Experimental and Numerical Investigations of Transition and Relaminarization of Boundary Layers

PASCAL BADER

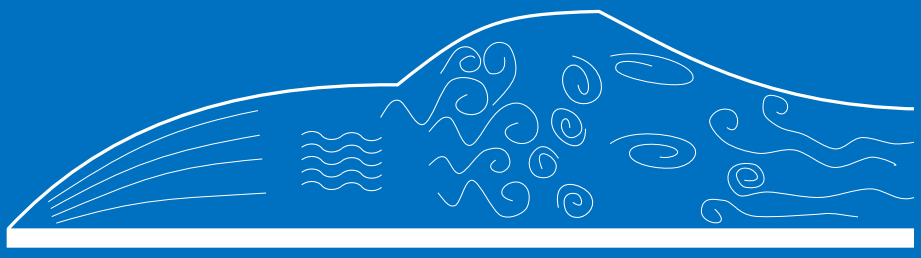

Doctoral Thesis
Graz, Austria. May 2017

Doctoral Thesis

Experimental and Numerical Investigations of Transition and Relaminarization of Boundary Layers

Dipl.-Ing. Pascal Bader, BSc

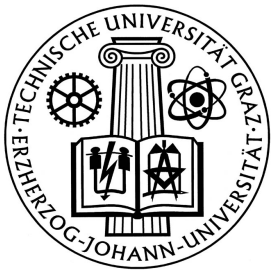

Doctoral School for Mechanical Engineering,
Graz University of Technology

This dissertation is submitted for the purpose of obtaining the academic degree *Doktor der technischen Wissenschaften (Dr. techn.)*

Supervisor: Ao. Univ.-Prof. Dipl.-Ing. Dr. techn. Wolfgang SANZ
Second advisor: Ao. Univ.-Prof. Dipl.-Ing. Dr. techn. Reinhard WILLINGER

Institute for Thermal Turbomachinery and Machine Dynamics
of Graz University of Technology, Austria

Graz, 2017

Abstract

Whenever a fluid flows along a surface with a different velocity than the velocity of the surface a boundary layer is formed. This small zone represents an area where the velocity difference is compensated. Within the boundary layer viscous effects are vital leading to losses due to shear or skin friction.

The boundary layer can have a laminar state, where the flow is regularly layered, or a turbulent state, where the flow is irregular, chaotic. The state depends on different parameters, like the length of the surface, the free stream velocity or the free stream turbulence. A laminar and a turbulent boundary layer also have highly different characteristics, influencing skin friction, heat transfer, the ability to follow curvatures or displacement of the surrounding flow. Thus it is important to know the state of the boundary layer.

At the beginning of a surface, the boundary layer is laminar, becoming turbulent at a certain position via a transitional zone. Under certain flow conditions, e.g. high acceleration a turbulent boundary layer can also undergo reverse-transition towards a laminar boundary layer. This process is called relaminarization.

The present work extensively investigates transition and relaminarization on simplified test cases both experimentally and numerically. Innovative measurement techniques focusing on non-invasive ones, are presented: The Laser interferometric vibrometer, which is commonly used for surface vibration measurements is successfully used in this work to measure transition. Also microphones which are embedded in the surface can be used as a non-invasive technique to measure the position of the transitional zone.

Regarding relaminarization, Laser-Doppler anemometry measurements are performed on three different relaminarization test cases. The results of these experiments reveal new details of emerging structures during relaminarization and give a further insight into the details of this process.

The numerical computations presented in this thesis show a comparison of different RANS based models – in particular the γ, γ-Re_θ and the k-k_l-ω model – and large eddy simulations with measurement results in order to show the capability of the different approaches in predicting transition and relaminarization. Although the RANS-based models show partly good results, LES is recommended to predict the change of the state of the boundary layer reliably and allow a better view on the processes during transition and relaminarization.

Furthermore a numerical studies of the effects of transition and relaminarization in turbomachines, in particular turbines, are presented in the work. The results point out that these processes can also occurring under real engine operating conditions. Thus it is recommended to consider the possible changes of the state of the boundary layer when e.g. computing efficiency or for the design of a blade.

Regarding relaminarization it is found, that it also occurs in turbomachines but it is problematic to potentially control the process in order to improve the efficiency. However, if the blade is properly designed regarding acceleration of the flow around it, the wall shear may be reduced, which lead to a decrease of the losses inside an aeroengine.

Summing up, the present work presents four main results with a focus on turbines:

- the successful testing of innovative measurement techniques for transition with a focus on non-invasive measurement systems which can be applied in narrow channels,
- a better understanding of the process of relaminarization due to acceleration,
- acquisition of a set of in-house test cases for benchmarking of CFD transition models,
- understanding of the effects of transition and relaminarization on flows through turbines.

Kurzfassung

Immer wenn ein Fluid entlang einer Wand strömt und sich die Strömungsgeschwindigkeit von der Geschwindigkeit der Wand unterscheidet, bildet sich eine Grenzschicht. Diese relativ dünne Zone gleicht eben diese Geschwindigkeitsdifferenz aus. Darüber hinaus sind in der Grenzschicht Zähigkeitseffekte dominant, was zu Reibverlusten führt.

Die Grenzschicht kann auf zwei Arten beschaffen sein: einerseits laminar, also stabil geschichtet, andererseits turbulent, was sich durch eine chaotische Strömung äußerst. Dieser Zustand hängt von mehreren Einflussfaktoren ab, beispielsweise von der Anlauflänge, der Freistromgeschwindigkeit oder der Freistromturbulenz. Hinsichtlich ihrer Eigenschaften unterscheiden sich diese beiden Grenzschichten in Bezug auf die Wandreibung, den Wärmeübergang, dem Folgevermögen von Umlenkungen oder die Verdrängungswirkung. Daher ist das Wissen über den Zustand der Grenzschicht an den unterschiedlichen Positionen essenziell.

Am Anfang einer Wand ist die Grenzschicht jedenfalls laminar und schlägt nach dem Durchlaufen einer Transitionszone in eine turbulente Grenzschicht um. Auch ist die Rückkehr vom turbulenten in den laminaren Zustand unter gewissen Voraussetzungen (z.B. hohe Beschleunigung) durchaus möglich. Dieser Vorgang wird als Relaminarisierung bezeichnet.

Die vorliegende Arbeit untersucht diese Transitions- und Relaminarisierungsvorgänge detailliert anhand vereinfachter Testfälle sowohl experimentell als auch numerisch. Darüber hinaus werden in dieser Arbeit innovative Messverfahren für die Grenzschichtmessung präsentiert, wobei der Fokus auf nicht-beeinflussenden Verfahren liegt. Dabei handelt es sich zum Einen um das Laser Interferometer, welches meistens für die Messung von Oberflächenvibrationen verwendet wird und das auch erfolgreich für die Detektion der Transition eingesetzt werden konnte, zum Anderen erweisen sich Mikrophone als effizientes Mittel zur experimentellen Bestimmung der Transitionsposition.

Um den Prozess der Relaminiarisierung experimentell zu untersuchen, werden Laser-Doppler-Anemometer-Messungen bei drei verschiedenen Testfällen durchgeführt. Aus diesen Messungen wurden neue Erkenntnisse und Details der Prozesse während der Relaminarisierung gewonnen.

Die durchgeführten numerischen Berechnungen zeigen die Ergebnisse verschiedener RANS-basierter Modelle, nämlich dem γ, γ-Re_θ und dem k-k_l-ω Modell sowie Large Eddy Simulationen im Vergleich zu den Messungen. Obwohl die RANS-Ergebnisse relativ gute Übereinstimmungen mit den Messergebnissen zeigen, ist für eine detaillierte Analyse LES sehr empfehlenswert.

Des Weiteren beschäftigt sich die vorliegende Arbeit mit den Effekten der Transition und Relaminarisierung in Turbomaschinen, im Speziellen in Turbinen. Es zeigt sich, dass diese Prozesse auch unter realen Bedingungen in Triebwerken geschehen. Daher empfiehlt es sich, diese Übergänge zwischen den Grenzschichtzuständen bei der Berechnung der Effizienz oder dem Designvorgang von Schaufeln zu beachten.

Betreffend der Relaminarisierung wird demonstriert, dass dieser Prozess auch in Turbinen vorkommt, wobei die Vorteile nur schwer kontrollierbar sind. Allerdings bestünde die

Möglichkeit – bei geeignetem Design der Schaufel bezüglich der Beschleunigung um das Profil – die Wandreibung zu reduzieren, was eine Verbesserung des Wirkungsgrades des Triebwerkes zur Folge hätte.

Zusammenfassend konnten in dieser Arbeit vier Hauptergebnisse mit Fokus auf Turbinen erzielt werden:

- der Test neuer Messverfahren für die Transitionsmessung, welche auch in kleinen Strömungskanälen, beispielsweise Turbinen, verwendet werden können,
- ein besseres Verständnis des Prozesses der Relaminarisierung aufgrund hoher Beschleunigungen,
- die Generierung neuer, institutseigener Transitions- und Relaminarisierungstestfälle, um CFD-Modelle erproben zu können,
- die Auswirkungen von Transition und Relaminarisierung auf Turbinenströmungen.

»*Jeder, der sich die Fähigkeit erhält, Schönes zu erkennen, wird nie alt.*«

– Franz Kafka, Austrian writer

Beschluss der Curricula-Kommission für Bachelor-, Master- und Diplomstudien vom 10.11.2008
Genehmigung des Senates am 1.12.2008

STATUTORY DECLARATION

I declare that I have authored this thesis independently, that I have not used other than the declared sources/resources, and that I have explicitly marked all material which has been quoted either literally or by content from the used sources.

EIDESSTATTLICHE ERKLÄRUNG

Ich erkläre an Eides statt, dass ich die vorliegende Arbeit selbstständig verfasst, andere als die angegebenen Quellen/Hilfsmittel nicht benutzt, und die den benutzten Quellen wörtlich und inhaltlich entnommenen Stellen als solche kenntlich gemacht habe.

Graz, am/at 15. Mai/May 2017

Dipl.-Ing. Pascal Bader, BSc

Danksagung

Auf meinem Weg hierher habe wurde ich von vielen Menschen inspiriert und unterstützt. Einigen dieser Personen will ich hier danken.

Allen voran gilt mein Dank meinem Betreuer Wolfgang Sanz, der mich während meines Studiums für thermische Turbomaschinen begeistert hat und mir schon während meiner Diplomarbeit hilfsbereit zur Seite stand. Seine Tür stand immer offen und er hat mich immer persönlich und fachlich unterstützt, auch wenn ich mir vorstellen kann, dass so manches Paper vermutlich anstrengend war.

Meinem Zweitgutachter, Reinhard Willinger will ich auch danken, dass er sich die Zeit genommen hat, sich mit dieser Arbeit auseinanderzusetzen.

Weiters möchte ich Jakob Woisetschläger für die tatkräftige Unterstützung während der Messkampagne danken sowie unserem Institutsvorstand Franz Heitmeir für die Möglichkeit der Dissertation.

Außerdem gilt mein Dank auch Günter Brenn und Walter Meile, die mir die Möglichkeit gegeben haben, meine Messungen in ihrem Windkanal durchzuführen sowie für die gemeinsame kritische Diskussion der Messergebnisse.

Dem Bundesministerium für Verkehr, Innovation und Technologie möchte ich auch besonders für die Finanzierung meines Projektes ReLam (Projekt 843999) im Rahmen des FTI-Förderprogramms TAKE OFF danken.

Neben den Professoren der Universität, möchte ich auch meiner Familie danken, allen voran meiner Mutter Gertrude und meinem Bruder Kevin. Beide haben mich stets unterstützt und ehrliches Interesse an meiner Tätigkeit am Institut gezeigt.

Ein ganz besonderer Dank geht an meine Verlobte Caroline, die mich während meiner ganzen Dissertationen unterstützt hat und mir stets meinen Rücken gestärkt hat, aber auch Verständnis gezeigt hat, falls es am Institut mal wieder länger gedauert hat; es ist sicher nicht einfach, mit einem Dissertanten zusammen zu sein. Ich danke auch ihren Eltern Karin und Werner für die Unterstützung während der letzten Jahre.

Natürlich möchte ich auch allen meinen Freunde, seien es alte aus der Heimat oder neu durch die Arbeit dazugewonnene besonders danken, die die letzten Jahre zu einem Erlebnis und so manche Konferenz besonders gemacht haben.

Graz, 15. May 2017 **Pascal Bader**

Für Caroline.

NOMENCLATURE

Greek symbols

Symbol	Description	Unit
α	Half of the angle between two LDA Laser beams	$^\circ$
δ	Boundary layer thickness, (see Eq. (3.2))	m
δ_1	Displacement thickness, (see Eq. (3.4))	m
δ_2	Momentum thickness, (see Eq. (3.4))	m
γ	Intermittency	$-$
κ	Von Kármán constant	$-$
λ	Laser beam wave length	m
Λ	Non-dimensional pressure gradient, (see Eq. (3.56))	$-$
ν	Kinematic viscosity	m^2/s
ρ/ρ_F	Fluid density	kg/m^3
ρ_P	Particle density	kg/m^3
σ	Standard deviation	$-$
σ	Suction rate	$-$
τ	Relaxation time, (see Eq. (4.30))	s
τ_w	Wall shear stress, (see Eq. (3.6))	N/mm^2
θ	Momentum thickness, (see Eq. (3.4))	m

Latin symbols

Symbol	Description	Unit
$\tilde{Re}_{\theta t}$	Local transition onset momentum-thickness Reynolds number	$-$
b	Plate width	m
B^+	Constant for the law-of-the-wall	$-$
c_f	Skin friction coefficient, (see Eq. (3.10))	$-$
c_f'	Local skin friction coefficient, (see Eq. (3.7))	$-$
C_τ	Shear stress correlation factor, (see Eq. (3.52))	$-$
d_L	Beam diameter inside the measurement volume, (see Eq. (4.21))	m
d_L	Laser beam diameter	m
$d_{x/y/z}$	Dimensions of the LDA measurement volume	m

Symbol	Description	Unit
F	Flatness (or Kurtosis)	–
F	Frequency of the Bragg cell inside the LIV	Hz
F	Rate of occurrence of streak breakup per unit span and time	Hz/m
F^+	Normalized burst rate, (see Eq. (3.49))	–
f	Frequency	Hz
f_b	LDA burst frequency	Hz
f_C	Cut-off frequency	Hz
F_D	Drag force	N
f_M	Frequency of the LIV measurement beam	Hz
f_S	Frequency of the LIV reference beam	Hz
f_{FL}	Focal length of the LDA lens	m
G	Gladstone-Dale constant	m^3/kg
$G(s)$	Transfer function for LDA seeding, (see Eq. (4.31))	–
H	Shape factor, (see Eq. (3.5))	–
h	Heat transfer coefficient	$W/(m^2K)$
K	(Launder) acceleration parameter, (see Eq. (3.51))	–
k	Turbulence kinetic energy, (see Eq. (3.40))	m^2/s^2
L	(Physical) integral length scale, (see Eq. (4.6))	m
l	Pseudo-integral scale	m
l_m	Mixing length	m
N	Number of samples	–
n	Independent samples	–
n	Refraction index, (see Eq. (4.15))	–
Nu_x	Nusselt number based on the streamwise position x, (see Eq. (3.13))	–
OPL	Optical path length, (see Eq. (4.14))	m
p	Static pressure	Pa
$\hat{p}_t$	Root mean square of the total pressure fluctuations, (see Eq. (4.3))	–
p_t	Total pressure	Pa
Pr_x	Prandtl number based on the streamwise position x	–
Q	Convective heat transfer, (see Eq. (4.11))	W
q/q_∞	Non-dimensional dynamic pressure, (see Eq. (4.1))	–
r	Seeding particle radius	m
Re	Reynolds number, (see Eq. (3.1))	–
Re_x	Reynolds number based on the streamwise position x	–
$Re_{\theta t}$	Transition onset momentum-thickness Reynolds number based on free stream conditions	–
S	Skewness	–
T	Temperature	K
Tu	Turbulence intensity, (see Eq. (4.2))	–
u'	Streamwise velocity fluctuation	m/s
$\hat{u}$	Root mean square of the streamwise velocity fluctuations	m/s
u^+	Non-dimensional streamwise velocity in wall coordinates, (see Eq. (3.38))	–
u_∞	Local free stream velocity	m/s

Symbol	Description	Unit
$u_{P,\perp}$	Seeding/Tracing particle velocity, (see Eq. (4.20))	m/s
v'	Lateral (plate normal) velocity fluctuation	m/s
$\hat{v}$	Root mean square of the lateral velocity fluctuations	m/s
w'	Spanwise (plate parallel) velocity fluctuation	m/s
x	Streamwise direction	m
Δx	Spacing between two fringes	m
y^+	Non-dimensional wall normal direction in wall coordinates	$-$
$z/\Delta z$	Geometrical path length / fluctuation	m

Abbreviation

Symbol	Abbreviation
ACF	Autocorrelation function
AF	Adjustable flap
AOM	Acousto-optic modulator
AP	Acceleration plate
CFD	Computational fluid dynamics
CTA	Constant temperature anemometry
DNS	Direct numerical simulation
FFT	Fast Fourier transformation
FLOPS	Floating point operations per second
FP	Flat plate
FPG	Favorable pressure gradient
FRAPP	Fast response aerodynamic pressure probe
HPC	High-performance computers
IATA	International Air Transport Association
ICAO	International Civil Aviation Organization
IR	Infrared thermography
ISW	Institute of Fluid Mechanics and Heat Transfer
ITTM	Institute for Thermal Turbomachinery and Machine Dynamics
LDA	Laser-Doppler anemometry
LES	Large eddy simulation
LIV	Laser interferometric velocimetry
LOS	Line of sight
OFI	Oil film interferometry
PC	Personal computers
PIV	Particle Image Velocimetry
PP	Parallel plate
RANS	Reynolds-averaged Navier-Stokes
RPK	Revenue passenger kilometers
SNR	Signal-to-noise ratio
SP	Stagnation plate
SRS	Scale resolving simulations
SSG	Semiconductor strain gauge

Symbol	Abbreviation
SSLCC	Shear sensitive liquid crystal coating
SST	Shear stress transport
T-S	Tollmien-Schlichting (waves)
TKE	Turbulence kinetic energy
TW	Trip wire
ZPG	Zero pressure gradient

TABLE OF CONTENTS

CHAPTER 1

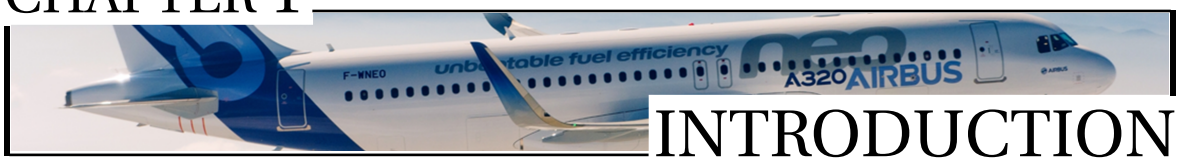

INTRODUCTION

As we battle the high price of fuel, cost efficiency will continue to be a top priority not only for airlines but for every partner in the value chain including airports and air navigation service providers.

Giovanni Bisignani
DIRECTOR GENERAL AND CHIEF EXECUTIVE OFFICER OF THE INTERNATIONAL AIR TRANSPORT ASSOCIATION (2002-2011)

1.1. Motivation

Although some scientists and politicians still doubt the existence of global warming, most people are aware of the risks combined with a rise of the global temperature. Carbon dioxide (CO_2) in the atmosphere plays a vital role regarding the greenhouse effect, leading to a rise of temperature. Although not all CO_2 emissions are caused by the human race, our contribution leads to an imbalance to the equilibrium of nature. In Fig. 1.1 the global carbon fluxes and reservoirs are shown as a simplified illustration. The natural cycle of carbon is indicated with black arrows and numbers, the man-made (anthropogenic) part in red. Clearly it can be observed from the illustration that the anthropogenic part of the carbon cycle is not negligible.

To reduce the influence of anthropogenic CO_2 emissions on the global balance four different approaches can lead to this goal:

- Reduce CO_2 emissions by reducing the usage of CO_2 emitting machines in general
- Improve the efficiency of machines, thus reducing their fuel consumption
- Enhance the capability of transferring CO_2 into O_2, thus enhancing the capability of the earth to withstand the higher CO_2 emissions
- Reduce the usage of fossil (CO_2-emitting) fuels by replacing them with alternative energy resources (e.g. H_2), thus reducing the emission of CO_2

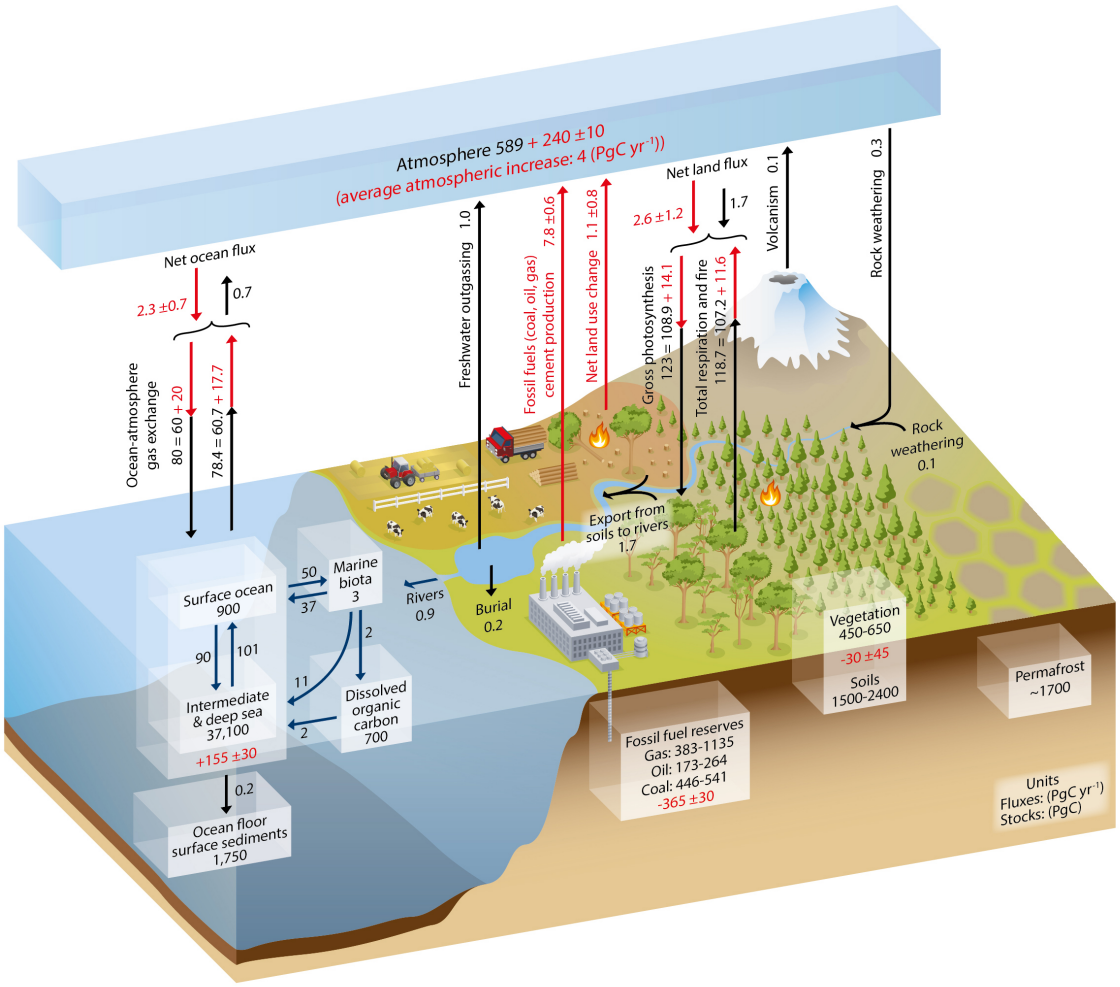

Figure 1.1: Simplified schematic illustration of the global carbon cycle, black numbers and arrows indicate fluxes and reservoirs before the industrial age (1750), red the anthropogenic fluxes as an average over a 2000-2009 time period, numbers in petagram (10^{15} g) [1]

For the future a combination of these four points will be inevitable.

Approximately a third of the global man-made CO_2 emissions can be accounted to mobility [2]. Thus when reducing the global CO_2 emissions, it is also necessary to reduce the emissions caused by mobility. Although according to the International Air Transport Association (IATA) air traffic accounts "only" for 2 percent of the global CO_2 emissions [3], it is also beneficial to reduce the emissions of aeroplanes. The reason is that the growing number of air passengers per year is immense. One reason for the strong rise of passengers is the progressive industrialization of Asia, South America and the Middle East. The growth in 2016 is illustrated in Fig. 1.2 showing the growth in revenue passenger kilometers[1] (RPK) presented by the International Civil Aviation Organization (ICAO) in Montréal on the 2nd of January 2017.

[1] RPK is a measure of sales volume of passenger traffic. [4]

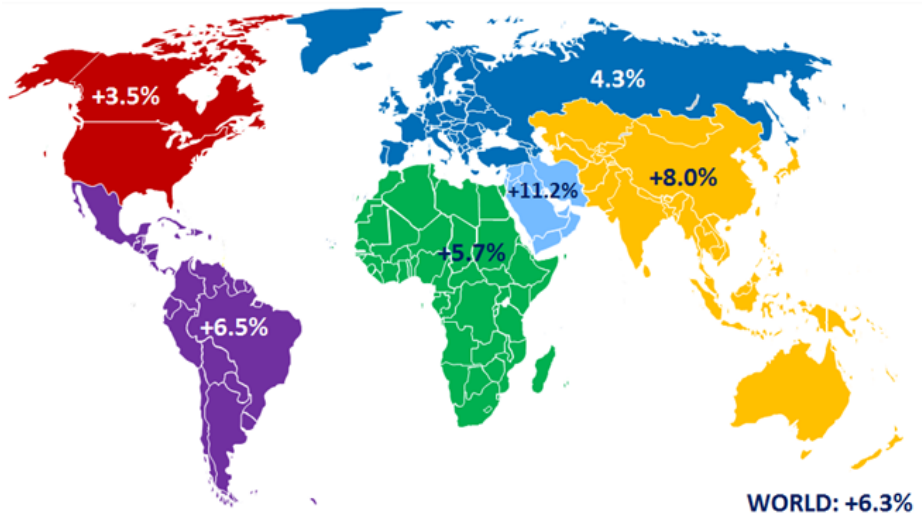

Figure 1.2: International growth of revenue passenger kilometers [5]

This figure clearly presents that the traditional industrial regions (first world) show a growth below the worlds average of 6.3 %, whereas the Middle East and Asia show an RPK growth of 11.2 % and 8.0 %, respectively. Although below the world's mean value, also Africa shows a higher growth as the so-called first world.

Therefore it is important to reduce emissions in air mobility. The four considerations above are already discussed broadly in public and are presented here in the following. However, the first above mentioned point is hardly accomplishable, since, as presented, the growth

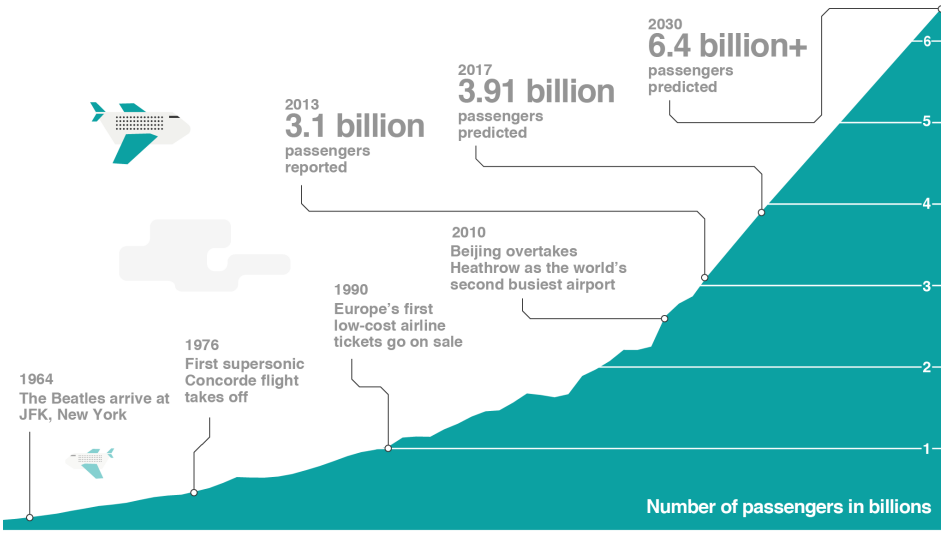

Figure 1.3: Number of passengers in billions showing reported and predicted data (data source: Marc Dierikx (1961-1969 and 1972); World Bank (1970-1971 and 1973-2012); IATA (2013 and 2017) and ICAO (2030)) [6]

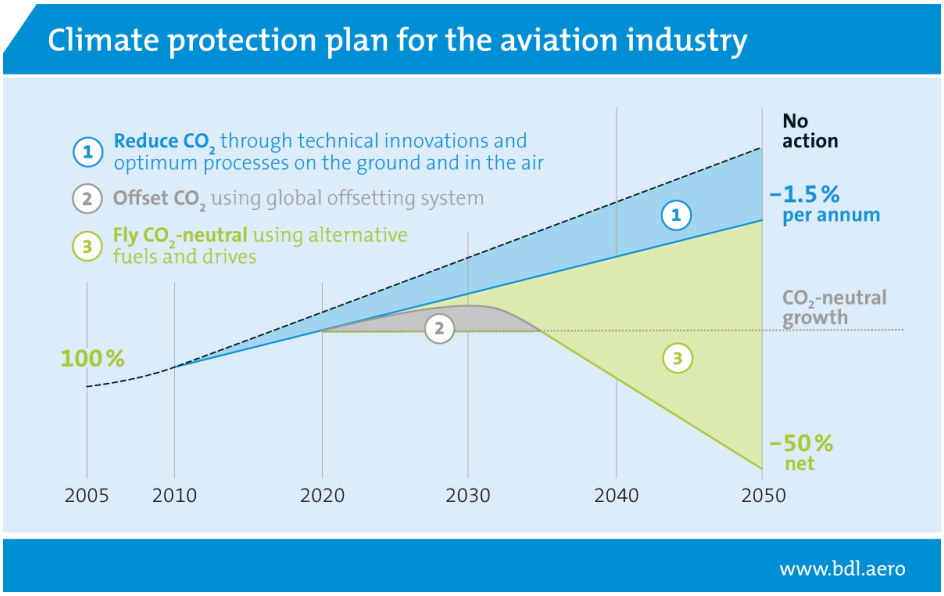

Figure 1.4: Climate protection plans presented by the Bundesverband der Deutschen Luftverkehrswirtschaft (BDL) [8]

of the number of passengers is still rising. In Fig. 1.3 the absolute number of passengers in billions is shown. It can be clearly seen that the number of passengers increases rapidly in the last years. In the figure also a forecast is given, showing 6.4+ billion passengers predicted in 2030.

Additionally one can observe from Fig. 1.3 that the air traffic is very resistant to crises. The first dent in the graph between 1976 and 1990 represents the second oil crisis in 1979. Between 1990 and 2010 four dents in the growth can be observed. Chronologically these four dents are related to the second Golf War (1990/91), the Asian crisis (1997/98), 09/11 and SARS (2002) an the financial crisis in 2007-09 [7]. All theses crises had global consequences on economical growth, however they represent only a relatively small decrease in the growth of the air traffic. Another interesting fact is, that the global RPK grows by 85 % since 09/11 [7].

So the first approach mentioned above is at the moment not manageable. The other three targets are reachable and are already under consideration.

In 2009 airlines, aircraft manufacturers, engine deliverers and airports worldwide agreed to a climate protection plan. This plan covers three main actions to reduce the CO_2 emissions of aeroplanes which agree to the latter three of the four points presented above. The first step is to reduce the emissions by improving the efficiency of aircraft and engine components. The second action is to offset CO_2 with the usage of a global offsetting system, e.g. planting of trees. The third step is the application of alternative fuels in order to fly CO_2 neutrally. These steps starting in 2010 are illustrated in Fig. 1.4. [8]

The graph shows how the CO_2 emissions would develop without and with these actions until 2050. One can observe that at the moment the first action already takes effect meaning an improvement of the efficiency of current aeroplanes and engines.

An improvement in efficiency is directly connected with a reduction of fuel consumption. Figure 1.5 presents some examples for the improvement of the fuel consumption per seat

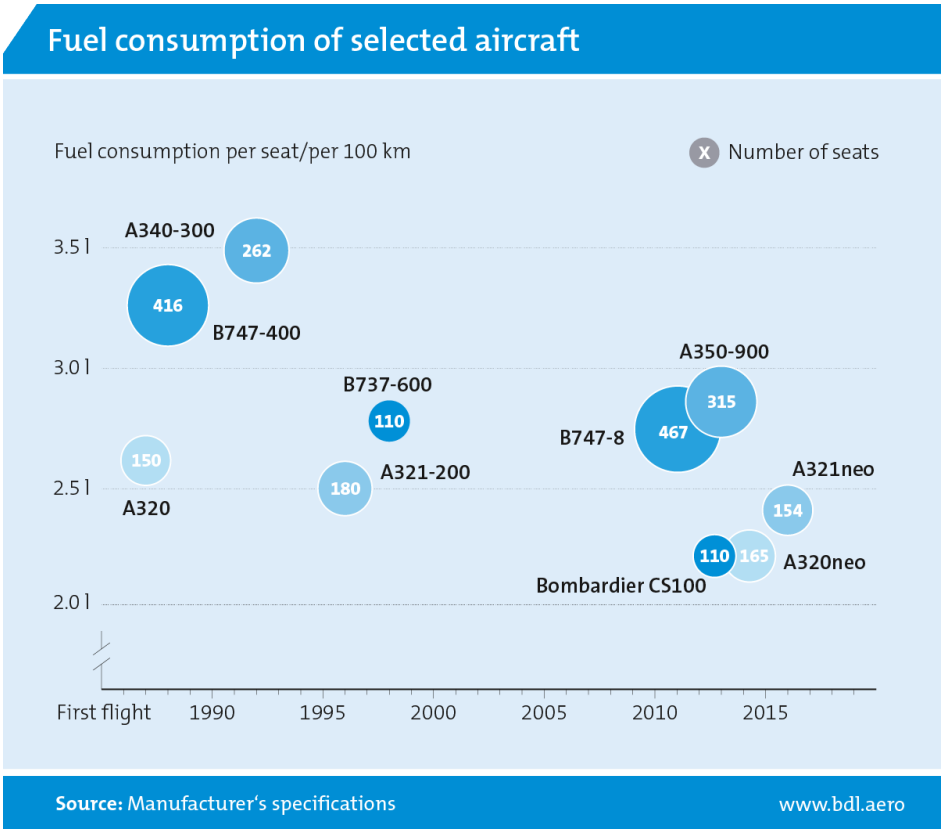

Figure 1.5: The decrease of fuel consumption of modern aircrafts over the years [8]

and 100 km over the last decades. The illustration clearly shows, how fuel consumption of different aircraft models decrease. The Airbus A320neo (shown at the chapter's heading) for example uses approximately 2.175 l/(seat 100 km), which represents a decrease of 16 % of fuel consumption compared to the first A320 (first flight in 1987).

The reduction of fuel consumption for the A320neo has been achieved by improving the efficiency of the engine, but also due to a reduction of the drag of the plane. Both of these approaches were achieved by a reduction of the frictional losses of the components.

The frictional losses of a surface depends on the state of the boundary layer, which develops when there is a velocity difference between a wall and the free stream. The boundary layer then evens this difference in velocity out, thus viscous effects and therefore shear losses are present within this rather small zone.

The boundary layer can have a laminar state, where the flow is equably layered, or a turbulent state where the flow is irregular, chaotic. The state of the boundary layer depends on different parameters, like the length of the surface, the free stream velocity or the free stream turbulence. A laminar and a turbulent boundary layer also have highly different characteristics, influencing skin friction, heat transfer, the ability to follow curvatures or displacement of the surrounding flow. Thus it is important to know the state of the boundary layer in order to potentially influence this state to reduce losses.

At the beginning of a surface, the boundary layer is laminar and becomes turbulent at a certain position via a transitional zone. Under certain flow conditions, e.g. high acceleration,

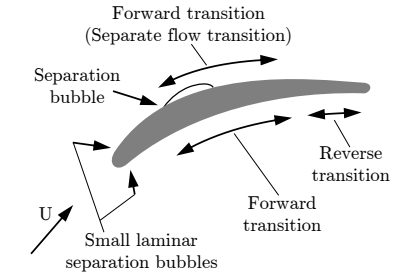

(a) Schematic drawing of a compressor blade showing the location of transition and reverse transition

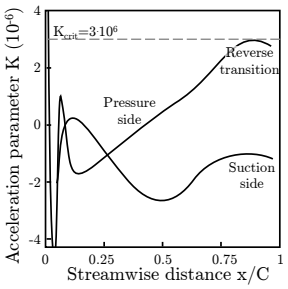

(b) Distribution of K along the pressure and suction side of a compressor blade

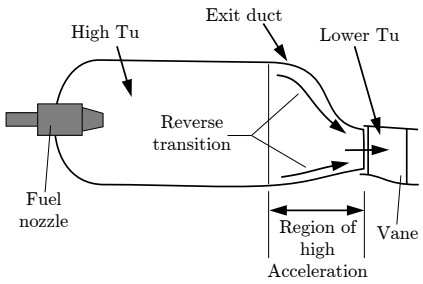

(c) Drawing of a combustion chamber showing reverse transition

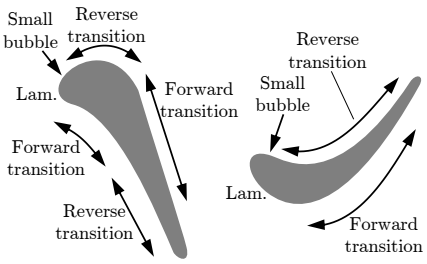

(d) Schematic drawing of a high pressure turbine stage showing the location of transition and reverse transition

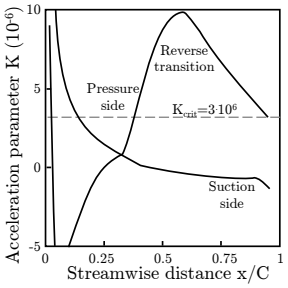

(e) Distribution of K along the pressure and suction side of a turbine blade

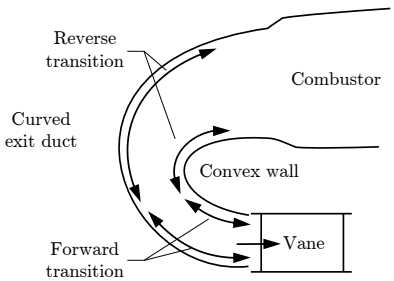

(f) Drawing of a curved duct showing the appearance of relaminarization

Figure 1.6: Schematic drawings showing transition and relaminarization in different turbomachinery components (renewed from [9])

a turbulent boundary layer can also undergo reverse transition towards a laminar boundary layer. This process is called relaminarization. It is important to know the position and length of the transitional and relaminarization zones in order to design components properly to rise the efficiency by a reduction of the shear losses or flow separations.

That transition and relaminarization happens within turbomachines, has already been shown by Mayle [9]. In Fig. 1.6 schematic illustrations of different engine components are given.

Figures 1.6a and b show a schematic drawing of the processes taking place along a compressor blade together with the acceleration parameter K (see Eq. (3.51)); Figs. 1.6d and e show the same for a turbine blade. It can be clearly observed, that transition as well as relaminarization can occur along a blade, influencing skin friction, heat transfer as well as boundary layer thickness which may change the downstream flow angle. All these effects also potentially influence the efficiency of the blades.

Additionally to the blades, also other parts of an engine can be affected by transition and relaminarization, for instance the exit duct of a combustion chamber (see Fig. 1.6c) or the outflow of an combustor with a U-Bend exit duct (see Fig. 1.6f). For these parts it is vitally important to know the state of the boundary layer, because of its high influence on the heat transfer, thus cooling of components.

(a) Photograph of the RedBull RB 10 formula one bolide with a split front wing [11]

(b) Schematic illustration of the influence of the separation behavior on the flow around the splitted wing (adopted from [12])

Figure 1.7: Photograph and working principle of a formula one front wing

Transition and relaminarization occur in various cases in a turbomachinery and also in many other flow cases in nature, however in the last decades the focus on this small part of the flow has been reduced, although many questions are still unanswered.

Rempfer [10] stated that the laminar-to-turbulent transition represents one of the most important processes which take place in and around many technical devices. Thus it is important to reliably predict this process, since it is not only important for turbomachines, but also for boats, ships, wings and also cars. Regarding the latter an application of transition-observations is presented in the following discussing a flow around the front wing of a formula one car (shown in Fig. 1.7a).

As mentioned above, a laminar and turbulent boundary layer shows also different separation behavior, meaning that a turbulent boundary layer can follow a turning of the flow around a convex contour better. Regarding the formula one car this is important for the front and rear wing. If the turning of the flow is too high, the boundary layer may separate. This is schematically shown in the top illustration of Fig. 1.7b. This separation happens earlier if the boundary layer has a laminar state. When splitting the front wing (lower illustration of Fig. 1.7b), the boundary layer is energized at the split of the wing, leading to an attached flow around the wing.

If it is possible to computationally predict the state of the boundary layer and also the separation position, this kind of wings can be numerically optimized in order to keep the losses low. The formula one is here a very good example, since computational fluid dynamics (CFD) codes are extensively used for the optimization of nearly every part. However, CFD is still just used for a preliminary selection of different designs. Experiments are then performed for the final selection of the design.

If with CFD a reliable prediction of the transition and relaminarization were be possible, we could use computers instead of expensive experiments for designing components and there-

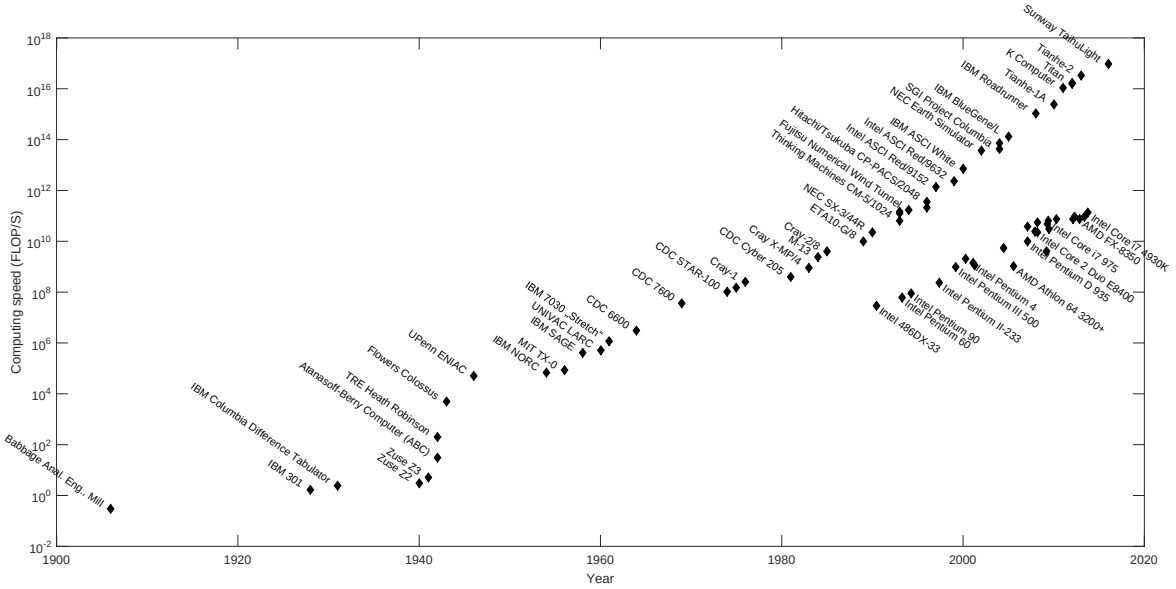

(a) Historical evolution of HPCs and PCs regarding FLOPS

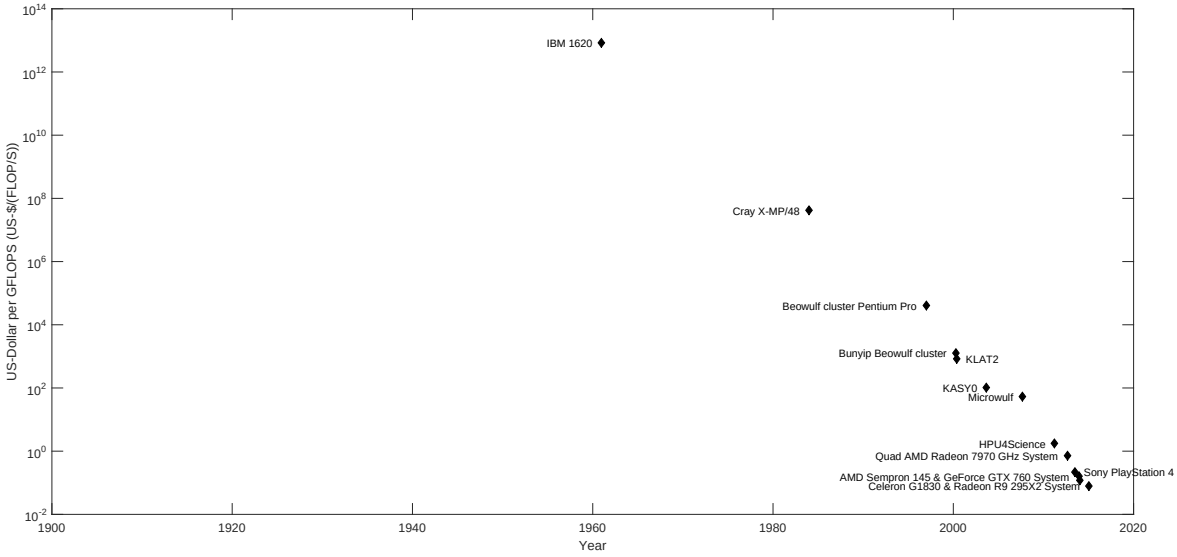

(b) Development of the costs of GFLOPS

Figure 1.8: Illustration of the development of computers (HPCs and PCs) over the years

fore save costs. Nevertheless CFD gets more and more important since modern computers can calculate faster at less costs.

In Fig. 1.8a the development of high-performance computers (HPC) and personal computers (PC) regarding floating point operations per second (FLOPS) over the years is shown. Clearly the fast increase regarding FLOPS can be seen (note that the ordinate is logarithmic): Whereas the IBM 301 (1928) could handle 1.7 FLOPS, the Tianhe-2 (2013) can manage about $3.39 \cdot 10^{16}$ FLOPS[2]. But not only the HPCs, also PCs show a rapid development which in-

[2] This means 1.7 FLOPS against 33,863,000,000,000,000 FLOPS

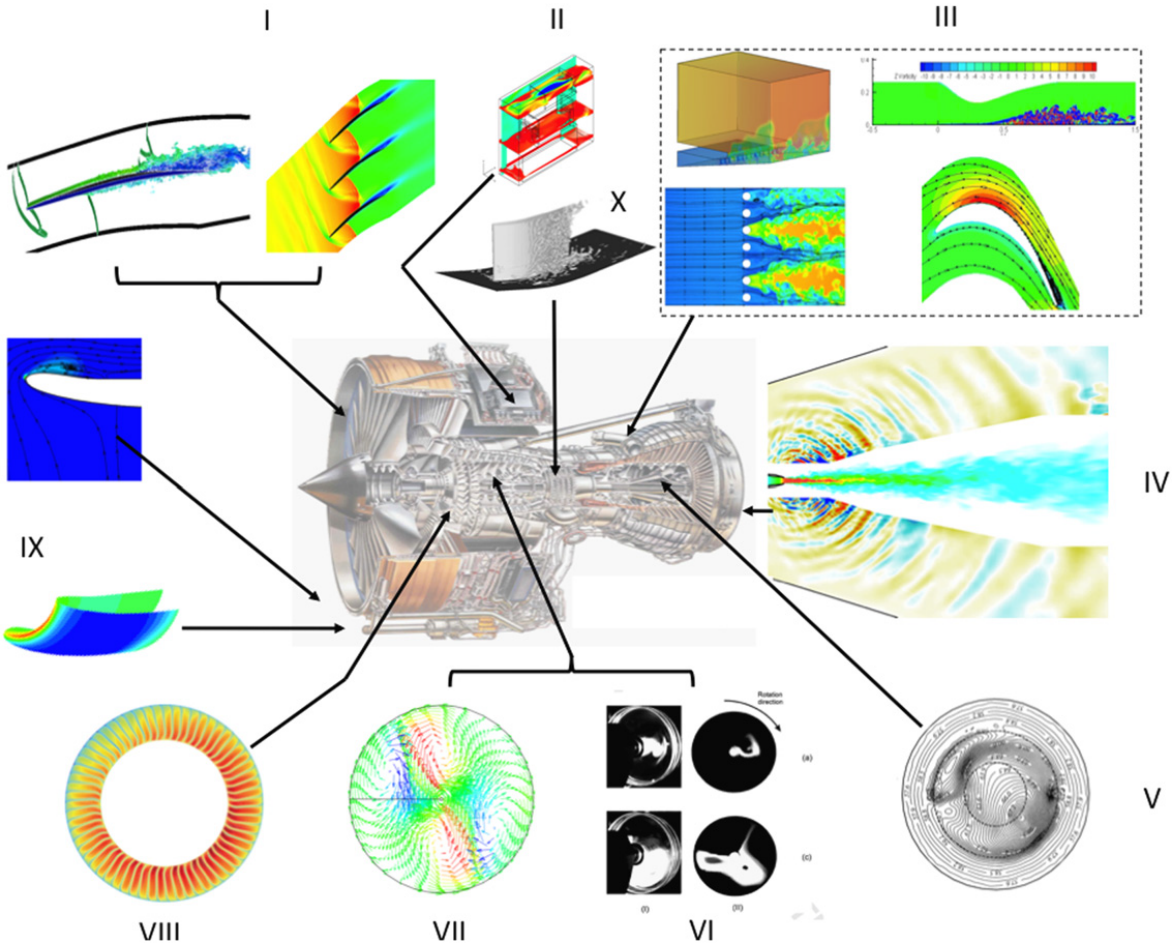

Figure 1.9: Illustration of a modern bypass engine with examples of the usage of CFD in aeroengines [13]

creases the importance of CFD since also small companies become able to compute highly sophisticated problems.

But beside the improvement in computational power also at the same time the costs decrease. In Fig. 1.8b the costs in US-Dollar per Giga FLOPS are given. Clearly one can observe that we are already far below 1 US-$/GFLOPS (ordinate is logarithmic).

The described rise in computational power with additionally lower costs made CFD already to a competitive tool for designing e.g. aeroengines. The calculations are used to analyze noise emissions, improve efficiency and performance and get a detailed insight into the flow. Many different parts of a modern aeroengine are already investigated using CFD. Figure 1.9 shows an overview of different parts which are numerically investigated and designed.

In the figure a section of a modern bypass aeroengine is given. Exemplary CFD results are plotted in the figure for different parts of the engine, including the compressor, combustor and turbine. The plots include date obtained by Reynolds-averaged Navier-Stokes (RANS) calculations and large eddy simulations (LES).

Although due to the high growth of computational power LES can be performed today

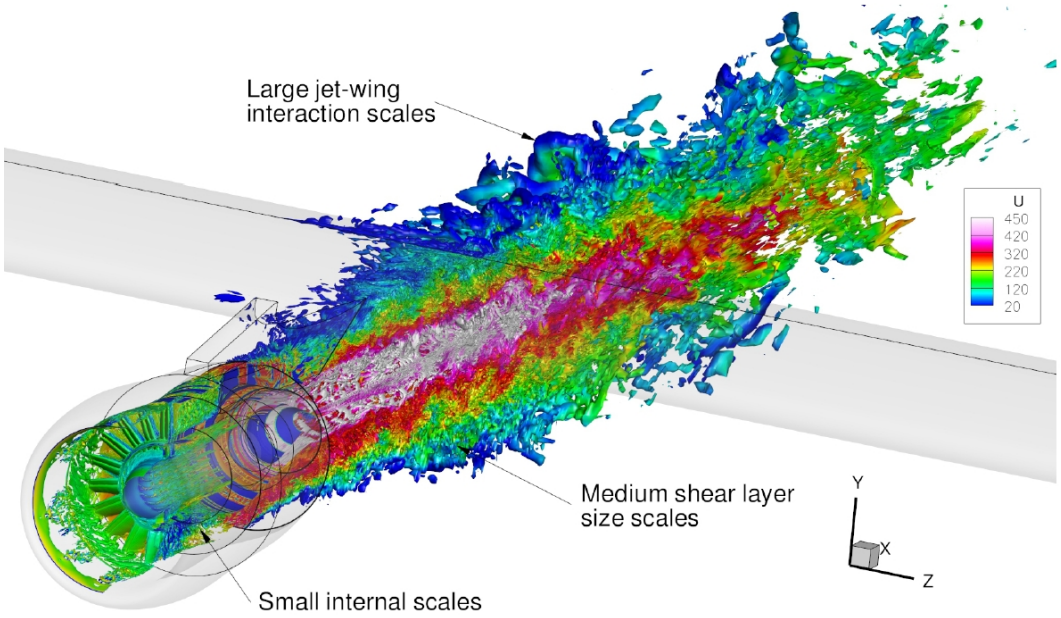

Figure 1.10: Illustration of an installed aeroengine with modeling of the inner geometry (RANS-NLES) [14]

on larger scales and in less time, RANS solutions, or a combination of the two (e.g. RANS-NLES) can be useful to get accurate results in less time and represents still the standard tool in the design process. In Fig. 1.10 the result of such a RANS-LES hybrid calculation is shown. The figure shows the computed flow of an installed aeroengine on a wing. Such large flow scales could be solved using LES, however this would take too much time and is not absolutely necessary.

So, although LES are already capable of simulating whole turbines or smaller parts with a very high accuracy, RANS approaches are still useful, since large eddy simulations still require long times to compute and evaluate the results. With RANS, computational results can be achieved rather quickly with a relatively good accuracy. However, RANS simulations can perform poorly regarding the simulation of strong curvatures, transition, relaminarization, separation and heat transfer [15].

The performance of RANS and LES in the prediction on transition and relaminarization is one of the main concerns of the present work, which will be described in more detail in the next section.

Another method to influence the skin friction in order to reduce losses is to apply so-called riblets on the surface. Riblets are micro-structures reducing drag and are inspired by the skin of a shark. In Fig. 1.11 the skin of a shark is shown together with technical riblets which may be applied to an aircraft wing. The working principle of these small structures is not yet fully understood, but the main impact on the flow is that the structures reduce the turbulence production within the wall-near area. Although the wall shear at the tip of a spike increases, the overall frictional losses can be reduced.

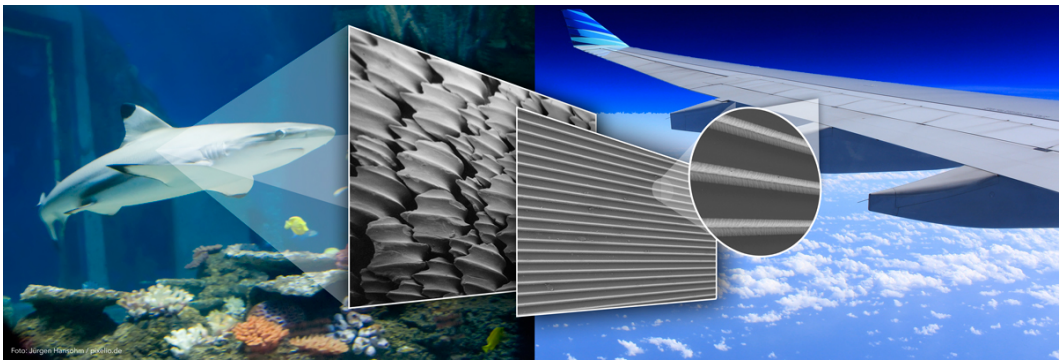

Figure 1.11: Illustration of the “riblets” at the skin of a shark and the technical use of riblets at the wing of an aircraft in order to reduce drag [16]

1.2. Objective and target

The just discussed need for an improvement of the efficiency of modern aeroplanes may lead to the question, if the state of the boundary layer can be potentially controlled by e.g. a proper design of turbomachinery parts in order to reduce the losses caused by wall friction. This optimization of the parts could be done numerically using accurate models, however existing transition model are not fully reliable at the moment.

The aim of the present thesis is first of all get a better understanding of the processes of transition from laminar to turbulent and relaminarization from turbulent to laminar. Secondly in-house experimental test cases should be acquired to test numerical models in order to point out their capabilities and drawbacks. In the following the main objectives of the present work are presented, thereafter the structure of the work is given:

One main object of this work is the implementation and application of innovative measurement techniques to measure transition in narrow channels should be tested within the scope of this work. A focus should be put on the non-invasive Laser interferometric vibrometer (LIV) which is commonly used to measure surface vibrations. However, if the surface reflecting the beam is rigid, the beam may detect density fluctuations along the line of sight, which then can be used to measure the position of transition.

Another object is to investigate the effects of riblets on the flow to test their potential in reducing skin friction of a surface.

A further target of the present work is to obtain a better understanding of the process of relaminarization due to high acceleration. Therefore a test bench should be built and different relaminarization cases should be analyzed. These experiments should lead to a deeper insight into the process.

Both, the transition and relaminarization measurement shall be used as in-house test cases for benchmarking of CFD turbulence/transition models. Also the capability of large eddy simulations in predicting these changes of the state of the boundary layer should be investigated.

Lastly, the influence of transition and relaminarization on turbine flows should be investigated. It should be discussed, if and how these processes may be influenced by a proper design of the blade in order to increase the efficiency of the blades.

In the following chapter (Chap. 2) an overview of turbulence research done in the last cen-

tury is given. In Chap. 3 the theory behind laminar and turbulent boundary layer is presented as well as a discussion of the current understanding of the transition and relaminarization processes.

In Chap. 4 the experimental and numerical approaches to reach the targets given above are presented. Thereafter experimental and numerical results for transition (Chap. 5) and relaminarization (Chap. 6) are given and discussed. Then a numerical discussion of the transition and relaminarization in turbomachines is presented in this work (Chap. 7).

The results and outcomes of the present work are summarized in Chap. 8 together with the main conclusions which can be drawn from the numerical and experimental works performed during this thesis. Additionally suggestions for future works are given within this last chapter.

Measurements of the influence of riblets attached to the surface are presented in App. A.

Although the main focus lies on turbines for aeroengines, most outcomes of this work can also be applied to other flows in industry, since laminar and turbulent boundary layers are formed at every surface with a velocity difference to the outer flow (plane wings, cars, wind turbines, heat exchangers, ...).

CHAPTER 2

TURBULENCE THEN AND NOW

> The problem is, and since the 1950s always have been, predicting the onset and length of transition, in other words, predicting the *birth*, *birth rate*, *growth*, and *propagation* of turbulent spots.
>
> Robert E. Mayle
> PROFESSOR

In this chapter an overview of fundamental works dealing with turbulence in free and wall-bounded flows done in the last century together with topic related experimental and numerical works is given. But before talking about specific publications, a short discussion of milestones on the path of understanding turbulence and transition is presented.

The first statistical concept of turbulence was formulated in the 19^{th} century by Joseph Boussinesq [17]. In 1877 [18] he proposed in his *concept of eddy viscosity* that Reynolds shear stresses are analogue to stresses triggered by viscosity.

One of the first experiments regarding turbulence was in 1883 when Osborne Reynolds [19] made his famous dye-streak studies which showed that a flow through a channel can be either laminar or turbulent depending on the dimensions of the channel, the velocity and the viscosity of the fluid. Figure 2.1 shows the original tank Reynolds used for his studies.

1895 Reynolds averaged the Navier-Stokes equations in order to describe unsteady fluctuation within a flow. He discovered apparent shear stresses, the so called Reynolds shear stresses which arise from the unsteady motion of the fluid. Along with this idea he used an energy method and discovered in this way the critical *Re* number for an unstable flow in a pipe. [21]

A next huge step forward made Ludwig Prandtl in 1904 [22] who described in his talk *"Über Flüssigkeitbewegung bei sehr kleiner Reibung"*[1] that the surrounding of a solid body consists of two zone: A small region close to the wall where friction effects play a dominant role (boundary layer) and a far-wall region where friction plays a minor role. This classification was not only new, but was also a major breakthrough combining the theoretical and experimental flow physics of these days. With the arising aviation this was a major step to calculate the drag of wings and flow separation. [23]

[1] On fluid movement at very low friction

Figure 2.1: The original tank from the experiment of Reynolds at the University of Manchester [20]

In 1914 Prandtl [24] showed experimentally that the boundary layer can be either laminar or turbulent, since the state of the boundary layer influenced the flow separation behavior of a sphere in a free flow. Prandtl's experiments were based on the speculation of Reynolds that instabilities within a laminar boundary layer lead to transition towards a turbulent boundary layer. [23]

Walter Tollmien (1929) [25] and Hermann Schlichting (1933) [26] managed to explain these instabilities within the boundary layer and experiments of H. L. Dryden [27] confirmed their deliberations [23]. In addition to these *Tollmien-Schlichting waves* they also determined a critical Reynolds number where these waves occur, so a critical value for the onset of transition from a laminar to a turbulent boundary layer.

In 1931 Tollmien [28, 29] published the first comprehensive report of the boundary layer theory. Prandtl made in 1935 [30] a considerable contribution to the understanding of the boundary layer theory. For the last eight decades many authors contributed to these publications, confirmed their findings and/or performed computations regarding instabilities which made the boundary layer theory to a research area with a huge scope. Thus it is close to impossible for a researcher to overlook the whole area, which also shows the importance of this field of research. [23]

The basic works presented above lead to a fundamental understanding of turbulence and processes within boundary layers. Over the years this knowledge base has been developed even further and the understanding of complex processes has been extended. In the following experimental contributions of different research groups are presented in chronological order. Although the main focus lies on research papers discussing relaminarization, also works of groups regarding transition are given. After a discussion of experimental works, important numerical publications are presented.

2.1. Experimental works

Although some experiments and studies regarding transition were done earlier, we want to start in 1954 with the pioneering set of measurements by Klebanoff [31] of a turbulent boundary layer in zero-pressure-gradient flows. He showed experimentally the distribution of the turbulent energy, its production, its dissipation, its spectra and also the viscous shear stress together with turbulent shear stresses in the boundary layer. Klebanoff also pointed out the importance of the area very close to the wall (laminar sublayer) and the buffer zone between this small area and the outer part. In this buffer layer, he stated that the highest turbulent production takes place and concluded that this zone plays a major role in the production of turbulent kinetic energy. He also confirmed the inadequacy of the concept of local isotropy of turbulence close to the wall.

Also in 1954 Francis Clauser [32] presented one of the first extensive studies of turbulent boundary layers in adverse pressure gradients. He performed many boundary-layer-tunnel experiments in order to analyze the influence of Reynolds number, pressure gradient and roughness on the development of skin friction along the investigated plate. Some years later Stratford [33] investigated flow separation of turbulent boundary layers. He developed a novel method to predict flow separation along a contour due to an adverse pressure gradient. He proposed a *two-layer theory* consisting of an outer layer which is driven by inertia following the deceleration of the flow and an inner layer, which has to fulfill the no-slip condition at the wall. Although his model predicts the position of separation too conservative, this model is still used today. His method of splitting the boundary layer into two parts has been picked up by Narasimha and Sreenivasan in 1973 [34] (see below).

Klebanoff et al. (1962) [35] presented a fundamental study regarding the three-dimensional nature of boundary-layer instabilities. They performed an experimental investigation to describe the nature of motion in the non-linear range of boundary layer instabilities leading to transition. Different approaches were investigated by Klebanoff et al. to describe the non-linear range of pre-transitional boundary layers and they concluded that three-dimensional disturbances dominate the behavior of collapsing of upstream wave motion. They also presented that the actual breakdown of these three-dimensional disturbances to turbulence involves the generation of hair-pin vortices. Their experiments were performed using a controlled vibrating ribbon, but their findings are also applicable to natural transition.

In 1964 Launder [36] presented laminarization by acceleration of a turbulent boundary layer. He showed a – as he calls it – *severe* acceleration, which leads to a complete transition to a fully laminar boundary layer. In Fig. 2.2 the development of the Launder acceleration parameter K (see Eq. (3.51)) and the shape factor H (see Eq. (3.5)) of his measurements are given. It can be clearly seen, that high acceleration is applied which leads to an increase of the shape factor towards $H \approx 2.4$, which represents a laminar state. Launder also showed in this experiment, that at decreasing acceleration, the boundary layer still developed as it was laminar. This is contradictory to the observations of Moretti and Kays (1965) [37] who showed a fast re-establishment of turbulent structures downstream of the relaminarization zone. However, they only reached partial relaminarization during the acceleration.

The basic structure of turbulent boundary layers has been analyzed by Kline et al. [38] (1967). They fundamentally investigated how the production inside the boundary layer happens in five different flow cases, from a strong adverse to a strong favorable pressure gradient. They found out, that fluid motions inside the laminar and turbulent boundary layer lead to *low-speed streaks* which then trigger different processes leading to a *burst of instabilities*.

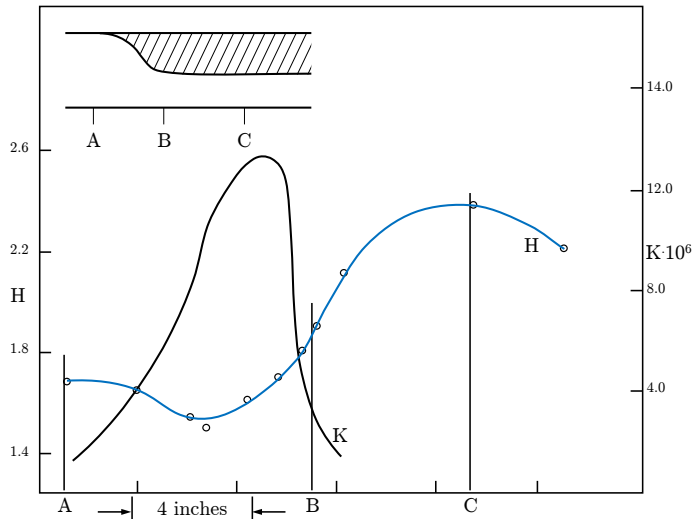

Figure 2.2: Shape factor and acceleration parameter along a plate under severe acceleration (renewed, original: [36])

Kline et al. state, that theses bursts occur in the buffer layer between the laminar sub-layer and the outer part of the boundary layer and are responsible for momentum, turbulence and vorticity transfer inside the boundary layer. Also these burst effects account for most of the turbulence production inside the boundary layer, therefore the rate of the bursts is a crucial factor of turbulence generation inside the boundary layer. Kline et al. displayed the burst rate as a function of the acceleration parameter K (see Eq. (3.51)). The result of this normalized burst rate is given in Fig. 2.3. It can be clearly observed that with high acceleration, the burst rate is close to zero, hence the production of turbulence vanishes leading to relaminarization of the boundary layer.

The observations of Launder (1964) and Moretti and Kays (1965) have motivated Launder

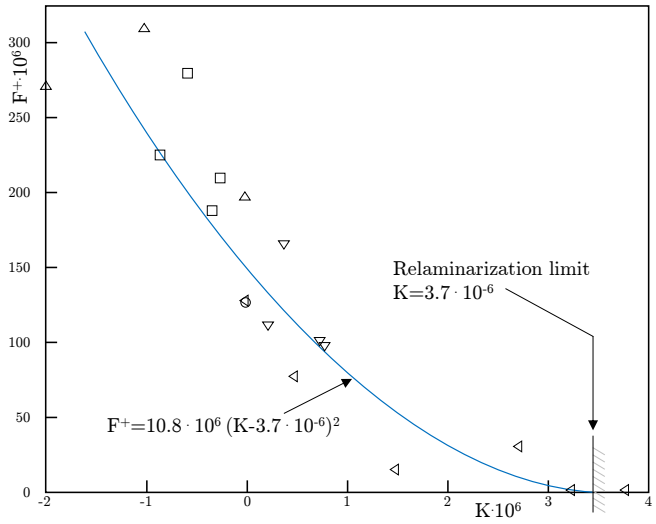

Figure 2.3: Normalized burst rate F^+ as a function of the acceleration parameter K [38]

and Jones (1969) [39] to divide the laminarization into two groups: (a) a *moderate acceleration* where the sublayer undergoes a change in structure, but the outer part of the boundary layer stays essentially turbulent and (b) a *severe acceleration* where a complete transition to a laminar boundary layer occurs if high acceleration is applied over a sufficient streamwise distance. They also proposed that there is not *a* single threshold value of K where relaminarization happens, but if K is higher than $2.0 \cdot 10^{-6}$ laminarization effects get more pronounced. Launder and Jones stated $K \approx 3 \cdot 10^{-6}$ as limit between moderate and severe acceleration.

In 1969 Badri Narayanan and Ramjee [40] presented hot-wire measurements of accelerated boundary layer flows. They tested different setups to come up with conditions for *reverse transition* – how they called relaminarization. They proposed that if the acceleration of a turbulent boundary layer exceeds a critical acceleration parameter $K = 3.0 \cdot 10^{-6}$ (definition see Eq. (3.51)) reverse transition can occur. Furthermore they presented that above this critical value the law-of-the-wall breaks down and the shape factor H (definition see Eq. (3.5)) shows a minimum.

1972 and 1973 two important papers regarding the understanding of relaminarization were published. The first one by Blackwelder and Kovasznay [41] in 1972 who performed hot-wire measurements on relaminarization cases. They investigated the role of large eddy structures on relaminarization. Blackwelder and Kovasznay presented that during the relaminarization process the inner viscous sublayer of the boundary layer becomes thicker. They argued this finding with the maximum of the streamwise fluctuations u' inside the boundary layer moving outwards. Also they found that less velocity defect can be observed in the outer layer, where the acceleration has nearly no effect on the turbulent energy. They also presented, that the acceleration decreases the total energy of the fluctuations together with the Reynolds shear stresses in respect to the local free stream velocity $U_\infty(x)$.

The second important paper has been published by Narasimha and Sreenivasan [34] in 1973. In this paper, *four stages of relaminarization* by acceleration have been described. This view on the relaminarization process has been used by other research groups over the years and will be also presented in section 3.4 (Page 52). In the third stage of this model, the boundary layer reaches a quasi-laminar state. In their paper they proposed a method to model this zone a priori and they reached a very good agreement with experimental data. In their work, they presented a short bubble-shaped reverse transitional zone which cannot be described with their quasi-laminar nor with a turbulent theory. They also found, that disturbances inside the boundary layer promote a fast re-transition into a turbulent boundary layer downstream of the relaminarization zone. Narasimha and Sreenivasan concluded, that the revision of the state of the boundary layer during the relaminarization process is caused by dominating pressure forces due to the acceleration over slow responding Reynolds shear stresses. Narasimha and Sreenivasan [34, 42] called this effect "frozen" Reynolds shear stresses.

Similar to the dye-streak studies of Reynolds Viswanath et al. [43] presented in 1978 a set of experiments to visualize relaminarization. They used two color dyes injected at two different positions, one into a fully turbulent and the second into laminarized flow (see Fig. 3.31). The experiment clearly showed that a flow can relaminarize under certain conditions. They showed relaminarization due to dissipative revision, revision is a stable stratified fluid (Richardson type), revision by domination and revision in coiled tubes.

A review of different modes of relaminarization including relaminarization by acceleration has been published by Narasimha and Sreenivasan in 1979 [42]. They also proposed some criteria which have to be fulfilled for relaminarization. They also stated that a relaminarization onset point cannot be defined for an accelerated boundary layer.

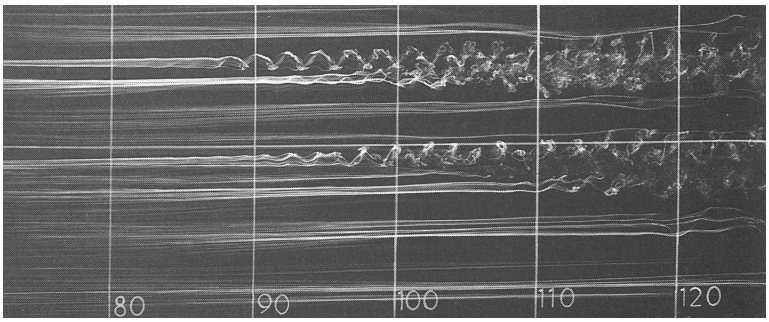

Figure 2.4: Instantaneous smoke wire visualization of low-speed streaks and their breakdown in a wall parallel plane (10 cm between two lines) [46]

Regarding transition, Abu-Ghannam and Shaw [44] presented in 1980 a comprehensive study discussing influencing parameters on natural transition. They investigated own and external experiments regarding the influence of turbulence intensity, pressure gradient and flow history. The reason for the work was that a lack of publications presenting measurements under high turbulence conditions and non-zero pressure gradient flow. Abu-Ghannam and Shaw also proposed a method to predict the boundary layer along a plate.

Sreenivasan (1982) [45] published a review about relaminarization by acceleration and compared the results of many different groups and also presented supplementary measurement results. In Tab. 2.1 experiments which he analyzed in his work are listed.

In 1987 Swearingen and Blackwelder [46] presented a study regarding streamwise vortices inside a boundary layer, about their growth and breakdown. They used Görtler vortices formed by a bending of a channel which are similar to streamwise vortices inside a boundary layer. In Fig. 2.4 a picture of smoke wire visualization is given, where low-speed streaks triggered by streamwise vortices are clearly visible. Also their breakdown into turbulence can be observed.

Up to now, most of the presented works here concentrated on results obtained under laboratory conditions making only little comment on the technical applicability and occurrence of transition and relaminarization. In 1991 Robert E. Mayle [9] presented how these effects play a role in gas turbine engines. He analyzed the influence of high turbulence intensities, momentum Reynolds number, acceleration and deceleration on transition and relaminarization, since theses parameters differ remarkably to many laboratory experiments. He also extensively reviewed processes of transition, e.g. turbulent spots.

Yip et al. (1993) [47] performed in-flight measurements with Preston tubes to predict transition and relaminarization. They found that during in-flight conditions a boundary layer along a wing experiences transition but also relaminarization along the chord. They were one of the first groups presenting theses effects not at laboratory conditions, but at real flight conditions.

1995 Volino and Simon [48] showed the effects of curvature and favorable pressure gradients on bypass transition. They showed how these effects influence the position and duration of the bypass transition and concluded that the curvature has a big influence on the boundary layer.

The question, if the design of a turbomachinery blade can be improved considering transition has been investigated by Narayan at al. in 1996 [49]. They performed an optimization

Table 2.1: Summary of relaminarization experiments up 1982 (adopted from [45])

Authors	Experimental code	Manner of producing acceleration	Initial Re_θ upstream of acceleration	Method of velocity measurement
Back and Seban	BS	Tunnel-wall liner	300	Pitot
Badri Narayanan and Ramjee	BR1	Tunnel-wall liner	1650	Pitot and hot-wire
	BR2		310	
	BR3		410	
	BR4	40° wedge (sink flow)	2050	
	BR5		1240	
	BR6		780	
	BR7	9° wedge (sink flow)	1700	
Badri Narayanan et al.	BRN	40° wedge	1850	Pitot
Blackwelder and Kovasznay	BK	Two-dimensional contraction	2500	Hot wire
Jones and Launder	JL	Wedge (sink flow)	391, 338, 475, 390, 340	Pitot
Launder	L1		320	Pitot and hot-wire
	L2		1000	
Launder and Stinchcombe	LS	Wedge (sink flow)	200	Pitot and hot-wire
Moretti and Kays	MK	Variable height tunnel	1400, 2800	–
Okamoto and Misu	OM1	Two dimensional contraction	470	Pitot
	OM2		580	
	OM3		640	
Patel and Head	PH1	Center body in a pipe	2100	Pitot
	PH2		5900	
Schruab and Kline	SK	Water channel with flexible wall	590	Hot-wire
Simpson and Shackleton	SS1	Two dim. contraction	1290	Hot-wire
	SS2		1650	
Simpson and Wallace	SW1	Flexible tunnel wall	1500	Hot-wire
	SW2		1700	
Sreenivasan	S1	(sink flow) 40° wedge	675	Pitot
	S2		940	
	S3		1250	

of a blade using a 2D panel code with the goal to reach a delayed transition due to an optimal acceleration distribution. As goal for the improvement they used the acceleration parameter K along the blade suction and pressure side.

In 1997 Mayle presented two publications worth mentioning. The first one of Mayle et al. [50] showed spectral analysis to find the *"turbulence that matters"* regarding heat transfer and transition processes inside turbomachines. They concluded that the effects of turbulence can only be explained when the full spectrum of the fluctuations is known. However, Mayle et al. concluded that this is almost impossible for complex flows as present in turbomachinery. They also admitted that their spectral distributions presented in their work may not apply, but so far there is nothing else to use.

The second paper of Mayle and Schulz (1997) [51] analyzed bypass transition and developed *laminar kinetic energy* equations to predict bypass transition within the k-ϵ model. They compared their prediction with experimental data and proposed a criterion for the onset of bypass transition.

Warnack and Fernholz [52] presented hot-wire measurements in 1998 and concluded that the relaminarization process is no catastrophic process, but caused by a gradual change of turbulent properties. They also point out, that the re-transition downstream of the relaminarization zone is triggered by remaining turbulent structures and concluded that this re-transition process can be compared to a bypass-transition. Ichimiya et al. [53] investigated the bursting phenomena during the re-transition process with a look on the statistical properties of hot-wire measurement signals.

1998 wavelet and frequency analysis of transition under high free-stream turbulence conditions have been presented by Volino [54]. Three years later he presented together with Hultgren [55] constant temperature anemometry (CTA) measurements of transition via a separation bubble with different turbulence levels. They showed with an analysis of fast Fourier transformation (FFT) spectra that the spectra downstream of the transition is essentially the same for different free-stream turbulence intensities.

Another relaminarization experiment has been performed by Bourassa and Thomas (2009) [56]. They used CTA probes and oil film interferometry (OFI) to measure the velocity fluctuations and skin friction, respectively. They used a four-quadrant method to analyze the effects leading to a decrease of Reynolds shear stress. Bourassa and Thomas showed how the mechanisms of *ejection* and *sweep*, which are responsible for the production of Reynolds shear stresses are effected by the acceleration of the boundary layer. They proposed that relaminarization occurs, if the near-wall autogeneration mechanisms of turbulence production and dissipation are interrupted.

In 2003 and 2006 Oyewola published experimental results of the influence of wall suction on a turbulent boundary layer in order to relaminarize it. First he and colleagues (2003) [57] made hot wire measurements and investigated also the influence of the Reynolds number on their setup. They found out that there is a critical suction rate Re_θ/σ, where σ is the suction rate, which is necessary to relaminarize a turbulent boundary layer with wall suction.

Later in 2006 Oyewola [58] used Laser Doppler anemometry (LDA) to measure the same setup and compared the data with the hot-wire results of 2003. Unfortunately the poor data rate of his LDA setup led to poor accuracy, however he showed promising results which need further investigation.

Also in 2006 Mukund et al. [59] published well-documented experiments about accelerated boundary layers. They made CTA measurements along a flat plate and a curved surface, both

with the same acceleration parameter K (definition see Eq. (3.51)). They found relaminarization in both cases, but for the convex surface the relaminarization was more pronounced.

Shahinfar and Fransson (2011) [60] showed with hot-wire experiments on normal transition the effects of free-stream turbulence characteristics on boundary layer transition length and onset position. They showed that not only the turbulence intensity is affecting the transition, but also the turbulent characteristics like the length scale. They presented how different characteristics of an incoming free-stream turbulence energy spectrum influence the growth of turbulent energy inside the boundary layer.

Mukund et al. (2012) [61] presented hot-film gauge time signals around a swept leading edge of a wing. They showed that the boundary layer experiences multiple transition and relaminarization cycles around the leading edge. Mukund et al. also see the computational modeling of these cycles very challenging. Like Yip et al. [47] they also showed in this work that relaminarization does not only occur under laboratory conditions in test benches.

In 2012 Widmann et al. [62] presented measurements of triggered Tollmien-Schlichting waves using phase-averaged particle image velocimetry (PIV). They successfully measured these harmonic instabilities leading to natural transition and proposed that these waves can be potentially controlled to shift the transition onset position downstream.

Lastly an extensive review of Robert E. Mayle of 2015 [21] should be mentioned. In his book he extensively reviews all important findings regarding pre-transitional, transitional and post-transitional flow. He presented old but also rather new information regarding all states of transition.

The here presented experimental works are of course far from complete, but summarize many important publications an their outcomes have been used in this thesis. Additionally it shows that research work in the field of boundary layer theory is a fascinating topic and there are still open questions.

2.2. Numerical works

Beside experimental works also numerical research has been done in the last decades. An advantage of numerical computations is, that effects which cannot be measured can may be modeled. In the following some important numerical publications are given briefly.

In 1987 Kim et al. [63] performed a direct numerical simulation (DNS) of a wall-bounded flow at low Reynolds numbers. They compared their results to experimental data and although the discrepancies were not negligible, the simulation pointed out problems of measurement techniques caused by a nearby wall.

Dietmar Rempfer [10] presented in 2003 a comprehensive review of numerical studies of transition. He discussed several models and ideas how transition to a turbulent boundary layer can be calculated and understood. As a concluding remark he stated, that *"there is still a sizeable chunk of 'gray area' on the map of our understanding of transition"* [10].

In 2002 and 2004 Brandt and Henningson [64] and Brandt et al. [65] investigated with DNS transition scenarios initiated by low and high-speed streaks close to the wall. They analyzed secondary instabilities triggered by these streaks and their influence on turbulence production.

Hœpfner er al. [66] presented in 2005 the influence of linear perturbations on boundary layer streamwise streaks on low streak amplitudes. They compared both sinuous and varicose symmetric modes on the energy growth rate for different frequencies.

In 2006 Robin B. Langtry [67] presented in his PhD thesis a correlation based two equation model, namely the γ-Re_θ (or γ-$\tilde{Re}_{\theta t}$) model. The empirical correlations used for the prediction of transition are based on the idea that after surpassing a critical boundary layer momentum thickness Reynolds number $Re_{\theta t}$ transition is triggered. But in this way it is a one-dimensional criterion which is only valid along the wall. Therefore Langtry introduced the transport variable $\tilde{Re}_{\theta t}$ as a transition criterion which is applicable in the whole flow field. For this reason the production term of the $\tilde{Re}_{\theta t}$ equation is designed in such a way, that $\tilde{Re}_{\theta t}$ is forced to adopt the value of the empirically prescribed transition onset Reynolds number $Re_{\theta t}$ in the free stream. With different empirical correlations the intermittency γ is influenced which is coupled with the turbulence production of the turbulence model. γ can vary between 0 (fully laminar) and 1 (fully turbulent). An exemplary result of a numerical calculation is given in Fig. 2.5 showing the intermittency around a blade. The coupling of the transition model with the underlying SST k-ω turbulence model is done by modifying the original production and dissipation term of the turbulence kinetic energy k. The model has also been presented by Menter et al.[2] in 2006 [68] but without all correlations. The full model was presented later (2009) by Langtry and Menter [69].

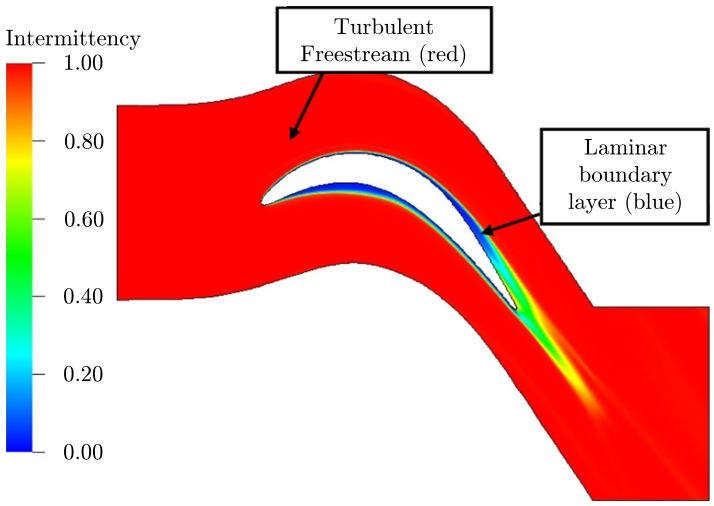

Figure 2.5: Contour plot of the intermittency γ calculated with the γ-Re_θ-model [67]

More or less at the same time (2009) Walters and Cokljat [70] presented a three-equation turbulence/transition model, the k-k_l-ω model. To predict low-frequency velocity fluctuations inside the pre-transitional boundary layer a third equation has been added to the k-ω framework. The idea of model terms is aimed to address the phenomenon of transition rather than be purely based on empirical methods.

Brandt and de Lange (2008) [71] presented a numerical investigation of streak interaction in wall bounded flows. They investigated numerically the differences between symmetric (high speed streak following low speed streak) and asymmetric (high and low speed streak slide along each other) streak interaction. The high shear produced in this way triggers irregular instabilities. The first scenario leads in later stages to hairpin or Λ vortices, whereas the latter leads to a bending of the streaks. Both lead to a formation of three dimensional shear layers.

[2] Florian R. Menter was the PhD supervisor of Langtry

In 2015 Menter et al. [72] presented a one-equation correlation based transition model using only the differential equation for the intermittency γ in addition to the k and ω equations of the SST turbulence model. This model is based on the local correlation-based transition modeling used by Langtry in 2006 but with an avoidance of the Re_θ equation by simplifying the onset criteria.

Lopez and Walters [73] also developed a new transition model, the k-k_l-v^2 model which is based on the k-k_l-ω model. They state that this new model has more capabilities and is more reliable than the k-k_l-ω model, especially for far-field computations.

CHAPTER 3

BOUNDARY LAYER THEORY

> Aber das Verständis des inneren Zusammenhangs wiegt unendlich viel mehr als die einfache Versicherung Anderer, und selbst mehr als der häufig wiederholte Versuch
>
> Galileo Galilei
> ITALIAN POLYMATH

Theoretical fluid mechanics investigations of flows at the beginning of the last century assumed inviscid flows of an ideal fluid, supposing that the fluid has no viscosity (potential theory). This is valid if viscous forces are negligible. This can be quantified with the well-known Reynolds number [19] which is defined as

$$Re = \frac{\rho u L}{\mu} = \frac{u L}{\nu} = \frac{\text{inertial forces}}{\text{viscous forces}} \tag{3.1}$$

where L is the characteristic length, u the velocity of the flow, ρ the density, μ the dynamic and ν the kinematic viscosity of the fluid, respectively.

If the Reynolds number is high, the assumption of an inviscid flow is accurate, since viscous forces play a minor role. In this case, only inertial forces e.g. pressure forces are taken into account. However, the theory fails when calculating the drag of bodies inside the flow. If a solid body moves with subsonic speed through an inviscid flow, the body does not experience any drag (D'Alembert's paradox, see most left illustration in Fig. 3.8) [23].

This is of course not acceptable and viscosity plays an even more important role, if the flow close to a wall is under investigation. Ludwig Prandtl [22] was the first who distinguished between a wall-near area, where friction and therefore viscous forces play a dominant role and a wall-far area, where inertial forces dominate over viscous ones. In his talk at the third International Congress of Mathematicians in Heidelberg, Germany, he established the boundary layer theory and presented his set of equations to calculate the boundary layer. The differences between the flow along a wall using the potential theory and the boundary layer approach are shown in Fig. 3.1.

The border between these wall-near and wall-far areas is not a clear line, but more an asymptotic change. However, in order to quantify the thickness of the boundary layer, the

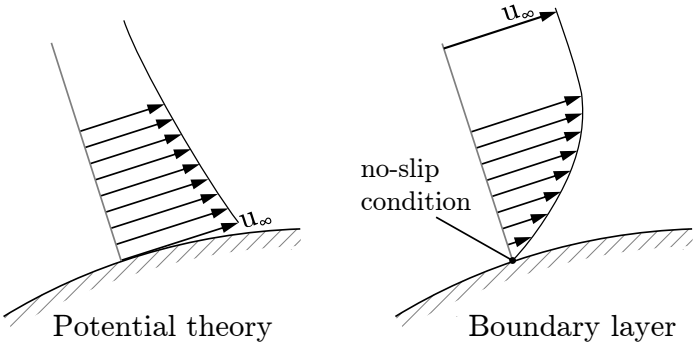

Figure 3.1: Illustration of the wall-near flow comparing the considerations of the potential theory (inviscid) and the boundary layer approach

99 % criteria is commonly used, which describes the coordinate normal to the wall $y(u)$, where 99 % of the free-stream velocity has been reached, as the edge of the boundary layer. The boundary layer thickness $\delta(x)$ can therefore be written as

$$\delta(x) = y\,(0.99 \cdot u_\infty) \tag{3.2}$$

where u_∞ represents the free stream velocity. This definition of the boundary layer thickness is also shown in Fig. 3.2. However, the boundary layer thickness is more or less just a mathematical number than an actual physical border.

In order to quantify physical effects due to the presence of a boundary layer, the displacement and momentum thickness can be calculated. The displacement thickness δ_1 quantifies the shift of streamlines in the outer flow due to the boundary layer. Thus, δ_1 represents the displacement effect by the boundary layer. For the outer flow the wall seems to be thickened by δ_1. The displacement thickness for an incompressible flow is calculated with

$$\delta_1 = \int_0^{\delta(x)} \left(1 - \frac{u(y)}{u_\infty}\right) \cdot dy \tag{3.3}$$

and the virtual shift is also shown in Fig. 3.3. The shaded zones have the same area and indicate the virtual shift of mass.

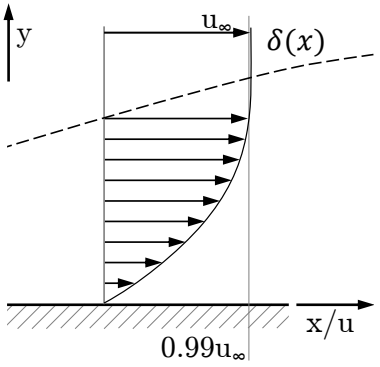

Figure 3.2: Illustration of the boundary layer thickness $\delta(x)$

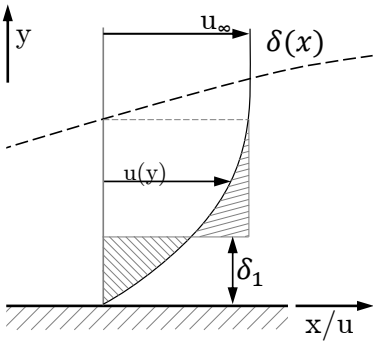

Figure 3.3: Illustration of the displacement thickness δ_1

The momentum thickness δ_2 describes the distance which the free stream fluid has to be shifted to reach the same momentum as the flow would have without boundary layer. In other words, the momentum thickness δ_2 describes the loss of momentum due to frictional forces inside the boundary layer [23]. δ_2 can be computed for an incompressible flow with

$$\delta_2 = \int_0^{\delta(x)} \frac{u(y)}{u_\infty} \cdot \left(1 - \frac{u(y)}{u_\infty}\right) \cdot dy \tag{3.4}$$

Note that the momentum thickness δ_2 is also often named as θ (e.g. in the transition model (Sec. 4.2.1))

The boundary layer, displacement and momentum thicknesses depend on some factors but mainly on the state of the boundary layer, whether it is laminar or turbulent. These states are described in more detail later in this chapter. Here in the following some general characteristic differences between the two states are given.

As said, the thickness parameters are influenced by the state of the boundary layer. In order to quantify the differences, the shape factor H can be calculated with

$$H = \frac{\delta_1}{\delta_2} \tag{3.5}$$

The shape factor is a measure of the velocity distribution within the boundary layer. This is shown in Fig. 3.4a and b, showing the shape of a laminar ($H \approx 2.6$) and a turbulent ($H \approx 1.4$) boundary layer.

Beside the different shape of a laminar and turbulent boundary layer, also other effects are caused by the different states, e.g. skin friction, heat transfer, and flow separation affinity, which are described in the following.

As can be seen in Fig. 3.4 the gradient at the wall is different between the two states. Since the shear, in particular the wall shear stress τ_w is calculated with this gradient du/dy according to

$$\tau_w = \mu \cdot \frac{du}{dy} \tag{3.6}$$

the wall shear of a turbulent boundary layer is higher compared to the laminar one. In Fig. 3.5 the differences between a laminar and turbulent boundary layer is shown. In the figure the local skin friction coefficient c_f', which is defined as

$$c_f' = \frac{\tau_w}{0.5\rho u_\infty^2} \tag{3.7}$$

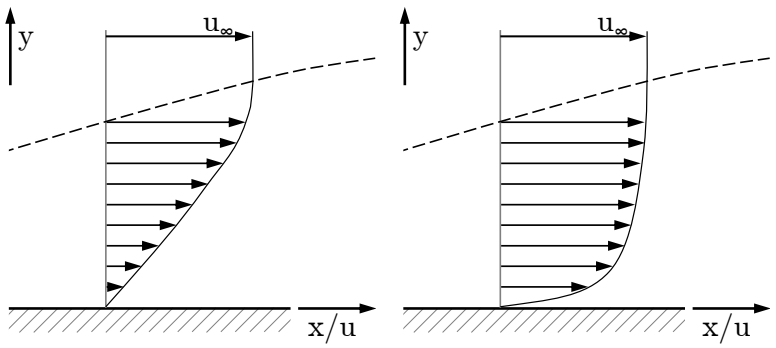

(a) laminar: $H \approx 2.6$ (b) turbulent: $H \approx 1.4$

Figure 3.4: Exemplary illustration of a laminar and turbulent boundary layer showing different shape factors

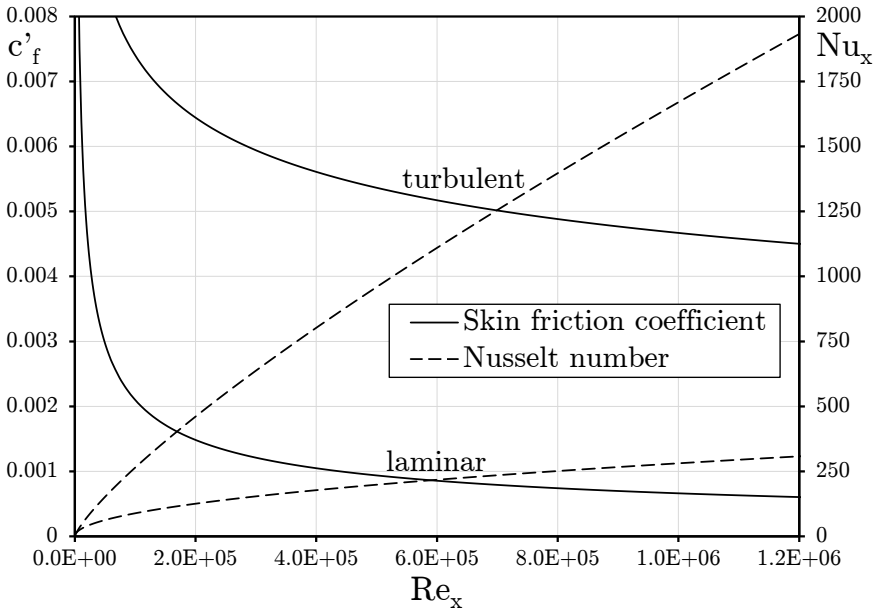

Figure 3.5: Comparison of the local skin friction coefficient c'_f and the local Nusselt number Nu_x of a laminar and a turbulent boundary layer against the plate Reynolds number Re_x

is plotted against the plate Reynolds number Re_x ($= u_\infty x/\nu$), where x represents the streamwise coordinate downstream of the start of the boundary layer. The two c'_f curves plotted in the figure show the exact Blasius solution (explained in Sec. 3.1) for the laminar boundary layer and an empirical distribution of Prandtl (1927) for the turbulent one:

$$c'_{f,lam} = 0.664 \cdot Re_x^{-1/2} \quad \text{Blasius solution [74]} \tag{3.8}$$

$$c'_{f,turb} = 0.0592 \cdot Re_x^{-1/5} \quad \text{Prandtl (1927) [75]} \tag{3.9}$$

It can be clearly seen, that the difference in skin friction due to the state of the boundary layer is not negligible and a turbulent boundary layer shows a far higher skin friction. This is

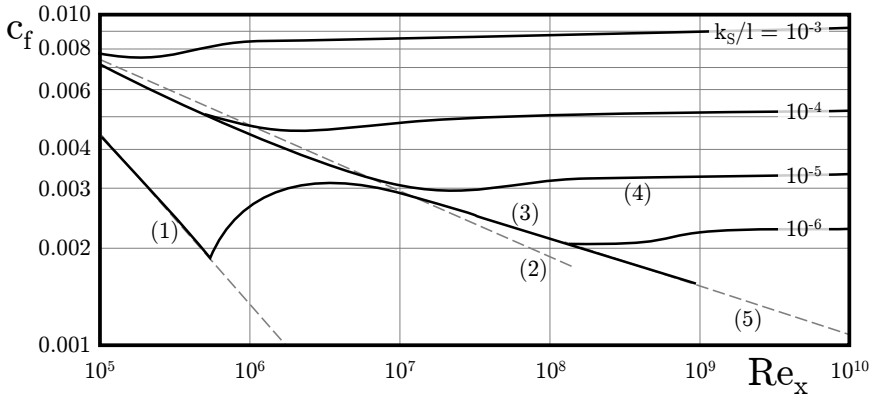

(1)	Blasius	$c_f = 1.3628\ Re^{-1/2}$	laminar
(2)	Prandtl	$c_f = 0.074\ Re^{-1/5}$	turbulent smooth
(3)	Prandtl-Schlichting	$c_f = 0.447\ \log(Re)^{-2.58}$	turbulent smooth
(4)	Prandtl-Schlichting	$c_f = [1.89+1.62\ \log(l/k_S)]^{-2.5}$	turbulent sand-rough
(5)	Schoenherr	extrapolated	turbulent smooth

Figure 3.6: Comparison of the skin friction coefficient c_f of a laminar and turbulent boundary layer against the plate Reynolds number Re_x (adopted from [75])

of special importance if the frictional losses (drag) of for instance an automobile or aeroplane should be reduced. So-called *laminar profiles/airfoils* consider these differences: The aim of the design of such an airfoil is to maintain the laminar boundary layer at the surface as long as possible to reduce drag.

Since in several publications the local skin friction coefficient c'_f is often mistaken for the skin friction coefficient c_f, it should be noted here, that c_f is defined with the drag force F_D for a plate with the length x and the width b according to

$$c_f = \frac{F_D}{0.5\rho u_\infty^2 b x} \tag{3.10}$$

Integration of Eqs. (3.8) and (3.9) leads for a fully laminar and a fully turbulent flow, respectively, to

$$c_{f,lam} = 1.328 \cdot Re_x^{-1/2} \tag{3.11}$$

$$c_{f,turb} = 0.074 \cdot Re_x^{-1/5} \tag{3.12}$$

Appendix B presents more information about the derivation and differences of c'_f an c_f.

The differences between the laminar and turbulent state regarding c_f are illustrated in Fig. 3.6 showing c_f against the plate Reynolds number Re_x. In the figure additionally to the skin friction coefficients presented in Eq. (3.11) and (3.12), other correlations are given, including the dependency of $c_{f,turb}$ on wall roughness.

Clearly the differences between a laminar and turbulent boundary layer can be seen. Additionally one can observe, that above a specific Reynolds number depending on the surface roughness, the skin friction coefficient stays constant.

In Tab. 3.1 the values of c_f' and c_f are given for a laminar and turbulent boundary layer, together with the values of δ, δ_1 and δ_2 of the two states.

Another distinguishing feature between a laminar and a turbulent boundary layer is the heat transfer. This is of interest for all kind of surfaces which should absorb or emit heat, e.g. heat exchangers or turbine blades. The difference in mean heat transfer can be described by the heat transfer coefficient α which can be calculated with the Nusselt number for a plate with the length x defined as

$$Nu_x = \frac{\alpha \cdot x}{\lambda_L} \tag{3.13}$$

where x represents the position downstream of the leading edge and λ_L represents the thermal conductivity of the fluid. Nu_x changes with the state of the boundary layer according to [77]

$$Nu_x = 0.332 \cdot {Re_x}^{0.5} \cdot Pr^{0.5} \quad \text{laminar} \tag{3.14}$$

$$Nu_x = 0.0296 \cdot {Re_x}^{0.8} \cdot Pr^{1/3} \quad \text{turbulent} \tag{3.15}$$

where Pr represents the Prandtl number. In Fig. 3.5 the differences between the two states are illustrated again over the plate Reynolds number Re_x, assuming a constant Prandtl number of $Pr = 0.71486$ (air at 20°C, 1 bar). It is observable that a turbulent boundary layer has a far higher Nusselt number and therefore heat transfer. Regarding turbomachines, this is of importance for the turbine blades just downstream of the combustion chamber. If the transition can be influenced, maybe less cooling of these blades is necessary.

Beside the just described differences of the boundary layer states on wall parameters, there are also differences regarding their ability to follow a convex contour, i.e. their sensitivity to pressure gradients regarding flow separation. Flow separation occurs when the gradient at the wall gets zero, according to

$$\frac{\partial u}{\partial y} = \tau_w = 0 \tag{3.16}$$

Figure 3.7 shows the stages of flow separation. The first profile (1) shows a normal profile. The second one (2) shows the beginning of flow separation. The wall shear of this profile is zero ($\partial u/\partial y = 0$) and the profile shows an inflexion point (IP). The third profile (3) shows a reverse flow inside the boundary layer due to flow separation.

Table 3.1: Overview of properties of a laminar and a turbulent boundary layer [76]

	laminar	turbulent
Boundary layer thickness δ	$5x \cdot Re_x^{-1/2}$	$0.37x \cdot Re_x^{-1/5}$
Displacement thickness δ_1	$1.72x \cdot Re_x^{-1/2}$	$0.046x \cdot Re_x^{-1/5}$
Momentum thickness δ_2	$0.665x \cdot Re_x^{-1/2}$	$0.036x \cdot Re_x^{-1/5}$
Local skin friction coefficient c_f'	$0.664 \cdot Re_x^{-1/2}$	$0.0592 \cdot Re_x^{-1/5}$
Skin friction coefficient c_f	$1.328 \cdot Re_x^{-1/2}$	$0.074 \cdot Re_x^{-1/5}$

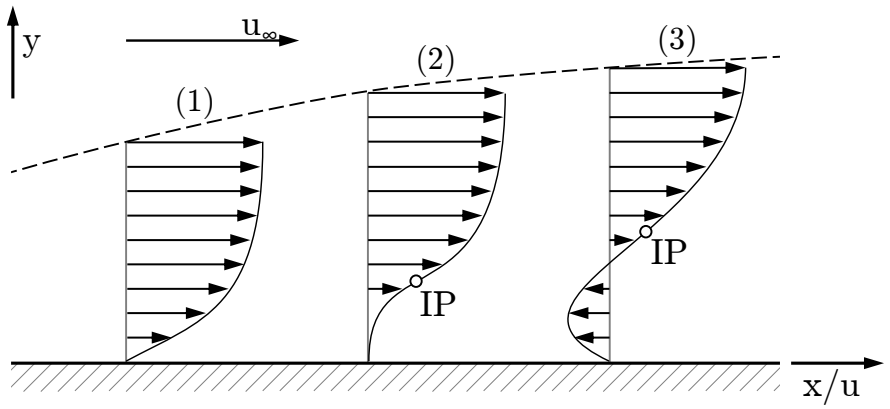

Figure 3.7: Illustration of flow separation in a boundary layer, (1) normal profile, (2) beginning separation ($\partial u/\partial y = 0$) and (3) reverse flow inside the boundary layer due to flow separation

So a criterion for separation of the boundary layer is the existence of an inflexion point along the velocity profile, or mathematically expressed [75]:

$$\left.\frac{\partial^2 u}{\partial y^2}\right|_{IP} = 0 \tag{3.17}$$

With this criterion we want to analyze two different cases: adverse ($\partial p/\partial x > 0$, deceleration) and favorable ($\partial p/\partial x < 0$, acceleration) pressure gradient.

The boundary layer equations at the wall ($u = v = 0$) is

$$\nu \left.\frac{\partial^2 u}{\partial y^2}\right|_{y=0} = \frac{1}{\rho}\frac{\partial p}{\partial x} \tag{3.18}$$

Additionally it can be noted, that at the border of the boundary layer ($y = \delta$)

$$\left.\frac{\partial^2 u}{\partial y^2}\right|_{y=\delta} < 0 \tag{3.19}$$

is valid, since the curvature at this position indicates a maximum. [75]

Therefore, if the criterion of Eq. (3.17) should be met, $\partial^2 u/\partial y^2$ at the wall must have a different leading sign compared to the position at the boundary layer edge to satisfy the IP condition of the profile to have a separation of the flow, thus

$$\left.\frac{\partial^2 u}{\partial y^2}\right|_{y=0} > 0 \tag{3.20}$$

According to Eq. (3.18) this can only be fulfilled for an adverse pressure gradient:

$$\frac{\partial p}{\partial x} > 0 \rightarrow \frac{\partial^2 u}{\partial y^2} > 0 \rightarrow \left.\frac{\partial^2 u}{\partial y^2}\right|_{IP} = 0 \quad \checkmark \tag{3.21}$$

For a flow exposed to a favorable pressure gradient the criterion cannot be fulfilled.

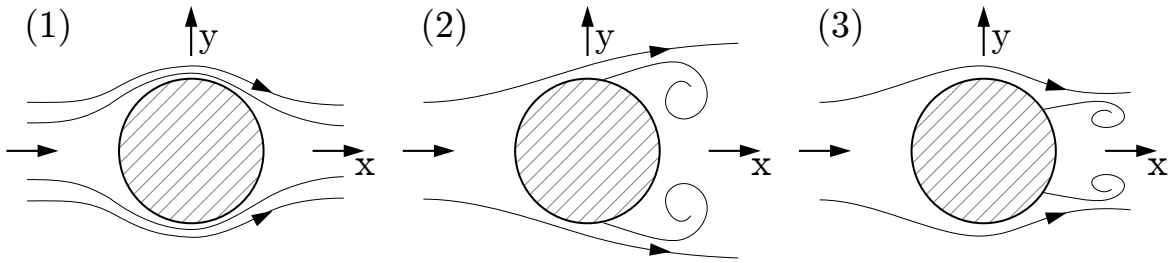

Figure 3.8: Illustration of the flow around a circular cylinder for an inviscid (1), a laminar (2) and a turbulent (3) flow showing the different separation behavior.

So flow separation can occur in the boundary layer when exposed to an adverse pressure gradient. The reason is that the kinetic energy of the boundary layer is lower compared to the free stream but is affected by the same pressure gradient. When the flow is decelerated the kinetic energy inside the boundary layer reduces until the streamwise velocity is zero, or even reverse flow occurs (flow separation). Inside a turbulent boundary layer flow more kinetic energy is transferred towards the wall due to the turbulent mixing inside the layer. This is the reason, why turbulent boundary layers can withstand much higher APGs compared to a laminar boundary layer. Thus a turbulent boundary layer can also follow higher flow turning. [75]

This is shown in Fig. 3.8 where the flow around a circular cylinder is given for an inviscid (1), a laminar (2) and a turbulent (3) flow. It can be clearly observed, that the separation point of the turbulent boundary layer is more downstream compared to the laminar one. Hence the turbulent layer follows the contour of the cylinder better and longer. The earlier separation of the laminar boundary layer causes a larger dead water area behind the cylinder

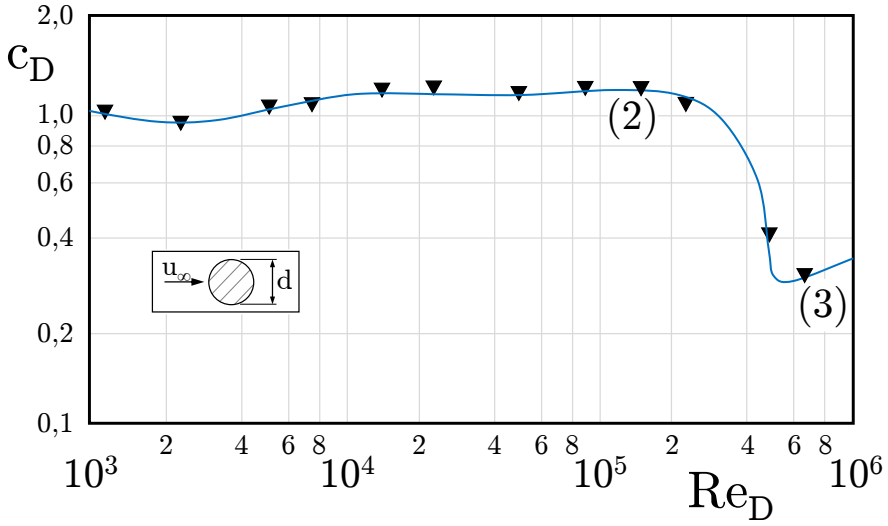

Figure 3.9: Dependence of the drag coefficient c_D of a circular cylinder from the Reynolds number Re_d, showing the difference between a laminar (2) (compare Fig. 3.8) and a turbulent (3) boundary layer (adopted from [75])

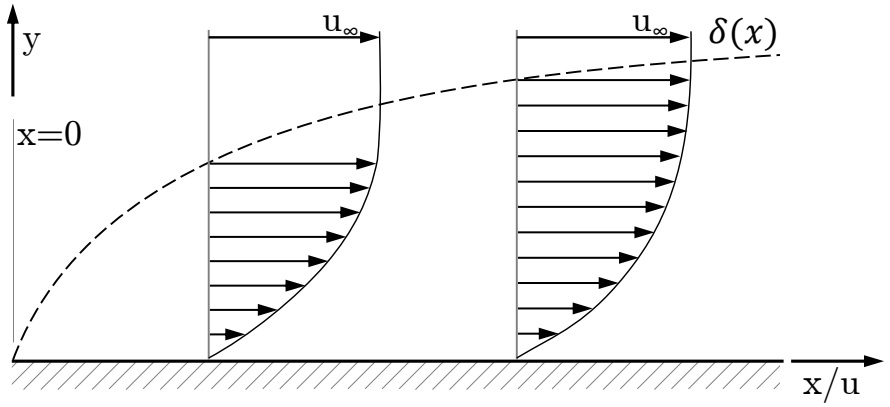

Figure 3.10: Illustration of the asymptotic growth of the boundary layer

which leads to a higher pressure drag of the cylinder. This is shown in Fig. 3.9 where the drag coefficient $c_D = F_D/(0.5\rho u_\infty^2)$ is given against the Reynolds number $Re_d = u_\infty d/\nu$. The effects of the boundary layer state are clearly visible: The drag coefficient drops remarkably at approximately $Re_d \approx 3 \cdot 10^5$ indicating the change of the boundary layer state to turbulent.

Up to now, main differences between the states of the boundary layer have been discussed. In the following (Secs. 3.1 and 3.2) the laminar and turbulent boundary layers are described in more detail. It is noted here that these sections mainly refer to the works of Meile [75] and Brenn and Meile [78].

Later the process of transition (Sec. 3.3) from laminar to turbulent and the process of relaminarization (Sec. 3.4) from turbulent to laminar are explained. In those sections the focus lies on transition and relaminarization by fluid mechanic effects rather than electrical, magnetical or buoyancy forces. Out of focus are problems of magnetohydrodynamics, plasma flows and flows driven by density convection effects.

3.1. Laminar Boundary Layer

At the beginning of a wall, the boundary layer starts to develop and gets asymptotically thicker. This is illustrated exemplary in Fig. 3.10. At this starting area the boundary layer is laminar.

If the problem is solved two dimensionally, and if it is generally assumed that the boundary layer thickness δ is far lower than the plate length L, so that

$$\frac{\delta}{L} = \epsilon << 1 \tag{3.22}$$

is valid. An order estimation of the continuity and Navier-Stokes equations leads then to following conclusions for a laminar boundary layer:

- The lateral velocity is much lower compared to the streamwise velocity
- The pressure gradient in y-direction is very small to fulfill the set of equations and is therefore negligible

For more details about the derivation please see Brenn and Meile [78].

This order estimation has been done by Prandtl [22] leading to *Prandtl's boundary layer equations*

$$\frac{\partial u}{\partial x} + \frac{\partial v}{\partial y} = 0 \tag{3.23}$$

$$\frac{\partial u}{\partial t} + u\frac{\partial u}{\partial x} + v\frac{\partial u}{\partial y} = -\frac{1}{\rho}\frac{\partial p}{\partial x} + \nu\frac{\partial^2 u}{\partial y^2} \tag{3.24}$$

$$\frac{\partial p}{\partial y} = 0 \tag{3.25}$$

It can be seen (Eq. (3.25)) that the pressure gradient in y-direction is zero. This leads to the condition that the pressure through the boundary layer and at the wall is specified by the outer free stream. This is of special meaning for accelerated and decelerated flows with a streamwise pressure gradient (see discussion about separation above).

The boundary conditions to solve the set of differential equations above are

- at the wall $y = 0$: $u = v = 0$
- in the free flow $y \to \infty$: $u = u_\infty$

As mentioned at the beginning of this chapter, for $y \to \infty$ the boundary layer thickness δ (see Eq. (3.2)) is used instead. With these boundary conditions, Blasius (1908) [74] solved Eqs. (3.23) to (3.25) using a similarity approach. With his exact solution the boundary layer thickness for a laminar boundary layer can be calculated with

$$\delta(x) = \frac{5 \cdot x}{\sqrt{Re_x}} \tag{3.26}$$

and also the skin friction coefficient c_f along the plate can be computed (see Eq. (3.8)).

3.2. Turbulent Boundary Layer

Similar to the laminar boundary layer, also for the turbulent boundary layer a set of equations can be formulated using order estimations. This leads for the turbulent boundary layer to the *Reynolds equations*. For these equations it is assumed that the turbulent fluctuation components are equal in all three dimensions (isotropic turbulence). The equations can be written as

$$\frac{\partial \overline{u}}{\partial x} + \frac{\partial \overline{v}}{\partial y} = 0 \tag{3.27}$$

$$\frac{\partial \overline{u}}{\partial t} + \overline{u}\frac{\partial \overline{u}}{\partial x} + \overline{v}\frac{\partial \overline{u}}{\partial y} = -\frac{1}{\rho}\frac{\partial \overline{p}}{\partial x} + \nu\frac{\partial^2 \overline{u}}{\partial y^2} - \frac{\partial \overline{u'v'}}{\partial y} \tag{3.28}$$

$$\frac{1}{\rho}\frac{\partial \overline{p}}{\partial y} + \frac{\partial \overline{v'^2}}{\partial y} = 0 \tag{3.29}$$

where the bar represents time-averaged values.

Integration of Eq. (3.29) leads to

$$\overline{p} + \rho\overline{v'^2} = const = p_\infty \tag{3.30}$$

From this equation it can be concluded that the pressure inside the boundary layer varies over the thickness δ, but the pressure at the wall is the pressure of the free stream.

The term $-\partial\overline{u'v'}/\partial y$ of Eq. (3.28) represents the a shear stress induced by the turbulence inside the flow, where $\tau_{xy} = -\rho\overline{u'v'}$ represents the so-called *Reynolds shear stress*.

A possible method to solve the boundary layer equations for a turbulent boundary layer is the integral method, the *von Kármán momentum integral equation*. This is an approximate solution where the equations are integrated from the wall to a position outside the boundary layer. This leads to a solution describing how the boundary layer evolves in time average. The von Kármán momentum integral equation is

$$\frac{d\delta_2}{dx} + \frac{1}{u_\infty}\frac{du_\infty}{dx}(2\delta_2 + \delta_1) = \frac{\tau_w}{\rho u_\infty^2} \tag{3.31}$$

Similar to the Blasius solution a similarity of the velocity profiles is assumed as

$$\frac{u}{u_\infty} = f\left(\frac{y}{\delta}\right) \tag{3.32}$$

Using a polynomial ansatz we can derive for a turbulent boundary layer

$$\frac{u}{u_\infty} = \left(\frac{y}{\delta}\right)^{1/n} \tag{3.33}$$

where the exponent n depends on the Reynolds number Re. For most of the cases $n = 7$ is used which does not represent a value based on physics but a best-fit curve. Additionally an equation for the wall shear stress can be received empirically:

$$\frac{\tau_w}{\rho u_\infty^2} = 0.0225\left(\frac{\nu}{u_\infty \delta}\right)^{1/4} \tag{3.34}$$

Using this correlation together with the von Kármán momentum integral equation, the boundary layer thickness δ can be derived accordingly to

$$\delta = 0.37 x Re_x^{-1/5} \tag{3.35}$$

Inserting Eq. (3.35) into Eq. (3.34) and using the definition of c'_f (see Eq. (3.7)), the equation for $c'_{f,turb}$ according to Prandtl (see Eq. (3.9)) can be derived.

In the following the layering of a turbulent boundary layer is described. Parts of the derivations have been taken from [79]. The total shear stress inside the turbulent boundary layer is assumed constant and is written as

$$\begin{aligned} \tau =& \mu\frac{d\overline{u}}{dy} - \rho\overline{u'v'} = \tau_w \\ \tau_l =& \mu\frac{d\overline{u}}{dy} \qquad \text{viscous shear stress} \\ \tau_t =& -\rho\overline{u'v'} \quad \text{turbulent shear stress} \end{aligned} \tag{3.36}$$

The mean velocity $\overline{u}$ is only dependent on y and τ_w, ρ and μ. Introducing the friction velocity $u_\tau = \sqrt{\tau_w/\rho}$ leads to

$$\frac{\overline{u}}{u_\tau} = f\left(\frac{y u_\tau}{\nu}\right) \tag{3.37}$$

Additionally the dimensionless wall coordinates $u^+ = \overline{u}/u_\tau$ and $y^+ = yu_\tau/\nu$ are introduced leading to

$$u^+ = f(y^+) \tag{3.38}$$

The relation between y^+ and u^+ for different distances from the wall can be written (without proof) as follows, where the values of the borders are approximate values: For an area close to the wall, the so-called viscous sublayer ($y^+ \leq 5$, $\tau_l >> \tau_t$), $y^+ = u^+$ must be true. If y^+ is larger ($5 \leq y^+ \leq 26$, $\tau = \tau_l + \tau_t$) no clear statement about the distribution of u^+ can be drawn. For a higher value of y^+ ($26 \leq y^+$, $\tau_l << \tau_t$) a logarithmic connection between y^+ and u^+ can be found, known as the *(logarithmic) law-of-the-wall* or log-law. [78]

The equation for the law-of-the-wall is

$$u^+ = \frac{1}{\kappa} ln(y^+) + B^+ \tag{3.39}$$

where κ is known as the *von Kármán constant* and B^+ is a constant. Both constants have been determined from experiments and for most cases $\kappa = 0.41$ and $B = 5.5$ is valid.

The profile resulting from this relations is shown in Fig. 3.11 together with a sketch of the layering of a turbulent boundary layer. The three above mentioned areas can clearly be seen as viscous sublayer ($y^+ \leq 5$), buffer layer ($5 \leq y^+ \leq 26$) and log-law region ($26 \leq y^+$) and can be summarized to the inner (boundary) layer. The outer border y^+ of this part of the boundary layer depends on the Reynolds number, but it covers more or less 20 % of the boundary layer height (see Fig. 3.23a). However, this relatively thin layer contributes to 80 % of the total turbulence production [38] (see Fig. 3.23b). This is described in more detail in Sec. 3.3.3.

The so-called outer part of the boundary layer consists of the logarithmic layer and an area, where the *wake law* is valid. The latter represents the largest part of te boundary layer and is described in more detail e.g. by Coles [80].

Since the logarithmic layer can be counted to the inner and outer part of the boundary layer, this part is also called *overlap layer*.

Lastly in this section, the turbulence distribution inside the boundary layer is discussed in more detail. First some turbulent properties are defined.

The velocity fluctuations in the three dimensions u' (streamwise), v' (lateral, plate normal) and w' (spanwise, plate parallel) are used to calculate the turbulence kinetic energy (TKE) k as

$$k = \frac{1}{2}\left(\overline{(u')^2} + \overline{(v')^2} + \overline{(w')^2}\right) \tag{3.40}$$

The TKE can be normalized with the mean streamwise velocity u_∞ leading to the turbulence intensity

$$Tu = \frac{\sqrt{\frac{1}{3}\left(\overline{(u')^2} + \overline{(v')^2} + \overline{(w')^2}\right)}}{u_\infty} = \frac{\sqrt{\frac{2}{3}k}}{u_\infty} \tag{3.41}$$

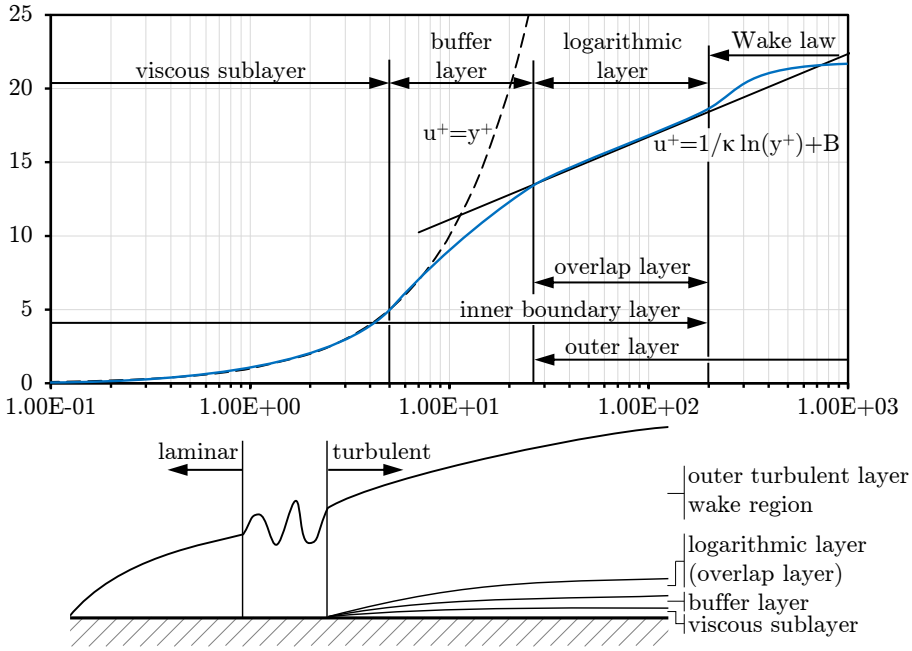

Figure 3.11: Non-dimensional wall coordinates u^+ and y^+ showing the different areas of a turbulent boundary layer including the law-of-the-wall; lower sketch shows the structure of a boundary layer

The turbulence intensities in the three dimensions are defined as

$$Tu_x = \frac{\sqrt{\overline{u'^2}}}{u_\infty} \tag{3.42}$$

$$Tu_y = \frac{\sqrt{\overline{v'^2}}}{u_\infty} \tag{3.43}$$

$$Tu_z = \frac{\sqrt{\overline{w'^2}}}{u_\infty} \tag{3.44}$$

In Fig. 3.12 measured distributions of these turbulence intensity Tu_x, Tu_y and Tu_z are shown against the non-dimensional wall distance $y^* = y/\delta$. Clearly it can be observed that the turbulence close to the wall is not isotropic. The streamwise turbulence intensity shows the highest values, whereas the spanwise velocity fluctuation show the lowest of the three fluctuation values. If only two dimensions (u and v) are measured, the turbulence kinetic energy can also be estimated as

$$k = \frac{3}{4}\left(\overline{(u')^2} + \overline{(v')^2}\right) \tag{3.45}$$

assuming that $\overline{(w')^2}$ is

$$w' = \frac{\overline{(u')^2} + \overline{(v')^2}}{2} \tag{3.46}$$

This assumption is supported by measurements as shown in Fig. 3.12 and is also used in this thesis in paper 5 (see Chap. 6) for the 2D LDA results.

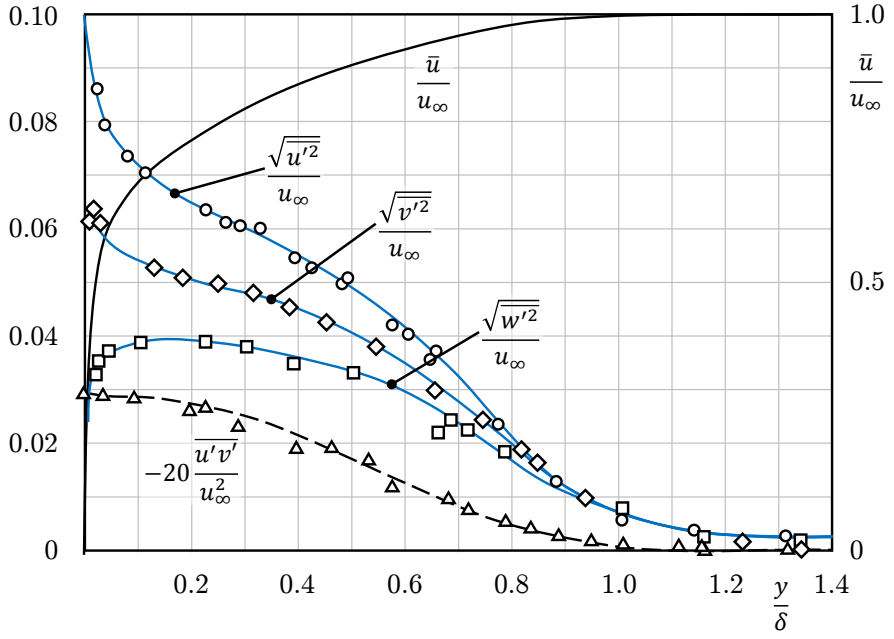

Figure 3.12: Measurement of the streamwise u', lateral v' and spanwise w' velocity fluctuations together with the non-dimensional turbulent shear stress $\overline{u'v'}$ within a turbulent boundary layer (renewed from [81])

Additionally to the turbulence intensities the non-dimensional turbulent shear $\overline{u'v'}/u_\infty^2$ and the distribution of $u^* = \overline{u}/u_\infty$ are given in the figure.

3.3. Transition

As already discussed, when a flow passes a wall, first the formed boundary layer is laminar. After a certain length disturbances inside the boundary layer start to appear, triggering the beginning of a transition process which leads to a turbulent boundary layer. So the transition process is not a rapid turnover into a fully turbulent flow, but passes several stages until the boundary layer becomes fully turbulent. This laminar-to-turbulent transition zone is intrinsically tied to the formation of turbulence, which happens beside inside the boundary layer also in e.g. a laminar pipe flow due to laminar instabilities.

As Rempfer [10] said, the process of transition is first of all a very interesting feature, since many questions of the stages to transition are still unanswered. Generally the boundary layer shows a continuous evolution from a laminar, stable flow to a chaotic complex and ultimately turbulent boundary layer. [10]

The process of transition represents *"the last frontier in fluid mechanics"* [21] and the description of its mechanisms are already filling thousands of pages of books, theses and papers. Therefore in the first part of this section, these different stages leading to a turbulent boundary layer are described in a nutshell. This overview has been partly taken from Mayle [21].

Later in this section, different forms of transition are discussed shortly. Although this work focuses on the process of relaminarization, the understanding of transition is crucial in

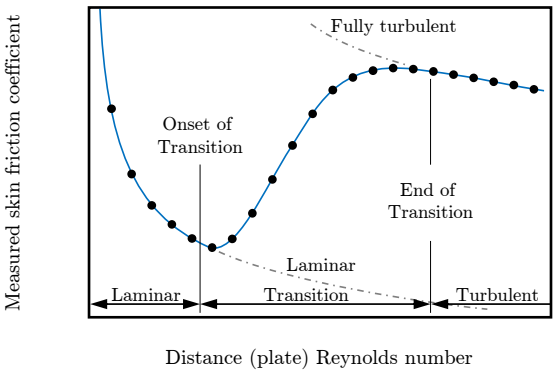

Figure 3.13: Local skin friction coefficient c'_f along a flat plate showing the laminar, transitional and turbulent zone along the plate (renewed from [21])

order to classify what happens during the relaminarization process.

One particular focus is laid on the formation of streaks which play an important role in the production of turbulence inside the boundary layer (see Sec. 3.3.3).

3.3.1. Transition in a nutshell

The simplest way to make transition visible is to plot the distribution of the local skin friction coefficient c'_f against the streamwise Reynolds number Re_x along a flat plate. This distribution is shown in Fig. 3.13 giving an indication of a laminar, transitional and turbulent boundary layer along the plate.

At low Reynolds numbers Re_x, which represent the beginning of the plate, the boundary layer shows a laminar behavior. The distribution of c'_f can be described with the laminar boundary layer theory which has already been presented in Sec. 3.1. $c'_{f,lam}$ (see Eq. (3.8)) is given by the lower dashed line in Fig. 3.13.

At a specific streamwise position the c'_f value shows a rise. Downstream of this increase in skin friction the boundary layer is fully turbulent. The boundary layer there can be described as presented in Sec. 3.2. The turbulent distribution of c'_f is again given as dashed line.

In between these two areas which can be explained using their corresponding theories lies the transitional zone, which cannot be predicted so easily. Also today the prediction of the onset as well as the extent of the transitional zone is challenging. One problem is the unsteadiness of the flow within this particular zone, because even in the laminar boundary layer "turbulent-like" velocity components are possible due to disturbances impressed by the free stream or caused by linear instabilities. The higher these disturbances (free stream turbulence) are, the higher is the amplification of those fluctuations inside the laminar boundary layer.

Generally the start of transition can be defined where these fluctuations *break down into turbulent eddies*, however, also this process is not fully understood. The breakdown into turbulent eddies happens randomly in space and time. The determination of the exact onset of transition is therefore challenging. Thus, the location of the onset of transition is simply defined, where the fluctuations inside the laminar boundary layer *most likely break down*. This position is always located upstream of the minimal local skin friction coefficient (see Fig. 3.13).

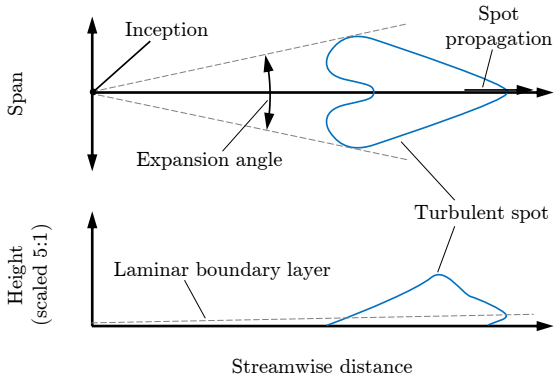

Figure 3.14: Top and side view of a turbulent spot in the laminar boundary layer (renewed from [21])

A critical Reynolds number for this onset of transition along a flat plate with a moderate turbulence intensity of the free stream is often given with [23]

$$Re_{x,crit} = 3.5 \cdot 10^5 \tag{3.47}$$

However, like Schlichting and Gersten [23] also remarked, this critical Reynolds number can be increased to $Re_{x,crit} = 3.5 \cdot 10^6$ if the free flow has a low turbulence intensity. The boundaries between low, moderate or high turbulence are not clearly distinguishable. Mayle [21] wrote that this critical Re_x value is more or less a relict of research dating back eighty years and is just a rule of thumb. He continued that today we know that transition can occur at any point, since the onset depends on a large amount of flow parameters.

The turbulent eddies which result from the breakdown of the fluctuations inside the laminar boundary layer quickly develop into turbulent spots. Figure 3.14 shows such a

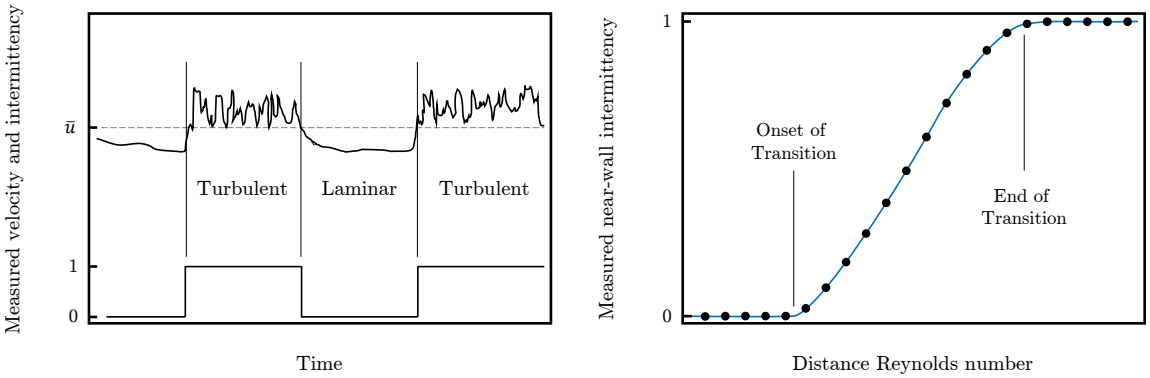

(a) Time signal of a CTA velocity measurement within the transitional zone together with the corresponding intermittency for laminar (zero) and turbulent (one) flow.

(b) Distribution of the intermittency γ along a flat plate showing the change from zero (laminar) to one (turbulent) during transition

Figure 3.15: Illustration of the intermittent behavior of the flow during transition (renewed from [21])

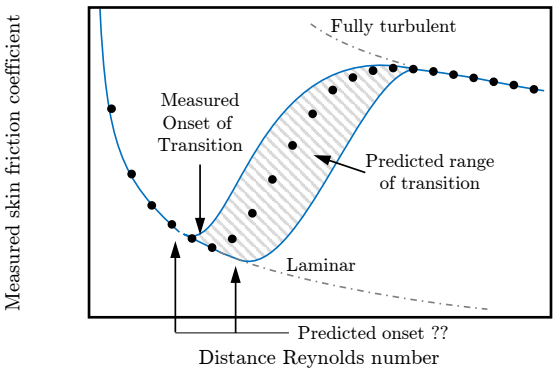

Figure 3.16: Comparison of skin friction measurement and the capability of today's models in predicting the transition (renewed from [21])

turbulent spot in top and side view. In the side view the height of the spot is increased by 5, thus the actual spot is a flat structure. Also the interface shown in Fig. 3.14 is not as sharp as shown but irregular. The turbulent spot spreads out turbulent eddies and protrude beyond the laminar boundary layer as shown in the figure.

The formed turbulent spots penetrate the laminar boundary layer leading to a very intermittent behavior of the boundary layer, which means that one specific position can show a laminar and a turbulent signal, respectively, depending on time. This is exemplary shown in Fig. 3.15a together with the intermittency γ. This value quantifies the fraction of time in which the fluctuations show a fully turbulent signal. Thus, an intermittency value of $\gamma = 0$ indicates a fully laminar flow whereas a value of $\gamma = 1$ a fully turbulent one.

Figure 3.15b shows the development of the intermittency γ along the flat plate. Clearly the rise from zero to one during transition can be observed.

Regarding turbulent spots, *Emmons' turbulent spot theory* represents a method to predict the *production*, *growth* and *propagation rate* of the spots, where the production represents the number of spots and the growth the expansion angle (see Fig. 3.14). Using this theory we can conclude, that the length of the transitional zone depends on the production, growth and propagation rate of the spots. So the length decreases if the production and growth increases but decreases if the propagation rate increases. Thus with Emmons' theory the distribution of c_f' within the transitional zone is predictable.

The end of transition can be found at a position, where the laminar fractions of the fluctuations *most likely disappear*. This position is always downstream of the maximum of c_f' (see Fig. 3.13).

To sum up, using different theories we can today predict the behavior of a laminar boundary layer, the development inside the transitional zone as well as the fully turbulent boundary layer. However, after even more than half a century of transition research we are still not able to predict the onset and length of the transitional zone reliably. In Fig. 3.16 the *best guess* of the transitional zone possible with today's theories/models is indicated by the gray area.

In 2015 Mayle [21] stated that since the 1970s the prediction capability of laminar-to-turbulent transition just slightly increased. Mayle does not see the difficulty in the prediction of the pre and post-transitional flow along a plate, as this can already be computed very

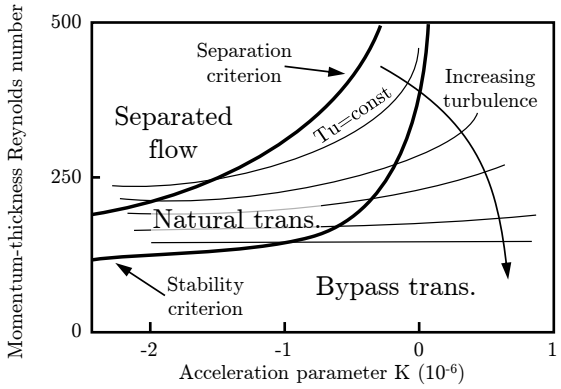

Figure 3.17: Basic modes of transition depending of the momentum-thickness Reynolds number Re_θ and the acceleration parameter K (renewed from [21])

accurately. He says the problem in predicting the onset and length of transition persists in the difficulty to predict *"the birth, birth rate and propagation of turbulent spots"*.

3.3.2. Modes of transition

As already discussed the onset and length of transition depend highly on several parameters, e.g. the turbulence level, the Reynolds number or the pressure gradient. These factors also influence the mode of transition. In general, three different modes of transition are distinguished:

- Natural transition
- Bypass transition
- Separated-flow transition

The condition of occurrence of these different modes are shown in Fig. 3.17 indicating the dependence of the modes on the turbulence level, momentum-thickness Reynolds number Re_θ[1] and the acceleration parameter K (definition see Eq. (3.51)).

Since the momentum-thickness θ (or δ_2) is a function of the streamwise direction x, it can also be seen proportional to the Reynolds number Re_x. The acceleration parameter K represents a non-dimensional pressure gradient and can therefore be used as criteria for separation of a boundary layer (separation criteria). A positive value of K represents an accelerated flow (FPG, $dp/dx < 0$), whereas a negative value of K represents a decelerated flow (APG, $dp/dx > 0$). As discussed at the beginning of this chapter, an APG is necessary for flow separation.

Additionally, Tu_{const} lines are given in the figure, indicating the dependency of the transition mode on the turbulence level. The different areas of the three modes natural, bypass and separated-flow transition are distinctly and visibly.

The latter mode is caused by a transition from laminar to turbulent above a separation bubble, leading to a reattachment of the flow since the turbulent boundary layer is able to overcome the pressure gradient leading to the separation. This mode is not described here

[1] Note that the momentum-thickness can be written as δ_2 or θ

further, since it is not in the scope of this work and the interested reader is referred to further literature, e.g. [21, 23, 81].

Natural transition occurs at relatively low turbulence intensities. This allows the development of eponymous natural instabilities within the laminar flow. Relatively small-amplitude unstable disturbances grow inside the laminar boundary layer and break down into turbulent spots. [21]

Bypass transition is associated with work done by unsteady pressure fluctuation impressed by the free stream and free stream turbulence on the fluctuations inside the boundary layer. This leads to large-amplitude disturbances inside the boundary layer which are forced to grow and will then again break down into turbulent spots and finally into fully turbulent flow. [21]

For both modes the condition of breakdown of the laminar flow into turbulence is still unknown, thus this process can still not be predicted.

In the following, the processes of natural and bypass transition leading to a fully turbulent boundary layer are discussed in more detail.

3.3.2.1. Natural transition

As already described, during natural transition the change towards a fully turbulent boundary layer is caused by natural instabilities inside the boundary layer. Mayle [21] divided this transition mode into four consecutive stages:

- At the leading edge and downstream along the wall the boundary layer is stable laminar and any unsteadiness is damped (1)

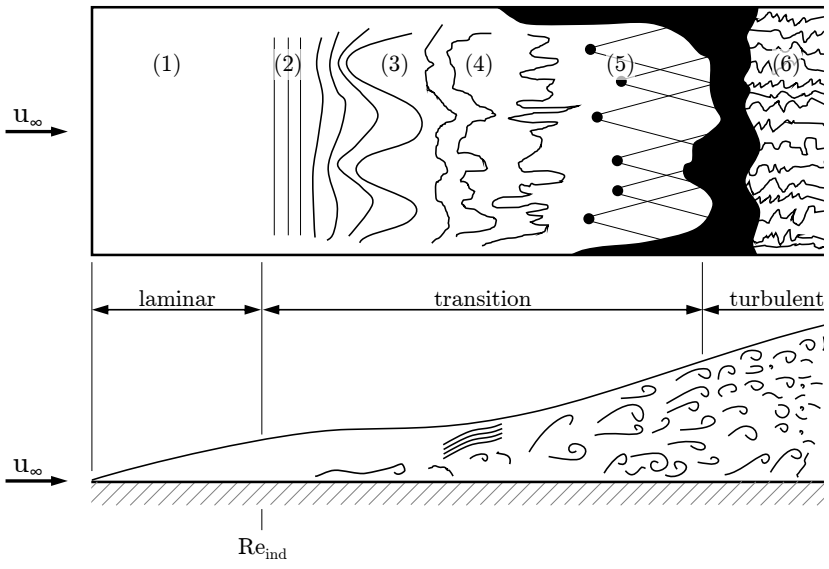

Figure 3.18: Schematic drawing of the process of natural transition showing the different stages: (1) stable laminar flow, (2) Tollmien-Schlichting (T-S) waves, (3) three dimensional waves and turbulent structures (Λ waves, streamwise streaks), (4) secondary instabilities, laminar breakdown, (5) turbulent spots, (6) fully turbulent flow (adopted from [82])

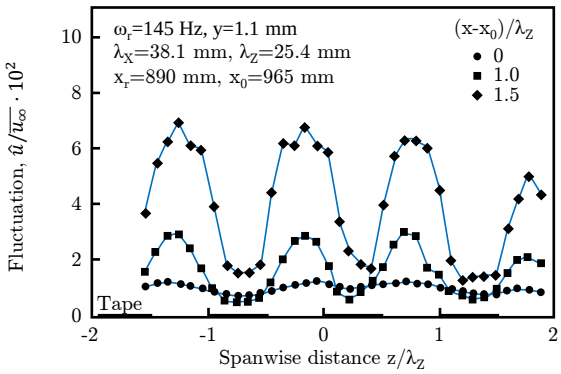

Figure 3.19: Experimental results showing the amplification of streamwise amplitude due to spanwise variations of the boundary layer thickness; initial disturbances are generated with a vibrating ribbon inside the boundary layer and boundary layer thickness variations have been generated with tape attached to the wall (data from [35], renewed from [21])

- When reaching the indifference (critical) Reynolds number Re_{ind}, two-dimensional (Tollmien-Schlichting (T-S) waves) and later three-dimensional unstable, unsteady waves form and grow (2)

- The growth continues and the "most amplified" waves influence the mean flow distribution inside the boundary layer. Additionally a secondary system of streamwise vortices develops inside the boundary layer (3)

- Secondary unsteadiness of high frequency develops with an upwelling of the vortex system. This promotes a rapid break down into turbulent eddies (4)

The numbers given above agree with the schematic drawing in Fig. 3.18. In this illustration additionally to the phases of Mayle just described, downstream turbulent spots (5) and the fully turbulent boundary layer (6) are shown. The different stages are described in the following in more detail.

In the laminar boundary layer, disturbances of small amplitude develop, which represent the first stage. A classical approach for solving this problem has been proposed by Orr [83,84] and Sommerfeld [85] who developed the *laminar stability theory*. These Orr-Sommerfeld equations have been first solved for a Blasius flow by Tollmien [25] and Schlichting [26]. They gave the name to the two-dimensional instabilities, the Tollmien-Schlichting waves, which occur within the laminar flow. These two dimensional waves are inherently unstable to spanwise disturbances, e.g. for spanwise variations of the boundary layer thickness. This has been shown by Schubauer [86], Klebanoff and Tidstrom [87], Klebanoff et al. [35] (experiments shown in Fig. 3.19), Kovasznay et al. [88] and others.

Figure 3.19 shows an experiment where a wave is generated with a vibrating ribbon, simulating T-S waves. This ribbon is mounted upstream of the first shown measurement position inside the boundary layer. Tape strips are attached partly beneath the vibrating ribbon to the surface leading to a spanwise variation of the boundary layer thickness. The positions of the tape strips are shown the figure. In Fig. 3.19 the spanwise variation of the

streamwise fluctuation intensity

$$\frac{\hat{u}}{\overline{u}_\infty} = \frac{\sqrt{\overline{(u')^2}}}{\overline{u}_\infty} = Tu \tag{3.48}$$

at three different streamwise positions is shown. Clearly the spanwise variation of streamwise fluctuation intensity ($\hat{u}/u_\infty$) is visible. Also the amplification of these variations in streamwise direction can be observed. The spanwise variation also triggers the formation of streamwise streaks inside the boundary layer (see below).

It can be concluded, that these spanwise variations of the streamwise velocity (streaks) are caused by an amplification of the Tollmien-Schlichting waves due to instability mechanisms by spanwise variations of the boundary layer thickness. Thus any spanwise variation of the boundary layer thickness triggers an unstable three-dimensional response.

For the sake of completeness it should be mentioned here, that in Fig. 3.19 the spanwise maximum of the fluctuation intensity occurs downstream of a position, where no tape was attached, thus inside a thinner part of the boundary layer. However, Klebanoff et al. [35] found, that if the frequency of the vibrating ribbon (T-S waves) is doubled, this effect inverses, leading to a maximum in the thicker parts of the boundary layer.

As the amplitude of fluctuation intensity increases, secondary effects in the originally two-dimensional flow emerge. These flow structures represent streamwise vortices, with alternating clockwise and counterclockwise rotation direction.

This system of streak structures is shown in Fig. 3.20. The solid circles show values at a position $y/\delta = 0.3$ (solid line in Fig. 3.20a) whereas the empty circles (in Fig. 3.20c) represent values at a position $y/\delta = 0.1$ (dashed line in Fig. 3.20a)

The spanwise distribution of the time-averaged streamwise velocity $\overline{u}$ normalized to the time-averaged free stream velocity $\overline{u}_\infty$ is shown in Fig. 3.20b together with the Blasius velocity at this position. It can be clearly observed, that downstream of the surface-attached tape (thicker boundary layer) the velocity is lower than the Blasius one, where the fluctuation intensity $\hat{u}/\overline{u}_\infty$ (Fig. 3.20d) shows its maximum, whereas the velocity is higher and the intensity is lower in the thinner parts of the boundary layer.

The time-averaged spanwise velocity $\overline{w}$ shows at these positions of maximum and minimum intensities $\hat{u}/\overline{u}_\infty$, a change in the sign. The position of maximum and minimum $\overline{w}$ values, respectively, are in between the maximum and minimum intensities. Additionally one can observe from the spanwise velocity distributions that $\overline{w}$ close to the wall ($\circ$) shows an opposite sign compared to the distribution away from the wall ($\bullet$). Note that the arrows close to the ordinate in Fig. 3.20c indicate the spanwise flow direction. This agrees with the streamwise vorticity system of alternating clockwise and counterclockwise rotating vortices as shown in Fig. 3.20a.

Between two streamwise vortices low speed fluid is moved away from the wall outside and at a different spanwise position faster moving fluid is moved towards the wall, respectively. This leads to the spanwise distribution of $\overline{u}/\overline{u}_\infty$ discussed above (Fig. 3.20b). This transport of fluid deforms the velocity profile of the boundary layer which is shown in Fig. 3.21 where instantaneous velocity profiles are shown. The transport of fluid due to these streamwise streaks and the related effects are described in more detail in Sec. 3.3.3.

Clearly the deformation of the Blasius profile can be observed, where the profile develops an inflexion point. According to Rayleigh [89–91] any profile with an inflexion point is

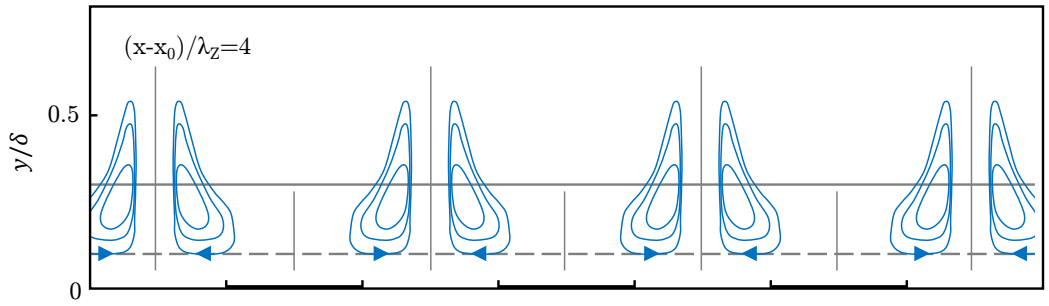

(a) Spanwise-lateral sketch through the boundary layer showing v-w streamlines

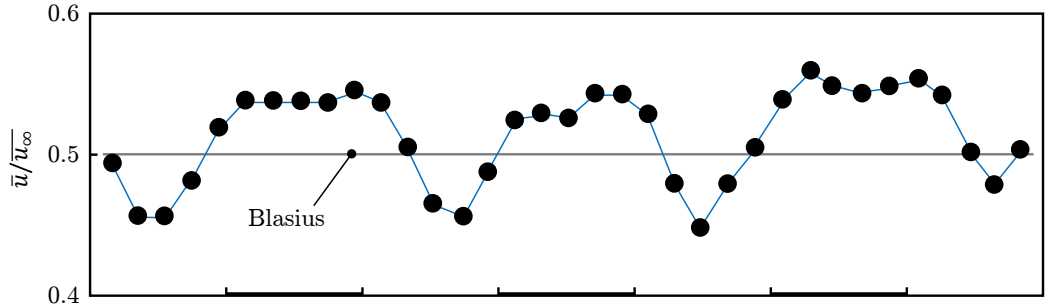

(b) Averaged normalized streamwise velocity

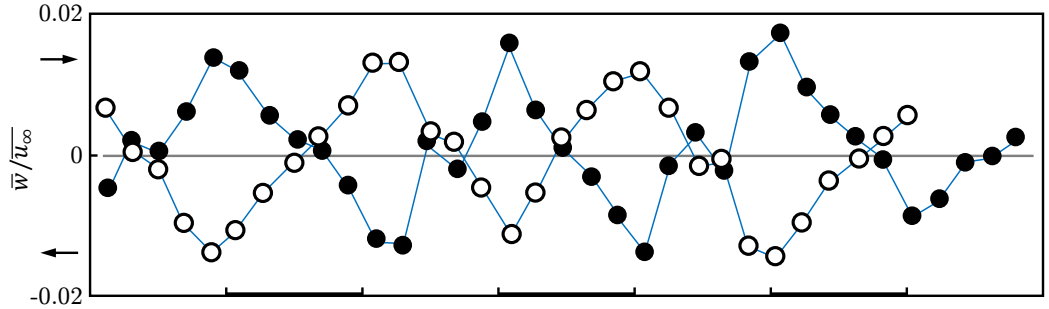

(c) Averaged normalized spanwise velocity, arrows at the ordinate indicate the flow direction

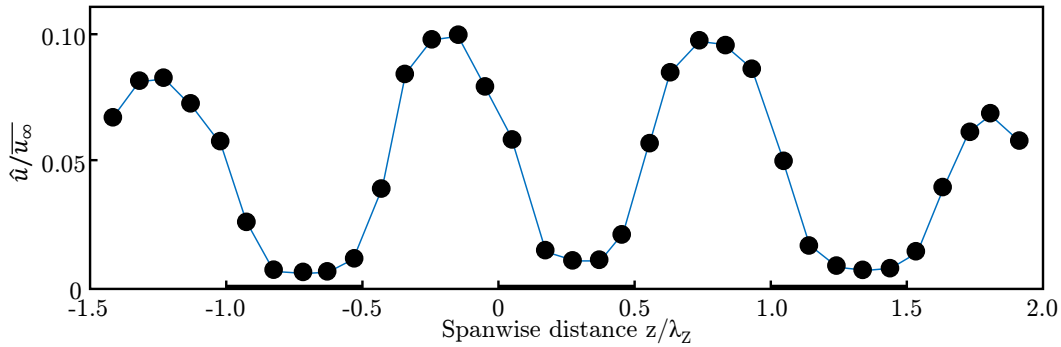

(d) Fluctuation intensity

Figure 3.20: Experimental results showing the secondary structures (streaks) during transition (data from [35], renewed from [21])

unstable. This instability of the profile leads to secondary instabilities which ultimately lead to a laminar breakdown into turbulent eddies.

Schubauer [86] states, that this breakdown happens, if the fluctuation intensity $\hat{u}/u_\infty$ is 0.074. However, Mayle [21] proposes as criterion for the breakdown, that the frequency of these secondary instabilities is five times the frequency of the Tollmien-Schlichting waves, thus these secondary instabilities may be Kelvin-Helmholtz like instabilities.

The turbulent eddies formed by the breakdown of the laminar layer accumulate to turbulent spots, (see above) which propagate downstream until the fully turbulent boundary layer is developed.

3.3.2.2. Bypass transition

If the amplification of the initial disturbances inside the boundary layer exceeds a certain value, the stages described by the laminar instability can be bypassed [23]. Thus the three dimensional and secondary instabilities can be triggered directly leading to turbulent spots. The propagation of a forced (triggered) instability is shown in Fig. 3.22. The snapshots have been made with a camera moving downstream with the propagating turbulence.

This amplification of disturbances can be caused by a higher free stream turbulence, thus this kind of transition is mostly present in turbomachines and other technical flows with high unsteadiness.

First serious measurements with elevated free stream turbulence have been done by Dyban et al. [92] who presented mean flow measurements as well as Reynolds shear stress data [21]. Morkovin [93] was the first pointing out the process of bypass transition.

Mayle and Schulz [51] and Mayle et al. [50] presented the "right" turbulence influencing the process of transition and analyzed the "effective turbulence" promoting the forced oscillations during the transition process.

But not only free stream turbulence can trigger the bypassing of transition stages, but also the roughness of the surface.

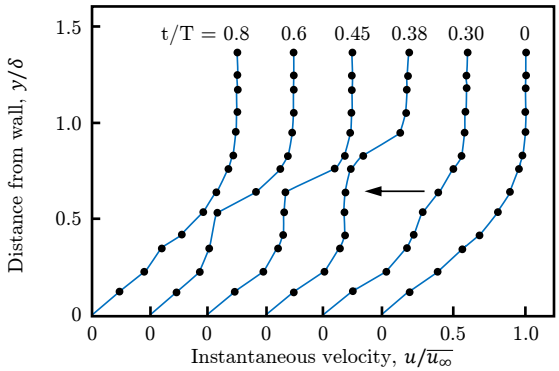

Figure 3.21: Instantaneous velocity profiles at a spanwise position between two streamwise streaks (data from [35], renewed from [21])

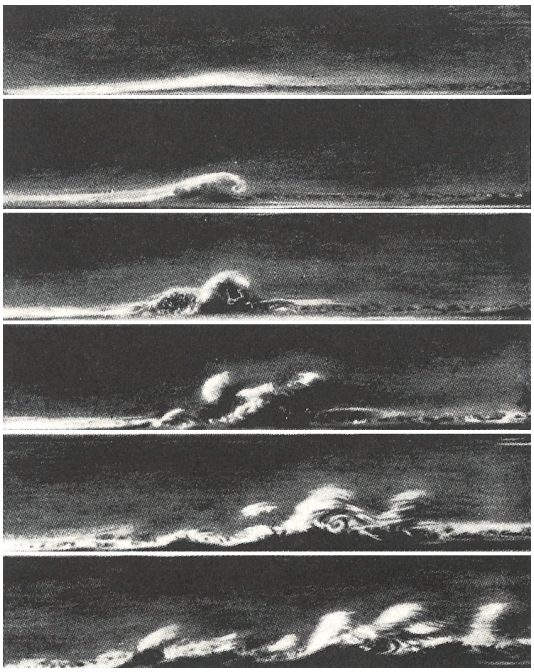

Figure 3.22: Propagation of an triggered disturbance inside the boundary layer leading to turbulence [79]

3.3.3. Streamwise streaks in the boundary layer

The streamwise streaks with are developing due to an instability of the laminar flow trigger further effects which are described in this section. These effects influence the production of turbulence close to the wall. According to Kline et al. [38] the turbulent production in this wall-near area represents 80 % of the total production of turbulence inside the boundary

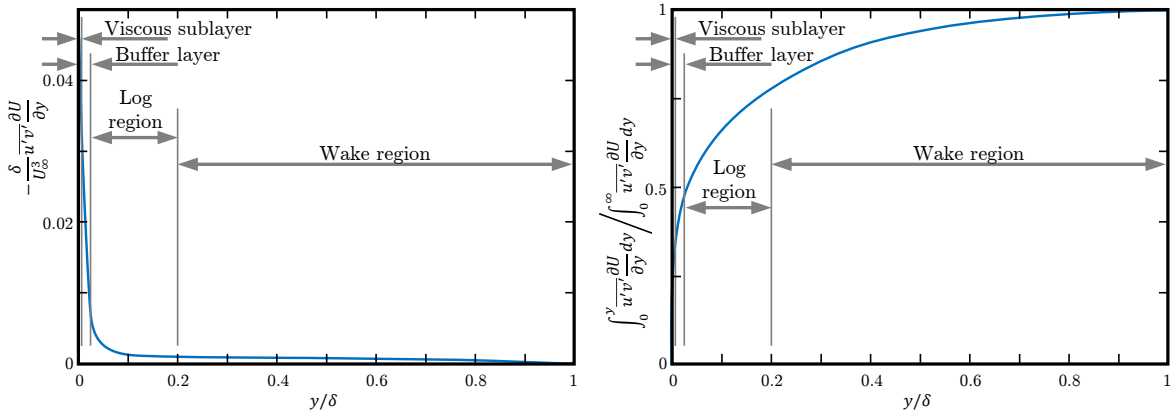

(a) Normalized turbulence energy production per unit volume

(b) Cumulative turbulence energy production

Figure 3.23: Production of turbulence energy inside a typical boundary layer [31]

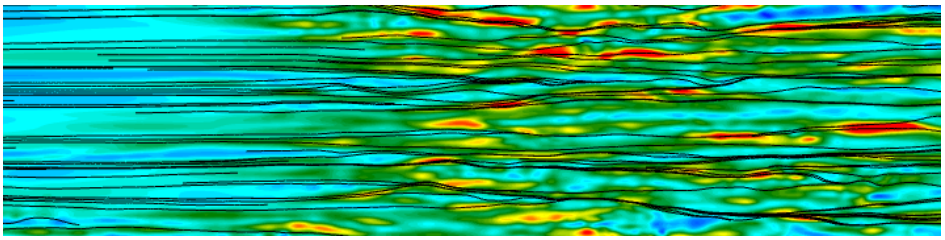

Figure 3.24: Contour plot of the wall shear stress τ_w computed with LES showing low and high-speed streaks causing lower (blue) and higher (red) wall shear, respectively

layer. This is also shown in Fig. 3.23 showing the turbulent production and the accumulated turbulent production in a turbulent boundary layer. It can be seen that the maximum production is situated inside the buffer layer. Also it can be observed that up to the end of the log region, which represents about 20 % of the boundary layer thickness, 80 % of the total turbulence production takes place. The effects leading to this production of turbulence is explained in the following and it is the author's opinion that these effects are important for the relaminarization process due to high acceleration. This is also the reason why this is explained here in more detail.

As described, Taylor-Görtler like streamwise vortices are present inside the boundary layer. They trigger a movement of low-speed fluid away from the wall and high-speed fluid towards the wall. This leads to a formation of high-speed and low-speed *streaks* inside the boundary layer at a distance of approximately $y^+ = 10$ which represents the zone of the buffer layer (see Fig. 3.11). These low and high-speed streaks can also be seen in the wall shear stress τ_w along the plate. Figure 3.24 shows the contours of τ_w along a plate during transition. The LES results clearly show this "streaky" distribution of the wall shear stress indicating the presence of streaks.

Above the low-speed streaks hairpin or horseshoe vortices develop, which have according to Kline et al. [38] a life cycle of *"lift-up"*, *"ejection"* and *"bursting"*. Due to the movement of fluid away from the wall (bursts), high speed fluid has to move towards the wall in order

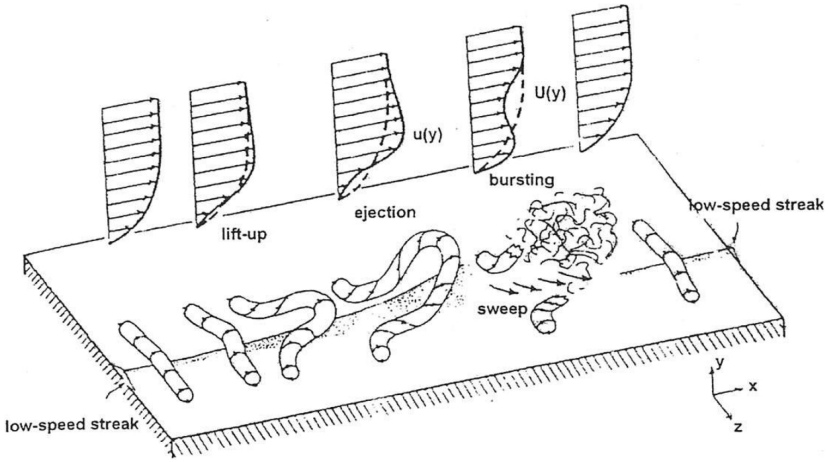

Figure 3.25: Streaks and hairpin vortices showing their life cycle close to the wall [17]

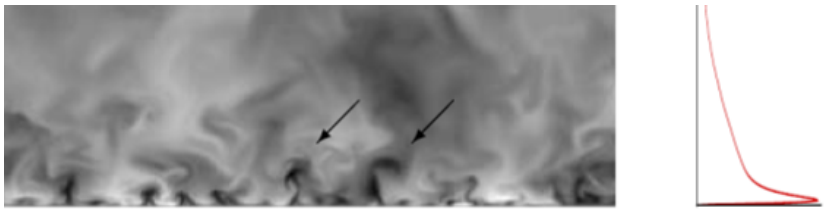

Figure 3.26: Contour plot of the streamwise velocity showing the bursting effects inside the boundary layer, data computed by DNS (adopted from [17])

to satisfy continuity. This effect is called "sweep". [17]

The stages are shown in Fig. 3.25. Clearly the formation of a vortex above the low-speed streak is visible. This vortex then lifts up, already deforming the velocity profile of the boundary layer, followed by an ejection of the vortex which then bursts into turbulence. This burst mechanism accounts for 80 % of turbulence production inside the boundary layer. During bursting, also the sweep effect (high-speed fluid towards the wall) can be seen also in the deformation of the velocity profile.

The bursting process can also be seen in Fig. 3.26 which shows a contour plot of the velocity instantaneous computed with DNS. Two bursting events are marked with arrows. Additionally on the right hand side of the figure the turbulence production is given, clearly showing a peak close to the wall. The position of this peak is about $y^+ = 10$.

The rate of bursting can also be quantified using the burst rate F, which describes the rate of occurrences of streak breakup per unit span and time, thus it represents the frequency of streak breakup per unit span [38]. Kline et al. [38] suggested a normalization of this value using wall-values according to

$$F^+ = \frac{F\nu^2}{u_\tau^3} \tag{3.49}$$

The movements of low and high-speed fluid can also be analyzed using a quadrant analysis of the streamwise u' versus the lateral v' velocity fluctuation, thus the Reynolds shear stresses (see e.g. [63, 94]). This is shown in Fig. 3.27 and can be done by measuring u and v coincidentally.

The first quadrant (top-right) indicates an outward motion of high speed fluid. The second (top-left) shows low-speed fluid which is moved away from the wall. This represents the ejection described above.

Measured velocities in the third quadrant (bottom-left) indicate an inward movement of low-speed fluid. The forth quadrant shows high speed fluid moved towards the wall. This represents the sweep effect.

If we consider that the turbulence production is proportional to $-\overline{u'v'}$, it can be seen from the quadrant analysis, that the velocity fluctuation in the first and third quadrant represent a positive Reynolds shear, thus a negative turbulence production, whereas fluctuations inside the second and fourth quadrant represent a positive production (negative Reynolds shear). Thus ejection and sweep effects contribute to the turbulence production inside the boundary layer.

The effects of the lift up of the streaks and their bursting have been visualized using particle tracing by Kim et al. [63] and is shown in Fig. 3.28. Particles generated by a pulsed

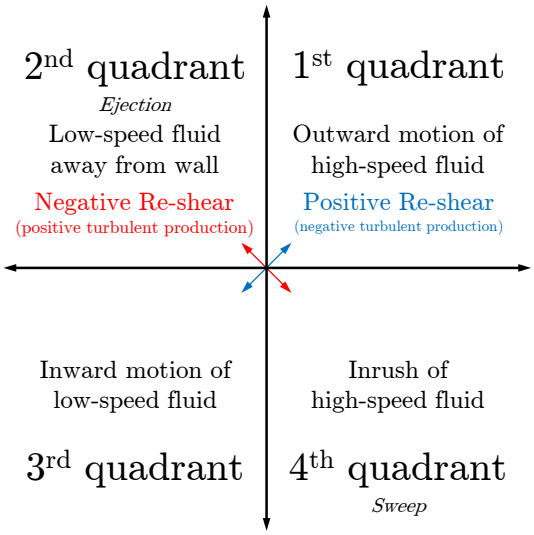

Figure 3.27: Quadrant analysis showing the streamwise u' versus the lateral v' velocity fluctuation

heated horizontal (Fig. 3.28a) and vertical wire (Fig. 3.28b) clearly show, how the streak slowly moves away from the wall and bursts into irregular movements. Kline et al. [38] describe, that the outwards moving streak starts to oscillate at around $y^+ = 8 \div 12$. This oscillation is amplified during the ongoing outward movement of the streak and it will break up between $y^+ = 10$ and $y^+ = 30$.

In Fig. 3.29 a contour plot of the instantaneous streamwise velocity for bypass transition

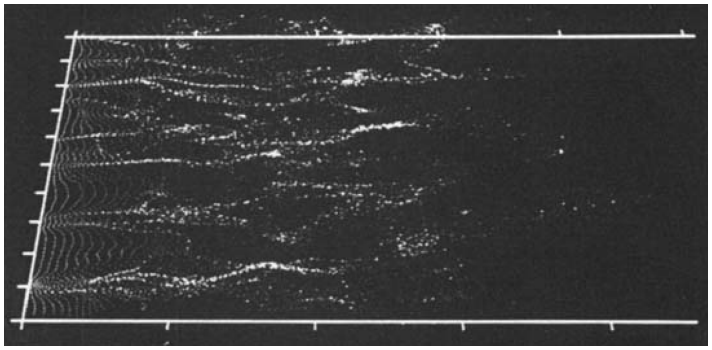

(a) Horizontal wire at $y^+ \approx 10$, top view

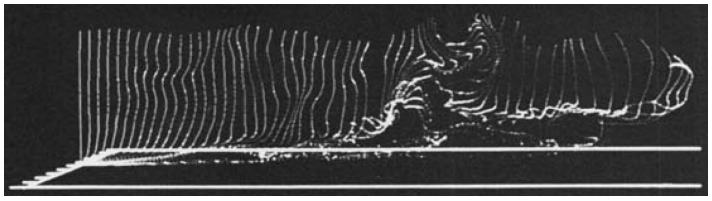

(b) Vertical wire, side view

Figure 3.28: Visualization of the flow structures inside the boundary layer [31]

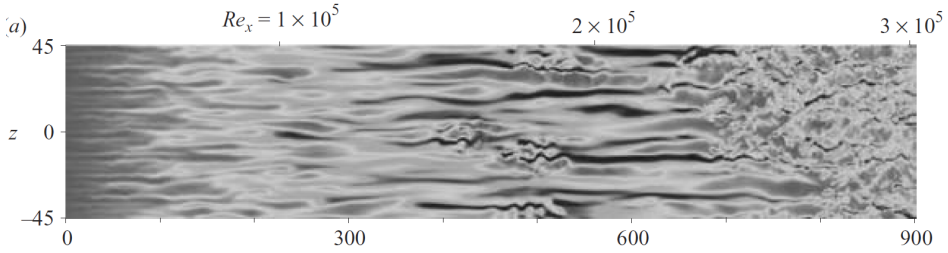

Figure 3.29: Instantaneous streamwise velocity during transition [65]

is shown. The data has been computed using DNS by Brandt et al. [65]. The plot shows clearly how instabilities of at first low amplitude are amplified leading to a breakdown and ultimately to a fully turbulent flow. Additionally in the figure the plate Reynolds number Re_x is given.

Figure 3.30 shows the structure of the streaks with the lift up to the hairpin vortex. In the figure iso-surfaces of λ_{ci}^2 are shown. λ_{ci}^2 is analogous to the enstrophy (the mean value of the quadratic vorticity), thus it is similar to the Q criterion. More details can be found in [95, 96]. The figure shows clearly, how the streaks lift up and form hairpin vortices.

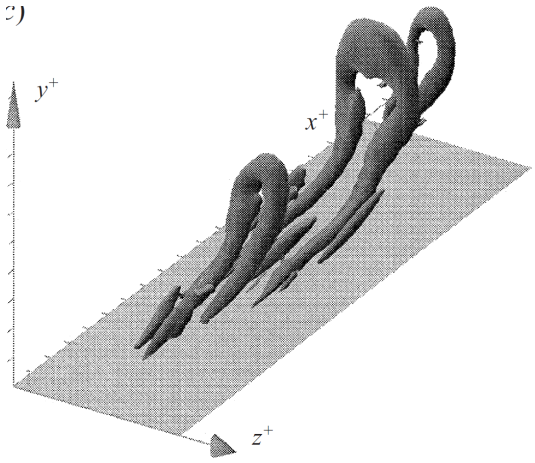

Figure 3.30: Vortical structures identified by an iso-surface of λ_{ci}^2 with 4.2 % of its maximum value [96]

3.4. Relaminarization

Relaminarization, also known as relaminisation, reverse transition or simply laminarization, describes a process where a chaotic turbulent flow turns into an ordered laminar flow. In the beginning of this field of research the process was seen as impossible, because it would violate the second law of thermodynamic, since the chaos inside a closed system would decay, which would mean, that the entropy would fall [42]. However, the system of relaminarization is not a closed one, thus relaminarization is possible. It is also easy to show, that relaminarization exists, which motivated Viswanath et al. [43] to publish some fundamental experiments to visualize relaminarization.

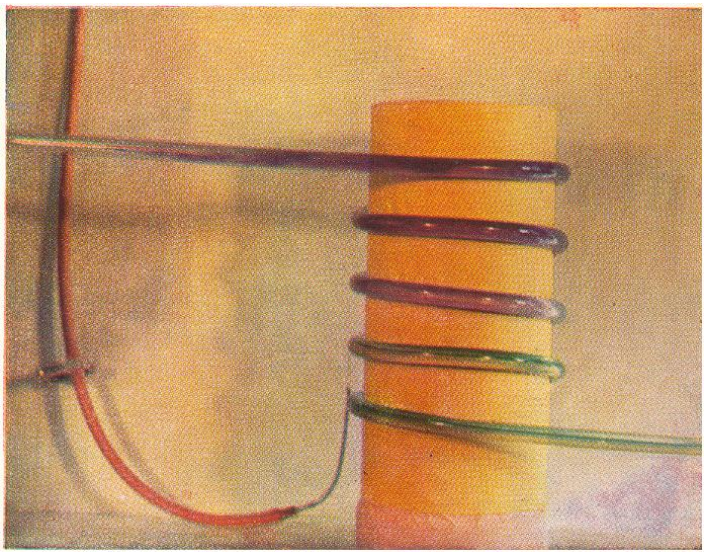

Figure 3.31: Dye-streaks used for visualization of relaminarization (reverse transition) in a coiled tube showing that a fully turbulent flow enters on the top left and a relaminarized flow leaves the system on the bottom right [43]

One of the most famous ones is shown in Fig. 3.31 for the relaminarization in a coiled tube. The experiment was originally presented by Taylor in 1929 [97] and rebuilt by Viswanath et al. and is similar to the dye streak experiment of Reynolds (1883) [19]. For the visualization a purple dye is injected upstream of a coiled tube, showing a mixing with the fluid, indicating a fully turbulent flow. In the forth coil a green dye is injected. In contrast to the purple dye, the green one is not mixed indicating a laminar behavior, thus the flow is relaminarized. In order to avoid a mixing of the two dyes, the photograph shown in Fig. 3.31 has been taken just before the purple dye reaches the injection point of the green one.

Narasimha and Sreenivasan [42] defined the relaminarization as a process, where the resulting turbulent fluctuations are negligible in contrast to the mean fluctuations of the flow. They distinguish three fundamental mechanisms leading to relaminarization:

- Relaminarization by dissipation
- Relaminarization in stable stratified flows
- Relaminarization in highly accelerated flows

These three mechanisms are described in the following, where a special focus is given on the relaminarization due to high acceleration, since this lies in the scope of this work. This process also takes place in turbomachines which represents the main focus of the present work. Parts of these explanations are taken from Narasimha and Sreenivasan [34, 42] and Viswanath et al. [43].

For the sake of completeness it should be mentioned that beside these three processes, relaminarization can also be caused by magnetic fields, rotation and others, but these processes are not discussed here.

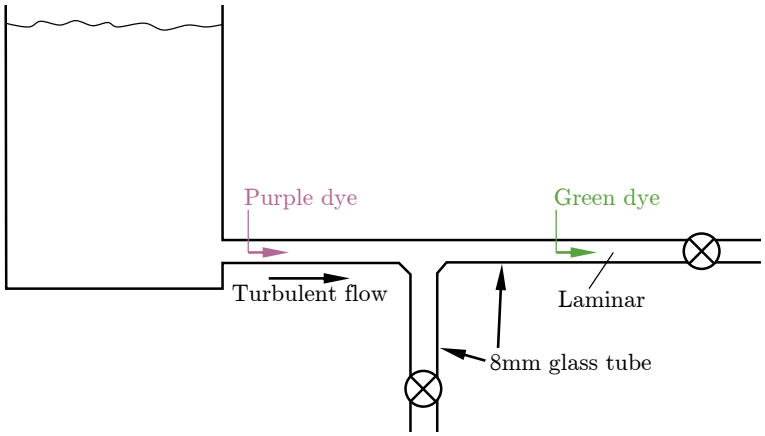

Figure 3.32: Experimental setup of a bifurcating pipe used for the visualization of relaminarization caused by dissipation (renewed from [43])

3.4.1. Relaminarization by dissipation

In fluid mechanics dissipation describes the conversion of high graded energy into energy of lower grade, in particular the dissipation of kinetic energy into heat. This is mainly caused by the influence of viscosity in the flow.

Regarding relaminarization, this is one of the mechanisms most easily to be understood: If the Reynolds number inside the flow decreases below the critical value, viscous effects dominate inside the flow, leading to dissipation of the turbulent kinetic energy. If the Reynolds number is sufficiently low the ratio of turbulent production and dissipation, which can be written as [42]

$$\frac{\text{production of turbulent energy}}{\text{dissipation}} = \frac{-\overline{u'v'}\ \partial u/\partial y}{\epsilon} \tag{3.50}$$

decreases.

Viswanath et al. [43] visualized this kind of relaminarization using a bifurcating pipe. The experimental setup is shown in Fig. 3.32.

The flow entering from the tank (upstream of the furcation) has a Reynolds number higher than the critical one. Thus the purple dye injected in this part of the pipe shows high mixing indicating a turbulent flow. At the furcation flow is split into two pipes, vertical and horizontal in Fig. 3.32. Since less mass continuous in the horizontal pipe but the diameter is the same compared to the flow upstream of the furcation, this will cause the velocity and thus the Reynolds number to drop. If the resulting Reynolds number is below the critical one, relaminarization can be expected. This has been visualized by Viswanath et al. using a second dye in the horizontal pipe. This dye streak is not mixed, indicating a laminar flow.

This mechanism also occurs in diffusers, where the cross-section is extended, leading to a decrease of the Reynolds number. In Fig. 3.33 the flow results in such a channel is shown. The opening angle is low enough to prevent separation of the flow. Upstream of the diffusor the Reynolds number is above the critical one ($Re_1 > Re_{crit}$), thus the flow is of a turbulent nature. As the cross-section increases the Reynolds number drops below the critical level ($Re_2 < Re_{crit}$). This leads as described above to dominating viscous forces leading to a higher turbulent dissipation compared to the production. It can be clearly observed that

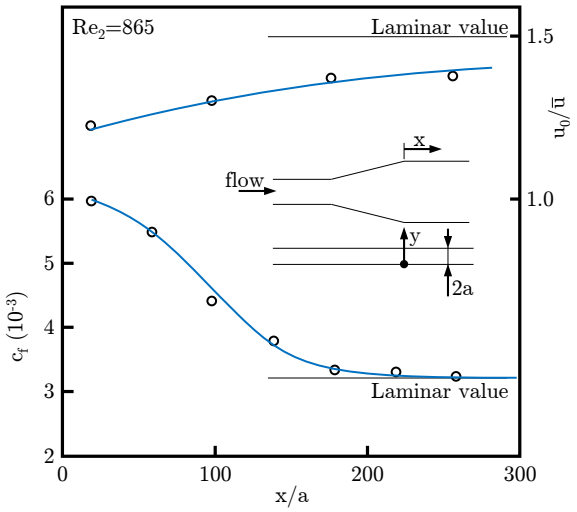

Figure 3.33: Distribution of the skin friction coefficient c_f (bottom) and the ratio of the velocity u_0 to the volume flow equivalent velocity $\overline{u}$ through a diffusor indicating relaminarization by dissipation (renewed from [42])

the mean velocity ratio $u_0/\overline{u}$ tends towards the laminar level. It is interesting that the skin friction coefficient c_f reaches the laminar level faster that the velocity distribution in the channel. Narasimha and Sreenivasan [42] stated that the rather fast response of the skin friction coefficient is caused by a development of a new viscous sublayer during the decay of Re.

Narasimha and Sreenivasan also found, that this mechanism is a rather slow relaminarization process, because the dissipation is just a little lower compared to the production of turbulence. The reason for the decay of turbulence production is a decorrelation of the velocity fluctuations leading to lower Reynolds shear stresses which decrease the production of turbulence inside the flow. The experiment presented in Fig. 3.33 clearly shows that it takes a streamwise distance of about $200 \cdot a$, where a represents the half channel width, for the relaminarization, although the Reynolds number is already far below the critical one ($Re_2 = 865 << Re_{crit}$).

This mechanism of relaminarization also takes place in our own body: Whereas the air flow entering our lungs during respiration is of turbulent nature, it is laminar inside our bronchial tubes due to relaminarization by dissipation as just described.

3.4.2. Relaminarization in stable stratified flows

A fluid is stable stratified, if heavier fluid is at the bottom and lighter fluid is at the top, respectively. This implies a density gradient which increases in the direction of gravity. The reason for relaminarization in such stable stratified flows is, that during the rising of the fluid, turbulent kinetic energy is converted into gravitational potential energy, reducing fluctuations of the flow. In other words the fluid has to work against gravity and this leads to an absorption of energy leading to revision towards a laminar flow.

Such stable stratifications are often seen in the atmosphere, e.g. caused by a sunset. An experiment for this kind of mechanism is shown in Fig. 3.34a. The experiment shows dye

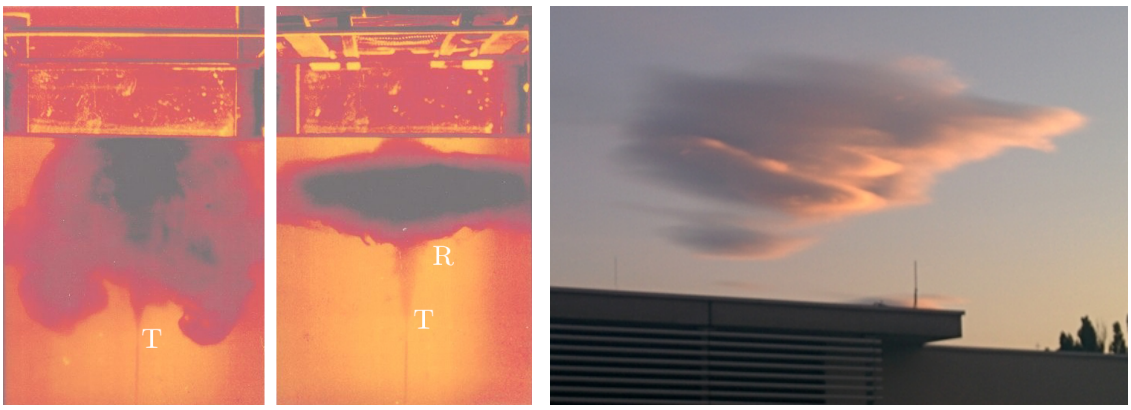

(a) Photograph of the distribution of injected dye without (a) and with (b) heating of the top wall showing transition (T) and relaminarization (R) [43]

(b) Picture of a relaminarized cloud in the sky over Graz, Austria

Figure 3.34: Illustration of the relaminarization phenomenon due to stable stratified flow

injected into a fluid tank from the bottom. In the left photograph of Fig. 3.34a the dye undergoes transition and breaks up into turbulent mixing. If the top wall is heated (right picture) a stable stratification is applied to the fluid inside the tank. One can clearly observe that the dye injected at the bottom undergoes transition as before, but shows relaminarization due to the density gradient. This cannot only be observed under laboratory conditions, but also in the sky with the occurrence of clouds showing flat, smooth shapes. Figure 3.34b shows such a cloud over the city of Graz, Austria.

Such clouds occur if a temperature gradient in the atmosphere leads to a stable stratification. This temperature gradient can e.g. be generated when the sun sets and sudden cooling of the ground due to radiation leads to a temperature gradient. Also a cooling rain

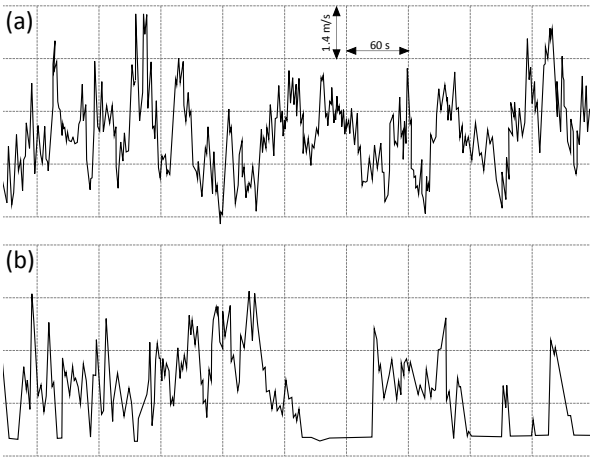

Figure 3.35: Time signal of the horizontal wind speed before (a) and after (b) a cooling rain shower showing laminar areas after the shower (renewed from [42])

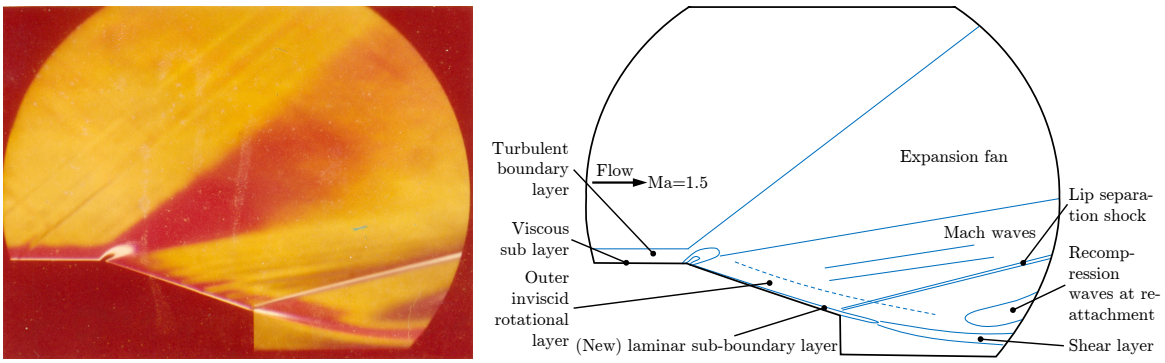

(a) Schlieren photography [43]

(b) Schematic diagram (renewed from [43])

Figure 3.36: Supersonic flow around a convex corner showing the formation of a Prandtl-Meyer expansion fan and a (new) laminar sublayer

shower can cause such a stable horizontal layering in the atmosphere. Figure 3.35 shows the time signal of the horizontal wind speed just before and after a cooling rain shower. The measurement has been performed by Prabhu in 1977 using a cup anemometer. Clearly the patches of laminar flow can be observed in the lower time signal after the shower.

3.4.3. Relaminarization due to high acceleration

This mechanism of relaminarization differs fundamentally regarding the process leading to a revision of the turbulent boundary layer towards a laminar state. In contrast to the other two processes, relaminarization in highly accelerated flows is not easily parametrizable, since the occurring processes inside the boundary layer leading to a laminar flow are more complex.

Regarding the scope of this work, this kind of relaminarization is of particular interest, since it takes place in turbomachines along blades, combustors or other flow channels as shown by Mayle [9] (see Fig 1.6, page 6).

One of the first works showing the influence of a favorable pressure gradient on transition were presented by Schubauer and Skramstad [98] and Liepmann [99, 100]. They performed transition measurements and observed a delay of transition, if the boundary layer is subjected to a FPG.

Regarding relaminarization, Sternberg [101] and Sergienko and Gretsov [102] found during their high speed experiments a first evidence, that the boundary layer may revert during high acceleration of the flow. Later Launder [36] presented results of relaminarization experiments with relatively low free stream velocity (see Fig. 2.2, page 16).

Although in this work a focus is put on relatively low speed cases, first high speed experiments are discussed.

Figure 3.36 shows a schlieren photography and a schematic drawing of high speed experiments ($Ma = 1.5$) by Viswanath et al. [43]. The experiment shows a turbulent boundary layer traversing a Prandtl-Meyer corner in a supersonic flow. Such a Prandtl-Meyer corner is characterized beside the formation of a Prandtl-Meyer expansion fan, by an acceleration around this corner, meaning that the velocity downstream of the corner M_2 is higher than the velocity upstream of the corner ($M_2 > M_1$). The schlieren photograph (Fig. 3.36a clearly

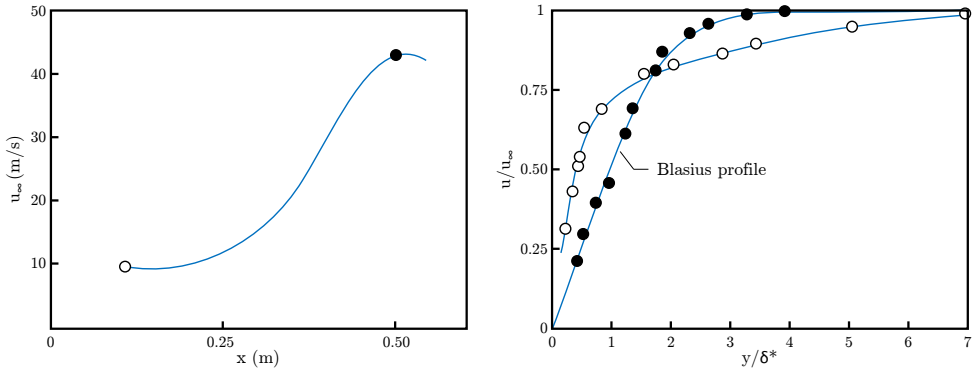

Figure 3.37: Relaminarization in a highly accelerated flow showing the velocity along the plate and the transformation of the boundary layer profiles (data from Ramjee [103])

shows that downstream of the corner a new laminar boundary layer occurs. Additional measurements also show a laminar-like distribution of c_f' and heat flux. This new formed viscous sublayer lies below the remains of the original turbulent boundary layer.

In general during relaminarization due to high acceleration of the flow a turbulent boundary layer at a position x_0 gets accelerated by a strong FPG. This leads to a decrease of the boundary layer thickness δ, to a rise of the shape factor H towards a laminar level and to a breakdown of the law-of-the-wall. Additionally the skin friction decreases leading to a lower c_f' value and also the relative turbulent intensity decreases. Thus it can be said, that the flow is effectively laminar, although velocity fluctuations may still remain in the flow.

In Fig. 3.37 experimental data obtained by Ramjee in 1968 [103] are given, showing the distribution of the free stream velocity indicating a high acceleration together with the velocity profiles before and after the acceleration. It can be clearly observed that during the acceleration, the shape of the velocity distribution develops towards the Blasius, therefore laminar solution, thus a complete relaminarization is present.

Beside these experiments, many other researches have been presented since the 1950s (see overview in Chap. 2), more recently for example by Savill [104]. His results are shown in Fig. 3.38, giving the distribution of the skin friction coefficient c_f' along a plate under FPG. The relaminarization process can be clearly identified by the strong decrease in c_f'. Additionally also the retransition from laminar to turbulent downstream of the relaminarization zone can be observed, which is discussed later in this section.

Within the works published different criteria for the onset of relaminarization have been presented, because the increase of velocity as shown in the left diagram of Fig. 3.37 is not sufficient as parameter.

Launder [36] differed between moderate and severe acceleration. For full relaminarization severe acceleration has to be applied to the flow, leading with enough streamwise extension of the acceleration zone, to full relaminarization of the flow. With a moderate acceleration only partial relaminarization can be reached.

In order to distinguish between severe and moderate acceleration Launder proposed a non-dimensional pressure gradient, namely the (Launder) acceleration parameter which can be written as

$$K = \frac{\nu}{u_\infty(x)^2} \cdot \frac{du_\infty(x)}{dx} \tag{3.51}$$

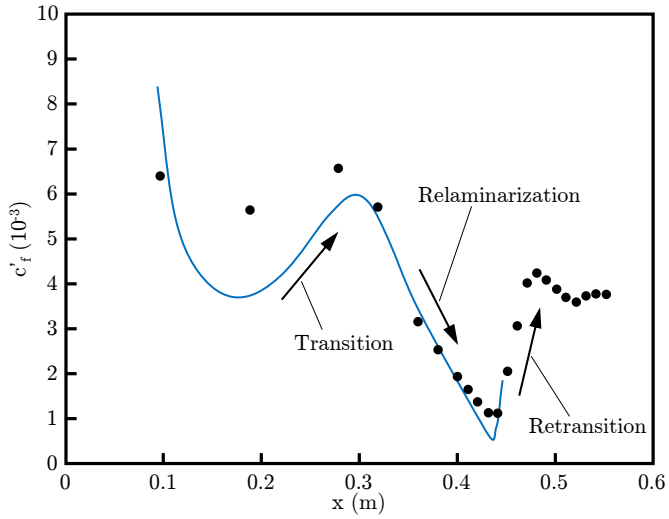

Figure 3.38: Skin friction coefficient c'_f distribution along a flat plate with severe acceleration showing relaminarization and retransition ($Tu = 0.1\%$) (renewed from [104])

where $u_\infty(x)$ represents the local free stream velocity and ν the kinematic viscosity. According to Launder, the critical value is $K_{crit} = 3 \cdot 10^{-6}$ as border between severe and moderate acceleration. Although other research groups have presented other values of K_{crit} (varying from $(2 \div 3.5) \cdot 10^{-6}$ [34, 40, 41, 59]), the parameter has been validated several times over the years, but it has some drawbacks, for instance only free stream values are used, and no information about the accelerated boundary layer (Re_x, Re_{δ_2}/Re_θ) is included. However, the acceleration parameter is widely used and a good parameter which is also easy to use.

As stated at the beginning of this section, relaminarization due to a high acceleration of the flow differs compared to the other two mechanisms described. The reason is, that in this case dissipation does not dominate production. This is shown in Fig. 3.39 presenting measurement results of Badri Narayanan et al. [105] comparing the production, dissipation, advection and diffusion for a zero and favorable pressure gradient case.

The comparison clearly show that production and dissipation decreases due to the acceleration, however the ratio of these two values stays quite the same. The dissipation in this case is always smaller than the production. Thus one can conclude that this mechanism of relaminarization is not caused by dissipation dominating production.

Additionally from the data of Badri Narayanan et al. [105] the shear stress correlation factor C_τ is given in Fig. 3.40. C_τ is defined as

$$C_\tau = \frac{\overline{u'v'}}{\hat{u} \cdot \hat{v}} \tag{3.52}$$

quantifying the amount of decorrelation of Reynolds shear stress, hence the production of turbulence.

From the data in Fig. 3.40 it can be observed that no significant difference in C_τ can be observed when comparing the ZPG and the FPG case. If major decorrelation would have been observed, one could conclude, that the turbulent production decreases within the relaminarization, but this is not the case.

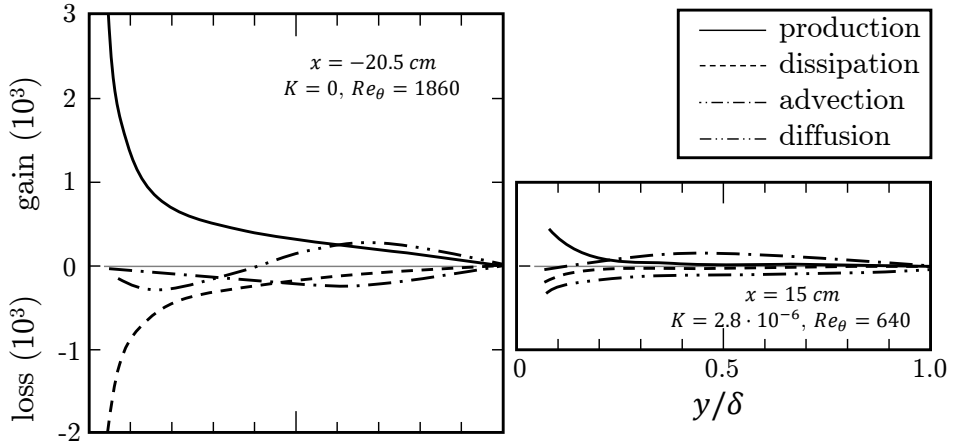

Figure 3.39: Comparison of production, dissipation, advection and diffusion of turbulent energy comparing a ZPG $K = 0$ and FPG $K = 2.8 \cdot 10^{-6}$ case (data from Badri Narayanan et al. [105], adopted from [42])

Thus Narasimha and Sreenivasan [34] concluded, that this mechanism of relaminarization is due to a domination of pressure forces over slowly responding – "frozen" – Reynolds shear stresses, rather than dissipation dominating production as in the other mechanisms, although this could contribute to the process.

To sum up, relaminarization can occur due to high acceleration, however the main observation can mainly be seen for the mean flow. Fluctuations from the original turbulent flow may still remain inside the relaminarized boundary layer, but compared to the kinetic energy of the flow, the turbulent kinetic energy of these remaining velocity fluctuations are negligible small inside this new laminar layer. Due to the remaining fluctuations, the resulting boundary layer may also be seen as quasi-laminar.

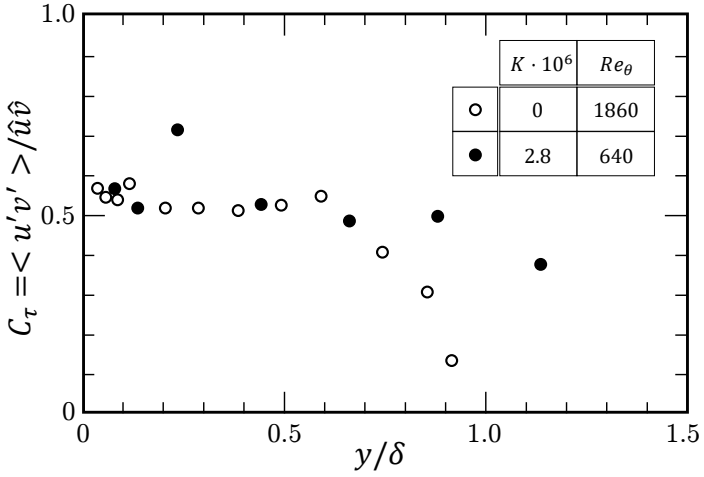

Figure 3.40: Comparison of the shear stress correlation coefficient for a ZPG $K = 0$ and FPG $K = 2.8 \cdot 10^{-6}$ case (same data as in Fig. 3.39 from Badri Narayanan et al. [105], adopted from [42])

For the time-mean flow during relaminarization, Narasimha and Sreenivasan [34] presented a quasi-laminar solution. Within their theory they used a two layer model of the boundary layer similar to Stratford [33] who discussed flow separation due to adverse pressure gradients.

The formulation of the model is done by using the two dimensional turbulent boundary layer equations according to [42]

$$\begin{aligned} \frac{\partial u}{\partial x} + \frac{\partial v}{\partial y} &= 0 \\ u\frac{\partial u}{\partial x} + v\frac{\partial u}{\partial y} &= -\frac{\partial p}{\partial x} + \nu\frac{\partial^2 u}{\partial y^2} + \frac{\partial \tau}{\partial y} \end{aligned} \tag{3.53}$$

and formulating the momentum equation separately for an outer inviscid layer [42]

$$u\frac{\partial u}{\partial x} + v\frac{\partial u}{\partial y} = -\frac{\partial p}{\partial x} \tag{3.54}$$

and an inner viscous flow [42]

$$u\frac{\partial u}{\partial x} + v\frac{\partial u}{\partial y} = -\frac{\partial p}{\partial x} + \nu\frac{\partial^2 u}{\partial y^2} \tag{3.55}$$

More details about their theory can be found in [34, 42].

From Eq. (3.54) Narasimha and Sreenivasan [42] draw following conclusion: According to the equation the total pressure head is conserved, leading to a rise of the inner velocity of the outer layer u_{o_i}, hence to a decrease of the difference $u_{o_i} - u_\infty$. In order to conserve the vorticity, the boundary layer thickness δ must decrease. This leads to an interesting behavior: Different Reynolds numbers behave differently during relaminarization. While Re_δ stays more or less constant, the plate Reynolds number Re_x rises whereas the momentum-thickness Reynolds number Re_{δ_2} (Re_θ) decreases.

Figure 3.41 shows a comparison of the quasi-laminar theory of Narasimha and Sreenivasan and measurement results of different research groups. Clearly a good agreement between experimental data and the theory can be observed during relaminarization. This also encourages the idea, that a new laminar layer is formed during relaminarization, thus supporting the quasi-laminar boundary layer theory.

The most right diagram (Fig. 3.41c) shows the distribution of c_f and Λ along the plate. The latter represents a non-dimensional pressure gradient defined as [42]

$$\Lambda = -\frac{\delta}{\tau_0} \cdot \frac{dp}{dx} \tag{3.56}$$

where δ represents the boundary layer thickness and τ_0 the turbulent wall shear just upstream of the relaminarization zone.

In the diagram again a good agreement between experiment and theory can be observed. However, downstream of relaminarization a retransition from laminar to turbulent can be observed (rise in c_f') in the experiments, which is not predicted by the theory. This process of retransition occurs, when the stabilizing pressure gradient (see Λ distribution) decreases, and distortions inside the inner layer trigger a sufficiently high turbulent energy production, leading to a fast retransition.

Narasimha and Sreenivasan [34] divided the boundary layer into three regimes. These are illustrated together with the c_f-distribution in Fig. 3.42. Regime I represents a fully

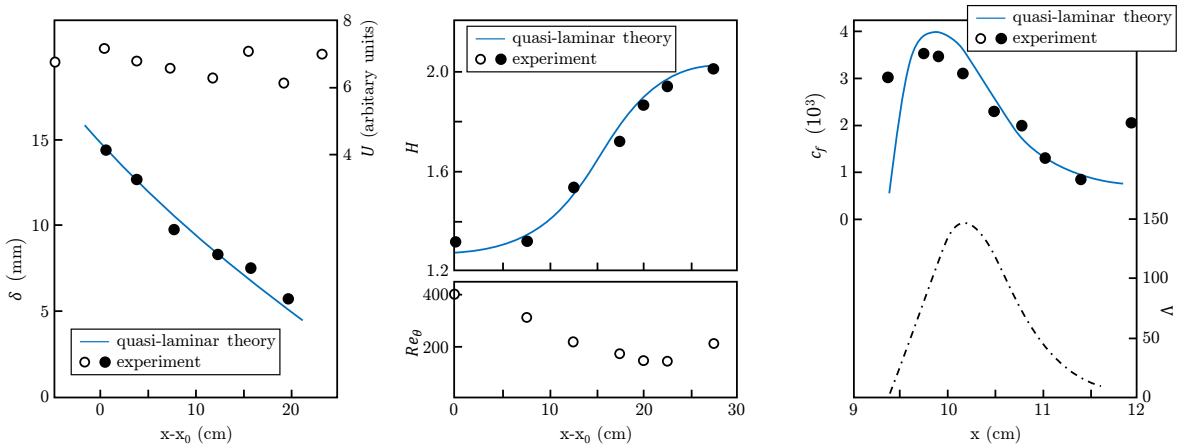

(a) with experimental data of Launder (1964) [36] showing the boundary layer thickness δ

(b) with experiments of Badri Narayanan and Ramjee [40] showing the shape factor H and the momentum-thickness Reynolds number Re_θ

(c) with experiments of Blackwelder and Kovasznay [41] showing the skin friction coefficient c_f

Figure 3.41: Distribution of various flow parameters comparing the quasi-laminar theory of Narasimha and Sreenivasan with experimental data (adopted and renewed from [42])

turbulent area upstream of relaminarization, whereas region III represents the quasi-laminar outer layer, which develops quickly at the beginning of the relaminarization zone. For these two areas, the c_f distribution in Fig. 3.42 show a good agreement with experimental data.

Region II represents a reverse transitional zone close to the wall. This relatively small, bubble shaped zone needs to be modeled and is not covered by the theory described above, since this zone is neither fully turbulent, nor quasi-laminar. However, this zone is relatively small and has a low impact on the mean flow.

Downstream of region II the quasi-laminar inner layer can be found, and again a good agreement of the c_f distribution is observable, until retransition takes place.

To sum up, this mechanism of relaminarization is not triggered by a higher turbulent dissipation compared to production, but the process is caused by "frozen" Reynolds shear stresses dominated by pressure forces. These forces are stabilizing the flow inside the new laminar boundary layer. However, fluctuations remain inside the laminar boundary layer, thus Narasimha and Sreenivasan speak about a quasi-laminar layer. When the pressure gradient decreases, the remaining fluctuations disturb the flow, leading to a high turbulent production which ends up in a fast retransition to a turbulent boundary layer.

A different explanation for the process of relaminarization due to acceleration has been given by Kline et al. [38] discussing the influence of the favorable pressure gradient on the burst rate F^+ (see Eq. (3.49)). As described in Sec. 3.3.3 the burst rate is proportional to a large share of the turbulence production. They stated, that F^+ decreases rapidly with an increasing FPG (see Fig. 2.3, page 16) which would lead to a lower turbulent production. Kline et al. extrapolated their measurement results and concluded, that the burst rate becomes zero ($F^+ = 0$) at $K = 3.7 \cdot 10^{-6}$.

Narasimha and Sreenivasan also found out, that F^+ decreases very rapidly with increasing Λ, but they did not find any evidence that the burst rate will be zero. So they state

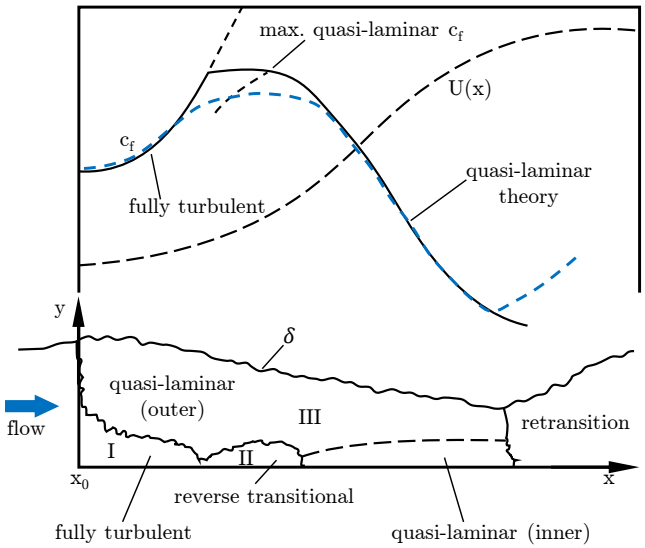

Figure 3.42: Schematic drawing of the different flow regimes together with the development of the skin friction coefficient c'_f, blue dashed line indicates experimental data (adopted and renewed from [34])

that it approaches zero asymptotically. In Fig. 3.43 their results supporting their findings are given, showing an exponential decrease of F^+ with increasing Λ. Therefore Narasimha and Sreenivasan are not convinced, that the reduction of the burst rate is the reason for relaminarization.

Note that beside F^+ also $\tilde{F}$ is given, which represents a different normalization of the burst rate suggested by Narasimha and Sreenivasan defined as

$$\tilde{F} = \frac{F \cdot \nu \cdot \delta_1}{U \cdot u_\tau} = \frac{1}{2} \cdot c'_f \cdot Re_{\delta_1} \cdot F^+ \tag{3.57}$$

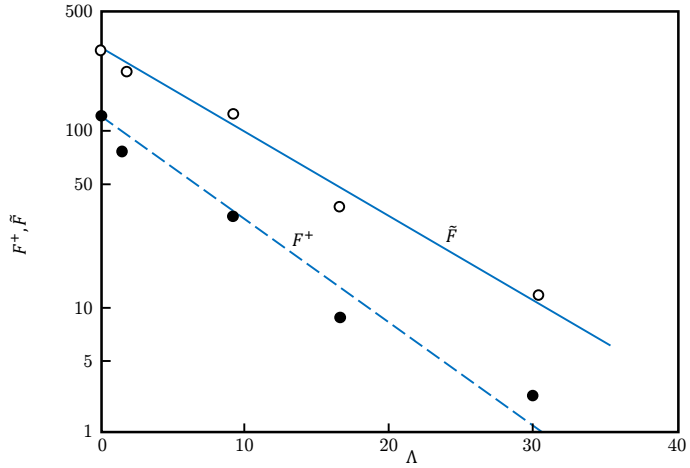

Figure 3.43: Distribution of the normalized burst rate $F^+/\tilde{F}$ over the acceleration factor Λ (data from Schraub and Kline [106], adopted and renewed from [34])

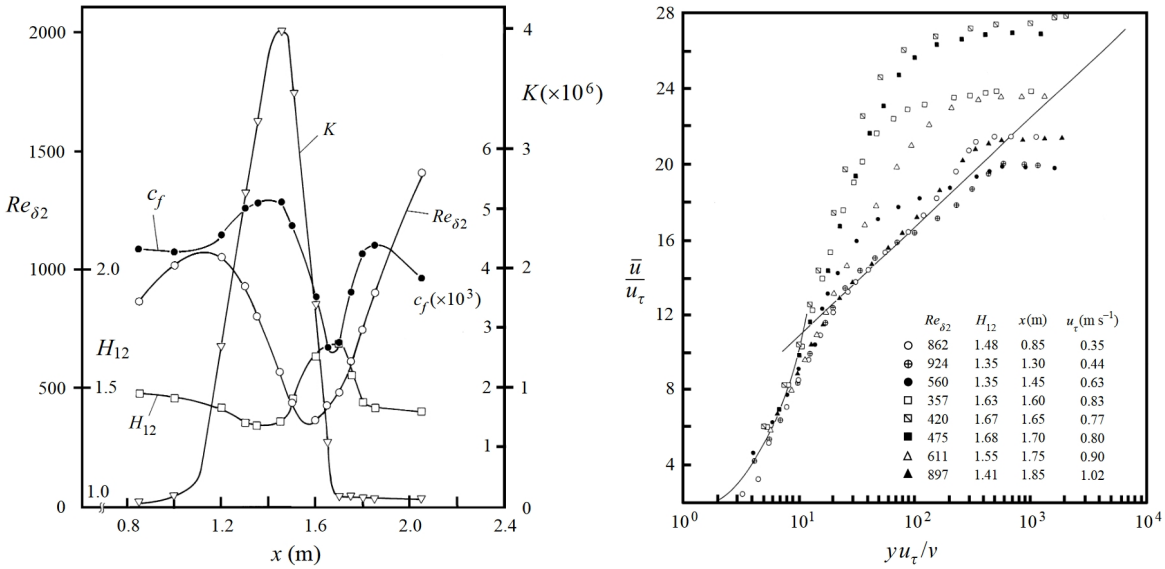

(a) Distribution of the acceleration parameter K, the skin friction coefficient c_f, the momentum-thickness Reynolds number Re_{δ_2} and the shape factor H

(b) Velocity profiles in wall coordinates y^+/u^+ at different streamwise positions together with the $y^+ = u^+$ curve and the law-of-the-wall as reference

Figure 3.44: DNS results of a relaminarizing flow [52]

However, the reduction of the burst rate does play an important role during the process of relaminarization, because a rapid drop of the burst rate does also mean a reduction of ejection, sweep and burst effects. This reduction is crucial for the building of the two layer model presented earlier in this section, since mixing of the layers is suppressed without the presence of these effects. Therefore it is essential for the validity of the quasi-laminar model, that F^+ decreases.

At the end of this section, the key developments of the skin friction coefficient c_f, the momentum-thickness Reynolds number Re_{δ_2}, the shape factor H and the velocity profiles during relaminarization are presented using DNS data of Warnack and Fernholz [52] in Fig. 3.44.

In Fig. 3.44a the streamwise distribution of the acceleration parameter K is given together with c_f, H and Re_{δ_2}. It can be clearly seen, that the acceleration parameter reaches a value above the critical one of $K_{crit} = 3 \cdot 10^{-6}$. The skin friction coefficient c_f first shows a rise up to a position, where K reaches its maximum. When the acceleration decreases, also the skin friction starts to drop. Downstream, where the stabilizing acceleration has nearly vanished, the remaining fluctuations inside the boundary layer promote a fast retransition which can be observed at about $x = 1.7$ m.

The momentum-thickness Reynolds number Re_{δ_2} shows a decrease during the zone of high acceleration. When the acceleration decreases Re_{δ_2} soon starts to increase again.

The shape factor H shows a slight decrease beneath the turbulent level of $H = 1.4$, which represents also a shift away from the laminar level of $H = 2.6$. This agrees with the overshoot of c_f above the fully turbulent level, which happens also at this streamwise position. As K decreases, the shape factor H shows a trend towards the laminar value, which is again in a good agreement with the c_f distribution. At the retransition position the shape factor drops rapidly towards the turbulent level.

For more insight in the development of the velocity profiles, in Fig. 3.44b the non-dimensional streamwise velocity in wall coordinates $u^+ = u/u_\tau$ is given against the non-dimensional lateral direction $y^+ = yu_\tau/\nu$ for several streamwise positions x. Beside the measurement results also the $u^+ = y^+$ line (lower left) and the log-law (see Eq. (3.39)) line are given as solid black lines. These lines represent the vicious (laminar) sublayer and the fully turbulent reference, respectively.

The first position, which lies upstream of the acceleration (see Fig. 3.44a) shows a fully turbulent profile. At the next given position, the boundary layer shows velocities lower than the law-of-the-wall. This represents also the area, where c_f and H show a trend above and below their turbulent reference values, respectively. More downstream it is observable that the velocity profiles tend more and more towards the laminar level, first close to the wall and as relaminarization continues, also the outer parts of the boundary layer start to agree with a more laminar shape of the velocity profile.

CHAPTER 4

METHOLOGY

> First I shall do some experiments before I proceed farther, because my intention is to cite experience first and then with reasoning show why such experience is bound to operate in such a way. And this is the true rule by which those who speculate about the effects of nature must proceed.
>
> Leonardo da Vinci
> ITALIAN POLYMATH

In this thesis transition and relaminarization have been investigated experimentally and numerically. For the experiments three different test benches have been used together with six measurement techniques. These are described in the following section 4.1. After this in section 4.2 the numerical models and methods are given.

4.1. Experimental Methods

4.1.1. Test benches

Experiments have been performed in three different wind tunnels which are described in the following. The tunnels labeled *A1* and *A2* are open-loop wind tunnels at the Institute for Thermal Turbomachinery and Machine Dynamics (ITTM) whereas *wind tunnel B* is a closed loop one at the Institute of Fluid Mechanics and Heat Transfer (ISW). In Tab. 4.1 an overview of these three tunnels is given with the boundary conditions and the measurement techniques used. More detailed operating and boundary conditions of the measurements in the different tunnels are given in the corresponding papers. Additionally the performed numerical computations performed are given in Tab. 4.1.

In the following the wind tunnels are explained with the measurement techniques used in the test sections. Details about the experimental techniques and instrumentation are given later in Sec. 4.1.2.

Table 4.1: Overview of the experiments and numerical studies performed in the different wind tunnels

Wind tunnel	A1	A2	B
Type	Open-loop		Closed-loop, Göttingen type
Compressor	Radial compressor, 125 kW		Two axial compressors, 2x37.5 kW
Inlet free-stream velocities	5.3 m/s 13.2 m/s	≈ 22 m/s[1] 14.79 m/s 18.12 m/s	5.2 m/s 10.8 m/s[2]
Inlet free-stream turbulence intensity	9.24 %	7.80 % 6.79 %	5.17 % 5.27 %
Transition measurement	• Preston tube • Thermography	• Preston tube • Acoustics	• Preston tube • Thermography • Hot-wire anemometry • Laser interferometric vibrometry • Laser-Doppler anemometry
Relaminarization measurements	—	—	• Laser-Doppler anemometry
Transition simulations	• RANS γ-Re_θ • RANS k-k_l-ω	• RANS γ-Re_θ[3] • RANS k-k_l-ω[3] • LES[4]	• RANS γ-Re_θ • RANS γ • RANS k-k_l-ω • LES
Relaminarization simulations	—	• RANS γ-Re_θ[4]	• RANS γ-Re_θ • RANS k-k_l-ω • LES

4.1.1.1. Wind tunnel A1

This wind tunnel was used for a feasibility study of measuring transition in wind tunnels with Preston tubes. In order to validate the Preston tube measurement results, also thermographic recording was applied to detect transition. The results of this study are presented in chapter 5, paper 1 (Sec 5.3).

The measurements were performed in a subsonic wind tunnel located at the Institute for Thermal Turbomachinery and Machine Dynamics. The test rig is a continuously operating open-loop wind tunnel. The air is delivered by a 125 kW radial compressor with a flow rate of approximately 0.6 kg/s. The compressor delivers the air into a flow settling chamber. From this chamber the air is transported via a flow-calming section formed by a diffusor with guiding vanes towards the test section. Figure 4.1a shows a picture of the subsonic compressor, settling chamber, air supply section and the diffusor. At the end of the diffuser honeycombs are installed in order to reduce velocity fluctuations and unsteadiness of the flow.

[1] Only for preliminary Preston tube measurements without turbulence measurements
[2] 9 m/s for the relaminarization case
[3] Results are presented in [107]
[4] Results are presented in [108]

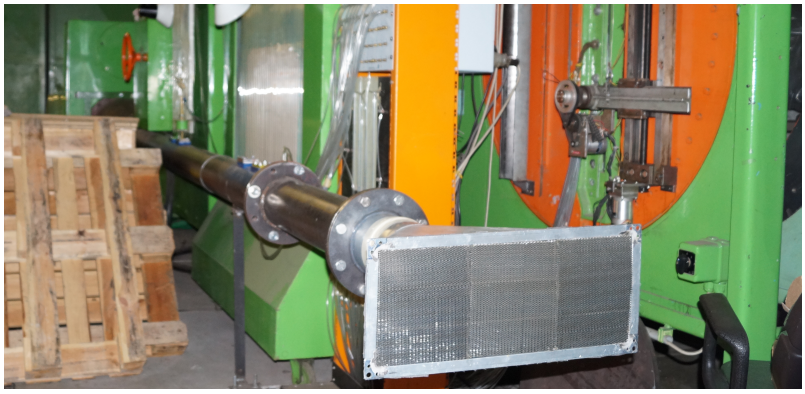

(a) Photograph of the wind tunnel up to the diffusor

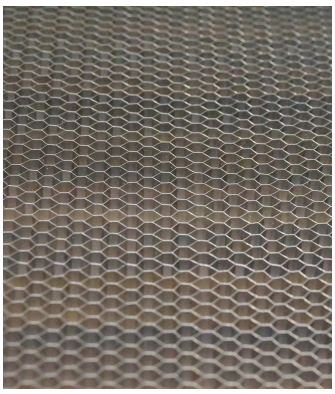

(b) Detailed view of the installed honeycombs

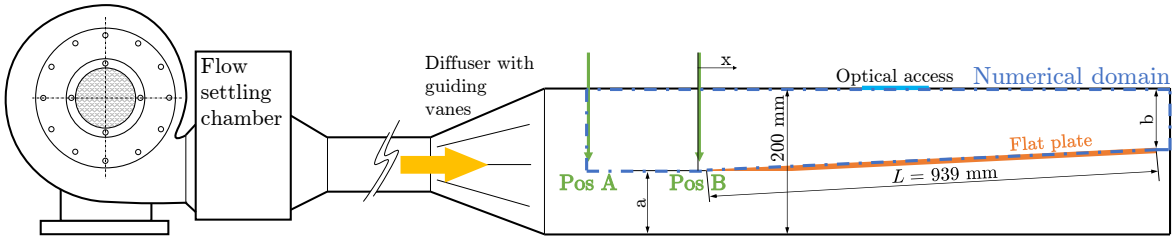

(c) Schematic drawing of the test bench showing (from left to right) the compressor, supply pipe, settling chamber, diffusor and test section

Figure 4.1: Wind tunnel A1

A detailed view of the used honeycombs is given in Fig. 4.1b. A schematic drawing of the whole test bench is shown in Fig. 4.1c.

The measurement plate is mounted in the middle of the tunnel and the boundary layer at the top surface is analyzed. The plate is inclined by 2° as recommended by Coupland [109] who performed the well-known ERCOFTAC (T3A, T3B, ...) flat plate experiments. This should ensure that the flow is attached to the plate without any leading edge separation. The plate is manufactured from a three millimeter thick metal plate to ensure a high stiffness. Along the plate several static pressure tappings with a diameter of 0.5 mm are embedded. These measurement positions are used for Preston-tube measurements.

The thermographic recordings of the heated plate have been made through an optical access at the top of the channel where a potassium-bromide (KBr) glass was mounted. This material has the characteristic that it is optically transparent for visible as well as for infrared light (from 0.23 to 4.0 μm).

Transition measurements have been performed for two different inlet velocities: $\overline{u}_\infty = 5.3$ m/s (low speed case) and $\overline{u}_\infty = 13.2$ m/s (high speed case). The tests were performed for two different channel cross sections WxH: 500x200 mm (low speed case) and 200x200 mm (high speed case).

At the inlet also turbulence intensity measurements have been performed using a fast response aerodynamic pressure probe (FRAPP).

A disadvantage of this tunnel is the relatively high opening angle of the diffuser. In order to suppress flow separation, guiding vanes are installed within this part. However, to

Figure 4.2: Photograph of the *wind tunnel A2* showing the elongated diffusor, test section and optical access (flow from left to right) [110]

improve the flow homogeneity further this tunnel has been adopted and will be presented as *wind tunnel A2* in the following section.

4.1.1.2. Wind tunnel A2

This wind tunnel is based on the design of *wind tunnel A1* with some improvements:

- Extended diffusor to prevent flow separation
- Elongated test section to ensure a fully developed flow
- Optical access on both side-walls of the plate to allow laser-assisted measurement techniques

Figure 4.2 shows a photograph of the tunnel where the elongated diffusor and test section are observable. Also the optical access is visible. In this tunnel Preston tube, FRAPP and acoustic measurements have been performed. For the latter it is very important to reduce all disturbing noise of the flow, which has been achieved successfully. More details of the design and first Preston tube measurements have been presented by Krasa [110].

Another focus on the design of the tunnel was to enable relaminarization measurements by acceleration. Therefore an acceleration can be achieved by a reduction of the cross section. In Fig. 4.3 the two plates which are used for a variable reduction of cross section are shown. For more details see [110].

Results obtained in this wind tunnel are presented in chapter 5, paper 2 (Sec 5.4) with a focus on transition measurement using microphones.

Wind tunnels *A1* and *A2* show good results, but due to their rather small dimensions also the boundary layers of the casing walls may influence the measurement. In order to reduce this influence of wall boundary layers, a larger wind tunnel has also been used, labeled as *wind tunnel B* which is presented next.

4.1.1.3. Wind tunnel B

The experiments were performed in the closed boundary-layer wind tunnel of the ISW. A sketch of the tunnel is given in Fig. 4.4. This Göttingen-type wind tunnel is powered by

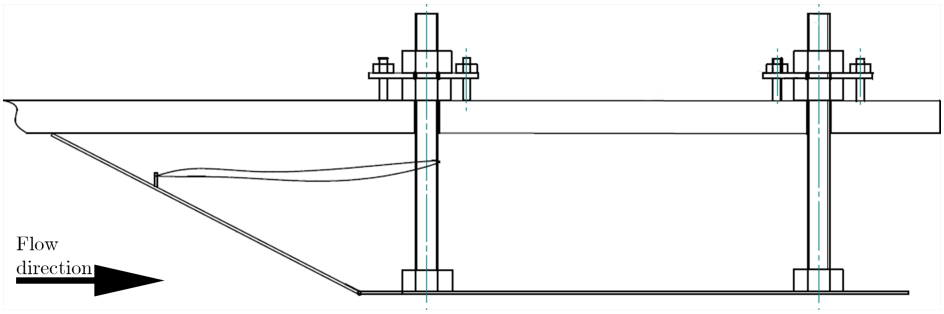

Figure 4.3: Acceleration plates with their mounting, flow from left to right [110]

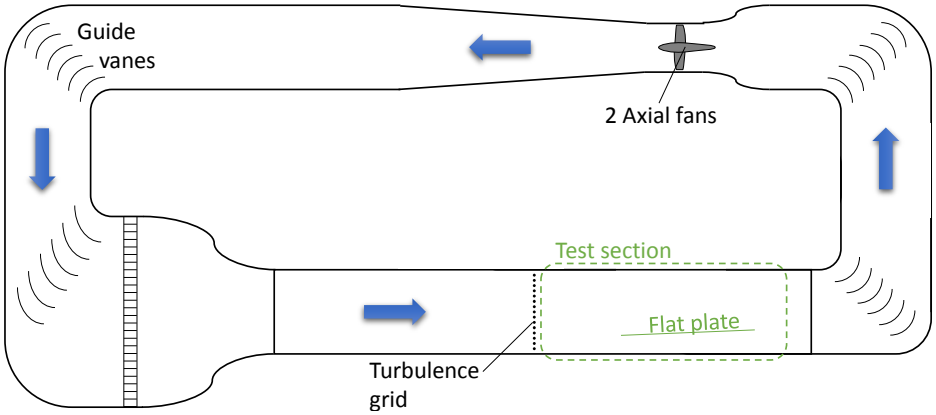

Figure 4.4: Sketch of the closed-loop Göttingen-type wind tunnel of the ISW

two axial fans with a total power input of 75 kW. The air is conveyed to a nozzle and the test section via two corners with guide vanes. The maximum achievable flow-rate equivalent velocity in the test section is about 30 m/s. The nozzle exit cross section is 2 m wide and 1 m high. Downstream from the nozzle, a 6 m long channel allows for developing flow velocity profiles. The test section itself is about 2.6 m long. The top panel of the tunnel is adjustable for setting a zero pressure gradient along the test section.

The turbulence intensity of the wind tunnel is well below 1 %. Therefore a turbulence generating grid is installed 2570 mm upstream of the investigated flat plate in order to raise the turbulence intensity to about 5 %, which is more representative for turbomachinery flows. The turbulence grid consists of equally spaced cylindrical rods. As suggested by Roach [111], the grid has a solidity below 50 %, and its position upstream from the first measuring point easily meets the $x/d > 10$ criterion, where x represents the streamwise distance and d the diameter of the rods. In the present case the turbulence grid consists of horizontal rods. The turbulence generated by horizontal rods is not isotropic, but this is not essential since a "2D" flow phenomenon is investigated. Hot wire measurements confirmed that at the first measurement position the individual wakes have completely smoothed out.

In this channel zero pressure gradient (ZPG) as well as favorable pressure gradient (FPG) flows have been measured. The latter is used to investigate relaminarization. For both the same flat plate is used. The plate is a 19 mm thick medium-density fiberboard and is mounted in such a way that the leading edge is at 205 mm height. This distance is used to ensure that

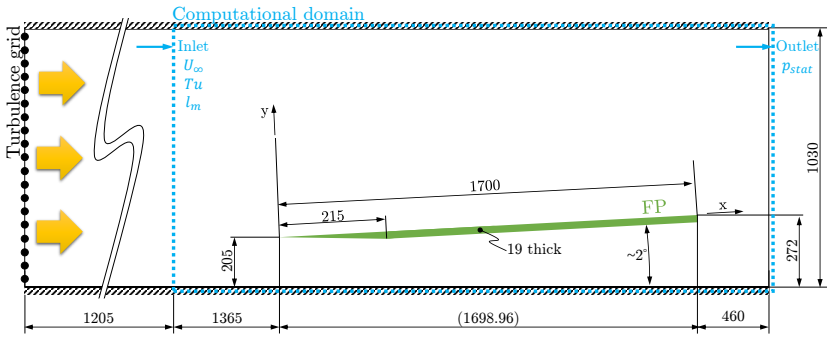

(a) Zero pressure gradient setup (Flat plate (FP))

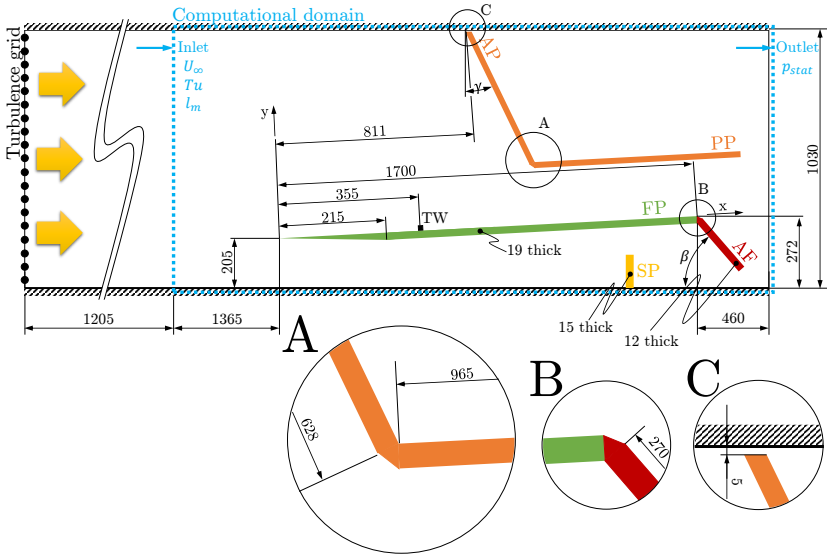

(b) Favorable pressure gradient setup (flat plate (FP), acceleration plate (AP), parallel plate (PP), adjustable flap (AF), stagnation plate (SP), trip wire (TW))

Figure 4.5: Detailed view of the zero and favorable pressure gradient cases

the boundary layer of the bottom channel wall does not extend to the leading edge of the plate. The plate has a length of 1700 mm and a width of 1500 mm. In respect to the channel width this results in a spanwise distance of 250 mm from each channel side wall, again to ensure no interaction with channel wall boundary layers.

1365 mm upstream of the plate leading edge the first measurement position is placed. At this position the inlet velocity, turbulence intensity and turbulent dissipation is determined. The latter is obtained by a numerical (CFD) fit comparing computed and measured turbulence intensity. Therefore the dissipation rate at the numerical inlet has been varied until the computed development of the turbulence fit with the five additional measurement locations placed downstream of the first (inlet) position.

The leading edge of the plate is sharpened to prevent a separation bubble and ensure a “clear” splitting in a flow above and below the plate. A schematic drawing is given in Fig. 4.5a. In this sketch also the computational domain is shown.

The plate is inclined by approximately 2 degrees. As for *wind tunnel A1* and *A2* one

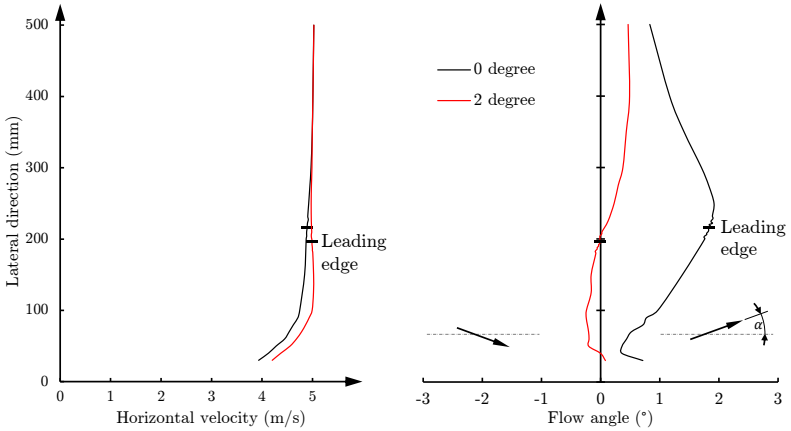

(a) Horizontal velocity $u(y)$ (b) Inflow angle α

Figure 4.6: CTA measurement results upstream of the leading edge of the plate with 0° and 2° inclination of the plate

reason is to ensure that the boundary layer is attached at the upper surface, but a second reason is to reach a zero incident inflow angle. In Fig. 4.6 hot-wire measurements are presented showing a comparison between 0° and 2° inclination. The measurements have been performed at midspan approximately 20 mm upstream of the leading edge. It is clearly observable, that the boundary layer of the lower wall does not hit the leading edge (see Fig. 4.6a) and that the incidence angle of the flow is reduced to zero upstream of the leading edge due to the inclination of the plate (see Fig. 4.6b). The reason of this effect is a slight suction underneath the plate due to the increasing cross section there.

The ZPG case was used to validate different measurement techniques, like Laser interferometric velocimetry (LIV) or Laser-Doppler anemometry (LDA). The results are presented in chapter 5, paper 3 (Sec 5.5).

In this channel also test cases for relaminarization by acceleration have been investigated. A schematic illustration is given in Fig. 4.5b. In order to accelerate the flow, the channel height cross section is reduced by a plate, called acceleration plate (AP). The inclination angle of the AP can be adjusted according the desired rate of acceleration. After a certain distance, a wall parallel plate (PP) is mounted subsequent to the AP. Since this reduction of cross section leads to a high blockage above the flat plate (FP), a flow resistance has to be installed below the plate. This has been achieved by using a fixed stagnation plate (SP) and an adjustable flap (AF) at the trailing edge of the plate.

In order to ensure that the boundary layer is turbulent upstream of the acceleration, a trip wire (TW) has been mounted at the plate for certain test cases. A picture of the test bench (without the tripwire) is given in Fig. 4.7. Along the plate static pressure tappings are mounted. In Fig. 4.8 the static pressure distributions along the plate taken from these tappings for three analyzed FPG cases are given. From the static pressure the velocity can be calculated with $u = \sqrt{2 \cdot (p_t - p)/\rho}$ assuming an incompressible flow (low Ma). This velocity is compared to LDA measurements in Fig. 4.8 where the acceleration of the flow is clearly visible. In the figure three different cases are compared: two low-speed cases and one high speed case, where the angle of the acceleration plate differs for the two low-speed cases.

Figure 4.7: Photograph of the relaminarization test section in *wind tunnel B*, flow from left to right

The used angle of the AP can be found in the legend of the figure. The pressure and LDA measurements show a good agreement for all three cases. Slight discrepancies can be seen for the high speed case, where the pressure measurement shows a higher velocity compared to LDA.

The acceleration can be varied by adjusting the angle of the acceleration plate. In order to reach similar flow conditions downstream of the acceleration zone despite the different inlet velocities, the parallel plate and the adjustable flap have to be adapted. The mechanism to adjust these three parts of the tunnel is shown in Fig. 4.9 and described in more detail by Pschernig [112].

Additionally it has been validated numerically and experimentally that separations and corner bubbles inside the channel do not interact with the boundary layer directly, meaning that these bubbles may influence the pressure gradient, but do not disturb the streamlines inside the investigated boundary layer. There are two bubbles present in the channel: One between the top wall and the acceleration plate (AP) and a second one downstream of the AP-PP edge which is attached to the parallel plate (PP).

In Fig. 4.10 the numerical and experimental validation of the setup is shown. The steady numerical results in Fig. 4.10a show a contour plot together with the streamlines at midspan. The bubble at the roof and the separation bubble is visible in the illustration. It can be observed, that both bubbles do not disturb the streamlines in the boundary layer along the BLP. However, as presented in paper 5, both bubbles do influence the pressure gradient distribution along the plate. Additionally, a numerical study has been performed for the small gap at the top end of the acceleration plate in order to reduce the size of the top-wall bubble.

Both bubbles have also been validated using light sheet visualization, also at midspan. The light sheet has been generated using a lens together with a 6 W Argon-Ion Laser. In Figs. 4.10b and c time-resolved photographs have been captured with a *Fastcam-SA 1* high speed camera by Photron® which records with a resolution of 1024x1024 pixels at $5,400$ frames-per-second and has a 12-bit CMOS sensor with a pixel size of 20 μm. The bubbles

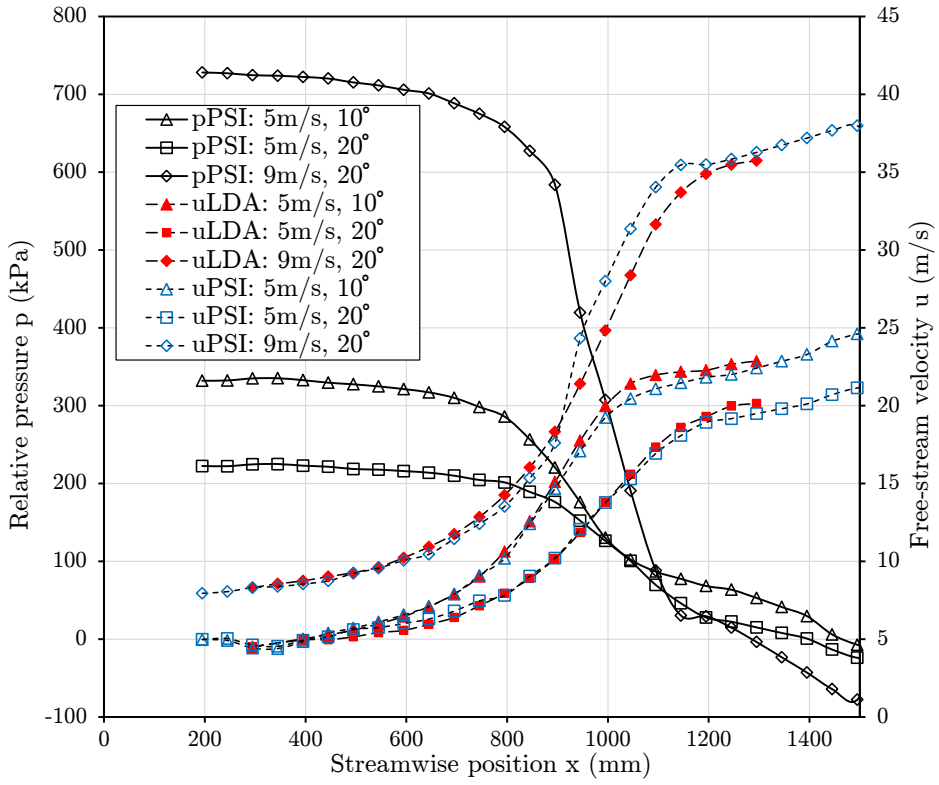

Figure 4.8: Distributions of the static pressure (solid lines) and velocity (dashed lines) along the plate measured with pressure tappings and LDA for three different FPG cases

are marked within the photographs. A good agreement with the computation results can be found, confirming that the bubbles do not disturb the boundary layer.

4.1.2. Measurement instruments and techniques

In the wind tunnels described above several measurement techniques have been used. Table 4.1 gives an overview which techniques are used in which setup. In the following these measurement techniques are described in detail. The physical measurement principle of the technique is explained together with the used instruments and their measurement accuracy.

4.1.2.1. Preston Tube

A Preston tube is traversed along the plate in the streamwise direction in order to locate the transition region. The probe is a Pitot tube with an inner diameter of 0.5 mm. The Preston tube allows the total pressure close to the wall to be measured. This pressure can be used to calculate the non-dimensional dynamic pressure according to [113]

$$\frac{q}{q_\infty} = \frac{p_{t,probe}(x) - p(x)}{p_{t,\infty} - p(x)} \tag{4.1}$$

where $p_{t,probe}(x)$ and $p(x)$ represent the local total and static pressures acquired by the probe and the tappings, and $p_{t,\infty}$ is the free-stream total pressure. The result gives an indication of

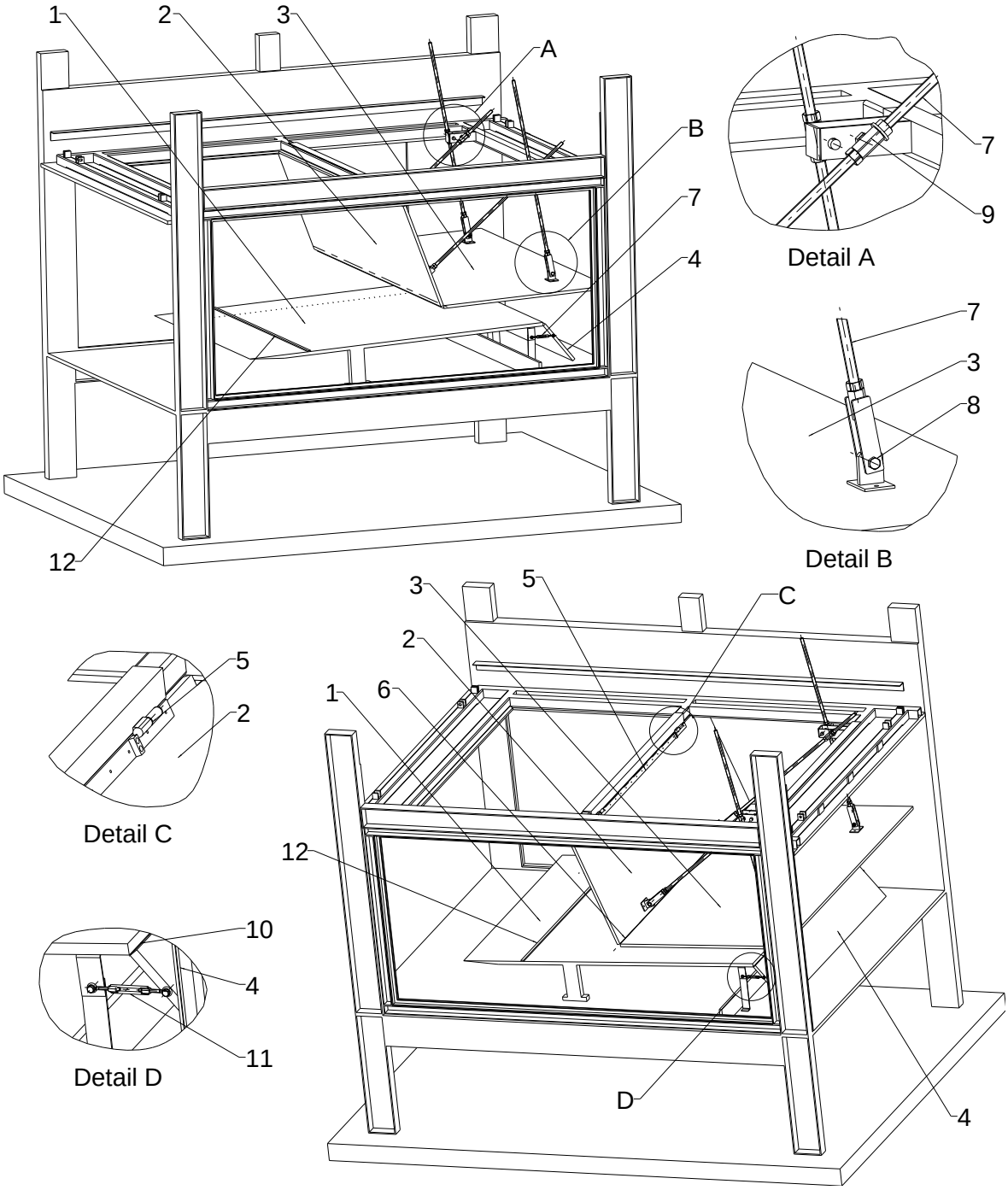

Figure 4.9: CAD drawing of the test bench *B* showing the mounting of the plates and mechanism for adjusting the adjustable flap (4), the acceleration (2) and parallel plate (3) in detail [112]

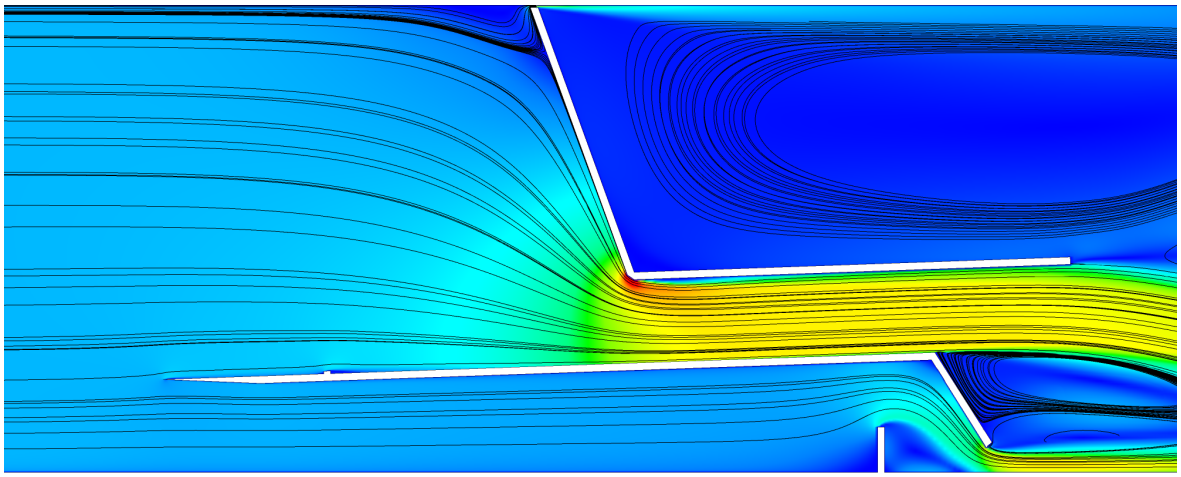

(a) CFD contour plot of the velocity together with streamlines

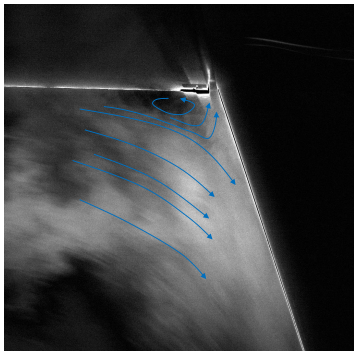

(b) light sheet visualization of the top wall-AP bubble

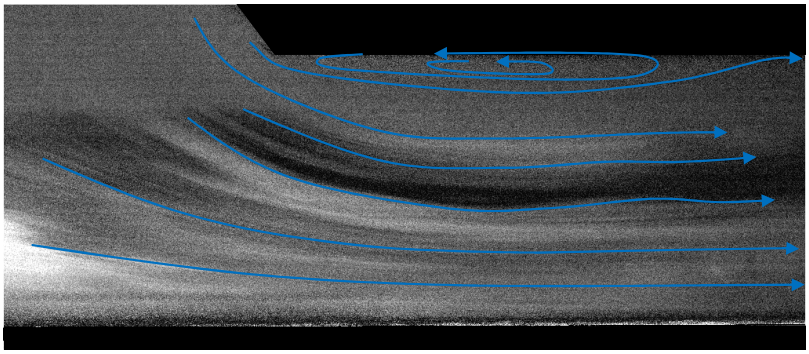

(c) light sheet visualization of the AP-PP bubble

Figure 4.10: Visualization of the two present bubbles in the test section at midspan

the shape of the velocity profile close to the wall, which is characteristic for the state of the boundary layer. Figure 4.11 explains this idea: The left sketch shows the different velocity profiles of the laminar and turbulent boundary layers. The steeper velocity gradient close to the wall in the turbulent boundary layer is due to the higher rate of momentum transport in the wall-normal direction because of its turbulent state. The right sketch in Fig. 4.11 shows the streamwise distribution of the non-dimensional total pressure $p_{t,probe}/p_{t,\infty}$ (denoted as q/q_1 in Fig. 4.11) and gives an example of its increase due to transition. The non-dimensional total pressure gives a similar trend as the non-dimensional dynamic pressure (Eq. (4.1)) on a flat plate due to the nearly constant static pressure $p(x)$ along the plate.

Three characteristic ranges of q/q_∞ can be distinguished: values of q/q_∞ around unity occur for probe positions at the edge or outside the boundary layer. Values between 0 and 1 occur for probe positions inside the boundary layer, and values close to zero indicate a separation bubble [113]. In the interpretation of the measurement results, however, the probe size must be accounted for, since the results are valid only for boundary layers whose thicknesses are at least twice the probe distance from the wall (y_1 in Fig. 4.11).

This measurement technique was used in all three channels but with different probes. For the channel *A1* the probe is shown in Fig. 4.12a with an additional static pressure probe at

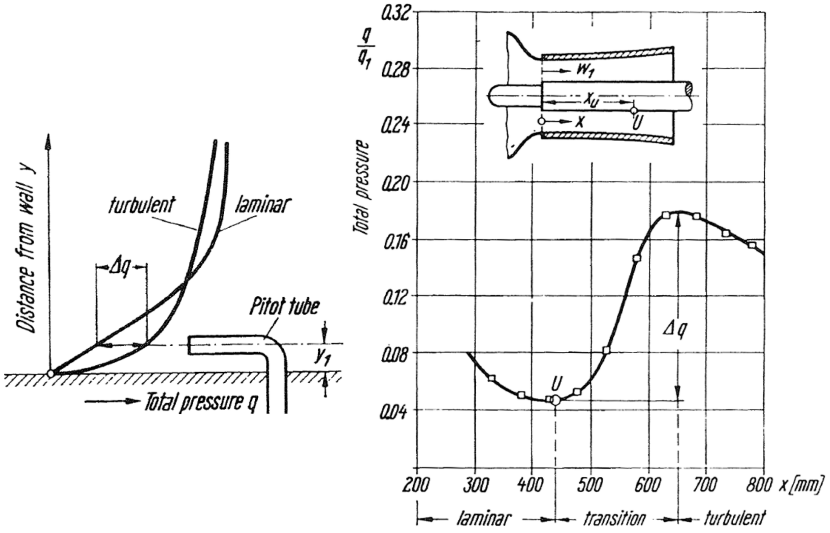

Figure 4.11: Concept of the Preston tube measurement [82]

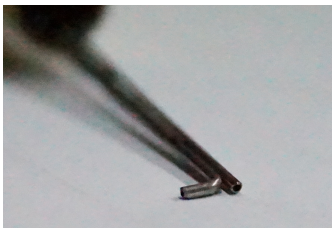

(a) used in channel *A1*

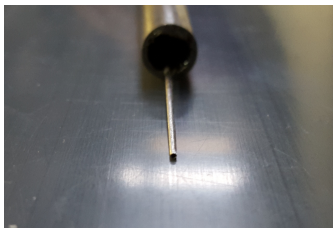

(b) used in channel *A2* [107]

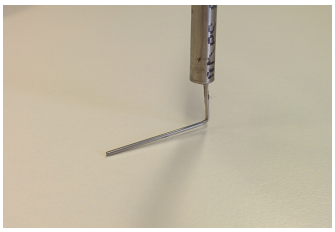

(c) used in channel *B*

Figure 4.12: Preston tube probes

the side of the Pitot tube; for channels *A2* and *B* the probs shown in Figs. 4.12b and c were used, respectively.

In channels *A1* and *A2* a NetScanner^{TM} pressure sensor, model 9116, was used. This sensor provides an accuracy of ± 0.05 % full scale and can sample up to 500 Hz. The scanner consists of 16 silicon piezo-resistive pressure sensors which measure a difference pressure. A reference pressure can be applied to the sensor, but in the present measurements the ambient pressure was used as reference for these measurements.

In channel *B* the pressure differences between the static tappings and the Preston tube were acquired with a differential pressure sensor PD9261 together with a data logger unit Clima Air 1 (both from *Rösler + Cie. Instruments GmbH*). The total system has been calibrated with the aid of a high-precision Betz-type manometer. The detected mean deviation from the reference values was 0.54 % in the relevant range.

4.1.2.2. Fast response aerodynamic pressure probe

The fast response aerodynamic pressure probe (FRAPP) consists of a thin 10 mm long cylindrical single-sensor probe. A miniaturized piezo-resistive pressure sensor (Kulite XCE-062) is mounted inside the probe head, which has an outer diameter of 1.85 mm. Figure 4.13a

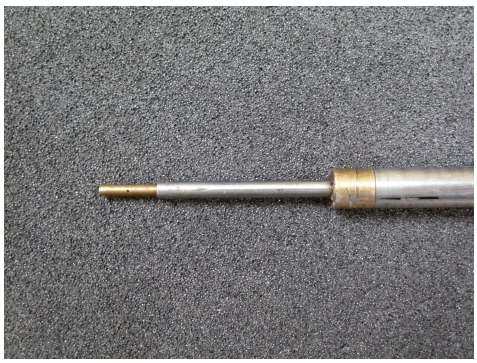

(a) Photograph of the probe

(b) cross section showing the pressure sensitive area

Figure 4.13: Fast response aerodynamic pressure probe

shows a picture of the probe and in Fig. 4.13b a cross section of the probe head is given showing the pressure sensor. The measurement bore with a diameter of 0.3 mm is clearly visible in both pictures. In Fig. 4.13b the pressure sensitive area is shown where the transducer records the pressure fluctuations.

Data acquisition has been performed using a DAQ-Board PCI-6052 which allows a resolution of 16 bit and a sample rate of 200 kHz. The probe is capable of measuring between 0°C and 80°C and up to a Mach number of 0.8.

The probe aerodynamic accuracy was evaluated in a calibrated nozzle, giving an extended uncertainty equal to ±0.5 % of the kinetic head for the pressure measurements and equal to ±0.3° for the flow angle. In order to obtain the transfer function of the probe, a dynamic calibration was carried out in a low-pressure shock tube; after digital compensation the probe bandwidth reaches up to 80 kHz. Persico et al. [114] presented more details about the probe design and calibration.

The FRAPP measurements in this work were used to measure the turbulence intensity Tu which can be calculated using

$$Tu = \frac{1}{\overline{u}} \cdot \sqrt{\frac{1}{N} \cdot \sum_{i=1}^{N} u_i'^2} = \frac{\hat{u}}{\overline{u}} \tag{4.2}$$

where $\overline{u}$ represents the mean velocity, u' the velocity fluctuations, $\hat{u}$ the root mean square value of the velocity fluctuations and N the number of samples. Therefore the measured pressure fluctuations have to be converted into velocity fluctuations. Equation (4.2) may be seen as the root mean square value of u_i divided by $\overline{u}$. In order to relate the total pressure fluctuations that are measured by the FRAPP probe to the velocity fluctuations, Persico et al. [114] provided the following formula, based on an approach by Wallace and Davis [115]:

$$\hat{p_t}^2 = 0.49\rho^2 \left(1 - 0.175\overline{Ma}^4\right) \widehat{u}^4 + \rho^2\overline{u}^2 \left(1 + 0.5\overline{Ma}^2\right) \hat{u}^2 \tag{4.3}$$

where $\hat{p_t}$ is the RMS value of the fluctuating total pressure, $\overline{Ma}$ represents the free stream

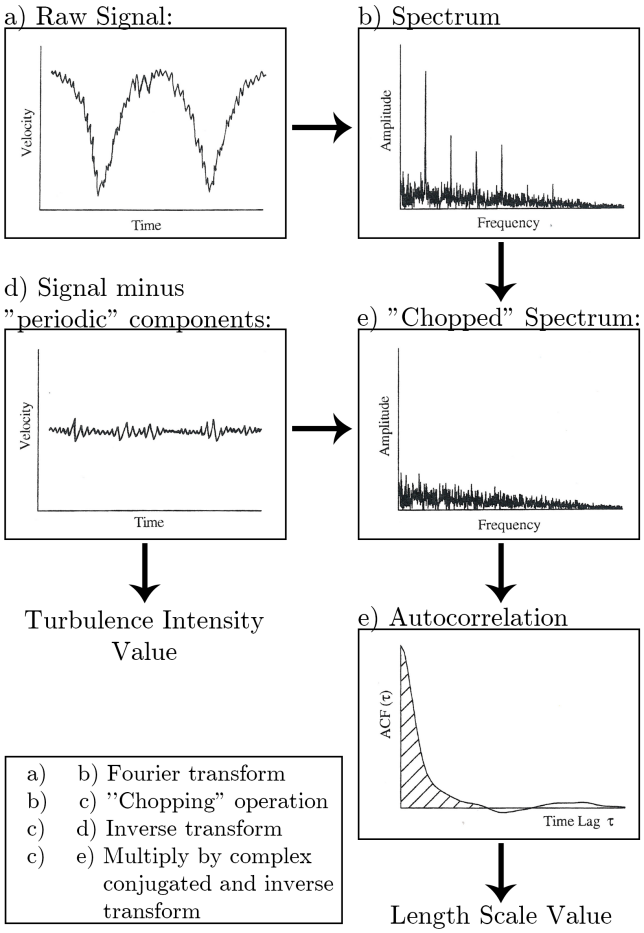

Figure 4.14: Illustration of the signal processing used for the FRAPP signal [117]

Mach number and ρ the fluid density. Reordering Eq. (4.3) leads to

$$\hat{u}^2 = \frac{-\rho^2\overline{u}^2 \pm \sqrt{\rho^4\overline{u}^4 + 4 \cdot 0.49\rho^2{\hat{p}_t}^2}}{2 \cdot 0.49\rho^2} \tag{4.4}$$

Before calculating $\hat{p}_t$ from the signal, it is necessary to remove all the periodic components of the measured raw signal, since only non-periodic stochastic parts of the signal represent turbulent fluctuations [116]. Therefore a procedure is used which was described by Camp and Shin [117] and is also exemplary given in Fig. 4.14. In order to perform this reduction, the measured signal is Fast Fourier Transformed (FFT) and the periodic components of the signal (like blade passing frequency and its harmonics) are "chopped" [117]. Only the non-periodic stochastic parts of the signal are modeled by a single-point turbulence model (like k-ω or k-ϵ) [116], hence this procedure is very important when using these values as CFD boundary conditions.

This chopped signal is illustrated in Fig 4.15, where the amplitude of the velocity fluctuations over the frequency is presented.

In this figure also the $-5/3$-line, known from the Kolmogorov-Obukhov [118–120] spectrum, can be observed. The spectrum shows, that the fluctuations fit the $-5/3$-line up to

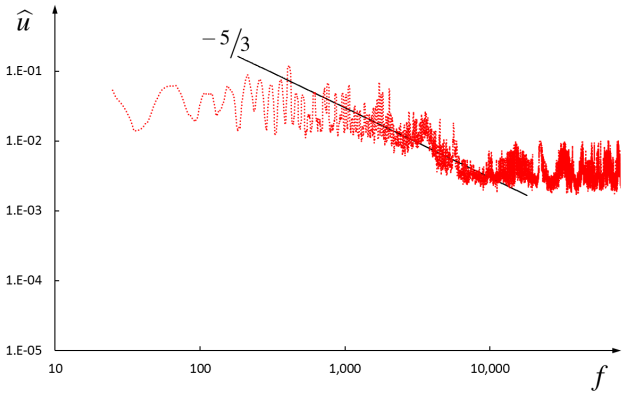

Figure 4.15: Moving average of the chopped velocity fluctuations over the frequency

about 10 kHz. Above this frequency it can be assumed that the detected fluctuations are caused by white noise and can not be considered as turbulence. Also low-frequency fluctuations (lower than 500 Hz) are assumed to have no contribution to the turbulence level. Thus, only the fluctuations between 500 Hz and 10 kHz have been taken into account for the calculation of the turbulence intensity.

The chopped and filtered spectrum was then processed with an inverse FFT to get a filtered time signal as also shown in Fig. 4.14. This time signal of the turbulent velocity fluctuations is then used to determine the turbulence intensity Tu according to Eq. (4.2).

An additional information which can be calculated from the FRAPP measurements is the turbulent length scale which describes the distribution of turbulent eddies, whether there are few large eddies, or many small ones. In Fig. 4.14 it is also shown how an autocorrelation of the chopped signal is used to calculate a characteristic length L describing this distribution. The autocorrelation function for a continuous signal is defined as [117]

$$ACF(\tau) = \frac{\frac{1}{\Delta T}\int_0^{\Delta T} u(t)u(t+\tau)dt}{\frac{1}{\Delta T}\int_0^{\Delta T} u(t)^2 dt} \tag{4.5}$$

where τ is the time-lag and ΔT represents the total time. The ACF adopts values between 1 and -1. According to Camp and Shin [117] by computing the ACF the integral length scale L can be derived with

$$L = \overline{u}\int_0^{\infty} ACF(\tau)d\tau \tag{4.6}$$

In practice the ACF function is integrated to the position where the ACF shows its first change of leading sign. Regarding numerical boundary conditions one should keep in mind that this physical integral length scale L is not equal to the mixing length l_m or the pseudo-integral scale l which are used by CFD codes.

A more detailed discussion of the measurement and signal processing of the FRAPP signal is given in [107].

4.1.2.3. Infrared thermographic recording

Another method to measure transition is to take into account the different heat transfer properties between a laminar and turbulent boundary layer. Since the heat transfer coefficient

depends highly on the state of the boundary layer, the surface temperature of a heated plate changes when the boundary layer transitions from laminar to turbulent, as described in Chap. 3. The correlation between Re_x and Nu_x and thus α is illustrated in Fig. 4.16 ($Pr = 0.71486$ for air at 20° C, 1 bar). In this graph the critical Reynolds number of $3 \cdot 10^5$ is assumed as transition onset criterion which is often stated in literature (see e.g. [23]).

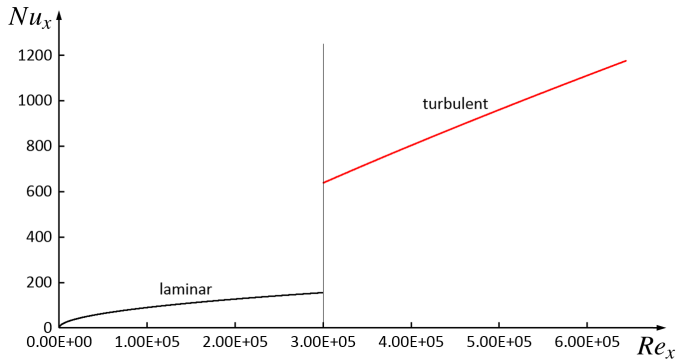

Figure 4.16: Nusselt number over Reynolds number for laminar and turbulent boundary layer

In order to measure transition using infrared thermography (IR), the thermal heating power output of a plate is held constant or a plate of constant temperature is cooled by the passing flow. The difference in wall temperature due to the different heat transfer coefficients of a laminar and turbulent boundary layer can be measured by an IR camera. The results of such measurements are discussed in chapter 5, paper 1 (Sec 5.3) and 3 (Sec 5.5), but also by Giepmann et al. [121], Joseph et al. [122] or Simon et al. [123].

Thermographic recordings have been performed for measurements in wind tunnels *A1* and *B*.

For the measurements in channel *A1* (presented in paper 1 (Sec 5.3)) a FLIR® SC620 thermographic camera was used which has a sensitivity of $< 40mK$ at $30°C$. The camera was placed above the optical access described in section 4.1.1.1 at the top of the channel (illustrated in Fig. 4.1c) and recorded about 100 *mm* of the plate length. The optical access was placed in such a way, that it is situated above the expected transition zone.

On the flat plate a heating foil by *thermo technologies* with a constant effective power output of 36 W was attached. In order to detect the transitional zone, the heating output was held constant and the temperature differences of the surface due to the laminar and turbulent boundary layer were recorded.

In contrast, the IR measurements for channel *B* (presented in paper 3 (Sec 5.5)) were made in a different way. The plate was heated to a constant, uniform temperature. Then the heating was switched off, and the plate cooled down at constant flow conditions for about 150 to 200 s, depending on the free-stream velocity. To quantify the uniformity of the temperature along the plate, the standard deviation of the initial mean temperature along the whole plate has been computed and is 0.56°C. The plate surface temperature was monitored over time, and the appearing temperature differences were used to determine the state of the boundary layer since the turbulent part cools faster due to the higher heat transfer.

For this purpose, we use the camera FLIR® T650sc with an accuracy of $\pm 0.1°C$. For heating the plate, five heating foils from *thermo technologies* with an effective output of 36 W each were mounted on the bottom side of the plate. This setup resulted in a homogeneous

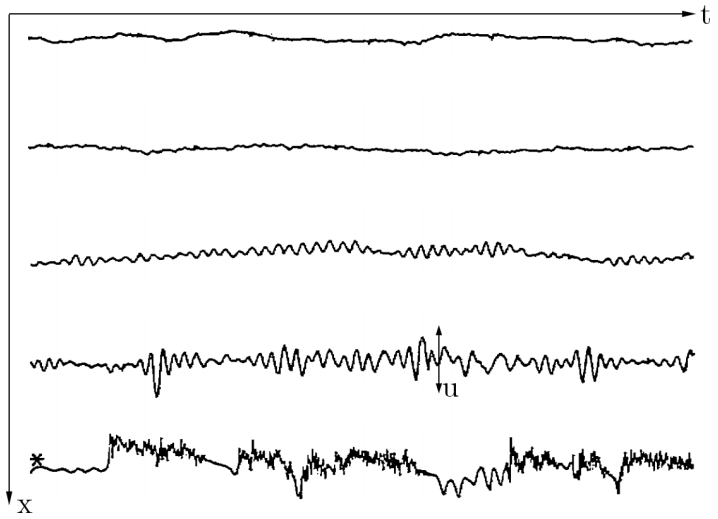

Figure 4.17: Velocity fluctuations measured with hot-wire within a boundary layer during transition (transition onset zone) [124]

heating of the plate. The foils were thermally insulated against the flow on the bottom side of the plate.

4.1.2.4. Microphone measurements

Another innovative measurement technique used within the frame of this work is the experimental investigation of the state of the boundary layer using microphones. An advantage is, that, since the microphones are flush-mounted, the flow is hardly disturbed. The idea is to measure the pressure fluctuations due to turbulent velocity fluctuations in a turbulent boundary layer. In Fig. 4.17 instantaneous velocity signals at different streamwise positions in the transition zone are given over time, showing the increase in velocity fluctuations from one position to the other (from top to bottom) aimed to measure with the microphones.

The microphones measure time-varying pressure, thus a coupling between the unsteady pressure and velocity fluctuations is necessary. The relation between the fluctuations can be expressed using the divergence of the Navier-Stokes equations in incompressible, two-dimensional, inviscid and steady-state form. This equation can be written as

$$\frac{1}{\rho}\nabla^2 p = -\frac{\partial u_i}{\partial x_j}\frac{\partial u_j}{\partial x_i} \tag{4.7}$$

where p represents the static pressure and indices i and j the two dimensions, in our case x and y direction. In order to split the equation into mean and fluctuating parts, Farabee [125] performed a Reynolds decomposition which leads to equation:

$$\frac{1}{\rho}\nabla^2\left(\overline{p}-p'\right) = -\frac{\partial\left(\overline{u_i}-u_i'\right)}{\partial x_j}\frac{\partial\left(\overline{u_j}-u_j'\right)}{\partial x_i} \tag{4.8}$$

Time averaging this equation yields to:

$$\frac{1}{\rho}\nabla^2\overline{p} = -\frac{\partial\overline{u_i}}{\partial x_j}\frac{\partial\overline{u_j}}{\partial x_i} - \frac{\partial^2\overline{u_i'u_j'}}{\partial x_j\partial x_i} \tag{4.9}$$

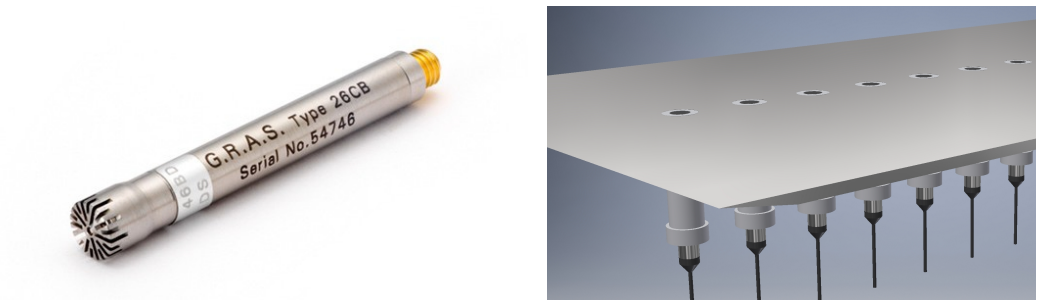

(a) Photograph of a G.R.A.S.® 40BD microphone (b) three dimensional drawing of the mounting of the microphones [107]

Figure 4.18: Microphone measurement details (wind tunnel *A2*)

By subtracting Eq. (4.9) from Eq. (4.8) a direct relationship between unsteady pressure and velocity fluctuations is obtained [107]

$$\frac{1}{\rho}\nabla^2 p' = -2\frac{\partial \overline{u_i}}{\partial x_j}\frac{\partial u_j'}{\partial x_i} - \frac{\partial^2\left(u_i'u_j' - \overline{u_i'u_j'}\right)}{\partial x_j \partial x_i} \tag{4.10}$$

This relation suggests, that the velocity fluctuations and their gradients lead to static pressure fluctuations. Therefore turbulent fluctuations can be measured by microphones, hence this measurement technique can be used to detect transition. [107]

Beside the measurements presented in this work (Chapter 5, paper 2 (Sec 5.4)) a similar approach has been used by Barrett [126], who presented also transition measurements with microphones.

The measurements presented here (see chapter 5, paper 2 (Sec 5.4)) have been performed in wind tunnel *A2*. The 24 microphones used are pre-polarized pressure microphones, model 40BD 1/4" by G.R.A.S.® with a high precision condenser technology (see Fig. 4.18a). The microphones have an accuracy for a frequency range from 4 Hz up to 70 kHz of ±2 dB and from 10 Hz to 25 kHz of ±1 dB, respectively. The microphones are flush mounted into the flat plate, as shown in Fig. 4.18b. In order to reduce noise and improve the signal quality a data processing similar to the one performed for the FRAPP measurements has been done (see Sec. 4.1.2.2). Additionally the Eigen-frequencies of the vibrations of the plate has been measured, using an impact hammer method. It is important to take this into account, because the microphones are mounted in the plate which is excited also by channel vibrations, thus it has to be ensured, that the flow and not the plate vibration is measured.

More details of the used equipment, mounting and signal processing are documented by Cinciripini [107].

4.1.2.5. Constant Temperature Anemometry

The measuring principle of constant temperature (or hot wire) anemometry (CTA) uses the cooling effect of a flowing fluid around an object, in particular a heated wire. The resulting convective heat transfer Q is proportional to the velocity u of the fluid according to [127]

$$\begin{aligned} Q &= (T_w - T_0)A_w h \\ &= A + Bu^n \quad \text{with } n \approx 0.5 \end{aligned} \tag{4.11}$$

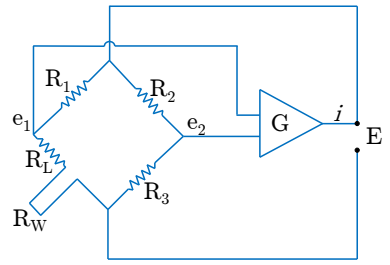

(a) Wheatstone bridge (renewed, original [127])

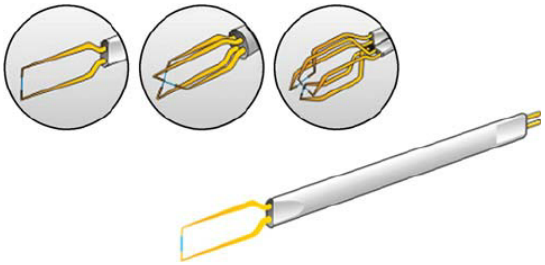

(b) Drawing of one, two and three-dimensional CTA probes [128]

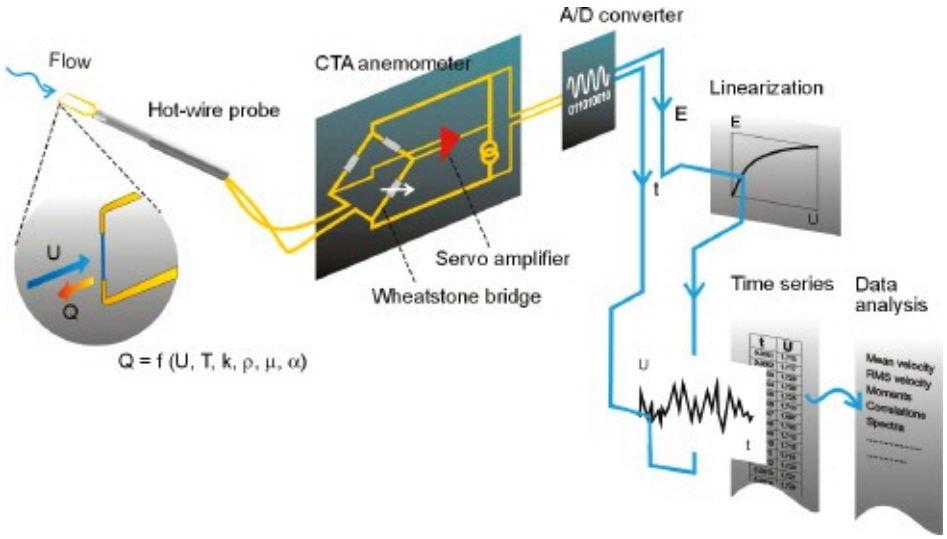

(c) Overview of the CTA system [127]

Figure 4.19: Constant temperature anemometry

where A_w is the wire surface, h the heat transfer coefficient, A/B are constants, T_w represents the temperature of the wire and T_0 of the fluid, respectively. The equation clearly shows the relation between the velocity u and the heat transfer Q. For CTA systems, the electrical resistance of the wire R_w is connected to one arm of a Wheatstone bridge (see Fig. 4.19a). A servo amplifier keeps the bridge in balance by controlling the current to keep the resistance of the wire R_w constant. In turn, a constant resistance corresponds to a constant temperature of the wire. So the current necessary to keep the bridge in balance is proportional to the heat transfer at the wire, hence the velocity. Systems sold today have a very high response to velocity fluctuations. Thus CTA systems are an ideal tool to solve high frequencies and therefore high turbulence frequencies. [127]

The voltage of the bridge and the velocity have an exponential or polynomial relation according to [127]

$$E^2 = (T_w - T_0) \cdot (A + Bu^n) \quad \text{or} \tag{4.12}$$

$$u = C_0 + C_1 E + C_2 E^2 + C_3 E^3 + C_4 E^4 + C_5 E^5 \tag{4.13}$$

With a calibration in a known flow the constants can be determined and the probe voltage can be converted into velocities (linearization). Additionally a compensation of the temperature

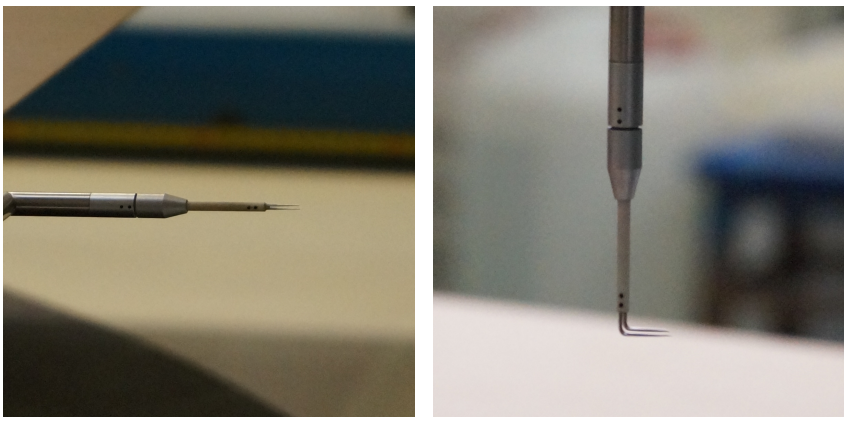

(a) Type 55P61 (b) Type 55P63

Figure 4.20: Used probes for the CTA measurements

is done with a temperature reference probe before the linearization. Lastly the measured signal is decomposed into the velocity components. [127]

CTA systems can measure one, two or three components of velocity fluctuations. In Fig. 4.19b the head of such probes is shown.

In Fig. 4.19c an overview of the of the system is given, showing the probe, the Wheatstone bridge with the sensor amplifier and the processing of the signal.

The hot wire measurements in this work have been performed in wind tunnel B using a multi-channel mini constant temperature anemometer system by Dantec Dynamics A/S. The probes used are two-dimensional probes, type 55P61 for the free-stream and 55P63 for the flow close to the wall. Both probes are shown in Fig. 4.20. The multichannel CTA of type 54N82 is used. For calibration the 54T29 velocity transducer is used together with the temperature probe 90P10.

The calibration of the probes has been performed directly in the channel, since the channel has a very low turbulence intensity and hardly any flow angle variations.

4.1.2.6. Laser Interferometric Vibrometry

Laser vibrometers are widely used to measure surface vibrations. In Fig. 4.21 the working principle of the vibrometer used in this work is shown: The Laser interferometric vibrometer consists of a He-Ne Laser where the beam is guided through a Mach-Zehnder-Interferometer. The Mach-Zehnder-Interferometer is an advancement of the Jamin-Interferometer and has been developed independently by Ludwig Mach[5] [129] and Ludwig Zehnder [130]. In this interferometer the beam is split into a reference and measurement (object) beam.

When the measurement beam hits a vibrating surface, the Laser beam is Doppler-shifted when reflected back into the interferometer. In this way the optical path length (OPL) is measured according to

$$OPL = n \cdot (z + \Delta z) \tag{4.14}$$

[5] Son of Ernst Mach

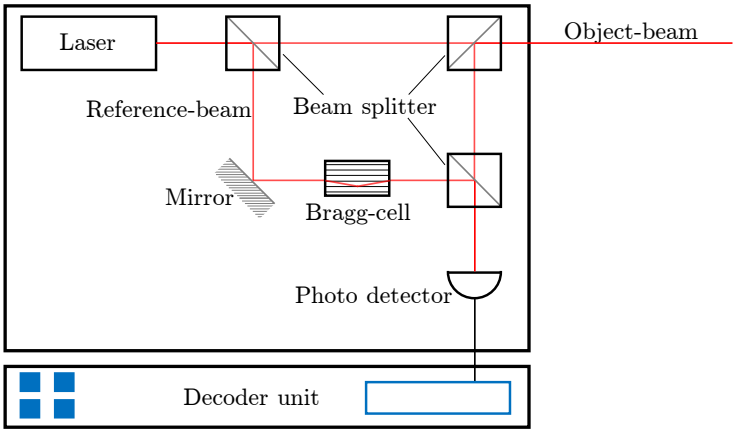

Figure 4.21: Working principle of a Laser interferometric vibrometry

where n represents the refraction index, z the geometrical path and Δz the amplitude of the vibration of the surface. The refraction index is defined with

$$n - 1 = G \cdot \rho \tag{4.15}$$

where ρ represents the density of the fluid and G the Gladstone-Dale constant.

Inside the Mach-Zehnder-Interferometer the reference beam is Doppler-shifted with an acousto-optic modulator (AOM), namely a Bragg-cell. The cell has been developed by the physicist and physic-Nobel-price winner William Henry Bragg. The working principle is shown in Fig. 4.22. Inside the Bragg-cell a part of the beam is modulated by an ultrasonic wave. The beam leaving the AOM is Doppler-shifted by an amount equal to the frequency of the acoustic-wave F:

$$f \rightarrow f + mF \quad \text{or} \tag{4.16a}$$
$$\omega \rightarrow \omega + \Omega \quad \text{(see Fig. 4.22)} \tag{4.16b}$$

After the Bragg cell the reference beam is superimposed with the measurement beam leading to a beat of the resulting signal. This signal is then processed and is proportional to the OPL. Without the Bragg cell and therefore without an frequency shift, the detected intensity would be [131]

$$I = \frac{I_0}{2} \cdot (1 + cos(2\pi(\pm\Delta f)t)) \tag{4.17}$$

where $\pm\Delta f$ represents the difference between the frequency of the reference beam f_S and the frequency of the measurement beam after having been reflected by the surface f_M ($\pm\Delta f = f_S - f_M$). It can be clearly seen in Eq. (4.17) that due to the cosine-function it is not possible to detect whether the sign of the frequency difference $\pm\Delta f$ is positive or negative, thus the direction of the vibration of the measured surface can not be determined. By modulating the reference beam in a Bragg-cell with a Doppler frequency of F the detected intensity can be computed with [131]

$$I = \frac{I_0}{2} \cdot (1 + cos(2\pi(F \pm \Delta f)t)) \tag{4.18}$$

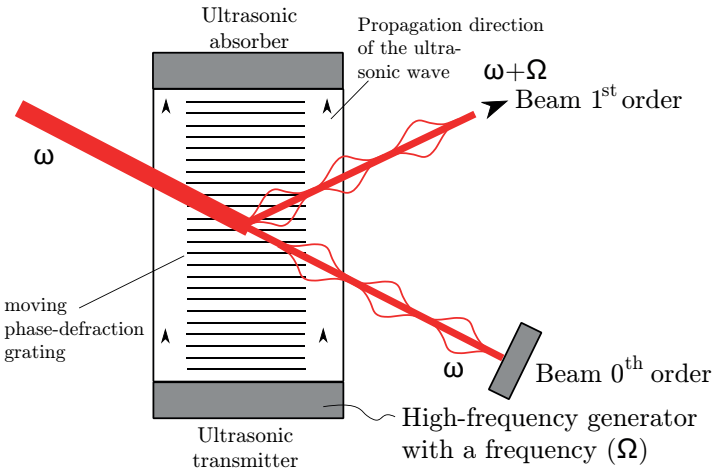

Figure 4.22: Working principle of an acousto-optic modulator (AOM), Bragg-cell [132]

Now it is possible to determine also the direction of the vibration.

If the surface which reflects the measurement beam is a rigid mirror, Δz of Eq. (4.14) equals to zero. Thus the optical path length is a function of the refraction index and therefore of the density. If the density is not constant, the Laser vibrometer can detect density fluctuations $\partial\rho/\partial t = \rho'(t)$. These fluctuations are integrated along the line-of-sight (LOS). This results in

$$OPL'(t) = G \int_0^{LOS} \rho'(t) dz \tag{4.19}$$

Regarding transition measurements it is assumed that the velocity fluctuations $u'(t)$ inside the boundary layer result in density fluctuations $\rho'(t)$. Therefore velocity fluctuations integrated along the line-of-sight are proportional to the change in $OPL'(t)\,[\propto \rho'(t)] \propto u'(t)$.

If the Laser beam shines through a laminar boundary layer, no integral density fluctuations are recorded, since the laminar boundary layer shows no fluctuations.

In a fully turbulent boundary layer also no integral fluctuations can be detected, since the mean value (integrated along LOS) of the velocity fluctuations of a fully turbulent boundary layer is again zero, although local fluctuations are present.

In the transitional zone, however, the integrated change of density is not equal to zero, because there are smaller and larger structures in the LOS, which eventually do not average to zero. Thus the transitional zone can be detected with the Laser interferometer. Theses three different states are illustrated in Figs. 4.23a to c.

For the measurements in wind tunnel B the Laser beam lights over the entire width and is reflected back from a rigid surface mirror. A schematic drawing of the setup is given in Fig. 4.24a. This mirror is mounted on a massive steel box filled with sand to reach a very low Eigen-frequency of approximately 10 Hz. This allows to easily differ between vibrations of the mirror and density fluctuations within the flow. Additionally the window in front of the laser which represents the optical access is tilted in respect to the X and Y axis, so that reflections at this glass window do not affect the measurement signal.

A lens in front of the LIV is adjusted in such a way that the Laser beam is cylindrical along the optical path. This lens and the used LIV are shown in Fig. 4.24b.

The laser beam was traversed over the length of the plate and the lateral direction in such a way, that the center of the beam is approximately in the middle of the boundary layer ($y_{beam} \approx \delta(x)/2$). The diameter of the laser beam is about 3 mm. It has to be kept in mind, that as long as the beam diameter is larger than the boundary layer thickness, the laser beam also reads parts of the free-stream.

This rather unconventional measurement tool for experimental investigations of boundary layer transition has been successfully tested within this work and the results are presented in chapter 5, paper 3 (Sec 5.5).

4.1.2.7. Laser-Doppler Anemometry

Laser-Doppler anemometry (LDA) is a common tool for measuring mean velocities together with turbulent fluctuations and statistical properties. LDA is an indirect, non-invasive measurement technique which uses tracer particles to measure velocities. In Fig. 4.25 the working principle is shown: A monochromatic Laser beam is split into a beam splitter in two beams of same intensity. The intensity of both beams have a Gaussian distribution over their diameter. A lens focus both beams into a point, which represents the so-called measurement volume. The resulting measurement volume is an equipotential ellipsoid as shown in Fig. 4.25. The two beams interfere with each other creating an interference fringe pattern in the measurement volume. If a tracer particle passes through this volume, it creates a burst due to the interference pattern, because it passes through darker and brighter zones. The frequency f_b of this burst is then detected by a photodetector and can be converted into the particle velocity $u_{P,\perp}$ according to

$$u_{P,\perp} = f_b \cdot \Delta x \tag{4.20}$$

where Δx represents the spacing between two interference fringes.

As indicated by the $\perp$ symbol, the velocity can be detected in the direction normal to the optical axis of the the two laser beams. In order to measure additional directions, it is necessary to focus two or more additional beams inside the measurement volume. In order to allow the photodetector to distinguish between the different beams and therefore directions, different wave lengths are used for different directions. Most common wavelengths are $\lambda = 514.4$ nm (green), 488 nm (blue) and 476.5 nm (violet).

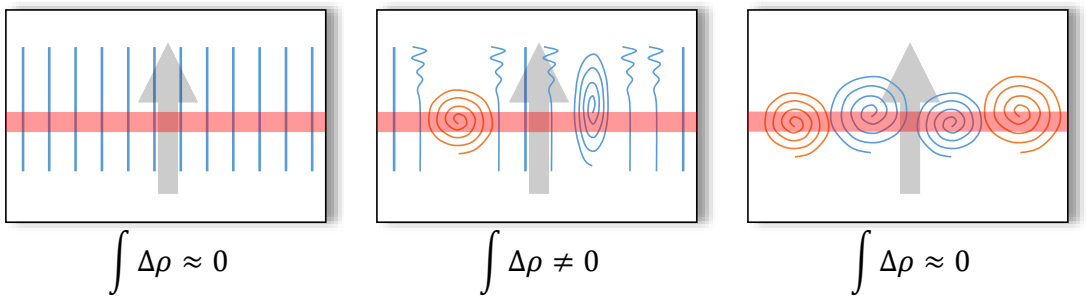

(a) Laminar boundary layer (b) Transitional boundary layer (c) Turbulent boundary layer

Figure 4.23: Measurement principle of transition detection with Laser interferometric vibrometry (red horizontal line indicates the Laser beam)

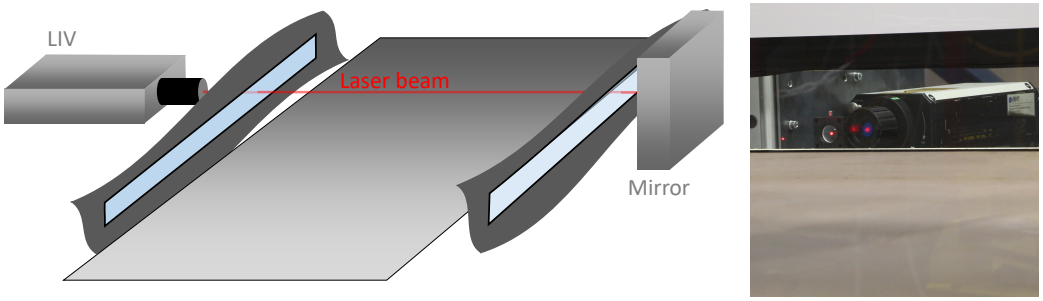

(a) Schematic drawing of the setup

(b) Photograph of the used LIV system and optical access and lens

Figure 4.24: Details of the Laser interferometric vibrometer

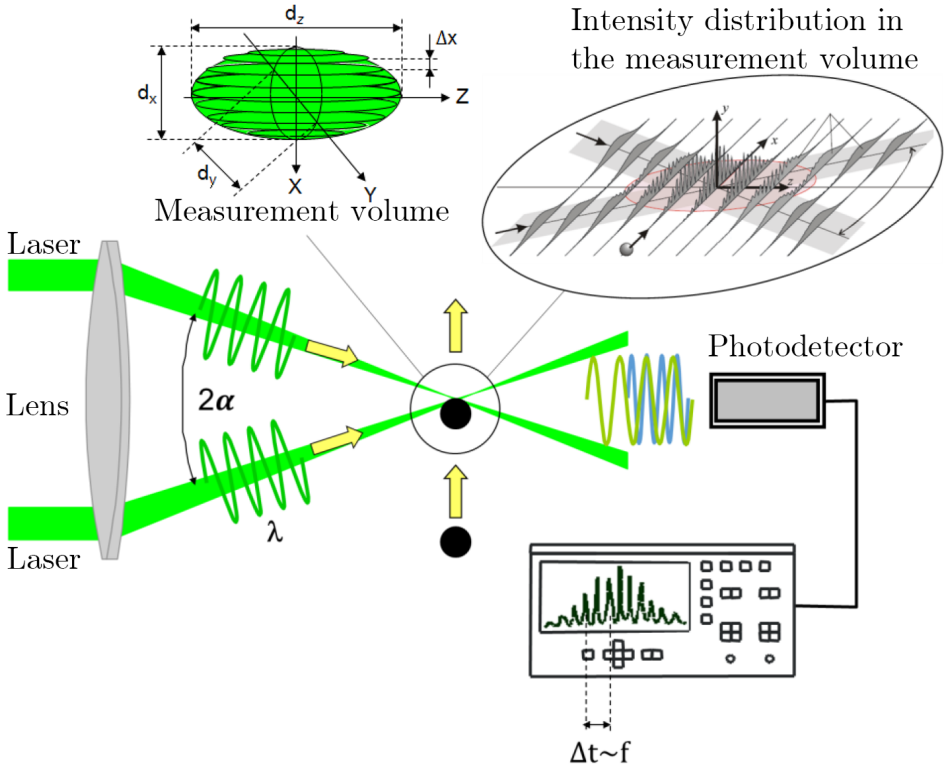

Figure 4.25: Measuring principle of the LDA system (adopted from [133, 134])

The principle of the LDA measurement technique can also be explained with the eponymous Doppler-Effect. This effect dates back to the Austrian mathematician and physicist Christian Doppler. When a particle passes through the measurement volume, the particle approaches one beam and removes from the other. According to the effect described by Doppler this results in two signals with slightly different frequencies, which then results in a beat with a burst-like shape. This resulting burst is again velocity proportional and has a frequency f_b (see Eq. (4.20)). [112]

The size of the equipotential ellipsoidal measurement volume d_x, d_y and d_z depends on

the angle between the two beams 2α. The focal length of the lens f_{FL} and the beam distance of the two Laser beams influence this angle (see Fig. 4.25).

The beam diameter d_f ($= d_y$ in Fig. 4.25) within the measurement volume can be calculated with

$$d_f = \frac{4}{\pi} \frac{f_{FL} \cdot \lambda}{d_L} \tag{4.21}$$

where d_L represents the beam diameter before the lens and λ the wave length of the Laser beam.

For the size of the measurement volume we can then derive

$$d_x = \frac{d_f}{cos(\alpha)} \tag{4.22}$$

$$d_y = d_f \tag{4.23}$$

$$d_z = \frac{d_f}{sin(\alpha)} \tag{4.24}$$

and further for the spacing between two interference pattern fringes

$$\Delta x = \frac{\lambda}{2 \cdot sin(\alpha)} \tag{4.25}$$

Finally the velocity of a passing particle can then be computed with

$$u_{P,\perp} = \frac{f_b \cdot \lambda}{2 \cdot sin(\alpha)} \tag{4.26}$$

It can be clearly seen, that the values of Eq. (4.26) do not depend on any calibration as it is necessary for e.g. CTA systems (compare Eq. (4.13)), which represents a big advantage of LDA systems.

Another matter which can be concluded from Eq. (4.26) is that the direction of a particle cannot be distinguished. The directional sensitivity can be achieved by shifting the frequency of one Laser beam slightly. The shift of the second beam is done by a Bragg-cell which is explained in Sec. 4.1.2.6. The different frequencies of the two beams lead to a moving interference pattern inside the measurement volume. The result is a different bursting frequency f_b modulated with a modulation frequency f_s depending on the direction a particle is moving. The resulting frequency is then lower ($f_b < f_s$) or higher ($f_b > f_s$) than the modulation frequency depending on if the particle is moving against or in the direction of the interference pattern moving direction, respectively. Figure 4.26 shows the differences between a setup with and without the modulation of the second beam. The diagrams given in Fig. 4.26 show the relation between the detected burst frequency f and the recorded particle velocity v. Particles (A) and (B) have the same velocity value, but an opposite moving direction. In the upper sketch, which represents a setup without frequency shift, the same frequency is detected for both particles, thus the system cannot distinguish between the moving directions. In the lower sketch one can clearly observe, that the different moving directions result in different detected burst frequencies.

The signal of the bursts detected by the photomultiplier are then processed in the so-called burst spectrum analyzer (BSA). Within this unit the bursts are filtered according to several criteria, amplified and counted and then the velocity is calculated. Additionally,

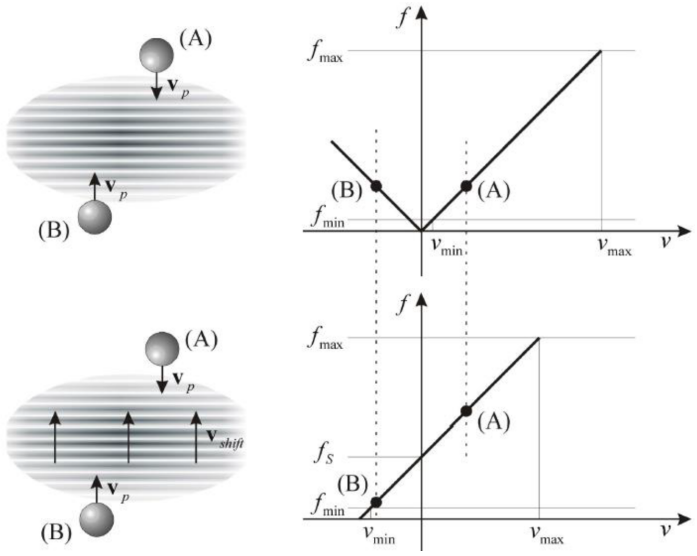

Figure 4.26: Principle of the directional sensitivity of an LDA system depending on the modulation of the second beam [134]

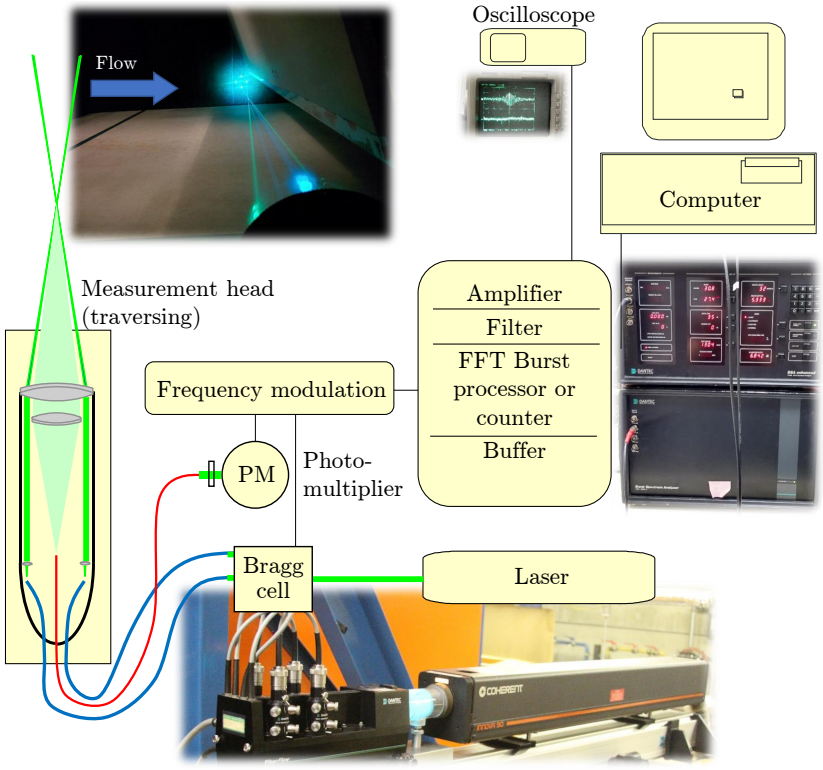

Figure 4.27: Scheme of the LDA system together with some used equipment (adopted from [133])

Table 4.2: Most important parameters of the used LDA system, optics and measurement volume (adopted from [112])

			BSA1	BSA2
Optics	Wave length λ	nm	514.5	488
	Color		green	blue
	Focal length f_{FL}	mm	1000	
	Beam diameter (lens exit) d	mm	2.2	
	Focused beam diameter d_f (Eq. (4.21))	mm	0.150	0.143
	Beam distance	mm	38	
	Enlargement factor	mm	1.98	
	Enlarged beam distance	mm	75.24	
Measurement volume	Number of interference lines	-	21	
	Distance between interference lines Δx (Eq. (4.25))	μm	6.844	6.492
	Half beam opening angle α	°	2.154	
	d_x (Eq. (4.22))	mm	0.150	0.143
	d_y (Eq. (4.23))	mm	0.150	0.143
	d_z (Eq. (4.24))	mm	4.001	3.795

statistical data like the standard deviation σ, the skewness S and the flatness (or kurtosis) F are calculated.

In Fig. 4.27 a schematic drawing of the LDA system is given. Additionally some photographs of the used equipment for the LDA measurements in wind tunnel B are shown. The light source is a 6 W Argon-Ion Laser of the type Innova 90 by *Coherent*. The beam enters a FibreFlow system by *Dantec Dynamics A/S*. First the beam is split in a wavelength-dependent beam-splitter into two monochromatic beams (in this case into two wavelengths $\lambda_1 = 514.5$ nm, $\lambda_2 = 488$ nm), one wave length per measurement direction. For each wavelength the beam is split again into two separate beams where the second beam is frequency shifted by the above described Bragg-cell. A 60 mm probe head (60x67 2D probe) with an enlarged beam distance of 75.24 mm, a focal distance of 1000 mm and a beam diameter of 2.2 mm (in front of the lens) was used as the laser light transmitter. The bursts are also "seen" by the same optic (see Fig. 4.27) and are forwarded towards a color separator to distinguish between the two measured velocity directions and a photo multiplier/detector (60x41 FiberFlow transmitter by *Dantec Dynamics A/S*). The signal is then processed by two burst spectrum analyzer processors (one for each direction), 57N35 model S (BSA1) and 57N20 (BSA2) by *Dantec Dynamics A/S*. The most important values of the used setup are summarized in Tab. 4.2.

The measurement uncertainties of the LDA system mainly depend on the number of independent samples (bursts) n and the turbulence level Tu and can be calculated with the Student's t distribution for the mean value $\overline{u}$ yielding

$$Mean_{err} = \pm t_{1-\alpha;n-1} \frac{\sigma}{\sqrt{n}} \tag{4.27}$$

where $t_{1-\alpha;n-1}$ represents the quantile of the Student's distribution, n the number of independent samples and $1-\alpha$ the confidence interval. With a confidence interval of 95 % this

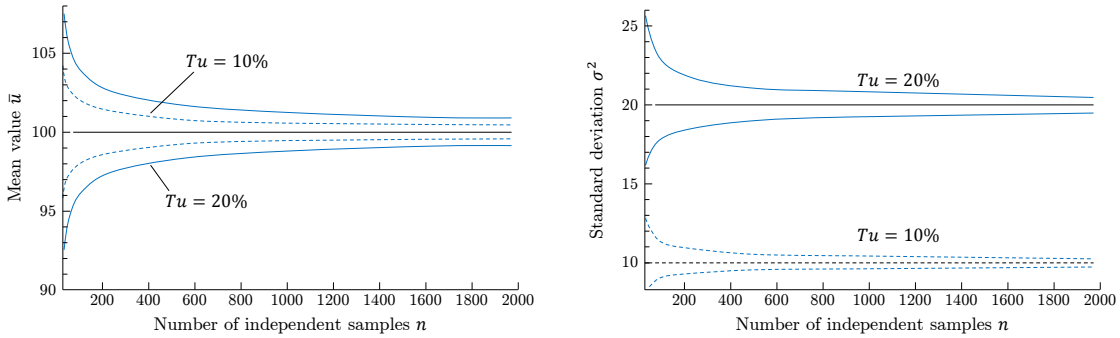

(a) Error of the mean value $\overline{u}$

(b) Standard deviation σ^2

Figure 4.28: Distribution of the error of the mean value $\overline{u}$ and standard deviation σ^2 depending on the turbulence intensity Tu and the number of independent samples n (adopted from [133])

results in 0.7 % error for the mean value close to the wall and 1 % for points in the outer regions due to a different number of samples n in those two areas. In the near-wall area, approximately $n \approx 8,000$ samples have been recorded and in the outer region $n \approx 4,000$. Close to the wall, a more samples were recorded due to the high local turbulence intensity (compare Fig. 4.28), whereas the number of samples was reduced in the outer region to reduce measurement time per point.

The error of the root mean square (RMS) – which is defined as

$$RMS = u_{RMS} = \sqrt{\frac{1}{n}\sum_{i=1}^{n}(u_i - \overline{u})^2} \quad (= \sqrt{\sigma}) \tag{4.28}$$

– can be calculated with the χ^2 distribution as

$$RMS_{err} = \sqrt{n-1}\frac{1}{\sqrt{\chi^2_{\alpha/2;n-1} - \chi^2_{1-\alpha/2;n-1}}} \tag{4.29}$$

This results in a mean RMS_{err} of 4.3 % (near-wall) and 3.1 % (outer region), respectively.

In Fig. 4.28 the distributions of the errors of the mean value $\overline{u}$ and the standard deviation σ depending on the number of independent samples n and the turbulence intensity Tu are given exemplary.

As described above, in near-wall areas with high turbulence levels 8,000 samples were recorded while far from the walls 4,000 samples were taken.

As already described the LDA system does not measure the velocity of the fluid directly, but the movement of tracer particles, also called seeding, which are injected into the stream. Therefore these particles should follow the flow without any slip. However, several forces are acting on the particles due to its density ρ_P and size d_P. These forces lead to a slip between the particles and the flow leading to an uncertainty of the velocity measurement results. Hence, these effects should be kept in mind and kept as small as possible.

The biggest influence is coming from inertia, drag, lift and gravity forces. Assuming a spherical shape of the particle and a presence of a Stokes flow (creeping flow $Re < 1$ [135])

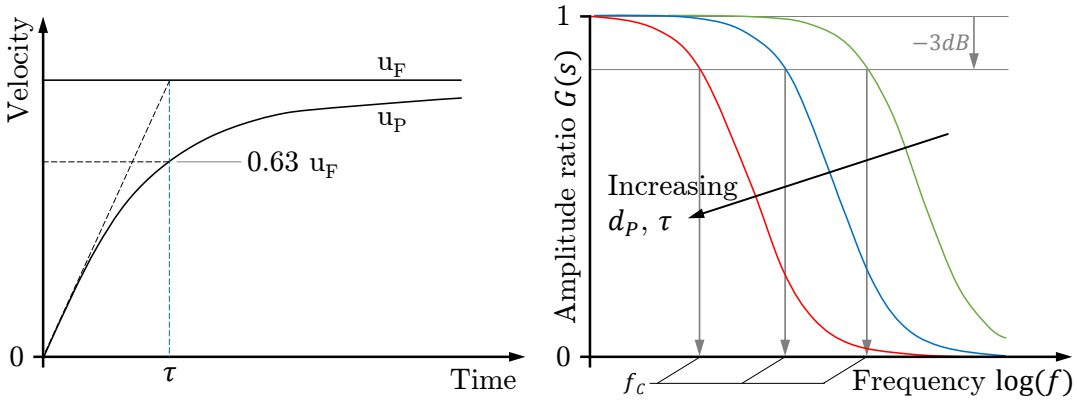

(a) Schematic approximation of the particle velocity u_P towards the fluid velocity u_F together with the relaxation time τ

(b) Qualitative distribution of the transfer function $G(s)$ showing the relation of the velocty amplitude of a seeding particle compared to the actual velocity amplitude of the flow

Figure 4.29: Influence of slip between a measured seeding particle and the actual flow (adopted from [112])

a relation between the fluid and particle velocity can be derived. This relation leads to an exponential approximation of the particle velocity u_P towards the fluid velocity u_F which is shown in Fig. 4.29a. Additionally a time-lag is shown in the figure, which marks that time, a stationary particle needs to reach 63 % of the fluid velocity. This lag, also called relaxation time τ, can be computed with

$$\tau = \frac{2 \cdot r^2 \cdot \rho_P}{9 \cdot \nu \cdot \rho_F} \tag{4.30}$$

where ν represents the kinematic viscosity of the fluid, r the radius of the particle, ρ_P and ρ_F the density of the particle and fluid, respectively. [112, 133]

As a direct consequence of these considerations it can be concluded that due to the lag of the particle the seeding acts as low-pass filter, damping higher frequencies. A relation between the velocity amplitude of a particle for different frequencies and the actual amplitude of the flow velocity at these frequencies – known as the transfer function $G(s)$ – can be calculated with

$$G(s) = \frac{1}{\tau s + 1} \quad \text{with } s = \mathbf{i} \cdot 2\pi f \tag{4.31}$$

where f represents the frequency of e.g. turbulent fluctuations. In Fig. 4.29b this low pass filtering is illustrated for varying particle diameters d_P and relaxation time τ influencing the cut-off frequency f_C. It can be clearly observed that larger particles ($d_P \uparrow$) and heavier particles ($\rho_P \uparrow \Longrightarrow \tau \uparrow$), respectively, lead to a higher damping of high frequency turbulence. Therefore small, light particles should be used. On the other hand the light scattering decreases for smaller, lighter particles which makes it more and more difficult for the LDA system to detect the above described Doppler bursts. [112]

Thus a compromise regarding the particle size has to be made between the low-pass filtering and an reasonable signal-to-noise ratio (SNR), to avoid an unnecessary decrease of the accuracy of the measurement and/or increase the necessary measurement time.

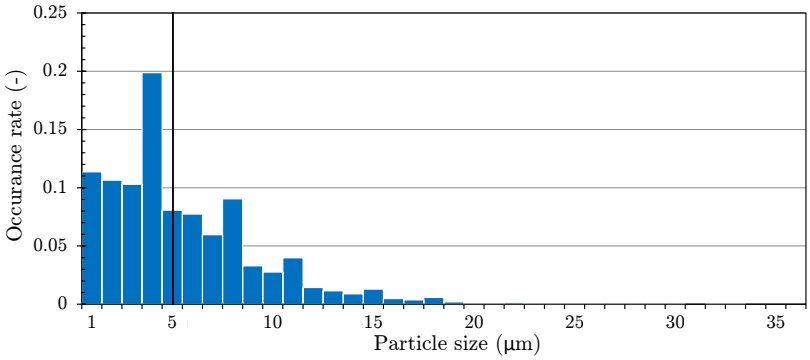

Figure 4.30: Size distribution of the seeding particles used for the LDA measurements, dashed line indicates the mean particle size (adopted from [112])

As already discussed, LDA measurements have been performed in wind tunnel *B*. For seeding the air flow within the channel, a fog generator from *EHLE-HD* was used with the *Slow Fog* glycol-water-based seeding fluid. The fluid density is $\rho \approx 1260$ kg/m^3 and was injected into the channel by a T-tube downstream of the measurement section. The seeding is then transported through the closed-loop channel towards the measurement section along a path of approximately 10 m. Therefore the seeding had enough time to be distributed homogeneously inside the channel. As discussed above the seeding acts as a low pass filter. In order to calculate the cut-off frequency the particle size has to be determined. Therefore Phase-Doppler measurements have been performed at the Institute of Fluid Mechanics and Heat Transfer in order to measure the particle sizes. In Fig. 4.30 the result of these measurements is given. Additionally to the distribution of the particle sizes the mean value of 4.7 μm is indicated by a dashed line. It can be also determined that 50 % of the particles are smaller than 4 μm. The cut-off frequency $f_C(-3dB)$ which represents the frequency where the the transfer function (see Fig. 4.29b and Eq. (4.31)) is reduced by 3 dB ($\approx$ 70.7 %) can be calculated to [136]

$$f_C(-3dB) = \frac{1}{2\pi\tau} \tag{4.32}$$

together with Eq. (4.30). Thus in our case the seeding particles act as low-pass filters up to about $f_C(-3dB) = 1.902$ kHz.

In Chap. 6, paper 5 (Sec 6.3) the results of the LDA measurements are presented. Beside standard measurements where the LDA optic is mounted in such a way that the plate parallel and lateral velocity directions are detected independently by the BSAs, also coincidence measurements have been performed. With this measurement method bursts are only recorded when they are recognized by both BSAs, therefore both velocity components (assuming 2D) are recorded at the same time. This allows to get e.g. Reynolds shear stresses $\overline{u'v'}$ or perform quadrant analysis of the velocity fluctuations (see Chap. 6).

If a dominant velocity is present in the flow or if the second component is zero, it is difficult to reach high burst rates since LDA BSA are not able to record for instance $v = 0$ m/s. In the accelerated case analyzed in this work this is the case and as long as the second BSA does not detect any bursts, the coincidence measurement does not find any coincident velocities. Therefore in this work the Laser beams are turned by 45° in respect to the optical axis in order to enhance the sample rate since now both BSA modules record parts of the main flow

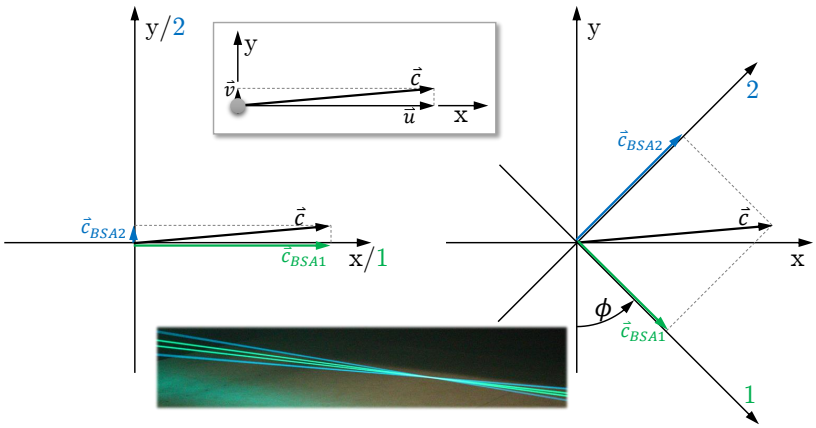

Figure 4.31: Coordinate transformation to reach a better burst rate, left: basis setup, right: Laser head turned by 45°. $\vec{c}_{BSA1}$ and $\vec{c}_{BSA2}$ represent the detected velocity components by the BSAs

direction u together with the lateral velocity coordinate v. The velocity components can then be transferred into the x/y-coordinate system by a standard coordinate transformation. Figure 4.31 shows this transformation by turning of the laser. It can be clearly observed that due to the 45° rotation both BSAs detect the dominant u component of the velocity together with the weak v component with a higher sample rate.

4.2. Numerical Models and Approach

One main goal of this work is to benchmark different existing numerical approaches for their capability in predicting transition and relaminarization. Different approaches are available for calculating wall bounded flows, for example direct numerical simulations (DNS), scale resolving simulations (SRS) or Reynolds-averaged Navier-Stokes (RANS) models. In Fig. 4.32 these three approaches are listed with some key characteristics. The main point is that DNS resolves all flow features without any modeling but has the highest computational effort; for RANS simulations this is vice versa. Large eddy simulations (LES) which belong to the SRS group, represent a trade-off regarding modeling degree and computational effort.

In this work RANS as well as LE simulations have been performed and compared to the experimental data obtained in the wind tunnels. In Tab. 4.1 the performed numerical calculations within the project are listed. The different models are described in sections 4.2.1 to 4.2.3.

Beside different approaches, also three different codes have been used: Fluent® and CFX® by ANSYS® and the in-house code LINARS.

For the numerical simulation with the commercial code ANSYS® CFX® version 15.0 was used. The code uses a pressure correction scheme. The high resolution scheme has been selected for the advection fluxes of the main and turbulent equations. The set of equations solved by the CFX solver, which describes the conservation of mass, momentum and energy, is commonly known as the Navier-Stokes equations, and is solved with the finite-volume method. The equations are discretized with first order accuracy in areas where gradients

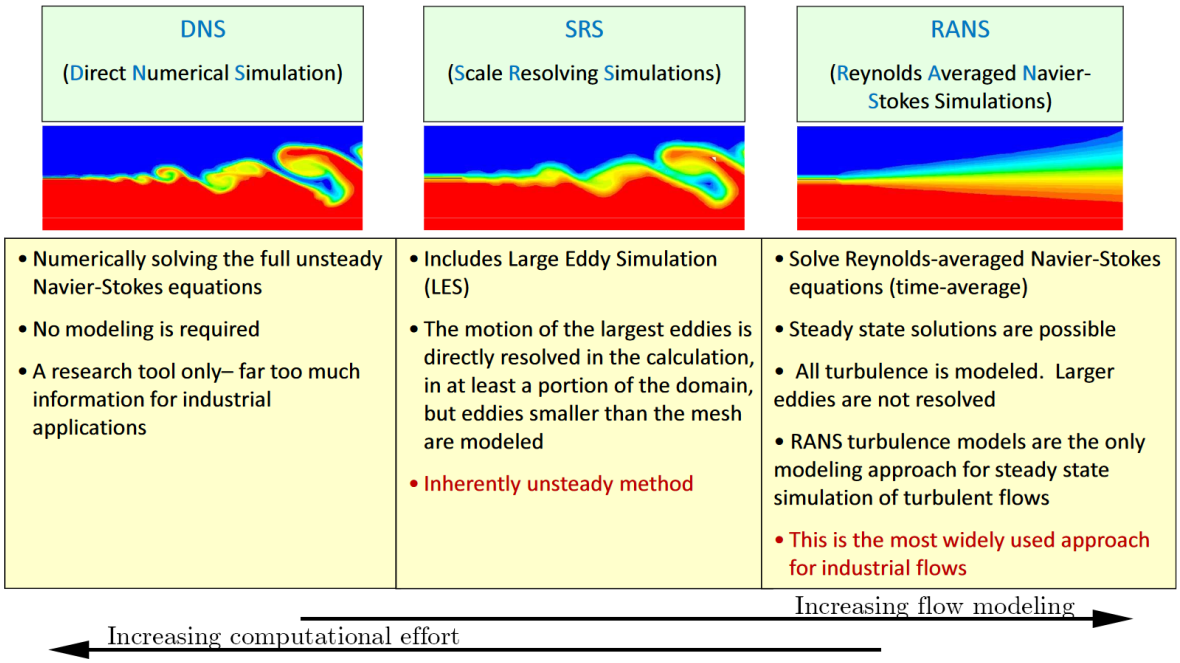

Figure 4.32: Overview of possible modeling approaches of turbulent flow in CFD (adopted from [137])

change sharply in order to prevent overshoots and undershoots and maintain robustness, and with second order in flow regions with low gradients to enhance accuracy [138]. In the results presented in this work (Papers 1-3, 8) CFX® was used together with the γ-Re_θ transition model.

The ANSYS® Fluent® version 15.0 code has broad modeling capabilities including beside classical CFD also combustion, heat transfer, chemical reactions, acoustics, etc. for all kind of fluids. Compared to CFX® Fluent® is more flexible regarding pressure-velocity coupling schemes (SIMPLE, PISO, ...), discretization methods (Standard, PRESTO!, MUSCL, ...) and solution methods. In this work, Fluent® was used with the RANS γ-Re_θ model (Papers 1, 3 and 4), the RANS k-k_l-ω model (Papers 1, 2, 4 and 6) and LES (Papers 4 and 6).

The third code used in this work is the in-house code LINARS. LINARS has been developed at Graz University of Technology at the ITTM by Pecnik et al. [139]. The code solves the Reynolds-averaged Navier-Stokes (RANS) equations in conservative form with a fully-implicit, time-marching finite-volume method. The inviscid (Euler) fluxes are discretized with the upwind flux-difference splitting method of Roe [140]. The incompressible solutions are obtained with a pseudo-compressibility method. LINARS provides the k-k_l-ω and the γ-Re_θ model. The computational results presented in Papers 1, 3, 7, 9 and 10 computed with LINARS were obtained with the latter of the two.

Within this work several models have been analyzed for different geometries. Therefore a bunch of meshes has been created. Here these meshes are not discussed and the interested reader is referred to the corresponding papers where the meshes are described in detail. However it should be mentioned that all meshes fulfill the requirements recommended for the particular solution method and less computational effort has not been favored at the expense of result accuracy.

4.2.1. The γ-Re_θ model

Traditional turbulence models, like the Spalart-Allmaras, the k-ϵ, the Wilcox k-ω or the Menter shear stress transport (SST) model, are not able to predict transition, but assume a fully turbulent boundary layer. Therefore Langtry [67] presented in his PhD thesis a correlation based two-equation model, namely the γ-Re_θ (or γ-$\tilde{Re}_{\theta t}$) model which is added to the Menter SST k-ω turbulence model [141]. The full model including the necessary correlations have been published by Langtry and Menter [69] later. Additionally several other correlations for the model have been developed, see e.g. [142–145].

The transition model solves two additional transport equations in order to influence the production and dissipation of the turbulence kinetic energy k within the turbulence model. The two equations are

$$\frac{\partial(\rho\tilde{Re}_{\theta t})}{\partial t} + \frac{\partial(\rho U_j \tilde{Re}_{\theta t})}{\partial x_j} = P_{\theta t} + \frac{\partial}{\partial x_j}\left[\sigma_{\theta t}(\mu + \mu_t)\frac{\partial \tilde{Re}_{\theta t}}{\partial x_j}\right] \tag{4.33}$$

$$\frac{\partial(\rho\gamma)}{\partial t} + \frac{\partial(\rho U_j \gamma)}{\partial x_j} = P_\gamma - E_\gamma + \frac{\partial}{\partial x_j}\left[\left(\mu + \frac{\mu_t}{\sigma_f}\right)\frac{\partial \gamma}{\partial x_j}\right] \tag{4.34}$$

where $\tilde{Re}_{\theta t}$ is the local transition onset momentum-thickness Reynolds number and γ represents the intermittency, i.e. the state of transition, and varies between 0 and 1, where 1 represents fully turbulent flow conditions.

The empirical correlations used for the prediction of transition are based on the idea that after surpassing a critical momentum thickness Reynolds number $Re_{\theta t}$ transition is triggered. But in this way it is a one-dimensional criterion which is only valid along the wall. Therefore Langtry and Menter [69] introduced the transport variable $\tilde{Re}_{\theta t}$ as a local transition criterion which is applicable in the whole flow field. For this reason the production term of the $\tilde{Re}_{\theta t}$ equation is designed in such a way, that $\tilde{Re}_{\theta t}$ is forced to adopt the value of the empirically prescribed transition onset momentum-thickness Reynolds number $Re_{\theta t}$ in the free stream. The production term of $\tilde{Re}_{\theta t}$ is defined as

$$P_{\theta t} = c_{\theta t}\rho\frac{\rho U^2}{500\mu}\left(Re_{\theta t} - \tilde{Re}_{\theta t}\right)(1.0 - F_{\theta t}) \tag{4.35}$$

where $Re_{\theta t}$ is based on free stream conditions. The blending function $F_{\theta t}$ is used to turn off the source term in the boundary layer and thus allow the transported scalar $\tilde{Re}_{\theta t}$ to diffuse in from the free-stream. $F_{\theta t}$ is equal to zero in the free-stream and one in the boundary layer. [69]

The correlation for $Re_{\theta t}$ suggested by Langtry and Menter [69] considers the influence of the free stream turbulence intensity Tu and the velocity gradient du/ds on the transition onset.

The production and the dissipation terms of the intermittency equation are defined as

$$P_\gamma = F_{\text{length}} c_{a1}\rho S\left[\gamma F_{\text{onset}}\right]^{0.5}(1 - c_{e1}\gamma) \tag{4.36}$$

$$E_\gamma = c_{a2}\rho\Omega F_{\text{turb}}(c_{e2}\gamma - 1) \tag{4.37}$$

where F_{length} and F_{onset} depend on the local $\tilde{Re}_{\theta t}$ value and determine the length and onset of transition in the flow field. On the other hand F_{turb} only depends on the local turbulence parameters (k and ω). The values of F_{length}, F_{onset} and F_{turb} can vary between $0 \leq F_{\text{length}} \leq$

40, $0 \leq F_{\text{onset}} \leq 2$ and $0 \leq F_{\text{turb}} \leq 1$, respectively. A discussion of the influences of these parameters on relaminarization prediction is discussed in paper 7 (Sec 6.7).

The coupling of the transition model is done by modifying the original production term P_k and dissipation term D_k of the k equation of the original SST turbulence model:

$$\tilde{P}_k = \gamma_{\text{eff}}\ P_k \tag{4.38}$$

$$\tilde{D}_k = \min(\max(\gamma_{\text{eff}}, 0.1), 1.0)\ D_k \tag{4.39}$$

Numerical results obtained with this model are presented in Chap. 5, papers 1 to 4 and Chaps. 6 and 7, papers 7 to 10, where the solutions have been calculated with Linars, ANSYS® Fluent® and CFX®.

4.2.2. The k-k_l-ω model

This model is based on the idea of the *laminar fluctuations* in a pre-transitional zone. In this zone the velocity profiles start to differ from the laminar Blasius solution, which influences skin friction as well as heat transfer. The fluctuations have a relatively high amplitude and eventually lead to a breakdown into a fully turbulent boundary layer. However, these fluctuations are not turbulence in the classical understanding, but fluctuations inside a laminar boundary layer. This distinction between laminar and turbulent fluctuations has been presented by Mayle and Schulz [51] proposing the idea of a transport equation for a laminar kinetic energy k_l. [146]

The model used in this work has been presented by Walters and Cokljat [70] and is an enhancement of the model by Walters and Leylek [147]. It is based on the k-ω framework where a third transport equation for the laminar kinetic energy k_l is added to include the phenomenological behavior of the pre-transitional flow. The concept of the laminar kinetic energy is that it represents the effects of Tollmien-Schlichting waves and Klebanoff waves which may lead to natural or bypass transition. Therefore this model is based on more physical considerations, rather than fully empirical correlations. The resulting three equations are for the laminar k_l and turbulent k_T kinetic energy and for the inverse turbulent time scale ω: [148]

$$\frac{\partial k_l}{\partial t} = P_{k_l} - R - R_{nat} - D_l + \frac{\partial}{\partial x_j}\left[\nu \frac{\partial k_l}{\partial x_j}\right] \tag{4.40}$$

$$\frac{\partial k_T}{\partial t} = P_{k_T} + R + R_{nat} - \omega k_T - D_T + \frac{\partial}{\partial x_j}\left[\left(\nu \frac{\alpha_T}{\alpha_k}\right)\frac{\partial k_T}{\partial x_j}\right] \tag{4.41}$$

$$\begin{aligned}\frac{\partial \omega}{\partial t} = C_{\omega_1}\frac{\omega}{k_T}P_{k_T} + \left(\frac{C_{\omega_R}}{f_W} - 1\right)\frac{\omega}{k_T}(R + R_{nat}) - C_{\omega_2}\omega^2 + \\ + C_{\omega_3} f_\omega \alpha_T f_W^2 \frac{\sqrt{k_T}}{d^3} + \frac{\partial}{\partial x_j}\left[\left(\nu \frac{\alpha_T}{\alpha_\omega}\right)\frac{\partial \omega}{\partial x_j}\right]\end{aligned} \tag{4.42}$$

where terms with P represent the production terms, R and R_{nat} represent the averaged effects of the breakdown into turbulence during bypass and natural transition, respectively [148].

Although the model was tested on different setups, Fürst and Příhoda [149] and also the results in paper 6 (Sec. 6.5) show that the model has difficulties with predicting transition and relaminarization if the flow is exposed to an adverse or favorable pressure gradient.

Numerical results using this model have been computed with ANSYS® Fluent® and are presented in papers 1, 2, 4 and 6 (Chaps. 5 and 6).

4.2.3. Large eddy simulation

Large eddy simulation is nowadays a common tool for solving flow problems. It offers a trade-off between physical accuracy (better than RANS) and computational effort (lower compared to DNS). A LE simulation solves vortical structures up to the so-called subgrid scale. The size of the smallest vortical structures which are resolved by the simulation is defined by the grid size.

Figure 4.33 shows the energy cascade of a fully turbulent flow. Clearly the breakup of larger vortices into smaller ones is visible indicated by the sketched vortices. This breakup leads to a the decrease in energy at higher frequencies.

Above a certain frequency where the mesh is not fine enough (grid limit) to resolve the vortices anymore these vortices ate higher frequencies are resolved by the LES subgrid model. This subgrid model considers the further dissipation of the vortices. It should be mentioned here, that the subgrid model is also necessary for the large eddy simulation to ensure stability of the calculation [150]. Thus a very high spatial resolution does not necessarily mean, that the simulation is more accurate.

The mesh used for an LES should be fine enough to resolve all relevant structures which matter for the use-case, and coarse as possible to reduce computational time and effort. In

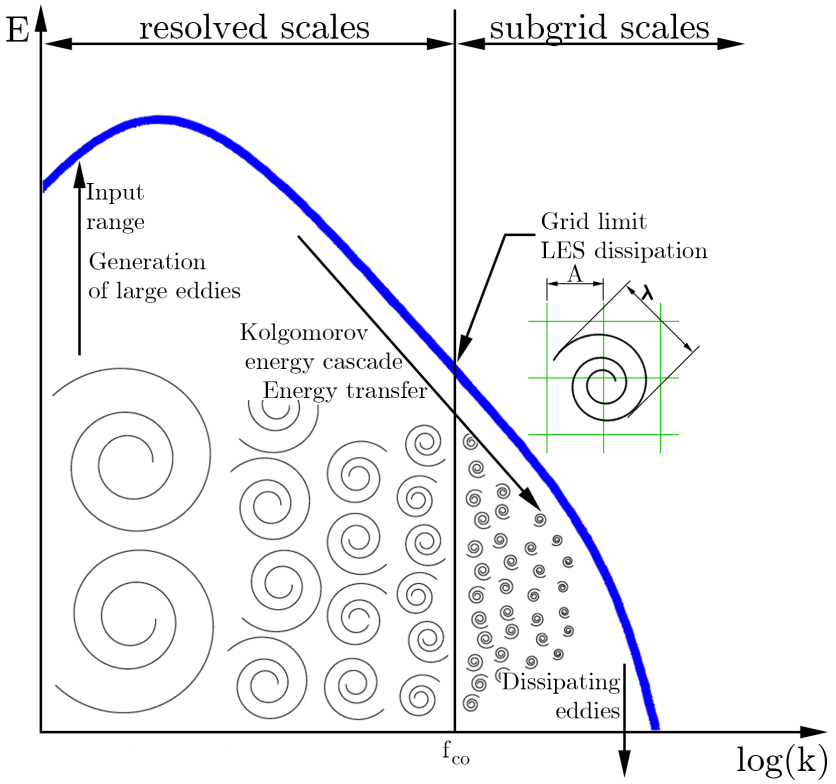

Figure 4.33: Energy spectrum of a fully turbulent flow indicating the resolved and subgrid scales of a large eddy simulation

order to compute the relevant frequencies, the resolution of the mesh should be chosen in such a way that four cells resolve the smallest eddies of interest. This is illustrated in Fig. 4.33, where an eddy with a wavelength of λ is resolved by four cells with the size of AxA ($\lambda/2$x$\lambda/2$). If the mean velocity $\bar{u}$ is known, the cut-off frequency f_{co} can be calculated with

$$f_{co} = \frac{\bar{u}}{\lambda} = \frac{\bar{u}}{2A} \tag{4.43}$$

This frequency represents the border between the resolved and modeled (subgrid) eddies. Beside this value, also the computational timestep should be kept in mind, since the highest eddy frequency which can be resolved depends on the timestep used during the calculation t_s. This leads to an effective cut-off frequency of

$$f_{co} = min\left[\frac{\bar{u}}{2A}, \frac{1}{t_s}\right] \tag{4.44}$$

More details about large eddy simulations and subgrid models have been presented in many works (e.g. [148, 150]), and the interested reader is referred to these publications.

The results of LES within this work have been computed with ANSYS® Fluent® v15.0 and are presented in Chap. 5, paper 4, and Chap. 6, paper 6.

CHAPTER 5

RESULTS: TRANSITION

> Life is one big transition.
>
> Willie Stargell
> ATHLETE

A first step of this work was the experimental and numerical investigation of the transition process from laminar to turbulent. The aim of these investigations was to understand the process, to validate different experimental techniques for their capability of measuring transition and to use the acquired experimental data for testing different numerical models and approaches.

Papers 1 to 3 present mainly experimental data and paper 4 discusses computational results.

5.1. Content

In the **first paper** [151] Preston tube measurements are presented for two different flow cases in wind tunnel A1. It is shown, that this measurement technique represents an easy but robust method to measure transition. The results of the Preston tube measurements are compared to thermographic recordings. Additionally, turbulence measurements at the inlet of the test section have been performed using a fast response aerodynamic pressure probe (FRAPP).

The results of the FRAPP measurements have been used to get the turbulence intensity at the inlet and also the turbulence dissipation. For the latter, different methods have been applied in order to find the right inlet dissipation scale. The values of turbulence intensity and dissipation at the inlet are necessary for CFD simulations, however, they are not often measured. With these values also first numerical studies are presented, showing the influence of free-stream turbulence on the numerical transition prediction and underlining the importance of an appropriate setting of the correct turbulent boundary conditions.

The paper also discusses different flow parameters which should be kept in mind when designing a flow channel for flat plate boundary layer measurements, like boundary layer thicknesses etc.

The outcomes of the first paper, mainly the results of the Preston tube and FRAPP measurements, have been considered in the **second paper**, which presents experiments performed in wind tunnel A2. This (yet unpublished) paper [152] presents an innovative measurement technique where transition is measured using microphones which are flush-mounted into the plate. The microphones measure the "noise" generated by the higher velocity fluctuations inside the boundary layer caused by arising turbulent vortices during transition.

The acoustic measurements show that upstream of the transitional zone the root-mean-square of the static pressure fluctuations $\hat{p}$ starts to increase (start of transition) and has its maximum within the transitional zone. After the maximum, $\hat{p}$ decreases again until it stays more or less constant (end of transition, fully turbulent). The results clearly show, that this technique can be used for measuring the transition along the plate. Since it does not influence the flow (no blockage effect) it is also perfectly suitable for applications inside narrow channels, so, for example, for relaminarization-by-high-acceleration test cases or within turbines.

Another innovative measurement technique is presented in the **third paper** [153], where beside the already discussed Preston tube and thermographic methods also constant temperature anemometry (CTA) and laser interferometric vibrometry (LIV) are used. The latter technique is used for the first time to analyze transition along a flat plate. Although the LIV is normally used to measure surface vibrations, it can also detect a variation of the refraction index due to density fluctuations, but it should be kept in mind, that the LIV records a mean value of the density fluctuations along the line of sight.

The results of the Preston tube measurements again clearly show the transitional zone. Also the thermographic recording detects the location of the transition along the plate. For the CTA measurements the boundary layer thickness and the time signal of the lateral fluctuations v' have been used as criteria for transition.

The laser vibrometer measurements show, that the density recordings for the laminar and turbulent boundary layers are similar. For the laminar layer hardly any density fluctuations are present, thus the signal of the vibrometer is low. In the turbulent boundary layer density fluctuations are present, caused by the turbulent fluctuations. However, the fluctuations are statistically normal distributed around the mean value. Since the laser vibrometer measures the average value along the line-of-sight, the resulting signal is again nearly zero. In the transitional zone, the velocity fluctuations are not equally distributed, since the first few emerging turbulent fluctuations are randomly distributed along the span. Thus the laser vibrometer measures a signal unequal to zero. These observation also agrees with the time-resolved velocity signal obtained by CTA in this zone.

Additionally to the transition measurements, free-stream turbulence intensities along the plate and at the inlet are measured with CTA. Also the dissipation is found by fitting CFD calculations to the measurement results. With ANSYS® CFX®, ANSYS® Fluent® and the in-house code Linars the transition zone is predicted along the plate using the γ-Re_θ transition model with boundary conditions from the measurement.

Regarding measurements, the paper shows, that due to the non-uniform distribution of velocity fluctuations along the span of the plate inside the transitional zone, this zone can be detected with LIV. This measurement technique also represents a non-invasive technique and can therefore also be used in narrow channels, so that it may be used for relaminarization experiments.

The simulations show a good agreement for the low-speed case, which is similar to the T3A test case of ERCOFTAC, but differ for the high speed case, which has other flow conditions as the ERCOFTAC flat plate test cases which were used for the calibration of the

model. This points out, that the transition model can predict transition but needs a proper calibration. Another interesting aspect is, that the two used CFD codes by ANSYS® show different transitional behavior, although the used boundary conditions, model and mesh were the same for both simulations.

A more detailed evaluation of the CTA measurements are given in App. D presenting profile data along the plate.

The last paper in this chapter [154] (**paper 4**) presents a computational study on the numerical prediction of transition along the flat plate. The test case is the setup used for the measurements presented in paper 3. The CFD results are compared with the measured results of paper 3 and LDA data acquired in wind tunnel B.

The presented RANS solutions have been computed using the k-k_l-ω transition/turbulence model, the γ-Re_θ and γ transition model. A comparison between these three approaches shows, that all models are able to predict transition, but the intermittency based models show a better agreement with the measurement results. Additionally, an embedded large eddy simulation (eLES) was performed. From the results of this simulation two conclusions could be drawn: (a) the eLES is capable of predicting transition, including the computation of streaks and (b) the necessary calculation time can be reduced using beside time-averaging also spatial averaging.

The large eddy simulation clearly shows the occurrence of streamwise streaks. A comparison of the time signals obtained by CTA and eLES shows a very similar behavior. Therefore the conclusion can be drawn, that a LE simulation not only predicts the transition of similar accuracy like RANS models based on empirical correlations, but also is able to simulate real processes occurring during transition.

5.2. Summary and Conclusions

The experimental results presented in papers 1-3 show clearly the advantages and disadvantages of the used measurement techniques for measuring transition. Beside Preston tube measurements, also thermographic recordings, laser vibrometer and acoustic measurement techniques have shown their capability in the prediction of the transition position and length in different wind tunnels.

All techniques are in a good agreement with each other, thus it can be concluded, that the measurement results can be used as a reliable set of tests for numerics. Additionally, the inlet boundary conditions have been measured which are necessary for CFD simulations.

The presented numerical results (paper 1-4) show, that the γ-Re_θ and the k-k_l-ω RANS models can predict transition. However, the accuracy for the intermittency-based model is only high for a test case which has similar flow conditions as in the ERCOFTAC test cases, which are used for the calibration of the model.

The embedded large eddy simulations presented in this chapter (paper 4) show their capability in predicting transition. A comparison with the measurement results shows good agreements, not only regarding the position and length of transition, but also the time signals of the LES and measurement show the same effects during transition.

5.3. Paper 1: On the Setup of a Test Bench for Predicting Laminar-to-Turbulent Transition on a Flat Plate

P. Bader and W. Sanz, "On the Setup of a Test Bench for Predicting Laminar-to-Turbulent Transition on a Flat Plate," *Journal of Energy and Power Engineering*, vol. 10, pp. 411–424, 2016.

Journal of Energy and Power Engineering 10 (2016) 411-424
doi: 10.17265/1934-8975/2016.07.005

On the Setup of a Test Bench for Predicting Laminar-to-Turbulent Transition on a Flat Plate

Pascal Bader and Wolfgang Sanz

Institute for Thermal Turbomachinery and Machine Dynamics, Graz University of Technology, Inffeldgasse 25/A, Graz 8010, Austria

Received: May 5, 2016 /Accepted: May 19, 2016 /Published: July 31, 2016.

Abstract: At turbomachinery relevant flow conditions the boundary layers are often transitional with laminar-to-turbulent transition occurring. The characteristics of the main flow can depend highly on the state of the boundary layer. Therefore it can be vitally important for the designer to understand the process of laminar-to-turbulent transition and to determine the position and length of the transitional region. In this paper the flow over a flat plate is experimentally studied in order to investigate and better understand transitional flow. Preston tube measurements as well as a thermographic camera system were performed for two different inlet velocities in order to determine the position of the transitional zone. The results of the experiment are compared to numerical flow solutions using a common transition model to determine its capability. The simulation has been performed with the two commercial codes CFX® and Fluent® by Ansys® and an in-house code called LINARS. As a result of this study, a better understanding of the experimental and numerical methods for determining transition shall be given.

Key words: Boundary layer transition, computational fluid dynamics, Preston tube, thermographic camera, flat plate boundary layers.

Nomenclature

a	Decay exponent
c_f	Wall friction coefficient
crit	Critical value
f	Frequency
H	Hydraulic/Characteristic diameter
H	Channel height
k	Turbulence kinetic energy
K	Acceleration parameter
L	Physical integral length scale
L	Plate length
l	Pseudo-integral scale
l_m	Mixing length
mean	Mean value
Nu	Nusselt number
p	Local static pressure
p_t	Total pressure
q_{probe}/q_∞	Non-dimensional dynamic pressure
Re	Reynolds number
Tu	Turbulence intensity
u	Local streamwise velocity
u_∞	Free-stream velocity
W	Channel width
x	Streamwise coordinate
y	Distance to the wall
y^+	Dimensionless wall distance
α	Heat transfer coefficient
δ	Boundary layer thickness
δ^*	Displacement thickness
ϵ	Dissipation rate
ν	Kinematic viscosity
τ_W	Wall shear stress
τ_t	Turbulent shear stress
∞	Free-stream value
$\bar{}$	Mean value
$\hat{}$	Fluctuation

Abbreviation

ACF	Autocorrelation function
BL	Boundary layer
CFD	Computational fluid dynamics
FFT	Fast fourier transformation
FRAPP	Fast-response aerodynamic pressure probe
ITTM	Institute for Thermal Turbomachinery and Machine Dynamics
LDV	Laser Doppler velocimetry
LE	Leading edge
PIV	Particle image velocimetry

Corresponding author: Pascal Bader, Dipl.-Ing., BSc, research assistant, research field: measurement and simulation of boundary layer behavior.

SST	Shear stress transport
TE	Trailing edge

1. Introduction

The boundary layer represents the small zone between the wall and the free stream where viscous effects are important. Due to its size, the influence of its state (laminar or turbulent) is often neglected although it can have a high impact on the flow characteristics like heat transfer or wall friction. These parameters influence the efficiency as well as the thermal stress of, for example a turbine blade.

Many parameters like free-stream velocity, acceleration, free-stream turbulence etc. have an influence, if a boundary layer is laminar or turbulent, but at the first contact of a flow with a stationary structure the boundary layer starts laminar and will become turbulent (under the right flow conditions) via a transitional area. The boundary layer passes through several stages within this transitional zone until it becomes fully turbulent [1].

It is vitally important to understand the influence of the above stated parameters on the onset and length of the transitional zone in order to influence and potentially control the state of the boundary layer.

Because of the possibility to increase efficiency, transition also plays a major role in turbomachinery flows. In such machines the efficiency of blades and stages can be improved when considering transition; thus this gives the possibility to improve the overall engine performance. In 1991, Mayle [2] published an interesting overview of the role of transition in gas turbines. He analyzed experiments performed by different research groups and showed the influence of several flow parameters on the transition process.

Additional experiments were performed in the last years by different research groups. Yip et al. [3] performed inflight measurements and predicted transition with the help of Preston tubes and analyzed the influence of the flight condition on the boundary layer around an airfoil. Oyewola et al. [4, 5] showed how the flow in the boundary layer can be measured with the help of hot-wire probes as well as LDV (laser-Doppler velocimetry). Another optical measurement technique has been used by Widmann et al. [6] who performed near-wall measurements with a PIV (particle image velocimetry) system. Also hot-film measurements were performed by Mukund et al. [7].

In addition to measurements, also different numerical approaches have been developed to predict the laminar-turbulent transition process. Common models, for example the $k - k_L - \omega$ [8] and the $\gamma - Re_\Theta$ [9, 10] model. For the latter model, various correlations for important model parameters have been developed [11-15].

So far, only the transition from laminar to turbulent has been described, but under certain flow conditions (like high acceleration) a reverse-transition or relaminarization from turbulent to laminar can occur. Up to now only few measurements and publications have been made in order to understand relaminarization. Therefore, a project has been launched at the ITTM (Institute for Thermal Turbomachinery and Machine Dynamics) at Graz University of Technology in order to understand the different mechanisms leading to relaminarization.

The first step of this project is to set up a test bench in order to measure transition from laminar to turbulent.

This should help to improve the understanding of transition even further and to test different measurement techniques. Another point of this measurement campaign is to acquire all data necessary for the simulation since the vital parameter of the turbulence scale is not documented in most experimental works. Some works discuss the measurement of turbulence length scales, for example Camp and Shin [16] who described in detail how to process the measured signal in order to get the necessary values. Also Axelsson et al. [17, 18], and Craft [19] discussed different length scales and measurements of turbulence intensity.

This work focuses on the set up of the test bench and will give an overview of technical considerations

which should be taken into account. Additionally measurement techniques are discussed and a special focus lies on measuring of the turbulence length scale.

Finally, several CFD codes and transition models will be compared in order to see their differences and their capabilities in predicting transition within the test bench.

2. Numerical Setup

The computational mesh models the flow region in the test bench which is described in the next section (Fig. 1b) and consists of about 13 million cells. To ensure a mesh independence of the simulation result, the y^+-value of the mesh was kept between 0.1 and 1 as recommended in Ref. [20]. The mesh consists only of the upper part of the channel and is illustrated in Fig. 1a.

The computational simulations have been performed with three different codes: ANSYS® CFX® v15.0, ANSYS® Fluent® v15.0.0 and the in-house code LINARS.

CFX® solves the Navier-Stokes equation system with first-order accuracy in areas where the gradients change sharply to prevent overshoots and undershoots to maintain robustness, and with second-order in flow regions with low variable gradients to enhance accuracy [20].

Fluent® uses the simple algorithm for the pressure-based solver. The pressure correction equation is solved with second-order accuracy and the momentum as well as the turbulence and transition equations are solved with a third-order MUSCL algorithm.

LINARS has been developed at Graz University of Technology at the ITTM [21]. The code solves the RANS (Reynolds-averaged Navier-Stokes) equations in conservative form with a fully-implicit, time-marching finite-volume method. The inviscid (Euler) fluxes are discretized with the upwind flux difference splitting method in Ref. [22]. The incompressible solutions are obtained with a pseudo-compressibility method.

For the simulation with all three codes Menter's $k-\omega$ SST turbulence model [23] was used with the $\gamma - Re_\Theta$ [12] transition model. Additionally, with Fluent® the $k - k_L - \omega$ [8] turbulence/transition model was also applied.

3. Experimental Setup

The measurements are performed in a subsonic wind tunnel located at the ITTM. The test rig is a continuously operating open-loop wind tunnel. The air is delivered by a 125 kW radial compressor with a flow rate of approximately 0.6 kg/s. The compressor delivers the air into a flow settling chamber. From this chamber the air is transported via a flow-calming section

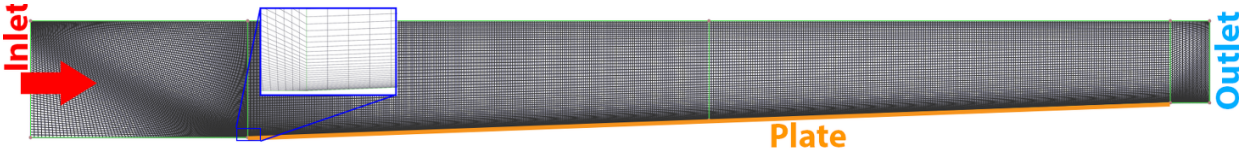

(a) Computational mesh

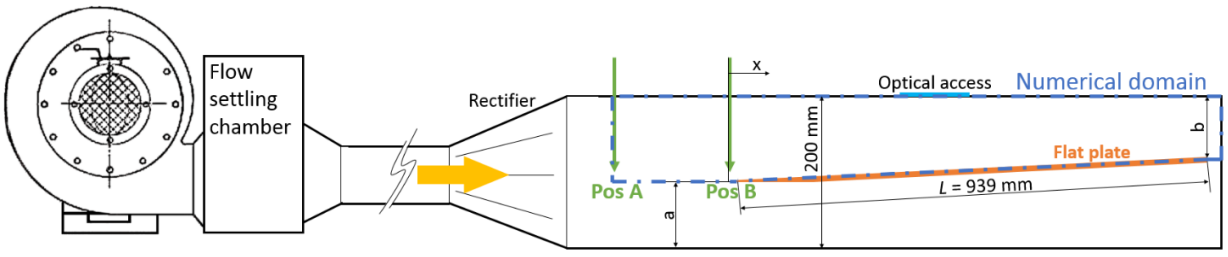

(b) Subsonic turbine with measurement area

Fig. 1 Illustration of the test bench and computational mesh.

formed by a diffuser with guiding vanes towards the test area. A schematic drawing of the test bench is given in Fig. 1b.

Transition measurements have been performed for two different inlet velocities: $u_{\infty,mean}$ = 5.3 m/s (low speed case) and $u_{\infty,mean}$ = 13.2 m/s (high speed case).

The plate in the channel is inclined by 2° as recommended by Coupland [24]. This should ensure that the flow is attached to the plate without leading edge separation bubbles.

In order to minimize the influence of the channel walls on the measured boundary layer some aspects have been kept in mind and will be discussed in the following.

First, the position (normal to streamwise direction) of the plate leading edge (distance *a* in Fig. 1b) has been chosen. One aspect here is that the plate must not be inside the boundary layer of the bottom or top wall of the channel. Therefore the approximate size of the boundary layer was estimated. The size of the boundary layer depends amongst others on the development length. It can be approximated with the Blasius solution for the laminar boundary layer:

$$\delta(x) \approx \frac{x}{\sqrt{Re_x}} \tag{1}$$

and for the turbulent boundary layer:

$$\delta(x) \approx 0.382 \cdot \frac{x}{Re_x^{1/5}} \tag{2}$$

where, δ is the local boundary layer thickness, x is the development length and Re_x is the Reynolds number based on x [1]. For the calculation of the Reynolds number u and v are taken at the inlet.

These two equations are illustrated in Fig. 2a which gives an example of the boundary layer growth for a specific velocity (here about 5 m/s). In this illustration of the boundary layer thickness $Re_{x,crit} = 3 \times 10^5$ is assumed for the onset of transition. According to Schlichting and Gersten [1], this is valid for "normal" longitudinal flow along a flat plate with a sharp leading edge. Additionally they state that, this critical Reynolds-number can be increased to $Re_{x,crit} \approx 10^6$ by ensuring a smooth flow (low turbulence intensity).

Although it is not clear, if these transition onset criteria stated by Schlichtung and Gersten are valid for the designed test bench, it is a good start for estimating the beginning of transition. In the following, $Re_{x,crit} = 3 \times 10^5$ is assumed as the onsetlocation of the transitional zone within the test bench of the institute.

The Re_L [1] value of the bottom and top wall, respectively, can be estimated with about $Re_L \approx 3.3 \times 10^5$ for the low-speed case and $Re_L \approx 8 \times 10^5$ for the high-speed case which results in a boundary layer thickness of about $\delta(x) \approx$ 30 mm and 25 mm, respectively, at the end of the plate. The plate leading edge is placed at about 100 mm above the bottom wall so that it certainly does not lie inside a wall boundary layer. But due to the small channel height, the influence of the sidewall and top wall BLs has to be considered in the numerical analysis. Another aspect which should be kept in mind is the vertical position of the TE (trailing edge) of the plate (distance *b* in Fig. 1b). It has to be ensured that the boundary layer of the top wall does not "collide" with the investigated boundary layer of the plate. As already described the boundarylayer grows along the plate, thus an important value is the boundary layer thickness $\delta(x_{TE})$ at the trailing edge of the plate. In Fig. 2b this value is illustrated for different free stream velocities u_∞. Also the values for the two test cases are marked in the figure. The graph shows that there is a maximal BL thickness (about $\delta(x_{TE}) \approx$ 30 mm) which can be reached for a given plate length under normal operating conditions.

The position of the trailing edge could not be chosen freely, since the length of the plate is fixed with 939 mm and the angle is set to 2° as discussed before. However, so the resulting position of the TE has sufficient distance towards the top wall.

[1] Computed with the plate length *L* and the thermophysical properties at the inlet.

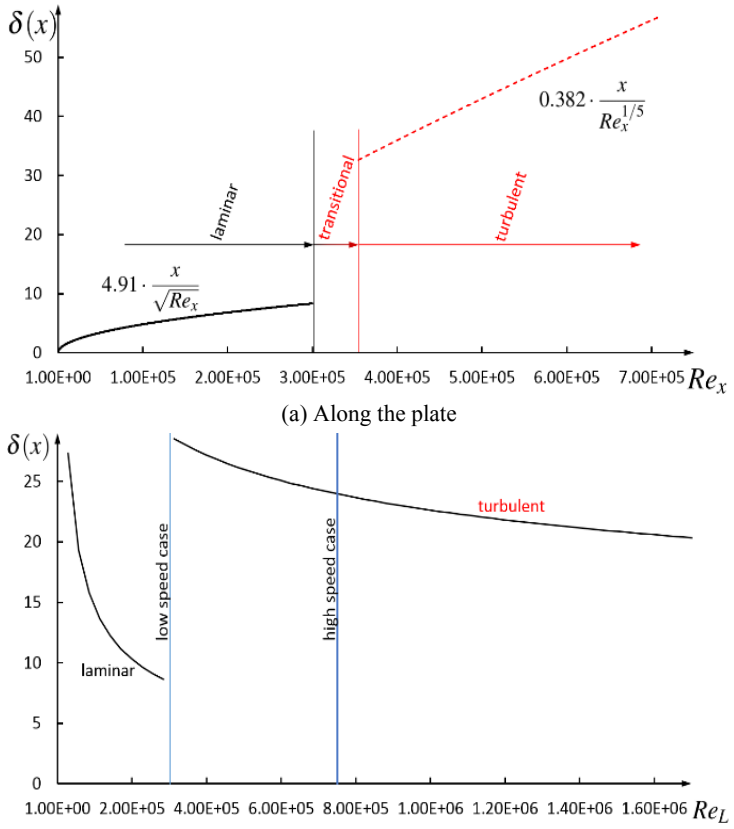

(a) Along the plate

(b) At the plate trailing edge where ν changes in Re

Fig. 2 Graph of the boundary layer thickness $\delta(x)$.

Also the displacement thickness δ^* is important which describes the shift of the free-stream streamlines away from the surface where the boundary layer develops. It gives the distance which a surface with a boundary layer would have to be moved in perpendicular direction to have the same flow rate compared to a case of a surface without a boundary layer [1]. The displacement thickness can be calculated for an incompressible fluid with

$$\delta^* = \int_0^\infty \left(1 - \frac{u(y)}{u_\infty}\right) dy \tag{3}$$

where, u represents the local streamwise velocity, y the direction normal to the wall and u_∞ represents the free stream velocity. δ^* influences the velocity of the free-stream within a channel (like in the test setup) since it narrows down the effective free stream flow area.

The tests were performed for two different channel cross sections W × H: 500 × 200 mm (low speed case) and 200 × 200 mm (high speed case).

4. Turbulence and Dissipation Measurements

Downstream of the diffuser with guiding vanes (position A in Fig. 1b) the free stream turbulence intensity Tu together with the total pressure p_t is measured. These values are measured about x = 220 mm upstream of the leading edge of the plate and are used as boundary conditions for the simulation.

Close to the leading edge (position B) again the turbulence intensity Tu is measured to be able to approximate the turbulence length scale of the flow which is necessary for the computational setup.

Tu measurements were performed by means of a cylindrical single-sensor FRAPP (fast-response aerodynamic pressure probe). A miniaturized

piezo-resistive pressure sensor (Kulite XCE-062) is mounted inside the probe head, which has an outer diameter of 1.85 mm.

The probe aerodynamic accuracy was evaluated in a calibrated nozzle, giving an extended uncertainty equal to $\pm 0.5\%$ of the kinetic head for the pressure measurements and equal to $\pm 0.5°$ for the flow angle. In order to obtain the transfer function of the probe, a dynamic calibration was carried out in a low-pressure shock tube; after digital compensation the probe bandwidth reaches up to 80 kHz. Persico et al. [25] presented more details about the probe design and calibration.

In order to get the turbulence intensity Tu out of the measured signal it is necessary to remove all periodic components of the raw measured signal. In order to perform this reduction, the measured signal is FFT (fast fourier transformed) and the periodic components (like blade passing frequency and its harmonics) of the signal are "chopped" [16]. Only the non-periodic stochastic parts of the signal are modeled by a single-point turbulence model (like $k-\omega$ or $k-\epsilon$) [17]. This chopped signal is illustrated in Fig. 3, where the amplitude of the velocity fluctuations over the frequency is presented.

In this figure also the $-5/3$-line, known from the Kolmogorov-Obukhov [26-28] spectrum, can be observed. The spectrum shows, that the fluctuations fit the $-5/3$-line up to about 10 kHz. Above this frequency it can be assumed that the fluctuations are due to white noise and cannot be considered as turbulence. Also low-frequency fluctuations (lower than 500 Hz) are assumed to have no contribution to the turbulence level. Thus, only the fluctuations between 500 Hz and 10 kHz have been taken into account for the calculation of the turbulence intensity.

The chopped and filtered spectrum was then processed with an inverse FFT to get a time signal again [16].

This time signal of the turbulent velocity fluctuations is then used to determine the turbulence intensity Tu according to Ref. [16]:

$$Tu = \frac{1}{\bar{u}} \cdot \sqrt{\frac{1}{N} \cdot \sum_{i=1}^{N} \hat{u}_i{}^2} \tag{4}$$

where, $\bar{u}$ represents the mean velocity and $\hat{u}_i$ represents the velocity fluctuations.

The turbulence intensity is a crucial and important inlet parameter for the simulation. Beside Tu another factor, the turbulence length scale l, needs to be defined at the inlet to determine the turbulence dissipation rate. Unfortunately the length scale is not often measured since it is more a descriptive quantity for explaining the dissipation. The idea of a mixing length was introduced by Prandtl [29] in 1925 describing it as "only a rough approximation" [30]. Prandtl made a correlation between the turbulence shear stress τ_t and the velocity

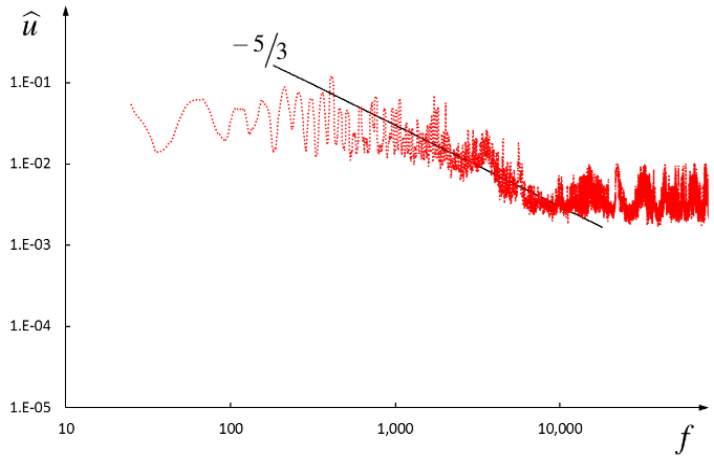

Fig. 3 Moving average of the chopped velocity fluctuations over the frequency.

gradient in a viscous layer. Therefore he introduced the mixing length l_m which describes the mean free distance between two eddies [1].

Although it is only a model for understanding the process of dissipation, it is still used in modern CFD codes. Since it is only a theoretical quantity, it is neglected in most measurements, and in most publications no focus on the length scale or dissipation is laid on.

In the following different definitions of the turbulence length scale are given. Several overviews have been published in the last years like Refs. [16, 17, 31, 32] and in the following the main outcomes will be discussed.

To use the above discussed mixing length in CFD calculations, a correlation between the mixing length l_m and the dissipation rate ϵ is necessary. This correlation is known as *Prandtl-Kolmogorov*-equation [1].

$$\epsilon = C_\mu^{3/4} \cdot \frac{k^{3/2}}{l_m} \tag{5}$$

where, k represents the turbulence kinetic energy and $C_\mu^{3/4}$ represents an empirical constant (usually ≈ 0.09) which is specified by the used turbulence model [33]. This correlation is used by codes like Fluent®, LINARS and several other codes. For estimating this mixing length the Fluent® modeling guide recommends l_m with

$$l_m = 0.07 \cdot H \tag{6}$$

where, H represents the hydraulic/characteristic diameter.

Other CFD codes (like CFX®) use a length scale defined as

$$l = \frac{k^{3/2}}{\epsilon} \tag{7}$$

This definition of a length scale is often called *pseudo-integral scale* as suggested by Gamard and George [31].

The two given definitions above (Eqs. (5) and (7)) represent a relation between the turbulence kinetic energy and dissipation, but the problem is that l and l_m are not directly measurable.

Since the length scale is used to define the turbulent dissipation rate ϵ it is obvious to measure this flow variable directly. Unfortunately this is almost impossible, since it would be necessary to measure down to very small spatial resolutions which cannot be resolved by probes [17].

A length which is measurable is the so-called (physical) integral length scale L which is defined as Ref. [16].

$$L = \bar{u} \cdot \int_0^k ACF(\tau) d\tau \tag{8}$$

where, $ACF(\tau)$ represents the ACF (autocorrelation function) of the turbulent velocity signal. In order to determine L the chopped FFT spectrum which was used within the signal processing for obtaining the turbulence intensity Tu is multiplied by its conjugated complex part and then transformed back with an inverse-FFT. The time signal obtained this way is then autocorrelated [16].

The idea behind the integral length scale L is that it describes the time a turbulence fluctuation needs to dissipate its energy. This time then is converted with the mean velocity $\bar{u}$ to a physical length.

The problem evolving from these definitions is that the idea of a turbulence length as parameter for the dissipation is more or less rough and dissatisfactory. So far, three different length scales have been defined:

(1) The physical integral scale L which is measurable;

(2) The pseudo-integral scale l which is used e.g. by CFX®;

Table 1 Measured and computed values of Tu and ϵ at the inlet (Pos. A) and within the channel (Pos. B).

Turbulence Tu	
Position A:	$Tu = 9.24\%$
Position B:	$Tu = 9.0\%$
Dissipation ϵ	
Linear develop:	$\epsilon_L = 14.686$ m²/s³
Exponent develop:	$\epsilon_E = 15.2485$ m²/s³

(3) The mixing-length idea l_m which is used e.g. by Fluent®;

While l and l_m have a clear relationship ($\frac{l_m}{l} = C_\mu^{3/4}$), the relation between l or l_m and L is not clear and depends on the investigated flow.

In order to get a boundary condition for the dissipation rate ϵ another approach will be discussed within this work.

As discussed before, the fluctuations are measured at two positions: At the inlet of the test section and within the channel (positions A and B in Fig. 1b). At these positions the turbulence intensity is determined. The Tu-values are given in Table 1.

Using the measured turbulence values at the two different positions the dissipation rate ϵ can be determined directly. Starting from the transport equation for k with the assumption of a non-accelerating flow with a isotropic turbulence the equation for the change of the turbulence kinetic energy [32]

$$\frac{dk}{dt} = P - \epsilon \tag{9}$$

can be used. For a steady flow without turbulence production between the two measurement positions following approximation can be used:

$$\bar{u} \cdot \frac{dk}{dt} = -\epsilon \tag{10}$$

Since the used evaluation system gives Tu the turbulent kinetic energy is obtained by using Eq. (11)

$$k = \frac{3}{2} \cdot \left[\frac{Tu[\%]}{100} \cdot \bar{u}\right]^2 \tag{11}$$

at both measurement positions. Since the distance between these two measurement positions is known as well as the kinetic energy k at these positions, ϵ can be estimated by using Eq. (10). In a first approach a linear decrease of the turbulence kinetic energy between the two positions is assumed, thus ϵ is constant.

Another approach is to assume an exponential decrease of k between the two measurement positions according to

$$k = k_0 \cdot e^{-a \cdot x} \tag{12}$$

where, a can be seen as decay exponent and describes how the turbulence dissipates within the flow. Eq. (12) can be used to calculate k at any position based on a starting value k_0.

Since $k(x)$, k_0 and the distance are known in our test case, the decay exponent a for the wind tunnel can be computed and thus the gradient of k at the inlet $[dk/dx]_{Inlet}$. Inserting this into Eq. (10) leads to the dissipation rate ϵ at the inlet which can be calculated with

$$\epsilon = -\bar{u} \cdot \left[\frac{dk}{dx}\right]_{Inlet} \tag{13}$$

The results of these evaluations are given in Table 1 where ϵ_L represents the solution with a linear and ϵ_E with an exponential decrease of k, respectively. Due to the small change of the measured turbulence intensity the difference between the two ϵ-values is small.

To sum up, five different options for the determination of the turbulence dissipation have been showed: Three length scales (physical integral length scale L, pseudo-integral scale l and mixing length l_m) and two ϵ-values.

In Table 2 the different length scales are listed: L represents the measured value, l_m represents the mixing-length used by LINARS and Fluent® (l_m^* is the mixing-length as recommend by the Fluent modeling guide (see Eq. (6))) and l represents the pseudo-integral length scale used by CFX®. The suffixes L and E represent the dissipation assumption whether it is linear or exponential.

Table 2 clearly shows that the differences between the different length scales are remarkable. To see the influence of the different length scales, simulation results computed with Fluent® and CFX® are given in Fig. 4. The graph shows the development of the turbulence intensity Tu from the inlet to the measurement position B.

The measured physical integral length scale L =

Table 2 Different length scale in meters.

Measurement	$L = 0.18158\ m$
Fluent, modeling guide value	$l_m^* = 0.014\ m$
Fluent, from measured ϵ_L	$l_{m,L} = 0.0575\ m$
Fluent, from measured ϵ_E	$l_{m,E} = 0.0554\ m$
CFX, from measured ϵ_L	$l_L = 0.35\ m$
CFX, from measured ϵ_E	$l_E = 0.337\ m$

0.18158 m shows a too weak dissipation, while the recommended mixing length $l_m^* = 0.014$ m shows a too high dissipation. Both length scales do not fit with the measured decrease of turbulence intensity.

The pseudo-integral scales l and mixing lengths l_m computed from the measured ϵ-values show nearly the same decrease of turbulence intensity as the measured one. It is also observable, that the differences between the assumed linear and exponential turbulence decrease are not high, but the exponential decrease fits slightly better to the measured results.

Both CFX® simulations show a too high turbulence intensity at the inlet, although the same value of $Tu = 9.24\%$ has been specified. However, CFX® computes the same decrease of Tu compared to Fluent® and the measurement.

For the sake of completeness it has to be mentioned that LINARS (also using the mixing-length approach) computes the same development as Fluent®, but is not illustrated in Fig. 4 due to clarity of the chart.

5. Transition Measurements

In this section the measurement and visualization of the transition process at the flat plate are discussed.

Along the flat plate several static pressure tappings are embedded into the plate. The diameter of the tappings is 0.5 mm. These measurement positions are used for Preston-tube measurements.

A Preston tube is traversed all over the plate in streamwise direction in order to locate the transition region. The probe consists of a pitot tube with an inner diameter of 0.5 mm. The Preston tube allows to measure the dynamic pressure close to the wall. This pressure can then be used to calculate the non-dimensional dynamic pressure according to Ref. [35]:

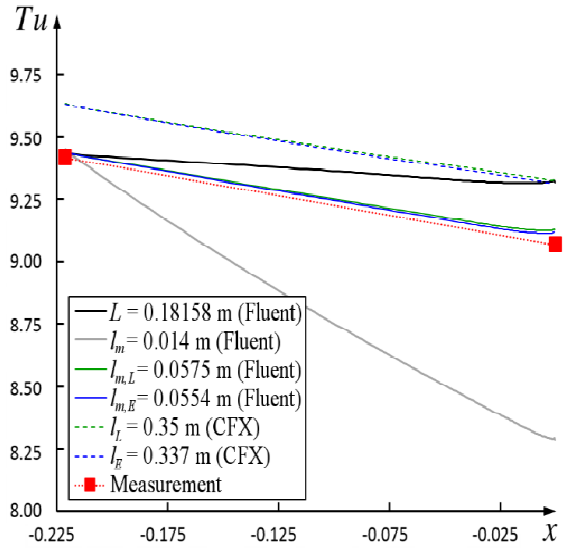

Fig. 4 Simulation results with different length scales.

$$\frac{q_{probe}}{q_\infty} = \frac{p_{t,probe}(x) - p(x)}{p_{t,\infty} - p(x)} \tag{14}$$

where, $p_{t,probe}(x)$ and $p(x)$ represent the total and static pressure acquired by the probe and the tappings, and $p_{t,\infty}$ represents the free-stream total pressure. The result gives an indication of the shape of the velocity profile close to the wall which is then characteristic for the state of the boundary layer. Fig. 5 explains this idea: The upper sketch shows the different velocity profiles of the laminar and turbulent boundary layer. The higher velocity close to the wall of the turbulent boundary layer is due to the fact that more energy can be transported normal to the streamwise direction towards the wall because of its turbulent state [34].

The lower sketch in Fig. 5 shows the streamwise distribution of the non-dimensional dynamic pressure q_{probe}/q_∞ (here q/q_1) and gives an example how the value increases when transition occurs.

However, the probe size has to be kept in mind, since the measured result can only be valid as long as the thickness of the boundary layer is at least twice the distance of the probe from the wall (y_1 in Fig. 5).

As already described, two measurements were performed for two different inlet velocities: $u_{\infty,mean} = 5.3$ m/s and $u_{\infty,mean} = 13.2$ m/s. The turbulence intensity together with the total pressure have been

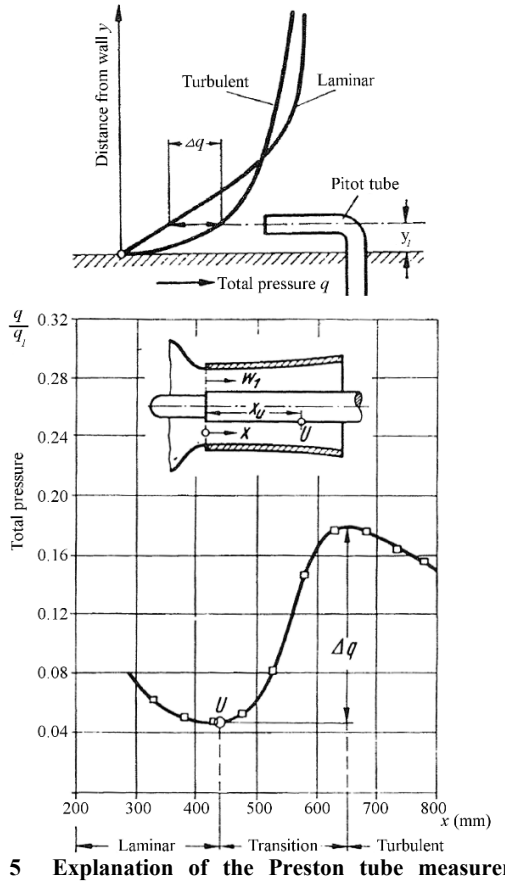

Fig. 5 Explanation of the Preston tube measurement theory.

measured at the inlet plane and the turbulence additionally close to the leading edge of the plate. The values at the inlet plane together with the static pressure at the outlet are used as boundary conditions for the simulations described later.

In Fig. 6 the static pressure along the flat plate is illustrated. The laminar and the turbulent zone are separated by a small peak within the static pressure which is caused by laminar-to-turbulent transition.

The measured q_{probe}/q_{∞} values of both test runs are given in Fig. 7. No transition can be observed for the low speed test case. This also agrees with the above mentioned critical Reynolds number $Re_{x,crit}$ as onset criterion. According to this, transition would start at about the position of the trailing edge of the plate.

The high speed measurements clearly show the start of transition (rise of q_{probe}/q_{∞}) at about 350-400 mm. This again agrees with the assumed onset criterion stated above.

In order to verify the measured transition location, the change of the boundary layer is visualized with the help of a thermographic camera. Since the heat transfer coefficient depends highly on the state of the boundary layer, the surface temperature of a heated plate changes when the boundary layer transitions from laminar to turbulent. The difference in heat transfer can be described by the heat transfer coefficient α which can be calculated with the Nusselt-number defined as

$$Nu_x = \frac{\alpha \cdot x}{\lambda_L} \tag{15}$$

where, λ_L represents the thermal conductivity. Nu_x changes with the state of the boundary layer according to Ref. [36]:

$$Nu_x = 0.332 \cdot Re_x^{0.5} \cdot Pr_x^{0.5} \quad \text{laminar} \tag{16}$$

$$Nu_x = 0.0296 \cdot Re_x^{0.8} \cdot Pr_x^{1/3} \quad \text{turbulent} \tag{17}$$

where, Pr represents the Prandtl number. The correlation between Re_x and Nu_x and thus α isillustrated in Fig. 8 (Pr = 0.71486 for air at 20 °C, 1 bar). In this graph again the critical Reynolds number

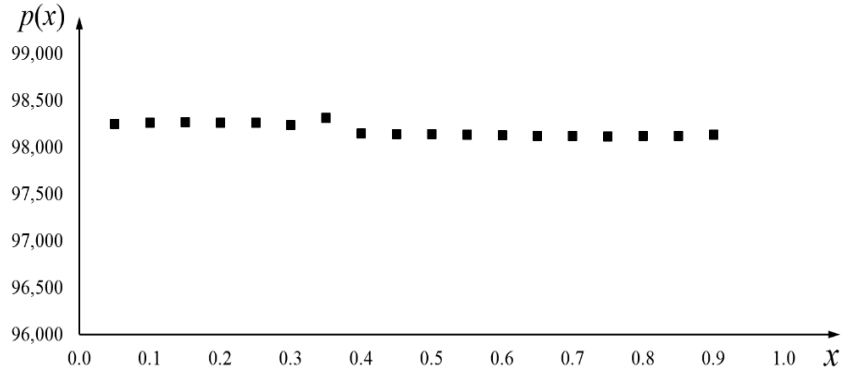

Fig. 6 Static pressure along the flat plate for the high speed test case.

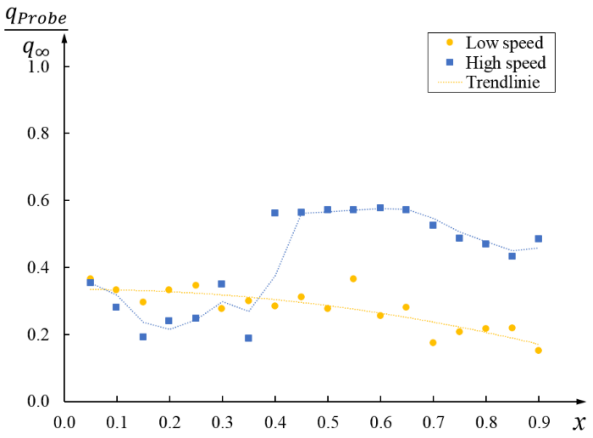

Fig. 7 q_{probe}/q_∞ measurements along the flat plate.

of 3×10^5 is assumed as transition onset criterion.

For the visualization a FLIR® SC620 thermographic camera was used which has a sensitivity < 40 mK at 30 °C. The camera was placed above an optical access at the top of the channel (illustrated in Fig. 1b) and recorded about 100 mm of the plate length.

On the flat plate a heating foil was glued with a constant heating input. The optical access was placed in such a way, that it is situated above the expected transition zone.

The result of the visualization is given in Fig. 9. The picture shows that the temperature of the heating foil drops at about 410 mm plate length. This most likely indicates a transitional zone and agrees well with the results of the Preston probe measurements.

6. Transition Simulation

Both measurement techniques showed that transition occurs at approximately 400 mm plate length. In the following numerical results are compared with the measurements to see how the transition model can predict the measured transition zone.

All inlet conditions are taken from the measurement. For the length scale $l_{m,L} = 0.0575\,m$ for Fluent® and LINARS and $l_L = 0.35\,m$ for CFX® are used which have been computed from the measured dissipation rate ϵ.

Fig. 10a shows the skin friction coefficient c_f at the plate for all three simulations. c_f is defined as

$$c_f = \frac{\tau_W}{\frac{1}{2} \cdot \rho \cdot u_\infty^2} \tag{18}$$

where, τ_W is the wall shear stress and u_∞ is the free stream velocity. All three codes used the $\gamma - Re_\Theta$-model and Fluent® additionally the $k - k_L - \omega$-model. All three codes failed in predicting the measured transition zone with the $\gamma - Re_\Theta$ model. The skin friction values show a fully turbulent boundary layer along the plate surface.

On the other hand, the $k - k_L - \omega$ turbulence model predicted successfully a transitional zone although it starts more upstream compared to the measured transition location.

A possible reason for not predicting transition with the $\gamma - Re_\Theta$-model is observable in Fig. 10b which shows the skin friction development along the flat plate for different turbulence intensities Tu computed with Fluent®. The chart shows, that for decreasing inlet

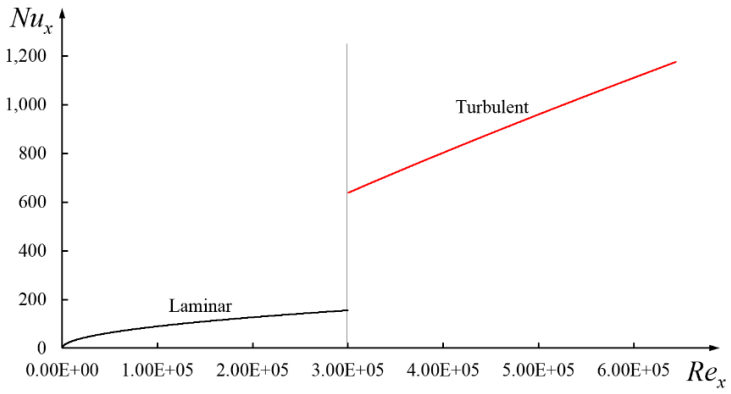

Fig. 8 Nusselt number over Reynolds number for laminar and turbulent boundary layer.

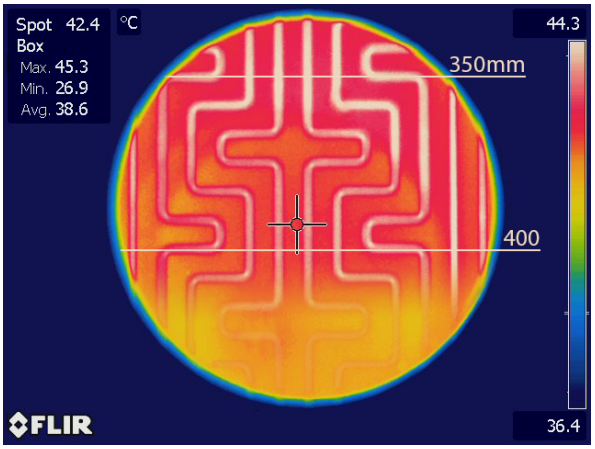

Fig. 9 Recording of the thermographic camera.

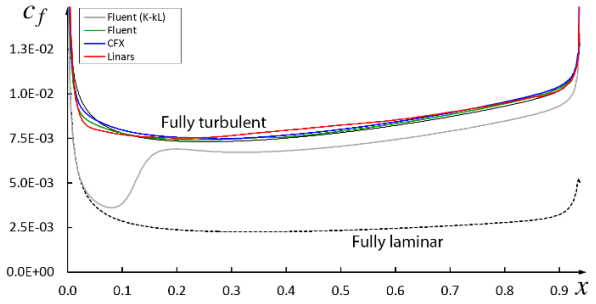

(a) Comparing the three codes

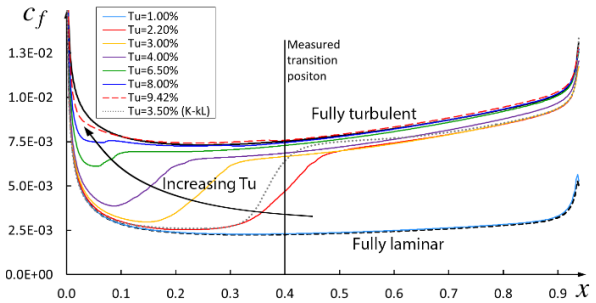

(b) Comparing different Tu levels with Fluent®

Fig. 10 Computed development of skin friction coefficient c_f along the flat plate.

turbulence intensity Tu transition is predicted. With an inlet turbulence intensity of about $Tu = 2.2\%$ the simulation shows a similar transition position as the measurements. At $Tu = 1\%$ no transition is observable anymore since the boundary layer stays laminar along the whole plate. It seems that for the high inlet turbulence the $\gamma - Re_\Theta$ transition model is not able to predict a laminar flow at the leading edge of the plate; thus no transition can be observed.

In Fig. 10b, also the $k - k_L - \omega$ model result is given for a lower inlet turbulence intensity. For $Tu = 3.5\%$ this model predicts a similar onset of the transition zone as the measurements. Compared to the $\gamma - Re_\Theta$-model result, the transitional zone is also smaller, which agrees better with the measurements, since the increase of q_{probe}/q_∞ spans only the distance between two measurement positions (see Fig. 7).

Both models show a different behavior when varying the turbulence intensity, but both react sensibly to the boundary condition.

7. Summary and Conclusions

In the present work the transition on a flat plate has been investigated. The measurements and simulations performed in the scope of this work are intended for a better understanding of transition prediction, both experimentally and numerically.

First, the paper describes the setup of a test bench. Therefore several important considerations are described which should be followed when designing such a test facility.

One major outcome of the study is that the turbulence inlet boundary conditions of the numerical simulations have a high impact on the result of the simulation, especially when it comes to transition. The investigation also showed that there are differences in the definition of the turbulence length scales and the needed length scale for the simulation cannot be measured directly. A general correlation between the measured integral length scale and the pseudo-length scale used by CFD would be helpful, but this needs more experimental data.

Two different techniques to measure and visualize transition have been tested successfully: Preston tube measurements and visualization with a thermographic camera. Regarding the computational results, the $\gamma - Re_\Theta$-model was not able to predict the transition process of this test case as observed in the measurements. On the other hand the $k - k_L - \omega$ turbulence model could predict transition but at a more upstream position.

Further numerical studies are necessary to understand the deficiencies of these models.

Further experimental and numerical studies are planned and should help to better understand the complex mechanism of transition. The result will form the basis for further studies on the mechanism of relaminarization.

Acknowledgement

The authors would like to especially thank Marn Andreas, Selic Thorsten and Bauinger Sabine for their immense support during the setup of the test bench and the measurement campaign.

The authors would also like to thank the Austrian Federal Ministry for Transport, Innovation and Technology who funded the project RELAM within the Austrian Aeronautics Program TAKE OFF.

References

[1] Schlichting, H., and Gersten, K. 2006. *Grenzschicht-Theorie (Boundary-Layer Theory)*. Springer-Verlag Berlin Heidelberg.

[2] Mayle, R. E. 1991. "The Role of Laminar-Turbulent Transition in Gas Turbine Engines." *Journal of Turbomachinery* 113 (October): 509-37.

[3] Yip, L. P., Vijgen, P., Hardin, J. D., and Van Dam, C. P. 1993. "In-flight Pressure Distributions and Skin-Friction Measurements on a Subsonic Transport High-Lift Wing Section." Presented at AGARD, High-Lift System Aerodynamics.

[4] Oyewola, O., Djenidi, L., and Antonia, R. A. 2003. "Combined Influence of the Reynolds Number and Localised Wall Suction on a Turbulent Boundary Layer." *Experiments in Fluids* 35 (July): 199-206.

[5] Oyewola, O. 2006. "LDV Measurements in a Pertubed Turbulent Boundary Layer." *Journal of Applied Science* 6 (14): 2952-5.

[6] Widmann, A., Duchmann, A., Kurz, A., Grundmann, S., and Tropea, C. 2012. "Measuring Tollmien-Schlichting Waves Using Phase-Averaged Particle Image Velocimetry." *Experiments in Fluids* 53 (3): 707-15.

[7] Mukund, R., Narasimha, R., Viswanath, P. R., and Crouch, J. D. 2012. "Multiple Laminar-Turbulent Transition Cycles Around a Swept Leading Edge." *Experiments in Fluids* 53 (6): 1915-27.

[8] Walters, K., and Cokljat, D. 2008. "A Three-Equation Eddy-Viscosity Model for Reynolds-Averaged Navier-Stokes Simulations of Transitional Flows." *Journal of Fluids Engineering* 130 (12): (121401) 1-14.

[9] Menter, F. R., Langtry, R. B., Likki, S. R., Suzen, Y. B., Huang, P. G., and Völker, S. 2006. "A Correlation Based Transition Model Using Local Variables Part 1: Model Formulation." *Journal of Turbomachinery* 128 (3): 413-22.

[10] Langtry, R. B. 2006. "A Correlation-Based Transition Model Using Local Variables for Unstructured Parallelized CFD Codes." Ph.D. thesis, University Stuttgart.

[11] Elsner, W., Piotrowski, W., and Drobniak, S. 2008. "Transition Prediction on Turbine Blade Profile with Intermittency Transport Equation." *Journal of Turbomachinery* 132 (1): 11-20.

[12] Langtry, R. B., and Menter, F. R. 2009. "Correlation Based Transition Modeling for Unstructured Parallelized Computational Fluid Dynamics Codes." *American Institute of Aeronautics and Astronautics Journal* 47 (12): 2894-906.

[13] Sorensen, N. N. 2009. "CFD Modeling of Laminar-Turbulent Transition for Airfoil and Rotors Using the $\gamma - Re_{\Theta}$ Model." *Wind Energy* 12 (8): 715-33.

[14] Malan, P., Suluksna, K., and Juntasaro, E. 2009. "Calibrating the $\gamma - Re_{\Theta}$ Transition Model for Commercial CFD." In *Proceedings of the 47th AIAA Aerospace Sciences Meeting Including the New Horizons Forum and Aerospace Exposition,* 1-20.

[15] Kelterer, M. E., Pecnik, R., and Sanz, W. 2010. "Computation of Laminar-Turbulent Transition in Turbomachinery Using the Correlation Based $\gamma - Re_{\Theta}$ Transition Model." In *Proceedings of the ASME Turbo Expo,* 613-22.

[16] Camp, T. R., and Shin, H. W. 1995. "Turbulence Intensity and Length Scale Measurements in Multistage Compressors." *Journal of Turbomachinery* 117 (January): 38-46.

[17] Axelsson, L.-U., and George, W. 2008. "Spectral Analysis of the Flow in an Intermediate Turbine Duct." In *Proceedings of the ASME Turbo Expo,* 1419-26.

[18] Axelsson, L.-U. 2009. "Experimental Investigation of the Flow Field in an Aggressive Intermediate Turbine Duct." Ph.D. thesis, Chalmers University of Technology.

[19] Craft, T. J. 2011. *Turbulence Length Scales and Spectra*. Lecture Notes for Advanced Turbulence modeling, The University of Manchester.

[20] ANSYS. 2012. *Ansys CFX-Solver Modeling Guide*. Release 14.5. ANSYS Inc.

[21] Pecnik, R., Pieringer, P., and Sanz, W. 2005. "Numerical Investigation of the Secondary Flow of a Transonic Turbine Stage Using Various Turbulence Closures." In *Proceedings of the ASME Turbo Expo,* 1185-93.

[22] Roe, P. L. 1997. "Approximate Riemann Solver, Parameter Vectors, and Differencing Scheme." *Journal of Computational Physics* 135 (2): 250-8.

[23] Menter, F. R. 1994. "Two-Equation Eddy-Viscosity Turbulence Models for Engineering Applications." *American Institute of Aeronautics and Astronautics Journal* 32 (8): 1598-605.

[24] Coupland, J. 1990. "Flat Plate Transitional Boundary Layers." ERCOFTAC "Classic Collection" Database. Accessed March 15, 2016. http://cfd.mace.manchester.ac.uk/cgi-bin/cfddb/ezdb.cgi?ercdb+search+retrieve+&&&SemiCFlow1g=Yes%%%%dm=Line.

[25] Persico, G., Gaetani, P., and Guardone, A. 2005. "Design and Analysis of New Concept Fast-Response Pressure Probes." *Measurement Science and Technology* 16 (9): 1741-50.

[26] Kolmogorov, A. N. 1991. "The Local Structure of Turbulence in Incompressible Viscous Fluid for Very Large Reynolds Numbers." *Proceedings: Mathematical and Physical Sciences* 434 (1890): 9-13.

[27] Kolmogorov, A. N. 1991. "Dissipation of Energy in a Locally Isotropic Turbulence." *Proceedings: Mathematical and Physical Sciences* 434 (1890): 15-17.

[28] Obukhov, A. M. 1941. "On the Distribution of Energy in the Spectrum of Turbulent Flow." *Doklady Akademii Nauk SSSR* 32 (1): 22-4.

[29] Prandtl, L. 1925. "Bericht Über Untersuchungen Ausgebildeter Turbulenz." *Zeitschrift Für Angewandte Mathematik und Mechanik* 5 (2): 136-9.

[30] Bradshaw, P. 1974. "Possible Origin of Prandtl's Mixing-Length Theory." *Nature* 249 (6): 135-6.

[31] Gamard, S., and George, W. K. 2000. "Reynolds Number Dependence of Energy Spectra in the Overlap Region of Isotropic Turbulence." *Flow, Turbulence and Combustion* 63 (1-4): 443-77.

[32] Pope, S. B. 2000. *Turbulent Flows*. Cambridge: Cambridge University Press.

[33] ANSYS. 2015. "Using Flow Boundary Conditions." In *Ansys Fluent Documentation*, Release 16.0. ANSYS Inc.

[34] Schlichting, H. 1965. *Grenzschicht-Theorie (Boundary-Layer-Theory)*. Verlag G. Braun, Karlsruhe.

[35] Händel, D., Rockstroh, U., and Niehuis, R. 2014. "Experimental Investigation of Transition and Separation Phenomena on an Inlet Guide Vane with Symmetric Profile at Different Stagger Angles and Reynolds Numbers." In *Proceedings of the 15th International Symposiumon Transport Phenomena and Dynamics of Rotating Machinery,* 1-9.

[36] Polifke, W., and Kopitz, J. 2005. "Wärmeübertragung." *Heat Transfer, Pearson Education, München*.

5.4. Paper 2: Innovative Acoustic Measurement Technique for Boundary Layer Transition Detection

---

A. Cinciripini, P. Bader, G. Persico and W. Sanz, "Innovative Acoustic Measurement Technique for Boundary Layer Transition Detection," *submitted to Journal of Mechanics Engineering and Automation.*

Innovative Acoustic Measurement Technique for Boundary Layer Transition Detection

Alessandro Cinciripini[2], Pascal Bader[1], Giacomo Persico[2] and Wolfgang Sanz[1]

1 Institute for Thermal Turbomachinery and Machine Dynamics
Graz University of Technology, Inffeldgasse 25/A, 8010 Graz, Austria
pascal.bader@tugraz.at, wolfgang.sanz@tugraz.at
2 Dipartimento di Energia
Politecnico di Milano, Via La Masa 34, 20158 Milano, Italy
alessandro.cinciripini@mail.polimi.it, giacomo.persico@polimi.it

Abstract

Different methods to detect boundary layer transition are investigated within the scope of this paper.
Laminar and turbulent boundary layers show a significantly different behavior, not only regarding skin friction but also for heat-transfer which affects the blade cooling design. Therefore, predicting the transition position in turbomachinery applications is often crucial.
Experimental measurements were performed for subsonic flow velocities over a flat plate with no pressure gradient. The flat plate is located in a channel with square section. In the first step, transition was investigated by a Preston tube which consists of a stagnation pressure probe together with static pressure tappings along the surface of the plate; this technique allows to evaluate the stream-wise variation of dynamic pressure due to transition. In the second step, microphones located along the plate were used to detect transition based on the fluctuations of pressure. The advantage of this measurement technique is that it is non-intrusive, i.e. it does not influence the flow within the boundary layer because there is no blockage effect in contrast to probe-based techniques.
Since the transition position is strongly dependent on the free-stream turbulence intensity, measurements with a Fast Response Aerodynamic Pressure Probe were performed in order to determine the turbulence intensity and the dissipation rate upstream of the plate.
Additionally, the results of the experimental studies are compared with numerical RANS simulations using different turbulence models in order to determine their capability to predict transition. It was assumed that the lateral sides of the channel do not influence the flow at mid section, so that a two-dimensional simulation was performed. The two commercial codes Fluent® and CFX® by Ansys® are used in addition to the open-source code OpenFOAM®, whereas the turbulence models that are applied are the k-k_L-ω and γ-$Re_{\theta t}$ models, since they are specifically developed to predict transition.
Keywords: Transition measurement, acoustic, Preston tube

Introduction

Transition is the process by which a laminar flow becomes turbulent. A laminar flow is characterized by a well ordered particle motion opposed to a turbulent one, where the paths of the particles are more chaotic. Transition is a very complex process, not yet fully understood, and its prediction is nowadays still subject of an intensive research. It occurs in most of turbomachinery and aeronautics applications, such as gas turbines, compressors, turbofan engines or plane wings.

The boundary layer is the small zone between the wall and the free-stream where viscous effects are relevant. In spite of its small size, the boundary layer is crucial because it determines the skin friction and the heat transfer between flow and solid surfaces. A boundary layer can present either a laminar or a turbulent nature, that affect substantially the skin friction and the heat transfer rate, due to a different gradient of velocity at the wall. A turbulent boundary layer presents a higher skin friction indeed. Also the heat transfer through solid surfaces increases considerably in a turbulent boundary layer. Depending on the application, this issue can be problematic, since overheating can take place. For these reasons, predicting where transition develops is crucial, not only from the economical point of view, but for safety reasons too. Moreover, a turbulent boundary layer presents a much more stable behavior, that means that flow separation (stall) occurs less often, in contrast to a more unstable behavior of a laminar boundary layer.

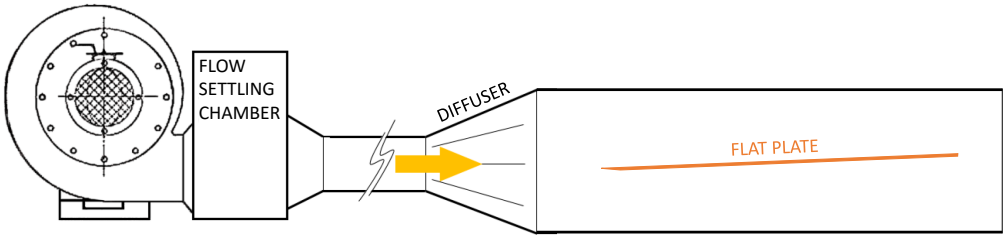

(a) Test bench scheme.

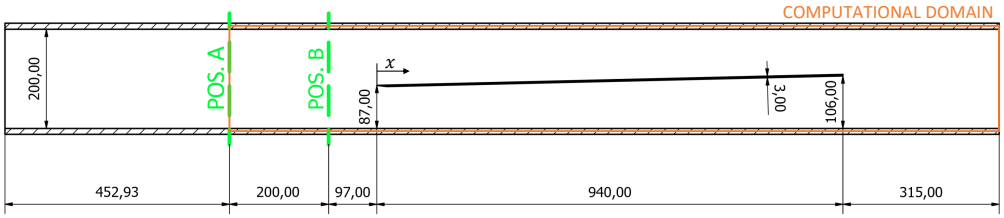

(b) Test facility geometry.

Figure 1 Schematic illustrations of the test bench

When a fluid flows past a stationary solid surface, a laminar boundary layer develops, growing from the leading edge. During its interaction with the solid structure, the boundary layer may become turbulent. This process passes through several stages within the transitional zone, until it reaches a fully turbulent behavior. The transition position and the length of this process are affected by many parameters like free-stream velocity, acceleration, free-stream turbulence etc. It is very important to study the influence of these parameters on the onset and the length of the transitional zone, in order to influence and possibly control the state of the boundary layer. In some machines, the efficiency of blades and stages can be improved by studying the influence of transition; this leads to the possibility to improve the overall engine performance.

In 1991, Mayle published one of the most important overviews about boundary layer transition [10]. He gathered and analyzed the main results of different experimental researches, in order to present the influence of several flow parameters on the transition process.

Additional experiments were performed in the last years by different research groups. Yip et al. [20] carried out in-flight measurements with a Preston tube. They detected the boundary layer transition over the wing surfaces and analyzed the influence of the flight conditions on the boundary layer behavior. Oyewola et al. [12] showed how to measure the turbulence generated within boundary layers with the help of hot-wire probes and Laser-Doppler velocimetry (LDV). In 2008 Døssing showed the results of acoustic measurements performed on an airfoil with the aim of detecting the boundary layer transition [7]. More recently, hot-film measurements were performed, e.g., by Mukund et al. [11], Preston tube and thermographic measurements by Bader and Sanz [2]. Recently, Bader et al. [3] used Laser Interferometric vibrometry (LIV) to predict transition.

Beside the experimental methods to observe the transition process, specific turbulence models for CFD simulations were developed with the scope of predicting this phenomenon. The most important transitional models are: k-k_L-ω [18] and γ-$Re_{\theta t}$ [9]. Both are based on the k-ω model [19], with the addition of one or more equations that model the transition process.

The aim of this work is to test an innovative acoustic measuring technique, that is supposed to be able to detect the boundary layer transition over a zero pressure gradient flat plate and compare these results to Preston tube measurements of the same flow, since it is a well-validated measuring technique. The results are also compared to a CFD simulation of the experimental case, that was carried out to verify the effectiveness of the transitional models employed. The turbulence quantities set at the inlet of the computational domain as boundary conditions are based on measurements performed directly on the test facility by means of a Fast Response Aerodynamic Pressure Probe. This is crucial in order to run an effective transition simulation.

Experimental setup

All experimental investigations were performed at the Institute for Thermal Turbomachinery and Machine Dynamics (ITTM) at Graz University of Technology, Austria. The test rig is a continuously operating open-loop wind tunnel. Within the flow channel, at about half of its height, a horizontal carbon steel flat plate is positioned. The flat plate entirely fills the transversal width of the inner cross section. The dimension of the channel internal cross-section is 200×200 mm and it is 2 m long. Figure 1b shows the vertical section of the channel.

The air flow is delivered by a centrifugal compressor with a max. power of 125 kW, corresponding to a mass flow rate of approximately 0.8 kg/s. The compressor delivers air into a flow settling chamber. From this chamber the flow is transported via a flow-calming section formed

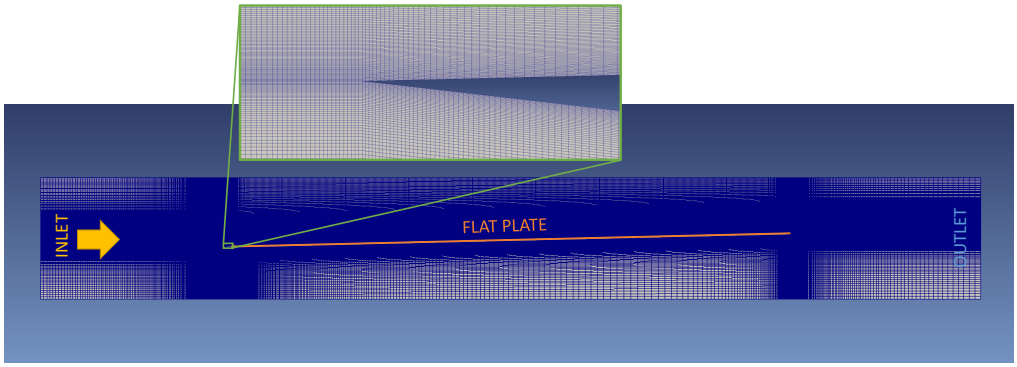

Figure 2 Computational domain

by a diffuser with guiding vanes towards the test area. A schematic drawing of the test bench is given in Figure 1a. A damping element made of polymeric rubber is inserted between the diffuser and the channel. The flow velocity was measured with the help of a rotating vane anemometer. It is equal to 18.12 m/s.

The flat plate is inclined about $1.3°$ to the mean stream vector. As reported in [6], a very small inclination of the plate ensures an attached flow over it and also a steady leading edge stagnation point. Nevertheless, this solution causes a small pressure gradient over the flat plate, but according to Mayle [10], the effect of this acceleration is considered negligible.

Every experimental measurement was performed in thermal steady-state conditions.

Numerical Setup

The computational domain shown in Fig. 2 is represents the entire channel section. The mesh was built 2-dimensional, so it was assumed that the external boundary layers in span-wise direction do not affect the channel mid section where the experimental investigations were carried out. Three grids with different cell density were built in order to perform a mesh independence analysis. The coarsest one has about 70k elements, the medium one about 192k elements, while the finest one about 507k. Figure 2 shows the coarse mesh. In all the three meshes a y^+ value between 0 and 1 is checked along the plate.

Regarding the boundary conditions, the inlet velocity is taken from the measurements with a rotating vane anemometer and the values of the turbulent kinetic energy and the turbulence dissipation rate are obtained from FRAPP measurements, which are described later. At every wall a no-slip velocity condition is set, but at the upper and the lower walls of the channel a wall-function for the turbulence models is activated, in order to save computational time.

Fluent® and CFX® by Ansys® in addition to the open-source code OpenFOAM® are employed. The main difference between Fluent® and CFX® is that the first one uses a SIMPLE algorithm that provides a lower computational time and it is more robust, while the second one uses a solver that fully-couples momentum and pressure equations. OpenFOAM® allows to use the SIMPLE algorithm as well.

The simulations performed with OpenFOAM® are run employing both the $k - k_L - \omega$ and the $\gamma - Re_{\theta t}$ transitional models. CFX® is run with the $\gamma - Re_{\theta t}$ model, while Fluent® employs the $k - k_L - \omega$ model. Hence, 4 different types of numerical simulations for the BL transition are analyzed and are going to be presented.

Turbulence and dissipation measurements

As already stated, the boundary layer transition is strongly affected by the turbulence level of the flow. Therefore, in order to execute a proper technical analysis of this issue, a direct measurement is crucial. Knowing the turbulence properties is essential for the numerical simulation within this work. In order to obtain the turbulence quantities, a cylindrical single-sensor *Fast Response Aerodynamic Pressure Probe* (FRAPP) is employed. A miniaturized piezo-resistive pressure sensor (Kulite XCE-062) is installed inside the probe head, which has an outer diameter of 1.85 mm. The probe aerodynamic accuracy was evaluated in a calibrated nozzle, giving an extended uncertainty equal to $\pm 0.5\%$ of the kinetic head for the pressure measurements and equal to $\pm 0.3°$ for the flow angle. Persico et al. [13] presented more details about the probe design and calibration.

The measurements were carried out downstream of the diffuser (Position A in Fig. 1b), in correspondence with the numerical domain inlet. Close to the leading edge (Position B) *Tu* is measured again to obtain the turbulence dissipation and the turbulence length scale, respectively. In both positions the measurements were carried out in seven different channel heights, in order to obtain a mean value of *Tu* along the channel cross-section.

The FRAPP sensor provides a total pressure time-signal, from which the flow fluctuations intensity can be obtained. According to the Reynolds decomposition technique, every fluid dynamic quantity can be split into two components, i.e. the time average and fluctuating parts of the quantity. Hence, this technique can be applied both to the time-varying pressure and to the time-varying velocity. According to Camp and Shin [5], the definition of turbu-

lence intensity *Tu* of a flow is given by:

$$Tu = \frac{1}{\overline{u}} \cdot \sqrt{\frac{1}{N} \sum_{i=1}^{N} {u_i}^2} \tag{1}$$

where N is the number of samples of the time-signal, $\overline{u}$ and u_i represent the average and the fluctuating components of the flow velocity respectively. Equation 1 may be seen as the root mean square value of u_i divided by $\overline{u}$. In order to relate the total pressure fluctuations that are measured by the FRAPP probe to the velocity fluctuations, Persico et al. [13] provided the following formula, based on an approach by Wallace and Davis [17]:

$$\begin{aligned} {p'_{t,rms}}^2 = 0.49\rho^2 \left(1 - 0.175\overline{M}^4\right) {u'_{rms}}^4 + \\ + \rho^2\overline{u}^2 \left(1 + 0.5\overline{M}^2\right) {u'_{rms}}^2 \end{aligned} \tag{2}$$

where $p'_{t,rms}$ is the RMS value of the fluctuating total pressure, $\overline{M}$ is the Mach number of the free-stream and ρ the fluid density. Working out this equation, u'_{rms} is obtained.

Before calculating $p'_{t,rms}$ from the data, it is necessary to remove all the periodic components of the measured raw signal, since only the non-periodic stochastic part of the signal represents turbulence [1]. These periodic components are the blades passing frequencies or flow fluctuations due to the rotor-stator interaction inside the centrifugal compressor. To perform this reduction, the acquired signal has to be Fast Fourier Transformed (FFT) in order to "chop" these frequency components. This procedure is explained in details in [5]. High-pass and low-pass filters have to be also applied at the frequency-transformed signal, in order to discard frequency ranges not related to turbulence. After that, every processed signal is transformed back into a time-signal, by means of an inverse Fast Fourier Transform (iFFT) algorithm, so that the RMS value of the velocity fluctuations can be evaluated.

Figure 3 shows an unchopped signal spectrum, measured with FRAPP. The green arrows point out the deterministic periodic components that have to be chopped. The main periodic component can be seen on the left, followed by the harmonics for higher frequencies. In this figure, also the Kolmogorov $-5/3$ energy cascade function is plotted. It can be observed that the spectrum fits the $-5/3$ up to about 7 kHz. Here, the low-pass filter is applied. In order to obtain the high-pass filter frequency, the integral length scale has to be estimated. The integral length scale L assigns a spatial dimension to the turbulent structures and can be identified as the average size of the largest eddies involved in a flow. Once the average size of these turbulence structures is known, their characteristic time scale τ_I, which corresponds to the high-pass frequency, can be estimated. Considering that u'_{rms} represents the characteristic velocity of the flow fluctuations, it may be assumed as the rotational velocity of the highest scale eddies: $\tau_I \simeq L/u'_{rms}$. Thus, the inverse of τ_I corresponds to the high-pass frequency f_I. According to [5], the integral length scale can be computed by means of an autocorrelation function $ACF(\tau)$ of the turbulent velocity time-signal. It is given by:

$$L = \overline{u} \int_0^\infty ACF(\tau)\, d\tau \tag{3}$$

This definition is effective only if every deterministic periodic component of the signal, such as the blade passing frequencies of the compressor, is removed. This calculation is performed with the processed time-signal, so, after the analysis in the frequency domain explained above and the iFFT are carried out. Nevertheless, both L and u'_{rms} at the first computation are based on a signal where no high-pass filter is applied, since this frequency is still unknown. Thus, an iterative procedure is required: after the first computation, f_I is applied to the Fourier transformed signal in order to cut out the low frequency range that is not related to turbulence. The iFFT is then computed and this procedure repeated with the new u'_{rms} and the new L. The iterations are repeated until convergence is obtained. Table 1 shows the results of the turbulence quantities, as averaged values of different measuring locations along the cross-section, in both Pos. A and Pos. B.

In order to simulate the experimental investigations with CFD, beside the turbulence intensity, also the dissipation is necessary. Therefore, an approach suggested by Bader and Sanz [2] is used. As discussed before, the turbulence level is calculated in two different positions (A and B). Using these values, ϵ can be calculated directly. The transport equation for the turbulent kinetic energy k, with the assumption of steady-state and non-accelerating flow, isotropic turbulence and with no turbulence production between the two measured positions reduces to [14]:

$$\overline{u}\frac{dk}{dx} = -\epsilon \tag{4}$$

According to Schlichting and Gersten [15], at a certain distance from screens or honeycombs, the turbulence in a wind tunnel becomes isotropic. Therefore, the turbulent kinetic energy k can be computed in both measuring positions by means of u'_{rms}:

$$k = \frac{3}{2}\left(u'_{rms}\right)^2 \tag{5}$$

Since the distance between these two measurement positions is known together with k of these positions, ϵ can be

Table 1 Turbulence quantities

	Position A	Position B
u'_{rms}	1.230 $[m/s]$	1.165 $[m/s]$
k	2.269 $\left[m^2/s^2\right]$	2.036 $\left[m^2/s^2\right]$
Tu	6.788 %	6.429 %
L	0.0025 $[m]$	
f_I	320 $[Hz]$	
ϵ	21.11 $\left[m^2/s^3\right]$	

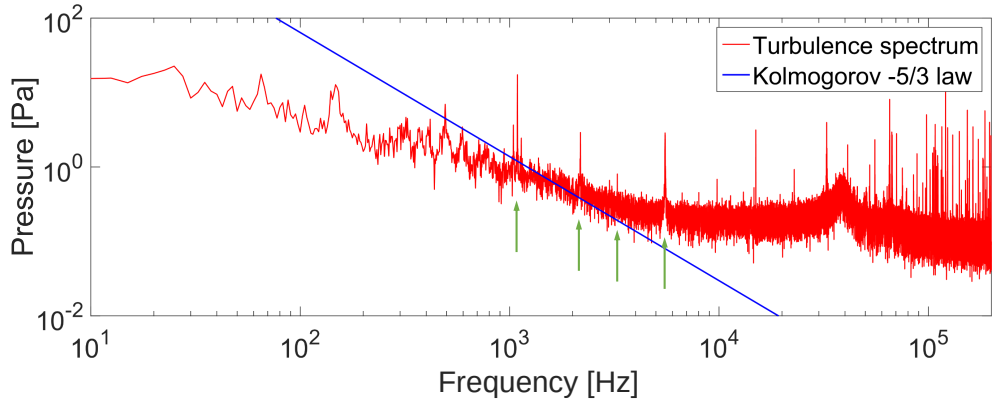

Figure 3 Measured FRAPP uncut signal

estimated by using Equation 4, assuming a linear decay. The results of these evaluations are given in Table 1. The values related to the Position A of the test facility, which corresponds to the inlet of the computational domain, can be used as boundary conditions for the numerical simulations.

Transition measurements

In this section, the experimental investigations that were carried out to detect the boundary layer transition are discussed. First, the Preston tube measurements are presented, followed by the acoustic measurements.

Preston tube measurements

Turbulent and laminar boundary layers present different velocity profiles $u(y)$ at the walls. A turbulent boundary layer is characterized by a high exchange of momentum in transverse direction, causing a more uniform distribution over the cross-section of a duct, if compared to a laminar BL. The Preston tube measuring method employs this different physical behavior to detect the boundary layer transition.

Along the flat plate surface, several static pressure tappings are embedded into the plate. The diameter of the tappings is $0.5\ mm$ and they are equally spaced with $50\ mm$, resulting in 18 static pressure tappings along the plate.

A Preston tube is traversed all over the plate in the stream-wise direction in order to capture the stagnation pressure of the flow. The probe consists of a Pitot tube with an outer diameter of $1\ mm$ and an inner diameter of $0.5\ mm$, that is the same dimension as the tappings. Considering the size of the tube section, it allows to measure the flow velocity at $y_1 = 0.5\ mm$ from the wall. The total pressure that the Preston tube measures can then be used, together with the static pressures, to calculate the non-dimensional dynamic pressure. Let x be the distance from the leading edge, according to [2] the non-dimensional dynamic pressure is given by:

$$\frac{q_{probe}}{q_\infty} = \frac{p_{t,probe}\,(x) - p\,(x)}{p_{t,\infty} - p\,(x)} \tag{6}$$

where p_t and p are the total pressure and the static pressure respectively. Before performing the measurements, the Preston tube size has to be validated: the distance between the probe middle axis and the wall y_1 has to be at least half of the boundary layer thickness, in every measuring position. The first measuring position ($50\ mm$ from the leading edge) is the most critical one – assuming that the transition occurs after this point – since the laminar boundary layer has just started to develop. The Blasius solution can be employed to estimate the boundary layer thickness $\delta_{99} = x\frac{4.9}{\sqrt{Re_x}}$ at $50\ mm$ from the leading edge, based on the local free-stream velocity. The formula provides a thickness of $1.16\ mm$. The minimum thickness is then confirmed because the value is greater than $1\ mm$ (twice y_1).

Figure 4 shows the non-dimensional dynamic pressure from the leading to the trailing edge fo the plate. The onset of transition can be seen at about $150/200\ mm$, after which the dynamic pressure suddenly changes from 0.4 to 0.8 of the free-stream value. This phenomenon indicates that the velocity profile changes from laminar to turbulent, where the momentum exchange is enhanced toward the wall. At about $x = 300\ mm$ the transition process is supposed to be completed.

Acoustic measurements

Acoustic measurements were performed with high frequency response microphones on the flat plate, with the scope to detect boundary layer transition. Several microphones were embedded into the structure of the flat plate, below the surface. The microphones do not generate a blockage effect, making this measurement method non-intrusive. They can measure the sound pressure level of the boundary layer through a series of thin holes, with a diameter of $1\ mm$ and a depth of $1\ mm$, that were drilled over the surface. The signals are then recorded simultaneously, monitoring the variation of the static pressure fluctuations along the plate.

The detection of the transition location is based on an evaluation of the RMS pressure fluctuations, registered by

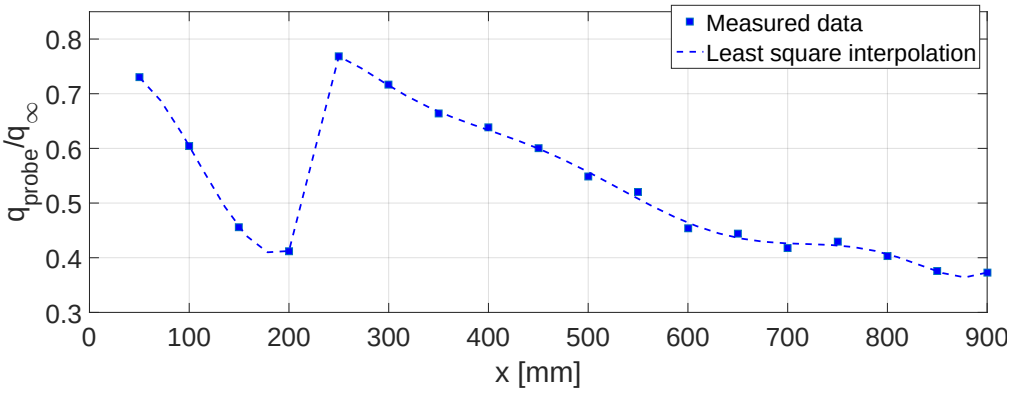

Figure 4 Non-dimensional dynamic pressure

the microphones along the plate. The transition from laminar to turbulent boundary layer is associated with a large increase in velocity fluctuations, due to the nature of the turbulent boundary layer. The velocity fluctuations are coupled to the pressure fluctuations, as it can be seen by analyzing the Navier-Stokes equation, after the divergence operator is applied. By assuming an incompressible, two-dimensional, inviscid and steady-state flow, the result is a relationship between pressure and velocity. The Equation takes the form:

$$\frac{1}{\rho}\nabla^2 p = -\frac{\partial u_i}{\partial x_j}\frac{\partial u_j}{\partial x_i} \tag{7}$$

Farabee [8] took this equation to perform a Reynolds decomposition into mean and unsteady terms. Splitting each quantity and then subtracting the time-averaged equation yields to:

$$\frac{1}{\rho}\nabla^2 p' = -2\frac{\partial \overline{u}_i}{\partial x_j}\frac{\partial u'_j}{\partial x_i} - \frac{\partial^2\left(u'_i u'_j - \overline{u'_i u'_j}\right)}{\partial x_j \partial x_i} \tag{8}$$

Equation 8 is a Poisson equation for the fluctuating pressure p in a turbulent flow. The source terms on the right hand side of Eq. 8 represent the *mean-shear-turbulence* (MT) interaction (first term) and the *turbulence-turbulence* (TT) interaction (second term) [8]. This relationship suggests that, in a turbulent flow, the pressure fluctuations are a result of the velocity fluctuations and their gradients.

A number of 24 microphones were used for this experimental investigation. The model is the 40BD 1/4" Prepolarized Pressure Microphone by G.R.A.S.®, operating with a high-precision condenser technology. Their precision respects the IEC 61094-4 requirements. They provide an high frequency response, from 4 to 70000 Hz with ± 2 dB of accuracy, and from 10 to 25000 Hz with ± 1 dB of accuracy. Their low sensitivity makes them ideal for sound measurements at high sound pressure levels, up to 174 dB. The shape of these microphones is cylindrical, the diameter is about 6 mm and they are 50 mm long. The head presents a diaphragm that transmits the sound vibrations to the condenser.

A data processing similar to that done for the FRAPP measurements has to be performed in order to chop the deterministic components related to blade passing frequencies and the ranges of the spectrum that do not belong to turbulence. For this reason, due to the presence of high amplitude deterministic components, a direct comparison between raw time signals cannot be carried out.

After the frequency-domain analysis, the iFFT is applied to each signal in order to obtain the RMS value of the pressure fluctuations. The first measurement results showed that the microphones were measuring the modes of vibration of the flat plate. Most of the sound pressure level that each microphone was registering came from the flat plate vibration which dominated the relatively low "noise" caused by turbulence.

In order to overcome this problem, a turbulator was mounted very close to the leading edge of the plate generating a turbulent boundary layer. If the turbulator is very thin, the dead-water region downstream is small too. The aim of this attempt is to create an experimental set that could be used as a fully turbulent reference case. The final result is obtained by dividing the RMS pressure value calculated in each measuring point without the turbulator by the corresponding value of the fully turbulent case. Theoretically, the resulting values should be equal to 1 in the locations where both cases are turbulent, and between 0 and 1 where the transitional case has a laminar boundary layer.

Figure 5 shows the graph of the non-dimensional p_{rms}, i.e. the RMS pressure values non-dimensiona-lized by the reference turbulent case. The values close to the leading edge are lower than 1, according to what stated before. Starting from the value at 50 mm from the leading edge, the graph increases until it reaches a peak. After that, a moderate decrease takes place, reaching a constant overall trend. The peak agrees with the theory because Equation 8 shows that the pressure fluctuations are the result of velocity fluctuations and their gradient. Within a transitional boundary layer, the pressure fluctuations arise from the point where small turbulent spots are formed to a fully developed turbulent boundary layer, so the sound pressure level measured by the microphones can reach a peak in this region. A peak of pressure fluctuations in transitional boundary layers was also shown by Døssing [7] and Bar-

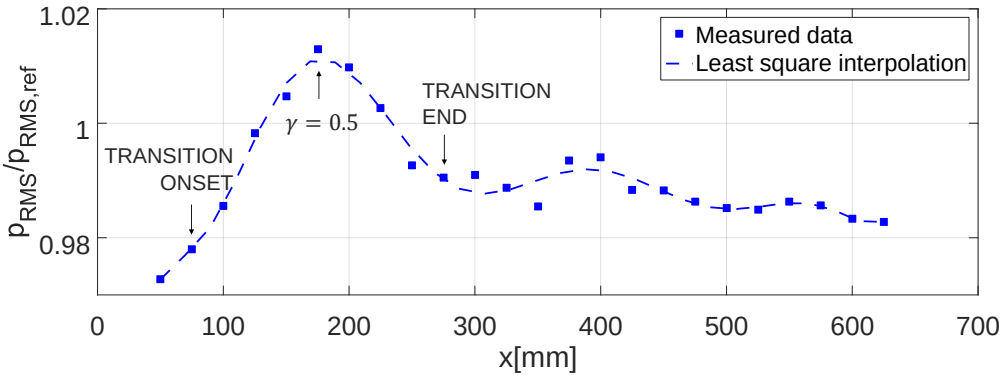

Figure 5 Non-dimensional RMS pressure data

rett [4]. In their works they both established that a peak of RMS pressure was registered with acoustic measurements. Furthermore, the location where the graph reaches the peak identifies the point of a laminar/turbulent equal distribution within the transitional boundary layer, i.e. the intermittency $\gamma = 0.5$. The intermittency γ, defined in every stream-wise position, identifies the fraction of time in which a boundary layer is turbulent, in the transitional zone. This quantity describes well the transition process because the turbulent spots appear and disappear continuously [16].

Comparision between experimental and numerical investigations

In this section, a comparison between numerical and experimental investigations is presented. Concerning the numerical results, in order to see the transition location, the skin friction coefficient c_f is plotted along the flat plate. c_f is a good parameter to point out the transition location, because the wall shear stress varies considerably between a laminar and a turbulent boundary layer. It is defined as:

$$c_f = \frac{\tau_0}{\frac{1}{2}\rho u_\infty^2} \tag{9}$$

where τ_0 is the wall shear shear. Thus, c_f is proportional to the velocity gradient in the wall-normal direction. u_∞ is the local free-stream velocity. The curves of the skin friction coefficient of laminar and turbulent boundary layers are provided by the Blasius solution and the 1/7 power law respectively. The 1/7 power law is defined as:

$$\frac{u}{u_\infty} = \left(\frac{y}{\delta_{99}}\right)^{\frac{1}{7}} \tag{10}$$

Figure 6 shows the transition results of both numerical simulations and experimental investigations. In order to make a comparison of the transition location, they are plotted on top of each other. For each type of investigation, the specific physical quantity that shows the transition process is plotted. The transition location is visualized by the point of a laminar/turbulent equal distribution in the transitional boundary layer (intermittency $\gamma = 0.5$). For the computation results, this location is supposed to be in the middle of the stretch where the curve detaches from the laminar level to reach the turbulent one.

The experimental results agree reasonably well with each other in the transition location. The little difference of the transition location may be due to different environmental conditions when the measurements were carried out and a different roughness of the surface between the experimental investigations. A thin metal plate with the drilled holes had to be placed over the flat plate to perform the acoustic measurements. These results agree very well with the numerical simulations that employ the $k - k_L - \omega$ model. Concerning this transitional model, OpenFOAM® and Fluent® present nearly the same transition onset and transition end. Therefore, providing the real turbulence intensity and the turbulence dissipation, $k - k_L - \omega$ is able to predict well the transition location. It can be seen that the OpenFOAM® $k - k_L - \omega$ simulation is the only one that fits the empirical turbulent profile. Considering that the Blasius solution is valid for flows with a very low level of perturbations [18], a reason why the theoretical laminar curve does not fit perfectly the calculated one is the fact that a bypass transition (high free-stream Tu level) occurs here.

Both OpenFOAM® and CFX® fail to predict the measured transition location zone with the $\gamma - Re_{\theta t}$ model. A fully turbulent boundary layer is predicted along almost the total length of the plate. Additional simulations that were performed with this model show that it predicts the correct transition location if an inlet *Tu* of about 3% is set. It this case, CFX® calculates a value of c_f that fits with the empirical turbulent value (1/7 power law).

Conclusion

In the present work, the boundary layer transition over a zero pressure gradient flat plate is investigated. Experimental investigations and numerical simulations were performed with the scope of better understanding the transition phenomenon, of verifying the capability of numerical transition models and of testing an innovative measuring technique. A direct measurement of the inlet flow turbulence level was carried out as well, in order to simulate properly the transition phenomenon with several CFD

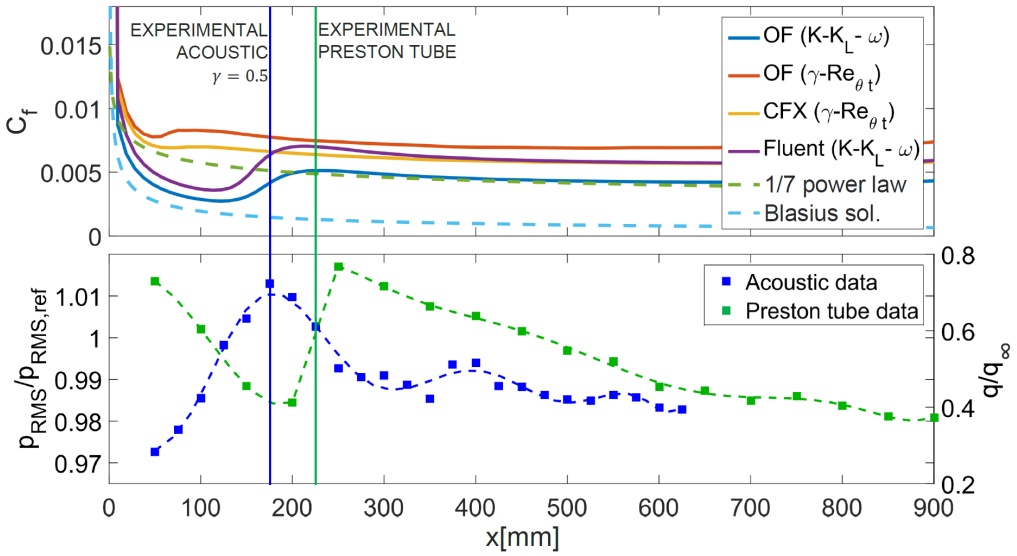

Figure 6 Comparison between numerical and experimental results

codes.

In the first part of the paper a new experimental technique to study the boundary layer behavior was tested and developed. Despite the high intensity vibration of the plate, the acoustic measurements performed by means of condenser microphones were able to detect the transition zone. The transition area fits quite well the one identified by the Preston tube and some CFD simulations. Due to the vibrations of the flat plate that hide the acoustic effects of turbulence, reference measurements were performed with a turbulator. Further investigations have to be performed with lower inlet velocity and turbulence level in order to generate the boundary layer transition more downstream. In this way, the acoustic behavior of the laminar boundary layer can be explored. In conclusion, this measuring technique is considered to be able to detect the boundary layer transition only if the solid body over which this transition occurs has a high stiffness, such as turbine blades or bluff bodies. This non-intrusive technique is very promising because it allows to measure the nature of boundary layers real-time in operating machines, because the microphones can be installed inside the body structure. To reach this results, it is necessary to validate cheap and robust condenser microphones that can be used in industrial applications.

A second important achievement of this work is a very good transition prediction of the CFD codes. To achieve this, a direct measurement of the turbulent inlet behavior of the flow is crucial. A specific data-processing procedure was developed to compute the turbulence quantities. OpenFOAM® and Fluent®, operating with the $k - k_L - \omega$ model, are able to predict the measured transition position, and OpenFOAM® also provided results that match very well with the empirical values. The $\gamma - Re_{\theta t}$ model is not able to detect the transition zone of this test case as observed in the measurements.

Acknowledgements

The authors gratefully acknowledge financial support from the Austrian Federal Ministry for Transport, Innovation and Technology in funding part of this work by the project ReLam within the Austrian Aeronautics Program TAKE OFF.

Also the authors would like to especially thank Marn Andreas, Bauinger Sabine, Laublättner Manuel and the staff of the laboratory of the ITTM for their immense support during the setup of the test bench and the measurement campaign.

References

[1] L.-U. Axelsson and W. K. George. Spectral analysis of the flow in an intermediate turbine duct. In *ASME Turbo Expo 2008: Power for Land, Sea, and Air*, pages 1419–1426. American Society of Mechanical Engineers, 2008.

[2] P. Bader and W. Sanz. On the setup of a test bench for predicting laminar-to-turbulent transition on a flat plate. *Journal of Energy and Power Engineering*, 10(7):411–424, July 2016.

[3] P. Bader, W. Sanz, J. Peterleithner, J. Woisetschläger, F. Heitmeir, W. Meile, and G. Brenn. Detecting transition on flat plate flow with laser interferometric vibrometry (LIV). *Proceedings of ASME Turbo Expo 2016: Turbine Technical Conference and Exposition, Seoul, South Korea*, 2016. GT2016-56043.

[4] R. Barrett. Transition detection for laminar flow aircraft using microphones beneath the surface of laser drilled suction panels. *Proceedings of the Institution of Mechanical Engineers, Part G: Journal of Aerospace Engineering*, 214(3):143–155, 2000.

[5] T. R. Camp and H.-W. Shin. Turbulence intensity and length scale measurements in multistage compressors. In *ASME 1994 International Gas Turbine and Aeroengine Congress and Exposition*. American

Society of Mechanical Engineers, 1994.

[6] Coupland. Flat plate transitional boundary layers. university lecture, University of Manchester, 1990.

[7] M. Døssing. High frequency microphone measurements for transition detection on airfoils. Technical report, Danmarks Tekniske Universitet, Risø Nationallaboratoriet for Bæredygtig Energi, 2008.

[8] T. M. Farabee. An experimental investigation of wall pressure fluctuations beneath non-equilibrium turbulent flows. Technical report, DTIC Document, 1986.

[9] R. B. Langtry. A correlation-based transition model using local variables for unstructured parallelized cfd codes. *AIAA journal*, 2006.

[10] R. E. Mayle. The role of laminar-turbulent transition in gas turbine engines. *Journal of Turbomachinery*, 113(4):509–536, 1991.

[11] R. Mukund, R. Narasimha, P. R. Viswanath, and J. D. Crouch. Multiple laminar-turbulent transition cycles around a swept leading edge. *Experiments in Fluids*, 53:1915–1927, 2012.

[12] O. Oyewola, L. Djenidi, and R. Antonia. Combined influence of the reynolds number and localised wall suction on a turbulent boundary layer. *Experiments in fluids*, 35(2):199–206, 2003.

[13] G. Persico, P. Gaetani, and A. Guardone. Design and analysis of new concept fast-response pressure probes. *Measurement Science and Technology*, 16(9):1741, 2005.

[14] S. B. Pope. Turbulent flows, 2001.

[15] H. Schlichting and K. Gersten. *Boundary-layer Theory*. McGraw-Hill, 8th edition, 1968.

[16] S. Stotz, C. Wakelam, Y. Guendogdu, and R. Niehuis. Detection of boundary layer transition on a low pressure turbine airfoil without separation using a preston tube and hot film anemometry. In *15th International Symposium on Transport Phenomena and Dynamics of Rotating Machinery (ISROMAC-15), Honolulu, HI, Feb*, pages 24–28, 2014.

[17] J. D. Wallace and M. R. D. Davis. Turbulence measurements with a calibrated pitot mounted pressure transducer. *13^{th} Symposium on Measuring Techniques in Turbomachinery, Zürich*, 1996.

[18] D. K. Walters and D. Cokljat. A three-equation eddy-viscosity model for reynolds-averaged navier-stokes simulations of transitional flow. *Journal of fluids engineering*, 130(12):121401, 2008.

[19] D. C. Wilcox. *Turbulence Modeling for CFD*. DCW Industries, 2nd edition, 1998.

[20] L. P. Yip, P. Vijgen, J. D. Hardin, and C. P. van Dam. In-flight pressure distributions and skin-friction measurements on a subsonic transport high-lift wing section. *AGARD CP-515*, 1993.

5.5. Paper 3: Detecting Transition in Flat Plate Flow with Laser Interferometric Vibrometry (LIV)

P. Bader, W. Sanz, J. Peterleithner, J. Woisetschläger, F. Heitmeir, W. Meile and G. Brenn, "Detecting Transition in Flat Plate Flow with Laser Interferometric Vibrometry (LIV)," *Proceedings of ASME Turbo Expo 2016: Turbine Technical Conference and Exposition, June 13-17, 2016, Seoul, South Korea*, GT2016-56043, 2016.

Proceedings of ASME Turbo Expo 2016: Turbine Technical Conference and Exposition
GT2016
June 13–17, 2016, Seoul, South Korea

GT2016-56043

DETECTING TRANSITION IN FLAT PLATE FLOW WITH LASER INTERFEROMETRIC VIBROMETRY (LIV)

Pascal Bader, Wolfgang Sanz,
Johannes Peterleithner, Jakob Woisetschläger
Franz Heitmeir
Institute of Thermal Turbomachinery and Machine Dynamics
Graz University of Technology
8010 Graz, Inffeldgasse 25/A, Austria
http://www.ttm.tugraz.at
pascal.bader@tugraz.at

Walter Meile
Günter Brenn
Institute of Fluid Mechanics and Heat Transfer
Graz University of Technology
8010 Graz, Inffeldgasse 25/F, Austria
http://www.isw.tugraz.at

ABSTRACT

Flow in turbomachines is generally highly turbulent. The boundary layers, however, often exhibit laminar-to-turbulent transition. Relaminarization from turbulent to laminar flow may also occur. The state of the boundary layer is important since it strongly influences transport processes like skin friction and heat transfer.

It is therefore vitally important for the designer to understand the process of laminar-to-turbulent transition and to determine the position of transition onset and the length of the transitional region. In order to better understand transition and relaminarization it is helpful to study simplified test cases first. Therefore, in this paper the flow along a flat plate is experimentally studied to investigate laminar-to-turbulent transition.

Measurements were performed for the different free-stream velocities of $5\ m/s$ *and* $10\ m/s$*. Several measurement techniques were used in order to reliably detect the transitional zone: the Preston tube, hot wire anemometry, thermography and Laser Interferometric Vibrometry (LIV). The first two measurement techniques are extensively in use at the institute ITTM and by other research groups. They are therefore used as a reference for validating the LIV measurement results.*

An advantage of the LIV technique is that it does not need any seeding of the fluid and that it is non-intrusive. Therefore this measurement technique does not influence the flow, and it can be used in narrow flow passages since there is no blockage, in contrast to probe-based measurement techniques.

Further to the measurements, computational simulations were performed with the Fluent® and CFX® codes from ANSYS®, as well as with the in-house code LINARS*. The Menter SST* k-ω *turbulence model with the* γ-Re_Θ *transition model was used in order to test its capability to predict the laminar-to-turbulent transition.*

NOMENCLATURE

c'_f	Local skin friction coefficient
$\delta(x)$	Boundary layer thickness
δ_1	Displacement thickness
δ_2	Momentum thickness
ε	Turbulence dissipation rate
G	Gladstone-Dale constant
H	Shape factor
k	Turbulent kinetic energy
λ	Light wavelength
p	Static pressure

p_t	Total pressure
ϕ	Light phase
Re	Reynolds number
ρ	Density
T	Temperature
t	Time
Tu	Turbulence intensity
τ_w	Wall shear stress
u	Streamwise velocity
v	Wall-normal velocity
x	Streamwise coordinate
y	Wall-normal coordinate
y^+	Non-dimensional wall coordinate

ABBREVIATIONS

AOM	Acousto-optic modulator
CFD	Computational Fluid Dynamics
He-Ne	Helium-Neon
ISW	Institute of Fluid Mechanics and Heat Transfer
ITTM	Institute for Thermal Turbomachinery and Machine Dynamics
LDA	Laser-Doppler Anemometry
LE	Leading edge
LIV	Laser Interferometric Vibrometry
OPL	Optical path length
PIV	Particle Image Velocimetry

INTRODUCTION

In flows along solid body surfaces, the boundary layer represents the narrow zone between the wall and the free stream where viscous effects are important. Its state of flow (laminar or turbulent) may have strong impact on transport processes like wall friction and heat transfer. These processes influence the efficiency as well as the thermal stress for example of a turbine blade. In turbomachines, the laminar or turbulent state of the boundary layer may therefore affect the efficiency of the blades and has an effect on other flow characteristics in the machine as well [1].

Many parameters, like free-stream velocity, acceleration, free-stream turbulence etc., may have an influence on the state of a boundary layer. At the first contact of a flow with a stationary structure, the boundary layer develops from laminar and becomes turbulent (under the appropriate flow conditions) via a transitional region. The boundary layer passes through several stages within this transitional zone before becoming fully turbulent. Schlichting and Gersten extensively discussed these different stages [2].

It is vitally important to understand the influences from the above parameters on the onset position and length of the transitional zone in order to predict and potentially control the state of the boundary layer. In turbomachinery, the efficiency of blades and stages can be improved considering transition. This allows the overall machine performance to be improved. In 1991, Mayle published a comprehensive review of the importance of transition in gas turbines [3]. He analyzed experiments performed by several research groups in order to find the influence of different flow parameters on the transition process.

Additional experiments were performed in the last years by many research groups. Yip et al. performed in-flight measurements, detected transition with the help of Preston tubes and analyzed the influence of the flight conditions on the boundary layer along an airfoil [4]. Oyewola et al. showed how the flow in the boundary layer can be measured with hot-wire anemometry and Laser-Doppler anemometry (LDA) [5, 6]. Widmann et al. performed near-wall measurements with Particle Image velocimetry (PIV) [7]. Hot-film measurements were performed, e.g., by Mukund et al. [8], Preston-tube and thermographic measurements by Bader and Sanz [9].

In addition to measurements, numerical models were developed to predict the laminar-turbulent transition process. Common models are, for example, the k-k_L-ω [10] and the γ-Re_Θ [11, 12] models. For the latter, various correlations for important model parameters were developed [13–17].

So far, only the transition from laminar to turbulent flow was described. Under certain flow conditions (like high acceleration), however, a reverse transition or relaminarization from turbulent to laminar can occur. Up to now, only few measurements on relaminarization were reported [18–20]. Therefore, at the Institute for Thermal Turbomachinery and Machine Dynamics (ITTM) of Graz University of Technology a project was launched in order to understand the process of relaminarization.

Since the interest is to investigate relaminarization at high acceleration, a test bench with a strongly convergent cross section is needed, leading to narrow channel cross section. In such a small flow area, probes like Preston tubes and hot wire probes would influence the flow considerably. Therefore, non-intrusive measurement techniques are used for measuring the state of the boundary layer.

Laser-Doppler Anemometry (LDA) or Particle Image Velocimetry (PIV) are widely used non-intrusive measurement techniques. However, they both rely on seeding of the flowing fluid with particles. It is a well known problem of particle-based anemometries that the flux of tracer particles close to the wall is insufficient for measuring inside the boundary layer.

As an alternative, laser interferometry allows for the measurement of line-of-sight integrated density fluctuations $\delta\rho/\delta t$ triggered by, e.g., turbulent structures. The measurements work with high temporal resolution up to high frequencies, without use of tracer particles. The density fluctuations are integrated along the path of the laser beam corresponding to the width of the plate, so that statistically distributed fluctuations along the beam are averaged out. Within the transition zone, however, the LIV signal

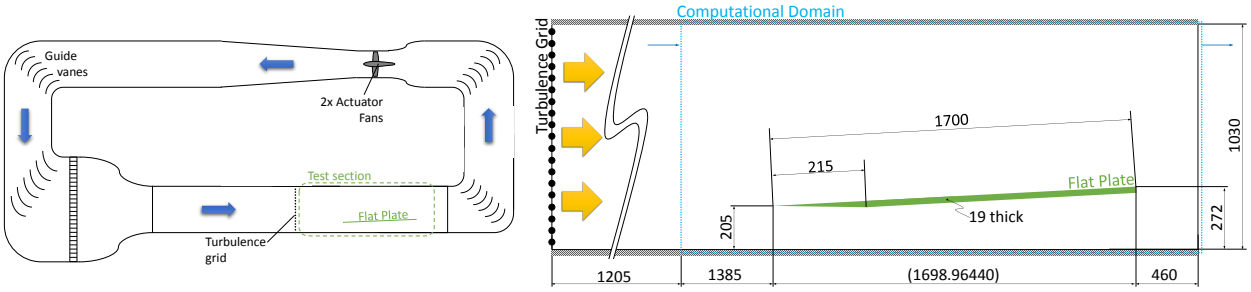

(a) SKETCH OF THE WIND TUNNEL.

(b) DETAILED VIEW OF THE TEST SECTION.

FIGURE 1. GÖTTINGEN-TYPE WIND TUNNEL WITH CLOSED TEST SECTION USED FOR THE EXPERIMENTS.

shows a significant rise in amplitude [21].

The following section presents the experimental setup, together with all the flow measuring techniques used for the study. Thereafter we present and discuss the measurement results, with a particular focus on the boundary layer thickness and velocity profiles. The paper ends with a summary and the conclusions.

EXPERIMENTAL SETUP

Test facility

The tests were performed in a Göttingen-type wind tunnel with closed test section at the ISW. A sketch of the tunnel is given in Fig. 1a. The wind tunnel is powered by two fans with a total power input of 75 kW. The air is conveyed to the nozzle and the test section via two corners with guide vanes. The maximum achievable flow-rate equivalent velocity is about 30 m/s. The nozzle exit cross section is 2 m wide and 1 m high. Downstream from the nozzle, a 6 m long channel for developing flow velocity profiles is installed. The test section itself is about 2.6 m long. The top panel of the tunnel is adjustable for setting a zero pressure gradient along the test section.

Since the turbulence of the wind tunnel flow is well below 1 %, a turbulence grid is installed upstream from the test section in order to raise the turbulence level to about 3 % to 4 %. The turbulence grid consists of equally spaced cylindrical rods. As suggested by Roach, the grid has a solidity below 50 %, and its position upstream from the first measuring point satisfies the $x/d > 10$ criterion, where x represents the streamwise coordinate and d the diameter of the rods [22].

Downstream from the turbulence grid, but upstream from the flat plate, the first measurement section is located (computational domain in Fig. 1b). Starting from this plane, the turbulence level and the free stream velocity were measured at six different streamwise positions in order to get the turbulence intensity Tu as well as the dissipation rate ε from the decrease of the turbulent kinetic energy k, which are important input parameters for the CFD simulations. The inlet boundary conditions of the numerical simulations are set at this plane. The measured boundary conditions used for the CFD simulation are given in Tab. 1 for both cases. The results of the turbulence measurements are given later in Fig. 10 in comparison with computational results.

Figure 1b also shows the position of the flat plate. The bottom side of the plate was trimmed along a length of 215 mm and the resulting leading edge is blunt with a thickness of 1 mm. The plate is inclined by two degrees against the bottom wall of the channel in order to ensure that the flow is attached at the upper surface. The plate distance from the side walls is larger than the boundary layer thickness there in order to avoid influences from the sidewall boundary layers on the flow along the plate.

Preston Tube

30 static pressure tappings with a streamwise spacing of 50 mm starting at $x = 195$ mm are placed along the flat plate, where x represent the position downstream of the leading edge. The inner diameter of the tappings is 0.5 mm. Their positions are used for Preston-tube measurements. A Preston tube is traversed along the plate in the streamwise direction in order to locate the transition region. The probe is a Pitot tube with an inner diameter of 0.5 mm. The Preston tube allows the total pressure close to the wall to be measured. This pressure can be used to calculate

TABLE 1. MEASURED BOUNDARY CONDITIONS FOR CFD SIMULATIONS.

	5 m/s	10 m/s
u_∞	5.223 m/s	10.815 m/s
T_{inlet}	$\approx$ 298 K	$\approx$ 298 K
Tu_{inlet}	5.166 %	5.267 %
Tu_{LE}	3.071 %	3.148 %
ε_{inlet}	0.8024 m^2/s^3	7.3821 m^2/s^3 m
$p_{stat,outlet}$	97700 Pa	97700 Pa

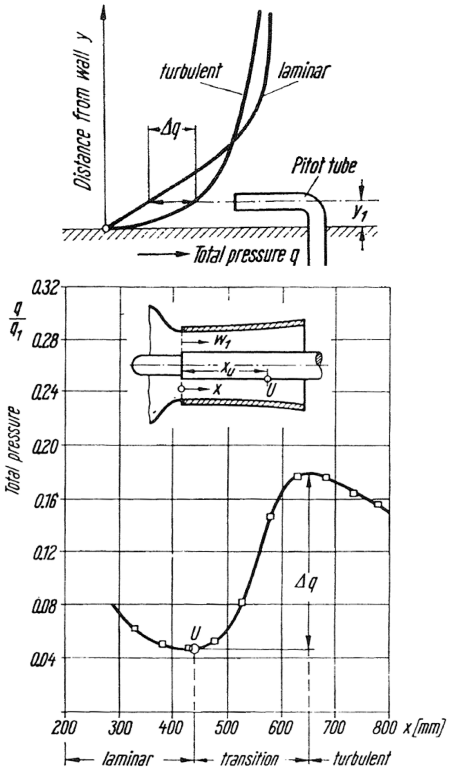

FIGURE 2. CONCEPT OF THE PRESTON TUBE MEASUREMENT [24].

the non-dimensional dynamic pressure according to [23]

$$\frac{q}{q_\infty} = \frac{p_{t,probe}(x) - p(x)}{p_{t,\infty} - p(x)} \tag{1}$$

where $p_{t,probe}(x)$ and $p(x)$ represent the total and static pressures acquired by the probe and the tappings, and $p_{t,\infty}$ is the free-stream total pressure. The result gives an indication of the shape of the velocity profile close to the wall, which is characteristic for the state of the boundary layer. Figure 2 explains this idea: The upper sketch shows the different velocity profiles of the laminar and turbulent boundary layers. The steeper velocity gradient close to the wall in the turbulent boundary layer is due to the higher rate of momentum transport in the wall-normal direction because of its turbulent state [9]. The bottom sketch in Fig. 2 shows the streamwise distribution of the non-dimensional total pressure $p_{t,probe}/p_{t,\infty}$ (denoted as q/q_1 in Fig. 2) and gives an example of its increase due to transition. The non-dimensional total pressure gives a similar trend as the non-dimensional dynamic pressure in Eq. (1) on a flat plate due to the nearly constant static pressure $p(x)$ along the plate.

Three characteristic ranges of q/q_∞ can be distinguished: values of q/q_∞ around unity occur for probe positions at the edge or outside the boundary layer. Values between 0 and 1 occur for probe positions inside the boundary layer, and values close to zero indicate a separation bubble [23]. In the interpretation of the measurement results, however, the probe size must be accounted for, since the results are valid only for boundary layers with thicknesses which are at least double the probe distance from the wall (y_1 in Fig. 2).

Pressure differences from the static tappings and the Preston tube were acquired with a differential pressure sensor PD9261 together with a data logger unit Clima Air 1 (both from *Rösler + Cie. Instruments GmbH)*). The total system has been calibrated with the aid of a high-precision Betz-type manometer. The detected mean deviation from the reference values was 0.54 % in the relevant range.

Thermography

The fact that the rate of heat transfer depends on the laminar or turbulent state of the flow in the boundary layer can be used for detecting transition with a thermographic camera. For this purpose, we use the camera FLIR® T650sc with an accuracy of $\pm 0.1^\circ C$ [9]. Applying this technique, the plate is heated up to a uniform temperature which is measured with the thermographic camera. For heating the plate, five heating foils from *thermo technologies* with an effective output of 36 W each were mounted on the bottom side of the plate. This setup resulted in a homogeneous heating of the plate. The foils were thermally insulated against the flow on the bottom side of the plate.

After reaching a uniform temperature, the heating was switched off, and the plate cooled down at constant flow conditions for about 150 to 200 s, depending on the free-stream velocity. The standard deviation of the initial mean temperature along the whole plate is $0.56^\circ C$. The plate surface temperature was monitored, and the appearing temperature differences were used to determine the state of the boundary layer since the turbulent part cools faster due to the higher rate of heat transfer.

Hot wire anemometry

In the present work, hot wire anemometry was also applied for measuring flow velocities. A multi-channel constant-temperature anemometer (CTA) 54N82 with a 54N95 transmitter from *Dantec Dynamics A/S* were used with miniature X-wire probes type 55P63 with 90° tilted heads for the velocity measurements along the plate. Straight probes type 55P61 were used for measuring the free-stream turbulence upstream from the plate. For the temperature compensation, a 90P10 reference temperature probe was used. The measurements were performed with a sampling frequency of 10 kHz, collecting a total number of 80,000 samples for each measuring position.

Preceding each measurement series, the hot wire probes have been calibrated with a reference velocity transducer 54T29 from *Dantec Dynamics A/S* within the full velocity range $1\ m/s \leq v \leq 15\ m/s$.

Laser interferometric vibrometry

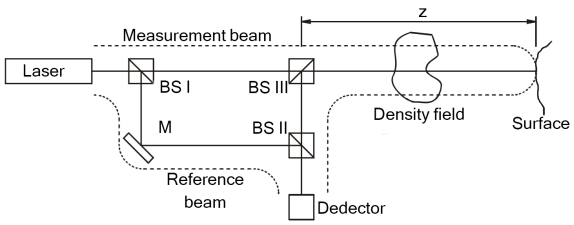

FIGURE 3. PRINCIPLE OF A LASER VIBROMETER, M - MIRROR, BS - BEAM SPLITTER [25].

Laser Interferometric Vibrometry (LIV) is typically used for point-wise measurements of surface vibrations of solid bodies. The vibrometer consists of a He-Ne Laser, whose beam shines through a Mach-Zehnder interferometer (see Fig. 3). The beam emitted from the device is reflected from the surface of the object [25, 26]. A reference beam, which does not interact with the object, interferes with the measurement beam.

A photo detector records the intensity fluctuations in the interfering measurement and reference beams at the exit of the interferometer. The frequency of these fluctuations is measured with the help of an FM-demodulator. For detecting the direction of the surface vibration, an acousto-optic modulator (AOM) shifts the frequency of the reference beam electric field relative to the measurement beam, thus producing a beat between the two electric fields even when the object is at rest. The object motion changes this frequency, which can be used for determining the direction and magnitude of the motion [25–27].

If an object at rest has a fixed reflecting surface, the vibrometer measures density fluctuations along the path of the laser beam. The relation between the change of the optical path length ΔOPL, the light phase ϕ and the integral of the variation of the density difference $\Delta\rho$, together with the Gladstone-Dale constant G and the light wavelength λ, is given in the following equation [21]:

$$G\int_z \Delta\rho(t)\,dz = \Delta OPL(t) = \frac{\lambda\phi(t)}{4\pi} \qquad (2)$$

Equation (2) shows that the LIV measures the integrated density fluctuations along the beam. In the case of the flat plate flow,

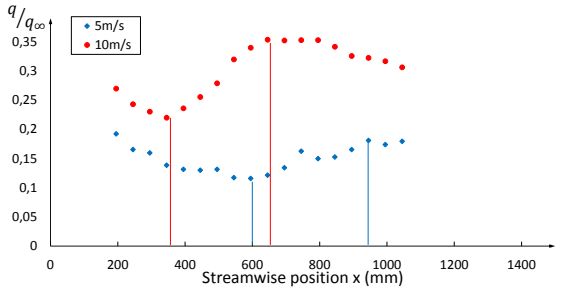

FIGURE 4. RESULTS OF PRESTON TUBE MEASUREMENTS FOR THE FREE STREAM VELOCITIES OF 5 m/s AND 10 m/s.

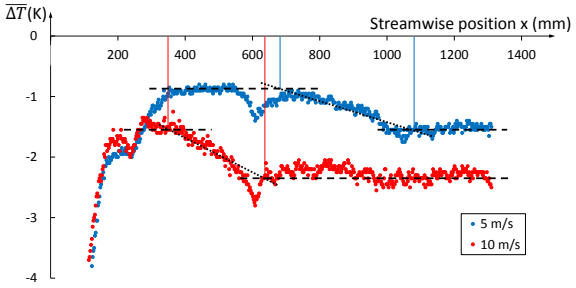

FIGURE 5. THERMOGRAPHICALLY RECORDED TEMPERATURE CHANGE $\overline{\Delta T}$ ALONG THE PLATE.

these fluctuations are caused by turbulence. Since they are statistically distributed, the mean value of $\Delta\rho$ is approximately zero. In the region of the transition, however, where larger structures develop randomly, the mean value of $\Delta\rho$ is not zero. The laser vibrometer rather detects an increase of the density fluctuations $\Delta\rho$ in the zone where transition takes place [21].

The LIV measurements in this paper were performed with a sampling frequency of 65.536 kHz, and 7,864,320 samples were recorded at each measurement position.

RESULTS AND DISCUSSION

Experiments

In this section, the results on the detection of transition obtained with the five different measuring techniques are presented. We first discuss the results from the Preston tube measurements. The results for the two free-stream velocities of 5 m/s and 10 m/s are plotted in Fig. 4. For the 5 m/s case, an increase of q/q_∞ starting about 600 mm downstream from the plate tip is visible. This is an indication for transition, and the values reach a maximum at approximately 950 mm. Downstream from this point, no further increase of q/q_∞ is seen, but it is not clear if transition is complete at 950 mm from the plate tip.

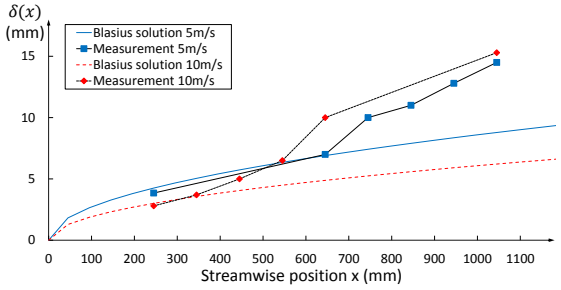

FIGURE 6. MEASURED BOUNDARY LAYER THICKNESS $\delta_{0.99}$ FOR THE LAMINAR BOUNDARY LAYER, TOGETHER WITH THE BLASIUS SOLUTION.

The result for the 10 m/s case is clearer: The graph in Fig. 4 shows the start and end of transition at about 350 mm and 650 mm from the plate tip, respectively.

In order to validate these measurement results, the flow is investigated by thermography. This measurement technique relies on the fact that the state of flow of the boundary layer affects the rate of heat transfer. The plate was heated up to reach a constant temperature $T(t_0)$ along the plate. At this time, the first thermographic image was taken. The heating power was then switched off, and further recordings were taken at different times t, yielding the temperatures $T(t)$, so that the temperature difference $\Delta T = T(t) - T(t_0)$ along the plate could be evaluated. The time differences $t - t_0$ for 5 m/s and 10 m/s are approximately 150 s and 200 s, respectively. This procedure was repeated several times, and the mean value $\overline{\Delta T}$ is shown in Fig. 5. In this figure also trendlines (dashed and dotted) are given. The decrease of $\overline{\Delta T}$ near $x = 600$ mm for both flow velocities may be due to the placement of the heating foils on the plate.

In both flow cases, the upstream part of the plate down to 200 mm from the tip cools down rapidly. The reason for this strong decrease is that the leading edge is sharpened, so that the heat capacity of the plate is smaller there than farther downstream. Furthermore, the heat transfer coefficient is very high on the upstream part of the plate.

Downstream from 200 mm, the 5 m/s case shows an increased temperature difference ΔT between about 675 mm and 1075 mm from the plate tip. In the 10 m/s case, an increase is also seen between approximately 350 mm and 625 mm. These stronger decreased temperatures most likely indicate transition in the regions and also agree with the Preston tube measurements discussed above.

Hot wire velocity measurements were then performed to measure profiles of the flow velocity component parallel to the wall. From these profiles, the boundary layer thickness $\delta(x)_{0.99}$

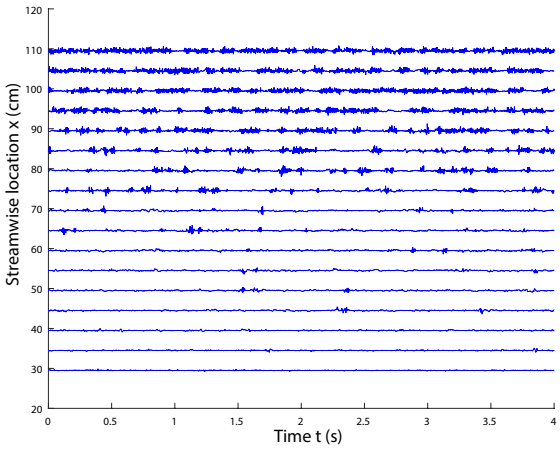

(a) AT 5 m/s.

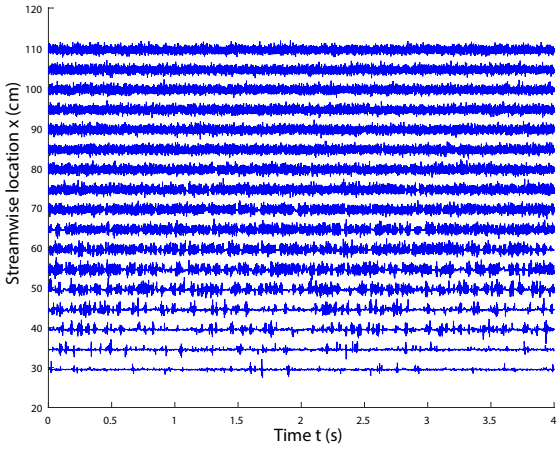

(b) AT 10 m/s.

FIGURE 7. TIME SIGNALS OF THE WALL-NORMAL VELOCITY FLUCTUATIONS v' WITHIN THE BOUNDARY LAYER OBTAINED BY CTA

was calculated using the criterion

$$u[y = \delta(x)_{0.99}] = 0.99\, u_\infty \tag{3}$$

In Eq. (3), x represents the streamwise and y the perpendicular coordinate in the flow field. The developments of $\delta(x)_{0.99}$ for the two free-stream velocities are illustrated in Fig. 6. Additionally, the Blasius solution for the laminar boundary layer thickness is

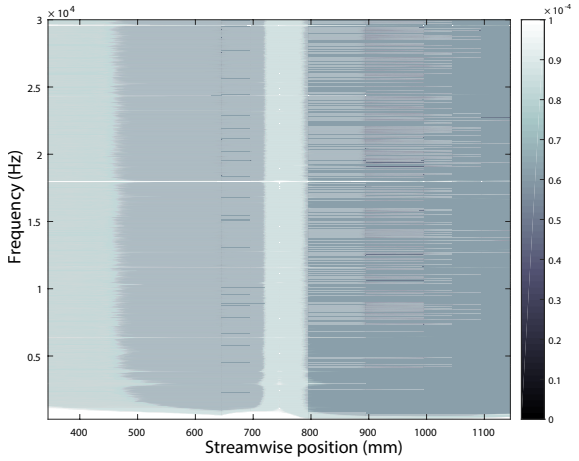

(a) FREE STREAM VELOCITY 5 m/s.

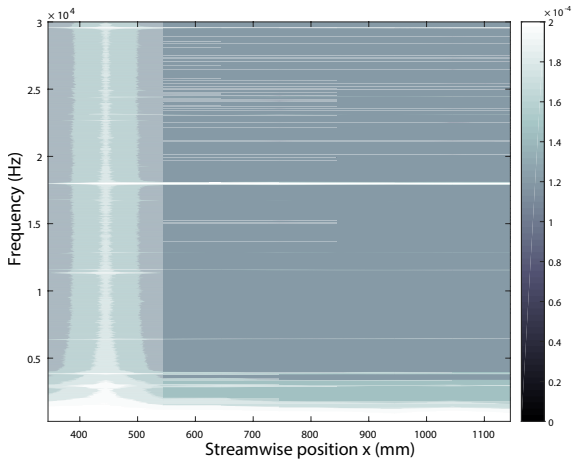

(b) FREE STREAM VELOCITY 10 m/s.

FIGURE 8. FREQUENCY SPECTRA OBTAINED BY LIV AT DIFFERENT POSITIONS AS A SURFACE PLOT

shown, which is given as

$$\frac{\delta(x)_{0.99}}{x} = \frac{5}{\sqrt{Re_x}} \tag{4}$$

with the Reynolds number at position x

$$Re_x = \frac{u_\infty \cdot x}{\nu} \tag{5}$$

The graph shows that the measured boundary layer thickness starts to deviate from the Blasius solution about 650 mm from the plate tip for the 5 m/s case, and about 350 mm at the 10 m/s case, respectively, indicating transition. The corresponding Reynolds numbers in the two cases are $2.06 \cdot 10^5$ and $2.22 \cdot 10^5$, respectively, thus representing well the generally accepted critical Reynolds number of transition in flat-plate flow. Again, the positions of transition found agree well with the other measurements above.

In order to see if the boundary layer is laminar or turbulent, the time signals of the wall-normal velocity fluctuations v' are investigated. Figure 7 shows the fluctuations for the two free stream velocities at different streamwise locations.

At the onset of transition, the flow in the boundary layer becomes three-dimensional and the velocity field fluctuates in the wall-normal direction also. In Fig. 7a first turbulent spots appear around $x = 650$ mm, indicating the onset of transition. The time signal does not indicate a fully turbulent boundary layer at the end of the plate (1100 mm), but transition seems to be nearly finished there.

At 10 m/s (Fig. 7b), the time signals of the wall-normal velocity fluctuations indicate the onset of transition about 350 mm from the plate tip. The fully turbulent time signal indicates completion of transition around $x = 700$ mm.

Above we applied several measurement techniques generally used for detecting transition in our flat plate flow. In the following, Laser Interferometric Vibrometry (LIV) is presented as an alternative to the above techniques. The advantages of LIV are that it is non-intrusive and that it works without any seeding of the flowing fluid. For the measurements, the laser beam was traversed along the plate and was kept at a distance from the wall of approximately half the local boundary layer thickness ($y = \delta(x)/2$).

Figure 8 shows the results of a Fast Fourier Transformation (FFT) of the LIV time signal. The amplitudes of the density fluctuations are color-coded along the plate (streamwise position x on the abscissa) for different frequencies displayed on the ordinate axis. The contour plot in Fig. 8a shows an increase around 775 mm for the 5 m/s case. An explanation for this finding is as follows: the LIV measurement integrates along the laser beam path way, which means that the measured value is a mean of the density fluctuations $\overline{[\Delta\rho]'}$ along the optical path length. As long as the laser beam travels inside the laminar boundary layer, the obtained value of $\overline{[\Delta\rho]'}$ is close to zero, since the flow in the laminar boundary layer does not fluctuate. In a turbulent boundary layer, on the other hand, fluctuations are present. These fluctuations are statistically distributed, so that the mean value of the density fluctuations $\overline{[\Delta\rho]'}$ is again close to zero if the measured ensemble is large enough. Only within the transitional zone, where, due to the appearance of turbulent spots, the probability distribution of the fluid density is not symmetric, non-zero density fluctuations $\overline{[\Delta\rho]'}$ are detected by the laser vibrometer. As long as only few structures lie within the optical path, LIV shows a rise in the signal. This seems to occur 775 mm from the

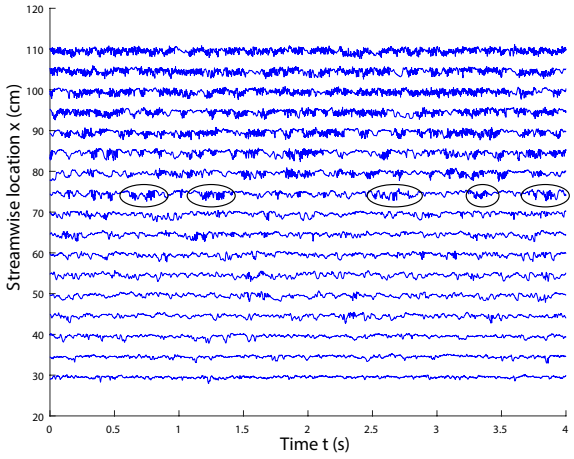

FIGURE 9. TIME SERIES OF THE STREAMWISE FLUCTUATIONS u' FOR THE 5 m/s CASE OBTAINED BY HOT WIRE ANEMOMETRY.

plate tip, which compares to the measurements discussed above.

Comparing with the Preston tube measurements, one can see that the position of 775 *mm* lies in the middle of the transition zone found. Exemplarily, hot wire time series of the streamwise fluctuations u' are given in Fig. 9 for the 5 m/s case. It is seen in this figure that, at the position where the LIV shows a rise in unevenly distributed density fluctuations (775 *mm*), some turbulent spots develop (encircled in Fig. 9). After the peak of the signal in Fig. 8a, the amplitude decreases to about 800 *mm* and then stays nearly constant. Looking at this position in the hot wire time series (Fig. 9), it can be observed that the turbulent fluctuations are more frequent and dominate the signal, so that an averaging out is stronger, which agrees with the LIV data.

The same comparison for the 10 m/s case (Fig. 8b) shows that the increase of the amplitude can be seen at 450 *mm*, which again lies in the middle of the transition zone observed with the other measurement techniques. This indicates that LIV is capable to detect transition. Although the exact start and end of transition could not be detected, the approximate middle of the transition zone is found. It is the region where the time signal shows a rapid development of turbulent spots. In both Figs. 8a and 8b, a horizontal line can be observed showing a rise in the signal at all positions. These peaks represent a solid body vibration.

CFD simulations

Computational Fluid Dynamics (CFD) is a powerful tool for fluid flow simulation and is widely used in a wide range of applications. The accuracy of its results depends, amongst others, on the reliability of the turbulence models and, if applicable, on

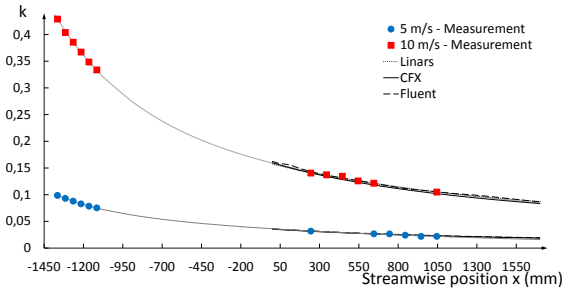

FIGURE 10. MEASURED AND SIMULATED VARIATION OF TURBULENT KINETIC ENERGY FOR BOTH SPEED CASES.

the transition models used. The latter were developed in the last decades for modeling transition in the boundary layer. Established models are, for example, the $k-k_L-\omega$ [10] and the $\gamma-Re_\Theta$ [11, 12] models, for which various correlations for important model parameters were developed [13–17]. Their evaluation and validation with test cases, however, is still ongoing to increase their reliability.

In order to verify the predictive capabilities of these transition models in the present test cases, simulations were per-

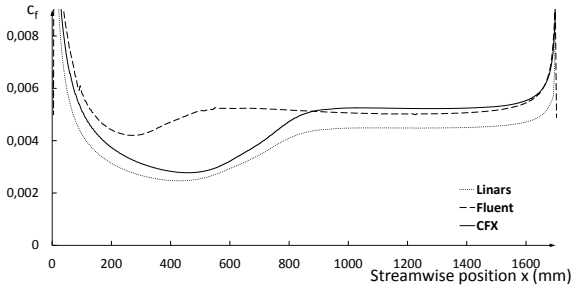

(a) FREE-STREAM VELOCITY 5 m/s.

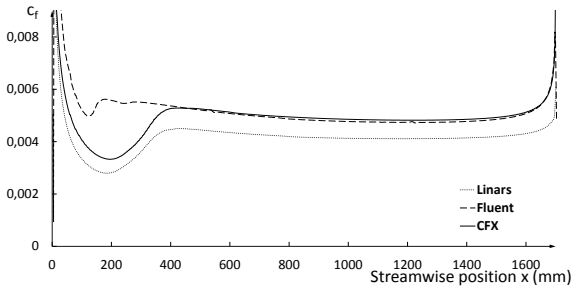

(b) FREE-STREAM VELOCITY 10 m/s.

FIGURE 11. COMPARISON OF THE SKIN FRICTION COEFFICIENT c_f OBTAINED WITH THREE DIFFERENT CFD CODES

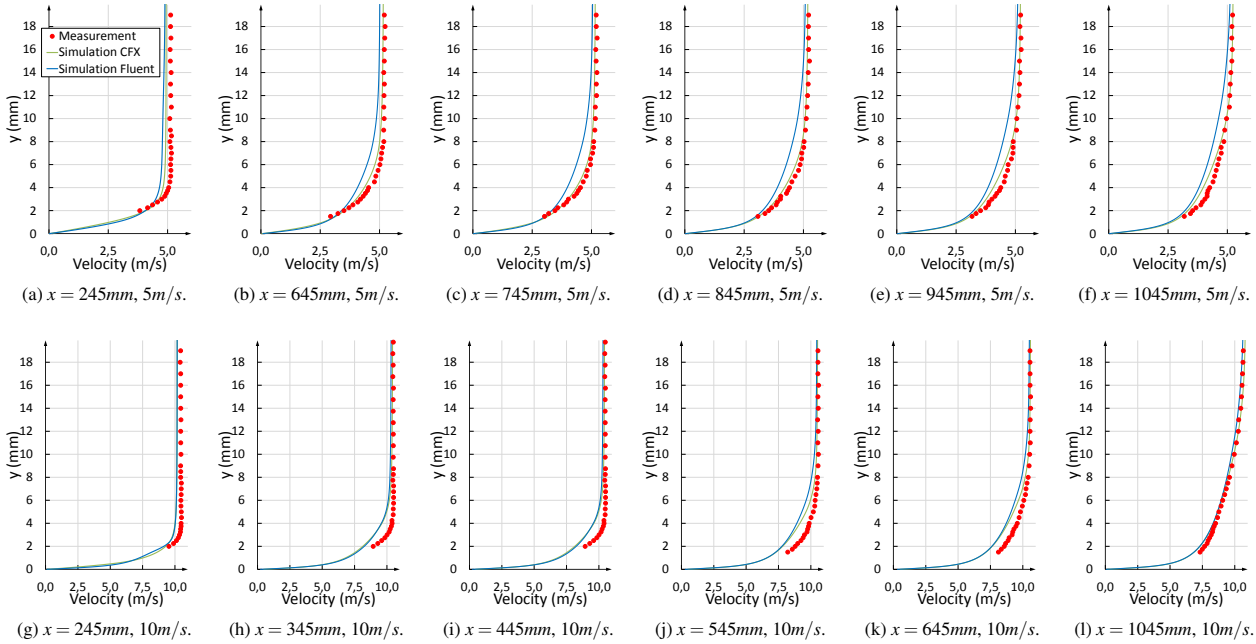

(a) $x = 245mm$, $5m/s$. (b) $x = 645mm$, $5m/s$. (c) $x = 745mm$, $5m/s$. (d) $x = 845mm$, $5m/s$. (e) $x = 945mm$, $5m/s$. (f) $x = 1045mm$, $5m/s$.

(g) $x = 245mm$, $10m/s$. (h) $x = 345mm$, $10m/s$. (i) $x = 445mm$, $10m/s$. (j) $x = 545mm$, $10m/s$. (k) $x = 645mm$, $10m/s$. (l) $x = 1045mm$, $10m/s$.

FIGURE 12. COMPARISON OF VELOCITY PROFILES FROM HOT WIRE MEASURMENTS AND CFD SIMULATIONS.

formed with CFX® v15.0 and Fluent® v15.0 by ANSYS® and with the in-house code LINARS. All the codes use the Menter SST k-ω turbulence model, together with the Menter γ-Re_Θ transition model. The boundary conditions were set such that the free stream velocity and the free stream turbulence of the simulation agree with the data measured along the plate. The 2D mesh consists of 368,512 nodes and y^+ was kept between 0.1 and 1 at the flat plate surface as recommended for the transition model [28]. The comparison of the measured and simulated turbulence properties is given in Fig. 10 displaying the variation of turbulent kinetic energy k along the plate. It can be clearly seen that all three simulation results agree very well with the measured CTA data.

Figure 11 shows the distribution of the local skin friction coefficient c'_f along the plate, which is defined as

$$c'_f = \frac{\tau_w}{\rho u_\infty^2/2} \tag{6}$$

where τ_w represents the wall shear stress, ρ the fluid density and u_∞ the free stream velocity.

Since the skin friction is higher in a turbulent than in a laminar boundary layer, c'_f can be used for determining the state of flow in the boundary layer. Figures 11a and b show the distributions of c'_f along the plate. The increase of the values indicates the position of transition onset.

The diagram for the 5 m/s case (Fig. 11a) shows an increase in the values of skin friction from all the three codes, indicating that transition is predicted. The positions of the transition regions from CFX® and LINARS agree well with the measurement data shown above, whereas Fluent® predicts the rise of c'_f, and thus transition, too far upstream.

Similar trends can be observed for the 10 m/s case: Here again CFX® and LINARS agree well with each other, but in this case the results indicate transition slightly too far upstream compared to the measurement data. Fluent® yields only a very small transitional zone near $x \approx 100$ mm and, thus, does not clearly show a laminar behavior at the front part of the plate at all.

LINARS generally predicts lower skin friction in the laminar and turbulent part compared to the two ANSYS® codes.

This difference in the prediction of the transitional region is also visible in the velocity profiles given in Fig. 12. The CFD results from CFX®, which are nearly identical to the LINARS results, and from Fluent® are illustrated together with the results from the hot wire measurements.

Figure 12a shows the velocity profile at $x = 245$ mm for the 5 m/s case in a zone where the boundary layer is still laminar. The profile from Fluent® is slightly flatter in the outer region compared to the CFX® simulation but shows a slightly steeper gradient close to the wall. However, all three curves agree quite well with each other at values slightly lower than the CTA measurements.

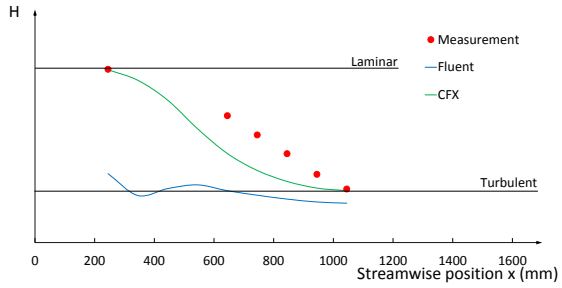

(a) FREE-STREAM VELOCITY 5 m/s.

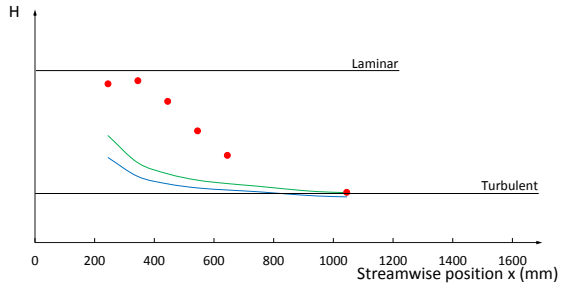

(b) FREE-STREAM VELOCITY 10 m/s.

FIGURE 13. COMPARISON OF THE SHAPE FACTOR H OBTAINED BY CFX AND FLUENT TOGETHER WITH THE CTA MEASUREMENT RESULTS

Figures 12b shows the velocity profiles at $x = 645$ mm, where the measurements indicate transition. The CFX® simulation results agree satisfactorily with the experimental data. The Fluent® results indicate an already turbulent state of the boundary layer (see also Fig. 11a) since the profile is more uniform in the outer region and the gradient close to the wall is steeper corresponding to the c'_f plots in Fig. 11a.

Figures 12c to f show the comparison of turbulent boundary layer profiles at farther downstream positions. It is again observable that the Fluent® solution yields a flatter profile compared the the CFX® solution. At these positions the gradient at the wall from the Fluent® simulation is slightly lower compared to the CFX® simulation which again agrees with the c'_f distribution in Fig. 11a.

The CFX® simulation agrees well with the measurement results at $x = 745$ mm and $x = 845$ mm (Figs. 12c and d), but also predicts a flatter profile compared to the measurement data at the last two positions (Figs. 12e and f).

A comparison of the velocity profiles at $x = 245$ mm and $x = 345$ mm for the 10 m/s case in Figs. 12g and h yields that there is hardly any difference. In the near wall region both curves agree quite well with the measurement data at $x = 245$ mm but differ at $x = 345$ mm. For the latter position, both codes predict a flatter profile compared to the CTA data.

At the farther downstream positions $x = 445$ mm, $x = 545$ mm and $x = 645$ mm (Figs.12i to k) the codes still predict a flatter profile compared to the measurements and, like in the 5 m/s case described above, the profile predicted by Fluent is more uniform than the CFX simulation.

Figure 12l shows the velocity profiles at $x = 1045$ mm where both simulations agree well with each other and with the measurement values. This indicates that, although the transition process is treated differently, farther downstream the simulated turbulent boundary layer does not show any evidence of the different transitional zones.

To quantify the shape of the velocity profiles, the shape factor H is given in Fig. 13 for the two speed cases. The shape factor is calculated as the ratio of the displacement thickness δ_1 to the momentum thickness δ_2, i.e.

$$H = \frac{\delta_1}{\delta_2} \quad \text{with} \tag{7}$$

$$\delta_1 = \int_0^{\delta(x)} \left(1 - \frac{u(y)}{u_\infty}\right) dy \tag{8}$$

$$\delta_2 = \int_0^{\delta(x)} \frac{u(y)}{u_\infty} \left(1 - \frac{u(y)}{u_\infty}\right) dy \tag{9}$$

A shape factor of $H \approx 1.4$ represents a turbulent boundary layer, and $H = 2.59$ a laminar velocity profile (Blasius solution).

Comparing the solutions for 5 m/s (Fig. 13a) it can be recognized that the Fluent solution yields earlier transition which has already been seen in the skin friction coefficient discussed above (Fig 11a). The CFX solution agrees better with the measurements.

From Fig. 13b it is evident that both codes show a similar trend for the 10 m/s case, but the shape factor of the Fluent solution is lower. This also agrees with the velocity profiles discussed above. Both simulations differ from the measurement data.

Within the measurement campaign of the present study, measurements with Laser-Doppler Anemometry (LDA) were also performed. The velocity profiles, together with the turbulence levels from the LDA measurements, were compared with the hot wire results. The results from the two measurement techniques agreed well. For reasons of clarity of the diagrams, however, only the hot wire velocity profiles are given.

SUMMARY AND CONCLUSIONS

This work presents the results of detecting laminar-to-turbulent transition in flat-plate boundary layer flow from different measurement techniques at two different free-stream velocities. Further to measurement techniques well established for transition detection, Laser Interferometric Vibrometry (LIV) was

employed as an alternative technique. This measurement technique is implemented in an easy-to-use system and offers the advantage of non-intrusive measurements without the need of seeding of the flowing fluid. Therefore its influence on the flow is negligible and it can be used in very different applications.

The results show that, although LIV is an integrating method, transition can be detected by sensing non-homogeneous structures in the transitional zone. The LIV results were validated with data from the established measurement techniques. In Table 2, a summary of the various results is given, revealing good agreement between the data from the different measurement techniques.

Further to the measurements, computational simulations were carried out using three different CFD codes, namely ANSYS® CFX®, ANSYS® Fluent® and the in-house code LINARS. The transition predictions by the two codes CFX® and LINARS agree satisfactorily with the measurement results. Details of the velocity profiles at 10 m/s free stream velocity, however, do not fit well to the measured data. The measured profiles show a more bouffant shape. The transitional zones predicted by the three codes are also listed in Table 2.

This good agreement between data from different measurement techniques and numerical simulations gives confidence in the applied methods. The present work therefore may be the basis for further investigations of transition in more complex flow situations. Additionally, experimental work on relaminarization is underway, where LIV will be used as a fast and non-intrusive measurement method.

ACKNOWLEDGMENT

The authors gratefully acknowledge the support from the Austrian Federal Ministry of Transport, Innovation and Technology by funding of a part of the work by the project RELAM in the frame of the Austrian Aeronautics Program TAKE OFF.

TABLE 2. SUMMARY OF MEASURED AND SIMULATED TRANSITION POSITIONS (APPROXIMATE VALUES IN *mm*)

Measurement	5 m/s		10 m/s	
technique	Start	End	Start	End
Preston tube	600	950	350	650
Thermography	675	1075	350	625
Hot wire	650	-	350	700
LIV	775		450	
LINARS	500	800	200	400
Fluent®	300	500	100	150
CFX®	500	800	200	400

The support by FWF project P24096-N24 (Laser Interferometric Research) is also gratefully acknowledged.

REFERENCES

[1] Bader, P., and Sanz, W., 2015. "Steady and unsteady CFD calculation of the laminar-to-turbulent transition in a turning mid turbine frame with embedded design". *Proceedings of ASME 2015 Turbo EXPO, Montreal, Canada*. GT2014-42617.

[2] Schlichting, H., and Gersten, K., 2006. *Grenzschicht-Theorie (Boundary-Layer Theory)*. Springer-Verlag Berlin Heidelberg.

[3] Mayle, R. E., 1991. "The role of laminar-turbulent transition in gas turbine engines". *Journal of Turbomachinery,* ***113***(4), October, pp. 509–537.

[4] Yip, L. P., Vijgen, P., Hardin, J. D., and van Dam, C. P., 1993. "In-flight pressure distributions and skin-friction measurements on a subsonic transport high-lift wing section". *AGARD CP-515*.

[5] Oyewola, O., Djenidi, L., and Antonia, R. A., 2003. "Combined influence of the reynolds number and localised wall suction on a turbulent boundary layer". *Experiments in Fluids,* ***35***, July, pp. 199–206.

[6] Oyewola, O., 2006. "LDV measurements in a pertubed turbulent boundary layer". *Journal of Applied Science,* ***6***(14), pp. 2952–2955.

[7] Widmann, A., Duchmann, A., Kurz, A., Grundmann, S., and Tropea, C., 2012. "Measuring tollmien-schlichting waves using phase-averaged particle image velocimetry". *Experiments in Fluids,* ***53***, pp. 707–715.

[8] Mukund, R., Narasimha, R., Viswanath, P. R., and Crouch, J. D., 2012. "Multiple laminar-turbulent transition cycles around a swept leading edge". *Experiments in Fluids,* ***53***, pp. 1915–1927.

[9] Bader, P., and Sanz, W., 2015. "On the setup of a test bench for predicting laminar-to-turbulent transition on a flat plate". *Proceedings of the 12th International Symposium on Experimental Computational Aerothermodynamics of Internal Flows, Genova, Italy*. ISAIF12-074.

[10] Walters, K., and Cokljat, D., 2008. "A three-equation eddy-viscosity model for reynolds-averaged navier-stokes simulations of transitional flows". *Journal of Fluids engineering,* ***130***, pp. 1214011–12140114.

[11] Menter, F. R., Langtry, R. B., Likki, S. R., Suzen, Y. B., Huang, P. G., and Völker, S., 2006. "A correlation based transition model using local variables part 1: Model formulation". *Journal of Turbomachinery,* ***128***(3), pp. 413–422.

[12] Langtry, R. B., 2006. "A correlation-based transition model using local variables for unstructured parallelized CFD codes". PhD Thesis, Institute of Thermal Turbomachinery and Machinery Laboratory, University Stuttgart.

[13] Elsner, W., Piotrowski, W., and Drobniak, S., 2008. Transition prediction on turbine blade profile with intermittency transport equations. ASME Turbo Expo 2008, Berlin, Germany. GT2008–50796.

[14] Langtry, R. B., and Menter, F. R., 2009. "Correlation-based transition modeling for unstructured parallelized computational fluid dynamics codes". *AIAA Journal,* ***47***(12), pp. 2894–2906.

[15] Sorensen, N. N., 2009. "CFD modeling of laminar-turbulent transition for airfoil and rotors using the $\gamma - \tilde{Re}_{\Theta}$ model". *Wind Energy,* ***12***(8), pp. 715–733.

[16] Malan, P., Suluksna, K., and Juntasaro, E., 2009. Calibrating the $\gamma - re_{\Theta}$ transition model for commercial CFD. AIAA Paper. 2009–1142.

[17] Kelterer, M., Pecnik, R., and Sanz, W., 2010. Computation of laminar-turbulent transition in turbomachinery using the correlation based $\gamma - re_{\Theta}$ transition model. ASME Turbo Expo 2010, Glasgow, Scotland. GT2010-22207.

[18] Ichimiya, M., Nakamura, I., and Yamashita, S., 1998. "Properties of a relaminarizing turbulent boundary layer under a favorable pressure gradient". *Experimental Thermal and Fluid Science,* ***17***, pp. 37–48.

[19] Mukund, R., Viswanath, P. R., Narasimha, R., and Praband Crouch, J. D., 2006. "Relaminarization in highly favourable pressure gradients on a convex surface". *Journal of Fluid Mechanics,* ***566***, pp. 97–115.

[20] Dorfer, S., 2011. "Auslegung und experimentelle untersuchung eines relaminarisierungs – testfalls". *Diploma Thesis at Graz University of Technology*.

[21] Mayrhofer, N., and Woisetschläger, J., 2001. "Frequency analysis of turbulent compressible flows by laser vibrometry". *Experiments in Fluids,* ***31***, pp. 153–161.

[22] Roach, P. R., 1987. "The generation of nearly isotropic turbulence by means of grids". *International Journal of Heat and Fluid Flow,* ***8***, pp. 82–92.

[23] Händel, D., Rockstroh, U., and Niehuis, R., 2014. Experimental investigation of transition and separation phenomena on an inlet guide vane with symmetric profile at different stagger angles and reynolds numbers. 15^{th} International Symposium on Transport Phenomena and Dynamics of Rotating Machinery, Honolulu, USA. ISROMAC-15.

[24] Schlichting, H., 1965. *Grenzschicht-Theorie (Boundary-Layer Theory)*. Verlag G.Braun, Karlsruhe, Germany.

[25] Hampel, B., Mayrhofer, N., and Woisetschläger, J., 2002. "Frequenzanalyse einer turbinenschaufelgitterströmung mittels laser-vibrometer und holographischer interferometrie". *Proceedings of GALA-Fachtagung Lasermethoden in der Strömungsmetechnik, Rostock, Germany*. paper No. 32.

[26] Hampel, B., Woisetschläger, J., Mayrhofer, N., Göttlich, E., and Heitmeir, F., 2005. "Recording local density fluctuations in turbine flows using laser vibrometry". *Proceedings of the 6^{th} Conference on Turbomachinery: Fluid Dynamics and Thermodynamics, Lille, France*. ETC2005-111050.

[27] Lewin, A., Mohr, F., and Selbach, H., 1990. "Heterodyn-interferometer zur vibrationsanalyse". *Technisches Messen,* ***57***, pp. 335–345.

[28] Langtry, R. B., Menter, F. R., Likki, S. R., Suzen, Y. B., Huang, P. G., and Völker, S., 2004. "A correlation based transition model using local variables part 2: Test cases and industrial applications". *Proceedings of ASME 2004 Turbo EXPO, Vienna, Austria*. GT2004-53454.

5.6. Paper 4: Comparison of RANS and embedded LES Calculations with Measurements of Transitional Flow along a Flat Plate

P. Bader, W. Sanz, C. Steinmayr and P. Leitl, "Comparison of RANS and embedded LES Calculations with Measurements of Transitional Flow along a Flat Plate," *ERCOFTAC Bulletin*, vol. 106, pp. 84–93, 2016.

Comparison of RANS and Embedded LES Calculations with Measurements of Transitional Flow Along a Flat Plate

P. Bader[1], W. Sanz[1], C. Steinmayr[2] and P. Leitl[2]

[1] *Institute of Thermal Turbomachinery and Machine Dynamics*
Graz University of Technology
8010 Graz, Inffeldgasse 25/A, Austria

[2] *bionic surface technologies GmbH*
8010 Graz, Brockmanngasse 49, Austria

Abstract

Flow in turbomachines is generally highly turbulent. The boundary layers, however, often exhibit laminar-to-turbulent transition. Relaminarization from turbulent to laminar flow may also occur. The state of the boundary layer is important since it strongly influences transport processes like skin friction and heat transfer.

It is therefore vitally important for the designer to understand the process of laminar-to-turbulent transition and to be able to determine the position of transition onset and the length of the transitional region. Several approaches exist to numerically predict transition along a solid body, but the uncertainty of these simulations are quite unknown. In order to get more insight into the process of transition and relaminarization it is often helpful to study simplified test cases first. Therefore, in this paper the transitional flow along a flat plate is experimentally and numerically studied and the capability of numerical approaches to predict the transition process accurately will be highlighted.

Constant temperature anemometry (CTA) as well as laser Doppler anemometry (LDA) measurements are performed to study the transitional flow. The measurement results are then compared with the results of different numerical simulations using the Reynolds-averaged Navier-Stokes (RANS) approach with different transition models as well as an embedded large eddy simulation (eLES). Time averaged and instantaneous velocity profiles are compared with the measurement data. Additionally time signals of the CTA probe are compared with the LES data.

In this way the capability of modern RANS models and of an embedded large eddy simulation in predicting transition are studied. The features of an eLES regarding the simulation of transition are presented.

1 Introduction

In flows along solid body surfaces the boundary layer represents the narrow zone between the wall and the free stream where viscous effects are important. Its state of flow (laminar or turbulent) may have strong impact on transport processes like wall friction and heat transfer. These processes influence the efficiency as well as the thermal stress for example of a turbine blade. In turbomachinery the laminar or turbulent state of the boundary layer may therefore affect the efficiency of the stages and has an effect on other flow characteristics in the machine as well [1].

At the first contact of a flow with a stationary structure, the boundary layer is laminar and then develops from laminar to turbulent (under the appropriate flow conditions) via a transitional region. There are mainly three different types of transition: Natural, bypass and separated-flow transition. Schlichting and Gersten [2] extensively discussed the different stages a boundary layer passes through within the natural transition zone before becoming fully turbulent. In turbomachinery, where generally high free-stream turbulence exists whose fluctuations act on the boundary layer flow, bypass transition is the dominant feature where the earlier stages of natural transition are bypassed.

Many parameters, like free-stream velocity, acceleration, free-stream turbulence etc., may influence the state of a boundary layer. It is therefore important to understand the effect of these parameters on the onset position and length of the transitional zone in order to predict and potentially control the state of the boundary layer. In turbomachinery, the efficiency of blades and stages can be improved considering transition, thus improving the overall machine performance. In 1991, Mayle published a comprehensive review of the importance of transition in gas turbines [3]. He analyzed experiments performed by several research groups in order to find the influence of different flow parameters on the transition process.

Additional experiments have been performed in the last years by many research groups. Yip et al. performed in-flight measurements, detected transition with the help of Preston tubes and analyzed the influence of the flight conditions on the boundary layer along an airfoil [4]. In this way they performed full-scale Reynolds number flow measurements including relaminarization and attachment-line transition. Oyewola et al. used hot-wire anemometry and laser Doppler anemometry (LDA) to investigate the effect of wall suction on a turbulent boundary layer [5, 6]. Widmann et al. performed near-wall measurements with particle image velocimetry (PIV) in order to measure Tollmien-Schlichting waves [7]. Hot-film measurements were performed, e.g., by Mukund et al. [8] who investigated relaminarization along a convex surface. Preston-tube and thermographic measurements by Bader and Sanz [9] and Bader et al. [10] showed an interesting comparison between different measurement

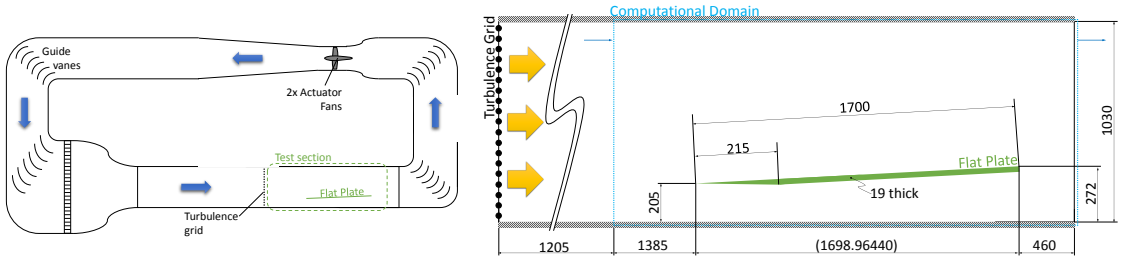

(a) Sketch of the wind tunnel.

(b) Detailed view of the test section

Figure 1: Göttinger-type wind tunnel with closed test section used for experiments

techniques regarding their capability to detect transition.

In addition to measurements, numerical models were developed to predict the laminar-to-turbulent transition process. Common models are, for example, the k-k_L-ω model by Walters and Cokljat [11], the intermittency γ model by Menter et al. [12] and the γ-Re_Θ model by Menter et al. [13] and Langtry [14]. For the latter, various correlations for important model parameters were developed [15, 16, 17, 18, 19].

So far, mainly the transition from laminar to turbulent flow was investigated. Under certain flow conditions (like high acceleration), however, a reverse transition or relaminarization from turbulent to laminar can occur. Up to now, only few measurements on relaminarization were reported [20, 21, 22]. Therefore, at the Institute of Thermal Turbomachinery and Machine Dynamics (ITTM) of Graz University of Technology a project was launched in order to understand the process of relaminarization.

The aim of this project is to understand the process of transition and relaminarization even further. Experimental and numerical means have been extensively applied to tackle this task. So several measurement techniques have been used to predict transition and have been validated against each other [9, 10]. In the present paper the results of constant-temperature anemometry (CTA) as well as laser Doppler anemometry (LDA) will be presented. The measurement results are compared to computational fluid dynamics (CFD) calculations.

For the CFD simulations Reynolds-averaged Navier-Stokes (RANS) simulations with different transition models as well as large eddy simulation (LES) have been performed. As transition models for the RANS simulations two intermittency models, namely the γ and the γ-Re_Θ model and the k-k_L-ω model have been used. The LES solution was obtained applying a RANS-LES hybrid approach to reduce the computational effort, called embedded large eddy simulation (eLES). The CFD simulations have been done by Bionic Surface Technologies GmbH (BST). Their special expertises are riblet simulations and their application. These numerical simulations also function as prestudies for investigations in the influence of riblets on transition.

2 Experimental Setup

In this section, the experimental setup used for the CTA and LDA measurements is presented. The detailed results of the hot wire measurements have already been presented by Bader et al. [10] and are only shortly discussed here. The measurement data is used for the evaluation of the simulations in the next section.

2.1 Test Facility

The tests were performed in a Göttingen-type wind tunnel with closed test section at the Institute of Fluid Mechanics and Heat Transfer. A sketch of the tunnel is given in Fig. 1(a). The wind tunnel is powered by two fans with a total power input of 75 kW. The air is conveyed to the nozzle and the test section via two corners with guide vanes. The maximum achievable flow-rate equivalent velocity is about 30 m/s. The nozzle exit cross section is 2 m wide and 1 m high. Downstream from the nozzle, a 6 m long channel for developing flow velocity profiles is installed. The test section itself is about 2.6 m long. The top panel of the tunnel is adjustable for controlling the pressure gradient along the test section.

Since the turbulence of the wind tunnel flow is well below 1 %, a turbulence grid is installed upstream from the test section in order to raise the turbulence level to about 3 % to 4 %. The turbulence grid consists of equally spaced cylindrical rods. As suggested by Roach, the grid has a solidity below 50 %, and its position upstream from the first measuring point satisfies the $x/d > 10$ criterion, where x represents the streamwise coordinate and d the diameter of the rods [23].

Downstream from the turbulence grid, but upstream from the flat plate, the first measurement section is located (inlet of the computational domain in Fig. 1(b). At this plane the turbulence level and the free-stream velocity were measured in order to get the inlet boundary conditions for the numerical simulations.

Figure 1(b) also shows the position of the flat plate. The plate is inclined by two degrees against the bottom wall of the channel in order to ensure that the flow is attached at the upper surface. The plate distance from the side walls is larger than the boundary layer thickness there in order to avoid influences from the sidewall boundary layers on the flow along the plate.

2.2 Hot Wire Anemometry

In the present work hot wire anemometry was also applied for measuring flow velocities. A multi-channel constant-temperature anemometer (CTA) 54N82 with a 54N95 transmitter from *Dantec Dynamics A/S* was used with miniature X-wire probes type 55P63 with 90° tilted heads for the velocity measurements along the plate. Straight probes type 55P61 were used for measuring the free-stream turbulence upstream from the plate. For the temperature compensation, a 90P10 reference temperature probe was used. The measurements were performed with a sampling frequency of 10 kHz, collecting a total number of 80,000 samples for each measuring position.

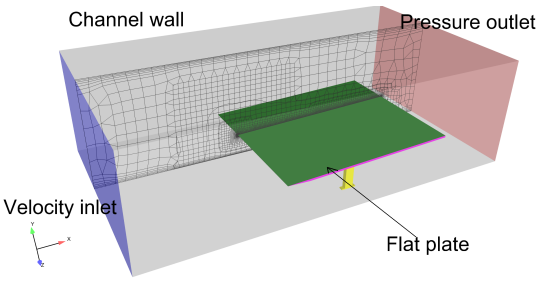

Figure 2: Numerical domain of the 3D RANS simulation

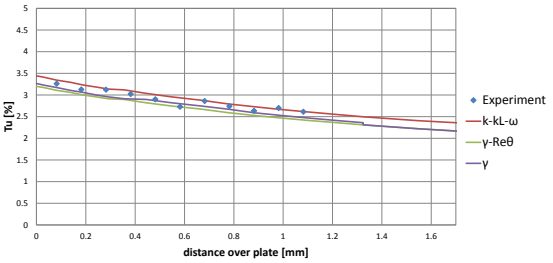

Figure 3: Comparison of measured and simulated free-stream turbulence intensity

2.3 Laser Doppler Anemometry

Additionally LDA measurements were performed in order to get the velocity and its fluctuations within the boundary layer. The two-dimensional LDA system by *Dantec Dynamics A/S* consists of a 6 Watt Argon-Ion Laser, two Burst Spectrum Analyzer (BSA) processors, 57N35 model S and 57N20, and a 60x41 FiberFlow transmitter ($\lambda_1 = 514.5\ nm$, $\lambda_2 = 488\ nm$).

As optic a 60 mm probe head (60x67 2D probe) with a beam distance of 75.24 mm, a focal distance of 1000 mm and a beam diameter of 2.2 mm (in front of the lens) is used.

For seeding a fog generator from *EHLE-HD* was applied with *Slow Fog* glycol-water-based seeding medium. The density is approximately $\rho = 1260\ {}^{kg}/_{m^3}$, thus the seeding particles act as a low pass filter up to about $f(-3dB) = 41\ kHz$ [24].

3 CFD Simulation

The simulations were performed for a free-stream velocity of 10 m/s where transitional flow was detected along the plate in the measurements. The measured turbulence intensity was $Tu = 3.15$ % in the free stream at the plate leading edge. The turbulent boundary conditions at the inlet of the computational domain were found by the requirement of matching the measured free-stream turbulence intensity along the plate.

3.1 3D RANS Simulations

In this section the CFD results of a Reynolds-averaged Navier-Stokes (RANS) simulation are presented. The calculations have been performed with the commercial solver ANSYS® Fluent® v15.0. In order to predict transition three different transition models have been used and are compared to each other. Two models, the γ [12] and the γ-Re_Θ model [13], are based on the intermittency approach. The intermittency which is defined as the ratio of time when the flow is turbulent to the total time is an indicator of the transitional state of the boundary layer. It is modelled with a transport equation and is used to modify the turbulence production in the SST turbulence model equations [13]. The γ model has been recently derived from the more complex γ-Re_Θ model and needs only one transport equation. The third model, the k-k_L-ω model [11], additionally considers the transport of the so-called laminar kinetic energy which precedes the transition process. It triggers the formation of turbulence kinetic energy in the transition process.

For the calculation a three dimensional mesh was used covering the whole flow domain with all details like the plate mounting. The domain starts 1385 mm upstream of the leading edge of the flat plate (see Figure 1(b)) with a velocity inlet boundary condition. The numerical mesh was generated with the program HEXPRESS™ of NUMECA. It is an unstructured mesh with a cell number of around 8 million cells. The geometry together with the applied numerical boundary conditions and a mesh sketch can be seen in Figure (2). The near wall condition on grid fineness of $y^+ \leq 1$ for transition modeling was fulfilled along the plate's upper side.

3.1.1 Development of Turbulence Intensity

At first the turbulence inlet boundary conditions were adjusted in order to capture the measured free-stream turbulence intensity along the flat plate (see Figure (3)). All three simulated cases exhibit a very good agreement with the measurement values, so that the flow conditions along the plate can be considered as similar. It is interesting that the k-k_L-ω model shows a slightly higher turbulence for the same inlet boundary conditions.

3.1.2 Skin Friction Coefficient

At the trailing edge in the center of the plate a foothold is mounted at the bottom side to hold the plate in its position. This support has a slight influence on the flow at the rear part of the plate at the centerline. To avoid this influence on the result the following evaluation of the skin friction coefficient was made at a z-position of 750 mm ($\approx 33\%$ plate width) where it is negligible.

The calculated skin friction coefficient c_f is plotted over the plate length in Figure (4). c_f is defined as

$$c_f = \frac{\tau_w}{1/2 \cdot \rho \cdot U_{\infty,0}^2} \tag{1}$$

where $U_{\infty,0}$ represents the inlet velocity of 10 m/s, τ_w the wall shear stress and ρ the fluid density.

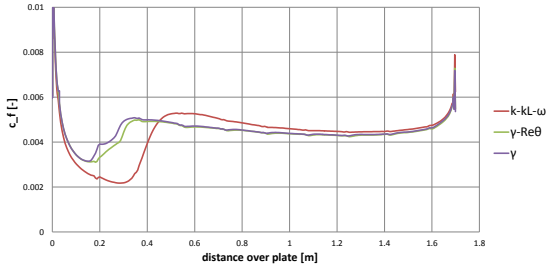

Figure 4: Calculated skin friction coefficient along the plate

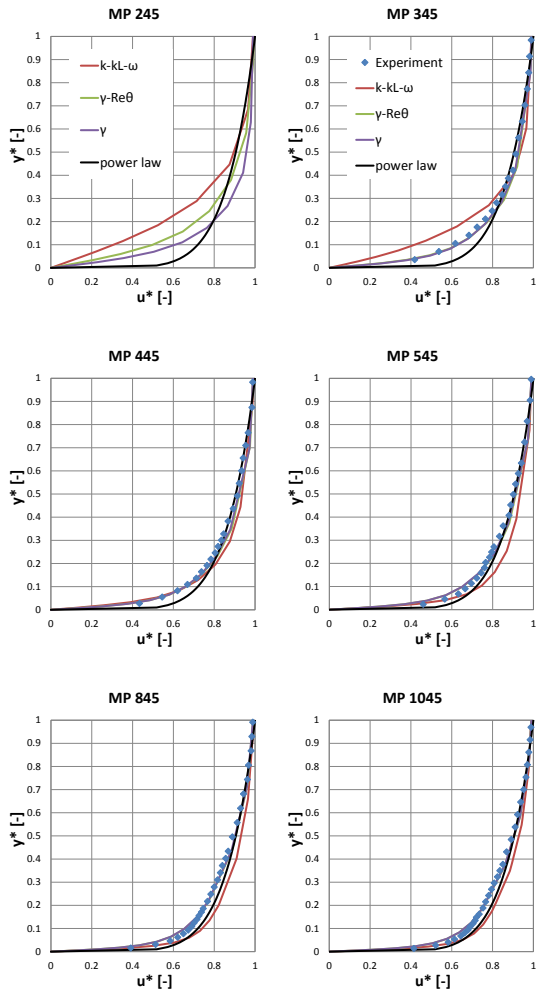

Figure 5: Dimensionless velocity profiles along the plate; comparison of RANS solutions with the measurements

All three models show a decrease of the skin friction coefficient in the leading edge region as expected in a laminar boundary layer flow upstream of the start of the transitional zone. The intermittency models both show a rise in skin friction and thus beginning transition significantly more upstream than the k-k_L-ω model. On the other hand this model predicts a slightly more rapid transition process. Due to the later transition the skin friction of the k-k_L-ω model is slightly higher after transition compared to the other models. The sudden rise of the skin friction coefficient at the trailing edge is caused by the enlargement of the flow area there which leads to an overspeed.

3.1.3 Velocity Profiles

A detailed insight into the boundary layer flow is given by the dimensionless velocity profiles at different positions along the plate. In Figure (5) the the non-dimensional velocity u^* is plotted for a dimensionless wall distance

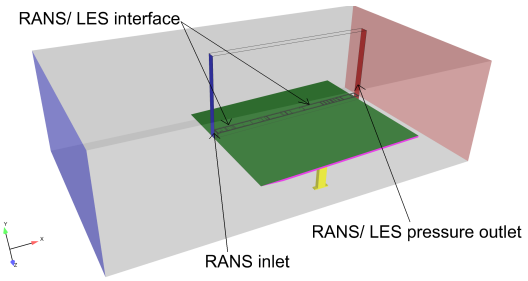

Figure 6: Position of eLES domain

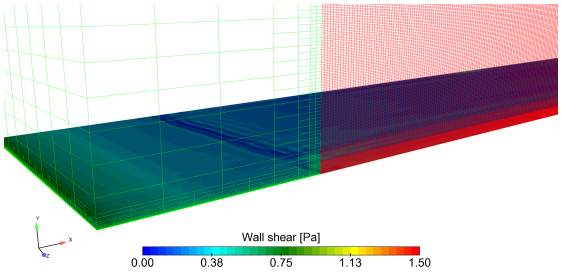

Figure 7: Sketch of the mesh in the RANS inlet section and in the LES region; instantaneous wall shear is shown along the plate

y^*. These values are defined as

$$y^* = \frac{y}{\delta(x)} \tag{2}$$

$$u^* = \frac{u(y)}{U_\infty(x)} \tag{3}$$

where $\delta(x)$ represents the local boundary layer thickness and $U_\infty(x)$ the local free-stream velocity at each position. The edge of the boundary layer is defined as the distance normal to the wall with

$$u(y = \delta(x)) = 0.99\ U_\infty(x) \tag{4}$$

Besides the measurement and simulation data the 1/7th-power law profile is plotted in Figure (5), which is a good approximation of a fully turbulent boundary layer and which is defined as

$$u^* = (y^*)^{\frac{1}{7}} \tag{5}$$

At the first location MP 245, which is located 245 mm downstream of the plate leading edge, the three calculated velocity profiles differ remarkably from the 1/7th-power law indicating that all simulations predict laminar or transitional flow which agrees with the results shown in Figure (4). The k-k_L-ω velocity profile deviates most; the boundary layer is still laminar. The transition predicted by the γ model is a little bit more advanced compared to the one of the γ-Re_Θ model.

Once transition is completed the two intermittency models predict identical results. So in measurement point MP 345, which is located 345 mm downstream of the plate leading edge, the intermittency results agree well with the measured velocity profile. The profile is not fully turbulent compared to the 1/7th-power law indicating that transition is not yet completed. The k-k_L-ω velocity profile rises linearly to approximately $y^* \sim 0.3$

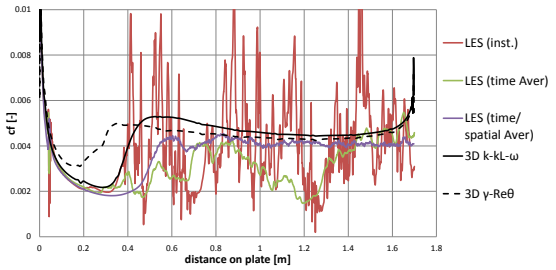

Figure 8: Comparison of skin friction coefficient along the plate for eLES and RANS simulations

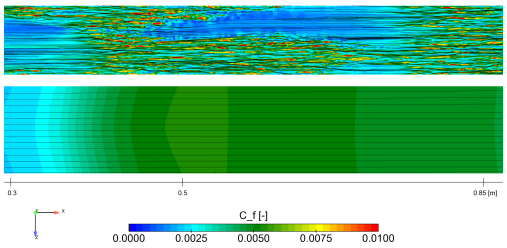

Figure 9: Detailed view of instantaneous eLES (top) and RANS (bottom) skin friction coefficient in the transitional region (245 mm-645 mm from leading edge.

revealing its still laminar character which agrees with the observations of the skin friction distribution of Figure (4).

At the next position MP 445 all calculated velocity profiles agree well with each other and with the measured profile especially close to the wall. This is approximately the location where all models predict the same skin friction coefficient value in Figure (4).

With rising distance from the leading edge measured and calculated profiles become more turbulent, converging towards the 1/7th-power law. But whereas the intermittency models nearly perfectly match the measured velocity profiles, the k-k_L-ω model exhibits a fuller profile. This observation agrees with the higher skin friction value in Figure (4). It also fits better to the 1/7th-power law at the last two positions which indicates a "more turbulent" flow at the back of the plate compared to the measured and intermittency model velocity profiles.

4 Embedded Large Eddy Simulation (eLES)

Large eddy simulation is said to be able to predict transition without additional modelling. In order to see its capability an embedded LES (eLES) is performed on the same test case. Embedded LES is a method that combines LES and RANS in such a way that an LES region is embedded in a surrounding RANS zone. Special interfaces are necessary for the information transport between the different regions.

For the simulation with eLES not the whole three dimensional test area of the wind tunnel was simulated, but a small section of 80 mm width as displayed in Figure (6). This is acceptable as the RANS simulations above show only small variations in transverse direction. Although the computational domain is reduced the mesh size increases due to the higher mesh density necessary for LES. The mesh was generated according to the guideline for transition modelling with eLES by Menter [25]. The dimensionless cell size within the boundary layer is $\Delta x^+ < 40$ (streamwise), $\Delta y^+ < 1$ (normal to wall) and $\Delta z^+ < 20$ (transveral).

The mesh used in this study has two different calculation domains. The near-wall part of the reduced flow domain is covered by an LES domain (see Figure (6)). A RANS domain is arranged in front and on top of the LES domain. Figure (7) shows the two flow domains at the inlet and gives a sketch of the RANS and LES meshes. The cell size in the LES mesh is about 1/20th of the one in the RANS zone. The requirements on grid fineness for the LES computation lead to about 45 million cells for the LES domain, the total cell number including the RANS zones is about 62 million.

Classical LES requires unsteady boundary conditions at turbulent inlets/interfaces. For the RANS–LES interface ANSYS® Fluent® v15.0 offers the vortex method and the spectral synthesizer. Both methods create stochastically discrete vortices at the inlet. Their distribution, strength, and size are modeled in order to provide the desirable characteristics of real turbulence. The input parameters are the turbulent scales (k and ω or k and ϵ) from an upstream RANS computation (for further details see [26] and [25]).

In order to use the stochastic turbulence generator at the interface, in this simulation a short RANS zone is placed in the leading edge region. The k-k_L-ω model is used there, the inlet boundary conditions were taken from the 3D RANS solution, with the variables velocity $\vec{v}$, turbulence kinetic energy k_T, laminar kinetic energy k_L and specific dissipation rate ω. At the streamwise plate position $x = 0.004\ m$ the LES domain starts, so that the interface between the RANS and LES domain is situated in the laminar region. The spectral synthesizer was chosen at the RANS–LES interface in front and on the top of the LES zone. With this configuration it was possible to generate a laminar flow in the first section of the flat plate which gets turbulent at downstream positions. Figure (7) shows the wall shear in the interface region. Small disturbances starting at the interface move into the LES region. In the side walls of the computational domain periodic flow conditions are assumed.

For the simulation a timestep of $t_s = 2.5 \cdot 10^{-5}$ has been used. Convergence of the solution is checked by plotting the total drag of the flat plate over time. 8000 time iterations were performed which took about 4 weeks on a 10-core computer; the solution was stored for every 100th step leading to 80 instantaneous distributions for the data evaluation.

Figure (8) shows a comparison of the skin friction coefficient c_f along the plate between the RANS results and the eLES. The diagram includes an instantaneous eLES result, a time-averaged result at mid line and a time- and transversely averaged result.

The instantaneous distribution shows large fluctuations starting approximately at the location of the transition onset as predicted by the k-k_L-ω model. The time-averaged result also indicates an increase of the c_f value at a similar location. But the fluctuations indicate that additional time snapshots should be used for averaging to obtain a "steady" result. The additional spatial averaging in transversal direction increases the number of instantaneous solutions used for averaging so that a smoother c_f distribution is obtained with values in the fully turbulent region close to the RANS results. But the averaged eLES solution predicts the most downstream transition

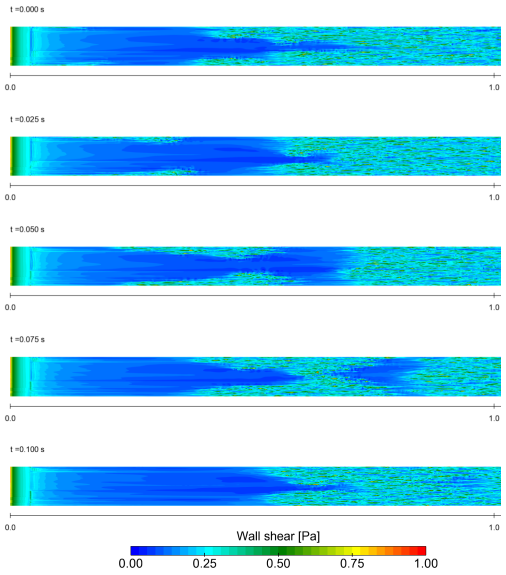

Figure 10: Instationary wall shear stress distributions from LES

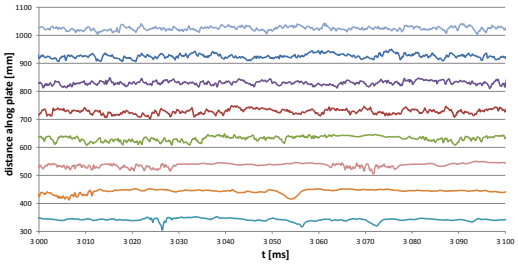

(a) Measurement

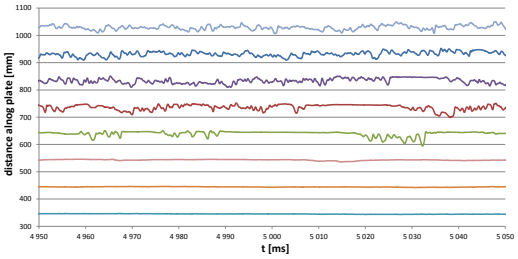

(b) eLES solution

Figure 11: Time signal of velocity at different streamwise positions

onset compared to all three RANS results.

The interface between RANS and LES domain can be observed in a slight spike shortly after the leading edge of the plate, but the nature of the laminar boundary layer is not influenced by the interface.

Figure (9) gives a comparison of an instantaneous c_f distribution (top view) with the RANS k-k_L-ω solution (bottom view) along the plate surface in the transitional region ($245\ mm \leq x \leq 645\ mm$). The peak values seen in Figure (8) are visible as red spots in the eLES domain and can be considered as turbulent bursts which are transported downstream. They also cause relatively strong lateral fluctuations which are shown by the streamlines close to the wall in the eLES solution. The large regions of low skin friction (blue zones) are of laminar character which is also shown by the nearly straight streamlines. It is interesting that the local c_f values show maxima about five times higher than the averaged c_f-values.

In order to better show the unsteady nature of the flow Figure (10) gives five snapshots of the wall shear stress distribution covering a time period of 0.1 s. In the first snapshot we see two spots of high wall shear evolving at both side walls of the computational domain. They grow and cover a more and more broad zone of the flow section until they eventually merge at $t = 0.75\ s$. The zone of low wall shear is pushed forward by the evolving turbulence and is finally trapped between regions of high turbulence ($t = 0.75\ s$). Finally it also transitions under the influence of the neighboring turbulent fluctuations.

Time signals of velocity fluctuations are also an appropriate indicator of the state of the boundary layer. Figure (11) compares the time signals of the CTA measurement with the eLES results. The signals are taken at several streamwise positions, 3 mm above the plate. It can be observed that measured and simulated signals have similar characteristics, although the measurement signal possesses additional higher-frequency oscillations. In the measurements the first two signals ($x = 345\ mm$ and $x = 445\ mm$) offer long laminar periods; further downstream, fluctuations start to increase but still laminar zones can be found between turbulent packages ($x = 545\ mm$ and $x = 645\ mm$). At $x = 745\ mm$ the boundary layer appears to be fully turbulent. In the eLES first turbulent packages turn up more downstream at $x = 645\ mm$; laminar periods can be still detected at $x = 745\ mm$ and $x = 845\ mm$. At $x = 945\ mm$ the time signal seems fully turbulent. This again indicates a later and shorter transition process as also observed in the c_f distribution of Figure (8).

In Figure (12) the non-dimensional velocity profiles $u^*(y^*)$ of the eLES solution are plotted in two ways: time-averaged at the mid line and time- and transversally-averaged. The measurement data and again the power law according to Equation (Eq. (5)) are also included. Additionally in Figure (13) several instantaneous velocity profiles are compared with each other. The small differences between time-averaged and time-space-averaged profiles show that more snapshots than 80 are necessary to obtain a "steady" result.

At the first position (MP 345) the eLES curves show similar behavior close to the wall and their slope indicates the laminar character there. This is confirmed by the instantaneous profiles of Figure (13) which all show the same slope close to the wall and only small deviations to each other. At larger wall distance the time-space-averaged profile approaches the 1/7th-power law. The difference to the measurement results again reveals that the measurement shows a transitional boundary layer there. At the next position (MP 445) there are small differences between both eLES results; and the simulation still shows a laminar profile whereas the measured profile approaches the power law indicating its turbulent character. At MP 645 the slope of both eLES profiles is steeper but has not yet reached the fully turbulent distribution. The instantaneous profiles also show partly laminar, partly turbulent character which agrees with the observations of Figure (10). At MP 845 measured and calculated profiles agree well with the 1/7th-power law; the flow is turbulent. The instantaneous profiles fluctu-

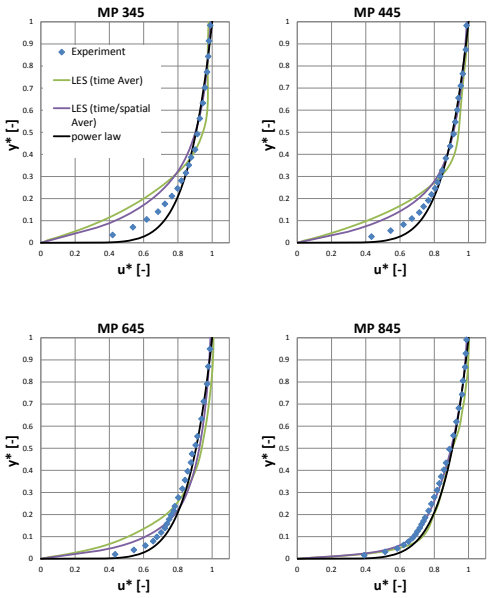

Figure 12: Dimensionless velocity profiles along the plate; comparison of LES results with the measurements

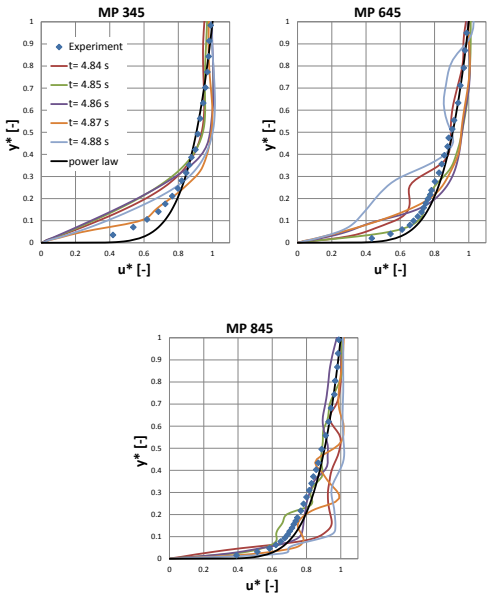

Figure 13: Instantaneous dimensionless velocity profiles from LES at three streamwise positions

ate and differ remarkably as expected from a turbulent boundary layer.

5 Summary and Conclusions

Accurate transition prediction is still a topic of research. Therefore in this work this problem is tackled by experimental and numerical investigations of the transitional flow along a flat plate. Three different RANS simulations with transition modeling and an eLES were evaluated based on CTA and LDA data of the velocity profiles. The best results are obtained with the intermittency based transition models which could capture the transition zone best based on a comparison between measured and calculated boundary layer velocity profiles. The γ model which was derived from the more complex γ-Re_Θ model gives nearly identical results at a reduced computational effort. The third RANS model, the $k - k_L - \omega$ model, gives also reasonable results but predicts a too late transition process compared to the experiments.

The eLES method which combines RANS and LES domains gives an insight into the unsteady development of transition. Very long computational times are necessary to obtain a converged time-averaged "steady" flow.The eLES could clearly capture the transition process. The evolution and development of turbulent bursts are visible in the wall shear stress contours. The associated velocity profiles in the boundary layer show laminar and turbulent profiles in the transition zone. But the predicted transition process takes place too far downstream similar to the $k - k_L - \omega$ model predictions.

Summarizing, for the test case presented all numerical approaches give reasonable results and are able to predict transition. But the simplest approach, the intermittency based RANS simulations, exhibits the best agreement with the measurement data especially regarding the transition process. Further evaluations will be performed on non-zero-gradient flows in order to improve the knowledge on the accuracy of transition modelling.

Acknowledgment

The authors would like to thank the Institute of Fluid Mechanics and Heat Transfer, especially Günter Brenn and Walter Meile, for providing their wind tunnel and parts of the measuring equipment and also for their continuous support during the test campaign.

The authors gratefully acknowledge the support from the Austrian Federal Ministry of Transport, Innovation and Technology by funding the project ReLam in the frame of the Austrian Aeronautics Program TAKE OFF.

References

[1] P. Bader and W. Sanz, "Steady and unsteady CFD calculation of the laminar-to-turbulent transition in a turning mid turbine frame with embedded design," *ASME Turbo EXPO 2015, Montreal, Canada*, 2015. GT2014-42617.

[2] H. Schlichting and K. Gersten, *Grenzschicht-Theorie (Boundary-Layer Theory)*. Springer-Verlag Berlin Heidelberg, 2006.

[3] R. E. Mayle, "The role of laminar-turbulent transition in gas turbine engines," *ASME Journal of Turbomachinery*, vol. 113, pp. 509–537, October 1991.

[4] L. P. Yip, P. Vijgen, J. D. Hardin, and C. P. van Dam, "In-flight pressure distributions and skin-friction measurements on a subsonic transport high-lift wing section," *AGARD CP-515*, 1993.

[5] O. Oyewola, L. Djenidi, and R. A. Antonia, "Combined influence of the reynolds number and localised wall suction on a turbulent boundary layer," *Experiments in Fluids*, vol. 35, pp. 199–206, July 2003.

[6] O. Oyewola, "LDV measurements in a pertubed turbulent boundary layer," *Journal of Applied Science*, vol. 6, no. 14, pp. 2952–2955, 2006.

[7] A. Widmann, A. Duchmann, A. Kurz, S. Grundmann, and C. Tropea, "Measuring Tollmien-Schlichting waves using phase-averaged particle image velocimetry," *Experiments in Fluids*, vol. 53, pp. 707–715, 2012.

[8] R. Mukund, R. Narasimha, P. R. Viswanath, and J. D. Crouch, "Multiple laminar-turbulent transition cycles around a swept leading edge," *Experiments in Fluids*, vol. 53, pp. 1915–1927, 2012.

[9] P. Bader and W. Sanz, "On the setup of a test bench for predicting laminar-to-turbulent transition on a flat plate," *Proceedings of the 12^{th} International Symposium on Experimental Computational Aerothermodynamics of Internal Flows, Genova, Italy*, 2015. ISAIF12-074.

[10] P. Bader, W. Sanz, J. Peterleithner, J. Woisetschläger, F. Heitmeir, W. Meile, and G. Brenn, "Measuring flat plate transition with laser interferometric vibrometry (LIV)," *ASME Turbo Expo 2016, Seoul, South Korea*, 2016. GT2016-56043.

[11] K. Walters and D. Cokljat, "A three-equation eddy-viscosity model for Reynolds-averaged Navier-Stokes simulations of transitional flows," *Journal of Fluids Engineering*, vol. 130, pp. 1214011–12140114, 2008.

[12] F. Menter, P. Smirnov, T. Liu, and R. Avancha, "A one-equation local correlation-based transition model," *Flow, Turbulence and Combustion*, vol. 95, no. 4, pp. 583–619, 2015.

[13] F. R. Menter, R. B. Langtry, S. R. Likki, Y. B. Suzen, P. G. Huang, and S. Völker, "A correlation based transition model using local variables part 1: Model formulation," *ASME Journal of Turbomachinery*, vol. 128, no. 3, pp. 413–422, 2006.

[14] R. B. Langtry, *A correlation-based transition model using local variables for unstructured parallelized CFD codes*. PhD Thesis, Institute of Thermal Turbomachinery and Machinery Laboratory, University Stuttgart, 2006.

[15] W. Elsner, W. Piotrowski, and S. Drobniak, "Transition prediction on turbine blade profile with intermittency transport equations." ASME Turbo Expo 2008, Berlin, Germany, 2008. GT2008–50796.

[16] R. B. Langtry and F. R. Menter, "Correlation-based transition modeling for unstructured parallelized computational fluid dynamics codes," *AIAA Journal*, vol. 47, no. 12, pp. 2894–2906, 2009.

[17] N. N. Sorensen, "CFD modeling of laminar-turbulent transition for airfoil and rotors using the $\gamma - \tilde{Re}_{\Theta}$ model," *Wind Energy*, vol. 12, no. 8, pp. 715–733, 2009.

[18] P. Malan, K. Suluksna, and E. Juntasaro, "Calibrating the $\gamma - Re_{\Theta}$ transition model for commercial CFD." Submitted to the 47^{th} AIAA Aerospace Sciences Meeting, Orlando, Floriada, 2009. AIAA 2009–1142.

[19] M. Kelterer, R. Pecnik, and W. Sanz, "Computation of laminar-turbulent transition in turbomachinery using the correlation based $\gamma - Re_{\Theta}$ transition model." ASME Turbo Expo 2010, Glasgow, Scotland, 2010. GT2010-22207.

[20] M. Ichimiya, I. Nakamura, and S. Yamashita, "Properties of a relaminarizing turbulent boundary layer under a favorable pressure gradient," *Experimental Thermal and Fluid Science*, vol. 17, pp. 37–48, 1998.

[21] R. Mukund, P. R. Viswanath, R. Narasimha, and J. D. Praband Crouch, "Relaminarization in highly favourable pressure gradients on a convex surface," *Journal of Fluid Mechanics*, vol. 566, pp. 97–115, 2006.

[22] S. Dorfer, *Auslegung und experimentelle Untersuchung eines Relaminarisierungstestfalls*. Diploma Thesis, Institute of Thermal Turbomachinery and Maschine Dynamics, Graz University of Technology, Austria, 2011.

[23] P. R. Roach, "The generation of nearly isotropic turbulence by means of grids," *International Journal of Heat and Fluid Flow*, vol. 8, pp. 82–92, 1987.

[24] J. Boree, L. Ben, and R. Bazile, "Optical methods for the measurement of constant and variable density flows," *International summer school on variable density turbulent flows, Barcelona, Spain*, 2003.

[25] F. R. Menter, "ANSYS FLUENT best practice: Scale-resolving simulations in Ansys CFD," *ANSYS Inc. Germany*, 2012.

[26] ANSYS Inc., Canonsburg, *ANSYS FLUENT Theory Guide*, 15 ed., 2013.

CHAPTER 6

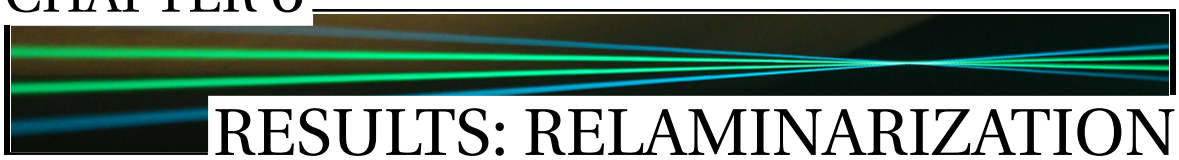

RESULTS: RELAMINARIZATION

> When I meet God, I am going to ask him two questions: Why relativity? And why turbulence? I really believe he will have an answer for the first.
>
> Werner Heisenberg,
> THEORETICAL PHYSICIST

In this chapter experimental (paper 5) and numerical (papers 6-8) results of relaminarization test cases are presented. The aims of the experimental work are on one side to get a better understanding of the process of relaminarization and on the other side to obtain a unique set of test cases, which are compared to the ERCOFTAC T** test cases, which are often used for calibration of numerical models.

The quantitative measurement results are then compared to RANS and LES solutions (paper 6 and 8) in order to test their capability and accuracy in computing relaminarization, whereas the qualitative outcome of the experimental campaign is used to evaluate the behavior of the γ-Re_θ transition model for a generic test case (paper 7).

6.1. Content

The first paper [155] of this chapter (**paper 5**) discusses the experimental program performed in wind tunnel B, where the cross section of the channel was reduced by integration of additional plates in order to accelerate the flow.

First, the setup of the acceleration plates is validated by CFD. The computation is used to confirm that the flow towards the leading edge is horizontal and no separation – neither at the leading edge nor at the acceleration plate edge – influences the measured boundary layer directly. This has also been validated using a light-sheet visualization technique (see Sec 4.1.1.3).

Laser-Doppler anemometry measurements have been performed for three different flow test cases: One sub- ($K < K_{crit}$) and two supercritical ($K > K_{crit}$) cases. The evaluation of the measurement data has been done by analyzing velocity profiles, skin friction and the shape factor. The skin friction and the shape factor have not been measured directly, but have been derived from the measured velocity profiles. The method to obtain the skin friction

which is used in this paper, is described in more detail in App. C together with other methods to measure the skin friction directly or indirectly.

Relaminarization occurs at a position downstream of the maximum of the acceleration factor K where the acceleration decreases. This can be observed with the shape factor, the skin friction and also with the velocity profiles. The latter also reveal, that relaminarization starts close to the wall. It seems that the viscous sublayer gets thicker, whereas the outer part follows the pressure gradient. When the maximum acceleration is reached, also the outer part starts to show a tendency towards a laminar boundary layer profile.

From these measurement data it can be observed that for all three cases at least partly relaminarization occurs, also for the subcritical case. The supercritical cases show an overshoot of the skin friction value upstream of the relaminarization zone.

Additionally, coincident two-dimensional LDA measurements give a detailed view on the development of the Reynolds shear stresses $\overline{u'v'}$, lateral velocity fluctuations v' as well as turbulence and statistical properties (skewness S, flatness F) inside the boundary layer during acceleration.

Additionally to the measurement program described in the paper a quadrant analysis of the coincidence measurements has been performed. The results are analyzed in Sec. 6.4 after paper 5. They show more clearly, what leads to the reduction of turbulence inside the boundary layer during relaminarization. Additionally, the disturbance leading to the retransition process is discussed in more detail.

Paper 6 [156] presents a comparison between measurement and simulation results, in particular computational results using the k-ω SST model (fully turbulent), the k-k_l-ω transition/turbulence model and a large eddy simulation. For comparison again the LDA measurement data obtained in wind tunnel B and presented in paper 5 are used.

The simulation results are validated by comparing the predicted free-stream velocities, turbulence intensities along the plate (not shown in the paper) and the acceleration parameter K with the measurement results. The comparison shows a good agreement for all three simulations with the experimental data.

Regarding the prediction of relaminarization it was found, that the k-k_l-ω model is not able to capture the relaminarization process. As Fürst [149] stated, the model does have problems with the prediction of transition if the flow is exposed to pressure gradients, thus the process of relaminarization cannot be captured using this model.

The LE simulation on the other hand clearly predicts the measured relaminarization. Beside the decrease in skin friction due to relaminarization, also the retransition following relaminarization can be observed. Although it retransition is computed too early compared to the measurements, the LES results can be used to get a more detailed insight into the relaminarization and retransition process.

A more detailed view on the LES results shows, that during relaminarization the vortices present in the boundary layer get elongated, and their number decreases. This can be interpreted as a reduction of the production of turbulence as observed by the measurements (see paper 4 and Sec. 6.4). More downstream an increase of the number of vortices is observed leading to a fast retransition into a fully turbulent boundary layer. This is most likely caused by the remaining fluctuations inside the boundary layer.

Similar to the post-processing of the LDA data, also a quadrant analysis has been performed for the LES results, which is presented in Sec. 6.6. The analysis shows, which quadrant events are influenced by the acceleration, reducing turbulent production. Additionally, a more detailed insight into the retransition process is given, showing which events dominate.

The last two papers 7 and 8 discuss numerical results obtained with the γ-Re_θ transition model.

Paper 7 [157] presents a generic study with the aim to understand how and why the γ-Re_θ model predicts relaminarization. The model basically compares the empirical transition onset momentum-thickness Reynolds number based on free stream conditions $Re_{\theta t}$ with the local transition onset momentum-thickness Reynolds number $\tilde{Re}_{\theta t}$ (see Sec. 4.2.1). If $Re_{\theta t}$ is higher than $\tilde{Re}_{\theta t}$, the intermittency γ, which influences the turbulent production of the flow, is close to 1, so that a fully boundary layer is computed.

It is presented in the paper, that due to the acceleration the value of the local transition onset momentum-thickness Reynolds number $\tilde{Re}_{\theta t}$ increases, therefore increasing the threshold for transition. This in turn leads to a reduction of the intermittency γ which decreases the production of turbulence within the boundary layer, finally leading to relaminarization. A delay to the onset of acceleration, which has also been observed by measurements, is caused by a slow transport of $\tilde{Re}_{\theta t}$ from the free-stream towards the wall.

Paper 8 [158] discusses a quantitative comparison of the γ-Re_θ model with the LDA measurements. The aim of the paper is to investigate the differences in the prediction of the relaminarization process by steady and unsteady simulations and it also discussed the question, what the "correct" turbulence intensity at the inlet is. The idea arose because a separation bubble at the top wall, which does not influence the streamlines within the boundary layer directly, induces velocity fluctuations due to pulsations of this bubble. These velocity fluctuations are measured by the LDA, but are not accounted for by the turbulence model or a steady simulation. Therefore four different simulations are discussed within the work, two steady and two unsteady, where for each type different inlet turbulence intensities are set as boundary conditions. The derivation of the method used to differ between the set turbulence intensities in this paper is described in more detail in App. E.

6.2. Summary and Conclusions

The results presented in this chapter show experimental and numerical data for three different relaminarization test cases. Relaminarization is found for all three test cases, both experimentally and numerically.

The measurement data (paper 5) gives a detailed view on the process of relaminarization together with a good set of relaminarization test cases which can be used to validate simulation results.

The numerical results presented in the papers 6-8 show that the γ-Re_θ model is able to predict relaminarization which has been validated with the LDA measurement results. The k-k_L-ω RANS simulation (paper 6) cannot predict relaminarization, because the model has difficulties with accurate prediction of the boundary layer when the investigated flow is exposed to pressure gradients.

The presented large eddy simulation (paper 6) shows good agreement with measurements and allows a more detailed insight into the relaminarization and the subsequent retransition process. The numerical results show how the vortices are reduced and stretched within the acceleration. Additionally, a quadrant analysis revealed which quadrant events are influenced by the acceleration, thus how the turbulence production is reduced within the relaminarization zone. It also shows how retransition is triggered.

Additionally, the numerical results presented in this chapter (paper 7) show how the γ-Re_θ RANS model is able to predict the relaminarization process and give an indication how the model could possibly be influenced. It is shown, that the free-stream turbulence level has a high influence on the length of relaminarization. Thus it can be concluded that the setting of the "right" inlet conditions is crucial. (see paper 8).

Therefore computations with different inlet turbulence intensities as well as steady and unsteady approaches have been compared. Surprisingly, the "most reasonable" case regarding the method and boundary conditions, which is an unsteady simulation with the most reasoned turbulence values, fits well with the measurements at the inlet, but not along the plate.

6.3. Paper 5: Flat-Plate Boundary Layers in Accelerated Flow

P. Bader, M. Pschernig, W. Sanz, J. Woisetschläger, F. Heitmeir, W. Meile and G. Brenn "Flat-Plate Boundary Layers in Accelerated Flow," *Proceedings of ASME Turbo Expo 2016: Turbine Technical Conference and Exposition, June 13-17, 2016, Seoul, South Korea*, GT2016-56044, 2016.

6.3.1. Errata for paper 5

During the measurement campaign a mistake happened for the $y = 0$ position identification. Thus in paper 5 the shown values for the skin friction coefficient c'_f (Fig. 5c in paper 5, Fig. 6.3.1), the shape factor H (Fig. 5d in paper 5, Fig. 6.3.1), the velocity profiles $u^*(y^*)$ (Fig. 6 in paper 5, Fig. 6.2) and $u^+(y^+)$ (Fig. 7 in paper 5, Fig. 6.3), respectively, have changed. The corrected diagrams are shown in the following, however the conclusions in paper five do not change due to this mistake.

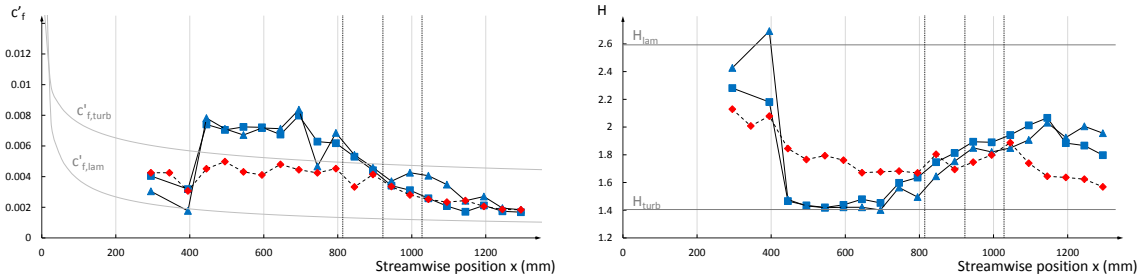

(a) Corrected local skin friction coefficient c'_f (Fig. 5c)

(b) Corrected shape factor H (Fig. 5d)

Figure 6.1: Corrected streamwise distribution of various flow parameters as recorded by one-component LDA (Fig. 5 in paper 5)

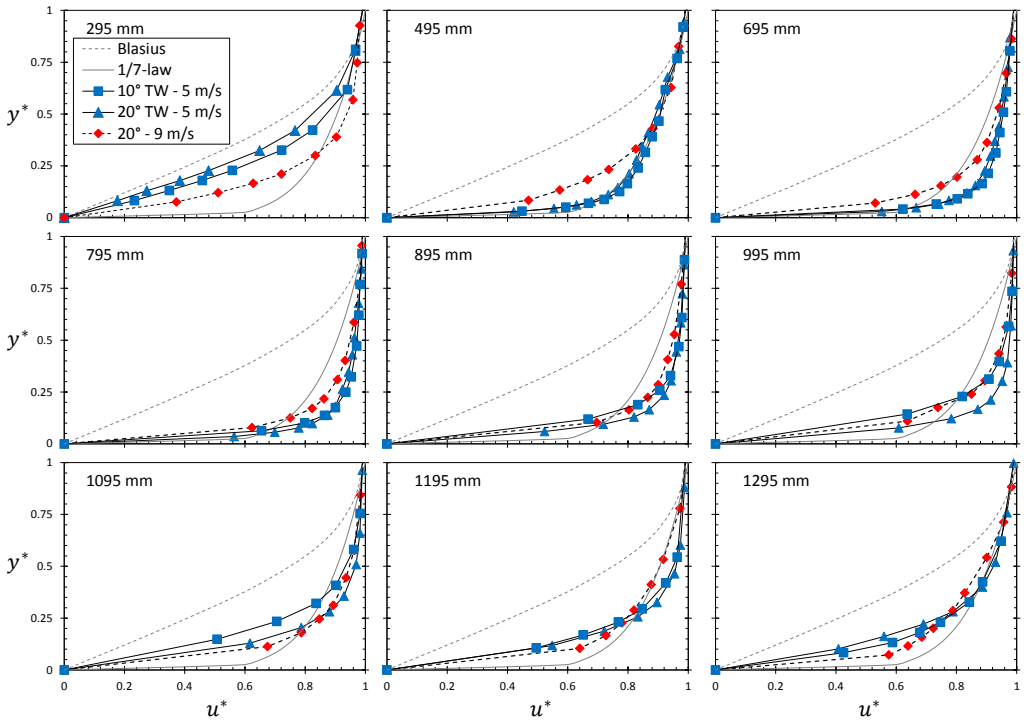

Figure 6.2: Corrected non-dimensional velocity profiles ($u^*(y^*)$ at different streamwise positions, LDA data (Fig. 6 in paper 5)

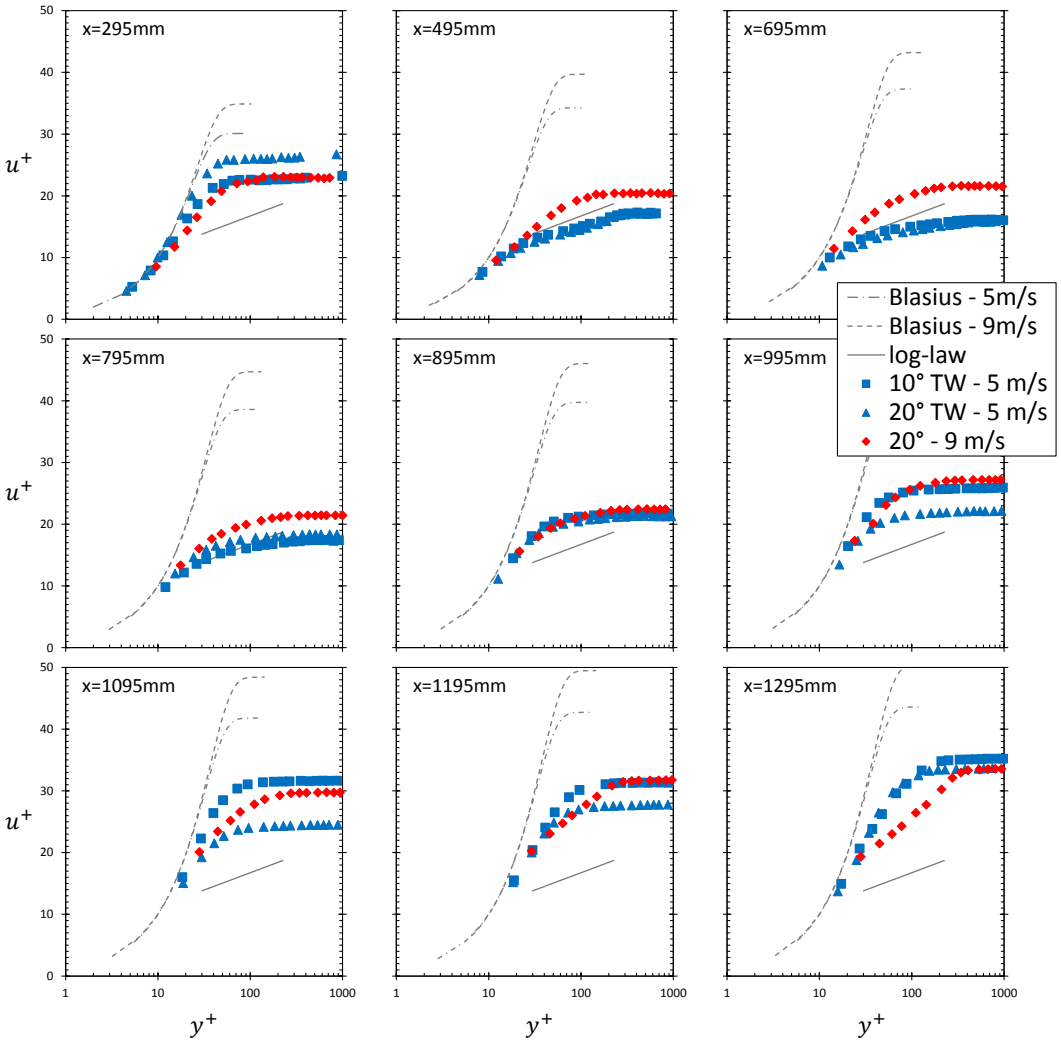

Figure 6.3: Corrected non-dimensional velocity profiles ($u^+(y^+)$ in wall coordinates at different streamwise positions (Fig. 7 in paper 5)

Proceedings of ASME Turbo Expo 2016: Turbine Technical Conference and Exposition
GT2016
June 13–17, 2016, Seoul, South Korea

GT2016-56044

FLAT-PLATE BOUNDARY LAYERS IN ACCELERATED FLOW

Pascal Bader, Manuel Pschernig,
Wolfgang Sanz, Jakob Woisetschläger
Franz Heitmeir
Institute for Thermal Turbomachinery and Machine Dynamics
Graz University of Technology
8010 Graz, Inffeldgasse 25/A, Austria
http://www.ttm.tugraz.at
pascal.bader@tugraz.at

Walter Meile
Günter Brenn
Institute of Fluid Mechanics and Heat Transfer
Graz University of Technology
8010 Graz, Inffeldgasse 25/F, Austria
http://www.isw.tugraz.at

ABSTRACT

Flow in turbomachines is generally highly turbulent. The boundary layers, however, often exhibit laminar-to-turbulent transition. But also relaminarization of the turbulent flow may occur. The state of the boundary layer is important, since it strongly influences transport phenomena like skin friction and heat transfer.

It is therefore vitally important for the designer to understand the process of boundary layer transition and to determine the position of transition onset and the length of the transitional region. In order to get into the details of transition and relaminarization it is helpful to study simplified test cases first. Therefore, in this paper a relaminarization test case for a simple geometry is investigated: The boundary layer flow along a flat plate is exposed to acceleration with three different acceleration parameters, which is known as a crucial parameter for relaminarization.

Measurements were performed for the inlet free-stream velocities of $5\ m/s$ *and* $9\ m/s$*. Several experimental techniques for detecting transition were tested at the institute before their application. In this work, Laser-Doppler anemometry (LDA) measurements were performed, since this optical technique is non-intrusive and does not disturb the flow. Therefore it can also be used in narrow flow passages where probe blockage can be crucial.*

As an outcome of this study, an insight into the process of relaminarization is presented.

Although the key onset values for relaminarization stated in literature are fulfilled with the test setup, full relaminarization over the whole boundary layer has not been achieved. It seems, that using only the skin friction as indicator for relaminarization is not sufficient.

NOMENCLATURE

B	Log-law of the wall constant
c'_f	Local skin friction coefficient
d	Diameter of rods (Turbulence grid)
$\delta(x)$	Boundary layer thickness
δ_1	Displacement thickness
δ_2	Momentum thickness
e_{kin}	Specific kinetic energy
ε	Turbulence dissipation rate
γ	Incidence angle (AP)
H	Shape factor
k	Turbulent kinetic energy
K	(Launder) acceleration parameter
κ	von Kármán constant
ν	Kinematic viscosity

p_{stat}	Static pressure
R	Energy ratio
Re_x	Reynolds number
RS	Reynolds stresses
ρ	Fluid density
T	Temperature
T_u	Turbulence intensity
τ_W	Wall shear stress
u	Plate parallel velocity
u'	Plate parallel velocity fluctuation
u_{RMS}	Root-mean-square of the plate parallel velocity fluctuations
U_{BLE}	Plate parallel velocity at the boundary layer edge
U_∞	Plate parallel free-stream velocity
$U_{\infty,inlet}$	Free-stream velocity at the inlet plane
u^+	Non-dimensional velocity (wall coordinates)
u^*	Non-dimensional velocity
v'	Lateral (plate normal) velocity fluctuation
v_{RMS}	Root-mean-square of the lateral (plate normal) velocity fluctuations
x	Streamwise position
y^+	Non-dimensional wall coordinate
y^*	Non-dimensional coordinate

ABBREVIATIONS

AF	Adjustable flap
AP	Acceleration plate
BLE	Boundary layer edge
BLP	Boundary layer plate
BSA	Burst spectrum analyzer
CFD	Computational fluid dynamics
ISW	Institute of Fluid Mechanics and Heat Transfer
ITTM	Institute for Thermal Turbomachinery and Machine Dynamics
LDA	Laser-Doppler anemometry
LIV	Laser Interferometric vibrometry
PP	Parallel plate
PIV	Particle Image velocimetry
RMS	Root mean square
SP	Stagnation plate
TW	Tripwire
ZPG	Zero pressure gradient

INTRODUCTION

In flows along solid body surfaces, the boundary layer represents the narrow zone between the wall and the free stream where viscous effects are important. Its state of flow (laminar or turbulent) may have strong impact on transport processes like wall friction and heat transfer. These processes influence the efficiency as well as the thermal stress, for example of a turbine blade, and may affect other flow characteristics in the machine as well [1].

Many parameters, like free-stream velocity, acceleration, free-stream turbulence etc., may have an influence on the state of flow of a boundary layer. At the first contact of a flowing fluid with a stationary structure under appropriate flow conditions, the boundary layer develops from laminar via a transitional zone and becomes turbulent. The boundary layer passes through several stages within this transitional zone before becoming fully turbulent. Schlichting and Gersten extensively discussed these different stages [2].

It is vitally important to understand the influences from the influencing parameters on the onset position and length of the transitional zone in order to predict and potentially control the state of the boundary layer. In turbomachinery, the efficiency of blades and stages can be improved considering transition. This allows the overall machine performance to be improved. In 1991, Mayle published a comprehensive review of the importance of transition in gas turbines [3]. He analyzed experiments performed by several research groups in order to find the influence of different flow parameters on the transition process.

In the last years, additional experiments were performed by many research groups. Yip et al. performed in-flight measurements, detected transition with the help of Preston tubes and analyzed the influence of the flight conditions on the boundary layer along an airfoil [4]. Oyewola et al. showed how the flow in the boundary layer can be measured with hot-wire anemometry and Laser-Doppler anemometry (LDA) [5, 6]. Widmann et al. performed near-wall measurements with Particle Image velocimetry (PIV) [7]. Hot-film measurements were performed, e.g., by Mukund et al. [8], Preston-tube and thermographic measurements by Bader and Sanz [9]. Additionally, Bader et al. used Laser Interferometric vibrometry (LIV) to predict transition [10].

So far, only the transition from laminar to turbulent flow was described. Under certain flow conditions (like strong acceleration), however, a reverse transition or relaminarization from turbulent to laminar can occur. Up to now, only few measurements on relaminarization were reported (e.g. [11–15]). Therefore, at the Institute for Thermal Turbomachinery and Machine Dynamics (ITTM) of Graz University of Technology a project was launched in order to understand the process of relaminarization and its phases even further and test common threshold values for relaminarization.

Experiments showed four different phases in relaminarization caused by acceleration [11–14]: In the first phase at the beginning of the acceleration zone, the skin friction increases along with a decrease of the shape factor H (ratio of displacement thickness to momentum thickness).

The second phase already shows the first signs of relami-

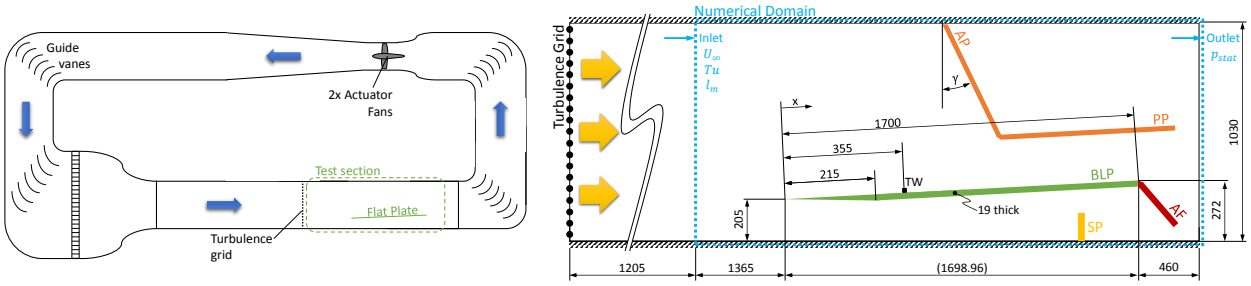

(a) SKETCH OF THE WIND TUNNEL.

(b) DETAILED VIEW OF THE TEST SECTION (BOUNDARY LAYER PLATE (BLP), ACCELERATION PLATE (AP), PARALLEL PLATE (PP), ADJUSTABLE FLAP (AF), STAGNATION PLATE (SP), TRIP WIRE (TW))

FIGURE 1. TEST SETUP AT THE INSTITUTE OF FLUID MECHANICS AND HEAT TRANSFER

narization, characterized by a break down of the law of the wall. Also, the boundary layer becomes thinner. Additionally, the local skin friction coefficient c_f' starts to decrease and the shape factor H starts to rise. The above authors state that this second zone is relatively short, within $x/\delta(x) = 20$ to 30. The turbulent velocity fluctuations are frozen within this zone [11]. These fluctuations promote a fast retransition into a turbulent boundary layer in the third phase when the acceleration falls below a certain threshold. Finally, in the fourth phase the boundary layer is turbulent again.

Since the interest of this work is to investigate relaminarization at high acceleration, a test bench with a strongly convergent cross section is needed, leading to a narrow channel cross section at the outflow. In such a small flow area, probes like Preston tubes and hot wire probes would influence the flow considerably. Therefore, non-intrusive techniques, such as, e.g., Laser-Doppler anemometry, are used for measuring the state of the boundary layer.

In a first step of this project, a test bench was set up to test different measuring techniques for flat plate flow transition [10]. In these tests, Laser-Doppler anemometry was also tested, and it was shown that LDA is capable of detecting transition.

In this paper the results of the LDA measurements are presented. This measuring technique is used in a test bench with a flat plate. The flow along the flat plate is accelerated differently, as described by three different values of the acceleration parameter.

The aim of the work is to investigate the process of relaminarization for different test cases. These test cases are convenient to verify the capability of CFD codes for predicting relaminarization and, thus, the appropriate boundary conditions are also specified in this work.

The following section presents the experimental setup together with all the flow measuring techniques used for the study. Thereafter we present and discuss the measurement results, with a particular focus on the development of the velocity profiles in the boundary layer and the wall friction. The paper ends with a summary and the conclusions.

EXPERIMENTAL SETUP

Test facility

The tests were performed at the closed wind tunnel of the ISW. A sketch of the tunnel is given in Fig. 1a. This Göttingen-type wind tunnel is powered by two fans with a total power input of 75 kW. The air is conveyed to the nozzle and the test section via two corners with guide vanes. The maximum achievable flow-rate equivalent velocity is about 30 m/s. The nozzle exit cross section is 2 m wide and 1 m high. Downstream from the nozzle, a 6 m long channel for developing flow velocity profiles is installed. The test section itself is about 2.6 m long. The top panel of the tunnel is adjustable for setting a zero pressure gradient along the test section.

Since the turbulence intensity Tu of the wind tunnel is far below 1 %, a turbulence generating grid is installed upstream from the test section in order to raise the turbulence intensity to about 3 % to 4 % which is more representative for turbomachinery flows. The turbulence grid consists of equally spaced cylindrical rods. As suggested by Roach, the grid has a solidity below 50%, and its position upstream from the first measuring point meets the $x/d > 10$ criterion, where x represents the streamwise distance and d the diameter of the rods [16].

In the present case the turbulence grid consists of horizontal rods. At the first measurement position the individual wakes have completely smoothed out which was confirmed by hot wire measurements. The turbulence generated by horizontal rods is not isotropic, but this is not essential since a ”2D”-flow phenomenon is investigated.

The first measurement section is situated downstream from the turbulence grid, but upstream from the flat plate (inlet of the computational domain in Fig 1b). Starting from this plane, the turbulence level and the free-stream velocity were obtained at six different measurement positions in order to get the turbulence

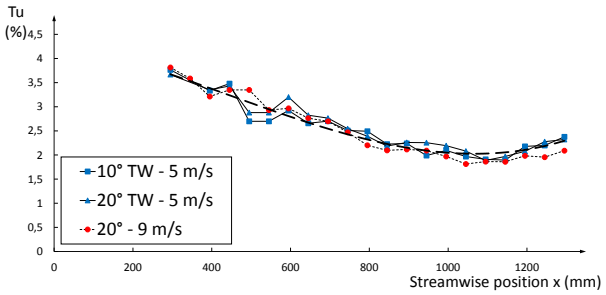

FIGURE 2. DEVELOPMENT OF THE FREE-STREAM TURBULENCE INTENSITY ALONG THE PLATE.

intensity Tu as well as the dissipation rate ε from the decrease of turbulent kinetic energy k which are necessary input parameters for the CFD simulations.

In Table 1 the boundary conditions for the CFD simulations are given. Additionally, Fig. 2 shows the streamwise distribution of the turbulence degree along the flat plate. Its variation is similar in all three cases so that a common trendline seems representative as given with the dashed line in Fig. 2 gives.

Figure 1b shows a sketch of the test section. The main components of the setup are the flat plate where the boundary layer develops (BLP), the acceleration plate (AP) and the parallel plate (PP). The BLP is inclined by two degrees in order to ensure that the flow is attached at the upper surface. The distance to the side walls is larger than their boundary layer thickness, so that the sidewall boundary layers do not affect the boundary layer of the plate.

Two different inclination angles of the AP against the vertical direction are investigated in this work: 10° and 20°. The PP is kept parallel to the BLP in both cases. Due to the relatively sharp corners between the AP and the top wall, as well as between the AP and the PP, large vortices develop in this regions. To minimize the top vortex, a small gap was placed between the AP and the top wall. The effect of the gap was analyzed with CFD. The 2D CFD simulations have been performed with ANSYS® CFX® v15.0 with the Menter SST turbulence model. The mesh consists

TABLE 1. MEASURED BOUNDARY CONDITIONS FOR CFD SIMULATIONS.

	$5\ m/s$	$10\ m/s$
$U_{\infty,inlet}$	$4.824\ m/s$	$8.541\ m/s$
T_{inlet}	$\approx 318\ K$	$\approx 330\ K$
Tu_{inlet}	$5.449\ \%$	$5.806\ \%$
ε_{inlet}	$0.2153\ m^2/s^3$	$1.948\ m^2/s^3$
$p_{stat,outlet}$	$97700\ Pa$	$97700\ Pa$

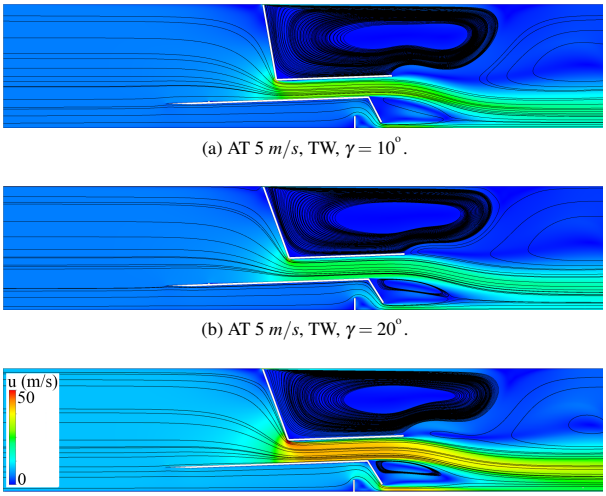

(a) AT 5 m/s, TW, $\gamma = 10^{\circ}$.

(b) AT 5 m/s, TW, $\gamma = 20^{\circ}$.

(c) AT 9 m/s, $\gamma = 20^{\circ}$.

FIGURE 3. VELOCITY DISTRIBUTION AT MIDPLANE SHOWING CFD STREAMLINES

of approximately 300,000 nodes, and y^+ was kept between 0.1 and 1 at the flat plate surface as recommended for the transition model [17]. The boundary conditions for the simulation have been obtained by measurements and are given in Tab. 1.

Figure 3 shows the contour plots of the midplane velocity together with the streamlines. It was shown by this CFD study that a relatively small separation bubble forms in this area while only little mass flow is lost. The detected bubble near the corner of AP and PP is small enough so that no direct influence on the boundary layer at the BLP can be expected. However, it influences the free-stream velocity and thus the acceleration parameter. This will be discussed later.

The second vortex downstream from the lower AP corner was also numerically investigated to ensure that this separation bubble does not influence the boundary layer at the BLP.

In order to reach an inlet flow parallel to the surface of the BLP, it is necessary to add additional blockage below the plate. Therefore, an adjustable flap (AF) was attached to the BLP and a stagnation plate (SP) installed below the BLP.

In this work, additionally to two zero pressure gradient cases, three different cases are discussed:

- $U_{\infty,inlet} \approx 5\ m/s$, $\gamma = 10^{\circ}$, with tripwire
- $U_{\infty,inlet} \approx 5\ m/s$, $\gamma = 20^{\circ}$, with tripwire
- $U_{\infty,inlet} \approx 9\ m/s$, $\gamma = 20^{\circ}$, without tripwire

where $U_{\infty,inlet}$ represents the free-stream velocity measured at the inlet plane (first measurement section), and γ the angle between the AP and the vertical direction. The tripwire for the $5\ m/s$ cases is mounted at $x = 355\ mm$ across the whole width of the BLP in

order to ensure a turbulent boundary layer in the low speed cases. The tripwire has a rectangular cross-section with $b = 15\ mm$ and $h = 5.8\ mm$. In relation to the local boundary layer thickness the height can be expressed as $h/\delta(x = 355\ mm)_{ZPG} = 1.14$.

For the zero-pressure gradient cases, the acceleration and parallel plates were entirely removed from the test setup.

Laser Doppler Anemometry

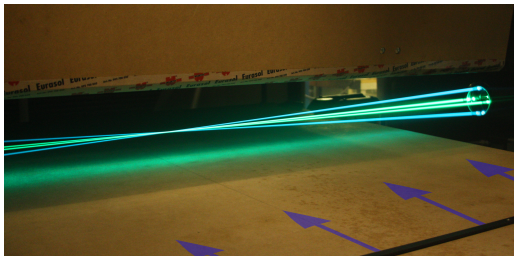

FIGURE 4. THE LDA SETUP TOGETHER WITH THE BLP, AP AND TRIPWIRE (FLOW FROM BOTTOM RIGHT CORNER)

In this study LDA measurements were performed in order to get the velocity and its fluctuations within the boundary layer. The two-dimensional LDA system by *Dantec Dynamics A/S* uses a 6 Watt Argon-Ion laser as the light source. The system consists of two Burst Spectrum Analyzer (BSA) processors, 57N35 model S and 57N20, and a 60x41 FiberFlow transmitter (wavelengths $\lambda_1 = 514.5\ nm$, $\lambda_2 = 488\ nm$).

A 60 *mm* probe head (60x67 2D probe) with a beam distance of 75.24 *mm*, a focal distance of 1000 *mm* and a beam diameter of 2.2 *mm* (in front of the lens) was used as the laser light transmitter.

In near-wall areas with high turbulence levels 8,000 samples were recorded while far from walls 4,000 samples were taken. The measurement uncertainties of the LDA system mainly depend on the number of samples and the turbulence level and can be calculated with the Student's t distribution for the mean value yielding

$$Mean_{err} = \pm t_{1-\alpha;n-1}\frac{\sigma}{\sqrt{n}} \tag{1}$$

where $t_{1-\alpha;n-1}$ represents the quantile of the Student's distribution, n the number of samples and $1-\alpha$ the confidence interval. With a confidence intervall of 95 % this results in 0.7 % error of the mean value close to the wall and 1 % for points in the outer regions (errors relative to the reading).

The error of the root mean square (RMS) value can be calculated with the χ^2 distribution as

$$RMS_{err} = \sqrt{n-1}\frac{1}{\sqrt{\chi^2_{\alpha/2;n-1} - \chi^2_{1-\alpha/2;n-1}}} \tag{2}$$

This results in a mean RMS_{err} of 4.3 % (near-wall) and 3.1 % (outer region), respectively.

For seeding the air flow, a fog generator from *EHLE-HD* was used with the *Slow Fog* glycol-water-based seeding fluid. The fluid density is $\rho \approx 1260\ {}^{kg}/_{m^3}$ and the mean particle size was determined with approximately 4.7 μm with 50 % of the particles smaller than 4 μm. Therefore, the seeding particles act as low-pass filters up to about $f(-3dB) = 1.902\ kHz$ [18].

RESULTS AND DISCUSSION

In the following, the results of the Laser-Doppler anemometer measurements are discussed. In the first part, the streamwise distributions of several flow properties are analyzed, followed by a discussion of the non-dimensional velocity profiles $u^*(y^*)$ and the velocity profiles in wall coordinates $u^+(y^+)$. In the last part, the development of turbulence within the boundary layer is discussed.

Five different cases are presented: Two zero pressure gradient (ZPG) cases with 5 m/s and 10 m/s free-stream velocity, and three accelerated cases as described above. In all the following figures, the low speed cases (5 m/s) are given with blue markers and solid lines, while the high speed cases (9 and 10 m/s) with red ones and dashed lines.

In Figure 5, the streamwise distributions of four different flow parameters are given: The velocity at the edge of the boundary layer $u(y = \delta(x)_{0.99})$, the acceleration parameter K, the skin friction coefficient c'_f and the shape factor H. The dotted lines mark the beginning and the end of the converging flow area, which differs depending on the inclination of the AP.

Figure 5a shows the streamwise distribution of the velocity at the edge of the boundary layer. The edge is defined as the distance normal to the wall where

$$u(y = \delta(x)_{0.99}) = 0.99\ U_\infty \tag{3}$$

with $\delta(x)$ as the local boundary layer thickness and U_∞ as the local free-stream velocity. In the following $u(y = \delta(x)_{0.99})$ is denoted as U_{BLE} and represents the local free-stream velocity at the boundary layer edge. It can be seen that the acceleration starts upstream from the decrease of the flow cross sectional area due to the strong contraction.

Acceleration also continues downstream from the AP, due to flow separation there. This effect is especially pronounced

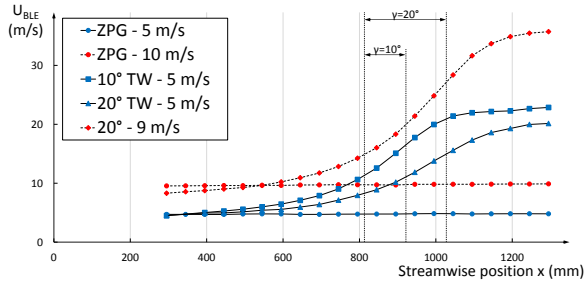

(a) VELOCITY AT THE BOUNDARY LAYER EDGE $u(\delta(x)_{0.99})$.

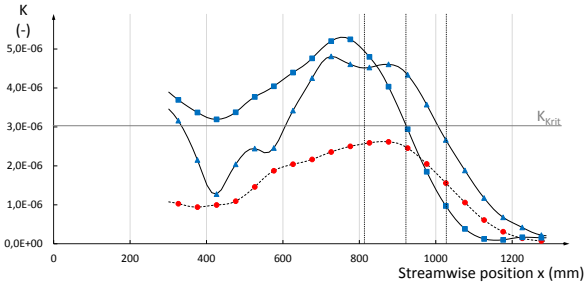

(b) ACCELERATION PARAMETER K.

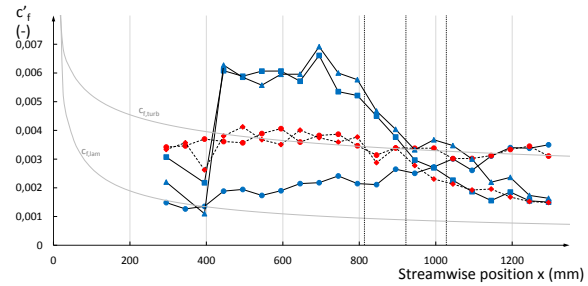

(c) LOCAL SKIN FRICTION COEFFICIENT c'_f.

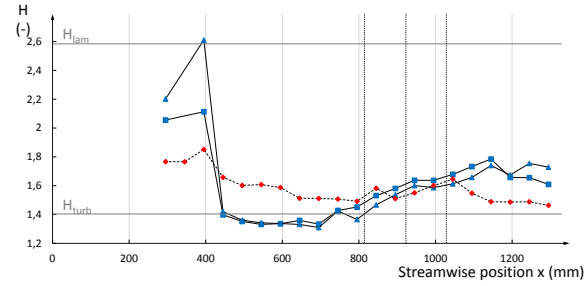

(d) SHAPE FACTOR H.

FIGURE 5. STREAMWISE DISTRIBUTION OF VARIOUS FLOW PARAMETERS AS RECORDED BY ONE-COMPONENT LDA

for the accelerated $\gamma = 20^{\circ}$ cases, whereas, for the $\gamma = 10^{\circ}$ case, acceleration ends about 200 *mm* downstream. The velocities at the end of the plate differ between the two 5 m/s cases.

In order to see if the acceleration is strong enough to relaminarize the boundary layer, the streamwise velocity gradient is not meaningful. Instead, the acceleration parameter K, also known as the Launder pressure-gradient parameter K, is used [19]. It is defined as

$$K = \frac{\nu}{U_\infty^2} \frac{du}{dx} \tag{4}$$

where ν is the kinematic viscosity, U_∞ the free-stream velocity and du/dx the streamwise velocity gradient. Since the free-stream velocity is not constant normal to the wall outside the boundary layer, in this work U_{BLE} is used for the calculation of K instead of U_∞.

In the literature, different critical values for the acceleration parameter for boundary layer relaminarization are given. Most publications specify critical acceleration parameters in the range $3 \cdot 10^{-6} \leq K_{crit} \leq 3.5 \cdot 10^{-6}$ [3, 11–14, 20–22]. Under these conditions, the boundary layer should relaminarize within the non-dimensional streamwise distance $\Delta x/\delta(x) = 20$ to 30 [8].

Figure 5b shows the acceleration parameter for the three accelerated flow cases. The graphs show that the 9 m/s case has an acceleration parameter slightly below the stated range of critical values K_{crit}. Both 5 m/s cases are super-critical: For the 20° case, the threshold is passed at approximately $x_{20^{\circ}} = 600$ *mm*, and for the 10° case already at about $x_{10^{\circ}} = 400$ *mm*. At these positions, the boundary layer thicknesses are $\delta(600)_{20^{\circ}} = 14.28$ *mm* and $\delta(400)_{10^{\circ}} = 12.54$ *mm*, respectively. This leads to theoretical streamwise relaminarization lengths of approximately $\Delta x_{20^{\circ}} = 280$ to 420 *mm* and $\Delta x_{10^{\circ}} = 250$ to 375 *mm*. Comparing these values with the length of the zone where K is above the critical value, the boundary layer should relaminarize in both cases. It is interesting that the acceleration parameter falls below the critical value where the AP ends, although the acceleration still continues.

In order to validate the full relaminarization of the boundary layer, the local skin friction coefficient c'_f and the shape factor H are examined together in the following. The local skin friction coefficient is calculated according to

$$c'_f = \frac{\tau_W}{\rho U_\infty{}^2/2} \tag{5}$$

where τ_W represents the wall shear stress and ρ the fluid density. The wall shear stress in Fig. 5c was derived from the measured velocity profiles. It is calculated with the velocity gradient between $y^+ = 0$ and $y^+ = 5$, where the dimensionless wall distance y^+ is found in an iterative way (see Eq. (14)). In Fig. 5c, the

values of c'_f for a fully turbulent and a laminar boundary layer are given together with the measured values. These values can be approximated with the Blasius solution as

$$c'_{f,lam} = 0.664 \frac{1}{\sqrt{Re_x}} \tag{6}$$

for the laminar boundary layer, and with [23]

$$c'_{f,turb} = 0.0592 \frac{1}{\sqrt[5]{Re_x}} \tag{7}$$

for the turbulent boundary layer, where Re_x represents the flow Reynolds number ($Re_x = U_\infty x/\nu$). The shape factor of Fig. 5d is calculated as the ratio of the displacement thickness δ_1 to the momentum thickness δ_2, i.e.

$$H = \frac{\delta_1}{\delta_2} \quad \text{with} \tag{8}$$

$$\delta_1 = \int_0^{\delta(x)} \left(1 - \frac{u(y)}{U_{BLE}}\right) dy \tag{9}$$

$$\delta_2 = \int_0^{\delta(x)} \frac{u(y)}{U_{BLE}} \left(1 - \frac{u(y)}{U_{BLE}}\right) dy \tag{10}$$

A shape factor of $H \approx 1.4$ represents a turbulent boundary layer and $H = 2.59$ a laminar velocity profile (Blasius solution). It should be mentioned that these H-values as well as the specified $c'_{f,lam}$ and $c'_{f,turb}$ apply to zero pressure gradient cases. Nevertheless, they represent suitable reference values for comparison.

Comparing the c'_f distribution between the accelerated cases, it can be seen that the c'_f values of the two $K > K_{crit}$ cases overshoot the turbulent level of c'_f. The $K < K_{crit}$ (9 m/s) case is more or less on the level of turbulent flow, thus as the ZPG-case.

The H distribution shows that this overshoot comes along with a drop of the H value below the stated $H_{turb} = 1.4$ level, which indicates a fuller profile.

In all accelerated flow cases, the local skin friction coefficient starts to decrease at a certain position towards the laminar c'_f level. This position does not coincide with the onset of the different K value plateaus. This decrease rather occurs past the location where the acceleration parameter already falls below the critical threshold. This late relaminarization onset may be caused by the inertia of the boundary layer.

It should be noted, however, that the skin friction assumes values far above the values of a turbulent boundary layer in zero pressure gradient flow, so that the location of the decrease in skin friction should be considered, and not its fall below the turbulent value. This observation is also strengthened by the shape factor H, which starts to rise towards the laminar level where the skin friction coefficient starts to decrease.

On the other hand, the high speed case, where K is below K_{crit}, does not show this overshoot. Its skin friction coefficient rather decreases towards the laminar value also, as in the other cases.

Although all the critical thresholds postulated by other research groups (e.g. [8]) are met by the present test setup, the boundary layer did not relaminarize totally. In order to evaluate the development within the boundary layer, the non-dimensional velocity profiles $u^*(y^*)$ will be discussed in Fig. 6. The non-dimensional values are calculated with

$$y^* = \frac{y}{\delta(x)} \tag{11}$$

$$u^* = \frac{u}{U_{BLE}} \tag{12}$$

The velocity profiles in Fig. 6 are given for the nine positions $x =$ 295 *mm*, 495 *mm*, 695 *mm*, 795 *mm*, 895 *mm*, 995 *mm*, 1095 *mm*, 1195 *mm* and 1295 *mm*. In all the graphs, the 1/7-law is added in order to have a representative of a turbulent boundary layer profile. The 1/7-law is defined as

$$u^* = (y^*)^{1/7} \tag{13}$$

The first position at $x = 295$ *mm* is located upstream from the tripwire used for the low-speed test cases (5 m/s). At this position, the boundary layer is laminar.

At the downstream positions, the profiles of the low-speed test case are turbulent due to the tripwire. Since the high-speed test case (9 m/s) transitions due to bypass transition, the profile is not yet fully turbulent, which can also be observed in the shape factor in Fig. 5d. Also, the boundary layer is already exposed to mild acceleration at this position, which delays the transition for the high-speed test case.

Even farther downstream, at $x = 695$ *mm*, where the acceleration is already high, the boundary layer profiles are fuller than the 1/7-law. It seems that the high favorable pressure gradient accelerates the boundary layer especially in the inner zones, so close to the wall. This leads to very high shear close to the wall, which can be observed in the overshoot of the turbulent skin friction coefficient discussed above. Due to the higher and earlier onset of the acceleration, the low-speed cases show this trend even more.

Starting at $x = 795$ *mm*, the high-speed test case follows the trend of the low-speed test case.

Position $x = 895$ *mm* shows that the three velocity profiles of the different cases are nearly identical. Also, a decrease of the velocity gradient close to the wall is seen, and the profile becomes flatter. This may be the reason of an equilibration within the boundary layer. These are the first effects of relaminarization.

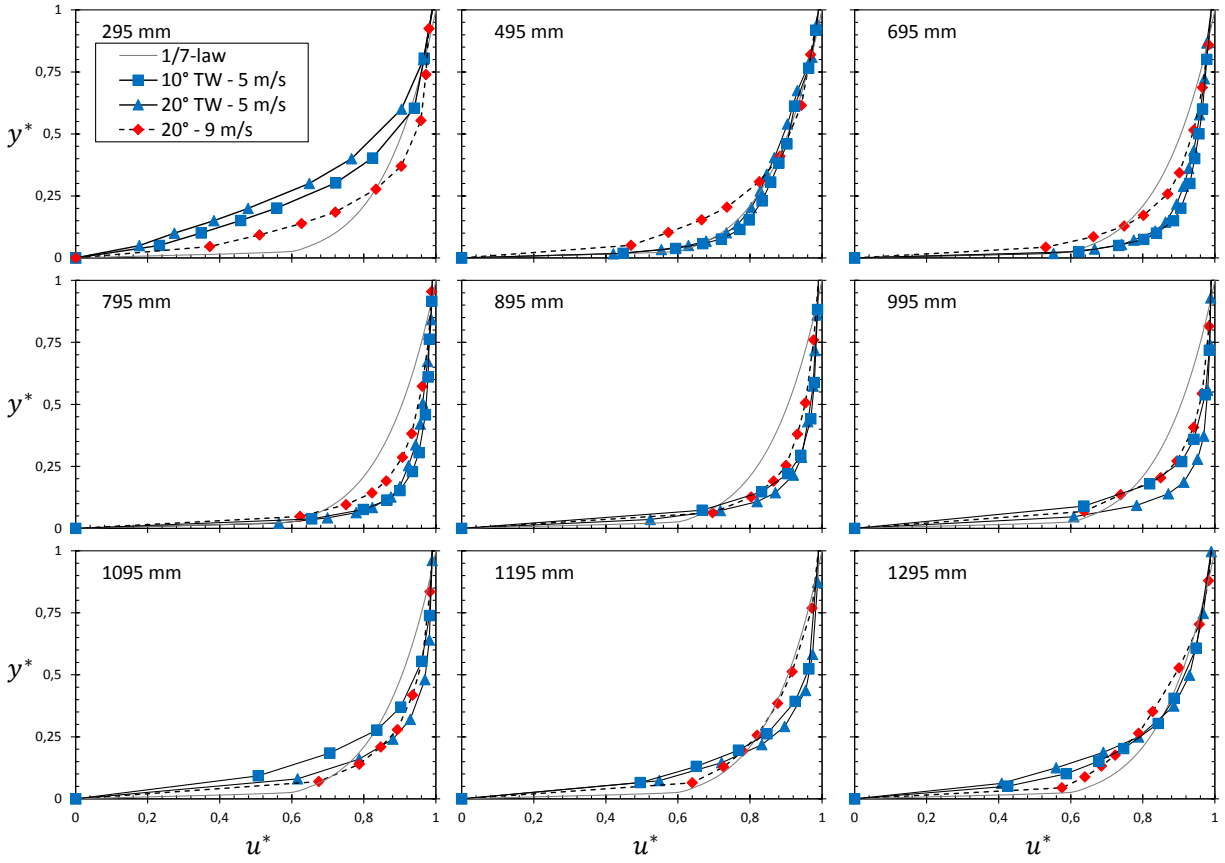

FIGURE 6. NON-DIMENSIONAL VELOCITY PROFILES $u^*(y^*)$ AT DIFFERENT STREAMWISE POSITIONS, LDA DATA.

For the $\gamma = 10^{\circ}$ case, the acceleration parameter drops below the critical threshold, so that this effect is more pronounced.

Downstream, at $x = 995$ *mm*, the velocity gradient close to the wall ($y^* < 0.15$) further decreases, while the outer part ($y^* > 0.60$))remains unchanged. This indicates that relaminarization starts close to the wall. It has to be mentioned that, at this position, the acceleration parameter K of all cases is already below the critical value K_{crit} (compare Fig. 5b).

At $x = 1095$ *mm*, the laminar-like profile covers already a quarter of the boundary layer ($y^* < 0.25$). It can also be observed that the velocity gradient up to this position decreases further.

The profile of the high-speed test case, which did not experience the high acceleration ($K < K_{crit}$), already indicates a retransition towards the 1/7-law at position $x = 1195$ *mm*.

At $x = 1295$ *mm*, the velocity profiles of all cases have returned to the 1/7-law at the beginning of acceleration. The low-speed test cases indicate a laminar boundary layer up to approximately ($y^* = 0.45$).

Summing up, there are two main processes: First, due to the high acceleration, the boundary layer overshoots the 1/7-law, which means that the profile becomes fuller than a zero pressure gradient turbulent profile. After this, the boundary layer starts to relaminarize, beginning close to the wall.

In order to see the different behaviors of the boundary layer better, the profiles in wall coordinates $u^+(y^+)$ are discussed in the following, where y^+ and u^+ are defined as

$$y^+ = \frac{y \cdot u_\tau}{\nu} \tag{14}$$

$$u^+ = \frac{u}{u_\tau} \tag{15}$$

$$\text{with } u_\tau = \sqrt{\frac{\tau_w}{\rho}} \tag{16}$$

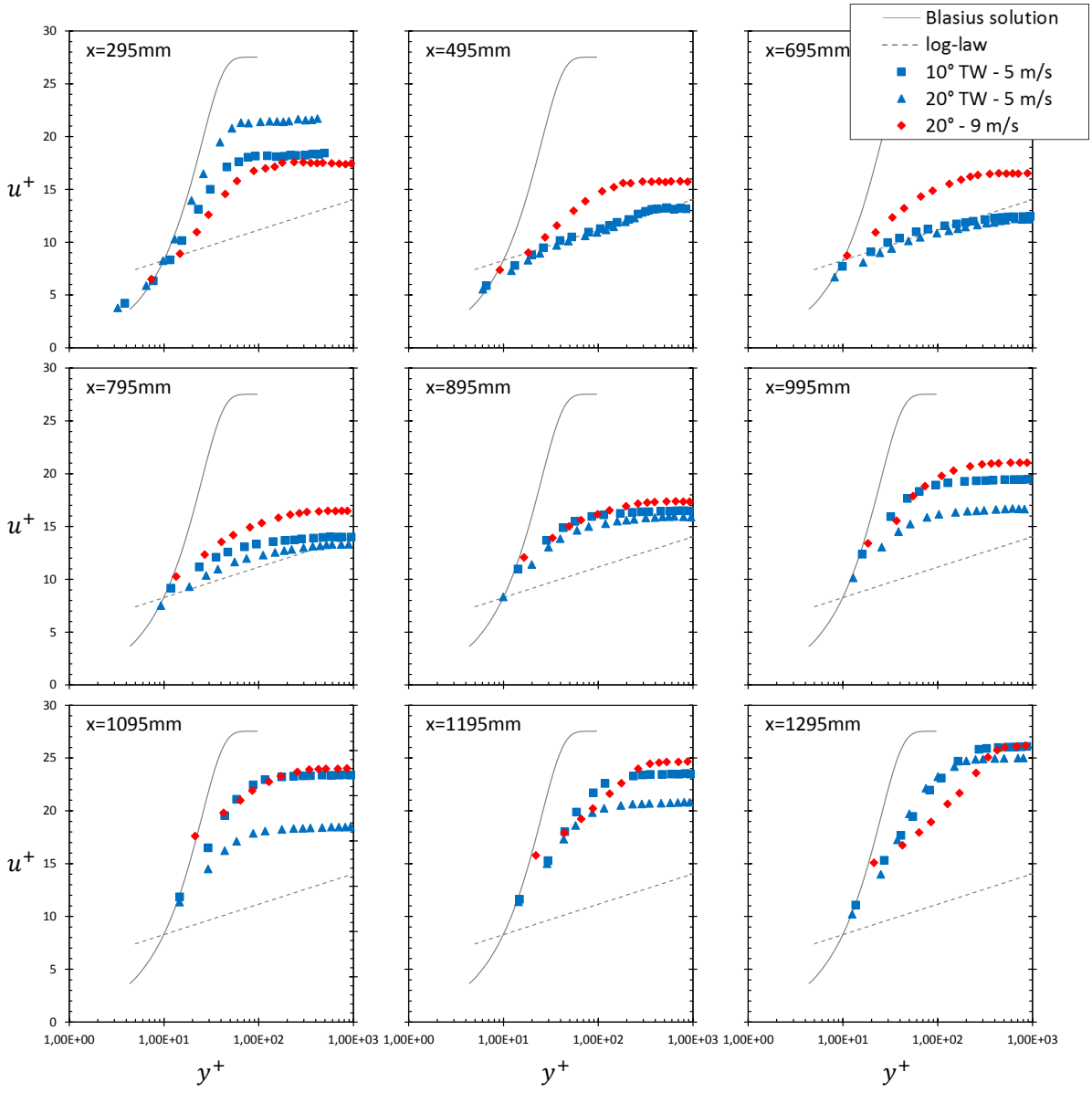

FIGURE 7. NON-DIMENSIONAL VELOCITY PROFILES $u^+(y^+)$ IN WALL COORINATES AT DIFFERENT STREAMWISE POSITIONS.

where u_τ represents the friction velocity.

In Fig. 7, the Blasius solution and the log-law $u^+ = (1/\kappa)\, log(y^+) + B$, with $\kappa = 0.4$ and $B = 5.5$, are added in order to have a reference for the profiles. Again the same nine positions discussed above are displayed.

At $x = 295$ *mm*, the profiles already differ from the Blasius solution, so that they are considered to be transitional.

Farther downstream, at $x = 495$ *mm* (downstream of the trip-wire in the 5 m/s cases), the profiles are fully turbulent for the low-speed cases, whereas they are still transitional for the high speed case. This was also observed in the velocity profiles of Fig. 6. As mentioned above, the acceleration parameter starts to

rise.

The two low-speed cases show similar trends at $x = 695\ mm$: The mid part of the profiles starts to rise above the log-law, and the outer part of the profiles falls below the log-law. This behavior of the outer part of the boundary layer is characteristic for accelerated flows (see e.g. [14, 20, 21]). Also, the high-speed test case deviates from the turbulent profile in the mid part of the boundary layer. This behavior of all cases already indicates the start of relaminarization.

Between $x = 795\ mm$ and $x = 995\ mm$, where all the cases have their high-K-value plateaus, this trend continues: All profiles tend towards the laminar Blasius solution. The inner part of the boundary layer ($y^+ < 11$) already fits well to the Blasius solution.

Although the acceleration parameter is below the critical value at the last three positions $x = 1095\ mm$, $x = 1195\ mm$ and $x = 1295\ mm$, the relaminarization continues. The tendency of the profiles agrees with the the observations in Fig. 6, where the inner part shows a more laminar profile, whereas the outer part is bulgy. Only the high-speed case starts to redevelop towards a turbulent boundary layer profile at the last position.

As already discussed above, relaminarization does not cover the whole boundary layer although all conditions for relaminarization are fulfilled. Relaminarization was detected close to the wall.

Up to now the development of the velocity profiles in the boundary layer has been discussed. But relaminarization should also go along with a reduction of the velocity fluctuations within the boundary layer towards a laminar state. Therefore in the following several parameters of the boundary layer are presented in Fig. 8. The values are given at three different relative wall distances inside the boundary layer: $y^* = 0.25$, 0.50 and 0.75. In the following only the overcritical low-speed test cases are presented.

In diagram Fig. 8a the ratio R between the turbulent kinetic energy k and the specific kinetic energy e_{kin} according to

$$R = \frac{k}{e_{kin}} \quad \text{with} \tag{17}$$

$$k = \frac{3}{4} \cdot (u_{RMS}^2 + v_{RMS}^2) \tag{18}$$

$$e_{kin} = \frac{1}{2} \cdot |\vec{u}|^2 \tag{19}$$

is presented. In the graph R is normalized with the value at $x = 495\ mm$ upstream of the relaminarization where the boundary layer is turbulent (compare Fig. 6). At all y^* positions at the beginning the ratio decreases rapidly for the overcritical cases ($5\ m/s$). All cases reach a minimum at a specific streamwise position. The decrease of R is caused by a decrease of the the turbulent kinetic energy k at a simultaneous rise of the specific kinetic energy e_{kin} of the boundary layer flow. Therefore there is not enough exchange of momentum with the outer layers of the boundary layer and the free stream to maintain the turbulent flow profile. The flow close to the wall starts to relaminarize as indicated by the velocity profiles in Fig. 6.

Downstream of the minimum the ratio R starts to increase sharply. In the $5\ m/s - 10^{\circ}$ case this increase takes place more upstream compared to the other case. This comes along with an earlier decrease in the acceleration parameter K (see Fig. 5b). In this case K is close to zero at about 1100 mm where the start of the sharp rise of R occurs. The same observation can be made for the $5\ m/s - 20^{\circ}$ case with the R increasing starting at about 1250 mm where the K parameter is approximately zero.

Generally, this increase is the result of a strong increase of the turbulent fluctuations given in Fig. 8b which shows the normalized lateral velocity fluctuations $v_{RMS}/v_{RMS,495}$, where $v_{RMS,495}$ represents the root-mean square value of the lateral fluctuations at $x = 495\ mm$.

It is observable that the lateral fluctuations decrease at the front section for the two presented cases.

Both cases have a minimum at similar positions of the minimum of the energy ratio R. Again downstream of this minimum the fluctuations increase again sharply. An explanation for this rapid increase is the assumption of "frozen" turbulent fluctuations within the boundary layer in zones of high acceleration as been presented e.g. by Narasimha [11]. They may still remain in the flow but their contribution on the flow dynamics is small. When the acceleration decreases, these fluctuations are not suppressed anymore and they burst rapidly promoting a fast re-transition.

Even though the lateral fluctuations v' do not decrease dramatically, the effect of these fluctuations decreases due to the high acceleration since the magnitude of the fluctuations decreases compared to the increasing streamwise velocity u. This can be seen in Fig. 8c which shows the turbulence intensity T_u according to

$$T_u = \frac{\sqrt{\overline{u'^2}}}{u} = \frac{u_{RMS}}{u} \tag{20}$$

The value is again normalized to the value $T_{u,495}$ at $x = 495\ mm$.

The graph shows, that for both cases the turbulence intensity T_u decreases so that the contribution of these fluctuations to the main flow dynamics reduces. According to Narasimha this comes along with a tendency of the Reynolds shear stresses to freeze [11]. In order to see this "freezing" of the Reynolds shear stress, Fig. 8d shows the normalized shear stresses $\overline{u'v'}$ relative to the wall shear velocity u_τ

$$RS = \frac{-\overline{u'v'}}{u_\tau^2} \tag{21}$$

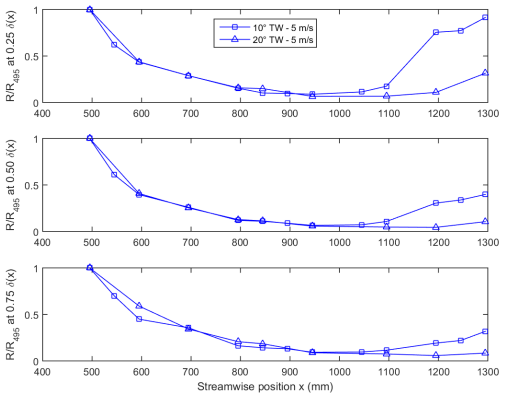

(a) RATIO OF TURBULENT KINETIC ENERGY VS. KINETIC ENERGY R/R_{495}.

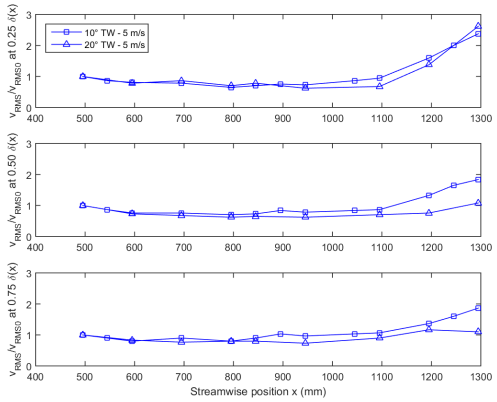

(b) NORMALIZED LATERAL VELOCITY FLUCTUATION $v_{RMS}/v_{RMS,495}$.

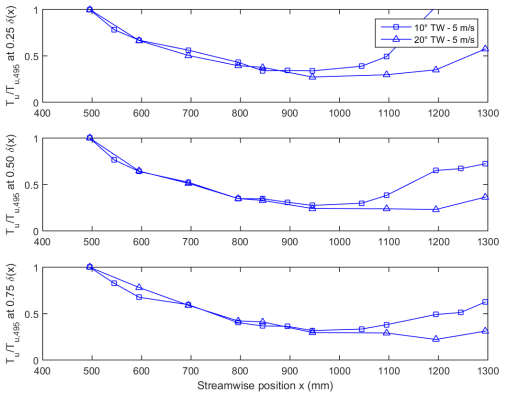

(c) NORMALIZED TURBULENCE INTENSITY $T_u/T_{u,495}$.

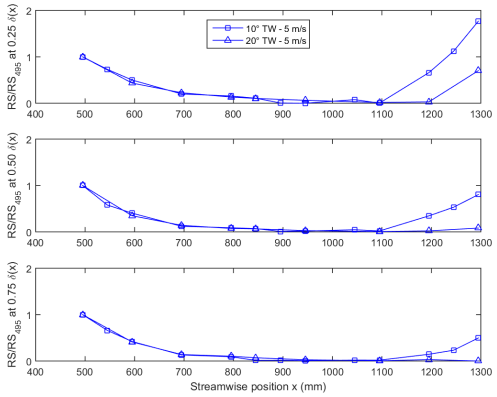

(d) NORMALIZED TUBULENT REYNOLDS SHEAR STRESSES RS/RS_{495}.

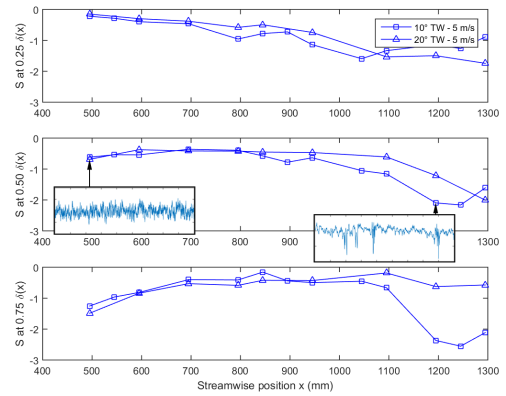

(e) SKEWNESS S.

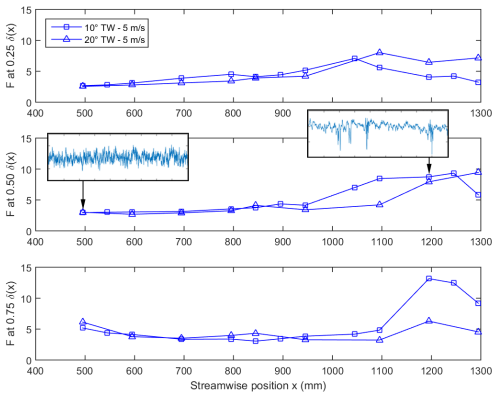

(f) FLATNESS (KURTOSIS) F.

FIGURE 8. STREAMWISE DISTRIBUTIONS AT DIFFERENT BOUNDARY LAYER POSITIONS (25%, 50% AND 75% RELATIVE HEIGHT) OBTAINED BY TWO COMPONENT LDA MEASUREMENTS.

with u_τ according to Eq. (16). Again, in the graph all values are normalized with the values at 495 *mm*.

It is observable that the values decrease for both cases and in nearly all positions. Comparing the two low speed cases, their trend is quite the same. The Reynolds stresses approach nearly zero, which results in more dominant viscous (laminar) stresses compared to the turbulent stresses. This leads to the relaminarization of the flow profiles as discussed above.

Downstream the Reynolds stresses again start to increase when the influence of the acceleration vanishes.

Finally the skewness parameter S and the flatness parameter F (or kurtosis) are presented in Figs. 8e and f. These parameters are known as indicators of the density probability function and are usually used to describe the time signal.

Figures 8e and f show that the skewness S and the flatness F have a minimum and a maximum, respectively, at the same positions. A minimum in skewness indicates a shift of the fluctuations to higher velocity, whereas a maximum in flatness indicates a lower amplitude of the fluctuations. In both figures also exemplary time signals of the velocity fluctuations are given to see the differences between these statistical properties. While the first velocity signal shows a turbulent profile, the second profile corresponding to low skewness and high flatness is characterized by longer periods of low fluctuations and short periods of high fluctuations. This is typical for a more laminar flow with few turbulent spots. This agrees again well with the statements above, that relaminarization occurs.

SUMMARY AND CONCLUSIONS

The boundary layer represents a narrow area of a flow field next to a wall, but has a strong influence on the overall performance of, e.g., a turbine blade. Therefore it is important to influence the transition and relaminarization in an optimal way.

The measurements presented in this paper were performed along a flat plate with strongly accelerated flow, with the objective to detect and investigate relaminarization. The acceleration parameter as a well-known indicator for relaminarization was varied. It is found that, even with acceleration parameters above the critical threshold, relaminarization over the whole boundary layer thickness does not take place.

Although a fully laminar profile could not be found in the acceleration zone, the campaign shows that the inner part of the boundary layer close to the wall relaminarizes. This leads to the conclusion, that the development of the skin friction along the plate alone is not sufficient in order to verify if relaminarization occurs.

Streamwise distributions of the lateral velocity fluctuation, the Reynolds shear stress or the statistical properties flatness and skewness show all similar trends: As a response to the high acceleration, all values tend towards a laminar state. Within this zone the contribution of the fluctuations within the boundary layer is reduced due to the high acceleration and the Reynolds shear stresses tend to "freeze" [22]. When the acceleration of the boundary layer is low, these suppressed fluctuations burst sharply and will eventually promote a fast retransition.

From these observations, relaminarization due to high acceleration is not so much the result of dissipation of turbulence, but more the reduction of the influence of these turbulent fluctuations. The pressure forces are dominating the slowly responding Reynolds shear stresses and a new laminar "sub-boundary-layer" is developed [11, 24].

Although a fully laminar boundary layer could not be achieved, important conclusions can be drawn due to the change of skin friction, which represents the economically important characteristic of the boundary layer since the skin friction influences the resulting total pressure loss.

It was found that, in strongly accelerating flows ($K > K_{crit}$), the skin friction coefficient assumes values significantly above the turbulent level for zero pressure gradient before relaminarization starts. Then, however, it decreases towards the laminar values. The high-speed case, which lies below the critical acceleration parameter, showed a lower skin friction in relaminarization, without overshoot above the turbulent c'_f value. This means that the overall friction is lower than the supercritical cases. When designing an optimized profile, this fact should be kept in mind: A high acceleration factor K may lead to relaminarization, and thus to a drop in skin friction. A too strong acceleration, on the other hand, can cause higher skin friction upstream.

From the present work following conclusions can be drawn:

1. High acceleration causes relaminarization, but the values for the key onset parameters given in the literature are not sufficient to achieve a fully relaminarized boundary layer
2. The change of the boundary layer state starts downstream of the peak of the acceleration parameter K
3. Due to the strong acceleration higher skin friction results upstream of the relaminarization area. This reduces the advantage of the lower skin friction caused by the relaminarization
4. Relaminarization also occurred in a subcritical case although the acceleration parameter K was below the critical value
5. Only validating the development of c'_f along the plate is not sufficient to analyze, if the boundary layer has relaminarized

ACKNOWLEDGMENT

The authors gratefully acknowledge financial support from the Austrian Federal Ministry for Transport, Innovation and Technology in funding part of the work by the project RELAM within the Austrian Aeronautics Program TAKE OFF.

REFERENCES

[1] Bader, P., and Sanz, W., 2015. "Steady and unsteady CFD calculation of the laminar-to-turbulent transition in a turning mid turbine frame with embedded design". *Proceedings of ASME 2015 Turbo EXPO, Montreal, Canada*. GT2015-42617.

[2] Schlichting, H., and Gersten, K., 2006. *Grenzschicht-Theorie (Boundary-Layer Theory)*. Springer-Verlag Berlin Heidelberg.

[3] Mayle, R. E., 1991. "The role of laminar-turbulent transition in gas turbine engines". *Journal of Turbomachinery,* ***113***(4), October, pp. 509–537.

[4] Yip, L. P., Vijgen, P., Hardin, J. D., and van Dam, C. P., 1993. "In-flight pressure distributions and skin-friction measurements on a subsonic transport high-lift wing section". *AGARD CP-515*.

[5] Oyewola, O., Djenidi, L., and Antonia, R. A., 2003. "Combined influence of the reynolds number and localised wall suction on a turbulent boundary layer". *Experiments in Fluids,* ***35***, July, pp. 199–206.

[6] Oyewola, O., 2006. "LDV measurements in a pertubed turbulent boundary layer". *Journal of Applied Science,* ***6***(14), pp. 2952–2955.

[7] Widmann, A., Duchmann, A., Kurz, A., Grundmann, S., and Tropea, C., 2012. "Measuring tollmien-schlichting waves using phase-averaged particle image velocimetry". *Experiments in Fluids,* ***53***, pp. 707–715.

[8] Mukund, R., Narasimha, R., Viswanath, P. R., and Crouch, J. D., 2012. "Multiple laminar-turbulent transition cycles around a swept leading edge". *Experiments in Fluids,* ***53***, pp. 1915–1927.

[9] Bader, P., and Sanz, W., 2015. "On the setup of a test bench for predicting laminar-to-turbulent transition on a flat plate". *Proceedings of the 12^{th} International Symposium on Experimental Computational Aerothermodynamics of Internal Flows, Genova, Italy*. ISAIF12-074.

[10] Bader, P., Sanz, W., Peterleithner, J., Woisetschläger, J., Heitmeir, F., Meile, W., and Brenn, G., 2016. "Detecting transition on flat plate flow with laser interferometric vibrometry (LIV)". *Proceedings of ASME Turbo Expo 2016: Turbine Technical Conference and Exposition, Seoul, South Korea*. GT2016-56043.

[11] Narasimha, R., and Sreenivasan, K. R., 1979. "Relaminarization of fluid flows". *Advances in applied mechanics,* ***61***, pp. 221–309.

[12] Ichimiya, M., Nakamura, I., and Yamashita, S., 1998. "Properties of a relaminarizing turbulent boundary layer under a favorable pressure gradient". *Experimental Thermal and Fluid Science,* ***17***, pp. 37–48.

[13] Escudier, M. P., Abdel-Hameed, A., Johnson, M. W., and Sutcliffe, C. J., 1998. "Laminarisation an re–transition of a turbulent boundary layer subjected to favourable presser gradient". *Experiments in Fluids,* ***25***, pp. 491–502.

[14] Mukund, R., Viswanath, P. R., Narasimha, R., and Praband Crouch, J. D., 2006. "Relaminarization in highly favourable pressure gradients on a convex surface". *Journal of Fluid Mechanics,* ***566***, pp. 97–115.

[15] Dorfer, S., 2011. "Auslegung und experimentelle untersuchung eines relaminarisierungs – testfalls". *Diploma Thesis at Graz University of Technology*.

[16] Roach, P. R., 1987. "The generation of nearly isotropic turbulence by means of grids". *International Journal of Heat and Fluid Flow,* ***8***, pp. 82–92.

[17] Langtry, R. B., Menter, F. R., Likki, S. R., Suzen, Y. B., Huang, P. G., and Völker, S., 2004. "A correlation based transition model using local variables part 2: Test cases and industrial applications". *Proceedings of ASME 2004 Turbo EXPO, Vienna, Austria*. GT2004-53454.

[18] Boree, J., Ben, L., and Bazile, R., 2003. "Optical methods for the measurement of constant and variable density flows". *International Summerschool on variable density turbulent flows, Barcelona, Spain*.

[19] Launder, B. E., 1987. "Laminarization of the turbulent boundary layer in a severe acceleration". *Journal of Applied Mechanics,* ***31***, pp. 707–708.

[20] Bardi Narayanan, M. A., and Ramjee, V., 1969. "On the criteria for reverse transition in a two–dimensional boundary layer". *Journal of Fluid Mechanics,* ***35***, pp. 225–241.

[21] Blackwelder, R. F., and Kovasznay, L. S. G., 1972. "Large–scale motion of a turbulent boundary layer during relaminarization". *Journal of Fluid Mechanics,* ***53***, pp. 61–83.

[22] Narasimha, R., and Sreenivasan, K. R., 1973. "Relaminarization in highly accelerated turbulent boundary layers". *Journal of Fluid Mechanics,* ***31***, pp. 417–447.

[23] Schlichting, H., 1979. *Grenzschicht-Theorie (Boundary-Layer Theory)*. Verlag G.Braun, Karlsruhe, Germany.

[24] Narasimha, R., 1977. "The three archetypes of relaminarization". *Proceedings of the 6^{th} canadian congress of applied mechanics. Vancouver*.

6.4. Quadrant analysis for relaminarization of experimental data

In this section a quadrant analyzes of the LDA measurements presented in paper 5 is given. Such analysis has also been performed by e.g. Nolan et al. [94] for transitional boundary layers.

With the Laser-Doppler system used, two velocity components are recorded simultaneously. One component in the flow direction along the plate surface, and the second one perpendicular to the surface, denoted u and v, respectively. These velocities were recorded in the points shown in the upper plots of Figs. 6.4 and 6.6, at wall distances of 25 %, 50 % and 75 % of the boundary layer thickness δ.

Each dot in the individual diagrams in the lower part of Figs. 6.4 and 6.6 represents the streamwise and lateral deviations u' and v' of an instantaneous velocity vector from the local mean. Each local data set consists of 5,000 velocity recordings. Figures 6.4 and 6.6 show these data for each of the two low-speed test cases presented in paper 5. The mean velocity components $\overline{u}$ and $\overline{v}$ and the standard deviations (RMS-values) of u and v are printed in the legends of the diagrams.

In the following we discuss the case of 5 m/s, 10° in Fig. 6.4. Similar behavior is seen for the case of 5 m/s, 20° case in Fig. 6.6, although about 100 mm farther downstream. In the first position at $x = 595$ mm downstream from the leading edge of the plate – the trip wire is at 355 mm – the plots show isotropic fluctuations in streamwise and lateral directions. At the next two positions 795 mm and 945 mm, the standard deviation in the lateral direction remains unchanged, wheras it increases slightly in the streamwise direction, together with the skewness as shown in Fig. 8e of paper 5 (also the representation of the velocity fluctuations in the diagrams makes the changes in skewness evident). At the two positions 795 mm and 945 mm, where the skin friction coefficient c'_f and the shape factor H already indicate relaminarization (see Figs. 5c and d in paper 5), the point plots indicate spikes of negative fluctuations u' caused by a occasionally appearing sudden decrease of the streamwise velocity, whereas the lateral fluctuations v' remain nearly unchanged. This effect is strongest at $x = 945$ mm, $y/\delta(x) = 0.25$, where the streamwise fluctuations are more than twice as strong as the lateral ones. This location is also the x position where the acceleration parameter K (see Fig. 5b in paper 5) falls below its critical value. This indicates two concurring, but opposed effects. On the one hand, due to the frozen turbulence as discussed by Narasimha and Sreenivasan [34] and the increase in main flow velocity, the turbulence intensity decreases. On the other hand, the increase in velocity fuels the turbulence.

At the next streamwise position of 1095 mm, at $y/\delta(x) = 0.25$, a bi-modal shape of the fluctuations v' becomes evident, indicating a vortical rotation in the plane of the u' and v' components. If we consider that this wall-layer vortex does not influence the fluctuations at $y/\delta(x) = 0.5$ at 1095 mm, the maximum spatial extent of this vortex is 1.35 mm. Using the estimate $f = v/\lambda$ for the fluctuation frequency inside the boundary layer, a minimum value of $f \approx 5\ kHz$ is found. This vortex moves downstream and from the near-wall layer ($y/\delta(x) = 0.25$) outwards to the main flow (1195 mm, $y/\delta(x) = 0.5$ and $y/\delta(x) = 0.75$ at $x = 1295$ mm), which is indicated by the red arrow. This can be explained by a hair-pin shape as described by Dennis [159] for a transitional boundary layer and agrees with streamwise streak structures described in Sec. 3.3.3. In the next positions, at 1195 mm and 1295 mm, close to the wall the streamwise velocity fluctuations increase significantly, showing

an increase in turbulence. This indicates re-transition.

The free stream flow conditions present at the position where the disturbances start would normally lead to bypass transition, with the transport of disturbances from the free stream into the boundary layer, triggering transition. However, this is not the case for the retransition process discussed here. Since the disturbance appears close to the wall, it is a direct consequence of the relaminarization process and not a classical transition process. This finding leads to another important conclusion: since retransition occurs as a direct consequence of relaminarization in accelerated flow, the laminar-like state of the boundary layer produced by the acceleration cannot be conserved. This means that relaminarization, as occurring in accelerated flow, can hardly exploited. The decrease of the wall shear – which represents a major advantage of relaminarization – happens at decreasing acceleration, but is immediately followed by rapid retransition.

For all diagrams in Figs. 6.4 and 6.6 a quadrant analysis can be performed as described in Sec. 3.3.3. As shown in Fig. 3.27 the fluctuations can be divided into four quadrants:

- Q1, $u' > 0 \wedge v' > 0$: Outward movement of high-speed fluid
- Q2, $u' < 0 \wedge v' > 0$: "Ejection", low-speed fluid moves away from the wall
- Q3, $u' < 0 \wedge v' < 0$: Inward motion of low-speed fluid
- Q4, $u' > 0 \wedge v' < 0$: "Sweep", inrush of high-speed fluid

Events (in our case dots) in Q1 and Q3 represent a positive Reynolds shear stress ($\overline{u'v'} > 0$) thus a negative turbulence production ($P_x = -\overline{u'v'}\ \partial\overline{u}/\partial y$) whereas events in Q2 and Q4 represent a positive turbulence production (negative Reynolds shear stress ($\overline{u'v'} < 0$)).

Applying these considerations to the diagrams of Fig. 6.4 (similar for Fig. 6.6) one can observe that upstream of $x = 1095$ mm the distribution of the fluctuations in the four quadrants is more or less equally distributed with slightly more events in Q2. This can be better seen in Fig. 6.5 (and Fig. 6.7 for the 20° case, respectively), where the events are averaged for several quadrant segments. The mean value illustrated by the red line represents the average value for all events ±15° of the line.

From this illustration one can observe, that the Q2 effects are dominant at $x = 595$ mm compared to the other quadrants for all heights. Downstream ($x = 795$ mm and $x = 945$ mm) the Q2 effects decrease in intensity, whereas Q1 and Q3 effects are rising, representing a negative turbulent production. If these observations are compared to the streamwise distribution of the Reynolds shear stress (see Fig. 8d in paper 5), it can be concluded that the Q1/Q3 effects are nearly equal to Q2/Q4 effects, thus the turbulence production is close to zero or even slightly below zero.

An interesting point are the Q3 events: These events represent an inward motion of low-speed fluid. For a "normal" boundary layer such events generally do not occur, but in the relaminarization case this means that already laminar-like profiles are present, since the velocity away from the wall is lower than the mean velocity at the wall. This proofs the existence of laminar-like profiles in this stage of the relaminarization.

Further downstream the remaining disturbances inside the boundary layer are amplified, since the stabilizing pressure gradient decreases. Besides a strong rise of the Q2 effects in the inner zone of $x = 1095$ mm[1] also the Q3 effects are increasing. This indicates beside the presence of a streamwise vortex as described above, also a higher occurrence of laminar-like profiles.

[1] Note that the axis scaling differs between $x = 945$ mm and $x = 1095$ mm

This amplification of the remaining disturbances dispreads along the streamline and outwards, which can be seen in both Figs. 6.4 and 6.5. Clearly it can be observed, how Q2 effects are dominating when comparing the averaged values in the diagrams, thus the turbulence production is rising again. This high rate of production can also be seen in Fig. 8d in paper 5, and it promotes a fast retransition.

The same conclusions can also be drawn for the 5 m/s, 20° case shown in Figs. 6.6 and 6.7, respectively.

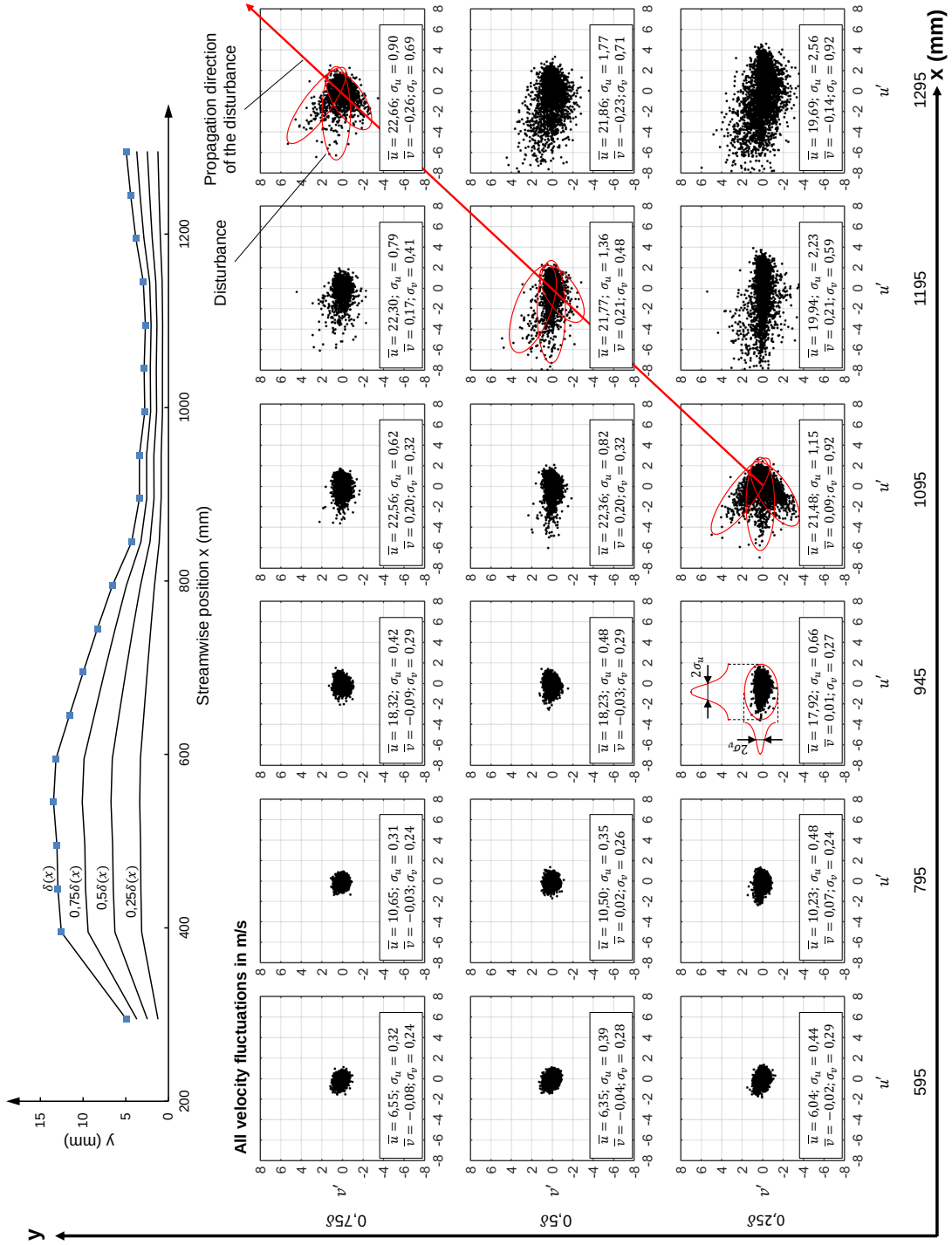

Figure 6.4: Boundary layer thickness profile $\delta(x)$, and streamwise u' and lateral v' velocity fluctuations at different x positions and wall distances for the 5 m/s, 10° case

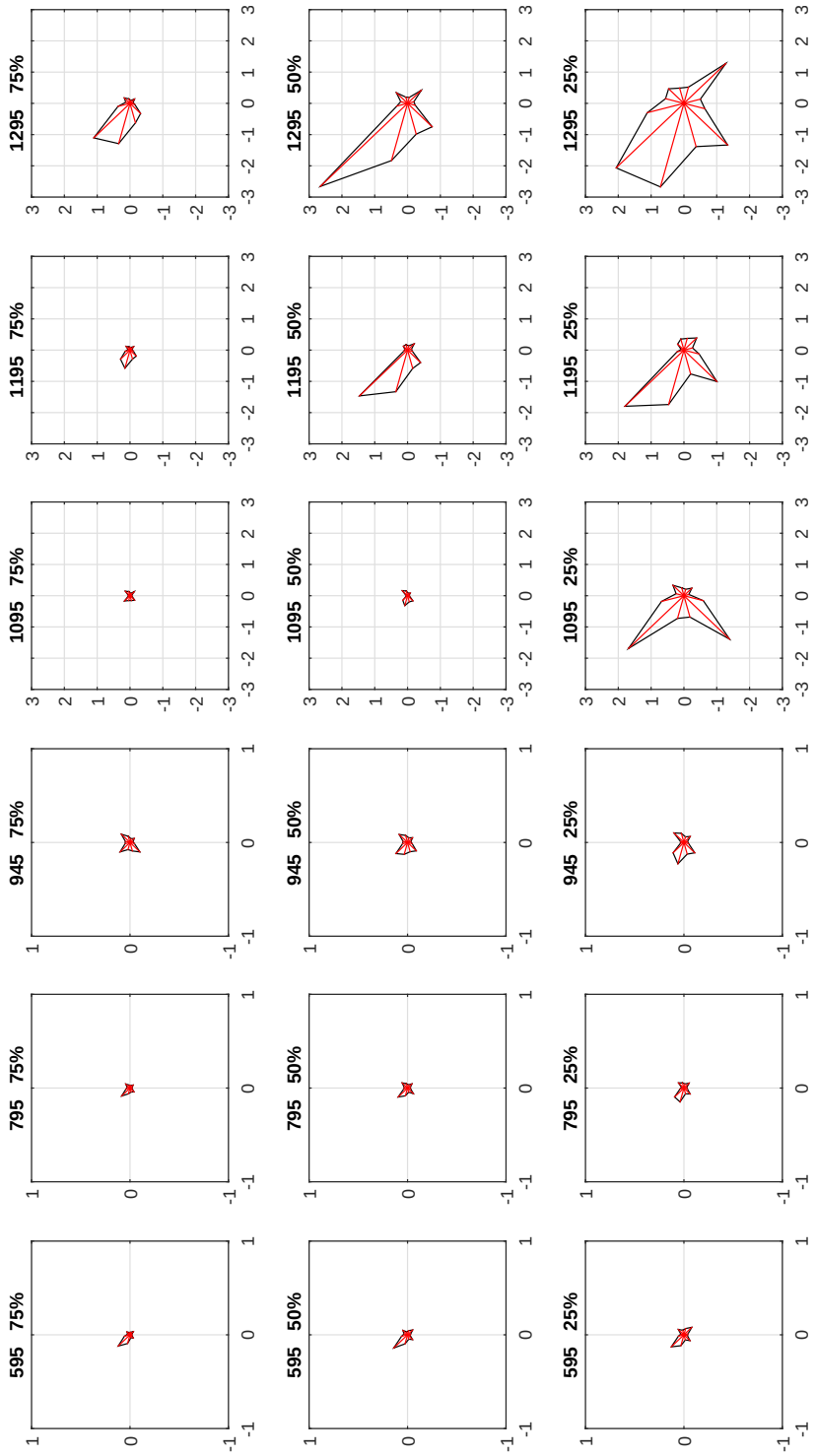

Figure 6.5: Averaged value $\overline{u'v'}$ ($\pm 15°$ around the red line) of the and streamwise u' and lateral v' velocity fluctuations for various quadrant segments at different x positions and wall distances for the 5 m/s, 10° case; the axis scaling differs between $x = 945$ mm and $x = 1095$ mm

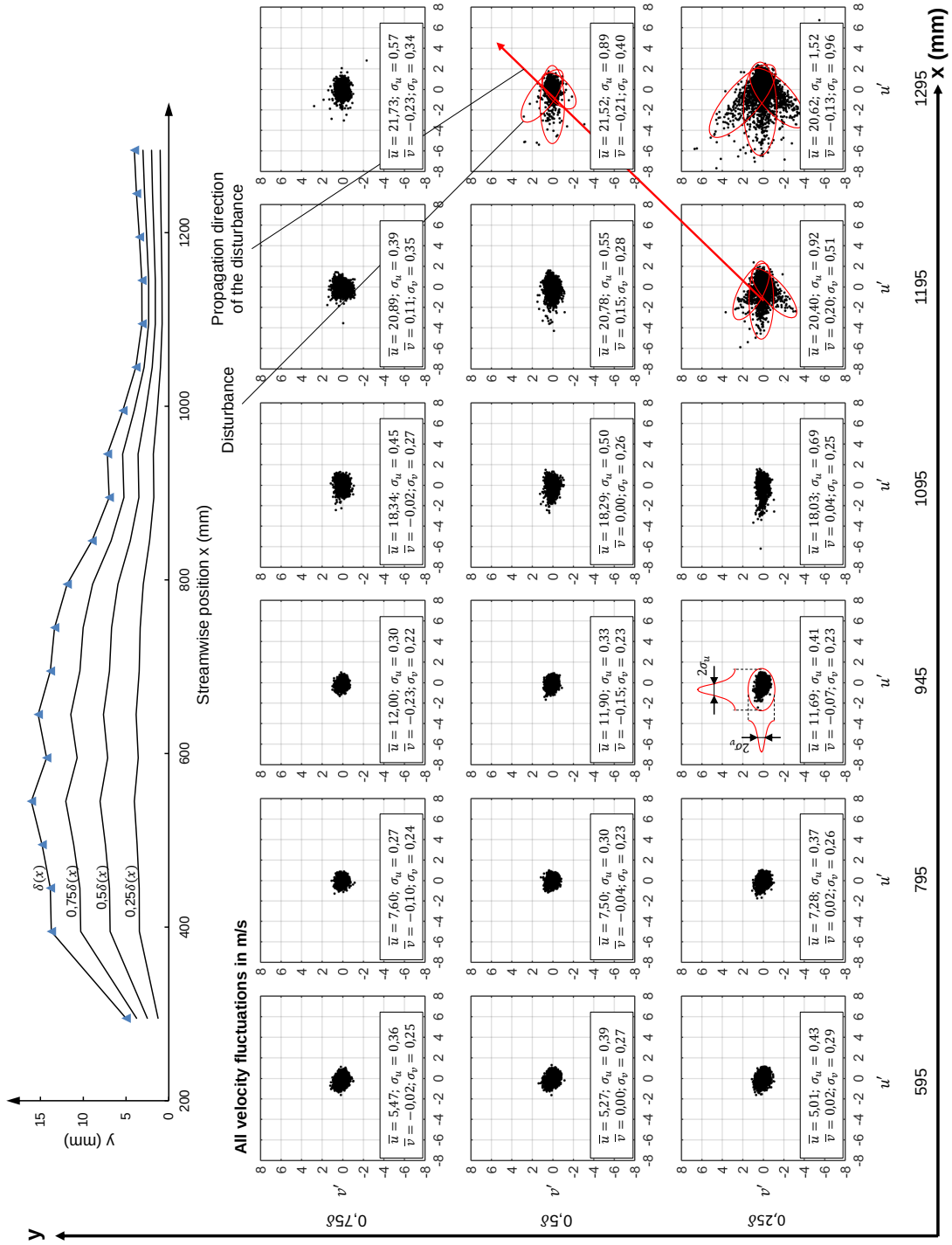

Figure 6.6: Boundary layer thickness profile $\delta(x)$, and streamwise u' and lateral v' velocity fluctuations at different x positions and wall distances for the 5 m/s, 20° case

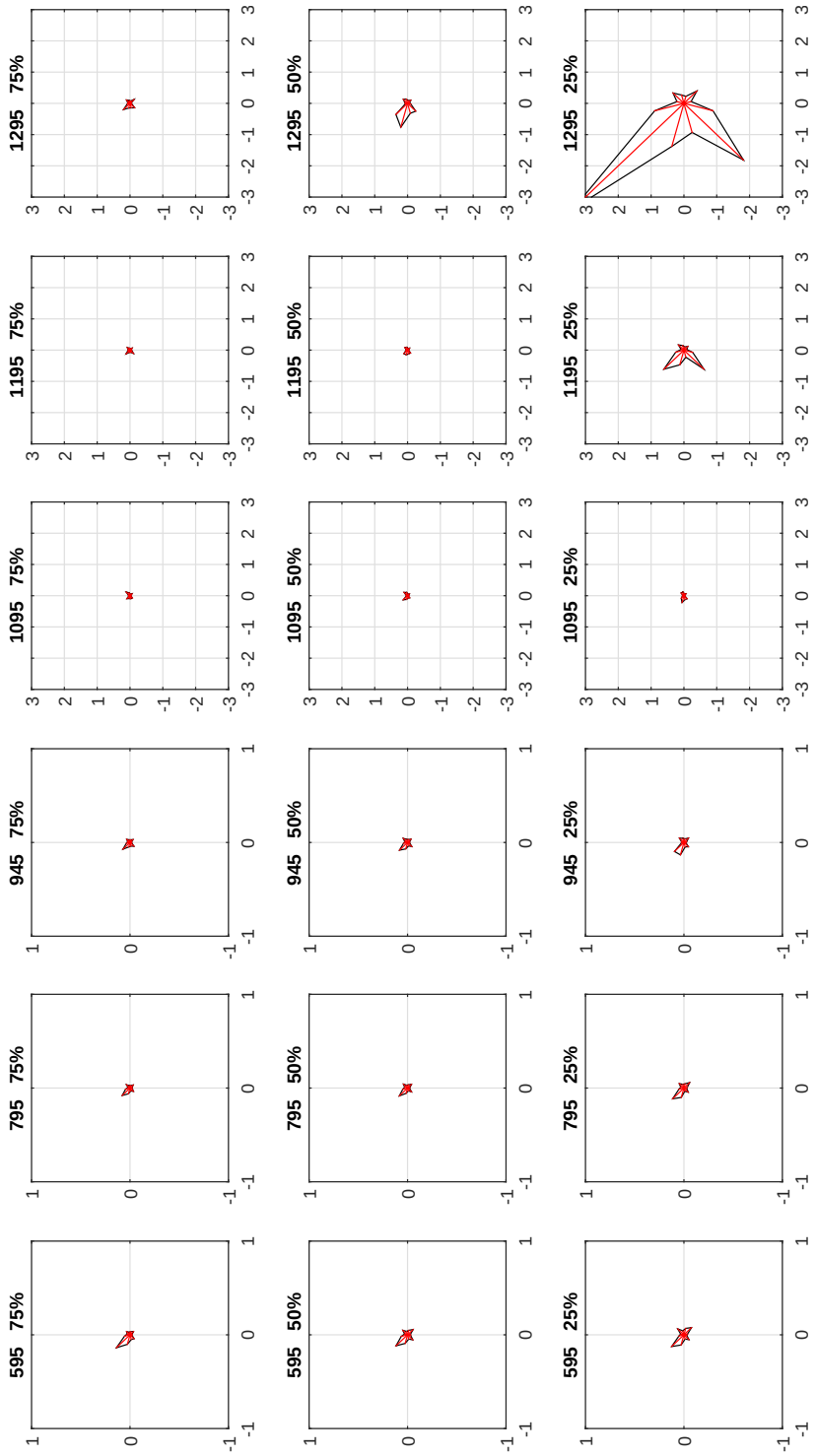

Figure 6.7: Averaged value $\overline{u'v'}$ ($\pm 15°$ around the red line) of the and streamwise u' and lateral v' velocity fluctuations for various quadrant segments at different x positions and wall distances for the 5 m/s, 20° case; the axis scaling differs between $x = 945$ mm and $x = 1095$ mm

6.5. Paper 6: The capability of Large Eddy Simulation to predict Relaminarization

P. Bader, W. Sanz, C. Steinmayr and P. Leitl, "The capability of Large Eddy Simulation to predict Relaminarization," *11^{th} International ERCOFTAC Symposium on Engineering Turbulence Modelling and Measurements*, SID-086, 2016.

THE CAPABILITY OF LARGE EDDY SIMULATION TO PREDICT RELAMINARIZATION

P. Bader[1], *W. Sanz*[1], *C. Steinmayr*[2] *and P. Leitl*[2]

[1] *Institute for Thermal Turbomachinery and Machine Dynamics, TU Graz, Austria*
[2] *bionic surface technologies GmbH, Graz Austria*

pascal.bader@tugraz.at, wolfgang.sanz@tugraz.at

Abstract

The boundary layer which represents the narrow zone between a solid body and the free stream can have a laminar or a turbulent state. This state influences on the one hand the properties of the near-wall flow like skin friction or heat transfer and on the other hand also the free-stream flow itself, e.g. the downstream flow angle of a turbomachinery blade. Thus it is important for designers of fluid machinery to understand and predict the state of the boundary layer as well as the transition processes between the two states.

In this work the so-called relaminarization is investigated which represents a reverse transition from a turbulent to a laminar boundary layer. At the Institute for Thermal Turbomachinery and Machine Dynamics at Graz University of Technology a test bench has been designed in order to produce a highly accelerated flow, thus triggering relaminarization. In the present work, this test bench is numerically investigated with Reynolds-averaged Navier-Stocks (RANS) flow simulation as well as with a large eddy simulation (LES).

An outcome of this paper is, that the LES shows a very good agreement to the measurement results and is capable in predicting relaminarization.

1 Introduction

In flows along solid body surfaces, the boundary layer represents the narrow zone between the wall and the free stream where viscous effects are important. Its state of flow (laminar or turbulent) may have strong impact on transport processes like wall friction and heat transfer. These processes influence the efficiency as well as the thermal stress, for example of a turbine blade, and may affect other flow characteristics in the machine as well (see e.g. Bader and Sanz (2015a)).

Many parameters, like free-stream velocity, acceleration, free-stream turbulence etc., may have an influence on the state of a boundary layer. At the first contact of a flowing fluid with a stationary structure the boundary layer flow is laminar before it develops via a transitional zone to become turbulent. The boundary layer passes through several stages within this transitional zone before becoming fully turbulent. Schlichting and Gersten (2006) extensively discussed these different stages.

It is vitally important to understand the influences of key parameters on the onset position and length of the transitional zone in order to predict and potentially control the state of the boundary layer. In turbomachinery, the efficiency of blades and stages may be improved considering transition. This may allow the overall machine performance to be enhanced. In 1991 Mayle (1991) published a comprehensive review of the importance of transition in gas turbines. He analyzed experiments performed by several research groups in order to find the influence of different flow parameters on the transition process.

Since then additional experiments were performed by other research groups. Yip et al. (1993) performed in-flight measurements, where they detected transition with the help of Preston tubes and analyzed the influence of the flight conditions on the boundary layer along an airfoil. Oyewola et al. (2003) and Oyewola (2006) showed how the flow in the boundary layer can be measured with hot-wire anemometry and Laser-Doppler anemometry (LDA), respectively. Widmann et al. (2012) performed near-wall measurements with particle image velocimetry (PIV). Hot-film measurements in the boundary layer were performed, e.g., by Mukund et al. (2012), Preston-tube and thermographic measurements by Bader and Sanz (2015b). Additionally, Bader et al. (2016b) used laser interferometric vibrometry (LIV) to predict transition.

So far, only the transition from laminar to turbulent flow was described. Under certain flow conditions (like strong acceleration), however, a reverse transition or relaminarization from turbulent to laminar can occur. Up to now, only few measurements on relaminarization were reported (e.g. (Narasimha and Sreenivasan, 1979; Escudier et al., 1998; Mukund et al., 2006)). Therefore, at the Institute for Thermal Turbomachinery and Machine Dynamics (ITTM) of Graz University of Technology a project was launched in order to understand the process of relaminarization and its phases even further and verify common threshold values for relaminarization.

Experiments showed four different phases in relaminarization caused by acceleration (Narasimha and

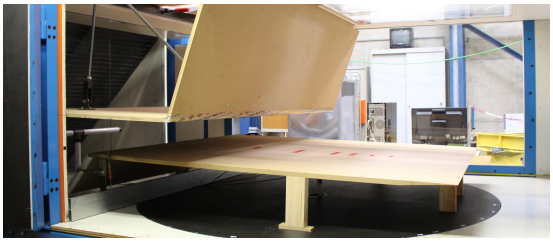

Figure 1: Photograph of the test bench at the ISW, flow from right to the left.

Sreenivasan, 1979; Escudier et al., 1998; Mukund et al., 2006; Ichimiya et al., 1998): In the first phase at the beginning of the acceleration zone, the skin friction increases along with a decrease of the shape factor H (ratio of displacement thickness to momentum thickness).

The second phase already shows the first signs of relaminarization, characterized by a break down of the law of the wall. Also, the boundary layer becomes thinner. Additionally, the local skin friction coefficient c_f' starts to decrease and the shape factor H starts to rise. The authors state that this second zone is relatively short, within $x/\delta(x) = 20$ to 30. Narasimha and Sreenivasan (1979) described the turbulent velocity fluctuations as "frozen" within this zone. These fluctuations promote a fast retransition into a turbulent boundary layer in the third phase when the acceleration falls below a certain threshold. Finally, in the fourth phase the boundary layer is turbulent again.

Since the interest of this work is to investigate relaminarization at high acceleration, a test bench with a strongly convergent cross section is needed, leading to a small channel cross section at the outflow. In such a small flow area probes like Preston tubes and hot wire probes can influence the flow considerably. Therefore, non-invasive techniques, such as Laser-Doppler anemometry, are used for measuring the state of the boundary layer.

In this paper, the results of these measurements by Bader et al. (2016a) are used to validate the simulation results. The numerical calculations presented here were done with a traditional RANS approach and a large eddy simulation (LES).

Within the present work, different numerical approaches should be tested regarding their capability of predicting relaminarization. The results of these numerical studies are instrumental in getting a better understanding of the process of relaminarization and retransition.

In the following section, the numerical setup together with the methodology used for the CFD simulations are discussed. Thereafter a discussion of the results is given, where the RANS and LES data are compared to experimental results. The paper ends with a summary and conclusion.

2 Numerical Setup and Methodology

The test bench numerically investigated is a closed-loop Göttingen-type wind tunnel at the Institute of Fluid Mechanics and Heat Transfer (ISW) which delivers air to the test section through several rectifiers and a turbulence grid. Approximately $1200\ mm$ downstream of the turbulence grid, the first measurement plane is situated which also represents the numerical inlet. Therefore all necessary inlet conditions for the simulation are measured at this position. The leading edge of the measurement plate is situated about $1350\ mm$ downstream of the numerical inlet. Along this plate, Laser-Doppler measurements have been performed. In order to have a fully turbulent boundary layer upstream of the acceleration area, a tripwire is mounted at the plate at about $x = 350\ mm$ downstream of the leading edge. A picture of the measurement plate including the acceleration board is given in Fig. 1. The reduction of the flow cross section starts at $x = 810\ mm$ and ends at $x = 1025\ mm$. A small gap is arranged between the outer wall and the acceleration board in order to reduce the corner vortex there.

As mentioned above, the experimental results of LDA measurements are compared with the numerical data calculated with RANS and LES. Bader et al. (2016a) discuss the measurement results together with more details of the setup of the experiment; so the interested reader is referred to their paper.

The numerical results discussed in this paper have been computed with ANSYS® Fluent® v15.0. The first step was a Reynolds-averaged Navier-Stokes (RANS) simulation. The k-k_L-ω transition/turbulence model by Walters and Cokljat (2008) was used in order to solve the turbulence equations. The used three dimensional mesh is shown in Fig. 2a and consists of approximately 35 million nodes. The wall distance of the first grid cells y^+ was kept between 0.1 and 1 in order to resolve the laminar sublayer. The boundary conditions at the inlet and outlet have been taken from the experiment.

Simulation results were extracted at three lines marked with their corresponding letter in Fig. 2a: (a) a line from the leading edge of the plate towards the top wall, (b) a line from the trailing edge of the plate towards the parallel plate and (c) a line in the gap between the acceleration board and the outer wall. These lines mark the geometrical boundaries of the LE simulation and the flow variables extracted from these lines are used as inlet and outlet conditions. This resulting smaller domain with a reduced width of $z = 80\ mm$ is shown in Fig. 2b and consists of approximately 66 million nodes. For the large eddy simulation the flow regime is divided into a coarse and a dense mesh which interact with each other. The finer domain is situated close to the wall and has a height of $y = 40\ mm$, whereas the coarser domain covers the free-stream flow. This division of the domain can be seen in

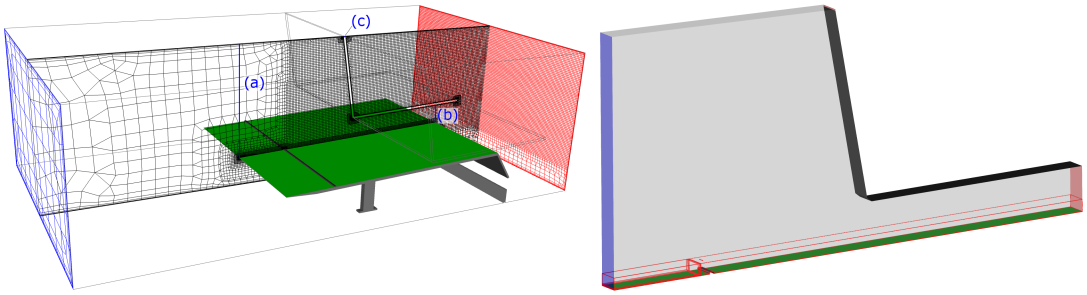

(a) mesh for the full 3D simulation.

(b) LES 3D domain.

Figure 2: Schematic drawings of the computational meshes

Fig. 3. Also the tripwire which generates the turbulence within the boundary layer is clearly apparent in the zone with the denser mesh. The dimensions of the wall cells for the three coordinates x^+, z^+ and y^+ is about 4.8, 4.7 and 0.6 respectively, at a representative position at $x = 695\ mm$.

The time step for the LE simulation has been set to $\Delta t = 2 \cdot 10^{-5}\ s$, thus resolving frequencies up to $f = 50,000\ Hz$. To reduce the necessary hard disc space, the extraction of data has been done for every 25^{th} timestep, resulting in a time interval of $5 \cdot 10^{-4}\ s$ which corresponds to a frequency limit of $f = 2,000\ Hz$. The total simulation time where the post processing has been performed is $t = 0.047\ s$.

3 Results and discussion

In this section the results of the RANS and LE simulations are compared with the measurement results obtained by Bader et al. (2016a).

In Fig. 4 three computational results are given together with the experimental data. The three numerical results are a RANS solution with the turbulence/transition model k-k_L-ω, a RANS solution with the standard k-ω turbulence model which represents the fully turbulent reference result and a LES result giving a time-averaged result at mid span.

Fig. 4a gives the free stream velocity u_∞ extracted $y = 32\ mm$ above the plate, and thus within the finer domain of the LES.

Comparing the curves with the experimental results, it can be observed that the CFD results show a good agreement with the measurement, however the LES results shows a slightly higher velocity compared to the measurement results from approximately $x = 0.80\ m$ on downstream. This difference is probably caused by three dimensional effects of the setup, like leakage flows at the sides of the plate, which are not accounted by the smaller LES domain. Both 3D RANS simulations show a very good agreement with the measurement results.

In order to see, if the acceleration is sufficient for relaminarization, the acceleration parameter K by Launder (1987) is plotted in Fig. 4b which is defined as

$$K = \frac{\nu}{u_\infty(x)^2} \frac{\partial u_\infty(x)}{\partial x} \tag{1}$$

where ν represents the kinematic viscosity of the fluid, $u_\infty(x)$ the free stream velocity and $\partial u_\infty(x)/\partial x$ the streamwise velocity gradient in the free stream. The critical value of $K_{crit} \approx 3 \cdot 10^{-6}$ in Fig. 4b represents a threshold value where, if exceeded, full relaminarization is most likely to occur(see e.g. (Narasimha and Sreenivasan, 1979)). But also K-values below this critical level may lead to partial relaminarization. In the present test case the distribution of K shows a value above the critical one, thus relaminarization is most likely to occur.

The comparison of the experimental and numerical results shows a very good agreement of all curves up to $x < 0.7\ m$. Downstream of this position, both RANS simulations predict a higher acceleration compared to the LES or measurement results. Also the LES results exceeds the measured K-value there.

To see if the boundary layer relaminarizes, the wall shear τ_w along the plate should be analyzed. During relaminarization, the wall shear should show a decrease due to the decrease of the velocity gradient at the wall by the more laminar boundary layer profile. In Fig. 4c the wall shear distribution along the plate is given for the three computational results and the experimental data. The wall shear is defined as

$$\tau_w = \mu \left(\frac{\partial u}{\partial y} \right)_{y=0} \tag{2}$$

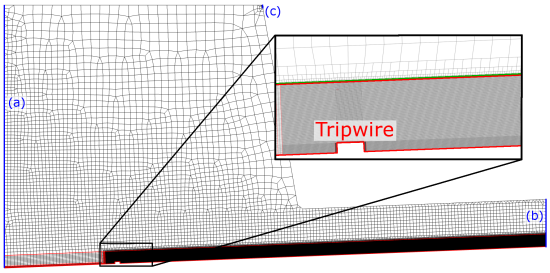

Figure 3: Meridional sketch of the mesh used for the LES showing the courser and finer zone.

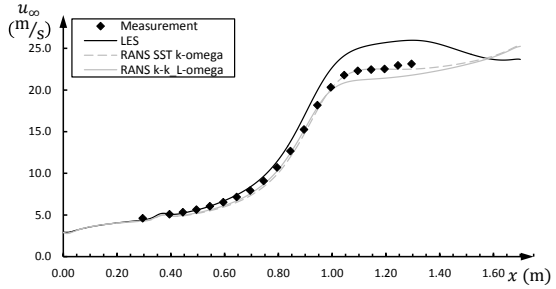

(a) of the free-stream velocity u_∞.

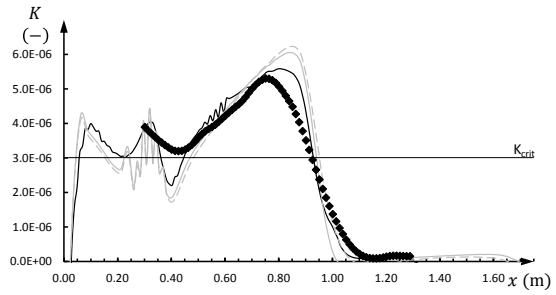

(b) of the acceleration parameter K.

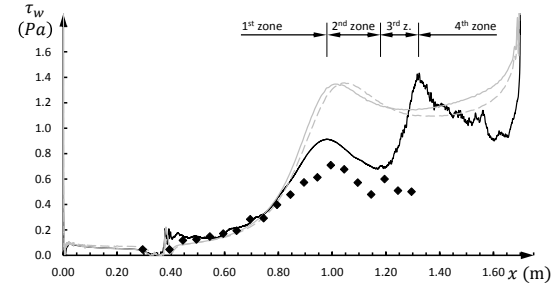

(c) of the wall shear τ_w (zones of relaminarization for LES marked).

Figure 4: Plots along the plate coordinate x

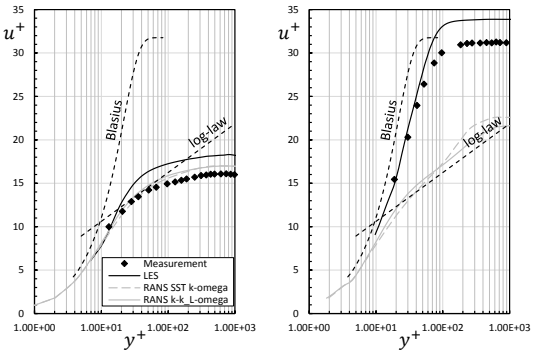

(a) at $x = 695\ mm$. (b) at $x = 1195\ mm$.

Figure 5: Velocity profile plots in wall coordinates $u^+(y^+)$

where $\partial u/\partial y$ represents the normal-to-wall gradient of the velocity at the wall ($y = 0\ mm$) and μ the dynamic viscosity.

Due to the acceleration, the wall shear starts to rise at approximately $x = 0.4\,m$. This rise is caused by the increasing free stream velocity due to the acceleration in addition to a decreasing boundary layer thickness $\delta(x)$. As described above, this effect indicates the first zone of relaminarization. Comparing the simulations with the experiment it can be observed, that all simulations agree well with the experimental data. Since the fully turbulent simulation also shows this increase of wall shear, this is not an effect of relaminarization, but caused by the high acceleration.

Starting at $x = 0.80\ m$ a discrepancy between RANS, LES and the experiment can be observed. The discrepancy between LES and the measurement is most likely caused by the differences in the free-stream velocity (see Fig. 4a), thus influencing the acceleration parameter K: Where the measurement results already indicate a decrease of the acceleration parameter (at about $x = 0.75\ m$), the numerical solutions still show a rise of K (up to approximately $x = 0.84\ m$). This position where the K factors of the LES and the experiment start to drop agrees with a position where the distributions of the wall shear τ_w differ from the fully turbulent reference solution. Thus, although the wall shear still rises in this area, first effects of relaminarization can be seen for LES and measurement data, however not for the k-k_L-ω solution.

More pronounced effects of relaminarization can be seen downstream of the position where the highest K value is reached at approximately $x = 0.95\ m$, where K drops below its critical value. At this position, τ_w starts to drop for the measurement results as well as for the LES. This is caused by a decreasing velocity gradient close to the wall, which indicates, that, at least close to the wall, the boundary layer changes to a laminar state. This decrease represents the second stage of relaminarization. On the other hand both RANS solutions still continue to rise. The SST k-ω solution as the fully turbulent reference case behaves as expected, but also the transitional solution with the k-k_L-ω model stays fully turbulent.

As described above, the discrepancy between LES and experiment can be explained by the velocity differences between the two results.

At approximately $x = 1.2\ m$ the wall shear increases sharply for the LES results, indicating a rapid retransition. This fast retransition represents the third of the four stages of relaminarization described above. Comparing with the measurements, it can be seen, that the experiment shows a larger second zone since no retransition is observable.

Downstream of the retransition zone, the boundary layer is turbulent again, which represents the forth and last zone of relaminarization. However, the wall shear of the LES differs to the results of the RANS solutions, so that the downstream turbulent boundary layer may be influenced by the relaminarization process. The four mentioned zones of relaminarization are indicated for the large eddy simulation in Fig. 4c.

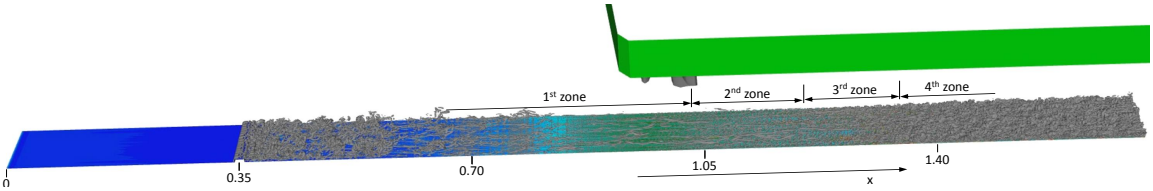

Figure 6: Instantaneous 3D illustration of iso-surfaces of the Q criterion together with a surface contour plot of the wall shear τ_w (LES result).

To verify relaminarization two velocity profiles are given in Fig. 5. The profiles at $x = 695\ mm$ and $x = 1195\ mm$ are given in wall coordinates $u^+(y^+)$, which are defined as

$$y^+ = \frac{y \cdot u_\tau}{\nu} \tag{3}$$

$$u^+ = \frac{u}{u_\tau} \tag{4}$$

$$\text{with } u_\tau = \sqrt{\frac{\tau_w}{\rho}} \tag{5}$$

In this illustration again the RANS and time- and spatial-averaged LE simulations are given together with the experimental data. Additionally, the Blasius solution, which represents a laminar boundary layer in a zero-pressure-gradient flow, is given together with the log-law.

At the first plotted position ($x = 695\ mm$) all curves show a relatively good agreement, since this position is upstream of the relaminarization zone (see Fig. 4c). Additionally, the influence of the acceleration can be seen by the discrepancies of the curves to the log-law.

At the second position ($x = 1195\ mm$) the differences between the LES and RANS solution are very high, caused by the relaminarization of the LE simulation, whereas the RANS solutions stay fully turbulent showing a good agreement with the log-law.

The measurement and the LES result show a good agreement of the trend but due to the different free stream velocities the profiles differ slightly (see Fig. 4a). However, both results show a trend towards the Blasius solution, which indicates, that the boundary layer is relaminarizing. The mechanism causing this relaminarization may be according to Bader et al. (2016a) a decreasing influence of the velocity fluctuations on the overall velocity field, or – in other words – the fluctuations stay more or less constant, while the overall velocity is increasing. This reduction of the share of energy of the velocity fluctuations causes the fluctuations to "freeze" within the boundary layer (Narasimha and Sreenivasan, 1979), so that the viscous forces within the boundary layer dominate the flow. Thus the boundary layer becomes laminar with a stable layering, but with remaining fluctuations inside the boundary layer. This "quasi-laminar" state leads ultimately to a reduction of the velocity gradient close to the wall, since the necessary energy to keep up a turbulent profile cannot be transferred in lateral direction towards the wall.

So basically the turbulent vortices are getting stretched, loosing their influence on the velocity field within the boundary layer. To visualize this effect, an instantaneous three dimensional plot of the LES data is given in Fig. 6 showing the wall shear τ_w as surface contour plot and iso-surfaces of the Q-criterion of (Hunt et al., 1988) . The Q-criterion defines a vortex as a spatial region where

$$Q = \frac{1}{2}\left[|\Omega|^2 - |S|^2\right] > 0 \tag{6}$$

with $S = \frac{1}{2}\left[\nabla v + (\nabla v)^T\right]$ representing the rate-of-strain tensor and $\Omega = \frac{1}{2}\left[\nabla v - (\nabla v)^T\right]$ the vorticity tensor. This criterion is helpful to visualize vortices in the flow, in our case the instantaneous vortices within the boundary layer.

In Fig. 6 also the four zones of the relaminarization process which have been identified above are given. In the first zone, the turbulent fluctuations related to the flow kinetic energy start to decay. In this area, where the wall shear rises and the boundary layer thickness decreases, the vortices get "stretched" and the interaction in the lateral direction between the vortices within this zone is reduced. As already mentioned, these "frozen" fluctuations represent structures with a very low turbulence, thus viscous forces are dominating, causing the boundary layer to laminarize in the second zone. In this zone, the wall shear decreases.

The iso-surfaces of the Q-criterion in this zone show that the "stretched" vortices are dominating but small vortices also arise. So although the boundary layer has developed a stable layering, where the wall shear decreases and the velocity profile shows a lami-

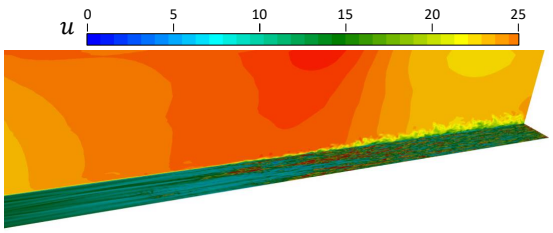

Figure 7: Instantaneous streamwise velocity at a midplane and surface contour plot of the wall shear; showing LES data.

nar distribution, new vortices occur again showing that the state of the boundary layer is "quasi"-laminar.

These small vortices remaining in the relaminarization zone (second zone) then promote a rapid retransition in the third zone, where the acceleration decreases. This is caused by the bursting of the above mentioned "frozen" fluctuations (Bader et al., 2016a). Downstream in the fourth zone, the boundary layer is turbulent again.

In order to see the retransition process in more detail, Fig. 7 shows the velocity at midplane together with the wall shear at the plate, both as instantaneous contour plots. It can be observed, that the wall shear and the velocity plot do not show stochasic fluctuations within the relaminarization zone (left hand side of Fig. 7), but a "streaky" distribution of wall shear. Downstream, where the rapid retransition takes place, it can be observed, that the wall shear increases together with the velocity fluctuations. It can be also observed, that no turbulent spots which would appear in a standard transition process (see e.g. Bader et al. (2016c)) can be found in this rapid-retransition zone. This again agrees with the statement above, that retransition is rather caused by the bursting of the "frozen" vortices than by a standard transition process.

4 Conclusions

The present work shows a simplified test case in order to study and understand the relaminarization of a turbulent boundary layer. Therefore measurements have been performed in a wind tunnel along a flat plate with a high acceleration caused by a reduction of the cross section. This simplified test case is numerically investigated within this paper to see the capability of two different numerical approaches: the transition/turbulence RANS model k-k_L-ω and a large eddy simulation.

The comparison showed, that the RANS solution was not capable in predicting relaminarization, although the model has performed very well in predicting transition in previous investigations. The LES results show a very good agreement with the measurement data and are able to predict relaminarization.

The paper also gives a more detailed view on the processes taking place within the four zones of relaminarization. The LES solution clearly shows, how the vortices are deformed leading to a laminar-like flow and how the "frozen" vortices then evolve again to trigger retransition.

So the large eddy simulation did not only agree well with the measurement results, but it also allowed a better understanding of the turbulent-to-laminar transition process and confirms conclusions drawn from experimental data.

Acknowledgments

The authors gratefully acknowledge financial support from the Austrian Federal Ministry for Transport, Innovation and Technology in funding this work by the project RELAM within the Austrian Aeronautics Program TAKE OFF.

Additionally the authors would to like to thank Günter Brenn and Walter Meile for providing their wind tunnel for the experimental work and their help during the test campaign. Last but not least, we would like to thank Jakob Woisetschläger for his guidance in the usage of the LDA equipment.

References

P. Bader and W. Sanz. Steady and unsteady CFD calculation of the laminar-to-turbulent transition in a turning mid turbine frame with embedded design. *Proceedings of ASME 2015 Turbo EXPO, Montreal, Canada*, 2015a. GT2015-42617.

P. Bader and W. Sanz. On the setup of a test bench for predicting laminar-to-turbulent transition on a flat plate. *Proceedings of the 12^{th} International Symposium on Experimental Computational Aerothermodynamics of Internal Flows, Genova, Italy*, 2015b. ISAIF12-074.

P. Bader, M. Pschernig, W. Sanz, J. Woisetschläger, F. Heitmeir, W. Meile, and G. Brenn. Flat-plate boundary layers in accelerated flow. *Proceedings of ASME Turbo Expo 2016: Turbine Technical Conference and Exposition, Seoul, South Korea*, 2016a. GT2016-56044.

P. Bader, W. Sanz, J. Peterleithner, J. Woisetschläger, F. Heitmeir, W. Meile, and G. Brenn. Detecting transition on flat plate flow with laser interferometric vibrometry (LIV). *Proceedings of ASME Turbo Expo 2016: Turbine Technical Conference and Exposition, Seoul, South Korea*, 2016b. GT2016-56043.

P. Bader, W. Sanz, C. Steinmayr, and P. Leitl. Comparison of rans and embedded les calculations with measurements of transitional flow along a flat plate. *ERCOFTAC Bulletin*, 106:84–91, 2016c.

M. P. Escudier, A. Abdel-Hameed, M. W. Johnson, and C. J. Sutcliffe. Laminarisation an re–transition of a turbulent boundary layer subjected to favourable presser gradient. *Experiments in Fluids*, 25:491–502, 1998.

J. C. R. Hunt, A. A. Wray, and P. Moin. Eddies, stream, and convergence zones in turbulent flows. *Center for Turbulence Research. Proceedings of the Summer Program 1988*, pages 193–208, 1988. N89-24555.

M. Ichimiya, I. Nakamura, and S. Yamashita. Properties of a relaminarizing turbulent boundary layer under a favorable pressure gradient. *Experimental Thermal and Fluid Science*, 17:37–48, 1998.

B. E. Launder. Laminarization of the turbulent boundary layer in a severe acceleration. *Journal of Applied Mechanics*, 31:707–708, 1987.

R. E. Mayle. The role of laminar-turbulent transition in gas turbine engines. *Journal of Turbomachinery*, 113(4):509–537, October 1991.

R. Mukund, P. R. Viswanath, R. Narasimha, and J. D. Praband Crouch. Relaminarization in highly favourable pressure gradients on a convex surface. *Journal of Fluid Mechanics*, 566:97–115, 2006.

R. Mukund, R. Narasimha, P. R. Viswanath, and J. D. Crouch. Multiple laminar-turbulent transition cycles around a swept leading edge. *Experiments in Fluids*, 53: 1915–1927, 2012.

R. Narasimha and K. R. Sreenivasan. Relaminarization of fluid flows. *Advances in applied mechanics*, 61:221–309, 1979.

O. Oyewola. LDV measurements in a pertubed turbulent boundary layer. *Journal of Applied Science*, 6(14):2952–2955, 2006.

O. Oyewola, L. Djenidi, and R. A. Antonia. Combined influence of the reynolds number and localised wall suction on a turbulent boundary layer. *Experiments in Fluids*, 35: 199–206, July 2003.

H. Schlichting and K. Gersten. *Grenzschicht-Theorie (Boundary-Layer Theory)*. Springer-Verlag Berlin Heidelberg, 2006.

K. Walters and D. Cokljat. A three-equation eddy-viscosity model for reynolds-averaged navier-stokes simulations of transitional flows. *Journal of Fluids engineering*, 130: 1214011–12140114, 2008.

A. Widmann, A. Duchmann, A. Kurz, S. Grundmann, and C. Tropea. Measuring tollmien-schlichting waves using phase-averaged particle image velocimetry. *Experiments in Fluids*, 53:707–715, 2012.

L. P. Yip, P. Vijgen, J. D. Hardin, and C. P. van Dam. In-flight pressure distributions and skin-friction measurements on a subsonic transport high-lift wing section. *AGARD CP-515*, 1993.

6.6. Quadrant analysis for relaminarization of numerical data

In order to analyze the remaining velocity fluctuations better and get more insight into the relaminarized boundary layer, a quadrant analysis is done. In Fig. 6.8 the streamwise u' and lateral v' velocity fluctuations inside the boundary layer at several streamwise positions x are given for three different heights: $y = 1\ mm$, $y = 1.5\ mm$ and $y = 3\ mm$. Every dot in this scatter plot represents one instantaneous value of LES in time.

The first position ($x = 1095\ mm$) shows a fully relaminarized profile. Clearly the remaining streamwise velocity fluctuations can be observed, with the highest amplitude at $y = 1\ mm$. Although the velocity fluctuations in streamwise and lateral direction are only isotropic at $y = 3\ mm$, the distributions of the fluctuations at the three positions are symmetric, meaning that non of the four quadrants shows a higher occurrence of dots/events indicating equality of turbulence production or destruction (see below).

The next streamwise position ($x = 1195\ mm$) which represents also the position of the laminar velocity profile shown in Fig. 5b of paper 6, already shows rising fluctuation amplitudes mainly in the lateral direction. At this position the acceleration parameter K (see Fig. 4b of paper 6) is very low, so that the stabilizing pressure gradient vanishes, leading to these emerging fluctuations. The fluctuations allow an energy transport inside the boundary layer, thus paving the way to retransition. Also the streamwise velocity fluctuations u' increase slightly compared to the upstream position.

The following two positions ($x = 1295\ mm$ and $x = 1395\ mm$) which are inside the retransition zone also show an increase of the lateral and streamwise fluctuations. The last two positions ($x = 1495\ mm$ and $x = 1595\ mm$) already show a fully turbulent boundary layer. The slight differences to the upstream position ($x = 1395\ mm$) is described below. Clearly the non-isotropy of the fluctuations can be observed at these positions.

In order to quantify these plots, the different quadrant events are evaluated by calculating the turbulent shear stress $\overline{u'v'}$ there. In Fig. 6.9 the shear stress $\overline{u'v'}$ for events in quadrants Q1 ($u' > 0 \wedge v' > 0$), Q2 ($u' < 0 \wedge v' > 0$), Q3 ($u' < 0 \wedge v' < 0$) and Q4 ($u' > 0 \wedge v' < 0$) are given separately. Q1 and Q3 events (given in blue) represent events with a positive shear stress $\overline{u'v'}$, thus a negative turbulent production, whereas events in Q2 and Q4 (marked in red) represent a positive turbulent production. In Fig. 6.9 also the accumulated turbulent production P is given computed with

$$P = \left|\overline{u'v'}\right|_{Q2} + \left|\overline{u'v'}\right|_{Q4} - \left|\overline{u'v'}\right|_{Q1} - \left|\overline{u'v'}\right|_{Q3} \tag{6.1}$$

If value of P larger then zero, indicates turbulent production.

Looking at the curves in Fig. 6.9 one can clearly observe that the turbulent production P is close to zero at the beginning, where the boundary layer is still quasi-laminar. More downstream where the retransition begins, an increase for all quadrant events can be observed, but Q2 events show the highest rise. This leads to a strong increase of the turbulent production P which agrees with the observations above. The Q2 events, which represent a movement of low speed fluid away from the wall (*ejection*) dominate the retransition process over the other quadrant events. It shows together with the turbulent production P a distinctive maximum at $y = 1\ mm$ and $x = 1400\ mm$ which represents the end of retransition (compare Fig. 4c of paper 6).

At the last position, where the boundary layer is again fully turbulent, decreasing Q2 are surpassed by further increasing Q4 events. Q4 events represent an inrush of high speed fluid

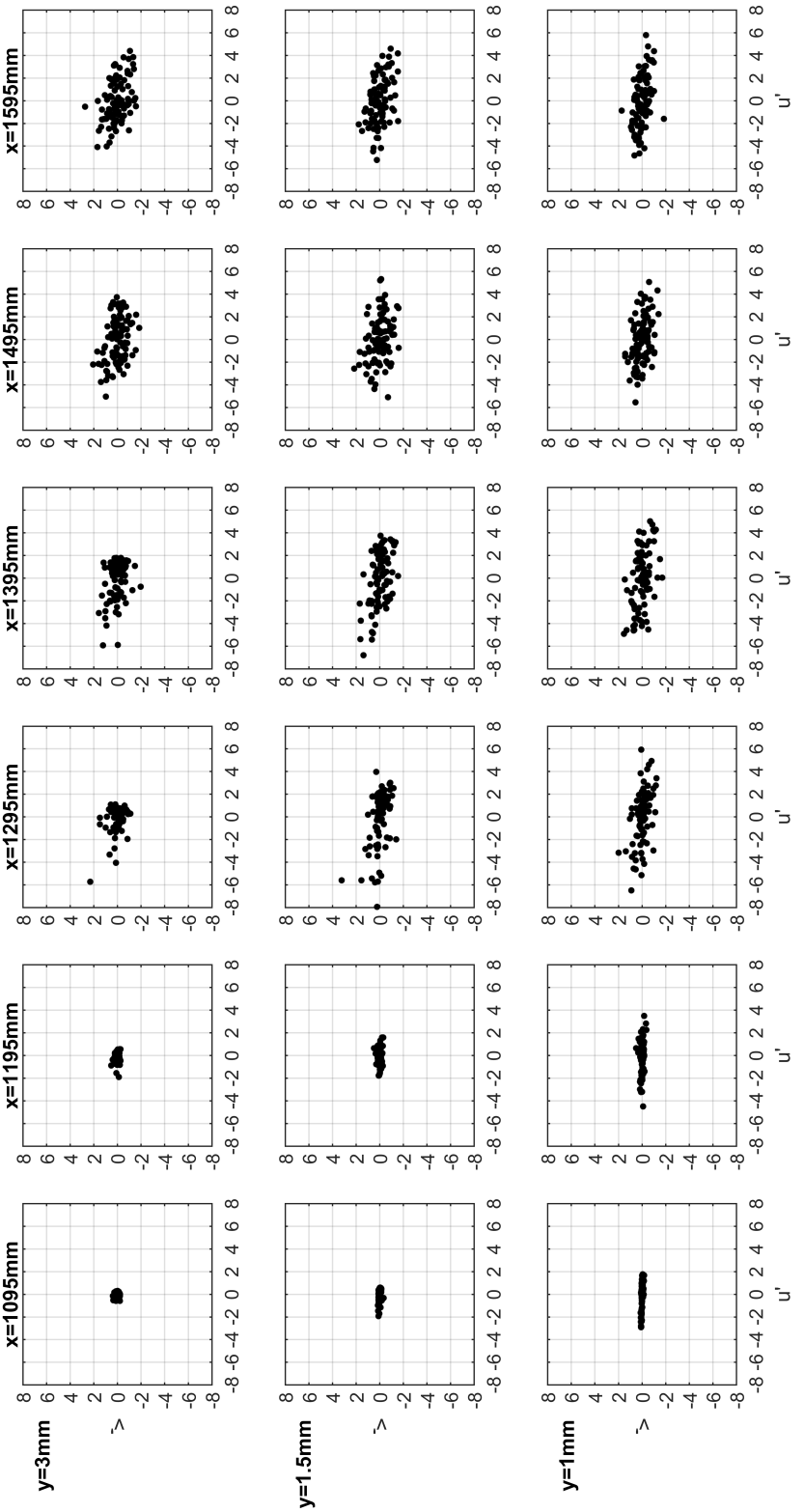

Figure 6.8: Quadrant analysis of the streamwise u' and lateral v' velocity fluctuations inside the boundary layer at several streamwise positions at $y = 1\ mm$, $y = 1.5\ mm$ and $y = 3\ mm$; showing LES data.

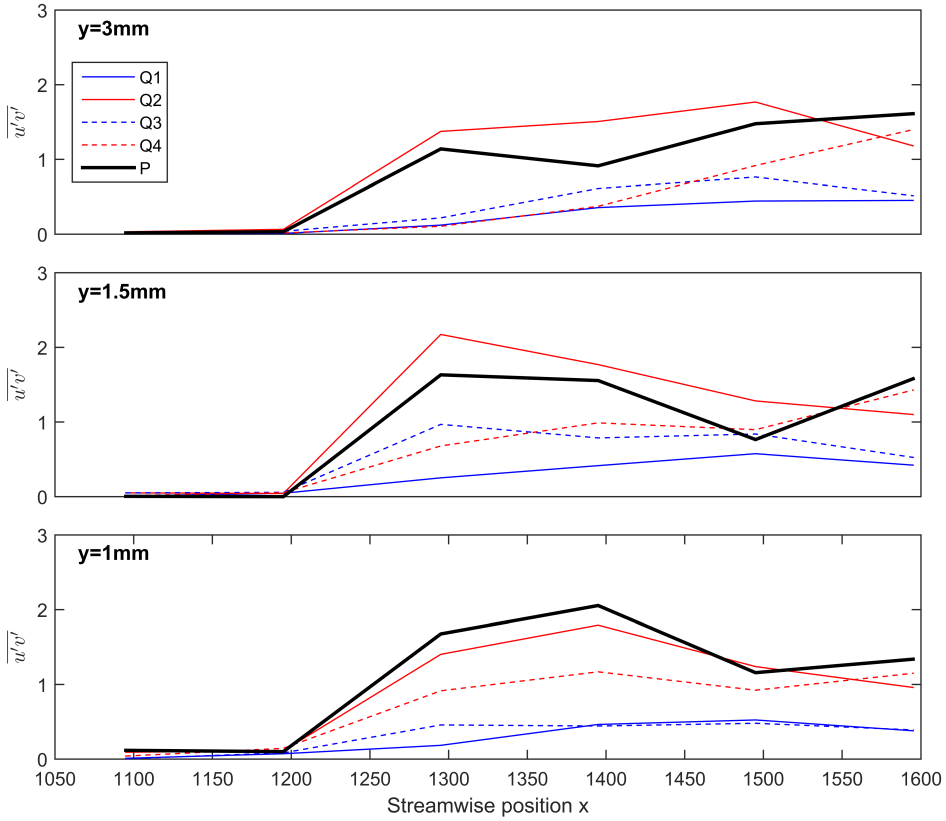

Figure 6.9: Quadrant analysis of the turbulent shear stress $\overline{u'v'}$ inside the boundary layer at $y = 1\ mm$, $y = 1.5\ mm$ and $y = 3\ mm$ along the plate; showing LES data.

(*sweep*). At this last position, also the Q1 and Q3 events decrease slightly and the production close to the wall increases again.

6.7. Paper 7: On the capability of the γ-Re_θ transition model to predict relaminarization

P. Bader, P. Pierigner and W. Sanz, "On the capability of the γ-Re_θ transition model to predict relaminarization," *Proceedings of 12th European Conference on Turbomachinery Fluid dynamics and Thermodynamics, April 3-7, 2017, Stockholm, Sweden*, ETC2017-328, 2017.

ON THE CAPABILITY OF THE γ-Re_θ TRANSITION MODEL TO PREDICT RELAMINARIZATION

P. Bader [a] *- P. Pieringer* [b] *- W. Sanz* [a]

[a] Institute for Thermal Turbomachinery and Machine Dynamics,
Graz University of Technology
Inffeldgasse 25A, 8010 Graz, Austria. pascal.bader@tugraz.at
[b] Springer und Pieringer EDV Dienstleistungen OG
Haydngasse 7/1 8010 Graz, Austria

ABSTRACT

In flows along solid body surfaces the boundary layer represents the narrow zone between the wall and the free stream where viscous effects are important. Its state of flow (laminar or turbulent) may have strong impact on transport processes like wall friction and heat transfer. These processes influence the efficiency as well as the thermal stress, for example of a turbine blade, and may affect other flow characteristics in a machine as well.
Under certain flow conditions (like strong acceleration), a reverse transition or relaminarization from turbulent to laminar can also occur. In this work, this type of process is numerically analyzed in order to see the capability of the the well-known γ-Re_θ transition model in predicting relaminarization. The model is used together with the Menter SST turbulence model which are both incorporated in the in-house code LINARS.
First, the behavior of the flow during acceleration is analyzed. The results of the present case are compared qualitatively to DNS and measurement results. It is shown, that the transition model successfully predicts relaminarization. Secondly it is found out, which processes inside the boundary layer are triggered by the model allowing us a better understanding how relaminarization is modeled.
The objective of this work reaching a better understanding of the model parameters influencing the relaminarization prediction by the γ-Re_θ transition model will enable an effective future parameter modification in order to enhance the accuracy of the model.

KEYWORDS

Relaminarization, transition modeling, CFD, flat plate testcase

NOMENCLATURE

C	Streamwise extend of the acceleration zone
D/E	Dissipation term
k	Turbulence kinetic energy
k_L	Laminar kinetic energy
K	(Launder) acceleration parameter
P	Production term
$\tilde{Re}_{\theta t}$	Local transition onset momentum-thickness Reynolds number
$Re_{\theta t}$	Transition onset momentum-thickness Reynolds number based on free stream conditions
Tu	Turbulence Intensity

u	Velocity
u^*	Non-dimensional velocity
u^+	Non-dimensional velocity in wall coordinates
u_∞	Local free stream velocity
$u_{\infty,in}$	Free-stream velocity at the inlet
x	Streamwise distance
x_0	Streamwise position of the start of the acceleration zone
y^*	Non-dimensional coordinate
y^+	Non-dimensional wall coordinate
$\delta(x)$	Boundary layer thickness
γ	Intermittency
ν	Kinematic viscosity
ρ	Density
τ_W	Wall shear stress

INTRODUCTION

The boundary layer represents the narrow zone between a solid body wall and the free stream where viscous effects are significant. The state of this boundary layer, whether it is laminar or turbulent, is on one hand influenced by free stream parameters, like the velocity, acceleration or turbulence level of the free stream and on the other hand influences the free stream as well as wall parameters, like skin friction or heat transfer. These parameters may influence for instance the efficiency of a blade and also the thermal stresses which the blade has to withstand. Therefore, an understanding of the state of the boundary layer, i.e. the position, length etc. of the transitional zone, is very important for the designer of turbomachines.

It is vitally important to understand the impact of the influencing parameters on the onset position and length of the transitional zone in order to predict and potentially control the state of the boundary layer. In turbomachinery, the efficiency of blades and stages can be enhanced considering transition. This allows the overall machine performance to be improved. Mayle [1991] published a comprehensive review of the importance of transition in gas turbines. He analyzed experiments performed by several research groups in order to find the influence of different flow parameters on the transition process.

In the last years, additional experiments were performed by many research groups. Yip et al. [1993] performed in-flight measurements, detected transition with the help of Preston tubes and analyzed the influence of the flight conditions on the boundary layer along an airfoil. Oyewola et al. [2003] showed how the flow in the boundary layer can be measured with hot-wire anemometry and Oyewola [2006] Laser-Doppler anemometry (LDA). Widmann et al. [2012] performed near-wall measurements with Particle Image velocimetry (PIV) . Hot-film measurements were performed, e.g., by Mukund et al. [2012], Preston-tube and thermographic measurements by Bader and Sanz [2015a] to investigate the transitional boundary layer. Additionally, Bader et al. [2016b] used Laser Interferometric vibrometry (LIV) to predict transition.

In addition to measurements, numerical models were developed to predict the laminar-turbulent transition process. Established models are, for example, the k-k_L-ω [Walters and Cokljat, 2008] and the γ-Re_θ [Langtry and Menter, 2009] model.

So far, only the transition from laminar to turbulent flow was described. Under certain flow conditions (like strong acceleration), however, a reverse transition or relaminarization from turbulent to laminar can occur. Up to now, only few measurements on relaminarization were

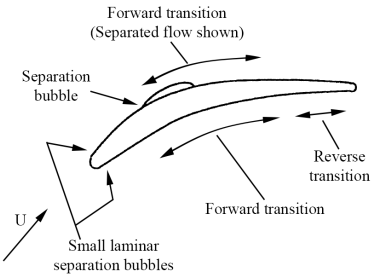

(a) Schematic drawing of a compressor blade.

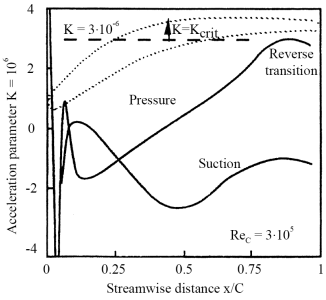

(b) K of a compressor blade.

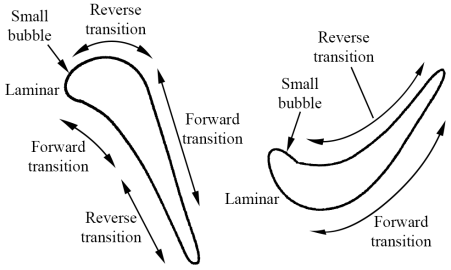

(c) Schematic drawing of a high pressure turbine blade.

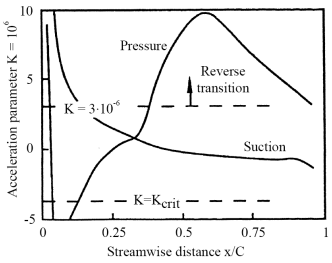

(d) K of a high pressure turbine blade.

Figure 1: Several applications where transition and relaminarization can occur (adopted from Mayle [1991]).

reported (e.g. Narasimha and Sreenivasan [1979], Ichimiya et al. [1998], Escudier et al. [1998], Mukund et al. [2006]). Therefore, at the Institute for Thermal Turbomachinery and Machine Dynamics (ITTM) of Graz University of Technology a project was launched in order to understand the process of relaminarization and its phases even further and test common threshold values for relaminarization by acceleration. First measurements performed at the institute already showed good results and relaminarization was detected [Bader et al., 2016a].

The studies performed within this project and by other research groups are not only applicable to simplified test cases, but they are also important under engine-representative conditions. As Mayle [1991] already showed, transition as well as relaminarization take place on compressor as well as turbine blades. Figures 1a and b, show a schematic drawing of the processes taking place along a compressor blade together with the acceleration parameter K (see Eq. (8)); Figs. 1c and d show the same for a turbine blade. It can be clearly observed, that transition as well as relaminarization occur along a blade, influencing skin friction, heat transfer as well as boundary layer thicknesses which may change the downstream flow angle.

The process of relaminarization has also been extensively analyzed by the works of Fernholz and Warnack [1998] and Warnack and Fernholz [1998] who analyzed axisymmetric turbulent flows under favorable pressure gradients. Their presented DNS studies impressively showed the influence of acceleration on the boundary layer.

Since the processes within the boundary layer are important for the design of turbomachinery, this work deals with the numerical prediction of relaminarization. It has already shown by the authors [Bader and Sanz, 2015b, 2017] that the γ-Re_θ model is able to predict relaminar-

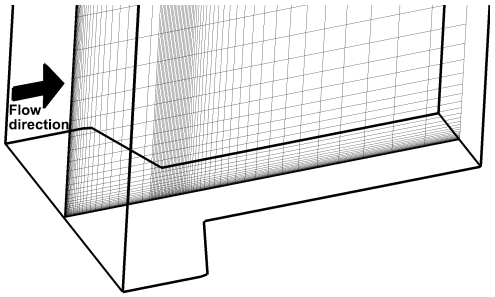

Figure 2: 3D illustration of the quasi-3D mesh.

ization, although there is an uncertainty in the location and streamwise extent. Therefore in this paper it should be investigated, how the model predicts relaminarization in order to be able to modify model parameters in an effective way to improve its prediction capabilities in the future.

The following section presents the numerical setup used for the study. Thereafter we present and discuss the simulation results with a focus on the model parameters. The paper ends with a short summary and the conclusions.

NUMERICAL SETUP

In this work, the CFD simulations have been performed with the in-house code LINARS. LINARS has been developed at Graz University of Technology at the ITTM by Pecnik et al. [2005]. The code solves the Reynolds-averaged Navier-Stokes (RANS) equations in conservative form with a fully-implicit, time-marching finite-volume method. The inviscid (Euler) fluxes are discretized with the upwind flux-difference splitting method of Roe [1981]. The incompressible solutions are obtained with a pseudo-compressibility method.

For the numerical study a generic test case has been designed. The flow along a flat plate was investigated, where the pressure gradient necessary for the acceleration was imposed by a decrease of the cross section in the quasi-3D direction. This has the advantage that no side wall effects like separation or sidewall boundary layer displacement influences the investigated flow along the plate. The structured mesh consists of 6,144 hexaeder elements and is shown in Fig. 2. The streamwise length upstream of the acceleration area has been set in such a way, that the boundary layer is able to fully transit to turbulent flow upstream of the acceleration zone for the calculations where the transition model was used. The y^+ value is kept between 0.1 and 1, which is recommended by Langtry et al. [2004] for the γ-Re_θ transition model.

At the inlet a total pressure of $p = 1.0005$ bar, a total temperature of 300 K and a turbulence intensity of $Tu = 5$ % and $Tu = 12$ %, respectively, depending on the case are imposed. Additionally the integral length scale l was set to 0.0001 m in order to specify the dissipation. At the outlet a static pressure was set, resulting in an inlet speed for all investigated cases of $u_{\infty,in} = 10$ m/s. The chord Reynolds number $Re_C = u_{\infty,in} \cdot C/\nu$, where C represents the length of the plate, is $Re_C = 3 \cdot 10^6$.

As turbulence model the well known SST k-ω turbulence model by Menter [1994] has been used. For modeling transition this turbulence model is coupled with a transition model, namely the γ-Re_θ transition model by Langtry and Menter [2009]. It solves two additional transport equations in order to influence the production and dissipation of the turbulence kinetic energy

k within the turbulence model. The two equations are

$$\frac{\partial(\rho\tilde{Re}_{\theta t})}{\partial t} + \frac{\partial(\rho U_j \tilde{Re}_{\theta t})}{\partial x_j} = P_{\theta t} + \frac{\partial}{\partial x_j}\left[\sigma_{\theta t}(\mu + \mu_t)\frac{\partial \tilde{Re}_{\theta t}}{\partial x_j}\right] \tag{1}$$

$$\frac{\partial(\rho\gamma)}{\partial t} + \frac{\partial(\rho U_j \gamma)}{\partial x_j} = P_\gamma - E_\gamma + \frac{\partial}{\partial x_j}\left[\left(\mu + \frac{\mu_t}{\sigma_f}\right)\frac{\partial \gamma}{\partial x_j}\right] \tag{2}$$

where $\tilde{Re}_{\theta t}$ the local transition onset momentum-thickness Reynolds number and γ represents the intermittency, i.e. the state of transition and varies between zero and one, where one represents fully turbulent flow conditions.

The empirical correlations used for the prediction of transition are based on the idea that after surpassing a critical momentum thickness Reynolds number $Re_{\theta t}$ transition is triggered. But in this way it is a one-dimensional criterion which is only valid along the wall. Therefore Langtry and Menter [2009] introduced the transport variable $\tilde{Re}_{\theta t}$ as a transition criterion which is applicable in the whole flow field. For this reason the production term of the $\tilde{Re}_{\theta t}$ equation is designed in such a way, that $\tilde{Re}_{\theta t}$ is forced to adopt the value of the empirically prescribed transition onset Reynolds number $Re_{\theta t}$ in the free stream. The production term of $\tilde{Re}_{\theta t}$ is defined as

$$P_{\theta t} = c_{\theta t}\rho\frac{\rho U^2}{500\mu}\left(Re_{\theta t} - \tilde{Re}_{\theta t}\right)(1.0 - F_{\theta t}) \tag{3}$$

where $Re_{\theta t}$ represents the transition onset momentum-thickness Reynolds number based on free stream conditions. The blending function $F_{\theta t}$ is used to turn off the source term in the boundary layer and allows the transported scalar $\tilde{Re}_{\theta t}$ to diffuse in from the free-stream. $F_{\theta t}$ is equal to zero in the free-stream and one in the boundary layer. [Langtry and Menter, 2009]

The correlation for $Re_{\theta t}$ used by Langtry and Menter [2009] considers the influence of the turbulence intensity Tu and the velocity gradient du/ds on the transition onset.

The production and the dissipation terms of the intermittency γ are defined as

$$P_\gamma = F_{\text{length}} c_{a1}\rho S\left[\gamma F_{\text{onset}}\right]^{0.5}(1 - c_{e1}\gamma) \tag{4}$$

$$E_\gamma = c_{a2}\rho\Omega F_{\text{turb}}(c_{e2}\gamma - 1) \tag{5}$$

where F_{length} and F_{onset} depend on the local $\tilde{Re}_{\theta t}$ value and determine the length and onset of transition in the flow field. On the other hand F_{turb} only depends on the local turbulence parameters (k and ω). The values of F_{length}, F_{onset} and F_{turb} can vary between $0 \leq F_{\text{length}} \leq 40$, $0 \leq F_{\text{onset}} \leq 2$ and $0 \leq F_{\text{turb}} \leq 1$, respectively.

The coupling of the transition model is done by modifying the original production term P_k and dissipation term D_k of the k equation of the SST turbulence model:

$$\tilde{P}_k = \gamma_{\text{eff}}\, P_k \tag{6}$$

$$\tilde{D}_k = \min(\max(\gamma_{\text{eff}}, 0.1), 1.0)\, D_k \tag{7}$$

RESULTS AND DISCUSSION

As described above a first step is to understand what the transition model does and more important why it can predict relaminarization and what happens during this process. Therefore the results of the generic test-case is presented in this section.

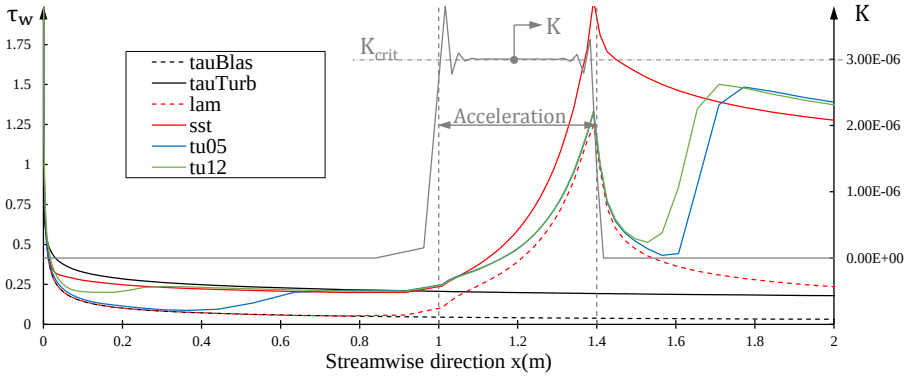

Figure 3: Local wall shear distribution τ_w along the test section.

In a first step it is shown, that relaminarization can be predicted by the transition model. Therefore in Fig. 3 the local wall shear τ_w is given together with the Launder acceleration parameter K. K is defined as

$$K = \frac{\nu}{u_\infty^2} \cdot \frac{du_\infty}{dx} \tag{8}$$

where u_∞ is the local free stream velocity, ν the kinematic viscosity and du_∞/dx the streamwise velocity gradient. According to literature, if this acceleration value surpasses a critical value $K > K_{crit} = 3.0 \cdot 10^{-6}$, relaminarization should most likely occur.

In the figure several curves are given, where the curve labeled as *tauBlas* shows the analytical Blasius (=laminar) solution for zero pressure gradient flow (ZPG), *tauTurb* the empirical turbulent solution for ZPG, *lam* a fully laminar simulation result, *sst* a fully turbulent SST solution, *tu05* and *tu12* a solution with the transition model activated for a free-stream turbulence intensity of $Tu = 5$ % and $Tu = 12$ %, respectively. The turbulence intensity of $Tu = 5$ % was chosen according to the measurement results presented by [Bader and Sanz, 2015b, 2017] and $Tu = 12$ % as an engine relevant value.

The curve for the empirical turbulent solution (ZPG) is defined as

$$\tau_{w,turb} = 0.0577 \cdot \frac{\rho \cdot u_{\infty,in}^2}{2} \cdot Re_x^{-1/5} \tag{9}$$

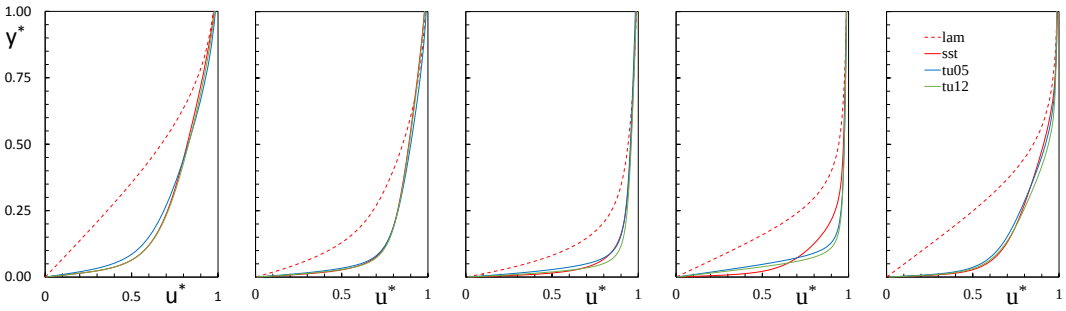

(a) $x = 0.76$ m. (b) $x = 1.11$ m. (c) $x = 1.31$ m. (d) $x = 1.50$ m. (e) $x = 1.93$ m.

Figure 4: Non-dimensional velocity profiles y^* vs. u^* at several x locations.

where $u_{\infty,in}$ represents the velocity at the inlet.

Looking at the results it can be observed that all cases except the fully laminar case (*lam*) are completely turbulent upstream of the acceleration zone. At the beginning of acceleration all curves begin to depart from their analytical/empirical ZPG solutions because the wall shear rises due to the acceleration.

The two curves for the activated transition model (*tu05* and *tu12*) start to differ from the fully turbulent CFD solution where the acceleration parameter K is just above the critical value K_{crit}. During the constant acceleration the two solutions approach the laminar solution, but they never coincide fully. This indicates a laminar-like boundary layer behavior at least close to the wall.

At approximately $x = 1.5$ m the boundary layer of these cases start retransition towards the fully turbulent solution.

It can also be clearly seen, that the free stream turbulence intensity Tu has no influence on the relaminarization, which is surprising, since it has an influence on laminar-to-turbulent transition, which can be seen by their retransitional behavior.

In order to see the change of the velocity distribution within the boundary layer the velocity profiles of the fully laminar (*lam*) and fully turbulent case (*sst*) are given together with the two transitional cases in Figs. 4a to e at different streamwise positions. The profiles are given as non-dimensional velocity profiles $y^* = y/\delta$ against $u^* = u/u_\infty$.

At the first position ($x = 0.76$ m, Fig. 4a) which is upstream of the acceleration, the transitional solution agrees more or less with the fully turbulent solution. At $x = 1.16$ m (Fig. 4b) which is the beginning of acceleration, the fully turbulent solution and the transitional solutions agree well. Fig. 4c shows the profiles at $x = 1.31$ m which represents a position, where according to the τ_w plot the boundary layer is laminar. In the graph it can be seen that close to the wall the transitional solutions coincide more with the laminar solution, whereas at the outer part of the boundary layer the two solutions agree more with the fully turbulent computation. More downstream at $x = 1.50$ m (Fig. 4d), which is already downstream of the acceleration zone, the profiles agree very well with the laminar profile over a larger distance from the wall. Fig. 4e which shows the profile at $x = 1.93$ m where retransition has already occurred, the profiles agree again with the fully turbulent solution in the near-wall region.

Additionally the results of the present simulation are compared qualitatively to the DNS data of Warnack and Fernholz [1998]. Therefore the velocity profiles are given in wall coordinates y^+/u^+ defined as

$$y^+ = \frac{y \cdot u_\tau}{\nu} \tag{10}$$

$$u^+ = \frac{u}{u_\tau} \tag{11}$$

where $u_\tau = (\tau_w/\rho)^{1/2}$ represents the friction velocity. The profiles in wall coordinates are given in Fig. 5a to e at the same streamwise positions as in Fig. 4 for the present simulation and in Fig. 5f the results of Warnack and Fernholz [1998] are given[1]. Additionally the $y^+ = u^+$ and $u^+ = 1/\kappa \ ln(y^+) + B^+$ profiles are given as laminar and turbulent reference, respectively.

At the first position ($x = 0.76$ m) one can clearly observe, that the transitional solutions agree with the fully turbulent one. Within the acceleration zone a typical behavior of all profiles

[1] Colored lines have been added to the DNS data for optical guidance, but only for profiles upstream of the retransition position

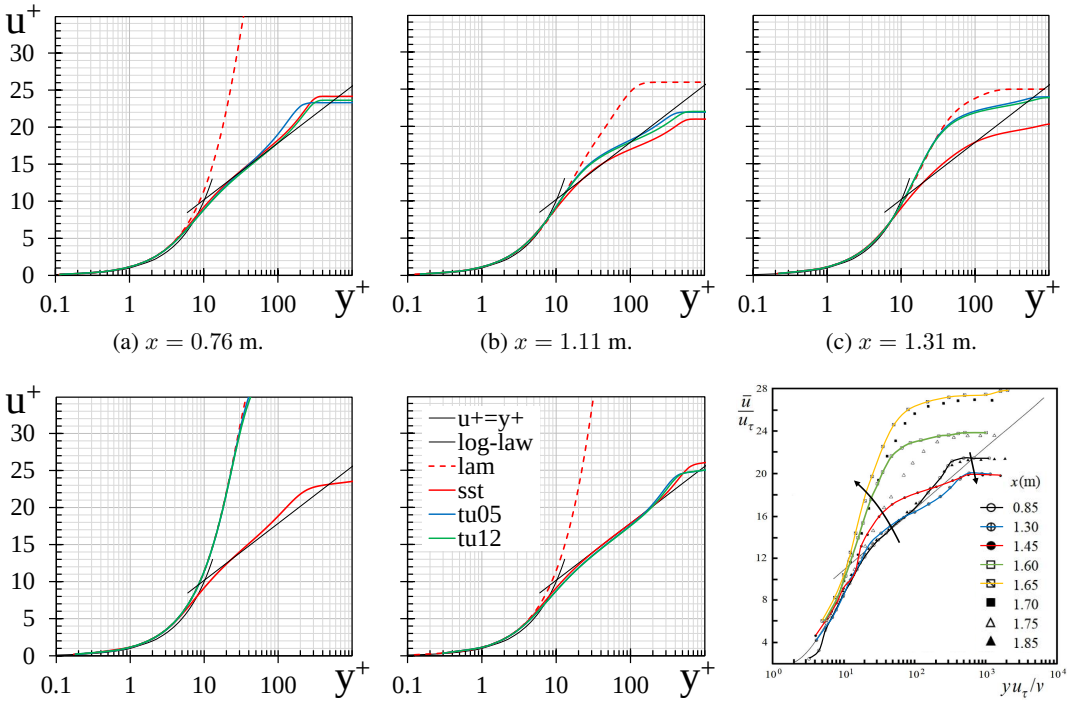

(a) $x = 0.76$ m. (b) $x = 1.11$ m. (c) $x = 1.31$ m.

(d) $x = 1.50$ m. (e) $x = 1.93$ m. (f) DNS of Warnack and Fernholz [1998] (color lines added for optical guidance).

Figure 5: Velocity profiles in wall coordinates y^+ vs. u^+ at several x locations together with the DNS results of Warnack and Fernholz [1998].

can be observed: Due to the strong FPG the outer part of the profiles ($y^+ > 100$) drops below the log-law. This behavior has also been observed by Warnack and Fernholz [1998] and is indicated by the right arrow in Fig. 5f which shows the change of the black to the blue profile. At $x = 1.11$ m it can be additionally observed that the transitional cases agree with the fully laminar one at the inner part of the boundary layer (up to $y^+ \approx 12$). We can therefore conclude, that relaminarization begins at the inner part of the boundary layer. The extend of this inner zone of good agreement between the laminar and transitional cases grows with streamwise position until these three curves agree with each other. This again agrees with the observations of Warnack and Fernholz [1998] (second arrow in Fig. 5f showing the change of the blue profile over the red and green one to the yellow one). At $x = 1.93$ m both transitional cases are fully turbulent again, thus agreeing with the SST solution.

To sum up, the wall shear stress and the velocity profiles have shown that the model is able to predict relaminarization. The behavior during relaminarization and retransition computed by the γ-Re_θ transition model agrees qualitatively well with published measurements [Bader et al., 2016a] and DNS data [Warnack and Fernholz, 1998].

In the following it should be explained how the relaminarization process is triggered within the transition model. Therefore in Fig. 6 the contour plots of several properties together with iso-lines are shown for the transitional case with a turbulence intensity of $Tu = 12$ %.

In Fig. 6a the intermittency γ is presented together with the boundary layer thickness $\delta(x)$

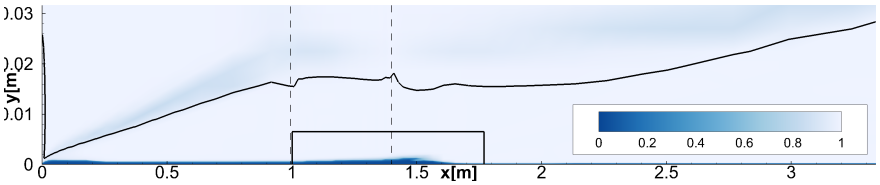

(a) Intermittency γ.

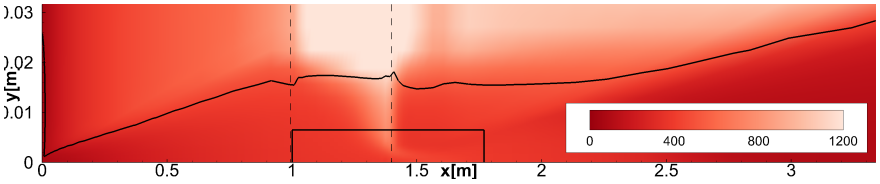

(b) Local transition onset momentum-thickness Reynolds number $\tilde{Re}_{\theta t}$.

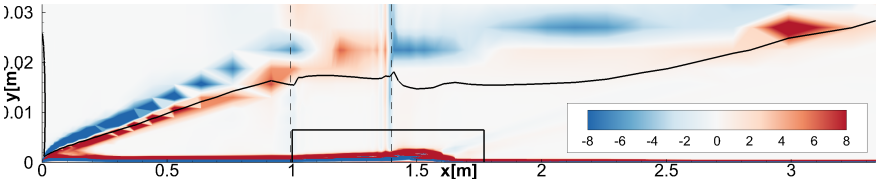

(c) Change of intermittency C_γ.

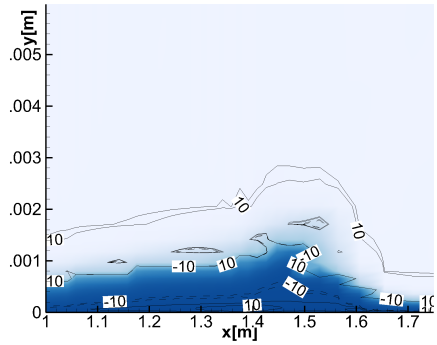

(d) Contour: γ, iso-lines: C_γ.

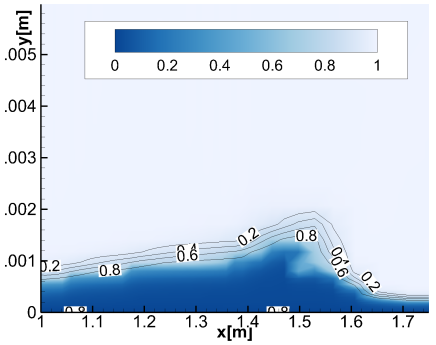

(e) Contour: γ, iso-lines: F_{turb}.

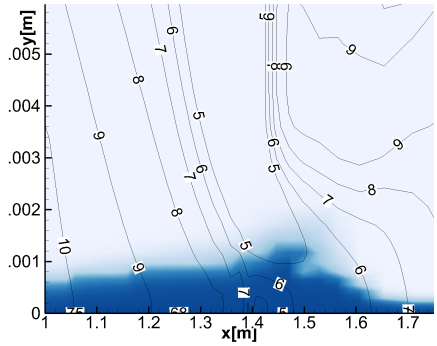

(f) Contour: γ, iso-lines: F_{length}.

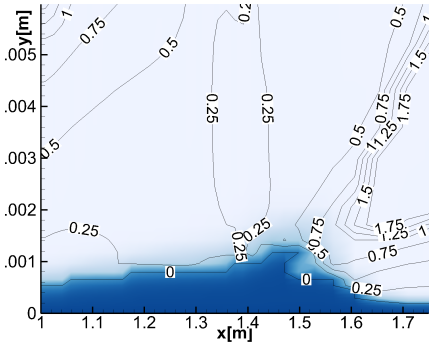

(g) Contour: γ, iso-lines: F_{onset}.

Figure 6: Contour plots at midspan.

(solid black line), which is defined as $u(y = \delta) = 0.99u_\infty$. It can be seen, that the intermittency in most parts of the boundary layer is approximately 1, only a small part close to the wall shows $\gamma = 0$. This small area represents the laminar sublayer. Within the acceleration zone (within the dashed black lines) this laminar sublayer increases its height in the latter part of this zone. This on the other hand leads to a reduction of the velocity gradient close to the wall which reduces the wall shear. This agrees with the observations above. The question is, what triggers this thickening of the inner part of the boundary layer and why it has a streamwise delay compared to the acceleration.

To answer these questions, $\tilde{Re}_{\theta t}$ is given in Fig. 6b. It can be clearly seen, that the value and thus the transition threshold rises in response to the acceleration in the free-stream, but as discussed above $\tilde{Re}_{\theta t}$ needs some streamwise distance in order to diffuse to the inner boundary layer. This delay fits to the delay of the thickening of the low-γ-zone described above. Downstream of the acceleration, $\tilde{Re}_{\theta t}$ decrease again, promoting retransition.

As shown above, $\tilde{Re}_{\theta t}$ influences the production term of the intermittency P_γ. On the other hand, the turbulent variables (F_{turb}) influence the dissipation term E_γ. In order to see which is dominating, Fig. 6c shows the source term of the γ equation C_γ defined as

$$C_\gamma = P_\gamma - E_\gamma. \tag{12}$$

Focusing on the behavior of C_γ close to the wall in Fig. 6c it can be seen that there is a high dissipation close to the wall were the thickening of the inner layer takes place. Just outside of this zone there is a high production of γ. To see this in more detail, Fig. 6d gives the intermittency as contour plot together with the source term C_γ as a magnified view of the black box in Figs. 6a to c. It can be clearly seen, that the area of destruction (negative C_γ) fits to the low-γ area, whereas the area of higher C_γ fits to areas with $\gamma \approx 1$.

As shown in Eq. (5) the dissipation depends on the factor F_{turb}. In Fig. 6e the iso-lines of this value are illustrated together with the intermittency γ as contour plot. It can be seen, that F_{turb} reaches its maximum value close to the wall, leading to a high dissipation. The shape of this high F_{turb} zone agrees well with the shape of the low-γ zone close to the wall.

The production of γ depends on the factors F_{length} and F_{onset} (compare Eq. (4)). These two values are influenced by - beside others - the local transition onset momentum-thickness Reynolds number $\tilde{Re}_{\theta t}$. The iso-lines of these two factors are given in Figs. 6f and g, respectively, with the contour plot of γ. It can be clearly seen that both values decrease with the increase of $\tilde{Re}_{\theta t}$ shown in Fig. 6b. This leads to a reduction of the production in this area. Together with the higher dissipation described above this results in a thickening of the inner laminar layer. At approximately $x \approx 1.65$ m where $\tilde{Re}_{\theta t}$ decreases again, F_{length} and F_{onset} increase. This leads to a high production of γ promoting the fast retransition explained earlier in this work.

To sum up, the acceleration leads to a rise of $\tilde{Re}_{\theta t}$ outside the boundary layer. This rise is then transported into the boundary layer and leads in the rear part of the acceleration to a drop of F_{length} and F_{onset}. This drop reduces the production of γ. On the other hand F_{turb}, which is not influenced by $\tilde{Re}_{\theta t}$ but by the turbulence values, rises which leads to a higher dissipation of γ. These two effects yield a thickening of a low-γ-region close to the wall and ultimately to a decrease of the velocity gradient, thus wall shear.

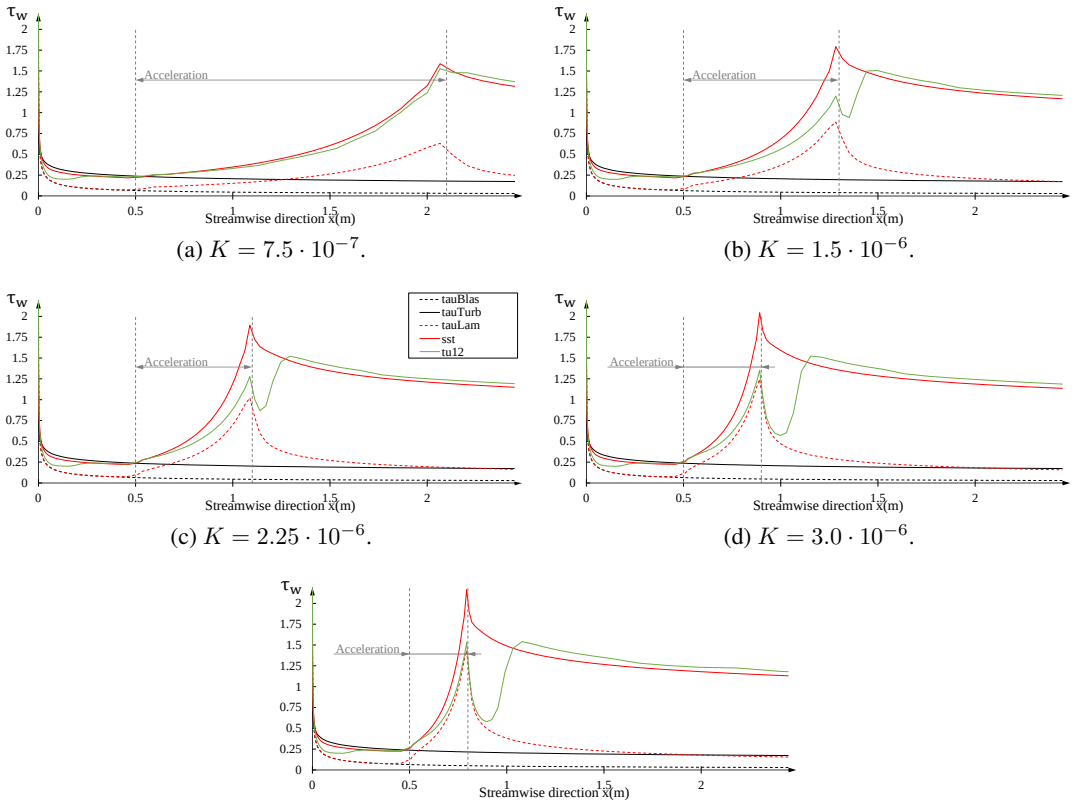

(a) $K = 7.5 \cdot 10^{-7}$.

(b) $K = 1.5 \cdot 10^{-6}$.

(c) $K = 2.25 \cdot 10^{-6}$.

(d) $K = 3.0 \cdot 10^{-6}$.

(e) $K = 4.0 \cdot 10^{-6}$.

Figure 7: Local wall shear distribution τ_w along the test section for different acceleration parameters K.

Influence of K on relaminarization prediction

As discussed above, the acceleration parameter K is considered as a critical parameter for relaminarization by acceleration. According to literature relaminarization occurs when the value surpasses $3 \cdot 10^{-6} \leq K_{crit} \leq 3.5 \cdot 10^{-6}$ [Bardi Narayanan and Ramjee, 1969, Blackwelder and Kovasznay, 1972, Narasimha and Sreenivasan, 1979, Mayle, 1991, Ichimiya et al., 1998, Escudier et al., 1998, Mukund et al., 2006]. Therefore a study was performed to see how the model reacts on the acceleration parameter. The variation of K has been done with a change of the acceleration length at the same inlet and outlet conditions and an inlet turbulence of $Tu = 12\%$.

Figure 7a to e shows different distributions of the wall shear τ_w along the streamwise coordinate x. The given curves in the figures represent the fully turbulent, transitional and fully laminar solution for acceleration parameters from $K = 7.5 \cdot 10^{-7}$ up to $K = 4.0 \cdot 10^{-6}$, and additionally the laminar and fully turbulent solution for zero-pressure-gradient flow.

At first, it is interesting to notice that the wall shear at the end of acceleration for the fully laminar and fully turbulent solution increases significantly with increasing acceleration parameter and thus decreasing length of acceleration. The reason for this behavior is that the boundary layer needs some flow length to adapt to the increasing free-stream velocity which is less available the shorter the acceleration zone is. This is visible by the decrease of wall shear after the

acceleration zone where the boundary layer has time to adapt to the higher free-stream velocity. But within the acceleration zone the gradient between boundary layer flow and free-stream flow increases the shorter the acceleration length is.

Regarding relaminarization prediction the trend of the transitional solution in relation to the fully turbulent and fully laminar solution is of interest. It can be seen, that the case with the lowest K-value ($K = 7.5 \cdot 10^{-7}$, Fig 7a) shows nearly no relaminarization and behaves similar to the fully turbulent solution. With increasing K (Figs. 7b and c) , the solutions tend more and more towards their laminar CFD solutions. When K reaches its stated critical value of $3.0 \cdot 10^{-6}$ (Fig. 7d), the local wall shear stress τ_w nearly fully approaches the laminar solution. If the acceleration is increased further above the critical value, nearly no difference regarding relaminarization can be observed. Thus the transition model is well calibrated to the critical value of $K = 3.0 \cdot 10^{-6}$. But the model also shows relaminarization in a weaker form for K values below the critical value.

Downstream of the acceleration zone, all cases which showed partial or full relaminarization show retransition at the same position, at approximately $\Delta x \approx 0.1$ m downstream of the end of the acceleration zone.

SUMMARY AND CONCLUSIONS

In this work a numerical study has been presented which gives a deep insight into the mechanism leading to relaminarization in the γ-Re_θ transition model making it capable of predicting relaminarization. The predicted behavior of the boundary layer velocity profiles has been also found from DNS calculations published. It has been found, that the local transition onset momentum-thickness Reynolds number $\tilde{Re}_{\theta t}$ rises due to acceleration. This rise causes the model parameters F_{length} and F_{onset} to drop, leading to a reduction of the production of the intermittency γ together with an increase of the intermittency dissipation E_γ. The resulting lower intermittency γ then leads to a decrease of the turbulence kinetic energy and thus to a reduced velocity gradient close to the wall and wall shear. This is visible by a change of the shape of the velocity profile in the boundary layer.

The following analysis of the influence of different acceleration parameters K on the relaminarization prediction showed, that the critical value of K stated in the literature is also well considered in the transition model. A higher K value only marginally changes the relaminarization behavior whereas for smaller K values partial relaminarization is also predicted by the simulation. Only for very low K values the flow remains fully turbulent.

So it can be concluded that the γ-Re_θ transition model can be also applied to highly accelerated flows where relaminarization can occur, but further calibration of the model with measurement data is recommended.

ACKNOWLEDGEMENTS

The authors gratefully acknowledge financial support from the Austrian Federal Ministry for Transport, Innovation and Technology in funding the work by the project RELAM within the Austrian Aeronautics Program TAKE OFF.

REFERENCES

P. Bader and W. Sanz. On the setup of a test bench for predicting laminar-to-turbulent transition on a flat plate. *Proceedings of the 12th International Symposium on Experimental Computational Aerothermodynamics of Internal Flows, Genova, Italy*, 2015a. ISAIF12-074.

P. Bader and W. Sanz. Measurement and simulation of flat-plate boundary layers in accelerated flow. *Poster presentation at ASME 2015 Turbo EXPO, Montreal, Canada*, 2015b. GT2016-58198.

P. Bader and W. Sanz. Measurements and simulation of a turbulent boundary layer exposed to acceleration along a flat plate. *Proceedings of 12th European Conference of Turbomachinery Fluid Dynamics & Thermodynamics ETC12*, April 2017. ETC2017-92.

P. Bader, M. Pschernig, W. Sanz, J. Woisetschläger, F. Heitmeir, W. Meile, and G. Brenn. Flat-plate boundary layers in accelerated flow. *Proceedings of ASME Turbo Expo 2016: Turbine Technical Conference and Exposition, Seoul, South Korea*, 2016a. GT2016-56044.

P. Bader, W. Sanz, J. Peterleithner, J. Woisetschläger, F. Heitmeir, W. Meile, and G. Brenn. Detecting transition on flat plate flow with laser interferometric vibrometry (LIV). *Proceedings of ASME Turbo Expo 2016: Turbine Technical Conference and Exposition, Seoul, South Korea*, 2016b. GT2016-56043.

M. A. Bardi Narayanan and V. Ramjee. On the criteria for reverse transition in a two–dimensional boundary layer. *Journal of Fluid Mechanics*, 35:225–241, 1969.

R. F. Blackwelder and L. S. G. Kovasznay. Large–scale motion of a turbulent boundary layer during relaminarization. *Journal of Fluid Mechanics*, 53:61–83, 1972.

M. P. Escudier, A. Abdel-Hameed, M. W. Johnson, and C. J. Sutcliffe. Laminarisation an re–transition of a turbulent boundary layer subjected to favourable presser gradient. *Experiments in Fluids*, 25:491–502, 1998.

H. H. Fernholz and D. Warnack. The effects of a favourable pressure gradient and of the reynolds number on an incompressible axisymmetric turbulent boundary layer. part 1: The turbulent boundary layer. *Journal of Fluid Mechanics*, 359:329–356, 1998.

M. Ichimiya, I. Nakamura, and S. Yamashita. Properties of a relaminarizing turbulent boundary layer under a favorable pressure gradient. *Experimental Thermal and Fluid Science*, 17: 37–48, 1998.

R. B. Langtry and F. R. Menter. Correlation-based transition modeling for unstructured parallelized computational fluid dynamics codes. *AIAA Journal*, 47(12):2894–2906, 2009.

R. B. Langtry, F. R. Menter, S. R. Likki, Y. B. Suzen, P. G. Huang, and S. Völker. A correlation based transition model using local variables part 2: Test cases and industrial applications. *Proceedings of ASME 2004 Turbo EXPO, Vienna, Austria*, 2004. GT2004-53454.

R. E. Mayle. The role of laminar-turbulent transition in gas turbine engines. *Journal of Turbomachinery*, 113(4):509–537, October 1991.

F. R. Menter. Two-equation eddy-viscosity turbulence models for engineering applications. *AIAA Journal*, 32(8):1598–1605, 1994.

R. Mukund, P. R. Viswanath, R. Narasimha, A. Prabhu, and J. D. Crouch. Relaminarization in highly favourable pressure gradients on a convex surface. *Journal of Fluid Mechanics*, 566: 97–115, 2006.

R. Mukund, R. Narasimha, P. R. Viswanath, and J. D. Crouch. Multiple laminar-turbulent transition cycles around a swept leading edge. *Experiments in Fluids*, 53:1915–1927, 2012.

R. Narasimha and K. R. Sreenivasan. Relaminarization of fluid flows. *Advances in applied mechanics*, 61:221–309, 1979.

O. Oyewola. LDV measurements in a pertubed turbulent boundary layer. *Journal of Applied Science*, 6(14):2952–2955, 2006.

O. Oyewola, L. Djenidi, and R. A. Antonia. Combined influence of the reynolds number and localised wall suction on a turbulent boundary layer. *Experiments in Fluids*, 35:199–206, July 2003.

R. Pecnik, P. Pieringer, and W. Sanz. Numerical investigation of the secondary flow of a transonic turbine stage using various turbulence closures. *In Proceedings of ASME Turbo Expo 2005, Reno-Tahoe, Nevada, USA*, 2005. GT2005-68754.

P. L. Roe. Approximate riemann solver, parameter vectors and differencing scheme. *Journal of Computational Physics*, 43:357–372, 1981.

K. Walters and D. Cokljat. A three-equation eddy-viscosity model for reynolds-averaged navier-stokes simulations of transitional flows. *Journal of Fluids engineering*, 130:1214011–12140114, 2008.

D. Warnack and H. H. Fernholz. The effects of a favourable pressure gradient and of the reynolds number on an incompressible axisymmetric turbulent boundary layer. part 2: The boundary layer with relaminarization. *Journal of Fluid Mechanics*, 359:357–381, 1998.

A. Widmann, A. Duchmann, A. Kurz, S. Grundmann, and C. Tropea. Measuring tollmien-schlichting waves using phase-averaged particle image velocimetry. *Experiments in Fluids*, 53:707–715, 2012.

L. P. Yip, P. Vijgen, J. D. Hardin, and C. P. van Dam. In-flight pressure distributions and skin-friction measurements on a subsonic transport high-lift wing section. *AGARD CP-515*, 1993.

6.8. Paper 8: Measurement and Simulation of a turbulent boundary layer exposed to acceleration along a flat plate

P. Bader and W. Sanz, "Measurement and Simulation of a turbulent boundary layer exposed to acceleration along a flat plate," *Proceedings of 12th European Conference on Turbomachinery Fluid dynamics and Thermodynamics, April 3-7, 2017, Stockholm, Sweden*, ETC2017-092, 2017.

MEASUREMENT AND SIMULATION OF A TURBULENT BOUNDARY LAYER EXPOSED TO ACCELERATION ALONG A FLAT PLATE

P. Bader - W. Sanz

Institute for Thermal Turbomachinery and Machine Dynamics, Graz University of Technology
Inffeldgasse 25A, 8010 Graz, Austria. pascal.bader@tugraz.at - wolfgang.sanz@tugraz.at

ABSTRACT

Flow in turbomachines is generally highly turbulent. The boundary layers, however, often exhibit laminar-to-turbulent transition. But also relaminarization of the turbulent flow may occur.
It is therefore important for the designer to understand the process of boundary layer transition in both directions and to determine the position of transition onset and the length of the transitional region. In the last decades several transition models have been developed to enable modern CFD codes to predict the transition and relaminarization processes. This has the advantage that the boundary layer behavior can be analyzed in advance, which enables the design of blades which trigger a "suitable" boundary layer. But in order to use CFD for designing tasks, the code must predict accurately and reliably the transition and relaminarization processes within the boundary layer.
Therefore in this work, the γ-Re_θ transition model is tested regarding relaminarization prediction. An in-house flat plate test case is analyzed where extensive measurement results are available. Since the test case shows flow pulsations caused by a separation bubble, different cases are investigated where either the full range of the measured velocity fluctuations or only the fluctuations above the integral subscale are prescribed as boundary conditions. Both boundary conditions are combined with either a steady or unsteady simulation where the latter allows to consider the velocity fluctuations additionally.
Aim of this variation is to understand the influence of inlet turbulence boundary condition of the predictions of the transition model regarding relaminarization.

KEYWORDS

Relaminarization, transition modeling, CFD, turbulence, RANS, URANS

NOMENCLATURE

c_f	Local skin friction coefficient
CFD	Computational fluid dynamics
ISW	Institute of Fluid Mechanics and Heat Transfer
ITTM	Institute for Thermal Turbomachinery and Machine Dynamics
K	(Launder) acceleration parameter
k, k_{tot}	Turbulent kinetic energy
k_T	Model-related turbulent kinetic energy
k_V	Turbulent kinetic energy resulting from velocity fluctuations
LDA	Laser-Doppler anemometry
LIV	Laser interferometric vibrometry

PIV	Particle image velocimetry
RMS	Root-mean square
SFF	Steady full frequency case
SHF	Steady high frequency case
TKE	Turbulent kinetic energy
Tu	Turbulence intensity
u_∞	Local free stream velocity
UFF	Unsteady full frequency case
UHF	Unsteady high frequency case
x	Streamwise distance (x = 0 mm - leading edge of the plate)
ν	Kinematic viscosity
ρ	Fluid density
τ_W	Skin friction
$'$	Fluctuation

INTRODUCTION

The boundary layer represents the narrow zone between a solid body wall and the free stream. In this small area viscous effects dominate the flow. The state of this boundary layer, whether it is laminar or turbulent, is on one hand influenced by free stream parameters, like the velocity, acceleration or turbulence level of the free stream and on the other hand influences the free stream itself as well as wall parameters, like skin friction or heat transfer (see e.g. Bader and Sanz [2015]).

These parameters are important in the real machine, since they strongly influence for instance the efficiency of a blade and also the thermal stresses which the blade has to withstand. Therefore, an understanding of the state of the boundary layer, moreover the position, length etc. of the transitional zone is very important for the designer of turbomachines.

At the first contact of a flowing fluid with a stationary structure, under appropriate flow conditions the boundary layer develops from laminar via a transitional zone to turbulent. The boundary layer passes through several stages within this transitional zone before becoming fully turbulent. Schlichting and Gersten [2006] extensively discussed these different stages.

It is vitally important to understand the influences from the various parameters on the onset position and length of the transitional zone in order to predict and potentially control the state of the boundary layer. In turbomachinery, the efficiency of blades and stages can be improved considering transition. This allows the overall machine performance to be improved. Mayle [1991] published a comprehensive review of the importance of transition in gas turbines. He analyzed experiments performed by several research groups in order to find the influence of different flow parameters on the transition process.

In the last years, additional experiments were performed by many research groups in order to better understand the processes in the boundary layer. Many different measurement techniques were used to find out more details of the boundary layer flow, e.g. Yip et al. [1993], Oyewola et al. [2003], Bader and Sanz [2016], Shin and Song [2015].

So far, only the transition from laminar to turbulent flow was described. Under certain flow conditions (like strong acceleration), however, a reverse transition or relaminarization from turbulent to laminar can occur. Up to now, only few measurements on relaminarization were reported (e.g. Narasimha and Sreenivasan [1979], Ichimiya et al. [1998], Escudier et al. [1998], Mukund et al. [2006]). Therefore, at the Institute for Thermal Turbomachinery and Machine

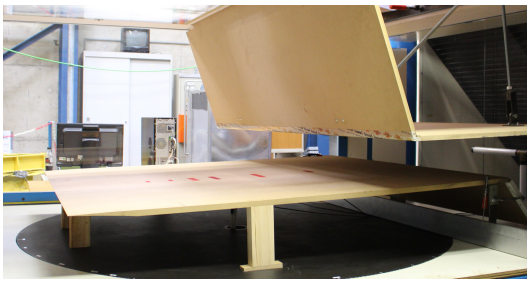

(a) Picture of the test bench.

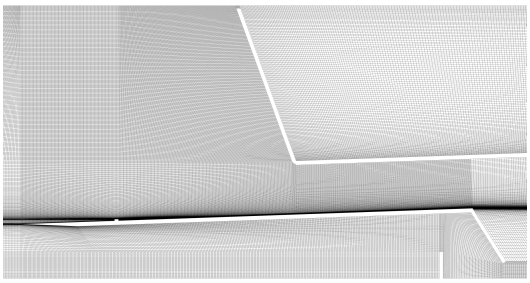

(b) Sketch of the 2D mesh used for the simulation.

Figure 1: Illustrations of the investigated case, the test bench and the used mesh (flow coming from left)

Dynamics (ITTM) of Graz University of Technology a project was launched in order to understand the process of relaminarization and its phases even further and evaluate common threshold values for relaminarization. First measurement performed at the institute showed the process of relaminarization (see Bader et al. [2016]).

Transition and relaminarization occurs in various cases in a turbomachinery (see e.g. [Mayle, 1991, Hampel et al., 2002, Händel et al., 2014]), however the focus in the last decades on this small share of the flow has been reduced, although it has an influence on the main flow as well as wall parameters like skin friction or heat transfer. The possibility to predict the state of the boundary layer in advance enables a design of a turbomachinery blade which benefits of the different advantages of the boundary layer stages. In order to enable such a design process, CFD codes can be used to analyze different variations of a blade. Therefore transition models have been developed, e.g. the γ-Re_θ [Langtry and Menter, 2009]. This model uses free-stream parameters like the turbulence intensity to trigger transition and relaminarization. As Bader et al. [2017] showed the model is capable of predicting relaminarization, but the length of the laminar-like zone before retransition is predicted too short. The authors found that this is caused by a too early decrease of Re_θ in the free stream.

In this paperthe role of turbulence intensity in causing this early retransition should be analyzed. The idea for this investigation is, that the turbulence which is measured by CTA or LDA does not always agree to Tu used within the simulation. The difference here lies in the definition of the turbulent kinetic energy k. While the simulation differs between unsteady velocity fluctuations and k representing turbulence within the model, the measurement accumulates fluctuations of all frequencies to one root-mean-square (RMS) value of the velocity fluctuations and thus to k_{tot}. In the present case these differences are quite high, since an unsteady pulsation of a separation bubble triggers velocity fluctuations of rather low frequency, which is not captured as turbulence (k) by the turbulence model. The discrepancies between these two types of fluctuations (velocity and turbulent fluctuations) influences the set inlet turbulence and thus also the distribution of turbulence along the plate. The latter influences the transition model, thus the prediction of transition and relaminarization.

In this work also the question should be answered, if a stationary simulation is sufficient to predict a relaminarization process since it neglects unsteady velocity fluctuations entirely.

The following section presents the numerical setup and the test case used for the study. Thereafter we present and discuss the simulation results compared to the measurements. The paper ends with a short summary and the conclusions.

INVESTIGATED CASE AND NUMERICAL SETUP

The investigated case in this paper represents a flat plate test case, where the flow is accelerated due to a decrease of the cross-section of the flow area. A picture of the test bench can be seen in Fig. 1a. At the corner of the upper wall, at the end of the decrease of cross-section, a separation bubble is present. This separation bubble is small and does not extend to the boundary layer at the flat plate, but it pulsates and thus triggers fluctuation is the free stream. It has been found, that these fluctuations are not accounted by the turbulence model, but are measured by the LDA. The difference of the turbulent kinetic energy k between measurement and simulation is illustrated in Fig. 2b and is discussed later in this section.

The plate normal extension has been validated numerically and experimentally, and it has been found, that the separation bubble is small enough and does not influence the boundary layer directly, which means that streamlines inside the boundary layer remain undisturbed.

For the numerical simulation the commercial code ANSYS® CFX® v15.0 was used. The code uses a pressure correction scheme. The high resolution scheme has been selected for the advection as well as the turbulent numerics. The Navier-Stokes equation system is discretized with first order accuracy in areas where the gradients change sharply to prevent overshoots and undershoots and maintain robustness, and with second order in flow regions with low variable gradients to enhance accuracy [Ansys Inc., 2013].

As turbulence model the well-known SST k-ω turbulence model by Menter [1994] has been used together with the γ-Re_θ transition model by Langtry and Menter [2009].

The mesh used for the simulation is a 2D mesh consisting of approximately 660,000 nodes and y^+ was kept between 0.1 and 1 which is recommend by Langtry et al. [2004] for the γ-Re_θ transition model. The mesh is shown in Fig. 1b. At the numerical inlet the boundary conditions have been taken from 2D hot-wire anemometry measurements and along the plate the experimental data has been acquired by 2D Laser-Doppler anemometry (LDA). The measurements have already been presented by Bader et al. [2016] and for more information the interested reader is referred to this publication.

As already described above, both measurement techniques measure fluctuations of all frequencies (between their minimum and maximum resolved frequencies) and return a time signal including all these fluctuations. The turbulent kinetic energy k can then be derived with

$$k = \frac{1}{2} \cdot \left(\overline{(u')^2} + \overline{(v')^2} + \overline{(w')^2} \right) \tag{1}$$

where u', v' and w' represent the fluctuations in the three spatial dimensions, respectively.

Figure 2a shows a typical distribution of k over the frequency. The range right of the maximum describes the dissipation of larger to smaller eddies (*inertial subrange*) and the final dissipation to heat (*dissipation scale*). These fluctuations are normally the turbulence which can be calculated by a turbulence model, in this work the SST k-ω model

Below the *inertial subrange* fluctuations of lower frequencies are present in the so-called *integral scale*. These fluctuations can be found by an unsteady CFD calculation as unsteady velocity fluctuations.

Fig. 2b shows the distribution of k along the plate from the measurement results, the model-related TKE k_T which represents k taken directly from the turbulence model, a velocity-fluctuation-related TKE k_V found from an unsteady simulation and derived according to Eq. (1) and a total TKE which is described in the next section (see Eq. (9)). It can be seen, that the model-related k_T does not predict a rise in TKE as measured, since this rise is triggered by unsteady velocity

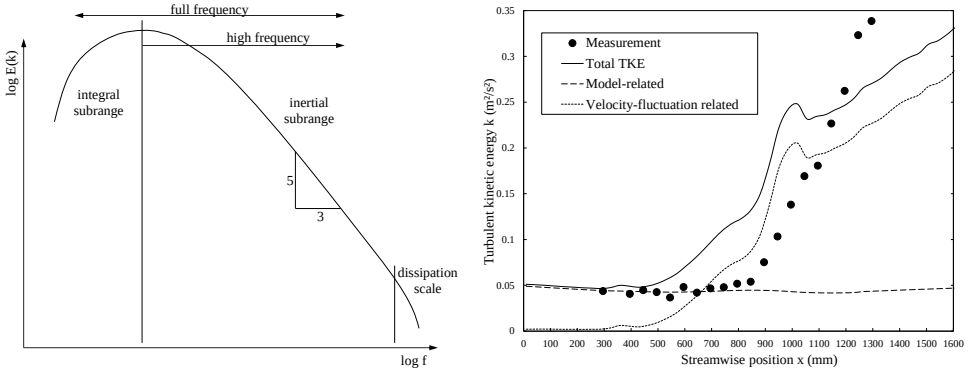

(a) Exemplary frequency spectrum of fluctuation energy (adopted from Mechanics of Turbulence [2016]).

(b) Comparison of measured an simulated turbulent kinetic energy along the plate

Figure 2: Explanation of the idea of the method used in this work showing the distinction between full and high frequency fluctuations and model and velocity-fluctuation related turbulent kinetic energy, respectively.

fluctuations. k_V predicts this rise, but too early. Although the curves do not agree perfectly with the measurement, it shows that the model-related k_T is not able to predict the measured distribution of k.

The question arising from these considerations is, how to set CFD boundary conditions correctly to enable the transition model – which is triggered beside others by the free stream turbulence – to predict transition and relaminarization correctly? In this work, this question should be answered together with the question, if the rise described above can only be predicted by an unsteady simulation and if a steady-state simulation for the present case with a pulsating separation bubble is acceptable? To answer these questions, four different simulations are performed within this work:

a) A steady state simulation, taking the measured k directly as boundary condition (Label: *SFF* (Steady - Full Frequency[1]))
b) A steady state simulation, taking a reduced k from the measurement, representing only the fluctuations above the *inertial subrange* as boundary condition (Label: *SHF* (Steady - High Frequency[1]))
c) An unsteady simulation, taking the measured k directly as boundary condition (Label: *UFF* (Unsteady - Full Frequency))
d) An unsteady simulation, taking a reduced k from the measurement, representing only the fluctuations above the *inertial subrange* as boundary condition (Label: *UHF* (Unsteady - High Frequency)

As described above, the result of the measurement returns a total turbulent kinetic energy, containing all ranges described above. In order to calculate a comparable TKE from the un-

[1]The range is also shown exemplary in Fig. 2a.

steady CFD result, the computed total fluctuations are found as

$$u_i' = u_{Ti}' + u_{Vi}' \tag{2}$$

accumulating the subranges shown in Fig. 2a. Combining this equation with the general definition of k

$$k_i = \frac{\overline{u_i' \cdot u_i'}}{2} \tag{3}$$

leads to

$$k = \frac{\overline{(u_T' + u_V')^2} + \overline{(v_T' + v_V')^2} + \overline{(w_T' + w_V')^2}}{2} \tag{4}$$

Dissolving this equation leads to

$$\begin{aligned} k = & \frac{\overline{(u_T')^2} + \overline{(v_T')^2} + \overline{(w_T')^2}}{2} \\ & + \frac{\overline{(u_V')^2} + \overline{(v_V')^2} + \overline{(w_V')^2}}{2} \\ & + \frac{\overline{2(u_T' u_V')} + \overline{2(v_T' v_V')} + \overline{2(w_T' w_V')}}{2} \end{aligned} \tag{5}$$

and substituting

$$k_T = \frac{\overline{(u_T')^2} + \overline{(v_T')^2} + \overline{(w_T')^2}}{2} \tag{6}$$

$$k_V = \frac{\overline{(u_V')^2} + \overline{(v_V')^2} + \overline{(w_V')^2}}{2} \tag{7}$$

leads to

$$k = k_{\text{tot}} = k_T + k_V + \overline{(u_T' u_V')} + \overline{(v_T' v_V')} + \overline{(w_T' w_V')} \tag{8}$$

where k_T represents – as discussed above – the model-related TKE and k_V the velocity-fluctuation-related kinetic energy. Both can be acquired directly from the unsteady CFD results. When both fluctuation parts (x_T' and x_V') are not correlated, the latter part of Equation (8) is equal to zero. In the present case these mean values of the fluctuations are set to be zero ($\overline{(u_T' u_V')} = \overline{(v_T' v_V')} = \overline{(w_T' w_V')} = 0$), because of their very low correlation coefficient caused by the high differences in frequency. Consequently the total turbulent kinetic energy is defined as:

$$k_{\text{tot}} = k_T + k_V \tag{9}$$

RESULTS AND DISCUSSION

In this section the four above mentioned simulations are compared with the measurement to see and understand, how they perform regarding the prediction of relaminarization. In this section, all unsteady results are time averaged over a sufficiently long time interval.

First, the comparability with the measurement should be ensured. Therefore in Fig. 3 the local free stream velocity u_∞ and the Launder acceleration parameter K are shown only for one case, since these values agree perfectly for all four cases. K is defined as

$$K = \frac{\nu}{u_\infty^2} \cdot \frac{du_\infty}{dx} \tag{10}$$

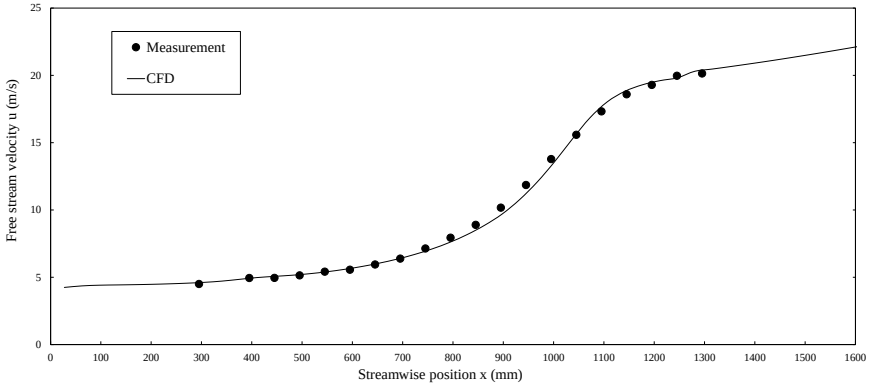

(a) Free stream velocity u_∞.

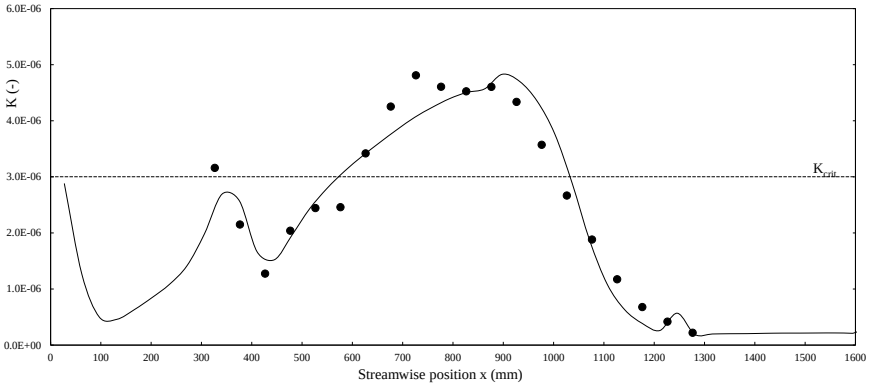

(b) Acceleration parameter K.

Figure 3: Free stream parameters along the plate comparing the measurement with the simulation results.

where u_∞ is the local free stream velocity, ν the kinematic viscosity and du_∞/dx the streamwise velocity gradient. This acceleration parameter represents a critical value for relaminarization. According to literature, if K exceeds a critical value according to $K > K_{crit} = 3.0 \cdot 10^{-6}$, relaminarization should most likely occur.

The free stream velocity u_∞ (Fig. 3a) shows, that the simulation is able to capture the experimental results well and also the acceleration parameter K in Fig. 3b gives a very good agreement.

To see the differences of the four mentioned simulations at the inlet in Fig. 4 the values of k_V, k_T and $k = k_{\text{tot}}$ are given in a bar diagram. The differences between the measurement and the simulations are not surprising. SHF does not consider any unsteady fluctuation but a lower k is set, thus the TKE is too low. On the other side UFF uses the unsteady fluctuations together with the full frequency k, thus this simulation has a higher TKE compared to the measurement. Obviously SFF and UHF show a very good agreement to the measurement values.

In order to see the difference between the simulations regarding turbulence along the plate, in Fig. 5a the total turbulent kinetic energy is plotted. For the steady simulations, the shown TKE represents only the k_T, because no unsteady fluctuations are computed. The differences between the unsteady and steady curves of the high and full frequency cases are therefore the

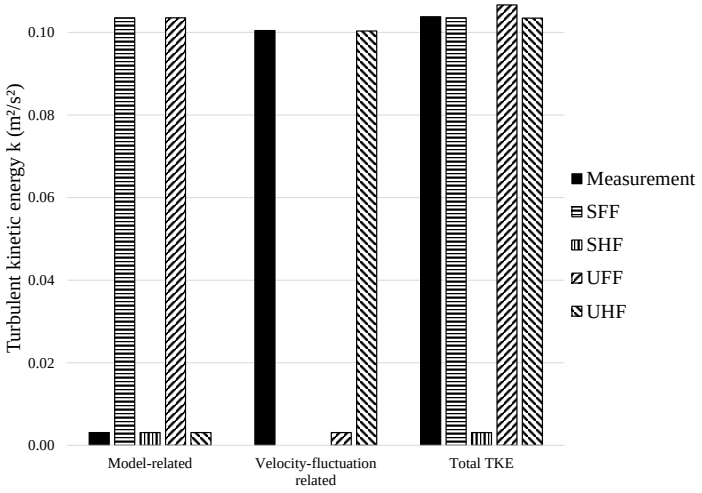

Figure 4: Bar diagram of the properties of k_V, k_T and k_{tot} measured/set at the inlet.

turbulent kinetic energy k_V caused by the velocity fluctuations.

It can be observed in Fig. 5a that the full frequency cases SFF and UFF show a very good agreement with the measurement at the beginning of the plate. The SFF solution starts to differ at approximately x = 850 mm, where the measurement values rises due to unsteady fluctuations which are not accounted for the steady simulation. On the other hand the UFF CFD result starts to differ at about x = 550 mm caused by a too early rise of k compared to the measurement.

The high frequency cases SHF and UHF differ completely from the measurement. This is not surprising for the steady simulation but for the unsteady simulation. Compared to the observations above done with the values at the inlet, the UHF solution should have the best fit to the measurement but it significantly exceeds the measured values. It seems, that the missing turbulence in the CFD equations leads to a reduced damping of unsteady fluctuations, thus to a far too high computed k_V.

It can be concluded here, that the "right" value of k in respect to the measurements lies in between the values of the full and high frequency cases for the unsteady simulation. Additionally it can be concluded that a stationary simulation does not address the distribution of the TKE accurately.

In order to compare the four different cases regarding their ability to predict relaminarization, the local skin friction coefficient c_f is compared with the measurement. c_f is defined as

$$c_f = \frac{\tau_W}{0.5 \cdot \rho \cdot {u_\infty}^2} \tag{11}$$

where τ_W represents the wall shear and ρ the density of the fluid. In Fig. 5b the c_f-value of the simulations together with the measurement is illustrated. At a streamwise position of about x = 800 mm the measurement value of c_f starts to decrease. This is a first indication of relaminarization as already shown by Bader et al. [2016]. With a slight streamwise delay, the simulations show the same trend. It can be observed that all simulations agree very well with the measurement up to a position of approximately x = 1200 mm. At this position the full frequency solutions SFF and UFF start a retransition to a turbulent boundary layer. The high frequency

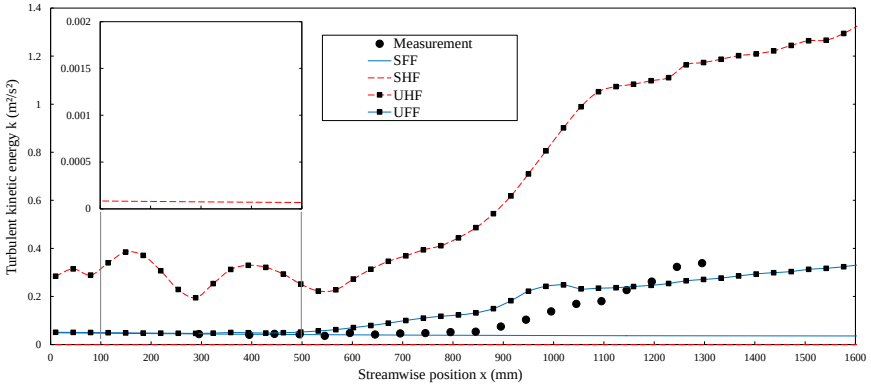

(a) Total turbulent kinetic energy k.

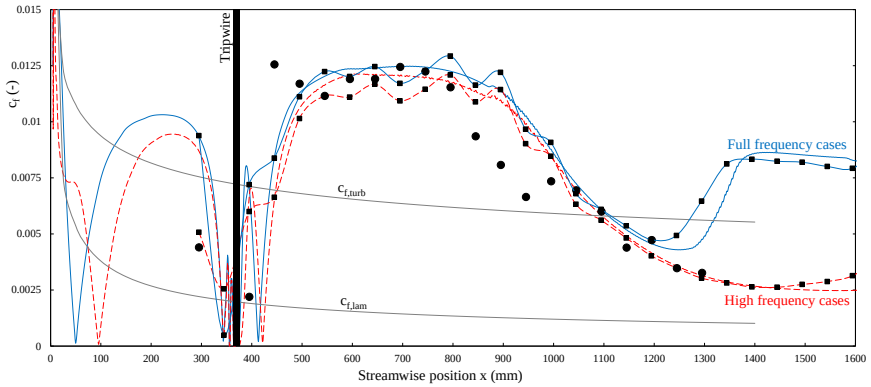

(b) Local skin friction coefficient c_f.

Figure 5: Comparison of the total turbulent kinetic energy and the skin friction coefficient along the plate comparing measurement results with values predicted by the four simulations (■ - unsteady; —— - full frequency; – – – - high frequency).

cases SHF and UHF still show a laminar behavior which agrees with the measurement.

Comparing steady and unsteady simulations it can be clearly observed, that the unsteady fluctuations do not influence the prediction of transition and relaminarization. Thus it can be concluded, that only the free-stream turbulence intensity k_T calculated by the turbulence model triggers changes in the state of the boundary layer. So a steady simulation is sufficient to calculate the boundary layer behavior even for the present case with a pulsating separation bubble. Therefore the validity of the model has to be verified, since low frequency unsteady fluctuations may have an effect on the transition and relaminarization process.

SUMMARY AND CONCLUSIONS

In this work, CFD simulations with the transition model γ-Re_θ are tested against measurement results. When applying measurement data one should keep in mind that the experimental data contains fluctuations of all frequencies, while in the numerical solution we can differ between a model-related turbulent kinetic energy k and unsteady velocity fluctuations. This may be crucial when using measurement data as boundary conditions for the simulation or comparing experimental with numerical data.

To analyze the best way to apply the turbulent boundary conditions, four different simulations have been analyzed within this work using the full frequency spectrum of the measurement and the high frequency part of the spectrum of fluctuations, respectively. For both boundary conditions steady and unsteady simulations have been performed.

The four simulations revealed some interesting facts:

a) The unsteady simulation with the high frequency fluctuations and the steady state simulation with the full frequency fluctuations show the best agreement with the measurement at the inlet, but
b) the unsteady simulation with the high frequency part shows too high unsteady fluctuations along the plate. This may be caused by a reduced damping by the missing turbulence.
c) Using only the high frequency parts of the fluctuations together with a steady state simulation leads to a too low TKE along the plate, but
d) although the steady simulations do not account for observed unsteady fluctuations, the results of the unsteady and steady simulations show the same behavior regarding transition and relaminarization, thus
e) regarding transition and relaminarization a steady state simulation is may sufficient, although unsteady fluctuations are present and entirely neglected by this simulation.

From these points, we can conclude that low frequency fluctuations, which are only considered by the unsteady simulations, have no influence on the predicted relaminarization by the model. The question arising from this point is, if this behavior is physically correct, since low frequency effects may also influence the position and length of the transitional and relaminarization zone.

Additionally is was found, that the unsteady simulation which the high frequency fluctuations which should be closest to the measured behavior shows a wrong increase fo turbulence intensity.

Further work is necessary to understand the relation between unsteady and turbulent fluctuations and their influence on the simulation of boundary layer behavior. The present paper showed surprisingly, that "right" turbulence intensity lies just somewhere in between the values resulting from the considerations made within the work.

ACKNOWLEDGEMENTS

The authors gratefully acknowledge financial support from the Austrian Federal Ministry for Transport, Innovation and Technology in funding the work by the project RELAM within the Austrian Aeronautics Program TAKE OFF.

Additionally the authors would to like to thank Günter Brenn and Walter Meile from ISW for providing their wind tunnel for the experimental work and their help during the test campaign. Last but not least we would like to thank Jakob Woisetschläger from ITTM for his guidance in the usage of the LDA equipment.

REFERENCES

Ansys Inc. ANSYS CFX-solver modeling guide. *Release 15.0*, November 2013.

P. Bader and W. Sanz. Steady and unsteady CFD calculation of the laminar-to-turbulent transition in a turning mid turbine frame with embedded design. *Proceedings of ASME 2015 Turbo EXPO, Montreal, Canada*, 2015. GT2015-42617.

P. Bader and W. Sanz. On the setup of a test bench for predicting laminar-to-turbulent transition on a flat plate. *Journal of Energy and Power Engineering*, 10(7):411–424, July 2016.

P. Bader, M. Pschernig, W. Sanz, J. Woisetschläger, F. Heitmeir, W. Meile, and G. Brenn. Flat-plate boundary layers in accelerated flow. *Proceedings of ASME Turbo Expo 2016: Turbine Technical Conference and Exposition, Seoul, South Korea*, 2016. GT2016-56044.

P. Bader, P. Pieringer, and W. Sanz. On the capability of transition models to predict relaminarization. *Proceedings of 12^{th} European Conference on Turbomachinery Fluid dynamics & Thermodynamics ETC12, April 3-7, 2017; Stockholm, Sweden*, 2017. ETC2017-328.

M. P. Escudier, A. Abdel-Hameed, M. W. Johnson, and C. J. Sutcliffe. Laminarisation an re–transition of a turbulent boundary layer subjected to favourable presser gradient. *Experiments in Fluids*, 25:491–502, 1998.

B. Hampel, N. Mayrhofer, and J. Woisetschläger. Frequenzanalyse einer turbinenschaufelgitterströmung mittels laser-vibrometer und holographischer interferometrie. *Proceedings of GALA-Fachtagung Lasermethoden in der Strömungsmesstechnik, Rostock, Germany*, 2002. paper No. 32.

D. Händel, U. Rockstroh, and R. Niehuis. Experimental investigation of transition and separation phenomena on an inlet guide vane with symmetric profile at different stagger angles and reynolds numbers. 15^{th} International Symposium on Transport Phenomena and Dynamics of Rotating Machinery, Honolulu, USA, 2014. ISROMAC-15.

M. Ichimiya, I. Nakamura, and S. Yamashita. Properties of a relaminarizing turbulent boundary layer under a favorable pressure gradient. *Experimental Thermal and Fluid Science*, 17: 37–48, 1998.

R. B. Langtry and F. R. Menter. Correlation-based transition modeling for unstructured parallelized computational fluid dynamics codes. *AIAA Journal*, 47(12):2894–2906, 2009.

R. B. Langtry, F. R. Menter, S. R. Likki, Y. B. Suzen, P. G. Huang, and S. Völker. A correlation based transition model using local variables part 2: Test cases and industrial applications. *Proceedings of ASME 2004 Turbo EXPO, Vienna, Austria*, 2004. GT2004-53454.

R. E. Mayle. The role of laminar-turbulent transition in gas turbine engines. *Journal of Turbomachinery*, 113(4):509–537, October 1991.

Mechanics of Turbulence. Length and time scales of turbulence, posted 29. February 2016. URL `http://www.mechturb.com/turbulence/length-and-time-scales-of-turbulence/`.

F. R. Menter. Two-equation eddy-viscosity turbulence models for engineering applications. *AIAA Journal*, 32(8):1598–1605, 1994.

R. Mukund, P. R. Viswanath, R. Narasimha, A. Prabhu, and J. D. Crouch. Relaminarization in highly favourable pressure gradients on a convex surface. *Journal of Fluid Mechanics*, 566: 97–115, 2006.

R. Narasimha and K. R. Sreenivasan. Relaminarization of fluid flows. *Advances in applied mechanics*, 61:221–309, 1979.

O. Oyewola, L. Djenidi, and R. A. Antonia. Combined influence of the reynolds number and localised wall suction on a turbulent boundary layer. *Experiments in Fluids*, 35:199–206, July 2003.

H. Schlichting and K. Gersten. *Grenzschicht-Theorie (Boundary-Layer Theory)*. Springer-Verlag Berlin Heidelberg, 2006.

J. H. Shin and S. J. Song. Pressure gradient effects on smooth- and rough-surface turbulent boundary layers - part II: Adverse pressure gradient. *J. Fluids Eng.*, 137(1):1–7, September 2015. doi: 10.1115/1.4027475.

L. P. Yip, P. Vijgen, J. D. Hardin, and C. P. van Dam. In-flight pressure distributions and skin-friction measurements on a subsonic transport high-lift wing section. *AGARD CP-515*, 1993.

CHAPTER 7

RESULTS: TRANSITION AND RELAMINARIZATION IN TURBOMACHINES

> The user of a turbulence model is more like a test pilot than a sunny Sunday Cessna flier
>
> Peter Bradshaw
> PROFESSOR, AERONAUTICAL ENGINEER

Papers 4, 6 and 8 show, that the γ-Re_θ model is capable of predicting transition and relaminarization along flat plates. This last result chapter presents the application of the γ-Re_θ transition model on flows through turbomachines.

7.1. Content

In two papers the flow through a two-stage two-spool turbine rig is analyzed. It consists of two counter-rotating spools, where between the high-pressure and low-pressure turbine an S-shaped mid turbine frame is mounted. This duct is necessary to guide the flow from the smaller, fast-turning high-pressure turbine to the rather slow-turning low-pressure turbine. Within this duct turning struts are installed which generate the necessary swirl for the downstream low-pressure (LP) rotor in order to replace the LP vane row. However, these load bearing turning struts have a rather large circumferential spacing between each other. This allows secondary flow structures from the high-pressure stage passing towards the LP rotor, influencing its efficiency. Also the rather large spacing minimizes the circumferential homogeneity of the swirl downstream of the turning struts. Thus additionally two splitter blades are added to the channel to reduce circumferential variations of the swirl leading to a more uniform flow towards the LP rotor. More details about this innovative setup can be found in [160–165].

Paper 9 [166] focuses on the high-pressure stator of the setup. Along this blade it is most likely that relaminarization occurs due to the high acceleration there caused by the high pressure ratio of the stator. To analyze the transitional behavior, RANS simulations with and without (fully turbulent) transition model are analyzed. The comparison of the results of the γ-Re_θ model with the fully turbulent simulation shows, that at the suction side of the blade transition is delayed due to the acceleration. Relaminarization can be found at the rear part of the blade pressure side.

The transitional behavior at the hub and shroud is similar to the pressure side of the blade with relaminarization at a similar streamwise position.

The last paper included in this thesis [167] (**paper 10**) also presents a look at transition and relaminarization in the turbine rig with a main focus on the turning mid turbine frame with splitters. For the analysis steady and unsteady CFD results with and without the γ-Re_θ transition model were compared. The data are discussed, focusing on the influence of the acceleration parameter K through the turbine with such a splitter design. The development of the intermittency γ along the blades and hub/shroud clearly shows transition and relaminarization. Additionally unsteady fluctuations along the blade are presented, influencing length and position of transition.

7.2. Summary and Conclusions

The numerical results of a two-spool two-stage turbine rig presented in this chapter show, that the differences between a fully turbulent simulation and a simulation considering transition and relaminarization are small, but not negligible.

Clear differences in skin friction caused by transition and relaminarization are found with the transitional solution.

Additionally, differences in losses between the fully turbulent and the transitional solution are discussed in detail. Although the differences are small, they should not be neglected. Thus as an outcome of this work, it can be concluded that transition and relaminarization should be taken into account in the design process.

The fully turbulent simulation in paper 9 shows a higher loss of the flow through the total stage, where the largest difference between the simulations can be found in the mid turbine frame.

Additionally, a slightly better agreement with measurement results can be achieved considering transition.

7.3. Paper 9: On Boundary Layer Relaminarization in an Highly Accelerated High Pressure Turbine Stator Flow

---

P. Bader and W. Sanz, "On Boundary Layer Relaminarization in an Highly Accelerated High Pressure Turbine Stator Flow," *Proceedings of ASME Turbo Expo 2016: Turbine Technical Conference and Exposition, June 26-30, 2017, Charlotte, North Carolina, USA*, GT2017-63296, 2017.

Proceedings of ASME Turbo Expo 2017: Turbine Technical Conference and Exposition
GT2017
June 26-30, 2017, Charlotte, North Carolina, USA

GT2017-63296

ON BOUNDARY LAYER RELAMINARIZATION IN AN HIGHLY ACCELERATED HIGH PRESSURE TURBINE STATOR FLOW

Pascal Bader
Institute for Thermal Turbomachinery
and Machine Dynamics
Graz University of Technology
8010 Graz, Inffeldgasse 25/A, Austria
http://www.ttm.tugraz.at
Email: pascal.bader@tugraz.at

Wolfgang Sanz
Institute for Thermal Turbomachinery
and Machine Dynamics
Graz University of Technology
8010 Graz, Inffeldgasse 25/A, Austria
http://www.ttm.tugraz.at
Email: wolfgang.sanz@tugraz.at

ABSTRACT

The boundary layer represents the thin layer between the wall and the free stream. Although this zone is small in respect to the free stream its state – whether it is laminar or turbulent – has a high impact on wall parameters like skin friction but also on the free stream.

The state of the boundary layer is influenced by free stream parameters like free stream turbulence intensity or acceleration. Transition can occur from laminar to turbulent, but also from turbulent to laminar. The latter process is called relaminarization.

Transition and relaminarization has already been detected in laboratory conditions but also occur in real-life flow around aeroplane wings, but also in turbomachines. In this work a high pressure stator of a two-spool, two-stage turbine is analyzed numerically regarding transition and relaminarization to show how the boundary layer flow along casing and blade is influenced by these phenomena.

It is found out in this work, that the boundary layer along the blade, hub and shroud undergoes transition and also relaminarization despite the high free stream velocities and turbulence levels inside the machine. The differences between a transitional and fully turbulent simulation regarding loss generation by wall friction are given.

NOMENCLATURE

BL	Boundary layer
c_f	Local skin friction coefficient
C	Axial chord length
CFD	Computational fluid dynamics
$D_{\nu,D}$	Van Driest damping function
D/E	Dissipation term
F_V	Integral viscous shear force
HP	High pressure
ITTM	Institute for Thermal Turbomachinery and Machine Dynamics
K	(Launder) acceleration parameter
k	Turbulence kinetic energy
k_L	Laminar kinetic energy
LDA	Laser-Doppler anemometry
LE	Leading edge
P_{TKE}	Turbulence kinetic energy production term
$\overline{p_{t,E}}$	Mass-weighted average of the total pressure in plane E
$\tilde{Re}_{\theta t}$	Local transition onset momentum-thickness Reynolds number
$Re_{\theta t}$	Transition onset momentum-thickness Reynolds number based on free stream conditions
RE	Relaminarization end
RS	Relaminarization start

s	Streamwise coordinate
S	Entropy difference $s - s_{in}$
TE	Trailing edge
TKE	Turbulence kinetic energy
TP	Transition position
Tu	Turbulence intensity
U	Velocity magnitude
U_∞	Local free stream velocity
u_τ	Frictional velocity $= \sqrt{\tau_w/\rho}$
u^+	Non-Dimensional velocity $(= u/u_\tau)$
x	Axial coordinate
y	Wall normal coordinate
y^+	Non-Dimensional wall coordinate $= y \cdot u_\tau/\nu$
α	Yaw angle $= \text{atan}(c_{tan}/c_{merid})$
$\delta(x)$	Boundary layer thickness
γ	Intermittency
μ	Dynamic viscosity
ν	Kinematic viscosity
ρ	Density
θ	Momentum thickness
Θ	Circumferential direction
τ_w	Wall shear stress
ω	Specific dissipation rate
Ω	Vorticity
ζ	Total pressure loss coefficient $(p_{t,1} - p_{t,2})/(p_{t,1} - p_1)$

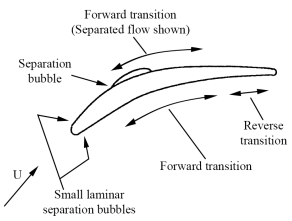

(a) SCHEMATIC DRAWING OF A COMPRESSOR BLADE.

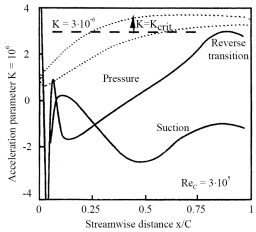

(b) K OF A COMPRESSOR BLADE.

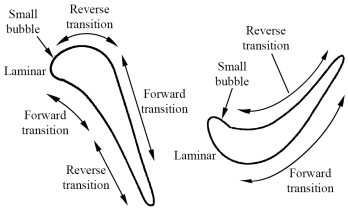

(c) SCHEMATIC DRAWING OF A HIGH PRESSURE TURBINE BLADE.

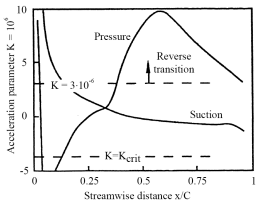

(d) K OF A HIGH PRESSURE TURBINE BLADE.

Figure 1. SEVERAL APPLICATIONS WHERE TRANSITION AND RELAMINARIZATION CAN THEORETICALLY OCCUR (ADOPTED FROM [1]).

INTRODUCTION

The boundary layer (BL) represents the narrow zone between a solid body wall and the free stream. In this small area viscous effects dominate the flow. The state of this boundary layer, whether it is laminar or turbulent, is on one hand influenced by free stream parameters, like the velocity, acceleration or turbulence level of the free stream and on the other hand influences the free stream as well as wall parameters, like skin friction or heat transfer (see e.g. [1]).

These parameters are important in turbomachinery, since they strongly influence for instance the efficiency of a stage and also the thermal stresses which blades have to withstand. Therefore, an understanding of the state of the boundary layer, i.e. the position, length etc. of the transitional zone, is very important for designers of turbomachines.

At the first contact of a flowing fluid with a stationary structure, under appropriate flow conditions the boundary layer develops from laminar via a transitional zone to a turbulent state. The boundary layer passes through several stages within this transitional zone before becoming fully turbulent. Schlichting and Gersten [2] extensively discussed these different stages.

It is vitally important to understand the impact of the influencing parameters on the onset position and length of the transitional zone in order to predict and potentially control the state of the boundary layer. In turbomachinery, the efficiency of blades and stages can be enhanced considering transition in the design process. This allows the overall machine performance to be improved. In 1991 Mayle [1] published a comprehensive review of the importance of transition in gas turbines. He analyzed experiments performed by several research groups in order to find the influence of different flow parameters on the transition process.

Under certain flow conditions (like strong acceleration), however, a reverse transition or relaminarization from turbulent to laminar can occur. Up to now, only few measurements on relaminarization were reported (e.g. [3–6]). In their basic work Narasimha and Sreenivasan [3] defined relaminarization by acceleration as a “freezing” of turbulent shear stress inside the boundary layer. The consequence is a suppressed production of the turbulent fluctuations inside the boundary layer. This leads to slow responding Reynolds stresses and dominating viscous forces inside the BL resulting in a quasi-laminar profile. This is characterized by a lower wall shear due to a lower velocity gradient at the wall.

Therefore, at the Institute for Thermal Turbomachinery and Machine Dynamics (ITTM) of Graz University of Technology a project was launched in order to understand the process of relaminarization and its phases even further and test common threshold values for relaminarization by acceleration. It has been found by LDA measurements, that relaminarization occurs under cer-

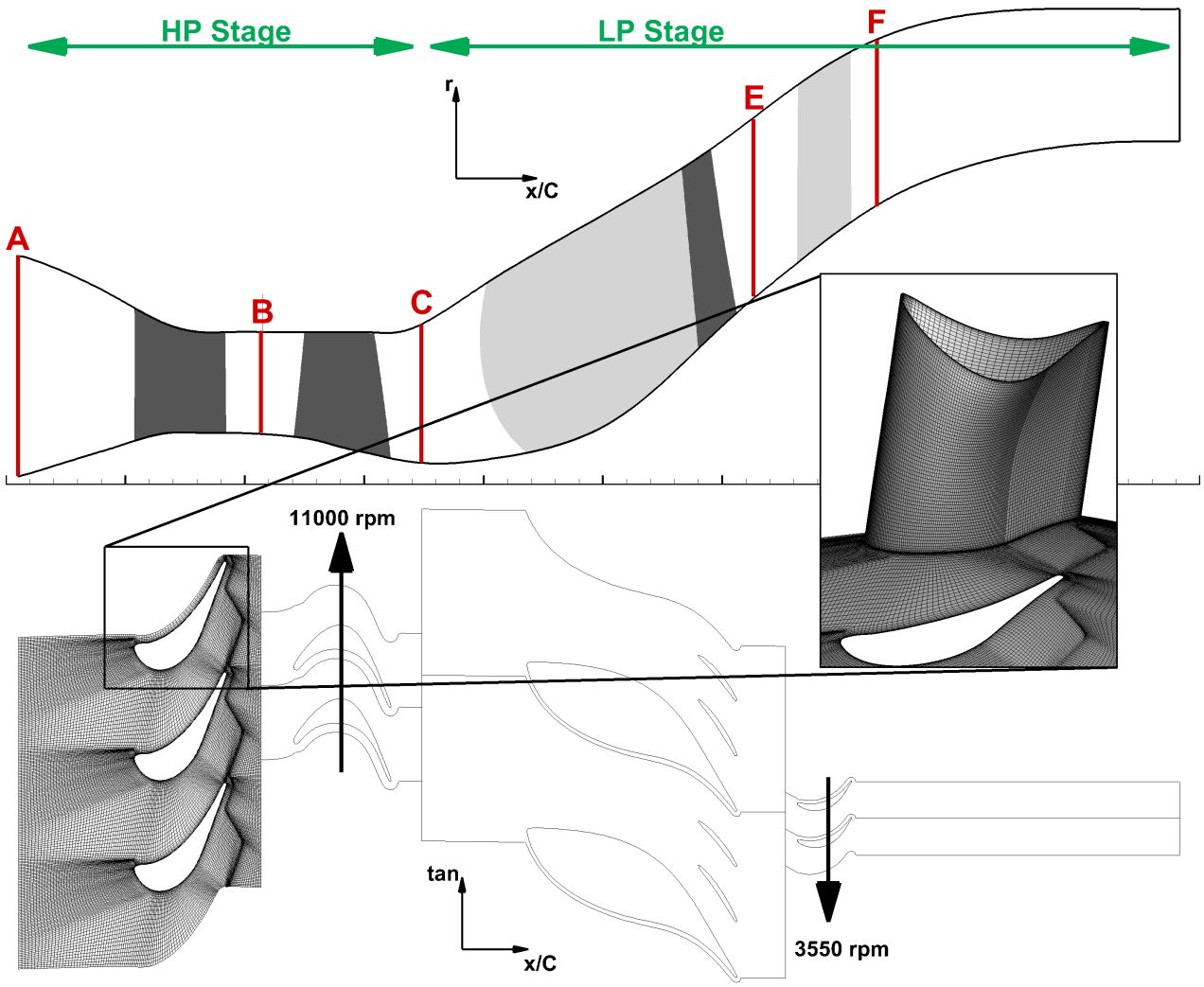

Figure 2. MERIODIONAL CONTOUR AND BLADE-TO-BLADE VIEW OF THE TWO-STAGE TEST TURBINE, DETAILED VIEW OF THE HIGH PRESSURE STATOR MESH.

tain flow conditions (see [7]). All these measurements were performed under laboratory conditions along flat plates.

Yip et al. [8] performed in-flight measurements with Preston tubes and presented transition and relaminarization along an aircraft wing. Also Mukund et al. [9] showed with hot-film gauge measurements along a swept leading edge the transition and relaminarization processes of the boundary layer. Thus these processes do not only happen under laboratory conditions, but also in real life. Regarding turbomachinery Mayle [1] already showed that transition as well as relaminarization theoretically take place on compressor as well as turbine blades. Figures 1a and b show a schematic drawing of the processes taking place along a compressor blade together with the acceleration parameter K (see Eq. 11); Figs. 1c and d show the same for a turbine blade. It can be concluded, that transition as well as relaminarization occurring along a blade influence skin friction, heat transfer as well as boundary layer thicknesses which may change the downstream flow angle.

Since BL measurements within turbomachines are difficult, numerical codes can be used to investigate the state of the bound-

ary layer. Therefore different models have been developed in order to predict the state of the boundary layer, e.g. the k-k_L-ω [10] and the γ-$\tilde{Re}_{\theta t}$ [11] model. It has already been shown by Bader et al. [12] that the γ-$\tilde{Re}_{\theta t}$ model is able to predict relaminarization for flat plate flows.

In this paper the development of the boundary layer within a transonic high pressure stator row is analyzed with a focus on relaminarization. The HP stator of a two-stage, two-spool test turbine has been used for the investigation within this paper, because due to the strong turning and the decreasing meridional flow area (see Fig. 2) high acceleration appears. It is shown how transition and relaminarization influences the performance of this particular vane row in respect to a fully turbulent boundary layer.

The following section presents the numerical setup used for the study. Thereafter we present and discuss simulation results of a fully turbulent simulation compared to one with activated transition. The paper ends with a short summary and the conclusions.

NUMERICAL SETUP

Solver

In this work, the CFD simulations have been performed with the in-house code LINARS. LINARS has been developed at Graz University of Technology at the ITTM by Pecnik et al. [13]. The code solves the Reynolds-averaged Navier-Stokes (RANS) equations in conservative form with a fully-implicit, time-marching finite-volume method. The inviscid (Euler) fluxes are discretized with the upwind flux-difference splitting method of Roe [14].

Mesh

The mesh used for this multirow simulation represents a three dimensional model of a counter-rotating two-stage, two-spool test turbine situated at the institute. A blade-to-blade sketch is given in Fig. 2 together with a three dimensional view of the high pressure stator. The full model consists of about 6.3 million nodes and the y^+ value is kept between 0.1 and 1, which is recommend for the γ-$\tilde{Re}_{\theta t}$ transition model (see [15]). The mesh has also been used in different other numerical investigations (see e.g. [16,17]) and mesh independence studies have been performed. For this study the normalized mean total pressure at plane E $\overline{p_{t,E}}$ has been compared to measurement results and it has been found that for a mesh size of 6.3 million and 12.3 million cells the difference between the two $\overline{p_{t,E}}$ values is negligible.

The boundary conditions for the steady simulation have been taken from measurements and are set at plane A and F (see Fig. 2). At the inlet (plane A) the total pressure, total temperature, turbulence kinetic energy (k=16.127 m^2/s^2) and specific turbulence dissipation rate ($\omega = 18.46 \cdot 10^3$ 1/s) have been set and at the outlet the static pressure is prescribed.

The validity of the CFD results have already been presented in previous works. Validation has been performed by comparing the blade loading of the TMTF blade, the radial distributions in plane F and the total pressure in plane E of simulation and measurement results (see e.g. [17]).

For the study in this work a focus is laid on the HP stator flow. This part of the mesh consists of approximately 1 million cells and about 18 mesh layers are used to resolve the boundary layers. Additional information about the high pressure stator and stage can be found in Tab. 1.

Turbulence model

As turbulence model the well known SST k-ω turbulence model by Menter [18] has been used. Since the SST model does not consider any transition or relaminarization, all BLs are computed as fully turbulent. The results of the SST simulation are used as the fully turbulent reference case. For modeling transition this turbulence model is coupled with a transition model, namely the γ-$\tilde{Re}_{\theta t}$ transition model by Langtry and Menter [11]. The model implementation in LINARS was successfully tested and compared with measurement results (see e.g. [19]). It solves two additional transport equations in order to influence the production and dissipation of the turbulence kinetic energy k within the turbulence model. The two equations are

$$\frac{\partial(\rho\tilde{Re}_{\theta t})}{\partial t} + \frac{\partial(\rho U_j \tilde{Re}_{\theta t})}{\partial x_j} = P_{\theta t} + \frac{\partial}{\partial x_j}\left[\sigma_{\theta t}(\mu+\mu_t)\frac{\partial \tilde{Re}_{\theta t}}{\partial x_j}\right] \quad (1)$$

$$\frac{\partial(\rho\gamma)}{\partial t} + \frac{\partial(\rho U_j \gamma)}{\partial x_j} = P_\gamma - E_\gamma + \frac{\partial}{\partial x_j}\left[\left(\mu + \frac{\mu_t}{\sigma_f}\right)\frac{\partial \gamma}{\partial x_j}\right] \quad (2)$$

with $\tilde{Re}_{\theta t}$ as the local transition onset momentum-thickness Reynolds number and γ representing the intermittency, i.e. the state of transition, which varies between zero and one, where one represents fully turbulent flow conditions.

The empirical correlations used for the prediction of transition are based on the idea that after surpassing a critical momentum thickness Reynolds number $Re_{\theta t}$ transition is triggered. But in this way it is a one-dimensional criterion which is only valid along the wall. Therefore Langtry and Menter [11] introduced the transport variable $\tilde{Re}_{\theta t}$ as a transition criterion which is applicable in the whole flow field. For this reason the production

Table 1. BLADING PARAMETERS AND OPERATION CONDITIONS.

HP vane		HP stage	
Vane/ blade no.	24	$n_{r,in}$ $(rpm/\sqrt{K})$	524.4
h/c_{ax}	1.15	$m_{r,in}$ $(kg/s \cdot \sqrt{K}/bar)$	81.2
Re (10^{-6})	2.38	Stage p_t ratio	3
Tip gap	-	Power (kW)	1710

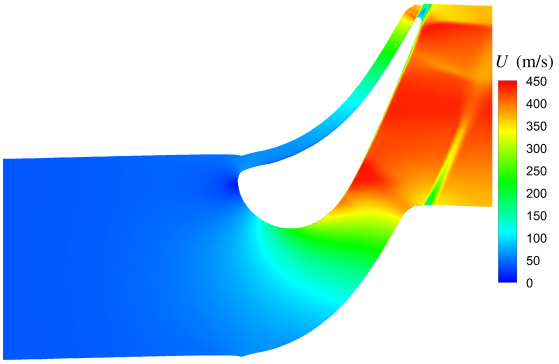

(a) VELOCITY MAGNITUDE U.

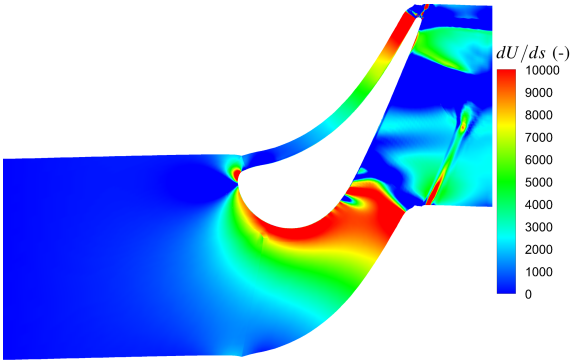

(b) STREAMWISE VELOCITY GRADIENT dU/ds.

Figure 3. CONTOUR PLOT OF VELOCITY AND VELOCITY GRADIENT AT MIDSPAN OF THE HIGH PRESSURE STATOR

term of the $\tilde{Re}_{\theta t}$ equation is designed in such a way, that $\tilde{Re}_{\theta t}$ is forced to adopt the value of the empirically prescribed transition onset Reynolds number $Re_{\theta t}$ in the free stream. The production term of $\tilde{Re}_{\theta t}$ is defined as

$$P_{\theta t} = c_{\theta t}\rho\frac{\rho U^2}{500\mu}\left(Re_{\theta t} - \tilde{Re}_{\theta t}\right)(1.0 - F_{\theta t}) \tag{3}$$

where $Re_{\theta t}$ represents the transition onset momentum-thickness Reynolds number based on free stream conditions. The blending function $F_{\theta t}$ is used to turn off the source term in the boundary layer and allow the transported scalar $\tilde{Re}_{\theta t}$ to diffuse in from the free stream. $F_{\theta t}$ is equal to zero in the free stream and one in the boundary layer. [11]

The correlation for $Re_{\theta t}$ used by Langtry and Menter [11] considers the influence of the turbulence intensity Tu and the velocity gradient dU/ds on the transition onset as

$$Re_{\theta t} = \left[1173.51 - 589.428\cdot Tu + \frac{0.2198}{Tu^2}\right] \cdot F(\lambda_\theta) \quad \text{for } Tu \le 1.3 \tag{4}$$

$$Re_{\theta t} = 331.50\cdot[Tu - 0.5658]^{-0.671} \cdot F(\lambda_\theta) \quad \text{for } Tu > 1.3 \tag{5}$$

$$\text{with } \lambda_\theta = \frac{\rho\theta^2}{\mu}\frac{dU}{ds} \tag{6}$$

where ρ represents the fluid density, θ the momentum thickness of the BL and μ the dynamic viscosity, respectively. Since θ is present on both sides of Eqs. (4) and (5), respectively, the momentum thickness can be computed by iteration [11].

The production and the dissipation terms of the intermittency γ are defined as

$$P_\gamma = F_{\text{length}}c_{a1}\rho S[\gamma F_{\text{onset}}]^{0.5}(1 - c_{e1}\gamma) \tag{7}$$

$$E_\gamma = c_{a2}\rho\Omega F_{\text{turb}}(c_{e2}\gamma - 1) \tag{8}$$

where F_{length} and F_{onset} depend on the local $\tilde{Re}_{\theta t}$ value and determine the length and onset of transition in the flow field. On the other hand F_{turb} depends on the local turbulence parameters (k and ω). The values of F_{length}, F_{onset} and F_{turb} can vary between $0 \le F_{\text{length}} \le 40$, $0 \le F_{\text{onset}} \le 2$ and $0 \le F_{\text{turb}} \le 1$, respectively.

The coupling of the transition model with the SST turbulence model is done by modifying the original production term P_{TKE} and dissipation term D_{TKE} of the turbulence kinetic energy k equation:

$$\tilde{P}_{TKE} = \gamma_{\text{eff}}\, P_{TKE} \tag{9}$$

$$\tilde{D}_{TKE} = \min(\max(\gamma_{\text{eff}}, 0.1), 1.0)\, D_{TKE} \tag{10}$$

RESULTS AND DISCUSSION

In this section the results of two simulations are presented: a fully turbulent case calculated with the SST model and a transitional case computed with the γ-$\tilde{Re}_{\theta t}$ transition model. As described above the investigation of the boundary layer shall focus on relaminarization caused by high flow acceleration. In Fig. 3 the velocity U and the streamwise velocity gradient dU/ds are given at midspan. The blade turns the flow in the front part and highly accelerates the flow to transonic conditions. In the rear part the velocity stays nearly constant with several weak shocks. The first weak shock emanates from the neighboring blade trailing edge and is reflected by the suction side surface. This weak shocks can be clearly observed in the velocity gradient plot as

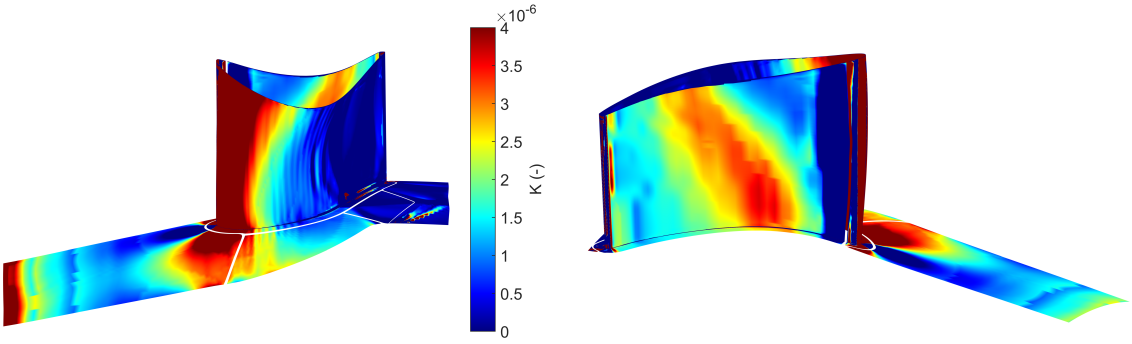

(a) SUCTION SIDE. (b) PRESSURE SIDE.

Figure 4. CONTOUR PLOT OF THE ACCELERATION PARAMETER K OF THE HIGH PRESSURE STATOR

areas with very low acceleration. A strong shock is seen downstream of the flow channel.

In order to quantify "high" acceleration with respect to relaminarization, the Launder acceleration parameter is used. This parameter is defined as

$$K = \frac{\nu}{U_\infty^2} \cdot \frac{dU_\infty}{ds} \tag{11}$$

where ν represents the kinematic viscosity and U_∞ the local free stream velocity. According to literature (see e.g. [1,3,5,6,20,21]) the critical value for relaminarization is $3 \cdot 10^{-6} \leq K_{crit} \leq 3.5 \cdot 10^{-6}$. If the acceleration of the flow is higher than this critical value relaminarization is most likely to occur.

Since K has to be evaluated at the edge of the boundary layer ($y = \delta(x)$), the boundary layer thickness is calculated by the method of Arnone and Pacciani [22]. The idea of this approach is to find the maximum of the function $G(y)$ which is defined as

$$G(y) = \frac{1}{y} \int_0^\infty y\Omega \left(1 - e^{-y^+/A^+}\right) dy \tag{12}$$

where Ω represents the vorticity of the flow field and y^+ represents the dimensionless wall coordinate and $A^+ = 26$. The position y_{max} where $G(y)$ is a maximum is then multiplied by a constant to find the boundary layer thickness:

$$\delta(x) = 1.145 \cdot y_{max} \tag{13}$$

In Fig. 4 the acceleration parameter evaluated at the BL edge is given as contour plot on the suction (Fig. 4a) and the pressure side (Fig. 4b) of the high pressure stator.

The view on the suction side of the blade (Fig. 4a) shows a zone of high acceleration factor at the leading edge region, which lies above the critical value of $K_{crit} = 3.0 \cdot 10^{-6}$. It is caused by the high turning of this front-loaded blade design together with a decrease of the meridional flow area. This zone of acceleration is also visible at the hub. Downstream on the suction side and the hub the location of the above mentioned weak shock is visible as a minimum of K. Although not shown, a similar distribution can be found at the shroud.

Looking at the pressure side of the blade (Fig. 4b) the very short zone of stagnation point acceleration is clearly visible. An extended zone of high acceleration can be observed in the mid part of the blade.

In order to see the effects of the high acceleration on the BL contour plots of the local skin friction coefficient c_f are compared in Fig. 5 between the SST and the transitional SST (γ-$\tilde{Re}_{\theta t}$) simulations. c_f is defined as

$$c_f = \frac{\tau_w}{0.5 \cdot \rho \cdot U_\infty^2} \tag{14}$$

where τ_w represents the wall shear stress.

On the suction side (Figs. 5a and c) the transitional solution shows a significant reduction of the skin friction coefficient in the zone of high acceleration compared to the fully turbulent solution. The lower skin friction level is maintained downstream until transition occurs shortly before the shock position at approximately $x/C = 0.6$ (see Eq. 15). This extended laminar boundary layer and transition is described later in this section in more detail. Downstream both solutions show similar values.

Looking at the c_f distribution at the hub it is observable, that up to the leading edge the trends are similar, but the predicted values of the transitional solution are slightly smaller. Inside the duct (between two blades) the differences are higher, but more downstream (after the weak shock) the two simulations agree again with each other.

At the pressure side just downstream of the leading edge the

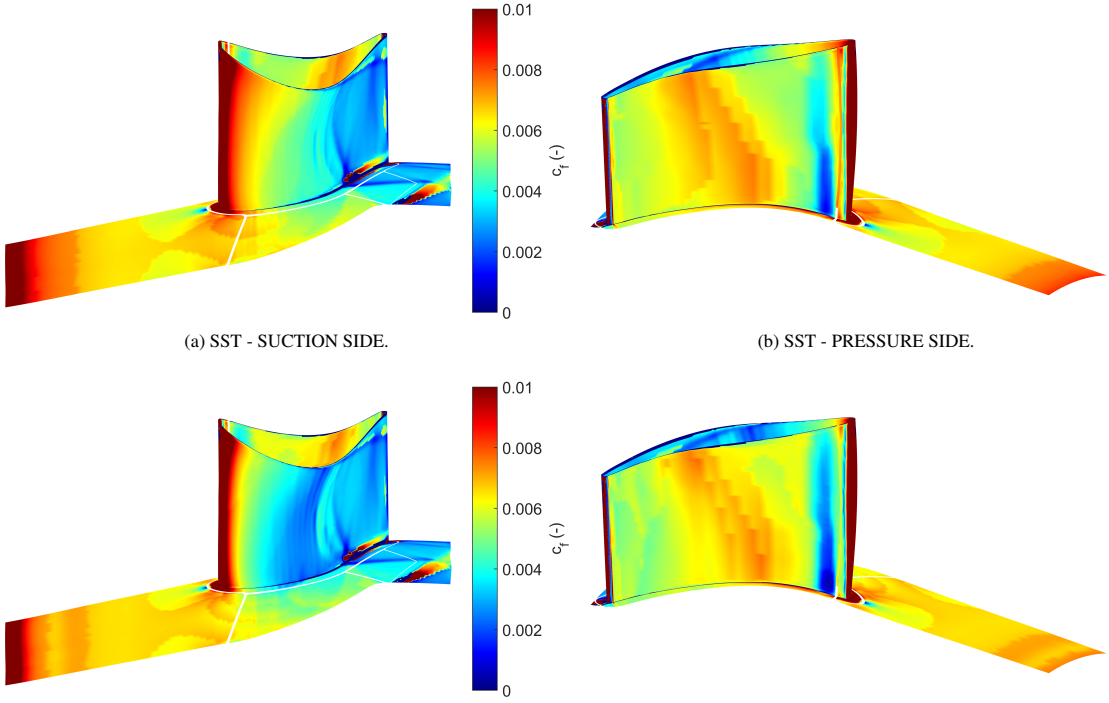

(a) SST - SUCTION SIDE.

(b) SST - PRESSURE SIDE.

(c) TRANSITIONAL SST - SUCTION SIDE.

(d) TRANSITIONAL SST - PRESSURE SIDE.

Figure 5. CONTOUR PLOT OF THE LOCAL SKIN FRICTION COEFFICIENT c_f OF THE HIGH PRESSURE STATOR

transitional solution shows lower skin friction (blue zone) which is followed by slightly higher skin friction values compared to the SST solution. This overshoot is described later. At mid-chord section of the blade and downstream both solution show zones of high skin friction but the transitional solution predicts lower skin friction at the rear part of the pressure side. This is caused by relaminarization due to the high acceleration observed here and is also discussed in more detail later in this section.

In order to analyze these results in more detail, in Figs. 6 and 7 distributions of the acceleration parameter K (see Eq. (11)), the boundary layer thickness $\delta(x)$ (see Eq. (13)) and the local skin friction coefficient c_f (see Eq. (14)) are plotted over the relative axial distance x/C defined as

$$\frac{x}{C} = \frac{x' - x_{LE}}{x_{TE} - x_{LE}} \tag{15}$$

where x' represents the local axial coordinate, x_{LE} and x_{TE} the axial location of the HP stator leading and trailing edge, respectively, and C the chord length of the blade.

In Fig. 6 the streamwise properties of the high pressure blade at 50% span are given. The suction side is given by dashed lines whereas the pressure side is plotted in solid lines.

First we want to focus on the suction side (dashed line) of the blade. Looking at the K values along the chord it can be seen that the acceleration is above the critical value of $K = 3 \cdot 10^{-6}$ (horizontal dash-dot line) up to about $x/C < 0.225$. Due to the high acceleration, the predicted skin friction of the transitional solution is remarkably lower than the SST solution indicating a laminar boundary layer. Transition from laminar to turbulent takes place at approximately $x/C = 0.55$ (marked as TP (transition position)). The transition is not induced by the shock which is at about $x/C = 0.7$. After the transition, the transitional and fully turbulent results agree very well in the c_f plot.

Comparing the predicted boundary layer thicknesses, it can be observed that the high acceleration suppresses the growth of $\delta(x)$ in the transitional solution, whereas $\delta(x)$ increases for the fully turbulent case. After the transition the growth rate of the predicted boundary layer thickness of both simulations is comparable.

Looking at the pressure side of the blade, it can be seen, that after decelerated flow region the acceleration parameter rises sharply at approximately $x/C = 0.2$ to about $K = 2 \cdot 10^{-6}$. During this increased acceleration the transitional c_f interestingly

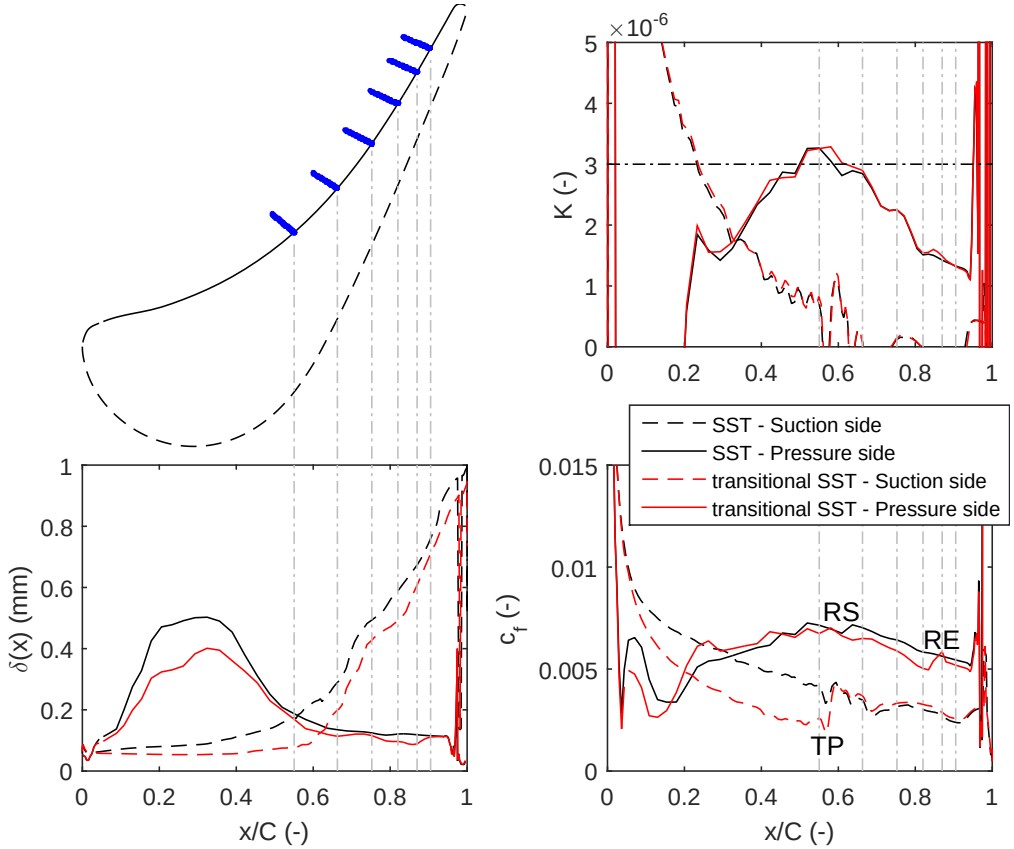

Figure 6. STREAMWISE PLOTS OF THE ACCELERATION PARAMETER K, BOUNDARY LAYER THICKNESS $\delta(x)$ AND LOCAL SKIN FRICTION COEFFICIENT c_f AT 50% SPAN ALONG THE BLADE.

switches from a lower to a higher value compared to the SST results. A local maximum of the skin friction predicted by the transitional solution coincides with the local peak of K value at about $x/C = 0.25$.

After a short reduction of acceleration the K value increases above the critical value at about $x/C = 0.55$. At this position, the boundary layer thickness $\delta(x)$ and the skin friction coefficient c_f of both simulations agree with each other. Downstream in the zone of decreasing acceleration the two simulations show a reduction of skin friction. The transitional solution then predicts relaminarization (marked as RS (relaminarization start)) indicated by a lower c_f as the fully turbulent result. This occurrence of relaminarization just downstream of the highest acceleration is often observed for relaminarization by acceleration (see e.g. [7]). More downstream, at approximately $x/C = 0.85$ the c_f-values indicate a re-transition (marked as RE (relaminarization end)), which typically follows relaminarization and is caused by "frozen" turbulent fluctuations inside the boundary layer, which start to burst if the acceleration is too low to keep this "frozen" state. Downstream of the re-transition, both simulations agree well.

In the region of increasing acceleration the boundary layer thickness $\delta(x)$ of the transitional solution is always smaller compared to the fully turbulent solution. In the relaminarization zone the difference is small and after retransition both simulations agree well.

In Fig. 7 the x/C-plots along the hub (solid line) and shroud (dashed line) both in the middle of the flow channel are given. The blade is located between $x/C = 0$ and $x/C = 1$. It has to be mentioned that the c_f distribution of the shroud is shifted $c_f + 0.0025$ along the y-axis to ensure a better distinction between the hub and the shroud distribution.

Looking at the hub it can be seen, that the acceleration parameter is higher than the critical value at the beginning and the

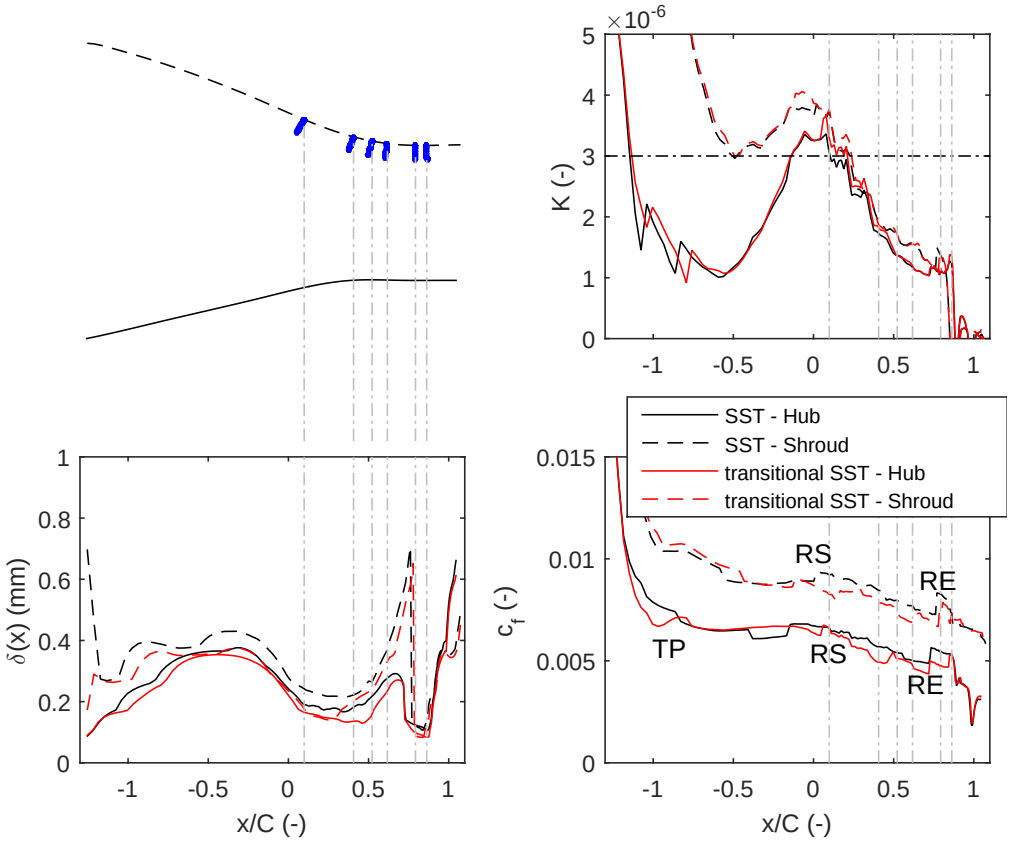

Figure 7. STREAMWISE PLOTS OF THE ACCELERATION PARAMETER K, BOUNDARY LAYER THICKNESS $\delta(x)$ AND LOCAL SKIN FRICTION COEFFICIENT c_f ALONG THE HUB AND SHROUD ENDWALLS.

boundary layer is predicted laminar. As the acceleration decreases, a transition from laminar to turbulent can be observed at about $x/C = -1$ (marked as TP). Then the acceleration increases to a value above the critical limit between $x/C = -0.2$ and $x/C = +0.2$. Due to the high acceleration, the flow relaminarizes downstream of the highest acceleration (marked as RS), which can be observed by the difference between the two simulated skin friction distributions. With decreasing acceleration re-transition can be found at approximately $x/C = 0.7$ (marked as RE). In the relaminarization zone the transitional boundary layer thickness $\delta(x)$ is smaller compared to the SST simulation and adopts the turbulent value after re-transition.

The distributions along the shroud are similar to the ones of the hub, but the acceleration parameter along the shroud is higher and up to $x/C = 0.2$ overcritical. At $x/C = 0$ with decreasing acceleration again relaminarization occurs (marked as RS) and extends up to $x/C = 0.75$ where re-transition can be seen (marked as RE) in the skin friction distribution. The boundary layer thickness $\delta(x)$ of the transitional calculation is slightly smaller compared to the fully turbulent case along the nearly whole flow path until the position of re-transition. Then the thicknesses agree again.

To illustrate the effect of relaminarization on the boundary layer, in Fig. 8a the velocity profiles in wall coordinates along the blade pressure side are given at different positions inside the relaminarization zone. The positions of these profiles are also given in the upper left corner in Fig. 6 as blue dots and represent a position of $x/C = 0.55$, $x/C = 0.66$, $x/C = 0.75$, $x/C = 0.82$, $x/C = 0.87$ and $x/C = 0.91$. In Fig. 8a additionally to the simulation results the $y^+ = u^+$-curves and the log-law are given, as a representation of the laminar sublayer which can be seen as a laminar and turbulent reference profile, respectively.

Looking at the different positions it can be observed that the transitional SST solution rises above the fully turbulent so-

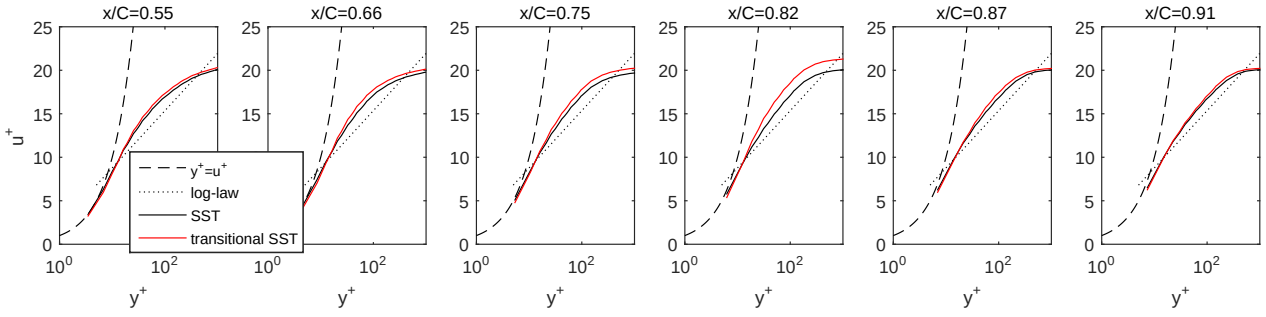

(a) VELOCITY PROFILES.

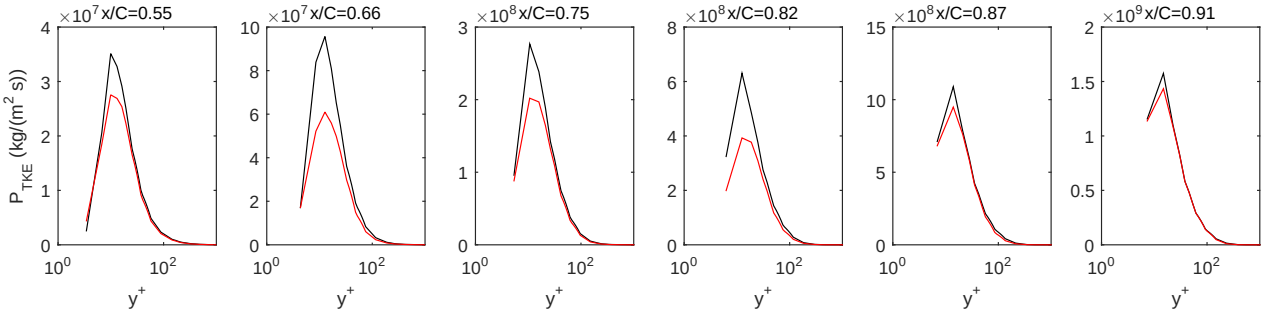

(b) PRODUCTION OF TURBULENCE KINETIC ENERGY P_{TKE}.

Figure 8. VELOCITY PROFILES AND THE PRODUCTION OF TURBULENCE KINETIC ENERGY P_{TKE} IN WALL COORINATES AT DIFFERENT STREAMWISE POSITIONS x/C AT THE PRESSURE SIDE OF THE BLADE.

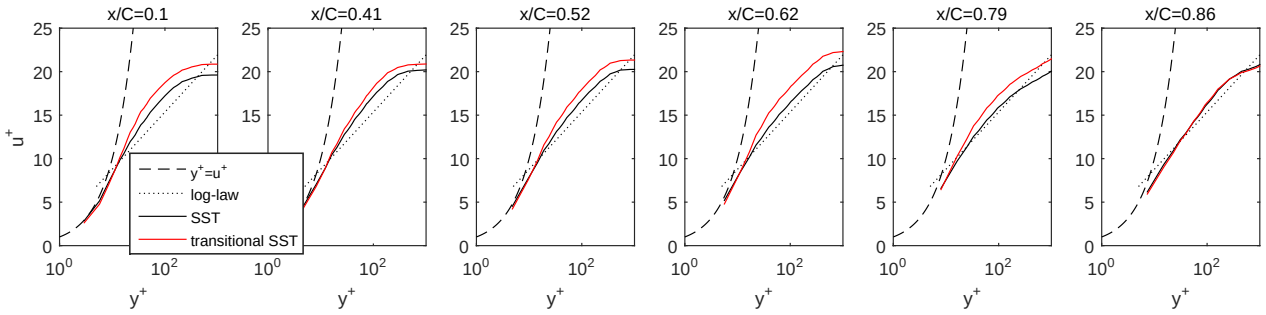

Figure 9. VELOCITY PROFILES IN WALL COORINATES AT DIFFERENT STREAMWISE POSITIONS x/C ALONG THE SHROUD.

lution and tends towards the laminar $y^+ = u^+$ reference curve. Although the differences are not high, this indicates a more laminar behavior along these positions.

At the latter positions both simulations again agree well, which indicates that the transitional simulation has undergone re-transition.

The changes in the boundary layer velocity profiles due to the transition model also cause a difference in the turbulence production P_{TKE} as shown in Fig. 8b for the same positions. In the case of the γ-Re_θ model the diagrams show the production term P_{TKE} before being multiplied with the intermittency γ (see Eq. (9)). The peak of production is clearly reduced by the intermittency model. The largest difference can be observed at position x/C=0.66, where the relaminarization starts. The the last two profiles which are after the retransition point the difference in turbulence production is small.

Additionally the velocity profiles at different positions in the relaminarization zone along the shroud are given in Fig. 9. These

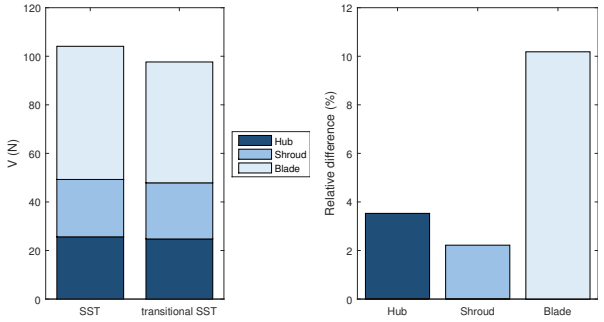

(a) INTEGRAL VISCOUS SHEAR FORCE F_V.

(b) RELATIVE DIFFERENCE.

Figure 10. COMPARISON OF THE SHEAR FORCES OF THE HIGH PRESSURE STATOR.

positions are shown in the upper-left picture in Fig. 7 with blue dots and represent relative positions of $x/C = 0.1$, $x/C = 0.41$, $x/C = 0.52$, $x/C = 0.62$, $x/C = 0.79$ and $x/C = 0.86$.

It can be seen, that the boundary layer is not fully turbulent at the first position. At the next position, the transitional solution tends towards the fully turbulent result. At $x/C = 0.52$ the transitional result again starts to tend towards the $y^+ = u^+$ laminar reference indicating relaminarization as observed in the c_f plots of Fig. 7. At the last position ($x/C = 0.86$) both simulations again agree well, which shows that the boundary layer has already undergone re-transition.

Beside detailed analysis, also the change of the skin friction between the two presented simulations is given in the following. Generally laminar boundary layers exhibit a lower wall friction than turbulent boundary layers. Therefore the state of the boundary layer influences losses generated by friction. The fully turbulent SST simulation represents the "worst-case", because it calculates all boundary layers as fully turbulent. In order to quantify these differences in Fig. 10a the integral viscous shear force F_V is given of the three walls hub, shroud and blade of the HP stator. F_V is defined as

$$F_V = \int \tau_w dA \tag{16}$$

It can be seen, that the transitional simulation predicts lower total viscous forces for all parts. The total difference in integral viscous shear force F_V is 6.46 N.

In Fig. 10b the relative differences of the three walls defined as

$$\frac{F_{V,\mathrm{SST}} - F_{V,\mathrm{transitional\ SST}}}{F_{V,\mathrm{transitional\ SST}}} \cdot 100\% \tag{17}$$

are given. The reduction of the blade friction is about $\approx 10\%$ and thus the biggest difference of the two simulations, whereas the hub and the shroud with $\approx 3.5\%$ and $\approx 2\%$, respectively, show a moderate reduction of the viscous drag forces.

In order to quantify the overall loss, the mass-flow weighted total pressure loss coefficients ζ of the two simulations are compared. The SST solution gives a total pressure loss of 3.57% related to the inlet dynamic pressure in contrast to 3.50% for the transitional solution. This means that taking transition into account in this numerical simulation, the predicted total pressure loss is 2% (0.07 percentage points) lower.

Although the skin friction and pressure difference give a good indication about losses, an entropy analysis gives a more detailed insight into the amount of irreversibility of the flow. Therefore the results of an entropy analysis are shown in Fig. 11.

Figure 11a shows the mass-weighted averaged entropy S from inlet to outlet of the stator passage. It can be clearly seen that up to the leading edge of the blade the differences between the setups are very small. Within the passage the entropy increases where the fully turbulent simulation shows a higher rise, indicating higher irreversible losses.

In order to break these losses down to the three components, similar to the relative viscous shear force F_V (see Eq. (17)) the entropy at the surface has been area averaged and the relative differences are shown in Fig. 11b. In contrast to the viscous force difference (see Fig. 10b) the relative difference are quite the same for all three parts, all showing approximately 0.25% lower rise of entropy compared to the fully turbulent SST simulation.

Beside discrepancies in losses, additional differences can be found which should be considered when designing a blade with CFD. The different boundary layer thicknesses between the two simulations lead to a different flow angle downstream of the stator. In Fig. 12, the circumferential distribution of the yaw angle α is given exemplary for 75% span for two stator pitches. The wakes of the stator blades are indicated by dashed lines.

It can be seen that there are flow angle differences of up to 0.5°, which may affect the exit metal angle of the stator (adjustment of the incidence). Interestingly the main differences can be found within the free stream and not in the wake region.

SUMMARY AND CONCLUSION

In this work a high pressure stator row of a two-spool, two stage turbine is computationally analyzed regarding transition. Is has shown in detail, that transition from laminar to turbulent and also relaminarization from turbulent to laminar occurs.

Within the stage, the necessary high acceleration for relaminarization occurs, despite the high free stream velocity. The main acceleration is caused by the turning of the front-loaded blade enhanced by a reduction of the meridional flow area. It is shown in this work that just downstream of the highest acceleration the skin friction coefficient decreases compared to a fully turbulent boundary layer. This behavior of beginning relaminarization af-

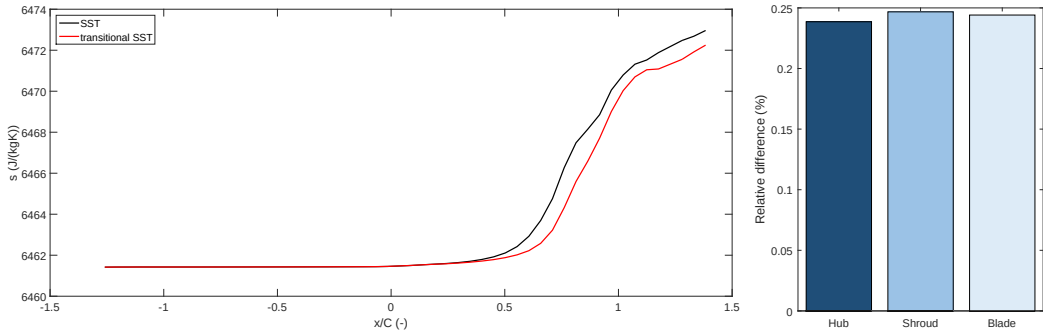

(a) FROM INLET TO OUTLET.

(b) BREAKDOWN OF THE RELATIVE DIFFERENCES.

Figure 11. ENTROPY FLUX THROUGH THE STATOR.

ter the position of highest acceleration has also been observed experimentally along flat plates. Also the fast re-transition from the laminar state to a turbulent boundary layer at decreasing acceleration downstream of the relaminarization zone has been detected numerically.

The relaminarization is not only observable in the skin friction coefficient, but also the boundary layer velocity profiles tend towards a more laminar profile. A fully laminar boundary layer could not be detected since the streamwise extend of the acceleration is too short.

Regarding skin friction a comparison of the integral viscous shear force has been given. It has been shown that differences up to 10% compared to the fully-turbulent case can be observed. Taking into account transition and relaminarization in the loss calculation also showed lower total pressure loss. This can also be seen by a reduced entropy increase in the blade channel.

It was also interesting to observe a change in the computed exit flow angle due to transition modeling.

So this numerical study shows well, that in turbomachinery flow computations a transition model should be taken into account since it can influence the results remarkably. This should also be considered in the design process.

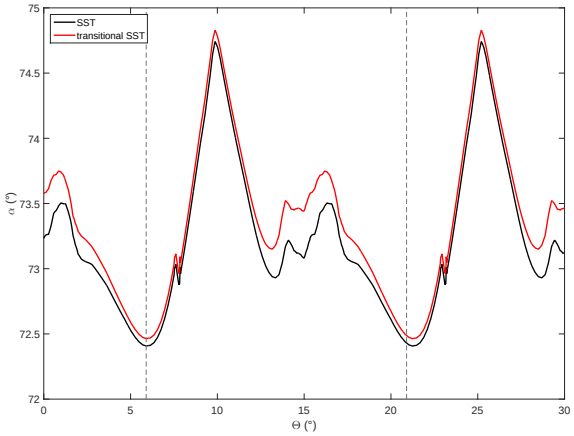

Figure 12. CIRCUMFERENTIAL YAW ANGLE α DISTRIBUTION AT 75% SPAN SHOWING TWO STRUT PASSAGES COMPARING THE SIMULATIONS.

ACKNOWLEDGMENT

The authors gratefully acknowledge financial support from the Austrian Federal Ministry for Transport, Innovation and Technology for funding the work by the project RELAM within the Austrian Aeronautics Program TAKE OFF.

REFERENCES

[1] Mayle, R. E., 1991. "The role of laminar-turbulent transition in gas turbine engines". *Journal of Turbomachinery,* ***113***(4), October, pp. 509–537.

[2] Schlichting, H., and Gersten, K., 2006. *Grenzschicht-Theorie (Boundary-Layer Theory).* Springer-Verlag Berlin Heidelberg.

[3] Narasimha, R., and Sreenivasan, K. R., 1973. "Relaminarization in highly accelerated turbulent boundary layers". *Journal of Fluid Mechanics,* ***31***, pp. 417–447.

[4] Ichimiya, M., Nakamura, I., and Yamashita, S., 1998. "Properties of a relaminarizing turbulent boundary layer under a favorable pressure gradient". *Experimental Thermal and Fluid Science,* ***17***, pp. 37–48.

[5] Escudier, M. P., Abdel-Hameed, A., Johnson, M. W., and Sutcliffe, C. J., 1998. "Laminarisation an re–transition of a turbulent boundary layer subjected to favourable pressure gradient". *Experiments in Fluids,* ***25***, pp. 491–502.

[6] Mukund, R., Viswanath, P. R., Narasimha, R., Prabhu, A., and Crouch, J. D., 2006. "Relaminarization in highly favourable pressure gradients on a convex surface". *Journal of Fluid Mechanics,* ***566***, November, pp. 97–115. doi: http://dx.doi.org/10.1017/S0022112006002473.

[7] Bader, P., Pschernig, M., Sanz, W., Woisetschläger, J., Heitmeir, F., Meile, W., and Brenn, G., 2016. "Flat-plate boundary layers in accelerated flow". *Proceedings of ASME Turbo Expo 2016: Turbine Technical Conference and Exposition, Seoul, South Korea.* GT2016-56044.

[8] Yip, L. P., Vijgen, P., Hardin, J. D., and van Dam, C. P., 1993. "In-flight pressure distributions and skin-friction measurements on a subsonic transport high-lift wing section". *AGARD CP-515*.

[9] Mukund, R., Narasimha, R., Viswanath, P. R., and Crouch, J. D., 2012. "Multiple laminar-turbulent transition cycles around a swept leading edge". *Experiments in Fluids,* ***53***, pp. 1915–1927.

[10] Walters, K., and Cokljat, D., 2008. "A three-equation eddy-viscosity model for reynolds-averaged navier-stokes simulations of transitional flows". *J. Fluids Eng.,* ***130***, pp. 1214011–12140114.

[11] Langtry, R. B., and Menter, F. R., 2009. "Correlation-based transition modeling for unstructured parallelized computational fluid dynamics codes". *AIAA Journal,* ***47***(12), pp. 2894–2906.

[12] Bader, P., Pieringer, P., and Sanz, W., 2017. "On the capability of transition models to predict relaminarization". *Submitted to 12th European Conference of Turbomachinery Fluid Dynamics & Thermodynamics ETC12*, April. ETC2017-328.

[13] Pecnik, R., Pieringer, P., and Sanz, W., 2005. "Numerical investigation of the secondary flow of a transonic turbine stage using various turbulence closures". *In Proceedings of ASME Turbo Expo 2005, Reno-Tahoe, Nevada, USA*. GT2005-68754.

[14] Roe, P. L., 1981. "Approximate riemann solver, parameter vectors and differencing scheme". *Journal of Computational Physics,* ***43***, pp. 357–372.

[15] Langtry, R. B., Menter, F. R., Likki, S. R., Suzen, Y. B., Huang, P. G., and Völker, S., 2004. "A correlation based transition model using local variables part 2: Test cases and industrial applications". *Proceedings of ASME 2004 Turbo EXPO, Vienna, Austria*. GT2004-53454.

[16] Akin, B. M., and Sanz, W., 2014. "The influence of transition on cfd calculations of a two-stage counter-rotating turbine". *Proceedings of ASME 2014 TURBO EXPO, June 16-20, 2014, CCD Congress Center Düsseldorf, Düsseldorf, Germany*. GT2014-26044.

[17] Bader, P., and Sanz, W., 2015. "Steady and unsteady CFD calculation of the laminar-to-turbulent transition in a turning mid turbine frame with embedded design". *Proceedings of ASME 2015 Turbo EXPO, Montreal, Canada*. GT2015-42617.

[18] Menter, F. R., 1994. "Two-equation eddy-viscosity turbulence models for engineering applications". *AIAA Journal,* ***32***(8), pp. 1598–1605.

[19] Kelterer, M., Pecnik, R., and Sanz, W., 2010. Computation of laminar-turbulent transition in turbomachinery using the correlation based $\gamma - re_\theta$ transition model. ASME Turbo Expo 2010, Glasgow, Scotland. GT2010-22207.

[20] Bardi Narayanan, M. A., and Ramjee, V., 1969. "On the criteria for reverse transition in a two–dimensional boundary layer". *Journal of Fluid Mechanics,* ***35***, pp. 225–241.

[21] Blackwelder, R. F., and Kovasznay, L. S. G., 1972. "Large–scale motion of a turbulent boundary layer during relaminarization". *Journal of Fluid Mechanics,* ***53***, pp. 61–83.

[22] Arnone, A., and Pacciani, R., 1996. "IGV-rotor interaction analysis in a transonic compressor using the navier-stokes equations". *Journal of Turbomachinery,* ***120***(1), pp. 147–155.

7.4. Paper 10: Steady and Unsteady CFD Calculation of the Laminar-to-Turbulent Transition in a Turning Mid Turbine Frame with Embedded Design

---

P. Bader and W. Sanz, "Steady and Unsteady CFD Calculation of the Laminar-to-Turbulent Transition in a Turning Mid Turbine Frame with Embedded Design," *Proceedings of ASME Turbo Expo 2016: Turbine Technical Conference and Exposition, June 15-19, 2015, Palais des Congres, Montreal, Canada*, GT2015-42617, 2015.

Proceedings of ASME Turbine Technical Conference and Exposition 2015
GT2015
June 15-19, 2015, Palais des Congres, Montreal, Canada

GT2015-42617

STEADY AND UNSTEADY CFD CALCULATION OF THE LAMINAR-TO-TURBULENT TRANSITION IN A TURNING MID TUBINE FRAME WITH EMBEDDED DESIGN

Pascal Bader, Wolfgang Sanz
Institute of Thermal Turbomachinery and Machine Dynamics
Graz University of Technology
8010 Graz, Inffeldgasse 25/A, Austria
Email: pascal.bader@tugraz.at
www: http://www.ttm.tugraz.at

ABSTRACT

In order to meet the weight requirements of future jet engines S-shaped intermediate turbine ducts can be supplied with turning load- carrying struts in order to save the first vane row of the subsequent low pressure rotor.

In such a duct large flow structures emanating from the outlet of the transonic high pressure stage are transported towards the low pressure rotor and are superimposed by secondary effects generated by the turning struts within the duct. To reduce the fluctuations behind the S-shaped duct and to homogenize the flow, the duct can be equipped with additional splitters. Such an embedded design has the advantage of a more homogenized flow entering the low pressure rotor, thus improving efficiency.

It is crucial for the overall efficiency to optimize the design of such an intermediate turbine duct. To understand all flow effects it is helpful to perform CFD calculations which do not neglect laminar-to-turbulent transition. Therefore this paper presents steady and unsteady CFD results of an S-shaped turbine duct with splitters considering boundary layer transition using Menter's γ-Re_Θ model. The differences between steady and unsteady simulation and the influence of transition are discussed.

NOMENCLATURE

C	Axial chord length
c	Velocity
c_f	Wall friction coefficient
c_p	Specific heat capacity
H	Relative channel height
K	Acceleration factor
p_{stat}	Static pressure
p_t	Total pressure
s	Entropy
T	Total temperature
t_{step}	Timestep
Tu	Turbulence intensity
U_∞	Free stream velocity
x	Axial coordinate
y^+	Dimensionless wall distance
α	Yaw angle
γ	Intermittency
δ	Boundary layer thickness
$\Delta\eta$	Lost efficiency
ν	Kinematic viscosity
τ_w	Wall shear stress

ABBREVIATIONS

BL	Boundary Layer
BPP	Blade passing period
CFD	Computational Fluid Dynamics
HP	High Pressure
ITTM	Institute for Thermal Turbomachinery and Machine Dynamics
LP	Low Pressure
PS	Pressure side
SS	Suction side
SST	Shear stress transport
TE	trailing edge
(T)MTF	(Turning) Mid Turbine Frame

INTRODUCTION

In modern two-spool engines an S-shaped intermediate turbine duct is used to connect the high and low pressure turbine. Such a duct has a great impact on the overall performance of the engine. Therefore it is important to analyze the efficiency and the flow through this mid turbine frame (MTF). In order to reduce weight and the overall axial dimensions of an engine, it is useful to locate the bearing underneath the MTF, thus load-carrying struts are necessary within the duct. These struts can also be aerodynamically optimized to generate the necessary swirl for the subsequent low pressure rotor, hence these turning struts replace the LP vane row. Such a design is called turning mid turbine frame (TMTF).

Since the circumferential space in between the struts is relatively large, the turning of the flow is quite inhomogeneous. In addition to that, the TMTF is characterized by strong secondary flows and it transports and even enhances secondary flow structures of the upstream high pressure stage. This leads to a strong rotor-rotor interaction (HP-LP rotor) and can trigger flow separation as well as vibrations at the downstream LP turbine blades. Many analyses have been performed in the past to understand the flow through an intermediate turbine duct. Götllich [1] published an interesting overview of the flow features in such a duct. Also measurements and simulations were performed, e.g. [2] and [3].

In order to homogenize the flow exiting the TMTF and thus the flow towards the LP rotor, splitters can be added between the struts to better guide the flow and to reduce the secondary vortices. Several designs were investigated in the last decade. In this paper the design of Spataro et al. [4] will be investigated. This TMTF consists of 16 strut blades with two additional split blades embedded between two struts (32 splitters in total). A three-dimensional view of this embedded design can be found in Figure 1a. This design was developed and investigated in a transonic two-stage counter-rotating turbine rig at the Institute for Thermal Turbomachinery and Machine Dynamics (ITTM) at Graz University of Technology. For more details about the rig references [6, 7] are recommended to the interested reader. For the sake of completeness, the investigated operation conditions of the rig are listed in Table 1.

TABLE 1. BLADING PARAMETERS AND OPERATING CONDITIONS [5].

Blading parameters				
	HP vane	HP blade	TMTF	LP blade
Vane/ blade no.	24	36	16	72
H/C	1.15	1.37	0.53	2.94
Re(10^{-6})	2.38	1.1	1.86	0.46
Tip gap	-	unshrouded	-	shrouded
Operating conditions				
		HP stage	LP stage	
$n_{r,in}$ $[rpm/\sqrt{K}]$		524.4	195.3	
$m_{r,in}$ $[kg/s \cdot \sqrt{K}/(bar)]$		81.2	214.6	
Stage p_t ratio		3	1.3	
Power [kW]		1710	340	

Previously steady [4] and unsteady [8] measurements as well as steady [5] and unsteady [9] CFD simulations have been performed at the institute to analyze the TMTF with embedded design. These publications discuss extensively the flow features through the TMTF. The purpose of this paper now is to understand and analyze the behavior of the boundary layer (BL) within the TMTF.

Already Mayle [10] published in 1991 an interesting paper about the role of transition in turbomachines. The state of the boundary layer, thus the transitional behavior, has a high influence on factors like skin friction, heat transfer and so on and is therefore vital for the analysis of the overall performance of the engine. But since transition is hardly measurable in complex flows like in turbomachines, not much focus is given on these vital details.

Due to the fact, that in complex turbomachinery flows it is difficult to measure the transitional behavior, numeric simulations for the prediction of transition are useful. For this reason iIn the last decades several transition models (e.g. the $\gamma - Re_\Theta$-model [11, 12]) have been developed and successfully tested (see e.g. [13–18].

In order to study the transitional behavior within a two-stage turbine, this work should give an insight in the behavior of the boundary layer with a focus on the turning mid turbine frame by using computational results obtained with the $\gamma - Re_\Theta$ transition model.

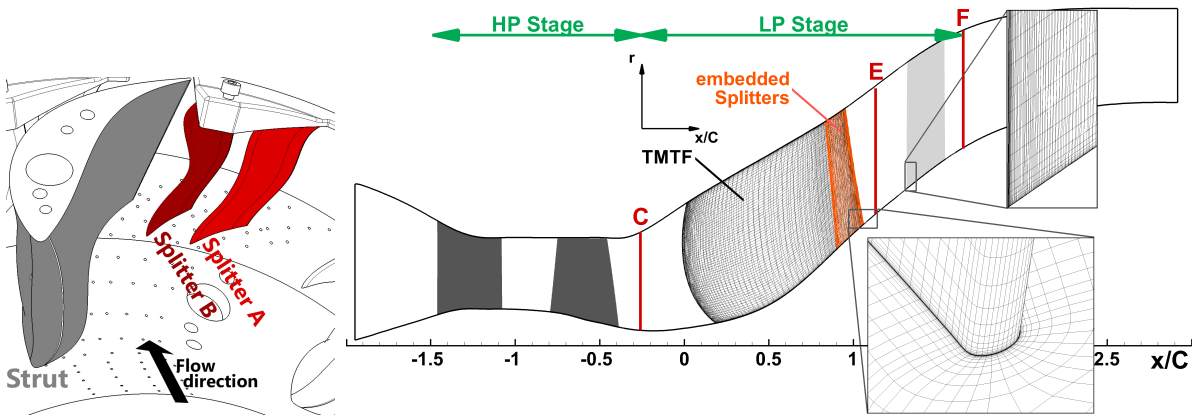

(a) SPLITTER DESIGN [4]. (b) MERIDIONAL PATH [5].

FIGURE 1. A CAD SKETCH OF THE TMTF TOGETHER WITH THE COMPUTATIONAL SETUP.

NUMERICAL SETUP

Both steady and unsteady simulations discussed in this paper have been computed with LINARS, an in-house code which has been developed at Graz University of Technology at the ITTM [19]. The code solves the Reynolds-averaged Navier-Stokes (RANS) equations in conservative form with a fully-implicit, time-marching finite-volume method. The inviscid (Euler) fluxes are discretized with an upwind flux difference splitting method of Roe [20].

As turbulence model Menter's k-ω SST model has been used [21] with two additional transition equations known as the $\gamma - Re_\Theta$ transition model [22].

In order to consider the circumferential periodicity, 90° of the whole turbine has been simulated. This results in 6 HP vanes, 9 HP rotor blades, 4 struts (with 8 splitters) and 18 LP rotor blades. The mesh consists of approximately 50 million cells with y^+ lower than 1.

Between the stationary and rotating domains transient rotor-stator interfaces were used for the unsteady simulation.

The timestep size t_{step} for the unsteady calculation was chosen in such a way, that every timestep the HP rotor rotates $^1/_{30}°$. This results in 300 timesteps for each high pressure blade passing period (HP-BPP). Several revolutions were calculated until a convergent periodic solution was achieved. Data evaluation was performed for the last 2700 time steps corresponding to 90° rotation of the HP rotor, which represents 9 HP-BPPs.

In Fig. 1b the meridional flow path through the computational domain is plotted. The inlet at the very left end was placed at a measurement plane of the test rig. Thus measurement values are available at this plane which were used as boundary conditions at the computational inlet. The outlet at the very right end of Fig. 1b was placed at an axial distance of $(x_{out} - x_{LP_{rotor},TE})/C_{LP_{rotor}} = 6$ downstream of the low pressure rotor trailing edge. At this position the static pressure p_{stat} was set implying radial equilibrium.

RESULTS

In this section the influence of boundary layer transition will be discussed. As a first step the basic state of the boundary layer is analyzed with the help of a stationary simulation.

The unsteady behavior of the boundary layer will be analyzed in the second part of this section.

In order to see the influence of transition modeling, a comparison between two unsteady simulations with and without transition modelling is given in the last section.

Steady behavior of the boundary layer

First, the stationary state of the boundary layer will be discussed. Figure 2 shows three-dimensional contour plots of the intermittency γ and the acceleration factor K of the HP rotor and the TMTF with the splitters of the steady state simulation. The intermittency γ describes the state of the boundary layer where $\gamma = 0$ represents a laminar boundary layer and $\gamma = 1$ a fully turbulent boundary layer. Since $\gamma = 0$ at the wall (laminar sublayer) the illustrated plane in Fig. 2a does not exactly show the results at the wall but at some grid levels offset of the wall.

The acceleration factor K is useful to determine whether transition or relaminarization is possible. K is calculated with

$$K = \frac{\nu}{U_\infty(x)^2} \cdot \left[\frac{dU_\infty}{dx}\right] \tag{1}$$

where $U_\infty(x)$ is the local free stream velocity, $^{dU_\infty}/_{dx}$ represents the streamwise velocity gradient and ν represents the kinematic

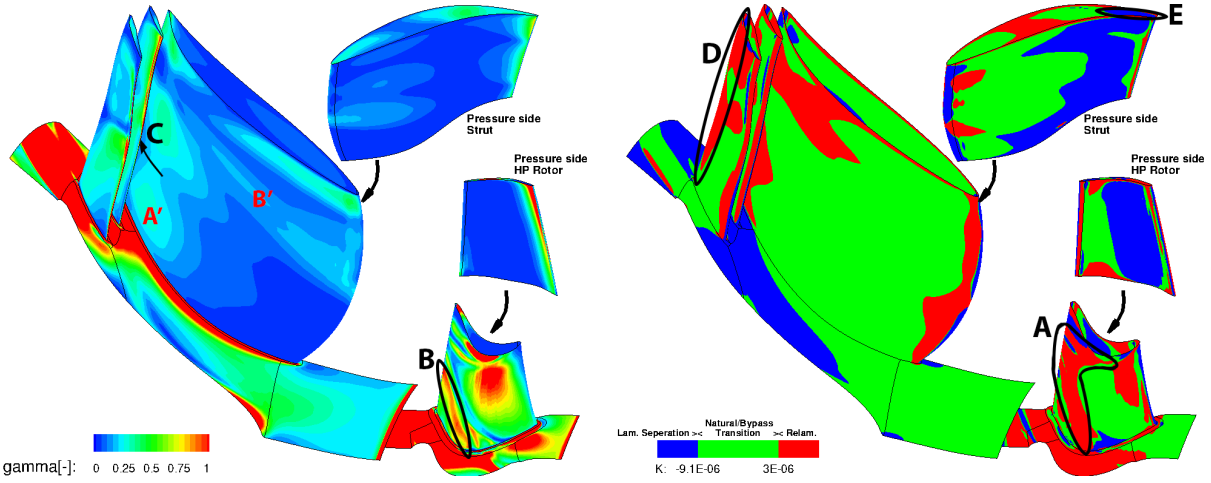

(a) INTERMITTENCY γ. (b) ACCELERATION FACTOR K.

FIGURE 2. THREE DIMENSIONAL PLOT OF A HP TURBINE BLADE AND THE TMTF WITH SPLITTERS.

viscosity of the fluid. If the acceleration factor exceeds $3 \cdot 10^{-6}$ relaminarization may occur. If K is lower, natural or bypass transition is most likely. If a strong deceleration takes place ($K < -9.1 \cdot 10^{-6}$) transition over a separation bubble may happen. The limit between natural/bypass transition and transition via a laminar separation bubble highly depends on the turbulence intensity Tu according to equation [10]

$$K_{limit} = -5.13 \cdot 10^{-7} \cdot Tu^{5/4} \tag{2}$$

where K_{limit} represents this limit. The above stated limit is calculated for $Tu \approx 10\%$ which is more or less the case within the TMTF.

Looking at the high pressure rotor blade in Fig. 2a and b it can be observed that the state of the boundary layer changes rapidly at the suction side. The intermittency distribution at the HP blade shows a strong variation of transition onset locations at different the blade height positions, which could lead to different boundary layer thicknesses δ at the trailing edge of the blade. At the upper part of the channel a rapid transition takes place. But due to a strong acceleration (marked with A in Fig. 2b) the boundary layer relaminarizes downstream.

At the lower part of the blade, the transition occurs more downstream (Indicated with B in Fig. 2a). A reason for the different boundary layer evolution can be observed in Fig. 2b: A strong acceleration at the HP rotor suction side (marked with A in Fig. 2b) leads to relaminarization. But shortly downstream, this transitional boundary layer gets turbulent again (marked with B in Fig. 2a).

The strong variations of transition and re-transition along the blade most likely lead to different boundary layer thickness $\delta(x)$. This can result in different downstream flow angles over the channel height due to the influence of the boundary layer.

The pressure side of the HP rotor shows a laminar boundary layer along the chord length.

Focusing on the TMTF, the plot in Fig. 2a of the intermittency shows, that the state of the boundary layer is transitional along the mid section of the strut, but does not change to a turbulent boundary layer. At the latter part of the blade the boundary layer relaminarizes (marked with arrow C in Fig. 2a), due to a strong acceleration caused by the blockage effect of the splitters (see [5]). Also the acceleration factor K in Fig. 2b agrees with these observations, since it shows a sufficiently high K at this part of the strut.

The diffusive part at the suction side of the strut close to the trailing edge is hidden by the splitters in Fig. 2. It is slightly visible at the top right picture (Fig. 2b) marked with E. The boundary layer is transitional there.

Also the splitters show transitional, but not fully turbulent boundary layers. The splitters also show a high acceleration rate close to their trailing edges (indicated with D in Fig. 2b) and also the intermittency decreases, thus relaminarization also occurs at the splitters.

Unsteady behavior of the boundary layer

In this section unsteady effects will be analyzed. The focus lies on the TMTF and on the flow reaching the subsequent low pressure rotor.

Unsteady fluctuations arising from the upstream high pressures stage have a high influence on the flow downstream. These unsteady effects were already analyzed in previous studies (see

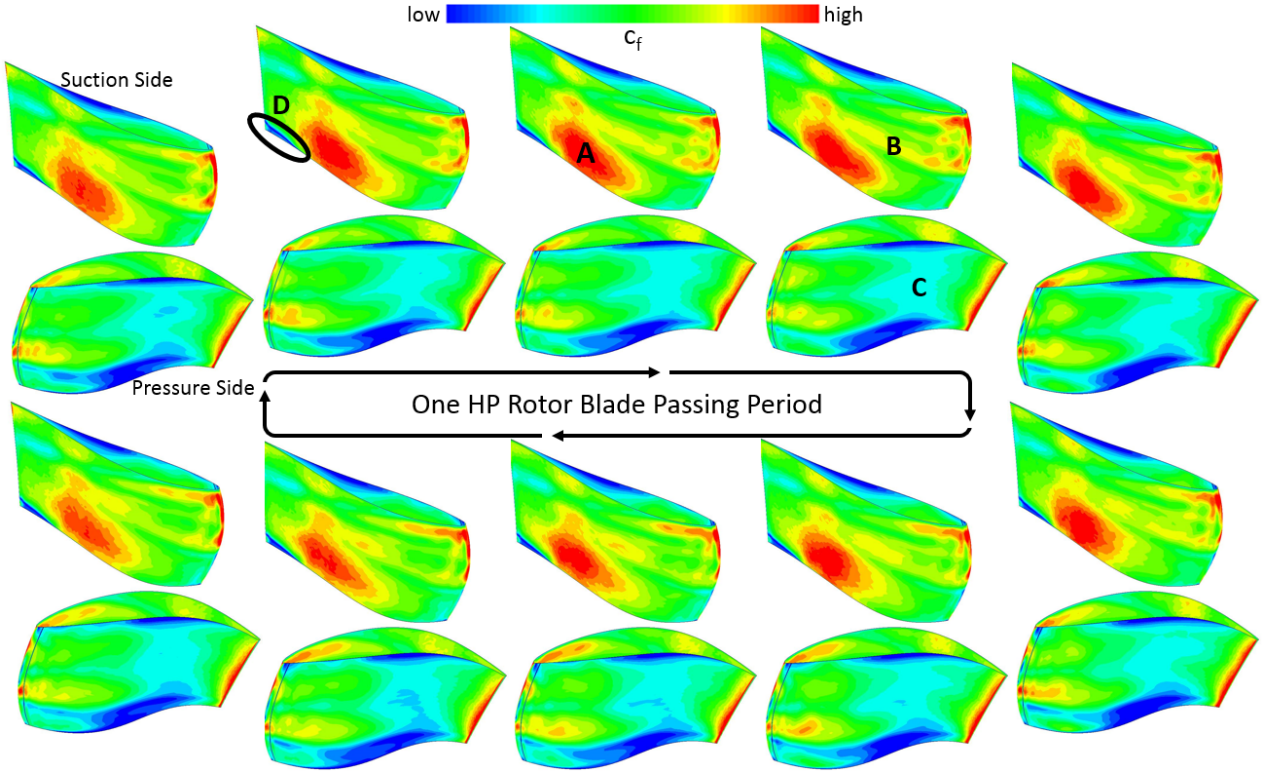

FIGURE 3. UNSTEADY FLUCTUATIONS OF c_f AT THE TMTF STRUT SHOWING ONE HP ROTOR BPP.

[9]), therefore in the following only the effects of the unsteady flow on the boundary layer should be discussed. Mainly the wakes of the HP rotor affect the boundary layer of the strut.

In order to see a change in the boundary layer the skin friction coefficient c_f is given as a contour plot on the TMTF strut surface[1] (see Fig. 3) at different timesteps. The skin friction coefficient is computed with

$$c_f = \frac{\tau_w}{1/2 \cdot \rho \cdot {U_\infty}^2} \tag{3}$$

where τ_w represents the wall shear stress and U_∞ the free stream velocity. c_f can be used to determine the state of the boundary layer because it increases rapidly if transition occurs since a turbulent BL has a larger wall friction as described in the previous section. The skin friction is also a quantity to estimate losses due to wall friction.

Each picture in Fig. 3 represents one degree of HP rotor revolution, thus the ten pictures in the figure represent one blade passing period (BPP) of a HP rotor blade. All contour plots show the suction side (upper part) and the pressure side (lower part) of the strut.

Focusing on the suction side of the strut a relatively huge zone of high c_f-values is visible (structure A). This area corresponds with the findings above (see Fig. 2a marked with A'). Comparing these structures at the different timesteps it is observable that the intensity fluctuates and the length of the structure in streamwise direction changes. This indicates that this area is transitional in all timesteps but the position of transition and relaminarization changes during one BPP.

Looking at the structure indicated with B (also B' in Fig. 2a), the transition zone is highly unstable. The skin friction c_f fluctuates highly during one BPP and therefore it can be assumed that transition does not always take place. The zone of high c_f shifts upstream and downstream in chordwise direction during one BPP. This indicates that these fluctuations are possibly triggered by the wakes of the upstream HP rotor.

At the pressure side it can be seen, that c_f also changes during one BPP, mainly in the center of the strut (indicated with C).

The low wall shear stress marked with D in Fig. 3 shows a

[1]Note that the view angle between Fig 2 and Fig. 3 differs!

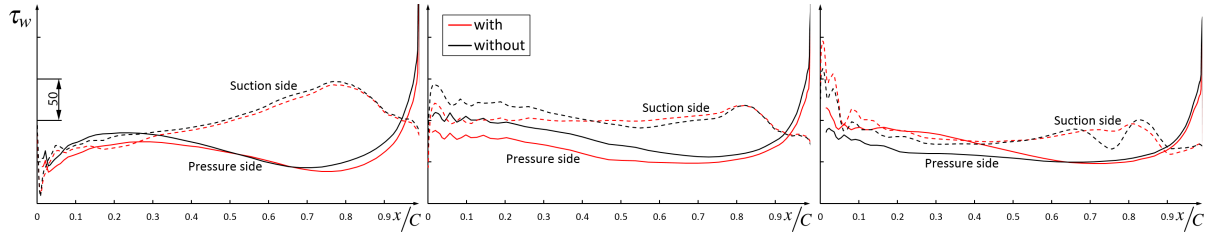

(a) AT 25% SPAN. (b) AT 50% SPAN. (c) AT 75% SPAN.

FIGURE 4. TIME-AVERAGED WALL SHEAR STRESS τ_w OF BOTH SIMULATIONS OF THE STRUT BLADE.

flow separation. This separation has already been observed in previous studies (see e.g. [4, 5]). Comparing this flow separation at the different timesteps it can be observed that this structure is more or less time independent.

Influence of transition on unsteady flow

In this section two unsteady simulations, one with and one without modeled transition, are compared to each other.

Friction at the strut: Fig. 4 shows the time-averaged wall shear stress τ_w at the pressure and suction side of the strut of both unsteady simulations at three different spanwise positions (25%, 50% and 75%). It has to be mentioned, that the calculation without transition model assumes a fully turbulent boundary layer.

The distribution in Fig. 4 confirms the result which was already discussed in Fig. 2. Looking at the streamwise distribution of τ_w at the pressure side at 25% span (Fig. 4a) it can be seen, that there are differences between the two simulations: The wall shear stress of the case without transition is slightly higher compared to the simulation with transition. Since a turbulent boundary layer has a higher wall shear stress, the reason for these differences may be a laminar boundary layer. Figure. 2a confirms that assumption: The γ-value at the pressure side indicates that the BL stays laminar over the whole chord length at 25% span of the strut.

The suction side at 25% span also shows similar differences, but at the aft part of the suction side the wall shear stress τ_w of both simulations has the same value. The reason is that the boundary layer gets turbulent at this position. This can again be validated with the γ-distribution of Fig. 2a.

At 50% span the differences between the two simulations are more distinct as at 25% span: As long as the boundary layer is laminar, the simulation without the enabled transition model has a higher wall shear stress due to the assumed turbulent boundary layer of this simulation. Both simulations approach nearly the same value at the aft part of the strut suction side and again this can be confirmed by the γ-distribution at 50% span in Fig. 2a. Surprisingly the wall shear stress of the simulation without transition is lower compared to the simulation with transition at the suction side between approximately $^x/_C > 0.45$ and $0.8 > {}^x/_C$.

The distribution of τ_w at 75% shows again that the boundary layer at the pressure side is predicted laminar by the simulation with transition. This is also observable in the γ-distribution in Fig. 2a. The differences at the suction side can be found mainly at the beginning of the blade, since the boundary layer gets transitional at aft parts of the strut, thus the differences between the curves are getting smaller.

Radial distribution at Plane E: Figure 5 shows the radial distributions of the total pressure p_t and the yaw angle α at plane E comparing the two simulations with steady measurements. Plane E represents the plane subsequent of the TMTF and upstream of the low pressure rotor. Thus these radial distributions describe the flow reaching the LP rotor.

The radial distribution of p_t does not show high differences, only a small deviation at the upper part of the channel, where the simulation with transition agrees slightly better with the measurement data. Generally both simulations agree well with the measurements.

The radial distribution of α clearly shows differences in the yaw angle and mainly at the lower part of the channel the simulation with transition also agrees better with the measurements. Since the yaw angle describes the direction of the flow reaching the subsequent LP rotor, thus influencing the efficiency of the rotor, this value is crucial and will be analyzed in the next section.

Flow downstream of the TMTF: As already discussed, a main focus lies on the flow entering the LP rotor since the design with splitters analyzed in this paper is used to homogenize the flow reaching the LP stage. The discussion deals mainly with the homogenization on the yaw angle α.

Figure 6 shows the circumferential distributions of the yaw angle at 25%, 50% and 75% span for both simulations. The graphs give the time-averaged values together with the envelope of the minimal and maximal fluctuations at these three posi-

tions. In the charts also the position of the wakes of the strut and splitters are marked. There are slightly differences between two neighboring struts because of the blade ratio of 3:2 between HP stator and TMTF (see [9]).

Comparing the two simulations it can be observed that the differences are remarkably high. At all three positions the simulation without transition shows higher local fluctuations. The most remarkable difference between the two simulations can be found at 75% span (Fig. 6c): Clearly the deviations caused by the wakes are computed higher by the simulation without transition. For all sections the local and temporal fluctuations are predicted smaller by the simulation with transition. Especially the wakes of splitter A are computed much thicker without transition model. A possible reason can be found in Fig. 2a where the γ-distribution at the splitters shows a laminar boundary layer at the trailing edge of the splitter which would lead to a thinner boundary layer as discussed above.

Although the simulations at 50% span (Fig. 6b) deviates less compared to 75% span, the differences are still clearly visible. It seems that both curves have a circumferential offset. Again a more laminar, thus thinner boundary layer as discussed may influence the yaw angle α downstream of the TMTF causing this circumferential shift.

At 25% span (Fig. 6a) the local fluctuations are again higher for the simulation without modeled transition.

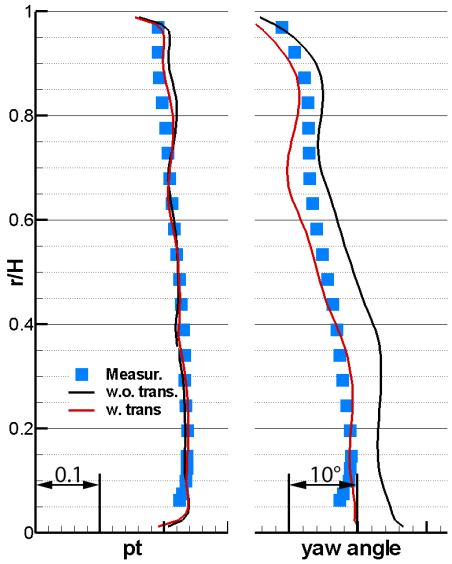

FIGURE 5. RADIAL DISTRIBUTIONS OF p_t AND α.

Effects on the stage performance: In this subsection the effect of the boundary layer on the overall stage performance will be discussed. The validation is made with the help of the lost efficiency $\Delta\eta$. Figure 7 shows this value through the different blade rows of the turbine. $\Delta\eta$ is computed with following formula [23]

$$\Delta\eta = \frac{\Delta s \cdot T_F}{c_p \cdot (T_A - T_F) + \Delta s_{AF} \cdot T_F} \tag{4}$$

where the entropy s and the total temperature T are mass-averaged. Δs represents the entropy differences within one stage, Δs_{AF} the total entropy difference of the engine and T_A and T_F represents the mass-averaged total temperature at plane A (Inlet) and F (downstream of the LP rotor), respectively. The losses were normalized with the total loss of the unsteady simulation without transition. The numbers in Fig. 7 show the relative differences in the losses for the different blade rows.

The highest difference between the two simulations appears in the TMTF: The simulation with modeled transition loses approximately $\approx 2.1\%$ less efficiency compared to the simulation without transition. On the other hand the loss through the HP and LP rotors is about $\approx 0.8\%$ and $\approx 0.6\%$ higher, respectively. Overall, the simulations differ about $\approx 0.9\%$ in normalized lost efficiency. The differences are remarkably since they are only caused by boundary layer transition. Thus, if turbomachines should be numerically improved it should be kept in mind, that transition has an influence on the overall performance.

CONCLUSION

In this paper an alternative TMTF design has been investigated. The setup has two additional splitter blades between two TMTF struts.

In order to understand how the boundary layer develops within such a channel, a steady and unsteady simulations have been performed with modeled transition. The computed unsteady results show that the boundary layer at the HP rotor blade is very unstable and changes its state along the chord.

The TMTF shows different boundary layer states along the chord of the strut and splitters. Also the transition and relaminarization positions differ over the blade height. These different transition effects over the blade height can lead to different boundary layer thicknesses.

To see how unsteady effects influence the boundary layer, the skin friction coefficient at the strut at different timesteps has been compared. It has been found, that the transition position of some parts of the boundary layer varies during one blade passing period. This effect is most likely caused by the wake of the HP rotor which triggers the laminar-to-turbulent transition.

In order to see the influence of the boundary layer transition, two different simulations have been compared, one with and one

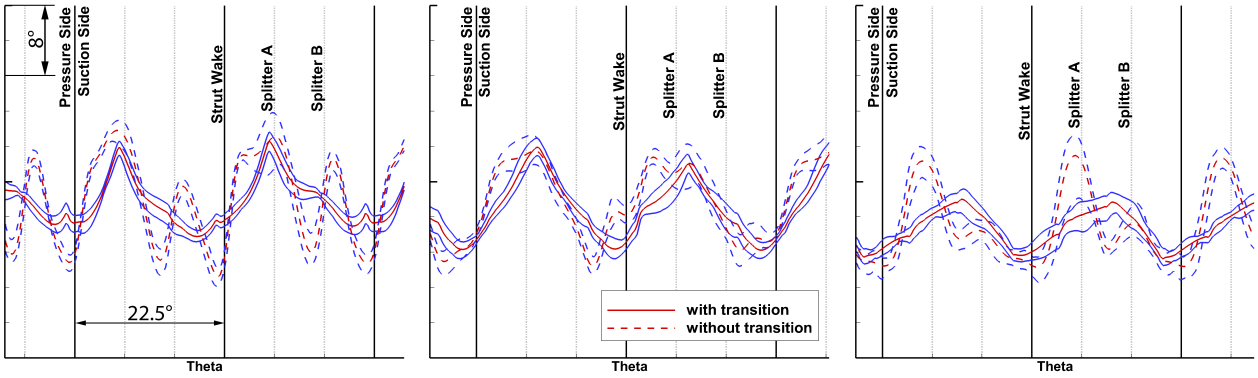

(a) AT 25% SPAN. (b) AT 50% SPAN. (c) AT 75% SPAN.

FIGURE 6. TIME-AVERAGED YAW ANGLE α TOGETHER WITH THEIR FLUCTUATION OF THE TWO SIMULATIONS.

without modeled transition. The comparison showed, that the differences are not marginal and that the modeled boundary layer has a high influence on the yaw angle distribution downstream of the TMTF blade. This is crucial since this distribution influences the performance of the downstream LP rotor.

Also the overall stage performance showed differences between the simulations.

Summarizing, the CFD simulations performed within this work gave an insight on boundary layer transition as predicted by a common transition model. It showed that the differences between modeled and not-modeled transition are not negligible. Since measurements of the state of the boundary layer are very difficult within such turbine rigs and thus are not available, this simulation can help to improve the view of the boundary layer development.

If future designs should be optimized with the help of CFD simulations, it should be kept in mind that the transition has an influence on the computed results.

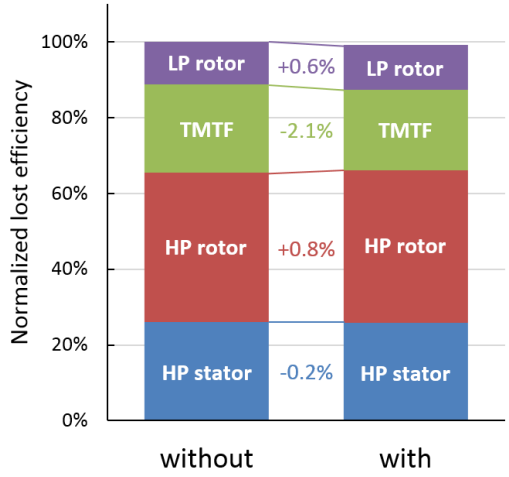

FIGURE 7. NORMALIZED LOST EFFICIENCY THROUGH THE STAGES.

ACKNOWLEDGMENT

The research leading to these results has been partially funded by the European Union within the EU-project DREAM (contract No. ACP7-GA-2008-211861) as well as from the Austrian Federal Ministry for Finance.

The authors would also like to thank the Austrian Federal Ministry for Transport, Innovation and Technology who funded part of the work by the project RELAM within the Austrian Aeronautics Program TAKE OFF.

REFERENCES

[1] Göttlich, E., 2011. "Research on the aerodynamics of intermediate turbine diffusers". *Progress in Aerospace Sciences 47*.

[2] Santner, C., Paradiso, B., Malzacher, F., Hoeger, M., Hubinka, J., and Göttlich, E., 2011. "Evolution of the flow through a turning mid turbine frame applied between a transonic HP turbine stage and a counter-rotating LP turbine". *Proceedings of 9th European Turbomachinery Conference 2011, Istanbul, Turkey*. Paper No. 110.

[3] Lengani, D., Santner, C., Spataro, R., Paradiso, B., and Göttlich, E., 2012. "Experimental investigation of the unsteady flow field downstream of a counter-rotating two-spool turbine rig". *Proceedings of ASME Turbo Expo, 2012*. GT2012-68583.

[4] Spataro, R., Göttlich, E., Lengani, D., Faustmann, C., and

Heitmeir, F., 2013. "Development of a turning mid turbine frame with embedded design: Part I design and steady measurements". *In Proceedings of ASME 2013 Turbo EXPO, June 3-7, San Antonio, Texas, USA*. GT2013-95279.

[5] Bader, P., Sanz, W., Spataro, R., and Göttlich, E., 2014. "Flow evolution through a turning mid turbine frame with embedded design". *Proceedings of ASME 2014 Turbo EXPO, Düsseldorf, Germany*. GT2014-25009.

[6] Hubinka, J., Santner, C., Paradiso, B., Malzacher, F., and Göttlich, E., 2009. "Design and construction of a two shaft test turbine for investigation of mid turbine frame flows". *Proceedings of ISABE 2009, Montreal, Quebec, Canada*. ISABE-2009-1293.

[7] Hubinka, J., Paradiso, B., Santner, C., Pirker, H. P., and Göttlich, E., 2011. "Design and operation of a two spool high pressure test turbine facility". *Proceeding of the 9^{th} European Turbomachinery Conference 2011, Istanbul, Turkey*, pp. 1531–1540. Paper No. B112.

[8] Spataro, R., Göttlich, E., Lengani, D., Faustmann, C., and Heitmeir, F., 2013. "Development of a turning mid turbine frame with embedded design - part II: Unsteady measurements". *Proceedings of ASME 2013 Turbo EXPO, San Antonio, Texas, USA*. GT2013-95280.

[9] Bader, P., Sanz, W., and Spataro, R., 2015. "Unsteady CFD simulation of a turning mid turbine frame with embedded design". *Proceedings of 11^{th} European Turbomachinery Conference 2015, Madrid, Spain*. ETC2015-007.

[10] Mayle, R. E., 1991. "The role of laminar-turbulent transition in gas turbine engines". *Journal of Turbomachinery,* ***113***(4), October, pp. 509–537.

[11] Menter, F. R., Langtry, R. B., Likki, S. R., Suzen, Y. B., Huang, P. G., and Völker, S., 2006. "A correlation based transition model using local variables part 1: Model formulation". *Journal of Turbomachinery,* ***128***(3), pp. 413–422.

[12] Langtry, R. B., 2006. "A correlation-based transition model using local variables for unstructured parallelized CFD codes". PhD Thesis, Institute of Thermal Turbomachinery and Machinery Laboratory, University Stuttgart.

[13] Elsner, W., Piotrowski, W., and Drobniak, S., 2008. Transition prediction on turbine blade profile with intermittency transport equations. ASME Turbo Expo 2008, Berlin, Germany. GT2008–50796.

[14] Sorensen, N. N., 2009. CFD modeling of laminar-turbulent transition for airfoil and rotors using the $\gamma - \tilde{Re}_{\Theta}$ model. Wind Energy. pp. 715–733.

[15] Malan, P., Suluksna, K., and Juntasaro, E., 2009. Calibrating the $\gamma - Re_{\Theta}$ transition model for commercial CFD. AIAA Paper. 2009–1142.

[16] Ramadani, K., Kelterer, M., Pecnik, R., and Wolfgang, S., 2009. Application of the zeta-f-turbulence model to steady transitional flow. Proceeding of the 8^{th} European Turbomachinery Conference 2009, Graz, Austria. Paper No. 093.

[17] Kelterer, M., Pecnik, R., and Wolfgang, S., 2010. Computation of laminar-turbulent transition in turbomachinery using the correlation based $\gamma - Re_{\Theta}$ transition model. ASME Turbo Expo 2010, Glasgow, Scotland. GT2010-22207.

[18] Kelterer, M., Burgstaller, R., and Sanz, W., 2011. Application of the $\gamma - Re_{\Theta}$ transition model to transitional flow. 10^{th} International Symposium on Experimental and Computational Aerothermodynamics of Internal Flows, Brussels, Belgium. ISAIF 10-091.

[19] Pecnik, R., Pieringer, P., and Sanz, W., 2005. "Numerical investigation of the secondary flow of a transonic turbine stage using various turbulence closures". *Proceedings of ASME Turbo Expo 2005, Reno-Tahoe, USA*. GT2005-68754.

[20] Roe, P. L., 1981. "Approximate riemann solver, parameter vectors and differencing scheme". *Journal of Computational Physics. Vol 43*, pp. 357–372.

[21] Menter, F. R., 1994. "Two-equation eddy-viscosity turbulence models for engineering applications". *AIAA Journal,* ***32***(8), pp. 1598–1605.

[22] Langtry, R. B., and Menter, F. R., 2009. "Correlation-based transition modeling for unstructured parallelized computational fluid dynamics codes". *AIAA Journal,* ***47***(12), pp. 2894–2906.

[23] Pullan, G., Denton, J., and Curtis, E., 2006. "Improving the performance of a turbine with low aspect ratio stators by aft-loading". *Journal of Turbomachinery, ASME. 2006. Vol. 128*.

CHAPTER 8

SUMMARY AND CONCLUSION

We have to learn a lot in order to be able to enquire about the things we do not know.

Jean-Jacques Rousseau
PHILOSOPHER, WRITER, AND COMPOSER

8.1. Summary

The present work gives a comprehensive review of transition and relaminarization, presents new measurement techniques for the experimental investigation of theses processes and shows new findings regarding relaminarization.

Regarding transition, innovative non-invasive measurement techniques for its measuring like the Laser vibrometer or acoustic probes are presented. Both successfully measured the position of transition without influencing the flow at all. These two techniques have been validated using commonly applied measurement techniques like the Preston tube, but also rather seldom techniques for measuring transition, like thermographic recordings.

One aim of these measurements was also to get new in-house test cases for benchmarking of numerical models. The comparison of CFD and experimental data shows that the three tested RANS models, the γ-Re_θ model, the γ model and the k-k_l-ω turbulence/transition model can predict transition, but the position and length of transition may not be predicted reliably. It has been shown, that as long as the free-stream and boundary conditions along the plate are similar to the test cases of ERCOFTAC, which are used for tuning the models, the results are good. But if the flow conditions differ, the quality of transition prediction by the above mentioned CFD model decreases.

Another interesting point is that there are different results between the solver codes, surprisingly also between CFX® and Fluent®, although both are published by ANSYS®.

Large eddy simulations of the transitional test case show promising results which also allow further insights into the process of transition. In contrast to the RANS simulations, physical effects are predicted which allow a better understanding of the boundary layer transition.

Regarding relaminarization, a well documented test case is obtained within this work. Laser-Doppler measurement results showed that relaminarization can occur when the boundary layer is accelerated. The three investigated test cases show relaminarization and new findings regarding the disturbances remaining inside the boundary layer have been found.

Coincidence measurements revealed beside an explanation for the decrease of turbulent shear stresses also a proof for the existence of laminar velocity profiles during relaminarization. This has been done using a quadrant analyzes. The presence of events in the third quadrant (inward motion of low speed fluid) is a proof for the presence of laminar-like velocity profiles, since such events are not present in a turbulent boundary layer.

As already described, the measurements within this work are also used as unique test sets for benchmarking the CFD transition models, like the k-k_l-ω or the γ-Re_θ RANS model and also to test the capability of large eddy simulation to predict transition and relaminarization numerically.

The turbulence/transition model k-k_l-ω shows a good agreement with the experimental transition measurement data, but cannot predict relaminarization. The model has problems in predicting transition and relaminarization for flows exposed to strong pressure gradients.

The intermittency based γ-Re_θ transition model shows a good agreement with the measurement results. In this work also a detailed discussion is given describing how the γ-Re_θ model can predict relaminarization. Although the model shows good results, it is still rather based on empirical correlations than on physical effects.

Large eddy simulations show a good agreement with the measurement data. The computational results also allow a better understanding of the relaminarization, in particular how vortices are influenced by to the acceleration of the flow and how quadrant-events and turbulent production develop during relaminarization.

Additionally, in the present work the flow through turbomachines has been investigated numerically with the γ-Re_θ transition model focusing on transition and relaminarization. It has been found that both processes happen inside turbomachines. This may be of special interest when optimizing blades regarding skin friction and heat transfer.

8.2. Conclusions

One of the main conclusions which can be drawn from this work is that – in contrast to some common opinions – relaminarization by acceleration occurs, also in turbomachines. It has been shown that due to high acceleration the boundary layer velocity profile deforms, reducing the turbulent production inside the boundary layer and the skin friction. However a direct consequence of the high acceleration is an overshoot of the skin friction upstream of the relaminarization zone. When the acceleration starts to decrease, the skin friction also drops leading to a benefit regarding frictional losses.

Downstream of the relaminarization zone a rapid retransition takes place. This is caused by a reduction of the stabilizing acceleration, allowing disturbances inside the boundary layer to grow, leading to this retransition. Thus it is the author's opinion that since relaminarization and retransition is a direct consequence of the decrease of acceleration, it is hardly possible to influence the contour of a blade in such a way to maintain the laminar boundary layer downstream of the relaminarization zone.

A further outcome of the relaminarization test cases is that if the acceleration leading to relaminarization is undercritical (moderate acceleration), the overshoot in skin friction up-

stream of the relaminarization zone is not present, which increases the benefit of the decrease of frictional losses due to relaminarization. Thus the shape of a blade should be optimized in such a way, that only moderate acceleration takes place, preventing the overshoot.

Regarding numerical results, it is shown that transition can be predicted by all models and approaches, however, not often very accurately. The error of the computations increases when the test case under investigation differs from the ERCOFTAC test cases.

Large eddy simulations show very promising results, the agreement with the measurement is good and LES allows a further insight into the physical processes during transition.

The numerical investigation of the relaminarization test cases shows, that the intermittency based transition models can predict relaminarization, but a critical analysis of the boundary conditions is mandatory, since they have a high influence on the prediction accuracy of the state of the boundary layer.

The turbulence/transition model k-k_l-ω fails in predicting relaminarization, because the model has problems if the boundary layer is exposed to strong pressure gradients which influence the onset and length of transition in general. Thus it is the author's opinion that this model should be used with care for turbomachinery flow calculations.

Also regarding relaminarization prediction the large eddy simulation does a good job and is also able to show the development of velocity fluctuations influenced by the high acceleration inside the boundary layer during relaminarization. LES here again give the opportunity to analyze the physical processes in more detail.

Generally the author thinks, that the intermittency models can achieve good results with relatively small computational effort/resources. The agreement with measurements is good, however, for a detailed analysis LES is recommend.

8.2.1. Future work

In this section recommendations for future works are given, which may improve the understanding of some effects discussed in this work.

- The measurement of the skin friction by using direct measurement techniques like the semiconductor strain gauge skin friction sensors should be improved. An overview of different methods to measure skin friction is given in App. C. This is of special interest, because the skin friction distribution gives an easy indication whether the boundary layer is laminar or turbulent and can also be easily compared to simulation results and although the method used for the results presented in this work is reliable, with a direct wall shear measurement technique the measurement time could be reduced by reducing measurement points close to the wall.

- Coincident Laser-Doppler measurements along the plate at $y^+ \approx 10$ should be performed. The idea behind this measurement is to experimentally obtain the bursts and burst rate leading to turbulent production, thus determine the effects of the high acceleration on the turbulent production. With this information a clearer differentiation between severe and moderate acceleration may be possible.

- Measurements of the boundary layer along blade profiles are of interest. Since it has been shown in this work, that transition and relaminarization can occur along turbine blades, these boundary layer modes should be measured in more detail. With the results

of such a study it would then be possible to control transition and relaminarization by e.g. applying suction at the surface.

- Regarding LDA measurements the data rate should be improved. This can be achieved by a reduction of the spanwise extend of the investigated channel (i.e. reducing the focal length) and a change of the seeding particles. This rise of the sample rate would decrease the measurement time per point, enabling a higher resolution of the measurement grid.
- The results of large eddy simulations should be investigated further regarding quadrant analysis and the spanwise velocity component. Also a focus should be set on embedded LES since the computational effort can be reduced remarkably with such a method. Additional LE simulations should be performed along blade profiles to analyze the boundary layer in turbomachines in more detail.

APPENDIX A

RIBLET MEASUREMENTS

Riblets are micro-structures in a surface, which are obtained e.g. by applying a foil at a surface or by directly manufacturing into the surface. “Riblets” are inspired by nature, in particular by the skin of sharks, which are known for their low resistance when gliding through the water. In Fig. 1.11 a close-up view of the skin of a shark and technical riblets derived are shown.

These structures may lead to a reduction of the skin friction. The mechanism behind is yet not fully understood, but in general the riblets suppress the turbulent production inside the boundary layer, thus “damping” turbulent fluctuations.

Within the scope of this work, riblet measurements have been performed. The riblets have been applied to the boundary layer plate of wind tunnel B, downstream of the acceleration area, where the free stream velocity is the highest. In the following the influence of the

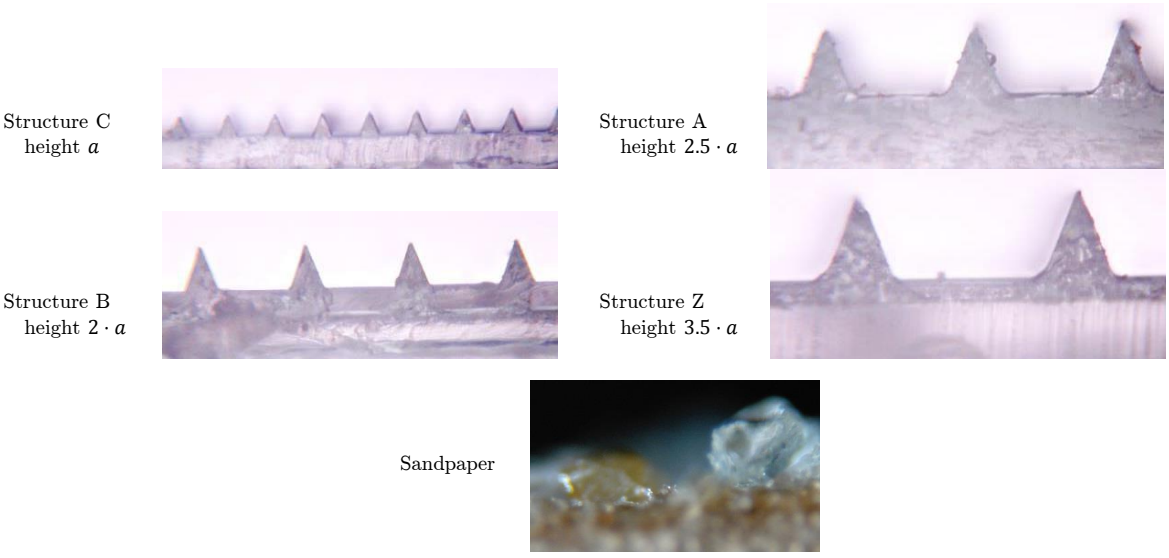

Figure A.1: Overview of the different measured riblet foils

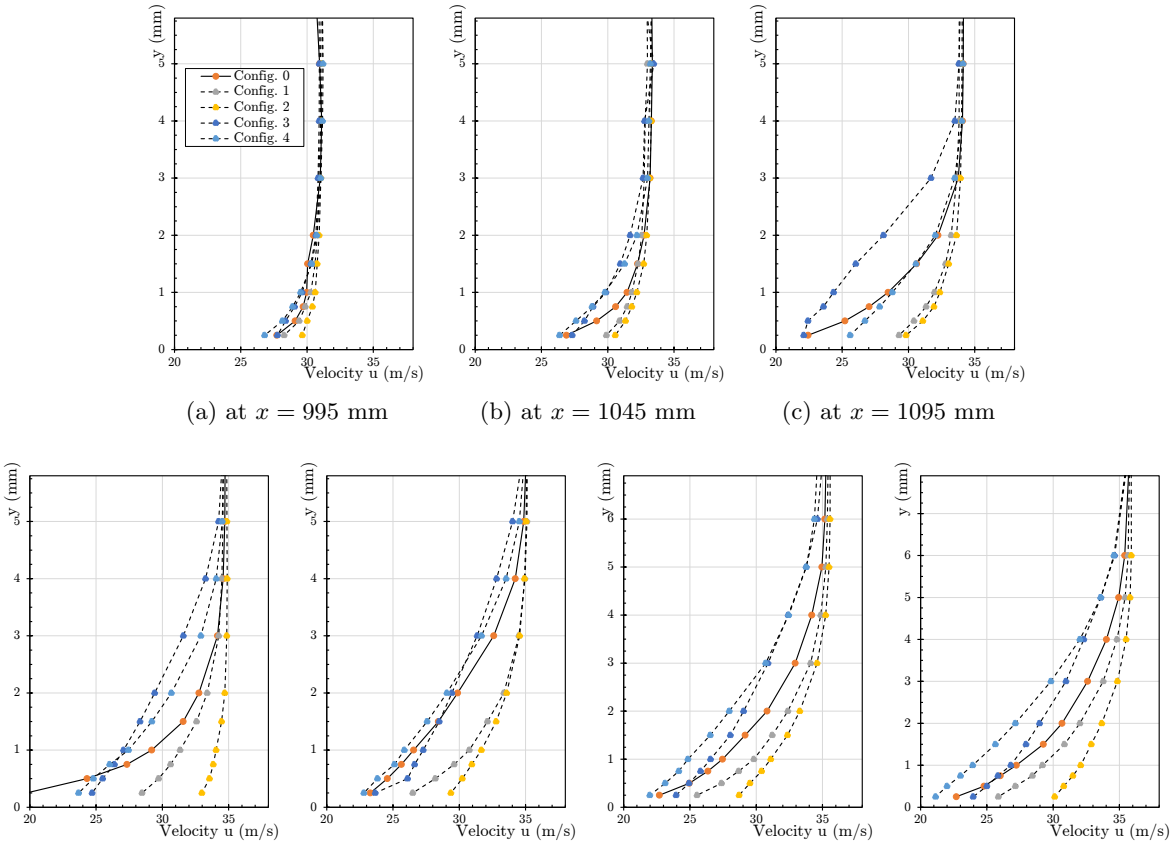

(a) at $x = 995$ mm (b) at $x = 1045$ mm (c) at $x = 1095$ mm

(d) at $x = 1145$ mm (e) at $x = 1195$ mm (f) at $x = 1245$ mm (g) at $x = 1295$ mm

Figure A.2: Streamwise velocity profiles at different streamwise positions showing the influence of the different riblet configurations

riblets on the streamwise velocity and fluctuation distributions are presented for five different configurations. An overview of the configurations is given in Tab. A.1.

Configuration 0 represents the smooth reference case, where smooth foils are applied along whole the surface, whereas configuration 4 represents the "rough" reference case. For configurations 1 to 3 different combinations of structures have been applied to the surface. The structures differ in size, depending on the local skin friction. The structures where selected using a preliminary CFD study performed by *bionic surface technologies*. According to this study, configuration 2 should show the best improvements compared to the baseline case. The differences of the structures are shown in Fig. A.1.

Table A.1: Overview of the measured riblet configurations

x (m)	Config. 0	Config. 1	Config. 2	Config. 3	Config. 4
0–0.9	smooth	smooth	smooth	smooth	smooth
0.9–1.06	smooth	Structure A	Structure B	Structure Z	Sand paper
1.06–1.7 (end)	smooth	Structure B	Structure C	Structure A	Sand paper

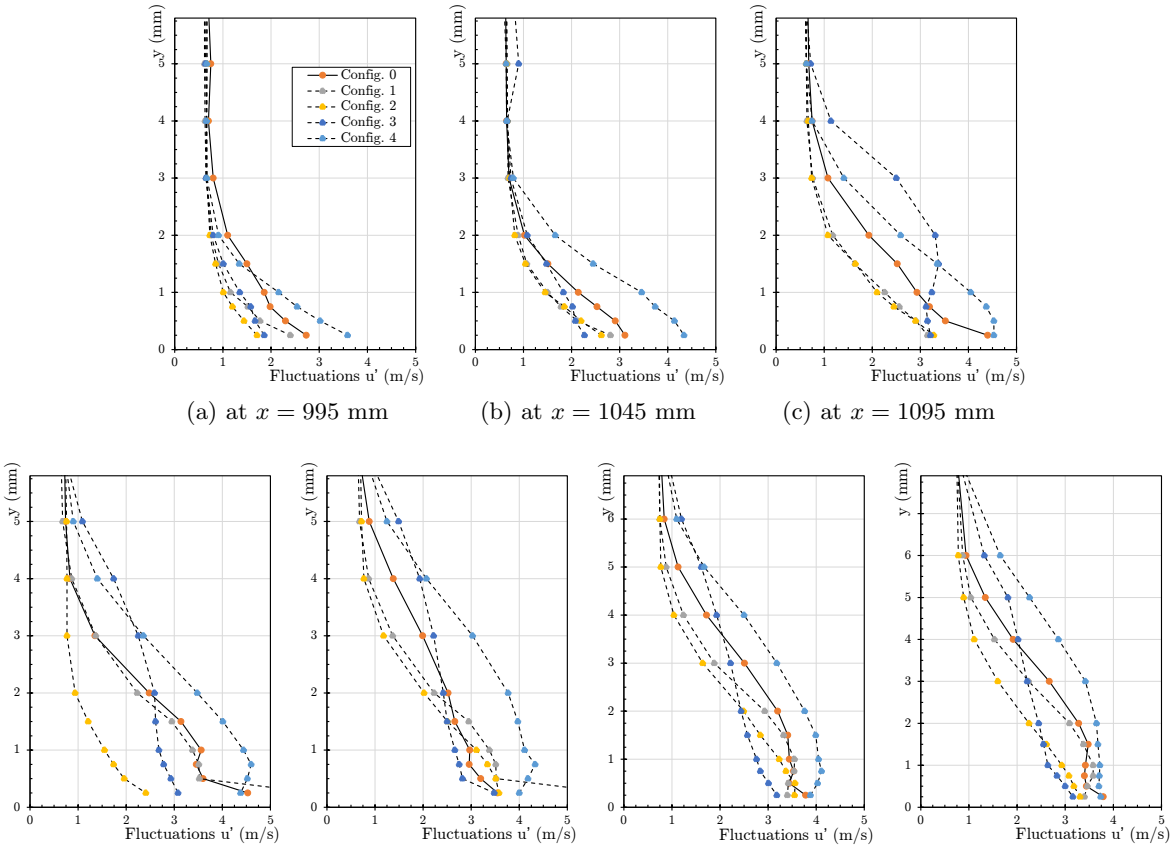

(a) at $x = 995$ mm (b) at $x = 1045$ mm (c) at $x = 1095$ mm

(d) at $x = 1145$ mm (e) at $x = 1195$ mm (f) at $x = 1245$ mm (g) at $x = 1295$ mm

Figure A.3: Streamwise velocity fluctuation profiles at different streamwise positions showing the influence of the different riblet configurations

In order to investigate differences caused by the riblets, LDA has been performed for the setups in wind tunnel *B*. More details of the measurement setup are presented by Baumgartner [168].

The measurements have been performed at seven different streamwise positions: At $x = 995$ mm, $x = 1045$ mm, $x = 1095$ mm, $x = 1145$ mm, $x = 1195$ mm, $x = 1245$ mm and $x = 1295$ mm.

In Fig. A.2 the lateral distributions of the streamwise velocity are shown. Clearly the differences between the configurations can be observed. Compared to configuration 0, which represents the smooth reference case, configurations 1 and 2 show higher velocities at the different streamwise positions. For all experiments the same power output of the wind tunnel fans has been used, thus this higher velocity is caused by a reduction of frictional losses leading to a slightly higher mass flow close to the wall.

Configuration 3 shows a lower velocity than the smooth reference case, and is at some positions close to the sand paper (config. 4). The reason is, that the structures are too large, i.e. too high, this increasing the wetted surface of the plate without any further reduction of the skin friction. Thus the losses due to skin friction increase.

In order to see, if the riblets successfully reduce turbulent fluctuations close to the wall,

the streamwise velocity fluctuations are analyzed. Figure A.3 shows the differences of the streamwise velocity fluctuations between the different configurations.

Comparing the configurations with the smooth surface (config. 0) in the diagrams at $x = 995\ mm$ all configurations except the sand paper show lower fluctuation values. More downstream the streamwise fluctuations of configurations 2 and 3 show lower values compared to configuration 0, with configuration 2 showing the lowest.

Configuration 3, which has already shown a worse performance regarding the velocity profiles, gives lower fluctuations only at the first positions. More downstream this configuration shows an increase in fluctuations away from the wall compared to the smooth reference case. Close to the wall the fluctuations are lower compared to configuration 0. But even though the fluctuations close to the wall are reduced by configuration 3, the size of the riblets lead to an increase in streamwise fluctuations a little away from the wall, resulting in higher losses inside the boundary layer.

APPENDIX B

COMPARISON OF C'_F AND C_F

As already discussed at the beginning of Chap. 3 the local skin friction coefficient c'_f defined with the wall shear stress (see Eq. (3.7)) and the skin friction coefficient c_f defined with the drag force F_D (see Eq. (3.10)) is often confound by many researchers. Additionally it should be kept in mind, that also the denominator in the definition of c'_f/c_f can differ, for example Brenn and Meile [78] use $c'_f = \tau_w/(\rho u_\infty^2)$ whereas Meile [75] uses $c'_f = \tau_w/(0.5\rho u_\infty^2)$. This can be additionally confusing, since the difference between c'_f and c_f for the laminar case is

$$\frac{c'_f}{0.5} = c_f \tag{B.1}$$

In the following the derivation of c_f should be explained for the laminar case. Later the derivation of c'_f for the turbulent case is described.

B.1. Laminar case

For the laminar boundary layer the Blasius solution is

$$c'_f = \frac{\tau_w}{0.5\rho u_\infty^2} = 0.664\frac{1}{\sqrt{Re_x}} \tag{B.2}$$

In order to get the overall skin friction c_f we first want to calculate the drag force F_D by integration of $\tau_w = 0.5\rho u_\infty^2 \cdot c'_f$:

$$F_D = 0.5\rho u_\infty^2 \cdot b \cdot \int_0^x 0.664\frac{1}{\sqrt{Re_x}}dx \tag{B.3}$$

$$F_D = 0.5\rho u_\infty^2 \cdot b \cdot 0.664\sqrt{\frac{\nu}{u_\infty}}\int_0^x x^{(-1/2)}dx \tag{B.4}$$

$$F_D = 0.5\rho u_\infty^2 \cdot b \cdot 0.664\sqrt{\frac{\nu}{u_\infty}}\left[2\sqrt{x}\right]_0^x \tag{B.5}$$

$$F_D = 0.5\rho u_\infty^2 \cdot b \cdot 2 \cdot 0.664\sqrt{\frac{\nu x}{u_\infty}} \tag{B.6}$$

To get c_f, Eq. (B.6) is reordered to

$$\frac{F_D}{0.5\rho u_\infty^2 \cdot b} = 1.328\sqrt{\frac{\nu x}{u_\infty}} \tag{B.7}$$

and multiplied by $1/x$ in order to get the definition of c_f

$$\frac{F_D}{0.5\rho u_\infty^2 \cdot bx} = 1.328\sqrt{\frac{\nu x}{u_\infty}} \cdot \frac{1}{x} \tag{B.8}$$

$$\frac{F_D}{0.5\rho u_\infty^2 \cdot bx} = 1.328\sqrt{\frac{\nu x}{u_\infty x^2}} = c_f \tag{B.9}$$

$$c_f = 1.328\frac{1}{\sqrt{Re_x}} \cdot \frac{1}{x} \tag{B.10}$$

B.2. Turbulent case

Since for turbulent boundary layers empirical correlations are often given for the c_f value, here the derivation of c_f' from c_f is described. Basically this is the reversal of the derivation above. Starting with c_f [75]

$$c_f = 0.074\frac{1}{\sqrt[5]{Re_x}} \tag{B.11}$$

$$c_f = 0.074\sqrt[5]{\frac{\nu}{u}}x^{-1/5} \tag{B.12}$$

$$\tag{B.13}$$

and similar to the calculation above

$$c_f x = \frac{F_D}{0.5\rho u_\infty^2 \cdot b} = 0.074\sqrt[5]{\frac{\nu}{u}}x^{4/5} \tag{B.14}$$

$$\frac{\tau_w}{0.5\rho u_\infty^2} = \frac{4}{5}0.074\sqrt[5]{\frac{\nu}{u}}\frac{1}{\sqrt[5]{x}} \tag{B.15}$$

and lastly

$$c_f' = 0.0592\frac{1}{\sqrt[5]{Re_x}} \tag{B.16}$$

A summary of the just discussed equations is given in Tab. B.1.

Table B.1: The local skin friction coefficient c_f' and the skin friction coefficient c_f for a laminar and turbulent boundary layer

	laminar	turbulent
$c_f' = \frac{\tau_w}{0.5\rho u_\infty^2}$	$0.664\frac{1}{\sqrt{Re_x}}$	$0.0592\frac{1}{\sqrt[5]{Re_x}}$
$c_f = \frac{F_D}{0.5\rho u_\infty^2 bx}$	$1.328\frac{1}{\sqrt{Re_x}}$	$0.074\frac{1}{\sqrt[5]{Re_x}}$

APPENDIX C

METHOD TO EXPERIMENTALLY OBTAIN THE SKIN FRICTION

In this chapter different experimental and post-processing techniques for measuring the skin friction are described. The aim of this overview is to support others to decide how to set up their test bench, since the skin friction distribution is crucial for transition and relaminarization observations. The chapter is divided into two parts: Direct measurement techniques, which describe methods for a direct acquisition of the skin friction, and indirect ones, where the skin friction is derived from the velocity profile.

C.1. Direct measurement techniques

C.1.1. Surface heat gauge – Hot-film anemometer

Surface heat gauges, also known as hot-film anemometers, are small foils which are applied to the surface similar to a strain gauge. They have the same working principle as hot-wire anemometers (described in Sec. 4.1.2.5): The wire within the foil is heated and kept at a certain constant temperature. The current necessary for this constant temperature is proportional to the velocity gradient along the foil, thus to the skin friction.

In Fig. C.1 an application of these hot-films is shown, where the gauges are applied to the surface of a blade. It can be observed, that the foils are streamwise and spanwise shifted. The necessary spanwise offset to prevent an influence between an upstream and downstream gauge is one of the disadvantages of this measurement technique. Other critical points are the influence of the thermal boundary layer and the lateral step due to the foil.

This measurement technique is described in more detail and applied by e.g. Österreicher [169] or Nichtawitz [170].

C.1.2. Stanton tube

The Stanton tube measures the stagnation pressure near the wall. The working principle is similar to the Preston tube described in Sec. 4.1.2.1 but with the difference that the Stanton

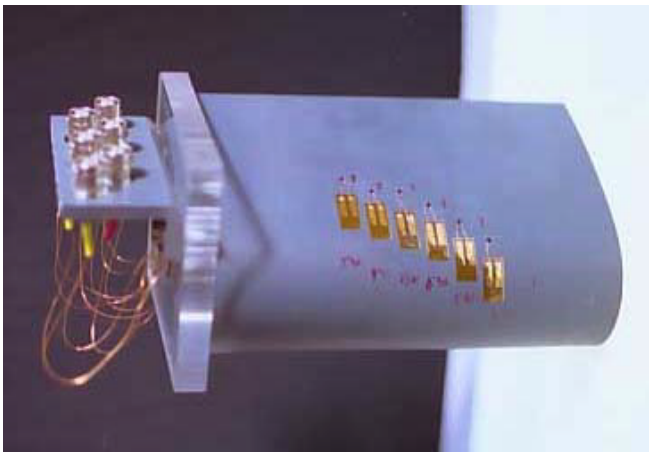

Figure C.1: Application of surface heat gauges (hot film anemometers) along a cascade blade [169]

tube is mounted into the wall. In Fig. C.2a a typical Stanton tube is shown and in Fig. C.2b a Pitot tube version of the Stanton tube. The disadvantage of the latter is its vulnerability to incidence.

More details of the Stanton tube are presented e.g. by Gadd [171].

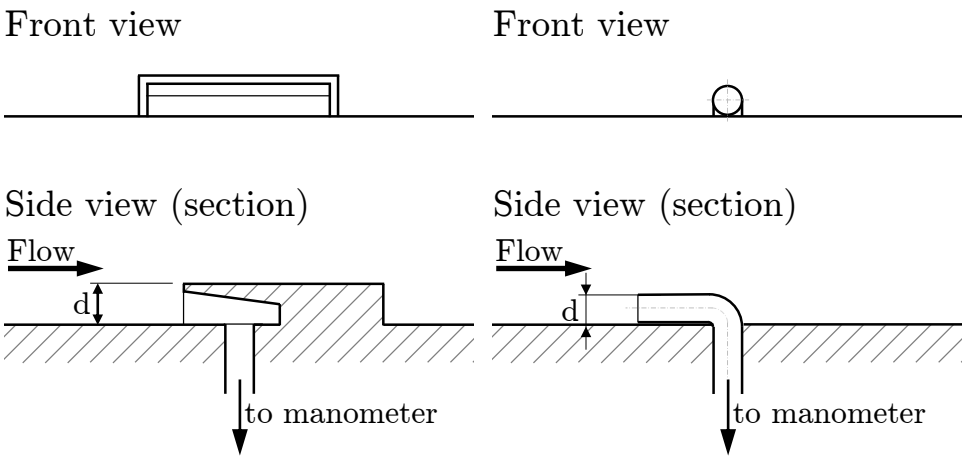

(a) A typical Stanton tube (renewed form [171])

(b) Pitot tube version

Figure C.2: Examples of applications of the Stanton tube principle

C.1.3. Shear sensitive liquid crystal coating

The shear sensitive liquid crystal coating (SSLCC) is a color which can be applied to a surface. The color consists of helical aggregates of long, planar molecules which are arranged in planes parallel to the plate where the color is applied. The height of this layered pack of molecules is in the order of the wavelength of visible light and the crystal is therefore extremely optical active. Under no-shear conditions, white light incident normal to the

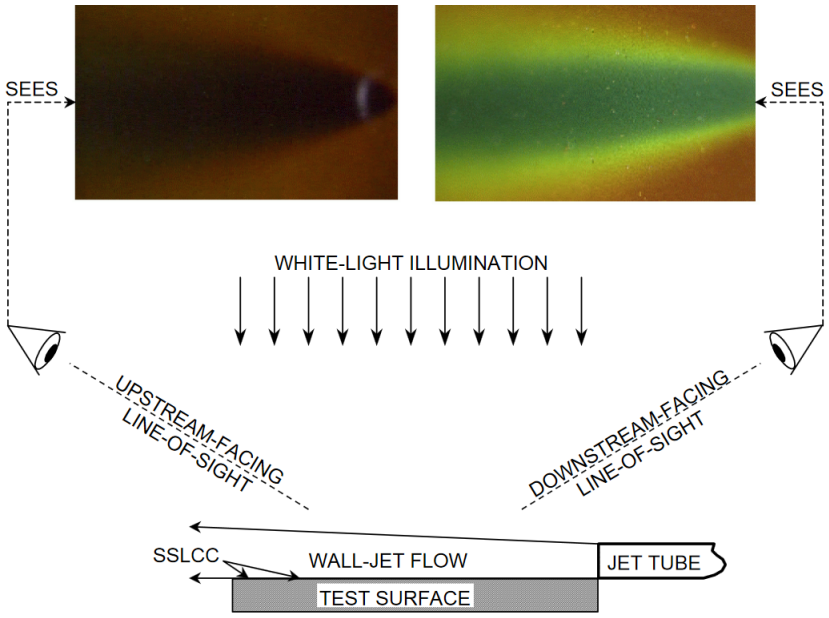

Figure C.3: Measurement setup for skin friction visualization using shear sensitive liquid crystal coating [172]

coating, is scattered at a certain wavelength. If shear is applied, the helix-axis is tilted. This results in a directional scattering as a three-dimensional color spectrum in space. [172]

In Fig. C.3 an experiment presented by Reda and Wilder [172] shows a test setup using the shear sensitive coating. For the experiment they used a jet flow close to the wall to shear the coating. Clearly the photograph shows how the SSLCC scatters the light depending on the shear stress. Also the directional sensitivity can be observed in Fig. C.3.

With a proper post-processing of the pictures one may can calculate the actual shear stress from the color distribution of the coating. This would enable this technique to rather

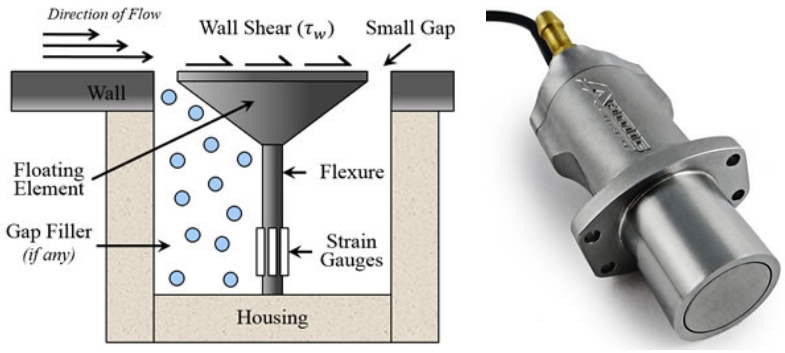

(a) Scheme of the measurement principle

(b) Photograph of a semiconductor strain gauge by Micron Instruments®

Figure C.4: Semiconductor strain gauge skin friction sensors [173]

fast measure skin friction directly.

C.1.4. Semiconductor strain gauges as skin friction sensors

The working principle of a semiconductor strain gauge (SSG) as a skin friction sensor is shown in Fig. C.4a: The wall shear at the top of a flexibly mounted plateau (floating element) leads to a deformation of the mounting. This deformation is proportional to the wall shear at the top of the plateau and is measured by strain gauges (e.g. DMS).

Figure C.4b shows a photograph of a SSG by Micron Instruments®. More details of the measurement technique is given by Chelner et al. [173].

C.1.5. Surface fence technique

A surface fence is a small obstacle mounted into a plate, where the pressure can be measured upstream and downstream of the obstacle. This fence should be smaller than $y^+ = 5$ so it is not depended on the validity of the law-of-the-wall. It is a rather simple method, since all is needed is a obstacle and a pressure sensitive measurement position upstream and downstream of the fence. The pressure difference is then proportional according to [174]

$$\Delta p = f\left(u_h, h, \rho, \nu\right) \tag{C.1}$$

to the velocity u_h which represents the velocity at the fence height h. Assuming that the velocity gradient is constant up to the fence tip, the wall shear can be computed with [174]

$$u_h = H^+ u_\tau = \frac{h\tau_w}{\nu} \tag{C.2}$$

As said, the fence should not be larger than $h^+ = y^+ = 5$, but also not smaller than $h^+ = 0.5$ since the presser difference would then be too small [174]. Since the height of the obstacle can vary due to manufacturing tolerances, the fence needs calibration.

More details can be found in e.g. [175–177].

C.2. Indirect techniques: Skin friction determination from the velocity profile

C.2.1. Schlichting method

This method has been presented by e.g. Schlichting [23]. It is necessary to solve a set of equations for different areas of the velocity profile in wall coordinates. These equations are

$$u^+ = \begin{cases} y^+ & \text{if } 0 \leq y^+ \leq 5 \\ Eq.\ C.3 & \text{if } 5 \leq y^+ \leq 70 \\ \frac{1}{\kappa} ln(y^+) + B^+ & \text{if } 70 \leq y^+ \end{cases}$$

$$u^+ = \frac{1}{\Lambda}\left[\frac{1}{3}\, ln\left(\frac{\Lambda y^+ + 1}{\sqrt{(\Lambda y^+)^2 - \Lambda y^+ + 1}}\right) + \frac{1}{\sqrt{3}}\, atan\left(\frac{2\Lambda y^+ - 1}{\sqrt{3}} + \frac{\pi}{3}\right)\right] + \\ + \frac{1}{4\kappa} ln\left(1 + \kappa b y^{+4}\right) \tag{C.3}$$

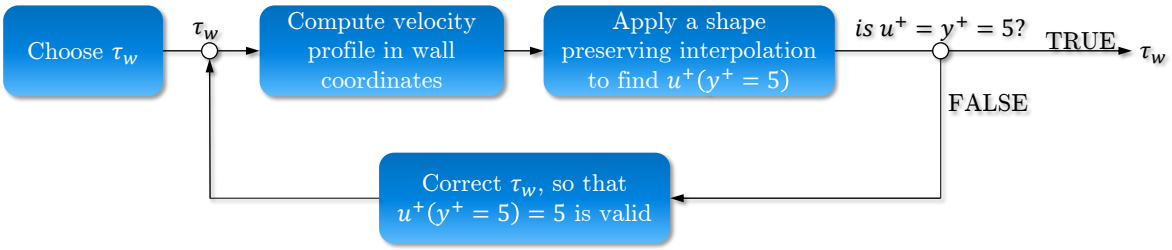

Figure C.5: Illustration of the iteration cycle used to obtain the skin friction with the method used for the calculation of the value presented in paper 5 (Bader method)

with

$$\kappa = 0.41; a = 6.1 \cdot 10^{-4}; b = 1.43 \cdot 10^{-3} \tag{C.4}$$

$$\Lambda = (a + b)^{1/3} = 0.127 \tag{C.5}$$

$$B^+ = \frac{2\pi}{3\sqrt{3}\Lambda} + \frac{1}{4\kappa}\, ln\,(\kappa b) \tag{C.6}$$

The most inner point of the measured velocity profile is used and the skin friction τ_w is found iteratively in such a way, that the point has to satisfy the equations above.

The equations assume a fully turbulent boundary layer, thus it may be used for profiles with mild pressure gradients, but can have difficulties with strong pressure gradients or laminar boundary layers.

C.2.2. Wall slope method

The wall slope method represents one of the easiest one. There are two different approaches to compute the skin friction with the wall slope technique: For the first, just the wall nearest point from the measurements is used to calculate the slope $\partial U/\partial y$ (see e.g. [41,106]). However, since the wall-near area, where the velocity gradient $\partial U/\partial y$ is constant is rather small [45], a high wall-near measurement grid resolution is necessary. Thus a second method, which describes a more reasonable and more sophisticated approach (see e.g. [178]) is to fit the velocity profile near the wall to a compensating curve [45]:

$$\frac{u}{u_\infty} = \frac{c_f}{2}\left(\frac{y u_\infty}{\nu}\right) - \frac{K}{2}\left(\frac{y u_\infty}{\nu}\right)^2 \tag{C.7}$$

The wall shear is then obtained by for example a least square fit. But the most inner 5 measurement points should be below $y^+ \leq 10$.

C.2.3. von Kármán method

The von Kármán method simply uses the von Kármán momentum integral equation (see Eq. (3.31)) to calculate the wall shear using the displacement thickness δ_1 and momentum thickness δ_2 together with the free stream velocity u_∞. The advantage is that these thicknesses and the velocity are quite easily obtainable. However, since also the gradient of the momentum thickness is needed which is prone to oscillations if not obtained accurately, also the computed wall shear may oscillate, thus the results may be of bad quality.

C.2.4. Bader method

This method has been used in paper 5. It is based on the assumption that the velocity gradient is constant up to a position of approximately $y^+/u^+ = 7$ ($u^+ = \overline{u}/u_\tau$ and $y^+ = yu_\tau/\nu$). The skin friction is computed from the velocity profile iteratively.

First a wall shear value τ_w is chosen. With this assumed value the non-dimensional y^+-u^+-profile in wall coordinates is calculated, where the $y^+ = u^+ = 0$ point is added. For the zone between the measured profile points, a shape preserving interpolation is applied. Then for $y^+ = 5$ the $u^+(y^+ = 5)$ value is evaluated, which most likely does not equal to 5. Therefore the wall shear is adjusted, so that $u^+(y^+ = 5) = 5$ is valid. With this new wall shear value the iteration cycle is repeated until the $u^+(y^+ = 5) = 5$ is fulfilled. In Fig. C.5 the method is illustrated schematically.

APPENDIX D

CTA TRANSITION MEASUREMENTS

In the following CTA measurement data for the 10 m/s transitional case are given. The graphs in Fig. D.2 show the mean streamwise velocity $\overline{u}$, the root-mean-square value of the streamwise $\left(\hat{u} = \sqrt{\overline{u'^2}}\right)$ and lateral $\left(\hat{v} = \sqrt{\overline{v'^2}}\right)$ velocity fluctuations (Figs. D.2a, d, g, j, m and o), the skewness S and flatness F for the streamwise velocity fluctuations (Figs. D.2b, e, h, k, n and p) and for the lateral velocity fluctuations together with time signals (Figs. D.2c, f, i, l, ñ and q) over the height y at various streamwise positions x.

The time signals in Figs. D.2b and c show the occurrence of streaks close to the wall, indicating vortices inside the laminar boundary layer. Clearly the amplification of these spikes within the time signal during transition downstream of the first position is observable. This effect comes together with a rise of quadrant 2 "ejection" events (compare Sec. 3.3.3, Fig. 3.27 or Sec. 6.4).

Another interesting point is that profile at a certain x position of the skewness S shows a minimum where the flatness F shows a maximum for the streamwise fluctuations. The y-position of this maximum and minimum, respectively, agrees with the value of to the boundary layer thickness $\delta(x)$ (shown in Fig. D.1). The y coordinate is at all positions slightly lower than $\delta(x)$. The LDA measurement results agree with these observations. This behavior is qualitative the same for all streamwise positions, although the value differs.

For the lateral fluctuations a similar trend is observable, but with the difference that the

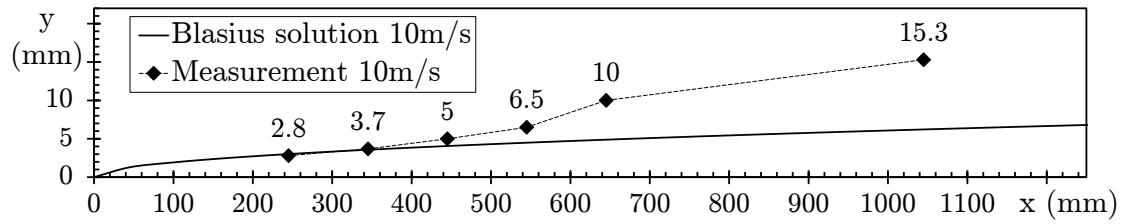

Figure D.1: Measured boundary layer thickness $\delta(x)$ along the plate for different streamwise positions together with the laminar Blasius solution

skewness and the flatness show a maximum at these y-position.

At the last position clearly a fully turbulent boundary layer can be observed from the time signals and the velocity profile.

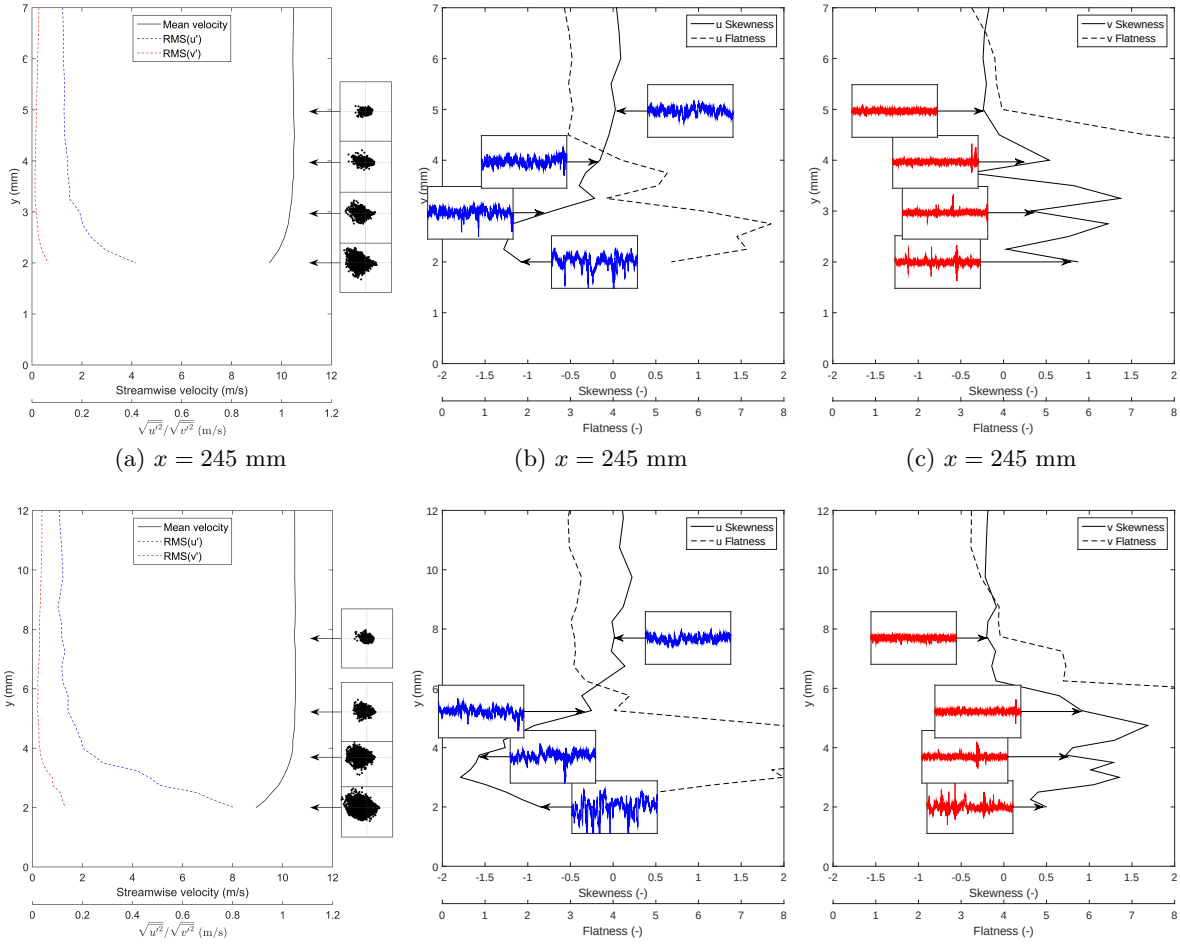

(a) $x = 245$ mm (b) $x = 245$ mm (c) $x = 245$ mm

(d) $x = 345$ mm (e) $x = 345$ mm (f) $x = 345$ mm

Figure D.2: Caption see following page

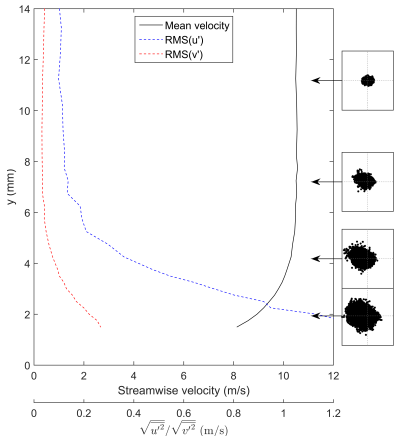

(g) $x = 445$ mm

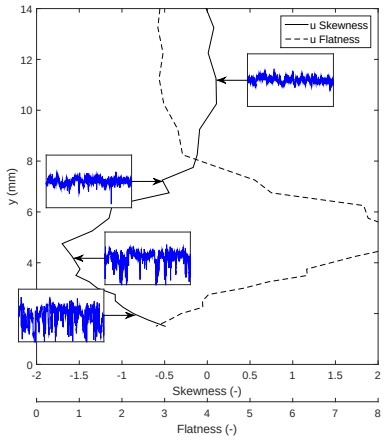

(h) $x = 445$ mm

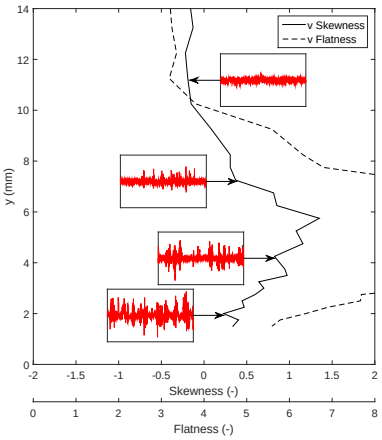

(i) $x = 445$ mm

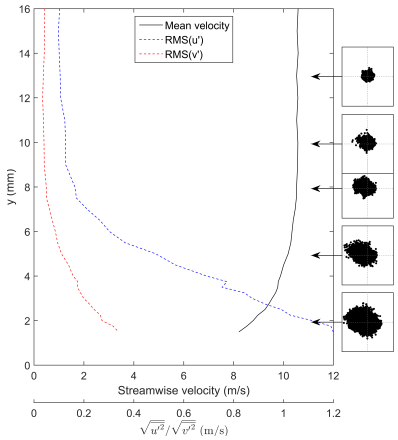

(j) $x = 545$ mm

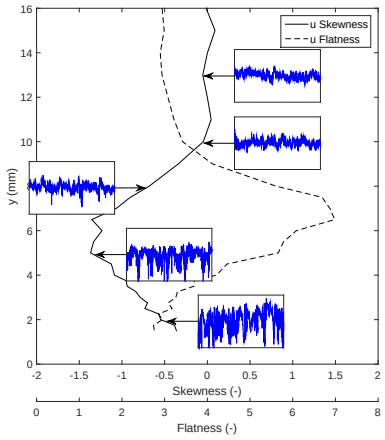

(k) $x = 545$ mm

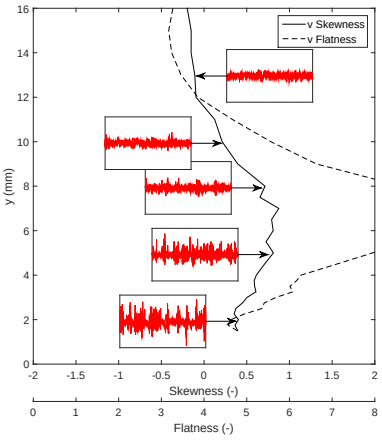

(l) $x = 545$ mm

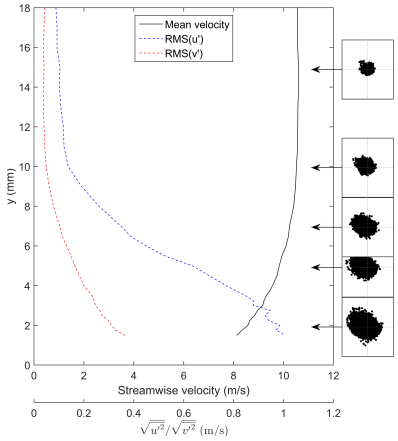

(m) $x = 645$ mm

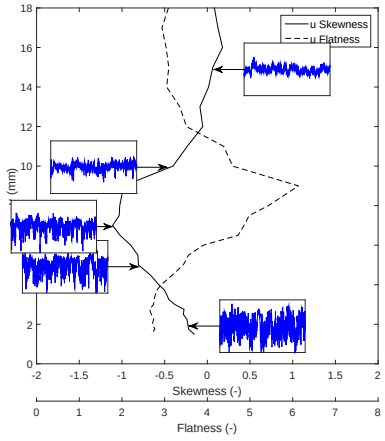

(n) $x = 645$ mm

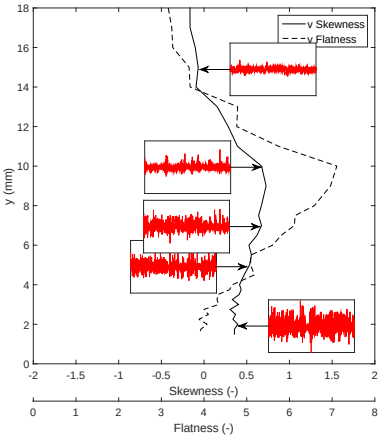

(ñ) $x = 645$ mm

Figure D.2: Caption see following page

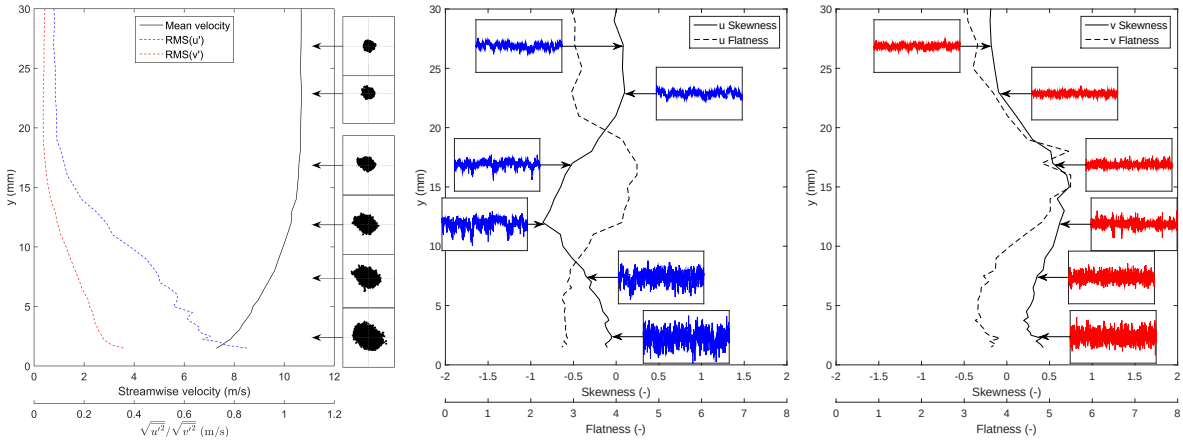

(o) $x = 1045$ mm (p) $x = 1045$ mm (q) $x = 1045$ mm

Figure D.2: CTA measurement data along the flat plate for the 10 m/s case at different streamwise positions x; left column: distribution of the mean streamwise velocity ($\overline{u}$), the root-mean-square value of the streamwise ($\hat{u}$) and lateral ($\hat{v}$) velocity fluctuations; middle column: distribution of the skewness S and flatness F for the streamwise velocity fluctuations together with time signals at various positions; right column: distribution of the skewness S and flatness F for the lateral velocity fluctuations together with time signals at various positions

APPENDIX E

DERIVATION OF THE TOTAL TURBULENT KINETIC ENERGY

As described in paper 7 (Sec. 6.7) the turbulence intensity, thus the turbulent kinetic energy, influences the prediction of the position and length of the transition and relaminarization zones. Thus the setting of the "right" inlet turbulence boundary conditions is crucial to predict reliably these changes of the state of the boundary layer.

One property of the relaminarization test case described in this work is the occurrence of a separation bubble at the top wall above the boundary layer plate (see Sec. 4.1.1.3). This bubble triggers unsteady velocity fluctuations of low frequencies. The fluctuations are measured by a measurement system (LDA, CTA etc.), but not modeled by the turbulence model (e.g. k-ω model), since these fluctuations are not seen as classical turbulent fluctuations. Thus it can be distinguished between low frequency velocity fluctuation which are triggered in our case by the bubble, and a high frequency part of the fluctuations, which are modeled by turbulence models. For more details see paper 8 (Sec. 6.8).

In this section the derivation for the turbulent kinetic energy including these low and high frequency velocity fluctuations presented in paper 8 is shown in more detail.

As described above, the data of the measurement give a total turbulent kinetic energy, containing all ranges of velocity fluctuations. In order to determine a comparable TKE from the unsteady CFD result, the computed total fluctuations are found as an accumulation of the subranges

$$u_i' = u_{Ti}' + u_{Vi}' \tag{E.1}$$

where u_{Vi}' represents low-frequency velocity fluctuations resolved by the unsteady simulation and u_{Ti}' model related fluctuations. Combining this equation with the general definition of k

$$k_i = \frac{\overline{u_i' \cdot u_i'}}{2} \tag{E.2}$$

results in

$$k = \frac{\overline{(u_T' + u_V')^2} + \overline{(v_T' + v_V')^2} + \overline{(w_T' + w_V')^2}}{2} \tag{E.3}$$

Dissolving this equation leads to

$$\begin{aligned} k =& \frac{\overline{(u'_T)^2} + \overline{(v'_T)^2} + \overline{(w'_T)^2}}{2} \\ &+ \frac{\overline{(u'_V)^2} + \overline{(v'_V)^2} + \overline{(w'_V)^2}}{2} \\ &+ \frac{\overline{2(u'_T u'_V)} + \overline{2(v'_T v'_V)} + \overline{2(w'_T w'_V)}}{2} \end{aligned} \tag{E.4}$$

and substituting

$$k_T = \frac{\overline{(u'_T)^2} + \overline{(v'_T)^2} + \overline{(w'_T)^2}}{2} \tag{E.5}$$

$$k_V = \frac{\overline{(u'_V)^2} + \overline{(v'_V)^2} + \overline{(w'_V)^2}}{2} \tag{E.6}$$

leads to

$$k = k_{\text{tot}} = k_T + k_V + \overline{(u'_T u'_V)} + \overline{(v'_T v'_V)} + \overline{(w'_T w'_V)} \tag{E.7}$$

where k_T represents – as discussed above – the model-related TKE and k_V the velocity-fluctuation-related turbulent kinetic energy. Both can be acquired directly from the unsteady CFD results. For the latter part of Eq. (E.7) we have to consider, how the two components are correlated.

For the sake of convenience we first look at one dimension (x-direction). To analyze the correlation between the two fluctuation values, we want to use the ansatz

$$\overline{(u'_T u'_V)} = \alpha \cdot \sqrt{\overline{(u'_T)^2} \cdot \overline{(v'_V)^2}} \tag{E.8}$$

where α represents a coefficient representing the correlation between the two parts. When taking the Pearson correlation coefficient ρ into account, which is defined as

$$\rho_{a,b} = \frac{\frac{1}{n}\sum_{i=1}^{n}(a_i - \overline{a})\left(b_i - \overline{b}\right)}{\sqrt{\frac{1}{n}\sum_{i=1}^{n}(a_i - \overline{a})^2}\sqrt{\frac{1}{n}\sum_{i=1}^{n}\left(b_i - \overline{b}\right)^2}} \tag{E.9}$$

will lead in our case to

$$\rho_{T,V} = \frac{\overline{(u'_T u'_V)}}{\sqrt{\overline{(u'_T)^2} \cdot \overline{(v'_V)^2}}} = \alpha \tag{E.10}$$

The correlation coefficient ρ can be easily calculated with two signals, in the present case the low-frequency and high-frequency signals of velocity fluctuations. In order to solve the latter part of Eq. (E.7), we need to reformulate the denominator of Eq. (E.10). For the 1D approach the two kinetic energies are written as

$$k_{T,x} = \frac{\overline{(u'_T)^2}}{2} \tag{E.11}$$

$$k_{V,x} = \frac{\overline{(u'_V)^2}}{2} \tag{E.12}$$

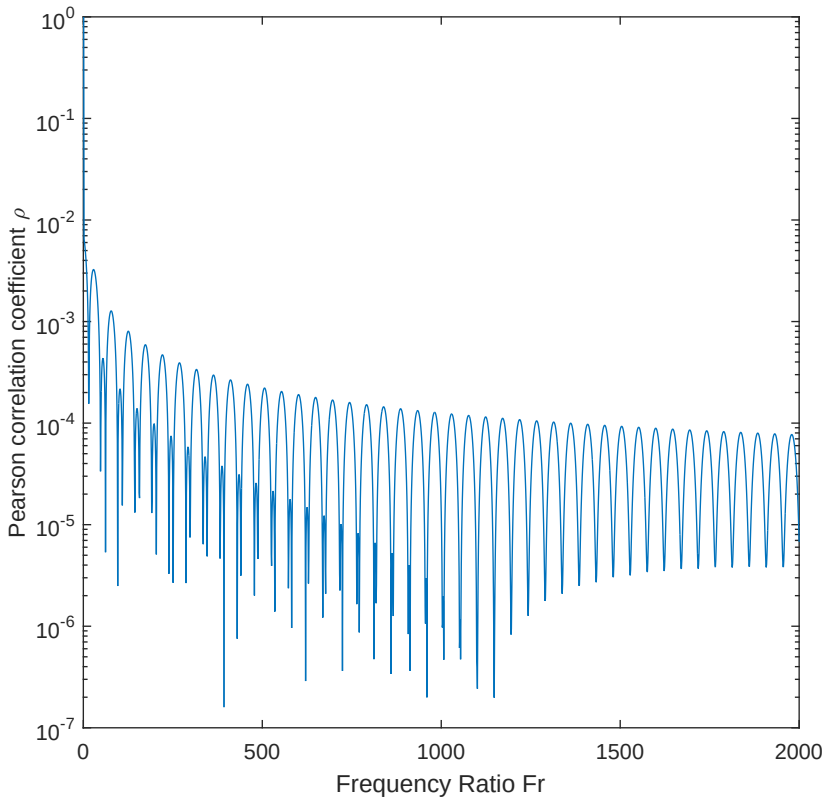

Figure E.1: Correlation factor ρ of two sine-signals against the frequency ratio $Fr = f_B/f_A$ for different amplitude ratios $Ar = a_b/a_A$ and phase shift ratios $\Phi = \phi_B/\phi_A$ between the two signals

Multiplying these two components leads to

$$4 \cdot k_{T,x} \cdot k_{V,x} = \overline{(u'_V)^2} \cdot \overline{(u'_V)^2} \tag{E.13}$$

Inserting Eq. (E.13) into Eq. (E.10) leads to

$$\overline{(u'_T u'_V)} = 2 \cdot \rho \cdot \sqrt{k_{T,x} \cdot k_{V,x}} \tag{E.14}$$

and for the three dimensional case this can be consequently written as

$$\overline{(u'_T u'_V)} + \overline{(v'_T v'_V)} + \overline{(w'_T w'_V)} = 2 \cdot \rho \cdot \left[\sqrt{k_{T,x} \cdot k_{V,x}} + \sqrt{k_{T,y} \cdot k_{V,y}} + \sqrt{k_{T,z} \cdot k_{V,z}}\right] \tag{E.15}$$

The calculated turbulent kinetic energy k_T cannot be split into three velocity components. Therefore we will assume isotropic turbulence:

$$k_{T,x} = k_{T,y} = k_{T,z} = \frac{1}{3} \cdot k_T \tag{E.16}$$

$$k_{V,x} = k_{V,y} = k_{V,z} = \frac{1}{3} \cdot k_V \tag{E.17}$$

which leads to

$$\overline{(u'_T u'_V)} + \overline{(v'_T v'_V)} + \overline{(w'_T w'_V)} = 2 \cdot \rho \cdot \left[\sqrt{\frac{1}{3}k_T \cdot \frac{1}{3}k_V} + \sqrt{\frac{1}{9}k_T \cdot k_V} + \sqrt{\frac{1}{9}k_T \cdot k_V}\right] \tag{E.18}$$

and finally to

$$\overline{(u'_T u'_V)} + \overline{(v'_T v'_V)} + \overline{(w'_T w'_V)} = 2 \cdot \rho \cdot \sqrt{k_T \cdot k_V} \tag{E.19}$$

So with Eq. (E.7) the total turbulent kinetic energy can be found from:

$$k_{\text{tot}} = k_T + k_V + 2 \cdot \rho \cdot \sqrt{k_T \cdot k_V} \tag{E.20}$$

As already described, k_T represents the model-related turbulent kinetic energy, thus this part is associated with high frequencies whereas k_V is associated with rather low frequencies. When correlating signals of different frequencies, the correlation and thus the correlation factor ρ is relatively low. This is exemplary shown in Fig. E.1, where the correlation factor ρ of two sine-signals is given against the frequency ratio $Fr = f_B/f_A$.

It can be clearly seen, that the correlation coefficient decreases with rising frequency ratio for all cases. For our case we can therefore conclude that $\rho \approx 0$ since u'_{Vi} and u'_{Ti} show per definition large differences in their frequency range. Thus for the present case in paper 8 the total kinetic energy is computed with

$$k_{\text{tot}} = k_T + k_V \tag{E.21}$$

LIST OF FIGURES

LIST OF TABLES

BIBLIOGRAPHY

[1] Intergovernmental Panel on climate change: Working group I, "Climate change 2013: The physical science basis," *ipcc report*, vol. WGI AR5, 2013.

[2] W. Sanz, "private communication," 2017. mar/2017.

[3] International Air Transport Association (IATA), "Fact sheet: Climate change," November 2016 2016.

[4] G. Pietersz, 2016. visited: mar/2017.

[5] International Civil Aviation Organization, "Traffic growth and airline profitability were highlights of air transport in 2016," 2017. visited: jan/2017.

[6] H. Czerski, "Is jet travel becoming the dirtiest way to cross the planet? Age of the jet set." BBC iWonder, 2017. visited mar/2017.

[7] I. Kernstock, "Forschung und Innovation im Luftfahrtsektor: Chancen nützen auf internationalen Märkten." Bundesministerium für Verkehr, Innovation und Technologie (bmvit), 2015. Die FTI-Strategie für den österreichischen Luftfahrtsektor 2020 plus.

[8] Bundesverband der Deutschend Luftverkehrswirtschaft e. V., "Klimaschutzreport 2016," *Klimaschutzplan für die Luftfahrt*, August 2016.

[9] R. E. Mayle, "The role of laminar-turbulent transition in gas turbine engines," *Journal of Turbomachinery*, vol. 113, pp. 509–537, October 1991.

[10] D. Rempfer, "Low-dimensional modeling and numerical simulation of transition in simple shear flows," *Annual Review of Fluid Mechanics*, vol. 35, pp. 229–265, 2003.

[11] www.f1technical.net Forum, "Red bull rb10 renault," 2014. jul/2016.

[12] scarbsf1, "Blown rear wings: seperating and stalling." ScrabsF1: everything technical in F1, 2010. jul/2016.

[13] P. G. Tucker, "Computation of unsteady turbomachinery flows: Part 1 – Progress and challenges," *Progress in Aerospace Sciences*, vol. 47, pp. 522–545, 2011.

[14] J. Tyacke, I. Naqavi, Z.-N. Wang, P. Tucker, and P. Boehning, "Predictive les for jet aeroacoustics – current approach and industrial application," *Journal of Turbomachinery*, vol. 139, no. 8, pp. 1–13, 2017.

[15] J. Tyacke and P. Tucker, "Future use of large eddy simulation in aero-engines," *Journal of Turbomachinery*, vol. 137, pp. 1–16, 2015.

[16] bionic surface technologies GmbH, "Strömungswiderstandsverminderung durch Riblets," 2017. visited: mar/2017.

[17] J. Fröhlich, *Large Eddy Simulation turbulenter Strömungen.* B.G. Teubner Verlag, Springer Scienece+Business Media, 2006.

[18] J. Boussinesq, "Théorie de l'écoulement tourbillant," *Mém. Acad. Sci. Paris 23*, vol. 23, pp. 46–50, 1877.

[19] O. Reynolds, "An experimental investigation of the circumstances which determine whether the motion of water in parallel channels shall be direct or sinuous and of the law of resistance in parallel channels," *Philosophical Transactions of the Royal Society*, vol. 174, pp. 935–982, 1883.

[20] D. Jackson and B. Launder, "Osborne Reynolds and the publication of his papers on turbulent flow," *Annual Review of Fluid Mechanics*, vol. 39, 2007. doi: 10.1146/annurev.fluid.39.050905.110241.

[21] R. E. Mayle, *Elements of Transitional Boundary-Layer flow.* Logos Verlag Berlin GmbH, 2015.

[22] L. Prandtl, "Über Flüssigkeitbewegung bei sehr kleiner Reibung," *Verhandlinger III. Internationaler Mathematiker Kongress Heidelberg*, pp. 484–491, 1904.

[23] H. Schlichting and K. Gersten, *Grenzschicht-Theorie (Boundary-Layer Theory).* Springer-Verlag Berlin Heidelberg, 2006.

[24] L. Prandtl, "Der Luftwiderstand von Kugeln," *Nachr. Ges.Wiss. Göttingen, Math. Phys. Klasse*, pp. 177–190, 1914.

[25] W. Tollmien, "Über die Entstehung der Turbulenz," *1. Mitteilung, Nachr. Ges. Wiss. Göttingen, Math. Phys. Klasse*, pp. 21–44, 1929.

[26] H. Schlichting, "Zur Entstehung der Turbulenz bei der Plattenströmung," *Nachr. Ges. Wiss. Göttingen, Math. Phys. Klasse*, pp. 182–208, 1933.

[27] H. L. Dryden, "Some recent contributions to the study of transition and turbulent boundary layers," *Sixth Internat. Congress for Appl. Mech., Paris, Sept. 1946*, 1946. NACA-TN-1168 (1947).

[28] W. Tollmien, "Grenzschicht-Theorie," *In: W. Wien; F. Harms (Publ.): Handbuch der Experimentalphysik, Leipzig*, vol. 4, no. 1, pp. 239–287, 1931.

[29] W. Tollmien, "Turbulente Strömungen," *In: W. Wien; F. Harms (Publ.): Handbuch der Experimentalphysik, Leipzig*, vol. 4, no. 1, pp. 289–339, 1931.

[30] L. Prandtl, "The mechanics of viscous fluids," *In W.F. Durand (Ed.): Aerodynamics Theory, Springer-Verlag, Berlin*, vol. 3, pp. 34–208, 1935.

[31] P. S. Klebanoff, "Characteristics of turbulence in a boundary layer with zero pressure gradient," *NACA report*, vol. 1247, pp. 1135–1153, 1955. supersedes P. S. Klebanoff, "Characteristics on a Boundary Layer With Zero Pressure Gradient," NACA TN 3178, 1954.

[32] F. Clauser, "Turbulent boundary layers in adverse pressure gradients," *Journal of the aeronautical science*, pp. 91–108, February 1954.

[33] B. S. Stratford, "The prediction of separation of the turbulent boundary layer," *Journal of Fluid Mechanics*, vol. 5, pp. 1–16, 1959.

[34] R. Narasimha and K. R. Sreenivasan, "Relaminarization in highly accelerated turbulent boundary layers," *Journal of Fluid Mechanics*, vol. 61, no. 3, pp. 417–447, 1973.

[35] P. S. Klebanoff, K. D. Tidstrom, and L. M. Sargent, "The three-dimensional nature of boundary-layer instability," *Journal of Fluid Mechanics*, vol. 12, no. 1, pp. 1–34, 1962.

[36] B. E. Launder, "Laminarization of the turbulent boundary layer by acceleration," *MIT Gas turbine lab. Report No. 77*, 1964.

[37] P. M. Moretti and W. M. Kays, "Heat transfer through an incompressible turbulent boundary layer with varying free-stream velocity and varying surface temperature – an experimental study," *International Journal of Heat and Mass Transfer*, vol. 8, no. 9, pp. 1187–1202, 1965.

[38] S. J. Kline, W. C. Reynolds, F. A. Schraub, and P. W. Runstadler, "The structure of turbulent boundary layers," *Journal of Fluid Mechanics*, vol. 30, no. 4, pp. 741–773, 1967.

[39] B. Launder and W. P. Jones, "On the prediction of laminarization," *Ministry of Technology. Aeronautical research council. Current papers*, vol. 1036, 1969.

[40] M. A. Badri Narayanan and V. Ramjee, "On the criteria for reverse transition in a two–dimensional boundary layer," *Journal of Fluid Mechanics*, vol. 35, no. 2, pp. 225–241, 1969.

[41] R. F. Blackwelder and L. S. G. Kovasznay, "Large–scale motion of a turbulent boundary layer during relaminarization," *Journal of Fluid Mechanics*, vol. 53, no. 1, pp. 61–83, 1972.

[42] R. Narasimha and K. R. Sreenivasan, "Relaminarization of fluid flows," *Advances in applied mechanics*, vol. 61, pp. 221–309, 1979.

[43] P. R. Viswanath, R. Narasimha, and A. Prabhu, "Visualization of relaminarizing flows," *Journal of the Indian Institute of Science*, vol. 60, pp. 159–165, March 1978.

[44] B. J. Abu-Ghannam and R. Shaw, "Natural transition of boundary layers — the effects of turbulence, pressure gradient, and flow history," *Journal of Mechanical Engineering Science*, vol. 22, pp. 213–228, October 1980.

[45] K. R. Sreenivasan, "Laminarescent, relaminarizing and retransitional flow," *ACTA Mechanica*, vol. 44, pp. 1–48, 1982.

[46] J. D. Swearingen and B. R. F, "The growth and breakdown of streamwise vortices in the presence of a wall," *Journal of Fluid Mechanics*, vol. 182, pp. 255–290, 1987.

[47] L. P. Yip, P. Vijgen, J. D. Hardin, and C. P. van Dam, "In-flight pressure distributions and skin-friction measurements on a subsonic transport high-lift wing section," *AGARD CP-515*, 1993.

[48] R. J. Volino and S. T. W, "Bypass transition in boundary layers including curvature and favorable pressure gradient effects," *Journal of Turbomachinery*, vol. 117, 1995.

[49] J. R. Narayan, C. A, and N. Pagaldipti, "Improvements in relaminarization characteristics of turbine blades using design optimization," *6^{th} AIAA, NASA and ISSMO Symposium on Multidisciplinary Analysis and Optimization*, pp. 1372–1381, 1996. AIAA-96-4143-CP.

[50] R. E. Mayle, K. Dullenkopf, and A. Schulz, "The turbulence that matters," *International Gas Turbine and Aeroengines Congress and Exhibition, Orlando, Floriada. June 2-5*, 1997. 97-GT-274.

[51] R. E. Mayle and A. Schulz, "The path to predicting bypass transition," *Journal of Turbomachinery*, vol. 119, pp. 405–411, July 1997.

[52] D. Warnack and H. H. Fernholz, "The effects of a favourable pressure gradient and of the reynolds number on an incompressible axisymmetric turbulent boundary layer. Part 2. The boundary layer with relaminarization," *Journal of Fluid Mechanics*, vol. 359, pp. 357–381, 1998.

[53] M. Ichimiya, I. Nakamura, and S. Yamashita, "Properties of a relaminarizing turbulent boundary layer under a favorable pressure gradient," *Experimental Thermal and Fluid Science*, vol. 17, pp. 37–48, 1998.

[54] R. J. Volino, "Effects analysis of trtransition flow data under high free-stream turbulence conditions," *Proceedings of the International Gas Turbine and Aeroengine Congress and Exhibition, Stockholm, Sweden. June 2–5 1998*, 1998. 98-GT-289.

[55] R. J. Volino and L. S. Hultgren, "Measurements in separated and trtransition boundary layers under low-pressure turbine airfoil conditions," *Proceedings of the International Gas Turbine and Aeroengine Congress and Exhibition, Stockholm, Sweden. June 2–5 1998*, 2001. 98-GT-289.

[56] C. Bourassa and T. F. O, "An experimental investigation of a highly accelerated turbulent boundary layer," *Journal of Fluid Mechanics*, vol. 634, pp. 359–404, 2009.

[57] O. M. Oyewola, L. Djenidi, and R. A. Antonia, "Combined influence of the reynolds number and localised wall suction on a turbulent boundary layer," *Experiments in Fluids*, vol. 35, pp. 199–206, July 2003.

[58] O. M. Oyewola, "LDV measurements in a pertubed turbulent boundary layer," *Journal of Applied Science*, vol. 6, no. 14, pp. 2952–2955, 2006.

[59] R. Mukund, P. R. Viswanath, R. Narasimha, A. Prabhu, and J. D. Crouch, "Relaminarization in highly favourable pressure gradients on a convex surface," *Journal of Fluid Mechanics*, vol. 566, pp. 97–115, 2006.

[60] S. Shahinfar and J. H. M. Fransson, "Effects of free-stream turbulence characteristics on boundary layer transition," *Journal of Physics: Conference Series*, vol. 318, 2011. 13$^{\text{th}}$ European Turbulence Conference.

[61] R. Mukund, R. Narasimha, P. R. Viswanath, and J. D. Crouch, "Multiple laminar-turbulent transition cycles around a swept leading edge," *Experiments in Fluids*, vol. 53, pp. 1915–1927, 2012.

[62] A. Widmann, A. Duchmann, A. Kurz, S. Grundmann, and C. Tropea, "Measuring tollmien-schlichting waves using phase-averaged particle image velocimetry," *Experiments in Fluids*, vol. 53, pp. 707–715, 2012.

[63] J. Kim, P. Moin, and R. Moser, "Turbulence statistics in fully developed channel flow at low reynolds number," *Journal of Fluid Mechanics*, vol. 177, pp. 133–166, 1987.

[64] L. Brandt and D. S. Henningson, "Transition of streamwise streaks in zero-pressure-gradient boundary layers," *Journal of Fluid Mechanics*, vol. 472, pp. 229–261, 2002.

[65] L. Brandt, P. Schlatter, and D. S. Henningson, "Transition in boundary layers subject to free-stream turbulence," *Journal of Fluid Mechanics*, vol. 517, pp. 167–198, 2004.

[66] J. Hœpfner, L. Brandt, and D. S. Henningson, "Transient growth on boundary layer streaks," *Journal of Fluid Mechanics*, vol. 537, pp. 91–100, 2005.

[67] R. B. Langtry, *A correlation-based transition model using local variables for unstructured parallelized CFD codes*. Phd thesis, University of Stuttgart, 2006.

[68] F. R. Menter, R. B. Langtry, S. R. Likki, Y. B. Suzen, P. G. Huang, and S. S. Völker, "A correlation-based transition model using local variables – Part I: Model formulation," *ASME Journal of Turbomachinery*, vol. 128, no. 3, 2006.

[69] R. B. Langtry and F. R. Menter, "Correlation-based transition modeling for unstructured parallelized computational fluid dynamics codes," *AIAA Journal*, vol. 47, no. 12, pp. 2894–2906, 2009.

[70] D. K. Walters and D. Cokljat, "A three-equation eddy-viscosity model for reynolds-averaged navier-stokes ssimulation of transitional flow," *Journal of Fluids Engineering*, vol. 130, no. 12, pp. 1–14, 2009.

[71] L. Brandt and H. C. de Lange, "Streak interactions and breakdown in boundary layer flows," *Physics of Fluids*, vol. 20, no. 024107, pp. 1–16, 2008.

[72] F. R. Menter, P. E. Smirnov, T. Liu, and R. Avancha, "A one-equation correlation-based transition model," *Flow Turbulence Combust*, vol. 95, pp. 583–619, 2015.

[73] M. Lopez and D. K. Walters, "Prediction of transitional and fully turbulent flow using an alternative to the laminar kinetic energy approach," *Journal of Turbulence*, vol. 17, no. 3, pp. 253–273, 2016.

[74] H. Blasius, "Grenzschichten in Flüssigkeiten mit kleiner Reibung," *Zeitschrift fÃ¼r angewandte Mathematik und Physik*, vol. 56, pp. 1–37, 1908.

[75] W. Meile, "Aerodynamik," lecture notes, 3 ed, Graz University of Technology, Institut for fluid mechanics and heat transfer, 2014/15.

[76] D. Thévenin, "Strömungsmechanik I / Strömungsdynamik I," arbeitsheft, part VII, University Magdeburg, Lehrstuhl Strömungsmechanik und Strömungstechnik, 2015/16.

[77] W. Polifke and J. Kopitz, *Wärmeübertragung (Heat transfer).* Pearson Studium, München, Germany, 2009.

[78] G. Brenn and W. Meile, "Stömungslehre und Wärmeübertragung I," Lecture notes, corrected edition 2010, Graz University of Technology, Institut for fluid mechanics and heat transfer, 2010.

[79] L. Prandtl, K. Oswatitsch, and K. Wieghardt, *Führer durch die Strömungslehre.* Vieweg Verlag, Berteksmann international, 9 ed., 1990.

[80] D. Coles, "The law of the wake in the turbulent boundary layer," *Journal of Fluid Mechanics*, vol. 1, no. 2, pp. 191–226, 1956.

[81] F. M. White, *Viscous Fluid Flow.* McGraw-Hill, 2 ed., 1991.

[82] H. Schlichting, *Boundary-Layer Theory.* Verlag G.Braun, Karlsruhe, Germany, 1965.

[83] W. M. F. Orr, "The stability or instability of the steady motions of a perfect liquid and of a viscous liquid. Part I: A perfect liquid," *Proceedings of Royal Irish Academy*, vol. 27, pp. 9–68, 1907.

[84] W. M. F. Orr, "The stability or instability of the steady motions of a perfect liquid and of a viscous liquid. Part II: A viscous liquid," *Proceedings of Royal Irish Academy*, vol. 27, pp. 69–138, 1907.

[85] A. Sommerfeld, "Ein Beitrag zur hydrodynamischen Erklärung der turbulenten Flüssigkeitsbewegung," *Atti del 4. Congresso Internazionale dei Matematici*, vol. III, pp. 116–124, 1908.

[86] G. B. Schubauer, *Grenzschichtforschung Symposium Freiburg im Brieslau (ed. Görtler, H.)*, ch. Mechanism of Transition at Subsonic Speeds, pp. 85–109. Springer Verlag, Berlin, 1957.

[87] P. S. Klebanoff and K. D. Tidstrom, "Evolution of amplified waves leading to transition in a boundary layer with zero pressure gradient," *NASA TN D-*, vol. 195, 1959.

[88] L. S. G. Kovasznay, H. Komoda, and B. R. Vasudeva, "Detailed flow field in transition," *Proceedings of the Heat Transfer and Fluid Mechanics Institute*, pp. 1–26, 1962. Stanford University Press, Stanford.

[89] J. W. S. Lord Rayleigh, "On the stability, or instability, of certain fluid motion," *Scientific Papers*, vol. I, pp. 474–487, 1880. Cambridge University Press.

[90] J. W. S. Lord Rayleigh, "On the stability, or instability, of certain fluid motion," *Scientific Papers*, vol. II, pp. 2–23, 1887. Cambridge University Press.

[91] J. W. S. Lord Rayleigh, "On the question of the stability of the flow of fluids," *Scientific Papers*, vol. III, pp. 575–584, 1892. Cambridge University Press.

[92] E. Dyban, E. Epik, and T. T. Suprun, "Characteristics of laminar boundary layer in the presence of elevated free-stream turbulence," *Fluid Mechanics – Soviet Research*, vol. 5, pp. 30–36, 1976.

[93] M. V. Morkovin, "Recent insights into instability and transition to turbulence in open-flow systems," *Final Report. NASA-CR-*, vol. 181693, 1988.

[94] K. P. Nolan, E. J. Walsh, and D. M. McEligot, "Quadrant analysis of a transitional boundary layer subject to free-stream turbulence," *Journal of Fluid Mechanics*, vol. 658, pp. 310–335, 2010.

[95] J. Jeong and F. Hussain, "On the identification of a vortex," *Journal of Fluid Mechanics*, vol. 285, pp. 69–94, 1995.

[96] J. Zhou, R. J. Adrian, S. Balachandar, and T. M. Kendall, "Mechanisms for gernerating coherent packets of hairpin vortices in channel flows," *Journal of Fluid Mechanics*, vol. 387, pp. 353–396, 1999.

[97] G. I. Taylor, "The criterion for turbulence in curved pipes," *Proceedings of the Royal Society*, vol. A124, pp. 243–249, 1929.

[98] G. B. Schubauer and H. K. Skramstad, "Laminar boundary layer oscillations and stability of laminar flow," *Journal of Aeronautical Science*, vol. 14, no. 69, 1947.

[99] H. W. Liepmann, "Investigations on laminar boundary layer stability and transition on curved boundaries," *National Advisory Committee for Aeronautics, Wartime report*, vol. W107, no. ACR 3H 30, 1943.

[100] H. W. Liepmann, "Investigations of boundary layer transition on concave walls," *National Advisory Committee for Aeronautics, Wartime report*, vol. W87, no. ACR 4J 28, 1945.

[101] J. Sternberg, "The transition from a turbulent to a laminar boundary layer," *Report No.*, vol. 906, 1954. Ballistic Research Laboratory, Aberdeen.

[102] A. A. Sergienko and K. V. Gretsov, "Transition from turbulent to laminar boundary layer," *Doklady Akademii Nauk SSSR*, vol. 125, 1959. RAE Translation No. 827.

[103] V. Ramjee, *Reverse transition in a two-dimensional boundary layer flow.* Phd thesis, Department of Aerospace Engineering, Indian Institute of Science, Bangalore, 1968.

[104] A. Savill, *In: Closure Strategies for Turbulent and Transitional Flow*, ch. New strategies in modelling Bypass transition, pp. 493–521. Launder, B. E. and Sandham, N. D. (eds.). Cambridge University Press, 2002.

[105] M. A. Badri Narayanan, S. Rajagopalan, and R. Narasimha, "Some experimental investigation on the fine structure of turbulence," *Report No.*, vol. 74, no. FM 15, 1974. Department of Aerospace Engineering, Indian Institute of Science, Bangalore.

[106] F. A. Schraub and K. S. J, "A study of the structures of the turbulent boundary layer with and without longitudinal pressure gradients," *Report No.*, vol. MD–12, 1965. Thermoscience Division, Stanford University, Stanford, California.

[107] A. Cinciripini, *An Investigation of Innovative Experimental and Numerical Techniques to Detect the Boundary Layer Transition.* Master thesis, Politecnico di Milano, 2016.

[108] P. K. Srinivasan, *Numerical study of Laminarization and Relaminarization of flows.* Master thesis, Aristotle University of Thessaloniki, 2017.

[109] J. Coupland, "Flat plate transitional boundary layers." http://cfd.mace.manchester.ac.uk/cgi-bin/cfddb/prpage.cgi?20&EXP&database/cases/case20/Case_data&database/cases/case20&cas20_head.html&cas20_desc.html&cas20_meth.html&cas20_data.html&cas20_refs.html&cas20_rsol.html&1&0&0&0&0, 1990. visited: nov/2016.

[110] J. Krasa, *Konstruktion und Bau eines Windkanals zur Messung der Grenzschicht einer ebenen Platte.* Bachelor thesis, Institut for Thermal Turbomaschinery and Machine Dynamics, Technische Universität Graz, 2016.

[111] P. R. Roach, "The generation of nearly isotropic turbulence by means of grids," *International Journal of Heat and Fluid Flow*, vol. 8, pp. 82–92, 1987.

[112] M. Pschernig, *Messaufbau und –durchführung der Transition und Relaminarisierung entlang einer ebenen Platte.* Master thesis, Institut for Thermal Turbomaschinery and Machine Dynamics, Technische Universität Graz, 2017.

[113] D. Händel, U. Rockstroh, and R. Niehuis, "Experimental investigation of transition and separation phenomena on an inlet guide vane with symmetric profile at different stagger angles and reynolds numbers," *15^{th} International Symposium on Transport Phenomena and Dynamics of Rotating Machinery, Honolulu, USA*, 2014. ISROMAC-15.

[114] G. Persico, P. Gaetani, and A. Guardone, "Design and analysis of new concept fast-response pressure probes," *Measurement Science and Technology*, vol. 16, pp. 1741–1750, 2005.

[115] J. D. Wallace and M. R. D. Davis, "Turbulence measurements with a calibrated pitot mounted pressure transducer," *$13^{t}h$ Symposium on Measuring Techniques in Turbomachinery, Zürich*, 1996.

[116] L.-U. Axelsson and W. George, "Spectral analysis of the flow in an intermediate turbine duct," *ASME Turbo EXPO 2008, Berlin, Germany*, 2008. GT2008-51340.

[117] T. R. Camp and H. W. Shin, "Turbulence intensity and length scale measurements in multistage compressors," *Journal of Turbomachinery*, vol. 117, pp. 38–46, January 1995.

[118] A. N. Kolmogorov, "The local structure of turbulence in incompressible viscous fluid for very large Reynolds numbers," *Proceedings: Mathematical and Physical Sciences*, vol. 434, pp. 9–13, 1991.

[119] A. N. Kolmogorov, "Dissipation of energy in a locally isotropic turbulence," *Doklady Akademii Nauk SSSR*, vol. 32, 1941.

[120] A. M. Obukhov, "On the distribution of energy in the spectrum of turbulent flow," *Doklady Akademii Nauk SSSR*, vol. 32, pp. 22–24, 1941.

[121] R. Giepmann, F. Schrijer, and B. van Oudheusden, "Tracking a moving boundary layer transition front in a supersonic flow using infrared themography," *Conference on Quantitative InfraRed Thermography, At Bordeaux, France*, 2014.

[122] L. A. Joseph, A. Borgoltz, and W. Devenport, "Infrared themography for detection of laminar-turbulent transition in low-speed wind tunnel testing," *Experiments in Fluids*, vol. 57, no. 77, 2016.

[123] B. Simon, A. Filius, C. Tropea, and S. Grundmann, "IR themography for dynamic detection of laminar-turbulent transition," *Experiments in Fluids*, vol. 57, no. 93, 2016.

[124] G. B. Schubauer and H. K. Skramstad, "Laminar boundary layer oscillations and transition on a flat plate," *NACA Report*, vol. 909, 1948.

[125] T. M. Farabee, "An experimental investigation of wall pressure fluctuations beneath non-equilibrium turbulent flows," *The Journal of the Acoustical Society of America*, vol. 83, no. 4, 1986.

[126] R. V. Barrett, "Transition detection for laminar flow aircraft using microphones beneath the surface of laser drilled suction panels," *Proceedings of the Institution of Mechanical Engineers*, vol. 214 Department of Aerospace Engineering, no. Part G, pp. 143–155, 2000.

[127] Dantec Dynamics A/S, "Measurement principles of CTA." http://www.dantecdynamics.com/measurement-principles-of-cta. visited dec/2016.

[128] L. Cattafesta, C. J. Bahr, and J. Mathew, *Encyclopedia of Aerospace Engineering*, vol. 1, ch. 60: Fundamentals of Wind-Tunnel Design, pp. 691–700. John Wiley & Sons, Ltd., 2010.

[129] L. Mach, "Über einen Interferenzrefraktor," *Zeitschrift für Instrumentenkunde*, vol. 12, pp. 89–93, 1892.

[130] L. Zehnder, "Ein neuer Interferenzrefraktor," *Zeitschrift für Instrumentenkunde*, vol. 11, pp. 275–285, 1891.

[131] L. Zipser, S. Lindner, and R. Behrendt, "Interferometrische Messung und Visualisierung von Schallwellen und Turbulenzen (Interferometric measurement and visualisation of acoustic waves and vortexes)," *Technisches Messen*, vol. 69, pp. 275–281, 2002.

[132] M. Lenz. https://commons.wikimedia.org/w/index.php?curid=7680121. visited dec/2016.

[133] J. Woisetschläger, *Lecture notes: Laser in der Schwingungs– und Strömungsmesstechnik*. Institute for Thermal Turbomaschinery and Machine Dynamics, Graz University of Technology, 2015.

[134] H. E. Albrecht, M. Borys, N. Damaschke, and C. Tropea, *Laser Doppler and Phase Doppler Measurement Techniques*. Springer-Verlag, Berlin-Heidelberg, 2003.

[135] H. Steiner, *Lecture notes: Höhere Strömungslehre und Wärmeübertragung*. Institute of Fluid Mechanics and Heat Transfer, Graz University of Technology, 2012.

[136] J. Boree, L. Ben, and R. Bazile, "Optical methods for the measurement of constant and variable density flows," *International Summerschool on variable density turbulent flows, Barcelona, Spain*, 2003.

[137] G. Eggenspieler, "Turbulence modeling." ANSYS Inc., 2012.

[138] ANSYS, Inc. Canonsburg, "ANSYS CFX-solver modeling guide," 2010.

[139] R. Pecnik, P. Pieringer, and W. Sanz, "Numerical investigation of the secondary flow of a transonic turbine stage using various turbulence closures," *In Proceedings of ASME Turbo Expo 2005, Reno-Tahoe, Nevada, USA*, 2005. GT2005-68754.

[140] P. L. Roe, "Approximate riemann solver, parameter vectors and differencing scheme," *Journal of Computational Physics*, vol. 43, pp. 357–372, 1981.

[141] F. R. Menter, "Two-equation eddy-viscosity turbulence models for engineering applications," *AIAA Journal*, vol. 32, pp. 1598–1605, August 1994. doi: 10.2514/3.12149.

[142] W. Elsner, W. Piotrowski, and S. Drobniak, "Transition prediction on turbine blade profile with intermittency transport equations," *ASME Turbo Expo 2008, Berlin, Germany*, 2008. GT2008–50796.

[143] N. N. Sorensen, "CFD modeling of laminar-turbulent transition for airfoil and rotors using the $\gamma - \tilde{Re}_\theta$ model," *Wind Energy*, vol. 12, no. 8, pp. 715–733, 2009.

[144] P. Malan, K. Suluksna, and E. Juntasaro, "Calibrating the γ-Re_θ transition model for commercial CFD," *47^{th} AIAA Aerospace Sciences Meeting*, 2009. 2009–1142.

[145] M. Kelterer, R. Pecnik, and W. Sanz, "Computation of laminar-turbulent transition in turbomachinery using the correlation based γ-Re_θ transition model," *ASME Turbo Expo 2010, Glasgow, Scotland*, 2010. GT2010-22207.

[146] D. Di Pasquale, A. Rona, and S. J. Garrett, "A selective review of CFD transition models," *39^{th} AIAA Fluid Dynamics Conference, San Antonio, Texas*, 2009. 2009–3812.

[147] D. K. Walters and J. H. Leylek, "New model for boundary layer transition using a single-point RANS approach," *Journal of Turbomachinery*, vol. 126, pp. 193–202, 2004.

[148] ANSYS, Inc. Canonsburg, "ANSYS fluent theory guide," 2013.

[149] J. Fürst and J. Příhoda, "On a modification of the three-equation k-k_l-ω model for natural transition in adverse pressure gradient flows," *11^{th} International ERCOFTAC Symposium on Engineering Turbulence Modelling and Measurements*, 2016. ETMM11–094.

[150] F. R. Menter, "Best practice: Scale-resolving simulations in ANSYS CFD." ANSYS Germany GmbH, 2012. Version 1.0.

[151] P. Bader and W. Sanz, "On the setup of a test bench for predicting laminar-to-turbulent transition on a flat plate," *Journal of Energy and Power Engineering*, vol. 10, pp. 411–424, 2016.

[152] A. Cinciripini, P. Bader, G. Persico, and W. Sanz, "Innovative acoustic measurement technique for boundary layer transition detection," *submitted to Journal of Mechanics Engineering and Automation*, 2017.

[153] P. Bader, W. Sanz, J. Peterleithner, W. Woisetschläger, F. Heitmeir, W. Meile, and G. Brenn, "Detecting transition in flat plate flow with laser interferometric vibrometry (LIV)," *Proceedings of ASME Turbo Expo 2016: Turbine Technical Conference and Exposition, June 13-17, 2016, Seoul, South Korea*, 2016. GT2016-56043.

[154] P. Bader, W. Sanz, C. Steinmayr, and P. Leitl, "Comparison of RANS and embedded LES calculations with measurements of transitional flow along a flat plate," *ERCOFTAC Bulletin*, vol. 106, pp. 84–93, 2016.

[155] P. Bader, M. Pschernig, W. Sanz, J. Woisetschläger, F. Heitmeir, W. Meile, and G. Brenn, "Flat-plate boundary layers in accelerated flow," *Proceedings of ASME Turbo Expo 2016: Turbine Technical Conference and Exposition, June 13-17, 2016, Seoul, South Korea*, 2016. GT2016-56044.

[156] P. Bader, W. Sanz, C. Steinmayr, and P. Leitl, "The capability of large eddy simulation to predict relaminarization," *11^{th} International ERCOFTAC Symposium on Engineering Turbulence Modelling and Measurements*, 2016. SID-086.

[157] P. Bader, P. Pieringer, and W. Sanz, "On the capability of the γ-Re_θ transition model to predict relaminarization," *Proceedings of 12^{th} European Conference on Turbomachinery Fluid dynamics & Thermodynamics, April 3-7, 2017, Stockholm, Sweden*, 2017. ETC2017-328.

[158] P. Bader and W. Sanz, "Measurement and simulation of a turbulent boundary layer exposed to acceleration along a flat plate," *Proceedings of 12^{th} European Conference on Turbomachinery Fluid dynamics & Thermodynamics, April 3-7, 2017, Stockholm, Sweden*, 2017. ETC2017-092.

[159] D. J. C. Dennis, "Coherent structures in wall-bounded turbulence," *Anais da Academia Brasileira de Ciencias*, vol. 87, no. 2, pp. 1161–1193, 2015.

[160] D. Lengani, C. Santner, R. Spataro, B. Paradiso, and E. Göttlich, "Experimental investigation of the unsteady flow field downstream of a counter-rotating two-spool turbine rig," *Proceedings of ASME 2012 Turbo EXPO, June 11-15 2012, Copenhagen, Denmark*, 2012. GT2012-68583.

[161] R. Spataro, C. Santner, D. Lengani, and E. Göttlich, "On the flow evolution through a lp turbine with wide-chord vanes in an s-shaped channel," *Proceedings of ASME 2012 Turbo EXPO, June 11-15 2012, Copenhagen, Denmark*, 2012. GT2012-68178.

[162] R. Spataro, E. Göttlich, D. Lengani, C. Faustmann, and F. Heitmeir, "Developement of a turning mid turbine frame with embedded design - part I: Design and steady measurements," *Journal of Turbomachinery*, vol. 136, no. 7, pp. 1–9, 2014.

[163] R. Spataro, E. Gï¿½öttlich, D. Lengani, C. Faustmann, and F. Heitmeir, "Developement of a turning mid turbine frame with embedded design - part ii: Unsteady measurements," *Journal of Turbomachinery*, vol. 136, no. 7, pp. 1–8, 2014.

[164] P. Bader, W. Sanz, R. Spataro, and E. Göttlich, "Flow evolution through a turning mid turbine frame with embedded design," *Proceedings of ASME 2014 Turbo EXPO, June16-20, Düsseldorf, Germany*, 2014. GT2014-25009.

[165] P. Bader, W. Sanz, and R. Spataro, "Unsteady CFDsimulation of a turning mid turbine frame with embedded design," *Proceedings of 11th European Conference on Turbomachinery Fluid dynamics & Thermodynamics, March 23-27, 2015, Madrid, Spain*, 2015. ETC2015-007.

[166] P. Bader and W. Sanz, "On boundary layer relaminarization in an highly accelerated high pressure turbine stator flow," *Proceedings of ASME Turbo Expo 2017: Turbine Technical Conference and Exposition, June 26-30, 2017, Charlotte, North Carolina, USA*, 2017. GT2017-63296.

[167] P. Bader and W. Sanz, "Steady and unsteady CFD calculations of the laminar-to-turbulent transition in a turning mid turbine frame with embedded design," *Proceedings of ASME Turbo Expo 2017: Turbine Technical Conference and Exposition, June 15-19, 2015, Palais des Congres, Montreal, Canada*, 2015. GT2015-42617.

[168] D. Baumgartner, *LDA–Messungen von Strömungsgeschwindigkeiten in Grenzschichtbereich von Riblets*. Bachelor thesis, Institut for Thermal Turbomaschinery and Machine Dynamics, Technische Universität Graz, 2016.

[169] W. Österreicher, *Messung des laminar/turbulent-Übergangs an Turbinenschaufeln mittels Heißfilmanemometrie*. Diploma thesis, Institute for Energy Systems and Thermodynamics, Technische Universität Wien, 2004.

[170] M. Nichtawitz, *Messung der Relaminarisierung der druckseitigen Grenzschicht einer Turbinenschaufel mittels Heißfilmanemometrie*. Diploma thesis, Institute for Energy Systems and Thermodynamics, Technische Universität Wien, 2009.

[171] G. E. Gadd, "A note on the theory of the stanton tube," *Aeronautical Research Council, Reports and Memoranda*, vol. 3147, 1960. A.R.C. Technical Report.

[172] D. C. Reda and M. C. Wilder, "Visualization of continuous surface shear stress vector distributions," *NASA - Ames Research Center Moffett Field, CA*, 2013. Lecture One.

[173] H. Chelner, R. A. Mueller, and R. J. Meritt, "Semiconductor strain gage applications to skin friction sensors for high-speed aerospace testing," *Piezo-Metrics, Inc.*, 2017.

[174] H. H. Fernholz, G. Janke, M. Schober, P. M. Wagner, and D. Warnack, "New developments and applications of skin-friction measuring techniques," *Measurement Science and Technology*, vol. 7, pp. 1396–1409, 1996.

[175] N. I. Konstantinov and G. L. Dragnysh, "The measurement of friction stress on a surface," *DSIR RTS 1499*, 1960.

[176] M. R. Head and I. Rechenberg, "The preston tube as a means of measuring skin friction," *Journal of Fluid Mechanics*, vol. 14, pp. 1–17, 1962.

[177] J. D. Vagt and H. H. Fernholz, "Use of surface fences to measure wall shear stress in three-dimensional boundary layers," *Aeronautical Quarterly*, vol. XXIV, pp. 87–91, 1973.

[178] R. L. Simpson and D. B. Wallace, "Laminarescent turbulent boundary layers: Exoeriments on sink flows," *Proj. SQUID Technical Report*, no. SMU-1-PU, 1975.

Sources of pictures used for the chapter headings and their caption

[Chapter 1] AVIONALE, "Airbus A320NEO Original Livery Aircraft Wallpaper 3849," *Aviation Ethusiasts*, `http://www.avionale.com/2014/10/airbus-a320neo\-original\-livery-aircraft-wallpaper-3849.html`, visited: 07.09.2016.

Chapter-Figure 1: Photograph of the Airbus A320neo

[Chapter 2] B. Cahalan, "Kàrmàn vortex street caused by wind flowing around the Juan Fernández Islands off the Chilean coast," *Wikimedia Commons*, `https://commons.wikimedia.org/wiki/File:Vortex-street-1.jpg`, visited: 01.09.2016.

Chapter-Figure 2: The photograph has been taken by the Landsat 7 satellite showing the clouds off the Chilean coast near the Juan Fernandez islands (also known as Robinson Crusoe islands)

[Chapter 3] J. Sillero, "Turbulent Boundary Layer visualization," *Blog-Post, posted on September 2, 2012*, `http://torroja.dmt.upm.es/jsillero/?p=31`, visited: 31.08.2016.

Chapter-Figure 3: Visualization of Enstrophy normalized with spanwise vorticity showing a lateral/spanwise (y/z) section at $Re_\theta = 6665$

[Chapter 4] Chapter-Figure 4: Light sheet visualization of vortices using a 1 W laser inside wind tunnel B

[Chapter 5] S. Y. Jung and T. A. Zaki, "The effect of a low-viscosity near-wall film on bypass transition in boundary layers," *Journal of Fluid Mechanics*, vol. 772, pp. 330–360, 2015.

Chapter-Figure 5: Contour plot of the instantaneous streamwise velocity fluctuation u' in the (x,z)-plane

[Chapter 6] Chapter-Figure 6: Photograph of the two-component LDA beams used for the measurements in wind tunnel B

[Chapter 7] Pinterest. "Rolls Royce Trent," `https://ru.pinterest.com/explore/rolls-royce-trent/`, visited: 02.11.2016.

Chapter-Figure 7: Composit fan blades of a future Rolls Royce *UltraFan* Trent engine

[Chapter 8] Amazing Photos, Designs, Quotes - ElsOar. "Idea concept with row of light bulbs and glowing bulb," *Best ideas – An Overview Supported by The Pictures*, `http://photo.elsoar.com/best-ideas-designs-images.html`, visited: 11.03.2017.

Chapter-Figure 8: Idea concept with row of light bulbs and glowing bulb